Design, Synthesis, and Fabrication of Soft Materials, Surfaces, and Interfaces

by

Matthew C. D. Carter

A dissertation submitted in partial fulfillment of

the requirements for the degree of

Doctor of Philosophy

(Chemistry)

at the

UNIVERSITY OF WISCONSIN-MADISON

2016

Date of final oral examination: 08/25/16

The dissertation is approved by the following members of the Final Oral Committee
David M. Lynn, Professor, Chemical and Biological Engineering
Padma Gopalan, Professor, Materials Science and Engineering
Nicholas L. Abbott Professor, Chemical and Biological Engineering
Lloyd M. Smith, Professor, Chemistry
Robert J. McMahon, Professor, Chemistry

Design, Synthesis, and Fabrication of Soft Materials, Surfaces, and Interfaces

Under the Supervision of Professor David M. Lynn

at the University of Wisconsin – Madison

The work presented in this thesis focuses on (i) the design and fabrication of azlactone-functionalized reactive polymers, surfaces, and interfaces, and (ii) the physicochemical characterization and self-assembly of a class of six-tailed synthetic amphiphiles. The first section describes the broad utility and versatile reactivity of polymers synthesized from vinyl azlactone monomers. Early chapters center around the assembly and post-fabrication functionalization of multilayer films fabricated by the reactive layer-by-layer assembly of poly(2-vinyl-4,4-dimethylazlactone) and branched poly(ethylenimine). The azlactone groups in these coatings can be modified with amine-, alcohol- and thiol-containing nucleophiles to impart new and useful surface properties. These materials were used to design interfaces that present dynamic and responsive surface features, as platforms for the top-down and bottom-up synthesis of biomolecule arrays, and to enable the design of superhydrophobic coatings amenable to surface patterning. These results highlight the broad utility of this reactive multilayer approach and open the door to a range of future applications where precise control over physicochemical surface properties is useful.

Subsequent chapters describe the self-assembly behavior of poly(styrene-*block*-2-vinyl-4,4-dimethylazlactone) (PS-*b*-PVDMA) reactive block copolymers (BCPs). Microphase

separated thin films of lamellae- and cylinder-forming BCPs yielded nanometer-scale reactive ‘lines’ or ‘dots’ of azlactone functionality onto which amine-containing compounds could be immobilized, enabling new approaches to nanometer-scale surface patterning. Low molecular weight PS-*b*-PVDMA BCPs were also used to identify new high-*X* materials, with high block-block chemical incompatibility. These results provide new approaches for advanced lithography and nanoscale patterning applications. Advances in azlactone-based materials design, including the development of electrospun nanofibers, degradable and reactive polymers, and new cationic polymers for gene delivery are also described.

The second section describes the synthesis and self-assembly behavior of a series of homologous six-tailed synthetic amphiphiles. These amphiphiles mimic key properties of bacterial Lipid A, including the ability to trigger optical transitions in liquid crystal droplets at exceedingly low picogram-per-milliliter concentrations. Investigations into the self-assembly behavior of this series of amphiphiles revealed several new lyotropic liquid crystalline phases with remarkably small domain sizes. These results represent important advances in the field of lipid self-assembly, and provide new insights into the morphological behavior of multi-tailed amphiphiles.

Acknowledgments

The work in this thesis represents the collective knowledge gained by many people over the last five years. My own successes as a scientist have been supported and encouraged by numerous mentors, colleagues, and collaborators. My advisor Prof. David Lynn has been an inexhaustible source of information and advice over the past five years. Dave supported my growth by suggesting ideas, experiments, and interpretations of my results, but he also left me free to choose my own path and to pursue my own ideas. I am proud that large portions of this thesis and many published papers represent the final product of my own ideas, and that I have taken the Lynn group in new research directions. Dave was willing to learn new things with me, and he was not hesitant to work in new areas where we did not yet have expertise. This willingness to learn and to experiment always made me feel like a new and exciting discovery was within reach.

Dave taught me to carefully consider hypotheses and results before moving forward, and he buoyed my spirits when things seemed to be 'going wrong'. Dave's reminder that well-thought out experiments, a solid understanding of past results, and a comprehensive literature search are often enough to break any problem is now a part of my own experimental design. I feel like I have learned Dave's holistic approach to data interpretation, looking at problems and solutions together from new angles, distilling complicated results into tangible insights, and reflecting on what the data is telling you while planning a next step. Dave's insistence on recognizing the fine details in both experimental results and critical thinking have led to many of the insights and discoveries reported in this thesis, and Dave's scientific touch will be readily recognized by the reader.

I am also indebted to many other professors who interacted, collaborated, and created the work described here with me. Prof. Mahesh Mahanthappa was, in many ways, a secondary advisor to me. During my time here, Mahesh welcomed me into his group where I was exposed to synthetic methodology, polymer physics, and new ways of thinking about materials science. Prof. Padma Gopalan supported my professional development on many projects through the UW NSEC, and Prof. Nicholas Abbott provided many helpful discussions through the MRSEC. Prof. Lloyd Smith and Prof. Michael Sussman were two other generous collaborators, letting my coworkers and me try many new experiments at times when positive results were rare. I wish to thank all of those people mentioned above as well as Prof. Robert McMahon, who introduced me to a wide range of materials chemistry and sparked much of my early interest in materials science.

I also wish to acknowledge Prof. Michael Serpe at the University of Alberta who saw promise in me and gave me his unwavering confidence when I was an undergrad in his lab. Mike's hands-on mentoring, patience, and excitement for research made me feel like anything and everything were possible in the lab; as long as you wanted to, you could always make something interesting happen in Mike's lab. Dr. Courtney Richman (née Sorrell) and Mike trained me on many of the instrumental techniques that I used extensively during my time here at UW, and the papers that we worked on together helped me develop my scientific writing style early. All of this prior knowledge helped me enjoy early successes at UW, and the experience I had in Mike's group, and with Mike himself, pushed me to pursue a Ph.D.

I have collaborated here with many people, both in the Lynn group and across campus, over the last five years. I want to acknowledge specifically the work of Adam Broderick (who helped me get started in the group), Frank Speetjens and Jon Choi, (block copolymer synthesis

and self-assembly), Matt Holden and Eric Codner (maskless array synthesis), Dan Miller and William Wang (LC droplets), and Dr. James Jennings (degradable and reactive polymers, and amphiphile self-assembly). Many former and current group members shaped my time here and I am grateful for the formal and informal interactions we have shared along the way. Shane Bechler, Selin Aytar, and John Muller were all helpful in the lab when I joined the group, while the majority of my time here was shared with Mike Kratochvil, Namrata Raman, Yan Yu, Yashira Zayas-Gonzalez, Dr. Uttam Manna, Gavin Guo, Visham Appadoo, and Benjamin Ortiz. Mike and Namrata deserve special recognition for their commitment to keeping the lab running smoothly, for their friendship, and for their shared humorous interpretations of grad school when they were needed most. Finally, I want to acknowledge here Maren Buck who worked on azlactone chemistry in the Lynn group before me. Maren kept meticulous notebooks and shared with me her knowledge and prior experiences with azlactone chemistry. Many of the insights and discoveries that I made as a graduate student were a direct result of the foundations Maren established.

There are many often unrecognized members of the campus community who truly made all of this work possible: Anna Kiyanova and Mike Efremov (Soft Materials Lab), Don Savage (SAXS), Rick Noll (SEM), Martha Vestling (MS), Charlie Fry (NMR), Rob McClain (chemistry instrument center) and the many other researchers and technicians who oversee and maintain the instruments that I used on a daily basis deserve my gratitude. In addition, the numerous people who work ‘behind the scenes’ in departmental offices, the mailroom, the stockroom, and the tradespeople who repair our facilities are all indispensable components of the research community; none of my work would have been possible without this system in place.

Finally, I would like to thank my family and my partner Keely. Keely made graduate school smoother and more enjoyable, and she has given it much more meaning. We have shared many happy times together in Madison and at UW, and the future holds a lot more. My parents passed on their gift and love of learning to me, and they have remained supportive and positive throughout this entire process. I also credit my sisters and my brothers-in-law, who have come to visit me, and always make me feel at home when I visit them. My family believes that nothing is too difficult with preparation, patience, and determination, and the completion of this thesis represents all three.

Table of Contents

Abstract i

Acknowledgments iii

List of Figures, Schemes, and Tables vii

Chapter 1: Introduction and Overview 1
Background – Part I 2
Background – Part II 9
Scope and Organization 11
References 21

Chapter 2: Covalently Crosslinked and Physically Stable Polymer Coatings 32
with Chemically Labile and Dynamic Surface Features Fabricated
by Treatment of Azlactone-Containing Multilayers with Alcohol-,
Thiol-, and Hydrazine-Based Nucleophiles

Abstract 33
Introduction 34
Materials and Methods 37
Results and Discussion 43
Summary and Conclusions 56
References 57
Supporting Information 63

Chapter 3: Fabrication of Oligonucleotide and Protein Arrays on Surfaces 68
Coated with Ultrathin Reactive Polymer Multilayers

Abstract 69
Introduction 70
Materials and Methods 74
Results and Discussion 79
Summary and Conclusions 93
References 94
Supporting Information 100

Chapter 4: Photolithographic Synthesis of High-Density DNA and RNA 102
Arrays on Flexible, Transparent, and Easily Sub-Divided Plastic
Substrates

Abstract 103
Introduction 104
Materials and Methods 105

Results and Discussion 112
Summary and Conclusions 123
References 124
Supporting Information 127

Chapter 5: 'Shrink-to-Fit' Superhydrophobicity: Thermally-Induced Microscale Wrinkling of Thin Hydrophobic Multilayers Fabricated on Shrink-Wrap Substrates 132

Introduction and Results 133
References 144
Supporting Information 146

Chapter 6: Influence of Partial Side Chain Hydrolysis on the Growth and Morphology of Reactive Polymer Multilayers Fabricated Using Poly(2-Vinyl-4,4-Dimethylazlactone) and Poly(ethylenimine) 155

Introduction 156
Materials and Methods 159
Results and Discussion 165
Summary and Conclusions 181
References 183
Supporting Information 188

Chapter 7: Post-Fabrication Placement of Arbitrary Chemical Functionality on Microphase Separated Thin Films of Amine-Reactive Block Copolymer 190

Abstract 191
Introduction and Results 192
References 203
Supporting Information 205

Chapter 8: Self-Assembly and Post-Fabrication Functionalization of Microphase Separated Thin Films of a Reactive Azlactone-Containing Block Copolymer 216

Abstract 217
Introduction 218
Materials and Methods 221
Results and Discussion 227
Summary and Conclusions 238
References 240

Chapter 9: A Reactive Platform Approach for the Rapid Synthesis and Discovery of High χ/Low N Block Polymers 246

Abstract 247
Introduction 248
Materials and Methods 250
Results and Discussion 256
Summary and Conclusions 267
References 269
Supporting Information 274

Chapter 10: Synthesis and Characterization of Backbone Degradable Azlactone-Functionalized Polymers 286

Abstract 287
Introduction 288
Materials and Methods 290
Results and Discussion 302
Summary and Conclusions 319
References 321
Supporting Information 328

Chapter 11: Controlling the Surface-Mediated Release of DNA Using 'Mixed Multilayers' 337

Abstract 338
Introduction 339
Materials and Methods 343
Results 350
Discussion 359
Summary and Conclusions 363
References 365
Supporting Information 370

Chapter 12: Non-Woven and Amine-Reactive Nanofiber Mats Fabricated by the Electrospinning of Azlactone-Functionalized Polymers 374

Abstract 375
Introduction 376
Materials and Methods 380
Results and Discussion 385
Summary and Conclusions 399
References 401
Supporting Information 407

Chapter 13: Synthetic Mimics of Bacterial Lipid A Trigger Optical Transitions in Liquid Crystal Microdroplets at Ultralow Picogram-per-Milliliter Concentrations 412

Abstract 413
Introduction 414
Results and Discussion 415
Summary and Conclusions 424
References 425
Supporting Information 428

Chapter 14: Characterization of Lyotropic Liquid Crystalline Assemblies of Synthetic Six-Tailed Amphiphiles 443

Abstract 444
Introduction 445
Materials and Methods 447
Results and Discussion 452
Summary and Conclusions 464
References 465
Supporting Information 469

Chapter 15: Cubic and Lamellar Lyotropic Liquid Crystals from Synthetic Six-Tailed Amphiphiles 475

Introduction 476
Materials and Methods 477
Results and Discussion 484
Summary and Conclusions 494
References 496
Supporting Information 499

Chapter 16: Summary and Future Work 500

Summary 501

Future Studies: Investigations into the Physicochemical. Parameters that Control Growth and Morphology in PEI/PVDMA Multilayer Films 503

Future Studies: Synthesis, Self-Assembly, and Reactivity in Azlactone-Containing Block Copolymers 504

Future Studies: LLC Particles as Hosts for Molecular Cargo 506

References 509

List of Figures, Schemes, and Tables

Chapter 2: Scheme 1 36
Figure 1 45
Figure 2 48
Figure 3 52
Figure 4 54
Figure S1 63
Figure S2 64
Figure S3 64
Figure S4 65
Figure S5 65
Figure S6 66
Figure S7 66
Figure S8 67

Chapter 3: Equation 1 72
Figure 1 81
Table 1 82
Figure 2 83
Figure 3 86
Figure 4 91
Figure S1 100
Figure S2 101

Chapter 4: Scheme 1 113
Figure 1 114
Figure 2 116
Figure 3 118
Figure 4 120
Figure 5 121
Figure 6 123
Figure S1 127
Figure S2 127
Table S1 128
Table S2 129
Table S3 130
Table S4 131

Chapter 5: Figure 1 136
Figure 2 138
Figure 3 141
Figure 4 143
Figure S1 150
Figure S2 151
Figure S3 152

Figure S4 153
Figure S5 154

Chapter 6: Scheme 1 166
Figure 1 167
Figure 2 169
Table 1 170
Figure 3 171
Figure 4 173
Figure 5 175
Figure 6 176
Figure 7 178
Figure 8 179
Figure S1 188
Figure S2 189
Figure S3 189

Chapter 7: Figure 1 195
Figure 2 197
Figure 3 198
Figure 4 201
Scheme S1 210
Figure S1 211
Figure S2 211
Figure S3 212
Figure S4 212
Figure S5 213
Figure S6 214
Figure S7 214
Figure S8 215
Figure S9 215

Chapter 8: Figure 1 228
Figure 2 230
Figure 3 233
Figure 4 235
Figure 5 237

Chapter 9: Scheme 1 256
Table 1 257
Figure 1 258
Table 2 259
Figure 2 260
Figure 3 262
Figure 4 264
Figure 5 266

Figure S1 274
Figure S2 275
Figure S3 276
Figure S4 277
Figure S5 278
Figure S6 279
Figure S7 280
Figure S8 281
Figure S9 282
Figure S10 283
Figure S11 284
Figure S12 285

Chapter 10: Scheme 1 289
Table 1 302
Figure 1 303
Scheme 2 306
Figure 2 308
Figure 3 310
Figure 4 314
Figure 5 316
Figure 6 318
Figure S1 328
Figure S2 329
Figure S3 329
Figure S4 330
Figure S5 331
Figure S6 332
Figure S7 333
Figure S8 334
Figure S9 335
Figure S10 336

Chapter 11: Figure 1 341
Figure 2 351
Figure 3 353
Figure 4 354
Figure 5 355
Figure 6 358
Figure S1 370
Figure S2 370
Figure S3-A 371
Figure S3-B 372
Figure S3-C 373

Chapter 12: Figure 1 379
Figure 2 386
Table 1 387
Figure 3 389
Table 2 390
Figure 4 392
Figure 5 395
Figure 6 399
Figure S1 407
Figure S2 407
Figure S3 408
Figure S4 409
Figure S5 410
Figure S6 411
Figure S7 411

Chapter 13: Figure 1 418
Figure 2 420
Figure 3 422
Figure 4 423
Figure S1 439
Figure S2 441
Figure S3 442

Chapter 14: Figure 1 453
Figure 2 455
Figure 3 457
Figure 4 460
Table 1 461
Figure 5 464
Figure S1 469
Figure S2 470
Figure S3 471
Figure S4 472
Figure S5 473
Figure S6 474

Chapter 15: Figure 1 486
Figure 2 489
Figure 3 490
Figure 4 493
Figure S1 499
Figure S2 499

Chapter 1

Introduction and Overview

Background – Part I – Design and Fabrication of Soft Materials Using Azlactone-Containing Polymers

Reactive polymers are useful and versatile platforms for the design of functional materials. Past studies have demonstrated that polymers containing a diverse range of chemically reactive functionalities can be used to (i) accelerate the rate at which new polymers can be prepared and screened for useful properties and (ii) design polymers and other macromolecular structures that can be further functionalized, post-fabrication, to tune physicochemical properties or provide access to useful structures that may not be possible using direct routes.[1-9] The work presented in this thesis aims to further develop the broad utility of azlactone-functionalized polymers for the reactive fabrication of new polymers, thin films, and reactive interfaces. In the following sections, we provide background and context on several areas, themes, and concepts relevant to the research described in the chapters that follow.

Reactive Polymers and Azlactone-Functionalized Materials

Polymers containing chemically reactive groups are powerful tools for the design of functional materials and interfaces. Through post-polymerization reactions, these polymers can be tailored to display diverse chemical functionalities and physicochemical properties. Reactive polymers are commonly synthesized directly from monomers that contain a functional group that is tolerant to the polymerization conditions, but that can be used, post-polymerization, to modify the properties of the resulting material.[1-9] This method can be particularly useful for several reasons: (i) the need to synthesize and then polymerize many different monomers with desired functionalities is avoided, (ii) reactive polymers can be used as templates to access a variety of macromolecular structures and (iii) a single reactive polymer can be elaborated into a library of

polymers with a common molecular weight and polydispersity. As a result, reactive polymers can greatly accelerate the rate at which new materials are identified and structure-property relationships can be elucidated.

Polymers functionalized with the azlactone (or oxazolone) functional group are a particularly useful class of reactive polymers. Azlactones are electrophilic cyclic esters that readily undergo ring-opening reactions at the carbonyl group with nucleophilic primary amines under mild conditions, generating stable 'amide/amide'-type linkages. These reactions are fast, do not require a catalyst, and are by-product free.[5,10] Azlactones can also ring-open with other nucleophiles, including alcohols and thiols,[10-12] but these reactions are relatively slow, require a catalyst and are less well understood. While several types of vinyl azlactone monomers have been synthesized and investigated, 2-vinyl-4,4-dimethylazlactone (VDMA) and its polymeric counterpart, PVDMA, is by far the most widely studied. Several recent reports highlight the broad utility of azlactone-functionalized polymers as reactive platforms for the design of new solution-phase functional polymers[13-27] and solid-phase interfaces in many fundamental and applied contexts; we describe specific examples of azlactone-functionalized surfaces and interfaces in more detail below.

Azlactone-Functionalized Polymers for the Design of Surfaces and Interfaces

Owing to the versatile reactivity of the azlactone group, homopolymers and copolymers of VDMA have been used to fabricate, functionalize, and modify the properties of a wide variety of surfaces.[5,10] From a historical perspective, some of the earliest interest in azlactone-functionalized polymers occurred in industry, in part because of the relative ease with which these reactive materials could be processed. An early patent, for example, describes the

incorporation of a small number of azlactone groups into commodity polymers, and the use of these materials as cross-linkable coatings with improved solvent resistance.[28] Rohm and Haas GmbH, Polaroid Corp., and the 3M Corp. have all pursued research in azlactone chemistry, with 3M being arguably the most prolific in the development of azlactone-functionalized materials. An excellent historical review and industrial perspective on this subject was published in 2001.[10]

The chemistry of azlactones at surfaces and interfaces has also been the subject of more recent academic research. Early work from several groups investigated azlactone-functionalized beads and porous monoliths as simple tools to reactively filter and capture amine-containing by-products of solution phase reactions[29-33] (elements of this technology have been commercialized by 3M under the Emphaze™ brand name). In a proteomics context, azlactone-functionalized monoliths have been also employed to spatially pattern enzymes and to promote directional biosynthesis.[34-36] Azlactone-functionalized polymer brushes have also been investigated for biotechnological applications. An early study used PVDMA brushes polymerized from the surface of poly(propylene) as scaffolds for the immobilization of short peptides and showed that surface properties could be tuned by the immobilization of small molecule amines.[37] The Gopalan group has also investigated the reactivity of surface-bound PVDMA. When polymerized from a silicon substrate, azlactone groups could be used to immobilize biologically relevant enzymes (*e.g.*, RNase A, DNase I, and glucose oxidase) with retention of enzymatic activity.[38] Similarly, when spin-coated onto plastic substrates, PVDMA thin films can be used as scaffolds to array peptides and spatially direct the growth and differentiation of stem cells.[39,40] Researchers at Oak Ridge National Laboratory have also developed coatings and scaffolds using azlactone-functionalized polymers. Their efforts have generated a number of publications related to azlactone chemistry[41-46] and they recently reported on the design of coatings that capture and

remove microbes from solution with high affinity.[47] Finally, our group has been developing a reactive layer-by-layer (LbL) assembly approach to surface functionalization using PVDMA[48,49]—that work is described in greater detail in the sections below.

Layer-by-Layer Assembly and Reactive Azlactone-Containing Polymer Multilayers

The layer-by-layer (LbL) assembly of polymer films is a well-studied method of surface functionalization, relying on attractive electrostatic forces or covalent bond formation between mutually interacting polymers to drive stepwise assembly into a multilayered thin film. LbL assembly affords precise control over film thickness and composition and can be used to coat a wide variety of substrates.[50-53] Although the aqueous assembly of polyelectrolytes into weakly-bound polymer multilayers is the more conventional approach, several groups have developed reactive or covalent methods for the fabrication of LbL films. Here, interfacial reactions between two reactive polymers lead to cross-linked and relatively stable films that contain residual reactive groups that can be used, post-fabrication, to install diverse chemical functionality and to tune surface properties.[49,54-56]

Our group has been developing cross-linked LbL films based on the assembly of PVDMA and branched poly(ethylenimine) (PEI).[5,48,49] As with conventional polyelectrolyte multilayers, the nanometer scale thickness of PVDMA/PEI multilayers can be easily controlled; however, because interfacial reactions lead to a film that is covalently cross-linked by 'amide-amide'-type linkages, these films are inherently more stable than their electrostatically-bound counterparts. Assembly can take place in many organic solvents, enabling the coating of substrates that may be inaccessible by aqueous-based methods.[57-60] Finally, a key outcome of this approach is that residual unreacted azlactones and amines remain in the film after fabrication,

and these chemical handles can be used for post-fabrication modification of film-coated surfaces; selected examples are described below.

Early work in our group with azlactone-containing multilayers demonstrated that PEI/PVDMA thin films can be easily modified with a wide range of amine-containing compounds. For example, treatment with hydrophobic or hydrophilic amines can be used to tune the wettability of film-coated surfaces and pattern surfaces with features that promote or prevent cell adhesion and protein adsorption.[61-63] These films are also useful for the immobilization of oligonucleotides and proteins, and are therefore of potential utility in biotechnological contexts, for example, as new platforms for the design of DNA and protein arrays.[64-66] Additionally, when films are fabricated in ways that promote the growth of nano- and microscale features, they exhibit superhydrophobic behaviors, repelling water with contact angles in excess of 150° (and with low water roll-off angles).[67-70] This new approach to reactive superhydrophobic coatings has led to the design of hydrophilic-superhydrophobic surface patterns useful for the guided transfer and manipulation of fluids,[71] multilayered coatings with other unique wetting behaviors,[72,73] as well as macroscopically thick films that prevent the ingress of water and promote the release of encapsulated agents over periods up to one year.[74,75]

Chapters 2-6 of this thesis build substantially on past work with the PEI/PVDMA film system. Chapter 2 expands the range of nucleophiles that can be used to functionalize azlactone groups in multilayered films to include alcohols, thiols, and hydrazines with the goal of introducing degradable linkages.[76] Chapter 3 and 4 further develop PEI/PVDMA films as a scaffold for the ‘bottom-up’ synthesis of DNA arrays and also present ‘top-down’ approaches for biomolecule patterning.[65,66] Chapter 5 describes the development of heat-shrinkable superhydrophobic films that are amenable to reactive surface patterning and feature

miniaturization.[69] Chapter 6 presents an emerging understanding and fundamental insights into the physicochemical properties that control the onset of nano- and microscale roughness and superhydrophobicity in these multilayered materials.

Reactive Block Copolymers and Microphase Separation

Block copolymers (BCPs) are a technologically important class of materials because they contain two (or more) chemically distinct polymers covalently bound into a single macromolecule. As a result of this unique structure, BCPs tend to exhibit physicochemical properties of both polymer blocks, and the degree of influence of either block can be tuned by manipulating block lengths.[77-80] Critically, if these blocks are sufficiently chemically dissimilar, they will tend to 'de-mix'. That is, BCPs will tend to phase separate into their pure components, driving self-assembly and microphase separation into well-ordered polymer morphologies with domains on the order of 10-100 nm.[79,81-83] In the bulk and as nanometer-scale thin films, BCPs can assemble into nanostructures such as spheres, cylinders, or lamellae. The parameters that determine BCP morphology are the relative volume fractions of each block, f_i, and the block segregation strength, χN, where χ is the Flory-Huggins interaction parameter (a measure of block-block chemical incompatibility) and N is the volume-normalized degree of polymerization. [79,81-84] Self-assembly in many BCP systems has been studied, with poly(styrene-*block*-methyl methacrylate) (PS-*b*-PMMA) having been the most rigorously investigated. As a result, the structure-property relationships for this system are well understood, and this material has been widely used in the thin film regime for surface patterning applications.[85,86] Broadly, self-assembled BCPs have been extensively applied as nanoporous membrane materials,[87-90]

components in inorganic or hybrid assemblies,[91-93] and as tools to obtain nanometer-scale surface patterns below the resolution limit of conventional photolithography.[94-98]

Much less is known about the behavior and physicochemical properties of reactive BCPs. BCPs in which one (or more) of the blocks bears reactive functional groups could be advantageous for rapidly synthesizing and screening for desired properties in new BCP constructs.[9] Our group has developed an approach to the synthesis of azlactone-containing poly(styrene-*block*-2-vinyl-4,4-dimethylazlactone) (PS-*b*-PVDMA) BCPs.[99] These polymers can be synthesized directly by reversible addition-fragmentation chain-transfer (RAFT) polymerization and, like their homopolymer counterparts, azlactone groups couple with amines in rapid and quantitative reactions.[99,100] Chapters 7 and 8 outline the use of microphase separated PS-*b*-PVDMA BCP thin films for reactive surface patterning applications, demonstrating that chemical functionality can be covalently immobilized and patterned on hexagonal and lamellar thin films with reactive, azlactone-containing nanometer-sized 'lines' or 'dots'.[99,101] Chapter 9 further exploits the reactivity of PS-*b*-PVDMA BCPs, using non-microphase-separated and low molecular weight polymers to rapidly screen and search for microphase separation in a library of side chain-functionalized polymer derivatives.[102] This new method of searching for high-χ materials provides a framework for the future discovery of new BCP constructs that microphase separate into morphologies with increasingly small feature sizes and that are potentially useful for nanometer-scale surface patterning and advanced BCP lithography techniques.

New Directions in Azlactone-Containing Materials

Finally, Chapters 10, 11, and 12 detail the design and development of new classes of reactive, azlactone-containing materials. Chapter 10 presents polymerization methods for the

introduction of degradable backbone units into the prototypical PVDMA scaffold, leading to the fabrication of hydrolytically degradable and reactive polymers and reactive assemblies, including reactive and degradable capsules, gels, and cationic polymers that promote gene delivery.[103] Chapter 11 builds on past studies showing the utility of conventional electrostatic LbL films for the surface-mediated delivery of DNA. We show that the combination of a side chain charge-shifting polymer and a poly(β-amino ester) into 'mixed multilayer' thin films yields surfaces that promote the long term and linear release of DNA.[104] Finally, Chapter 12 presents guiding principles for the fabrication and control over electrospun polymer nanofibers that display the azlactone group, together with subsequent investigations into the reactivity and the immobilization of diverse chemical functionality onto electrospun non-woven mats.[105]

Background – Part II – Synthesis and Self-Assembly of Synthetic Six-Tailed Amphiphiles

Like BCPs, amphiphilic molecules can self-assemble into nanostructured morphologies containing discrete, well-organized domains, depending on the nature and volume of the hydrophilic and hydrophobic amphiphile components.[106-109] During the course of our studies, we became interested in the self-assembly behavior of a series of structurally-related synthetic six-tailed amphiphiles as a result of their ability to mimic properties of bacterial Lipid A.

Lipopolysaccharides are a class of biomolecule preserved across species and found in the bacterial cell wall. One common lipopolysaccharide motif known as endotoxin contains a terminal six-tailed lipid, Lipid A, that anchors the antigen-containing polysaccharide domain within the cell wall.[110,111] The Lipid A portion of endotoxin is acutely toxic, and the Federal Drug Administration requires that it be detected and kept below certain levels in a variety of consumer and medical-use products (*i.e.*, frequently below a picogram-per-millilitre

threshold).[112,113] As a result, the development and deployment of analytical methods for the rapid and inexpensive point-of-care detection of Lipid A and bacterial endotoxins is an active area of research.

Detection of Lipid A Using Liquid Crystal Droplets

Over the last several years, the Abbott group has pursued the development of liquid crystal (LC) droplet-based approaches for the detection of Lipid A and bacterial endotoxins.[114-116] Lipid A can trigger ordering transitions in micrometer-size droplets of the nematic LC 4'-pentyl-4-cyanobiphenyl (5CB) at remarkably low concentrations (*e.g.*, as low as 1 pg/mL in water) from the so-called "bipolar" to the "radial" state. These LC droplet states can be readily and rapidly observed and detected using polarized light microscopy or a bench-top flow cytometer.[114,115,117] In contrast, all one- and two-tailed synthetic and naturally-occurring surfactants and other biological lipids investigated to date trigger transitions at much higher concentrations, (*e.g.*, in the 10−100 μg/mL range). These concentrations lead to near or complete monolayer coverage of the LC droplets by the amphiphiles, and they are 5−6 orders of magnitude higher than those at which Lipid A elicits a LC droplet response.[114,115] The results of past studies suggest that Lipid A promotes bipolar-to-radial optical transitions at these ultralow concentrations through a fundamentally new mechanism that involves the formation of self-assembled nanostructures at topological defects in the LC.

Self-Assembly in a Homologous Series of Synthetic Six-Tailed Amphiphiles

The observation that Lipid A, with a high multiplicity of tails and large tail volume, could trigger LC droplet transitions at extremely low concentrations motivated us to study the origin

and mechanism of this response. Similar to the biological amphiphile, we discovered that synthetic amphiphiles bearing six aliphatic tails connected to a tertiary amine-containing headgroup can trigger changes in the internal ordering of LC microdroplets at picogram-per-milliliter concentrations. The primary focus of Chapter 13 is the synthesis and physicochemical characterization of six-tailed amphiphiles that mimic key structural properties of Lipid A, including the LC droplet response.[118] These results suggested that LC orientational transitions may be due to self-associative amphiphile interactions and the formation of an amphiphile nanostructure within specific regions of the LC droplet. This hypothesis led to the characterization and systematic study of the phase behavior and the morphologies accessible in this homologous series of synthetic amphiphiles. Chapter 14 describes a series of synchrotron SAXS experiments on amphiphile self-assembly, where tail length and headgroup counter-ion identity are systematically varied, and the subsequent discovery of several new lyotropic liquid crystalline (LLC) lipid phases. Chapter 15 exploits the self-assembly behavior of these six-tailed amphiphiles to fabricate colloidally-stable LLC particles. These so-called cubosome, hexasome, or lamellarsome particles (depending on the structure of the internal morphology) contain well-ordered, nanometer-scale networks of discrete hydrophobic and hydrophilic domains.[119,120] These materials, assembled from synthetic six-tailed amphiphiles, are among the first examples of fully-synthetic LLC particles, and they can potentially be used for a variety of applications, including to host and deliver molecular cargo.

Scope and Organization

The following section provides a brief overview of the chapters of this thesis. The chapters are organized into two broad areas of research: Chapters 2 to 6 describe work related to

the design of functional materials and interfaces using PEI/PVDMA multilayer films. Chapters 7 to 9 outline the development of reactive azlactone-containing BCPs and their use in both (i) reactive nanoscale surface patterning applications, and (ii) the rapid elaboration BCP libraries in the search for high-χ materials. Chapters 10-12 describe new advances in the area of azlactone-containing materials, including the development of reactive electrospun nanofibers, mixed multilayer thin films that promote the extended and linear release of DNA, and the synthesis of reactive and hydrolytically backbone-degradable VDMA-containing copolymers. The second part of this thesis, Chapters 13 to 15, describes the design, synthesis, and characterization of the self-assembly behavior of a series of synthetic six-tailed amphiphiles. While the chapters are generally grouped and arranged to provide a logical progression within each focus area, the individual chapters in each section were written in a manner that permits reading independently or out of the sequence in which they appear. The relevant introductory material, critical references, and a description of the experimental techniques used for each investigation are provided in each chapter.

Chapter 2 describes approaches to the design of covalently crosslinked and physically stable polymer coatings with chemically labile and dynamic surface features based on the functionalization of PEI/PVDMA films with alcohol-, thiol-, and hydrazine-based nucleophiles.[76] Past work has demonstrated that a wide variety of surface features and properties can be obtained by the post-fabrication functionalization of PEI/PVDMA films with primary amine-containing compounds.[5,58,61-63,65,68,69,71-73,121,122] In this chapter, we demonstrate that the azlactone groups in these materials can also be functionalized using less nucleophilic alcohol- or thiol-containing compounds, or converted to reactive acylhydrazine groups by treatment with hydrazine. These methods have (i) broadened the pool of molecules that can be

used for post-fabrication functionalization to include compounds containing alcohol, thiol, or aldehyde groups, and (ii) yield surface coatings with chemically labile amide/ester-, amide/thioester-, and amide/imine-type bonds that enable the design of new dynamic and stimuli-responsive materials (*e.g.*, surfaces that release covalently-bound molecules or undergo changes in extreme wetting behaviors in response to specific chemical stimuli). These results significantly expand the range of functionality that can be installed in azlactone-containing multilayers.

Chapter 3 exploits the well-studied reaction of amine-containing compounds and azlactone groups for the fabrication of oligonucleotide (DNA) and protein arrays on thin LbL films.[65] Manual spotting of amine-terminated oligonucleotide sequences on film-coated glass slides yielded arrays of immobilized probes that hybridized to fluorescently labeled complementary sequences with high signal intensities, high signal-to-noise ratios, and high sequence specificity. Furthermore, treatment of residual azlactone functionality with the non-fouling molecule D-glucamine resulted in regions between array features that resisted adsorption of protein and permitted hybridization in complex biologically-relevant media. The residual azlactone groups in these films were also exploited to fabricate functional arrays of proteins and enzymes. The ability to coat substrates of arbitrary size, shape, and composition with PEI/PVDMA multilayers permitted the fabrication of biomolecule arrays on the surfaces of poly(ethylene terephthalate) (PET) and heat-shrinkable polymer sheets. Arrays fabricated on these flexible substrates could be bent, cut and physically manipulated. This approach could thus contribute to the development of new assay formats and applications of biomolecule arrays.

The ‘top-down’ approach to the design of biomolecule arrays described Chapter 3 is complemented by a ‘bottom-up’ synthesis approach outlined in Chapter 4. This chapter

describes the photolithographic fabrication of high-density DNA and RNA arrays on flexible and transparent plastic substrates by Maskless Array Synthesis (MAS).[66] The azlactone groups in thin sheets of multilayer-coated PET are functionalized to present hydroxyl groups suitable for light-directed phosphoramidite-based nucleic acid synthesis. By modifying conventional and previously reported MAS procedures[64] to accommodate the physical and chemical properties of film-coated PET, the synthesis of oligonucleotide arrays with feature sizes as small as 14 x 14 μm and feature densities in excess of 125 000/cm^2 is achieved. These results are comparable to specifications attainable using conventional rigid substrates such as glass or glassy carbon. These plastic-backed arrays are tolerant to a wide range of hybridization temperatures, and improved synthetic procedures are described that enable the fabrication of arrays with sequences up to 50 nucleotides in length. This platform also supported the enzymatic conversion of DNA into RNA arrays, and we have outlined proof of concept experiments demonstrating that these plastic arrays can be readily sub-divided into smaller arrays (or 'millichips') using laboratory-scale laser cutting tools. These results have expanded the utility of oligonucleotide arrays, and could open the door to new potential applications for these important bioanalytical tools.

Chapter 5 continues to investigate the reactive properties of PEI/PVDMA multilayer coatings on plastic materials. Superhydrophobic surface coatings (*e.g.*, advancing water contact angles >150°, with low roll-off angles) can be obtained when films are deposited onto commercially available heat-shrinkable plastic film and the material is shrunk.[69] We demonstrated that superhydrophobicity arises from a combination of thermally-induced microscale folding and wrinkling in these materials, and the inherent roughness of the polymer multilayers coated on the heat-shrink films. This approach is relatively straightforward and

yielded superhydrophobic materials that can be bent, cut, or transferred onto other surfaces. The reactive nature of the surface coatings could be exploited to impart new properties, for example, to create superhydrophobic/hydrophilic surface patterns. Furthermore, we show that this method can be used to design materials that 'shrink-to-fit' around complex surfaces and three dimensional geometries, and that shrinking can be used to increase the density of patterned surface features. This innovative approach also makes it possible to repair full-thickness defects in these superhydrophobic films by further heat treatment after damage. These material properties and features could all prove useful for future advanced applications of superhydrophobic surfaces.

Chapter 6 continues the theme of investigating the physicochemical properties and reactivity of PEI/PVDMA multilayers. We show that partially hydrolyzed PVDMA (*i.e.*, polymer containing a significant fraction of azlactone groups hydrolyzed to side chain carboxylic acids) contributes to the evolution of nano- and microscale features that arise during film growth and that contribute to the onset of superhydrophobicity in these materials. We demonstrate that there is an apparent optimal 'percent hydrolysis' of azlactone groups required to drive superhydrophobic film growth, and propose that a combination of covalent bond formation between azlactone groups and amines in PEI, together with electrostatic interactions between the hydrolyzed side chains in PVDMA and the amines in PEI, drive film growth and lead to thick and porous film morphologies. These new observations provide fundamental insight into the growth and onset of roughness and superhydrophobicity in PEI/PVDMA thin films—features that lead to a variety of advanced applications—and establish principles for the future development and control over physicochemical properties in these versatile reactive coatings.

Chapters 7 through 9 report on the synthesis, self-assembly, and post-fabrication

functionalization of azlactone-containing block copolymers (BCPs). Chapter 7 reports an approach to the post-fabrication installation of chemical functionality on microphase-separated reactive BCP thin films.[99] We exploited the reactivity of a symmetric PS-*b*-PVDMA BCP that could self-assemble into perpendicularly-oriented lamellar domains (~15 nm wide) when spin-coated as a thin film. These materials presented nanoscale 'lines' of azlactone groups that served as chemical handles for the immobilization of primary amine-containing functionality. We demonstrated that a range of chemical functionalities could be installed on these films by treatment with aqueous solutions of desired amines, and that these mild conditions did not perturb the underlying microphase-separated pattern. This post-fabrication and reactive template approach provides a basis for the development of modular design of microphase-separated BCP thin films, and gives access to coatings with patterned chemical domains and surface properties that would be difficult to prepare by the self-assembly and processing of functionally complex BCPs.

Chapter 8 builds upon the results described in Chapter 7, extending our work to the thin film self-assembly and post-fabrication functionalization of cylinder-forming PS-*b*-PVDMA BCPs.[101] Using FTIR spectroscopy and ellipsometry, we demonstrate that self-assembly by thermal annealing leads to physicochemical interactions between reactive azlactone groups and underlying substrates that can lead to BCP 'pinning' and decreased polymer chain mobility, ultimately resulting in relatively high defect densities and poor long-range order in thin films. Solvent annealing circumvented these issues and could be used to drive thin film microphase separation to high quality morphologies. We show that parallel and perpendicularly-oriented cylinders with diameters of ~12 nm and a center-to-center distance of 23.7 nm can be obtained by solvent annealing a cylinder-forming PS-*b*-PVDMA BCP, and that the azlactones in the

PVDMA block remained available for reaction with primary amine-functionalized nucleophiles. X-ray photoelectron spectroscopy (XPS) depth-profiling analyses revealed that reactions between azlactone groups and amines occurred primarily in the uppermost portions of the reactive domains. Finally, we demonstrate that the azlactone groups in both parallel and perpendicularly-oriented films provide robust platforms for the selective infusion of trimethylaluminum vapor, and that this metal precursor can subsequently be converted into aluminum oxide nanowires and nanodots, depending on thin film orientation. The principles reported here open the door to new nanopatterned surfaces decorated with diverse chemical or biological functionality and provide new and useful templates for the fabrication of metallic and inorganic features of potential utility in lithography applications.

Chapter 9 continues the theme of azlactone-containing BCP self-assembly, reporting on a reactive templating approach for the rapid discovery of strongly segregated diblock polymers that microphase separate into well-defined morphologies with sub-5 nm features in the bulk. This strategy employed reactive PS-*b*-PVDMA polymers with low degrees of polymerization (N) obtained by RAFT polymerization in which the VDMA blocks could undergo quantitative reactions with primary amine-containing nucleophiles, to identify new poly(acrylamide)-like side chains that were highly immiscible with PS and therefore induced BCP self-assembly.[102] Using a combination of optical birefringence and small-angle X-ray scattering (SAXS), we characterized a library of 17 side chain-functionalized BCPs generated from four parent PS-*b*-PVDMA diblocks. We demonstrated that VDMA blocks functionalized with terminal side chain hydroxy and methoxy groups yielded polymers that ordered into lamellar mesophases with half-pitches as small as 3.8 nm—among the smallest feature sizes observed to-date. This azlactone-based, reactive platform approach enables the combinatorial generation of polymer libraries with

diverse side chain structures that can be rapidly screened to identify new high χ/low N systems for self-assembly at ever decreasing length scales.

Chapters 10-12 describe new innovations in the design and fabrication of reactive, azlactone-containing materials. Chapter 10 reports on the design of reactive and hydrolytically degradable copolymers that contain both azlactone side chain functionality and hydrolyzable backbone ester groups. We showed that copolymerization of VDMA with the cyclic ketene acetal 2-methylene-1,3-dioxepane (MDO) using conventional or reversible-deactivation radical polymerization techniques yields copolymers and block copolymers that exhibit the amine-reactivity associated with poly(vinyl azlactone)s but also the hydrolytic degradability associated with conventional polyesters.[103] Control over monomer feed ratios and other parameters could be used to tune both copolymer composition (*e.g.*, the number/ratio of azlactone and ester repeat units) and the physical properties of the resulting materials (*e.g.*, glass transition temperatures and ability to self-assemble into nanostructured morphologies). Post-fabrication functionalization of azlactone groups in MDO-*co*-VDMA copolymers with primary amine-containing compounds proceeded rapidly and, critically, could be achieved without disruption of backbone ester groups. We showed that azlactone-functionalized copolymers are well-suited for use as templates for the design of new degradable polymers and as building blocks for the design of covalently and ionically-crosslinked macromolecular thin films, capsules, and polymer gels that degrade in aqueous environments.

Chapter 11 reports the design of erodible 'mixed multilayer' coatings fabricated using plasmid DNA and combinations of both hydrolytically degradable and charge-shifting cationic polymer building blocks. LbL films fabricated using combinations of a model poly(β-amino ester) and a model charge-shifting polymer (obtained by functionalization of PVDMA) exhibited

DNA release profiles that were substantially different from those assembled using either polymer alone.[104] The order in which the DNA/polymer layers were deposited during assembly had a profound impact on release profiles when these materials were incubated in physiological buffer. Mixed multilayers fabricated by depositing layers of poly(β-amino ester)/DNA onto films of charge-shifting polymer/DNA released DNA into solution over ~60-80 days, with multi-phase release profiles intermediate to and exhibiting some general features of poly(β-amino ester) films or charge-shifting only films (*e.g.*, a period of rapid release, followed by a more extended phase). In sharp contrast, 'inverted' mixed multilayers fabricated by depositing layers of charge-shifting polymer/DNA onto films composed of poly(β-amino ester)/DNA exhibited release profiles that were nearly completely linear over ~70 days. These and other results are consistent with substantial interdiffusion and co-mixing among the individual components of these compound materials. Our results lead to new, unanticipated release profiles useful for the design of polymer-based coatings for the local, surface-mediated delivery of DNA from the surfaces of topologically complex interventional devices, such as intravascular stents, with predictable long-term release profiles.

Chapter 12 reports on the development of methods for electrospinning azlactone-containing polymers into reactive nanofiber materials. We demonstrate that randomly oriented nanofibrous mats can fabricated using a model copolymer of methyl methacrylate (MMA) and VDMA, and that azlactone groups can be used to introduce new functionality and modulate important interfacial properties of these materials (e.g., wetting behaviors) by post-fabrication treatment with primary amine-containing nucleophiles without substantial changes to nanofiber morphology.[105] This approach enabled the macroscale or microscale patterning of new functionality on mat-coated surfaces by treatment with bulk solutions or using methods such as

microcontact printing. Our results also demonstrated that these reactive nanofiber mats could be transferred or printed onto other secondary surfaces by pressing them into contact with other amine-functionalized objects. Additionally, infusion of a viscous oil into decylamine-functionalized mats resulted in a slippery liquid-infused surface (SLIPS) anti-wetting surface. The approaches described in this chapter enable the introduction of new properties to electrospun nanofibers after fabrication and reduce the need to design new functional polymers with desired properties or surface functionality. We anticipate that the strategies reported here can be used to design new azlactone-functionalized copolymers, or be used in combination with other azlactone-reactive nucleophiles (*e.g.*, alcohols or thiols) to design nanofibers and nanofiber-based coatings with new physical properties, surface features, and behaviors of potential utility in a broad range of contexts.

Chapter 13 changes the focus significantly from the previous chapters, and investigates the characterization of synthetic, six-tailed amphiphiles designed to mimic key properties of bacterial Lipid A. We showed that, like six-tailed Lipid A, synthetic six-tailed amphiphiles obtained by the ring-opening reaction of alkyl-epoxides and tris(2-aminoethyl)amine could trigger changes in the internal ordering of water-dispersed liquid crystal (LC) microdroplets at ultralow (picogram-per-milliliter) concentrations.[118] These molecules are the first class of synthetic amphiphiles discovered that mimic the ability of Lipid A to trigger LC droplet optical responses at these ultralow concentrations. This behavior differs significantly from all previously investigated synthetic surfactants and lipids, which require near-complete monolayer coverage of the LC droplet surface to trigger ordering transitions. Surface-pressure measurements and SAXS experiments reveal these six-tailed synthetic amphiphiles to mimic key aspects of the self-assembly of Lipid A at aqueous interfaces and in solution. These results suggest that these

amphiphiles trigger orientational transitions at ultralow concentrations through a unique mechanism that is similar to that of Lipid A and involves the formation of inverted self-associated nanostructures at topological defects in the LC droplets.

Finally, Chapters 14 and 15 describe the self-assembly behavior and breadth of self-assembled morphologies accessible in a homologous series of six-tailed synthetic amphiphiles. Chapter 14 describes in-depth morphological studies by temperature-dependant synchrotron SAXS studies, where amphiphile tail length and headgroup counter-ion identity were systematically varied, and the subsequent discovery of new, inverse cubic LLC phases with remarkably small domain sizes. Chapter 15 details the fabrication of colloidally stable, water-dispersed LLC particles (so-called 'isasome' particles) composed of the six-tailed amphiphiles studied in the two preceding chapters. These nanometer-sized cubosomes, hexasomes, and lamellarsomes contain internal self-assembled morphologies dictated by the amphiphile employed for their assembly. These materials are among the first examples of entirely synthetic LLC particles, and can be used to host molecular cargo (*e.g.*, the model antibacterial agent triclosan) and affect a response in living cells.

Finally, Chapter 16 provides a summary of the work described in Chapters 2-15 and a discussion of potential directions for future studies based on the work described in this thesis.

References

(1) Boaen, N. K.; Hillmyer, M. A. Post-polymerization functionalization of polyolefins. *Chemical Society Reviews* **2005,** *34* (3), 267.

(2) Fournier, D.; Hoogenboom, R.; Schubert, U. S. Clicking polymers: a straightforward approach to novel macromolecular architectures. *Chemical Society Reviews* **2007,** *36* (8), 1369.

(3) Gauthier, M. A.; Gibson, M. I.; Klok, H.-A. Synthesis of functional polymers by post-polymerization modification. *Angewandte Chemie International Edition* **2009,** *48* (1), 48.

(4) Golas, P. L.; Matyjaszewski, K. Marrying click chemistry with polymerization: expanding the scope of polymeric materials. *Chemical Society Reviews* **2010,** *39* (4), 1338.

(5) Buck, M. E.; Lynn, D. M. Azlactone-functionalized polymers as reactive platforms for the design of advanced materials: Progress in the last ten years. *Polymer Chemistry* **2012,** *3* (1), 66.

(6) Tempelaar, S.; Mespouille, L.; Coulembier, O.; Dubois, P.; Dove, A. P. Synthesis and post-polymerisation modifications of aliphatic poly(carbonate)s prepared by ring-opening polymerisation. *Chemical Society Reviews* **2013,** *42* (3), 1312.

(7) Theato, P.; Klok, H.-A.; Editors *Functional Polymers by Post-Polymerization Modification: Concepts, Guidelines, and Applications*; Wiley-VCH Verlag GmbH & Co. KGaA, **2013**.

(8) Günay, K. A.; Theato, P.; Klok, H.-A. Standing on the shoulders of Hermann Staudinger: Post-polymerization modification from past to present. *Journal of Polymer Science Part A: Polymer Chemistry* **2013,** *51* (1), 1.

(9) Romulus, J.; Henssler, J. T.; Weck, M. Postpolymerization Modification of Block Copolymers. *Macromolecules* **2014,** *47* (16), 5437.

(10) Heilmann, S. M.; Rasmussen, J. K.; Krepski, L. R. Chemistry and technology of 2-alkenyl azlactones. *Journal of Polymer Science Part A: Polymer Chemistry* **2001,** *39* (21), 3655.

(11) Rasmussen, J. K.; Heilmann, S. M.; Palensky, F. J.; Smith, H. K., II; Melancon, K. C. Chemistry of Alkenylazlactones. 2. Reaction with Thiols. *Macromolecular Rapid Communications* **1984,** *5* (2), 67.

(12) Heilmann, S. M.; Moren, D. M.; Krepski, L. R.; Pathre, S. V.; Rasmussen, J. K.; Stevens, J. The chemistry of 2-alkenyl-5(4H)-oxazolones. VIII - Acid-catalyzed reaction with alcohols. *Tetrahedron* **1998,** *54* (40), 12151.

(13) Sun, B.; Liu, X.; Buck, M. E.; Lynn, D. M. Azlactone-functionalized polymers as reactive templates for parallel polymer synthesis: synthesis and screening of a small library of cationic polymers in the context of DNA delivery. *Chemical Communications* **2010,** *46* (12), 2016.

(14) Ho, T. H.; Levere, M.; Soutif, J.-C.; Montembault, V.; Pascual, S.; Fontaine, L. Synthesis of thermoresponsive oxazolone end-functional polymers for reactions with amines using thiol-Michael addition "click" chemistry. *Polymer Chemistry* **2011,** *2* (6), 1258.

(15) Gardner, C. M.; Stover, H. D. H. Reactive Polyanions Based on Poly(4,4-dimethyl-2-vinyl-2-oxazoline-5-one-co-methacrylic acid). *Macromolecules* **2011,** *44* (18), 7115.

(16) Ho, H. T.; Leroux, F.; Pascual, S.; Montembault, V.; Fontaine, L. Amine-Reactive Polymers Synthesized by RAFT Polymerization Using an Azlactone Functional Trithiocarbonate RAFT Agent. *Macromolecular Rapid Communications* **2012,** *33* (20), 1753.

(17) Ho, H. T.; Levere, M. E.; Fournier, D.; Montembault, V.; Pascual, S.; Fontaine, L. Introducing the Azlactone Functionality into Polymers through Controlled Radical Polymerization: Strategies and Recent Developments. *Australian Journal of Chemistry* **2012,** *65* (8), 970.

(18) Laquievre, A.; Allaway, N. S.; Lyskawa, J.; Woisel, P.; Lefebvre, J.-M.; Fournier, D. Highly Efficient Ring-Opening Reaction of Azlactone-Based Copolymer Platforms for the Design of Functionalized Materials. *Macromolecular Rapid Communications* **2012,** *33* (9), 848.

(19) Gardner, C. M.; Brown, C. E.; Stöver, H. D. H. Synthesis and properties of water-soluble azlactone copolymers. *Journal of Polymer Science Part A: Polymer Chemistry* **2012,** *50* (22), 4674.

(20) Gardner, C. M.; Potter, M. A.; Stöver, H. D. H. Improving covalent cell encapsulation with temporarily reactive polyelectrolytes. *Journal of Materials Science: Materials in Medicine* **2012,** *23* (1), 181.

(21) Ho, H. T.; Levere, M. E.; Pascual, S.; Montembault, V.; Casse, N.; Caruso, A.; Fontaine, L. Thermoresponsive block copolymers containing reactive azlactone groups and their bioconjugation with lysozyme. *Polymer Chemistry* **2013,** *4* (3), 675.

(22) Jones, M. W.; Richards, S.-J.; Haddleton, D. M.; Gibson, M. I. Poly(azlactone)s: versatile scaffolds for tandem post-polymerisation modification and glycopolymer synthesis. *Polymer Chemistry* **2013,** *4* (3), 717.

(23) Quek, J. Y.; Zhu, Y.; Roth, P. J.; Davis, T. P.; Lowe, A. B. RAFT Synthesis and Aqueous Solution Behavior of Novel pH- and Thermo-Responsive (Co)Polymers Derived from Reactive Poly(2-vinyl-4,4-dimethylazlactone) Scaffolds. *Macromolecules* **2013,** *46* (18), 7290.

(24) Li, Y.; Duong, H. T. T.; Jones, M. W.; Basuki, J. S.; Hu, J.; Boyer, C.; Davis, T. P. Selective Postmodification of Copolymer Backbones Bearing Different Activated Esters with Disparate Reactivities. *ACS Macro Letters* **2013,** *2* (10), 912.

(25) Delplace, V.; Harrisson, S.; Ho, H. T.; Tardy, A.; Guillaneuf, Y.; Pascual, S.; Fontaine, L.; Nicolas, J. One-Step Synthesis of Azlactone-Functionalized SG1-Based Alkoxyamine for Nitroxide-Mediated Polymerization and Bioconjugation. *Macromolecules* **2015,** *48* (7), 2087.

(26) Zhu, Y.; Batchelor, R.; Lowe, A. B.; Roth, P. J. Design of Thermoresponsive Polymers with Aqueous LCST, UCST, or Both: Modification of a Reactive Poly(2-vinyl-4,4-dimethylazlactone) Scaffold. *Macromolecules* **2016,** *49* (2), 672.

(27) Barkakaty, B.; Browning, K. L.; Sumpter, B.; Uhrig, D.; Karpisova, I.; Harman, K. W.; Ivanov, I.; Hensley, D. K.; Messman, J. M.; Kilbey, S. M.et al. Amidine-Functionalized Poly(2-vinyl-4,4-dimethylazlactone) for Selective and Efficient CO2 Fixing. *Macromolecules* **2016,** *49* (5), 1523.

(28) Acrylic azlactone coatings. *Brit.* **1968,** (GB1121418), 8 pp.

(29) Tripp, J. A.; Stein, J. A.; Svec, F.; Frechet, J. M. J. "Reactive filtration": Use of functionalized porous polymer monoliths as scavengers in solution-phase synthesis. *Organic Letters* **2000,** *2* (2), 195.

(30) Tripp, J. A.; Svec, F.; Frechet, J. M. J. Grafted macroporous polymer monolithic disks: A new format of scavengers for solution-phase combinatorial chemistry. *Journal of Combinatorial Chemistry* **2001,** *3* (2), 216.

(31) Guyomard, A.; Fournier, D.; Pascual, S.; Fontaine, L.; Bardeau, J.-F. Preparation and characterization of azlactone functionalized polymer supports and their application as scavengers. *European Polymer Journal* **2004,** *40* (10), 2343.

(32) Fournier, D.; Pascual, S.; Montembault, V.; Haddleton, D. M.; Fontaine, L. Well-Defined Azlactone-Functionalized (Co)polymers on a Solid Support: Synthesis via Supported Living Radical Polymerization and Application as Nucleophile Scavengers. *Journal of Combinatorial Chemistry* **2006,** *8* (4), 522.

(33) Lucchesi, C.; Pascual, S.; Dujardin, G.; Fontaine, L. New functionalized polyHIPE materials used as amine scavengers in batch and flow-through processes. *Reactive Functional Polymers* **2008,** *68* (1), 97.

(34) Xie, S.; Svec, F.; Frechet, J. M. J. Design of reactive porous polymer supports for high throughput bioreactors: poly(2-vinyl-4,4- dimethylazlactone-co-acrylamide-co-ethylene dimethacrylate) monoliths. *Biotechnology and Bioengineering* **1999,** *62* (1), 30.

(35) Peterson, D. S.; Rohr, T.; Svec, F.; Frechet, J. M. J. Enzymatic microreactor-on-a-chip: Protein mapping using trypsin immobilized on porous polymer monoliths molded in channels of microfluidic devices. *Analytical Chemistry* **2002,** *74* (16), 4081.

(36) Geiser, L.; Eeltink, S.; Svec, F.; Frechet, J. M. J. In-line system containing porous polymer monoliths for protein digestion with immobilized pepsin, peptide preconcentration and nano-liquid chromatography separation coupled to electrospray ionization mass spectroscopy. *Journal of Chromatography A* **2008,** *1188* (2), 88.

(37) Fontaine, L.; Lemele, T.; Brosse, J.-C.; Sennyey, G.; Senet, J.-P.; Wattiez, D. Grafting of 2-vinyl-4,4-dimethylazlactone onto electron-beam activated poly(propylene) films and fabrics. Application to the immobilization of sericin. *Macromolecular Chemistry and Physics* **2002,** *203* (10/11), 1377.

(38) Cullen, S. P.; Mandel, I. C.; Gopalan, P. Surface-Anchored Poly(2-vinyl-4,4-dimethyl azlactone) Brushes as Templates for Enzyme Immobilization. *Langmuir* **2008,** *24* (23), 13701.

(39) Schmitt, S. K.; Xie, A. W.; Ghassemi, R. M.; Trebatoski, D. J.; Murphy, W. L.; Gopalan, P. Polyethylene Glycol Coatings on Plastic Substrates for Chemically Defined Stem Cell Culture. *Advanced Healthcare Materials* **2015,** *4* (10), 1555.

(40) Schmitt, S. K.; Trebatoski, D. J.; Krutty, J. D.; Xie, A. W.; Rollins, B.; Murphy, W. L.; Gopalan, P. Peptide Conjugation to a Polymer Coating via Native Chemical Ligation of Azlactones for Cell Culture. *Biomacromolecules* **2016,** *17* (3), 1040.

(41) Barringer, J. E.; Messman, J. M.; Banaszek, A. L.; Meyer, H. M., III; Kilbey, S. M., II. Immobilization of Biomolecules on Poly(vinyldimethylazlactone)-Containing Surface Scaffolds. *Langmuir* **2009,** *25* (1), 262.

(42) Lokitz, B. S.; Messman, J. M.; Hinestrosa, J. P.; Alonzo, J.; Verduzco, R.; Brown, R. H.; Osa, M.; Ankner, J. F.; Kilbey, S. M. Dilute Solution Properties and Surface Attachment of RAFT Polymerized 2-Vinyl-4,4-dimethyl Azlactone (VDMA). *Macromolecules* **2009,** *42* (22), 9018.

(43) Messman, J. M.; Lokitz, B. S.; Pickel, J. M.; Kilbey, S. M., II. Highly Tailorable Materials based on 2-Vinyl-4,4-dimethyl Azlactone: (Co)Polymerization, Synthetic Manipulation and Characterization. *Macromolecules* **2009,** *42* (12), 3933.

(44) Lokitz, B. S.; Wei, J.; Hinestrosa, J. P.; Ivanov, I.; Browning, J. F.; Ankner, J. F.; Kilbey, S. M.; Messman, J. M. Manipulating Interfaces through Surface Confinement of Poly(glycidyl methacrylate)-block-poly(vinyldimethylazlactone), a Dually Reactive Block Copolymer. *Macromolecules* **2012,** *45* (16), 6438.

(45) Ramanathan, M.; Lokitz, B. S.; Messman, J. M.; Stafford, C. M.; Kilbey, S. M., II. Spontaneous wrinkling in azlactone-based functional polymer thin films in 2D and 3D geometries for guided nanopatterning. *Journal of Materials Chemistry C* **2013,** *1* (11), 2097.

(46) Kumar, R.; Lokitz, B. S.; Sides, S. W.; Chen, J.; Heller, W. T.; Ankner, J. F.; Browning, J. F.; Kilbey, S. M., II; Sumpter, B. G. Microphase separation in thin films of lamellar forming polydisperse di-block copolymers. *RSC Advances* **2015,** *5* (27), 21336.

(47) Hansen, R. R.; Hinestrosa, J. P.; Shubert, K. R.; Morrell-Falvey, J. L.; Pelletier, D. A.; Messman, J. M.; Kilbey, S. M.; Lokitz, B. S.; Retterer, S. T. Lectin-Functionalized Poly(glycidyl methacrylate)-block-poly(vinyldimethyl azlactone) Surface Scaffolds for High Avidity Microbial Capture. *Biomacromolecules* **2013,** *14* (10), 3742.

(48) Buck, M. E.; Zhang, J.; Lynn, D. M. Layer-by-Layer Assembly of Reactive Ultrathin Films Mediated by Click-Type Reactions of Poly(2-Alkenyl Azlactone)s. *Advanced Materials* **2007,** *19* (22), 3951.

(49) Broderick, A. H.; Lynn, D. M. In *Functional Polymers by Post-Polymerization Modification*; Wiley-VCH Verlag GmbH & Co. KGaA, **2013**.

(50) Schönhoff, M. Self-assembled polyelectrolyte multilayers. *Current Opinion in Colloid & Interface Science* **2003,** *8* (1), 86.

(51) Hammond, P. T. Form and Function in Multilayer Assembly: New Applications at the Nanoscale. *Advanced Materials* **2004,** *16* (15), 1271.

(52) Decher, G. In *Multilayer Thin Films: Sequential Assembly of Nanocomposite Materials, 2nd Edition*; Decher, G.;Schlenoff, J. B., Eds.; Wiley-CVH, 2012.

(53) Xiao, F.-X.; Pagliaro, M.; Xu, Y.-J.; Liu, B. Layer-by-layer assembly of versatile nanoarchitectures with diverse dimensionality: a new perspective for rational construction of multilayer assemblies. *Chemical Society Reviews* **2016**.

(54) Quinn, J. F.; Johnston, A. P. R.; Such, G. K.; Zelikin, A. N.; Caruso, F. Next generation, sequentially assembled ultrathin films: beyond electrostatics. *Chemical Society Reviews* **2007,** *36* (5), 707.

(55) Bergbreiter, D. E.; Liao, K.-S. Covalent layer-by-layer assembly-an effective, forgiving way to construct functional robust ultrathin films and nanocomposites. *Soft Matter* **2009,** *5* (1), 23.

(56) Rydzek, G.; Schaaf, P.; Voegel, J.-C.; Jierry, L.; Boulmedais, F. Strategies for covalently reticulated polymer multilayers. *Soft Matter* **2012,** *8* (38), 9738.

(57) Buck, M. E.; Lynn, D. M. Free-Standing and Reactive Thin Films Fabricated by Covalent Layer-by-Layer Assembly and Subsequent Lift-Off of Azlactone-Containing Polymer Multilayers. *Langmuir* **2010,** *26* (20), 16134.

(58) Buck, M. E.; Lynn, D. M. Functionalization of Fibers Using Azlactone-Containing Polymers: Layer-by-Layer Fabrication of Reactive Thin Films on the Surfaces of Hair and Cellulose-Based Materials. *ACS Applied Materials & Interfaces* **2010,** *2* (5), 1421.

(59) Buck, M. E.; Lynn, D. M. Reactive Layer-by-Layer Assembly of Suspended Thin Films and Semipermeable Membranes at Interfaces Created Between Aqueous and Organic Phases. *Advanced Materials* **2010,** *22* (9), 994.

(60) Broderick, A. H.; Manna, U.; Lynn, D. M. Covalent Layer-by-Layer Assembly of Water-Permeable and Water-Impermeable Polymer Multilayers on Highly Water-Soluble and Water-Sensitive Substrates. *Chemistry of Materials* **2012,** *24* (10), 1786.

(61) Buck, M. E.; Breitbach, A. S.; Belgrade, S. K.; Blackwell, H. E.; Lynn, D. M. Chemical Modification of Reactive Multilayered Films Fabricated from Poly(2-alkenyl azlactone)s: Design of Surfaces that Prevent or Promote Mammalian Cell Adhesion and Bacterial Biofilm Growth. *Biomacromolecules* **2009,** *10* (6), 1564.

(62) Fredin, N. J.; Broderick, A. H.; Buck, M. E.; Lynn, D. M. Nanoimprinted Thin Films of Reactive, Azlactone-Containing Polymers: Combining Methods for the Topographic Patterning of Cell Substrates with Opportunities for Facile Post-Fabrication Chemical Functionalization. *Biomacromolecules* **2009,** *10* (4), 994.

(63) Broderick, A. H.; Azarin, S. M.; Buck, M. E.; Palecek, S. P.; Lynn, D. M. Fabrication and Selective Functionalization of Amine-Reactive Polymer Multilayers on Topographically Patterned Microwell Cell Culture Arrays. *Biomacromolecules* **2011,** *12* (6), 1998.

(64) Broderick, A. H.; Lockett, M. R.; Buck, M. E.; Yuan, Y.; Smith, L. M.; Lynn, D. M. In situ Synthesis of Oligonucleotide Arrays on Surfaces Coated with Crosslinked Polymer Multilayers. *Chemistry of Materials* **2012,** *24* (5), 938.

(65) Broderick, A. H.; Carter, M. C. D.; Lockett, M. R.; Smith, L. M.; Lynn, D. M. Fabrication of Oligonucleotide and Protein Arrays on Rigid and Flexible Substrates Coated with Reactive Polymer Multilayers. *ACS Applied Materials & Interfaces* **2013,** *5* (2), 351.

(66) Holden, M. T.; Carter, M. C. D.; Wu, C.-H.; Wolfer, J.; Codner, E.; Sussman, M. R.; Lynn, D. M.; Smith, L. M. Photolithographic Synthesis of High-Density DNA and RNA Arrays on Flexible, Transparent, and Easily Subdivided Plastic Substrates. *Analytical Chemistry* **2015,** *87* (22), 11420.

(67) Buck, M. E.; Schwartz, S. C.; Lynn, D. M. Superhydrophobic Thin Films Fabricated by Reactive Layer-by-Layer Assembly of Azlactone-Functionalized Polymers. *Chemistry of Materials* **2010,** *22* (23), 6319.

(68) Manna, U.; Broderick, A. H.; Lynn, D. M. Chemical Patterning and Physical Refinement of Reactive Superhydrophobic Surfaces. *Advanced Materials* **2012,** *24* (31), 4291.

(69) Manna, U. M.; Carter, M. C. D.; Lynn, D. M. 'Shrink-to-Fit' Superhydrophobicity: Thermally-Induced Microscale Wrinkling of Thin Hydrophobic Multilayers Fabricated on Flexible Shrink-Wrap Substrates. *Advanced Materials* **2013,** *25* (22), 3085.

(70) Manna, U.; Lynn, D. M. Restoration of Superhydrophobicity in Crushed Polymer Films by Treatment with Water: Self-Healing and Recovery of Damaged Topographic Features Aided by an Unlikely Source. *Advanced Materials* **2013,** *25* (36), 5104.

(71) Manna, U.; Lynn, D. M. Patterning and Impregnation of Superhydrophobic Surfaces Using Aqueous Solutions. *ACS Applied Materials & Interfaces* **2013,** *5* (16), 7731.

(72) Manna, U.; Lynn, D. M. Fabrication of Liquid-Infused Surfaces Using Reactive Polymer Multilayers: Principles for Manipulating the Behaviors and Mobilities of Aqueous Fluids on Slippery Liquid Interfaces. *Advanced Materials* **2015,** *27* (19), 3007.

(73) Manna, U.; Lynn, D. M. Synthetic Surfaces with Robust and Tunable Underwater Superoleophobicity. *Advanced Functional Materials* **2015,** *25* (11), 1672.

(74) Manna, U.; Kratochvil, M. J.; Lynn, D. M. Superhydrophobic Polymer Multilayers that Promote the Extended, Long-Term Release of Embedded Water-Soluble Agents. *Advanced Materials* **2013,** *25* (44), 6405.

(75) Kratochvil, M. J.; Tal-Gan, Y.; Yang, T.; Blackwell, H. E.; Lynn, D. M. Nanoporous Superhydrophobic Coatings that Promote the Extended Release of Water-Labile Quorum Sensing Inhibitors and Enable Long-Term Modulation of Quorum Sensing in Staphylococcus aureus. *ACS Biomaterials Science & Engineering* **2015,** *1* (10), 1039.

(76) Carter, M. C. D.; Lynn, D. M. Covalently Crosslinked and Physically Stable Polymer Coatings with Chemically Labile and Dynamic Surface Features Fabricated by Treatment of Azlactone-Containing Multilayers with Alcohol-, Thiol-, and Hydrazine-Based Nucleophiles. *Chemistry of Materials* **2016,** *28* (14), 5063.

(77) Bates, F. S.; Fredrickson, G. H. Block copolymer thermodynamics: theory and experiment. *Annual Review of Physical Chemistry* **1990,** *41*, 525.

(78) Bates, F. S.; Fredrickson, G. H. Block Copolymers—Designer Soft Materials. *Physics Today* **1999,** *52*, 32.

(79) Hadjichristidis, N.; Pispas, S.; Floudas, G. *Block Copolymers: Synthetic Strategies, Physical Properties, and Applications*; John Wiley & Sons, Inc., **2003**.

(80) Hadjichristidis, N.; Pitsikalis, M.; Iatrou, H. Synthesis of block copolymers. *Advances in Polymer Science* **2005,** *189* (Block Copolymers I), 1.

(81) Leibler, L. Theory of Microphase Separation in Block Copolymers. *Macromolecules* **1980,** *13* (6), 1602.

(82) Lodge, T. P. Block Copolymers: Past Successes and Future Challenges. *Macromolecular Chemistry and Physics* **2003,** *204* (2), 265.

(83) Mai, Y.; Eisenberg, A. Self-assembly of block copolymers. *Chemical Society Reviews* **2012,** *41* (18), 5969.

(84) Epps, I. I. I. T. H.; O'Reilly, R. K. Block copolymers: controlling nanostructure to generate functional materials - synthesis, characterization, and engineering. *Chemical Science* **2016,** *7* (3), 1674.

(85) Guarini, K. W.; Black, C. T.; Yeung, S. H. I. Optimization of Diblock Copolymer Thin Film Self Assembly. *Advanced Materials* **2002,** *14* (18), 1290.

(86) Ham, S.; Shin, C.; Kim, E.; Ryu, D. Y.; Jeong, U.; Russell, T. P.; Hawker, C. J. Microdomain Orientation of PS-b-PMMA by Controlled Interfacial Interactions. *Macromolecules* **2008,** *41* (17), 6431.

(87) Olson, D. A.; Chen, L.; Hillmyer, M. A. Templating Nanoporous Polymers with Ordered Block Copolymers. *Chemistry of Materials* **2008,** *20* (3), 869.

(88) Jackson, E. A.; Hillmyer, M. A. Nanoporous Membranes Derived from Block Copolymers: From Drug Delivery to Water Filtration. *ACS Nano* **2010,** *4* (7), 3548.

(89) van Rijn, P.; Tutus, M.; Kathrein, C.; Zhu, L.; Wessling, M.; Schwaneberg, U.; Boker, A. Challenges and advances in the field of self-assembled membranes. *Chemical Society Reviews* **2013,** *42* (16), 6578.

(90) Ahn, H.; Park, S.; Kim, S.-W.; Yoo, P. J.; Ryu, D. Y.; Russell, T. P. Nanoporous Block Copolymer Membranes for Ultrafiltration: A Simple Approach to Size Tunability. *ACS Nano* **2014,** *8* (11), 11745.

(91) Bockstaller, M. R.; Mickiewicz, R. A.; Thomas, E. L. Block copolymer nanocomposites: Perspectives for tailored functional materials. *Advanced Materials* **2005,** *17* (11), 1331.

(92) Kao, J.; Thorkelsson, K.; Bai, P.; Rancatore, B. J.; Xu, T. Toward functional nanocomposites: taking the best of nanoparticles, polymers, and small molecules. *Chemical Society Reviews* **2013,** *42* (7), 2654.

(93) Orilall, M. C.; Wiesner, U. Block copolymer based composition and morphology control in nanostructured hybrid materials for energy conversion and storage: solar cells, batteries, and fuel cells. *Chemical Society Reviews* **2011,** *40* (2), 520.

(94) Segalman, R. A. Patterning with block copolymer thin films. *Materials Science and Engineering: Reports: R.* **2005,** *48* (6), 191.

(95) Bang, J.; Jeong, U.; Ryu, D. Y.; Russell, T. P.; Hawker, C. J. Block Copolymer Nanolithography: Translation of Molecular Level Control to Nanoscale Patterns. *Advanced Materials* **2009,** *21* (47), 4769.

(96) Killops, K. L.; Gupta, N.; Dimitriou, M. D.; Lynd, N. A.; Jung, H.; Tran, H.; Bang, J.; Campos, L. M. Nanopatterning Biomolecules by Block Copolymer Self-Assembly. *ACS Macro Letters* **2012,** *1* (6), 758.

(97) Bates, C. M.; Maher, M. J.; Janes, D. W.; Ellison, C. J.; Willson, C. G. Block Copolymer Lithography. *Macromolecules* **2014,** *47* (1), 2.

(98) Sinturel, C.; Bates, F. S.; Hillmyer, M. A. High Chi-Low N Block Polymers: How Far Can We Go? *ACS Macro Letters* **2015,** *4* (9), 1044.

(99) Speetjens, F. W., II; Carter, M. C. D.; Kim, M.; Gopalan, P.; Mahanthappa, M. K.; Lynn, D. M. Post-Fabrication Placement of Arbitrary Chemical Functionality on Microphase-Separated Thin Films of Amine-Reactive Block Copolymers. *ACS Macro Letters* **2014,** *3* (11), 1178.

(100) Pascual, S.; Blin, T.; Saikia, P. J.; Thomas, M.; Gosselin, P.; Fontaine, L. Block Copolymers Based on 2-Vinyl-4,4-dimethyl-5-oxazolone by RAFT Polymerization: Experimental and Computational Studies. *Journal of Polymer Science Part A: Polymer Chemistry* **2010,** *48* (22), 5053.

(101) Choi, J. W.; Carter, M. C. D.; Wei, W.; Kanimozi, C.; Speetjens, F. W., II; Mahanthappa, M. K.; Lynn, D. M.; Gopalan, P. Self-Assembly and Post-Fabrication Functionalization of Microphase-Separated Thin Films of a Reactive Azlactone-Containing Block Copolymer. **2016,** *Submitted.*

(102) Carter, M. D. C.; Jennings, J.; Speetjens, F. W., II; Mahanthappa, M. K.; Lynn, D. M. A Reactive Platform Approach for the Rapid Synthesis and Discovery of High *X*/Low N Block Polymers. **2016,** *DOI: 10.1021/acs.macromol.6b01268*.

(103) Carter, M. C. D.; Jennings, J.; Appadoo, V.; Lynn, D. M. Synthesis and Characterization of Backbone Degradable Azlactone-Functionalized Polymers. *Macromolecules* **2016,** *49* (15), 5514.

(104) Appadoo, V.; Carter, M. C. D.; Lynn, D. M. Controlling the Surface-Mediated Release of DNA Using 'Mixed Multilayers'. *Bioengineering & Translational Medicine* **2016**, DOI: 10.1002/btm2.10023.

(105) Kratochvil, M. J.; Carter, M. C. D.; Lynn, D. M. Non-Woven and Amine-Reactive Nanofiber Mats Fabricated by the Electrospinning of Azlactone-Functionalized Polymers. **2016,** *Submitted*.

(106) Nguyen, S. T.; Gin, D. L.; Hupp, J. T.; Zhang, X. Supramolecular chemistry: functional structures on the mesoscale. *Proceedings of the National Academy of Sciences U.S.A.* **2001,** *98* (21), 11849.

(107) Gin, D. L.; Bara, J. E.; Noble, R. D.; Elliott, B. J. Polymerized lyotropic liquid crystal assemblies for membrane applications. *Macromolecular Rapid Communications* **2008,** *29* (5), 367.

(108) Zhao, X.; Pan, F.; Xu, H.; Yaseen, M.; Shan, H.; Hauser, C. A. E.; Zhang, S.; Lu, J. R. Molecular self-assembly and applications of designer peptide amphiphiles. *Chemical Society Reviews* **2010,** *39* (9), 3480.

(109) Fong, C.; Le, T.; Drummond, C. J. Lyotropic liquid crystal engineering-ordered nanostructured small molecule amphiphile self-assembly materials by design. *Chemical Society Reviews* **2012,** *41* (3), 1297.

(110) Molinaro, A.; Holst, O.; Di Lorenzo, F.; Callaghan, M.; Nurisso, A.; D'Errico, G.; Zamyatina, A.; Peri, F.; Berisio, R.; Jerala, R.et al. Chemistry of Lipid A: At the Heart of Innate Immunity. *Chemistry-A European Journal* **2015,** *21* (2), 500.

(111) Raetz, C. R. H.; Whitfield, C. Lipopolysaccharide Endotoxins. *Annual Review of Biochemistry* **2002,** *71*, 635.

(112) Weary, M. E. Understanding and Setting Endotoxin Limits. *PDA Journal of Pharmaceutical Science and Technology* **1990,** *44* (1), 16.

(113) Malyala, P.; Singh, M. Endotoxin Limits in Formulations for Preclinical Research. *Journal of Pharmaceutical Sciences* **2008,** *97* (6), 2041.

(114) Lin, I. H.; Miller, D. S.; Bertics, P. J.; Murphy, C. J.; de Pablo, J. J.; Abbott, N. L. Endotoxin-induced structural transformations in liquid crystalline droplets. *Science* **2011,** *332* (6035), 1297.

(115) Miller, D. S.; Abbott, N. L. Influence of droplet size, pH and ionic strength on endotoxin-triggered ordering transitions in liquid crystalline droplets. *Soft Matter* **2013,** *9* (2), 374.

(116) Miller, D. S.; Wang, X.; Abbott, N. L. Design of Functional Materials Based on Liquid Crystalline Droplets. *Chemistry of Materials* **2014,** *26* (1), 496.

(117) Miller, D. S.; Wang, X.; Buchen, J.; Lavrentovich, O. D.; Abbott, N. L. Analysis of the Internal Configurations of Droplets of Liquid Crystal Using Flow Cytometry. *Analytical Chemistry* **2013,** *85* (21), 10296.

(118) Carter, M. C. D.; Miller, D. S.; Jennings, J.; Wang, X.; Mahanthappa, M. K.; Abbott, N. L.; Lynn, D. M. Synthetic Mimics of Bacterial Lipid A Trigger Optical Transitions in Liquid Crystal Microdroplets at Ultralow Picogram-per-Milliliter Concentrations. *Langmuir* **2015,** *31* (47), 12850.

(119) Mulet, X.; Boyd, B. J.; Drummond, C. J. Advances in drug delivery and medical imaging using colloidal lyotropic liquid crystalline dispersions. *Journal of Colloid and Interface Science* **2013,** *393*, 1.

(120) Zabara, A.; Mezzenga, R. Controlling molecular transport and sustained drug release in lipid-based liquid crystalline mesophases. *Journal of Controlled Release* **2014,** *188*, 31.

(121) Kinsinger, M. I.; Buck, M. E.; Abbott, N. L.; Lynn, D. M. Immobilization of Polymer-Decorated Liquid Crystal Droplets on Chemically Tailored Surfaces. *Langmuir* **2010,** *26* (12), 10234.

(122) Guo, X.; Manna, U.; Abbott, N. L.; Lynn, D. M. Covalent Immobilization of Caged Liquid Crystal Microdroplets on Surfaces. *ACS Applied Materials & Interfaces* **2015,** *7* (48), 26892.

Chapter 2

Covalently Crosslinked and Physically Stable Polymer Coatings with Chemically Labile and Dynamic Surface Features Fabricated by Treatment of Azlactone-Containing Multilayers with Alcohol-, Thiol-, and Hydrazine-Based Nucleophiles‡

‡ Portions of this chapter have previously been published as: Carter, M.C.D.; Lynn, D.M. "Covalently Crosslinked and Physically Stable Polymer Coatings with Chemically Labile and Dynamic Surface Features Fabricated by Treatment of Azlactone-Containing Multilayers with Alcohol-, Thiol-, and Hydrazine-Based Nucleophiles." *Chemistry of Materials* **2016**, *28*, 5063-5072.

ABSTRACT: We report approaches to the design of covalently crosslinked and physically stable surface coatings with chemically labile and dynamic surface features based on the functionalization of azlactone-containing materials with alcohol-, thiol-, and hydrazine-based nucleophiles. Past studies demonstrate that residual azlactone groups in polymer multilayers fabricated by the reactive layer-by-layer assembly of poly(2-vinyl-4,4-dimethylazlactone) and branched poly(ethylenimine) can react with amine-based nucleophiles to impart new surface and bulk properties through the creation of chemically stable amide/amide-type bonds. Here, we demonstrate that the azlactone groups in these covalently crosslinked materials can also be functionalized using less nucleophilic alcohol- or thiol-containing compounds, using an organic catalyst, or converted to reactive acylhydrazine groups by direct treatment with hydrazine. These methods (i) broaden the pool of molecules that can be used for post-fabrication functionalization to include compounds containing alcohol, thiol, or aldehyde groups, and (ii) yield surface coatings with chemically labile amide/ester-, amide/thioester-, and amide/imine-type bonds that make possible the design of new dynamic and stimuli-responsive materials (e.g., surfaces that release covalently-bound molecules or undergo changes in extreme wetting behaviours in response to specific chemical stimuli). Our results expand the range of functionality that can be installed in, and thus the range of new functions that can be imparted to, azlactone-containing coatings beyond those that can be accessed using primary amine-based nucleophiles. The chemical approaches demonstrated here using model polymer-based reactive multilayer coatings are general, and should thus also prove useful for the design of new responsive surfaces based on other types of azlactone-functionalized materials.

Introduction

The layer-by-layer assembly of polymers on surfaces is a well-studied and versatile method for the fabrication of composite materials and provides means to define many important physical and chemical properties of polymer-based coatings.[1-9] These layer-by-layer approaches generally fall into one of two broad categories depending on the types of molecular interactions that are used to drive film growth—e.g., either (i) polyvalent weak interactions between mutually interacting polymers[1,5,6,9,10] or (ii) the formation of covalent bonds between mutually reactive polymers.[11-14] The latter 'reactive' or 'covalent' approaches offer several potential practical advantages relative to methods that rely on assembly coordinated through weak interactions, including the fact that they lead to covalently crosslinked coatings that can exhibit enhanced physical and chemical stability in complex media.[11-14] In addition, the use of reactive polymers to drive assembly often yields reactive coatings that can be further functionalized to impart new surface or bulk properties after fabrication. Many different reactive polymers have been investigated with these goals in mind,[11-14] with the overall facility and extent to which physical stability, chemical reactivity, and other features can be exploited depending heavily upon the chemical nature of the reactive materials that are used as building blocks during assembly.

The work reported here was motivated by a series of past studies from our group demonstrating that polymers bearing amine-reactive azlactone functionality can be used to drive reactive layer-by-layer assembly with polymers that contain primary amines.[14,15] We have investigated this approach extensively using poly(2-vinyl-4,4-dimethylazlactone) (PVDMA) and branched poly(ethylenimine) (PEI) as a model for the design of new classes of functional thin films.[15-22] Azlactones react rapidly, through ring-opening reactions, with primary amines under mild conditions,[15,23] leading to unique and stable 'amide/amide'-type crosslinks between

polymer chains, and residual azlactone functionality in the resulting PEI/PVDMA multilayers can be used as reactive handles for further functionalization by treatment with any of a broad range of readily available amine-based nucleophiles to impart new surface and bulk properties[16-21,24-28] (again, through the creation of unique and chemically stable 'amide/amide'-type bonds; Scheme 1). Several recent reports highlight the utility of azlactone groups and the use of azlactone-functionalized polymers as reactive platforms for the design of new functional materials, surfaces, and interfaces of interest in many other contexts.[15,23,29-42]

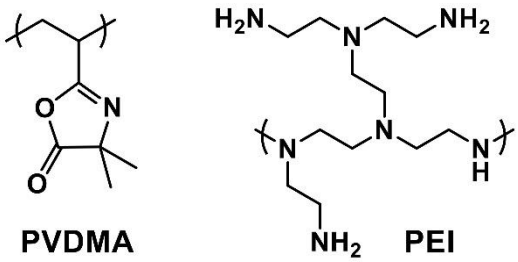

In this current study, we sought to develop new approaches to tailor the surface and bulk properties of azlactone-containing materials using other classes of non-amine-based nucleophiles (Scheme 1). Azlactone groups are understood to react with primary alcohols and thiols under certain conditions (e.g., in the presence of a catalyst and at higher temperatures),[23,43-45] but the use of these nucleophiles to design new materials is far less developed than approaches that exploit the reactivity of azlactones with more nucleophilic primary amines.[39,40,46] We reasoned that strategies for the rapid and robust functionalization of azlactone groups in polymer multilayer assemblies using primary alcohols and thiols could be broadly useful in at least two ways. First, such methods would substantially increase the pool of commercially or readily available molecules that is available for post-fabrication functionalization (and, thus, expand the range of new properties that could be imparted to azlactone-containing assemblies). Second, the

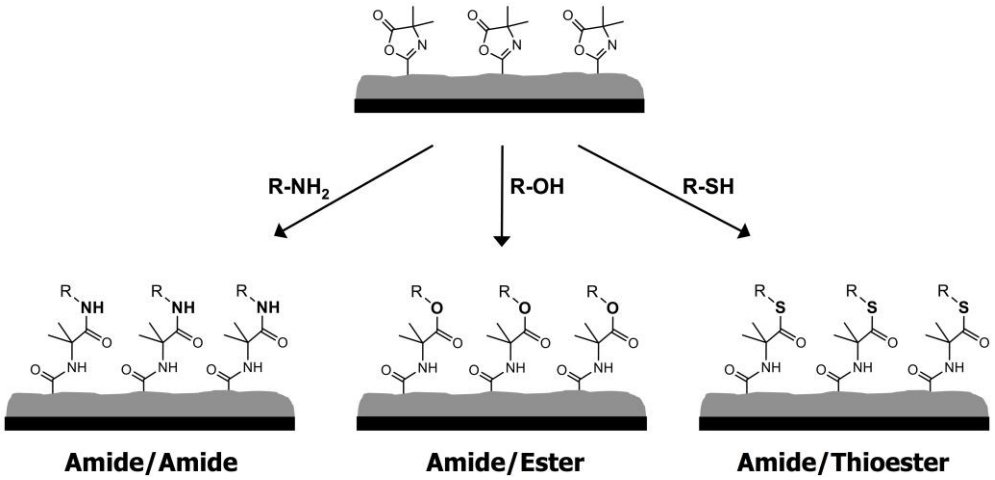

Scheme 1. Schematic illustration showing the chemical structures of residual azlactone groups in PEI/PVDMA polymer films and the products of the reaction of these azlactone groups with amine-, alcohol- and thiol-based nucleophiles.

reaction of azlactones with primary alcohols and thiols results in the formation of unique 'amide/ester'- and 'amide/thioester'-type bonds (e.g., Scheme 1) that, in contrast to the chemically stable amide/amide bonds formed by reactions with primary amines, can be hydrolyzed under relatively mild conditions. Methods for the functionalization of otherwise stable and covalently crosslinked coatings with these chemically labile and dynamic surface features could thus provide new strategies for the design of surfaces and coatings with dynamic and stimuli-responsive properties.

Here, we report new approaches to the functionalization of azlactone-containing PEI/PVDMA multilayers using primary alcohol- and thiol-containing nucleophiles. We demonstrate that alcohol- or thiol-containing compounds can react uniformly and extensively with the residual azlactone functionality in these materials when an organic catalyst is used, and that the physical and chemical properties of these nucleophiles (e.g., whether they are hydrophobic or hydrophilic, etc.) can be used to dictate interfacial properties and pattern useful

surface features. We demonstrate further that the amide/ester and amide/thioester groups that result from these reactions can be cleaved under mild conditions in aqueous environments, leading to dynamic and responsive materials that can release covalently-bound molecules into surrounding media or undergo changes in extreme wetting behaviours that cannot be achieved using coatings functionalized with primary amines. Finally, we report approaches to the post-fabrication conversion of installed thioester groups to acylhydrazine functionality that can react through 'click-like' reactions with aldehydes[47,48] to anchor new surface features through acid-responsive imine bonds. Our results expand the range of chemical functionality and new functions that can be imparted to azlactone-containing materials beyond those that can be attained by functionalization using primary amines. The strategies reported here, demonstrated using model polymer-based reactive multilayer coatings, should also prove useful for the design of new materials based on other types of azlactone-functionalized polymers, assemblies, and coatings.

Materials and Methods.

Materials. 2-Vinyl-4,4-dimethylazlactone (VDMA) was a kind gift from Dr. Steven M. Heilmann (3M Corporation, Minneapolis, MN). Poly(2-vinyl-4,4-dimethylazlactone) (PVDMA) used to fabricate polymer multilayers was synthesized by polymerization of VDMA in the presence of 7 wt% of intentionally added cyclic azlactone-functionalized oligomers, as described previously.[24] Solution-phase functionalization of PVDMA was performed using PVDMA synthesized in the absence of cyclic azlactone-functionalized oligomers.[22] Branched poly(ethyleneimine) (PEI; MW ~25,000), ethylenediamine (99%), *n*-decylamine (95%), *n*-decanol (99%), decanethiol (96%), pyrenebutanol (99%), pyrene (98%), 1,8-diazabicycloundec-

7-ene (DBU, 98%), hydrazine (anhydrous, 98%), octyl aldehyde (99%), acetone (ACS grade), hexanes (technical grade), methanol (MeOH, ACS grade), dichloromethane (DCM, ACS grade), dichloroethane (DCE, ACS grade), tetrahydrofuran (THF, HPLC grade), and deuterated chloroform ($CDCl_3$, 99.8%) were purchased from Sigma-Aldrich (Milwaukee, WI). Tetramethylrhodamine (TMR) was obtained from Anaspec (Fremont, CA). Ethanol (EtOH, 200 proof) was obtained from Decon Labs (King of Prussia, PA). Glass microscope slides and phosphate-buffered saline (PBS 10X) were purchased from Fisher Scientific (Pittsburgh, PA). Sheets of poly(ethylene terephthalate) (PET 0.004 in. thick) were purchased from McMaster Carr (Elmhurst, IL). Water with a resistivity of 18.2 MΩ was obtained from a Millipore filtration system. All chemicals were used as received.

General Considerations. ^{1}H NMR spectroscopy was performed using a Bruker Avance-500 (500 MHz) spectrometer using a relaxation delay of 10 seconds. Spectra were referenced relative to the residual proton peak of $CDCl_3$ (δ7.26 ppm). Gel permeation chromatography (GPC) was performed using a Viscotek GPC Max VE2001 equipped with two Polymer Laboratories PolyPore columns (250 mm × 4.6 mm) and a TDA-302 detector array, using THF as the eluent at a flow rate of 1 mL/min at 40 °C. The GPC instrument was calibrated using 10 narrow dispersity polystyrene standards with M_n = 0.580−377.4 kg/mol (Agilent Technologies Santa Clara, CA). Solid-state fluorescence emission traces of dry thin films were obtained using a Hitachi FL-4500 FL spectrophotometer. Samples were placed in a quartz cuvette at 45° relative to the incident beam (λ_{ex} = 343.0 nm) and data were collected over a range from 350 – 700 nm. Excitation and emission slits were set to 5.0 nm and the PMT operated at a voltage of 950 V with a response time of 0.1 s. Data was smoothed by 7 points. Fluorescence micrographs were obtained using an

Olympus IX70 microscope equipped with a Lumen Dynamics XCite 120PC-Q fluorescence source and a Q Imaging EXi Aqua camera at a magnification of 4x and an exposure time of 400 ms. Images were analyzed and false-colored using MetaMorph Advanced software, version 7.7.8.0 (Molecular Devices, LLC). Fluorescence measurements of pyrenebutanol and pyrene released from thin films into PBS buffer solution were made using a Jobin Yvon FluoroMax-3 fluorimeter. Films (0.9 x 1 cm) were submerged in 800 μL of PBS solution (pH 7.4) and incubated at 37 °C in the dark. The fluorescence emission of the release solution was measured in a low-volume quartz cuvette (QS 10,00 Sigma Aldrich, Milwaukee, WI) over a range from 350 – 700 nm by excitation at λ = 343 nm. The fluorescence of the release solution was measured three times for each sample and then returned to the original solution; data was corrected by measuring a blank solution (PBS only) in the same cuvette. Attenuated total reflectance (ATR) infrared (IR) measurements were obtained on a Bruker Tensor 27 FTIR spectrometer outfitted with a Pike Technologies Diamond ATR stage (Madison, WI.) Data was analyzed using Opus Software version 6.5 (Bruker Optik GmbH). Spectra were collected at a resolution of 2 cm^{-1} and were an average of 32 scans. Data were smoothed by applying a 9-point average and baseline corrected using a concave rubberband correction (10 iterations, 64 points). Contact angle measurements were made using a Dataphysics OCA 15 Plus contact angle goniometer at ambient temperature with 4 μL of either 18.2 MΩ Millipore water or DCE in at least 3 different locations on each film. Where DCE contact angles were measured underwater, films were submerged in a vial containing Millipore water. Fluorescence images of TMR-loaded films were acquired using a GeneTAC UC 4 x 4 fluorescence scanner (Genomic Solutions) and analyzed using ImageJ (NIH, Bethesda, MD). Digital images were acquired using a Canon

PowerShot SX130 IS digital camera. Compressed air used to dry samples was filtered through a 0.2 μm membrane nylon syringe filter.

Substrate Preparation. Prior to the fabrication of reactive PEI/PVDMA multilayer films, glass and PET substrates were prepared as follows. Glass slides (~0.9 cm x 5.5 cm) were cleaned with deionized water and acetone and dried under a stream of compressed air. Amine functionality was installed on PET strips (~0.9 cm x 5.5 cm) by adopting a procedure described previously.[49] Briefly, strips of PET were sonicated for 15 mins in EtOH and then rinsed with fresh EtOH and dried with compressed air. The substrates were placed in a solution of ethylenediamine in MeOH (70 % v/v) in an oil bath set to 50 °C for 25 minutes. Substrates were removed and rinsed copiously with deionized water and MeOH and then dried with compressed air. Immediately prior to film fabrication, substrates were submerged in a NaOH solution (20 μL of 1M NaOH in 20 mL H_2O) for ~1 min and then rinsed with acetone and dried in compressed air.

Film Fabrication. PEI/PVDMA multilayers were fabricated on glass substrates using the following general procedure: (i) substrates were submerged in a solution of PEI (20 mM in acetone with respect to the polymer repeat unit) for 20 s; (ii) substrates were removed and immersed in an initial acetone bath for 20 s followed by a second acetone bath for 20 s; (iii) substrates were submerged in a solution of PVDMA (20 mM in acetone with respect to the polymer repeat unit) for 20 s; and (iv) substrates were removed and rinsed again using the procedure outlined under step (ii). For thin, transparent films on glass, this cycle was repeated 10 times and the rinse solutions were changed every two cycles to give films composed of 10 layer pairs (or 'bilayers'). For thicker, hydrophobic films, this cycle was repeated 35 times, without

changing the rinse solutions to yield films 35 bilayers thick. After fabrication, films were washed copiously with acetone from a spray bottle and then dried under a stream of compressed air. For PEI/PVDMA multilayers deposited on aminated PET substrates, the same general procedure was followed; however, fabrication began with submersion of the substrate in a solution of PVDMA, as described previously,[22,26] to allow for covalent attachment of the first layer. These films were terminated with a final layer of PVDMA.

Solution-Phase Functionalization of PVDMA with Pyrenebutanol. In a typical reaction, 44.26 mg (0.318 mmol) of PVDMA and 4.37 mg (0.0159 mmol) of pyrenebutanol were dissolved in 4 mL of DCM in a glass vial charged with a stir bar to give a light yellow solution. DBU [0.23 μL (0.0016 mmol; 0.1 equiv. w.r.t. pyrenebutanol)] was added to the solution and the vial was capped, sealed with parafilm, and stirred at 50 °C overnight. This light yellow solution was concentrated on a rotary evaporator to ~1 mL total volume and then precipitated into ~10 mL of hexanes. The resulting white powder was dissolved in ~1.5 mL of DCM and precipitated once more into ~10 mL hexanes and dried overnight under high vacuum.

Functionalization of Polymer Multilayers Using Amine-, Alcohol-, and Thiol-Containing Nucleophiles. Films were functionalized with nucleophiles using the following general procedure. Treatment with pyrenebutanol and pyrene (serving as a control) was performed by immersing a 10-bilayer film (0.9 x 1 cm) on a glass substrate in 1.5 mL of the desired fluorophore solution (40 mg/mL in DCE) in a glass vial, followed by the addition of 2 μL of DBU. The vial was capped, sealed with parafilm, and left on a shaker plate overnight at room temperature. Films were removed and rinsed copiously with DCE, and then placed in large vials

containing fresh DCE rinse solution for several days in order to remove any non-specifically adsorbed fluorophore and the DBU catalyst. The rinse solution was changed several times each day. Films were finally rinsed with ~25 mL each of DCM, methanol, water, and acetone, and then dried in a stream of compressed air. Decanol and decanethiol treatments were performed in a similar manner by immersing films (~0.9 cm x 3 cm) in ~4 mL of the desired nucleophile solution (1:1 wt/wt in DCE) in a glass vial followed by addition of 54 μL of DBU. The vial was capped, sealed with parafilm, and left on a shaker plate overnight. Films were rinsed copiously with DCE and then DCM before being placed in DCM rinse vials for several days, as above. Decylamine and hydrazine functionalization reactions were performed by immersing a film (~0.9 cm x 3 cm) in a ~4 mL solution of either decylamine (20 mg/mL in THF) or anhydrous hydrazine (20 mg/mL in MeOH) overnight and then rinsing with THF or MeOH, respectively, and then acetone, before drying in a stream of compressed air.

Hydrolysis of Ester and Thioester Bonds in Functionalized Films. Experiments designed to characterize the hydrolysis of the ester bonds in multilayers functionalized using decanol were performed by placing small droplets (see main text) of aqueous NaOH (0.05 M) onto the surface of a film and incubating it in a humid chamber for pre-determined periods of time. The NaOH droplet was rinsed from the surface of the film using Millipore water and then subsequently with acetone before drying in compressed air. To facilitate imaging, newly created hydrophilic spots on these films were loaded selectively with TMR by submersion of the entire film into an aqueous solution of the dye (~0.05 mg/mL) for ~2 seconds. To demonstrate the reactivity of thioester bonds in decanethiol-treated films, samples (0.9 x 1 cm) were immersed in 1.5 mL of

hydrazine solution (20 mg/mL in MeOH) at 50 °C, removed after pre-determined periods of time, rinsed in MeOH and acetone, and then dried in compressed air prior to characterization.

Reversible Reactions of Imine Bonds in Hydrazine-Functionalized Multilayers. Films functionalized by treatment with hydrazine were treated with octyl aldehyde (20 mg/mL in MeOH) for 1 hour at room temperature and then rinsed copiously with MeOH and acetone before being dried in a stream of compressed air. The superhydrophobic films were cut to desired sizes (1 x 1 cm) and immersed in 2 mL of a 1 M HCl solution (1:1 H_2O:THF, v/v) overnight at room temperature. The resulting hydrophilic films were then removed and rinsed copiously with THF, water, and acetone before being dried in a stream of compressed air for contact angle analysis. Experiments were also performed without HCl by placing films into solutions of 1:1 v/v H_2O:THF and removing after pre-determined periods of time. This process (octyl aldehyde/acid treatment) was repeated several times to characterize the reversibility of the imine bond formation/hydrolysis reaction (see main text for details).

Results and Discussion

Functionalization of Azlactone-Containing Multilayers Using Alcohol-Based Nucleophiles

We first characterized the reactivity of the residual azlactone groups in PEI/PVDMA multilayers[16] with primary alcohol-based nucleophiles. These initial experiments were conducted using PEI/PVDMA multilayers 10 bilayers (~160 nm) thick and pyrenebutanol as a model fluorescent primary alcohol to facilitate characterization. Prior to experiments using azlactone-containing multilayers, we conducted studies using solutions of pyrenebutanol and PVDMA to identify reaction conditions that lead to efficient coupling. Past studies demonstrate that reactions

between azlactones and alcohols do not occur substantially in the absence of a catalyst, but that these reactions can be promoted by catalytic amounts of trifluoroacetic acid or strong amidine bases such as 1,8-diazabicycloundec-7-ene (DBU).[23,45,50] We selected DBU as a catalyst for these studies because this approach is more general and can also be used to promote reactions between azlactones and thiols (described below). The addition of pyrenebutanol to solutions of PVDMA in the presence of DBU (0.05 eq. pyrenebutanol, 0.1 eq. DBU with respect to pyrenebutanol) yielded copolymers containing both reactive azlactone functionality and pyrenebutanol-based side chains attached to the backbone through amide/ester linkages, as characterized by ^{1}H NMR spectroscopy and gel permeation chromatography (Fig. S1 and Fig. S2, respectively. Supporting Information can be found at the end of this chapter).

We functionalized PEI/PVDMA multilayer films by incubating film-coated substrates in solutions of pyrenebutanol using the general reaction conditions described above. Fig. 1A-C shows results of fluorimetry and fluorescence microscopy experiments performed using films treated with solutions of either pyrenebutanol or pyrene (as a non-nucleophilic and non-reactive control). Inspection of Fig. 1A reveals films treated with solutions of pyrenebutanol (solid line) to exhibit fluorescence emission characteristic of the pyrene moiety (λ_{ex} = 343 nm). In contrast, films treated with solutions of non-reactive pyrene did not exhibit any significant fluorescence (Fig. 1A; dashed line). Characterization of these films by fluorescence microscopy (Fig. 1B) also revealed that films treated with pyrenebutanol exhibit uniform fluorescence over large areas of the substrate (the inset of Fig. 1B shows an image of a pyrene-treated control film, which did not exhibit fluorescence). These results, when combined, are consistent with the DBU-catalyzed nucleophilic ring-opening of azlactone functionality by pyrenebutanol and the immobilization of this compound to the film through a covalent amide/ester bond (further support for this view is

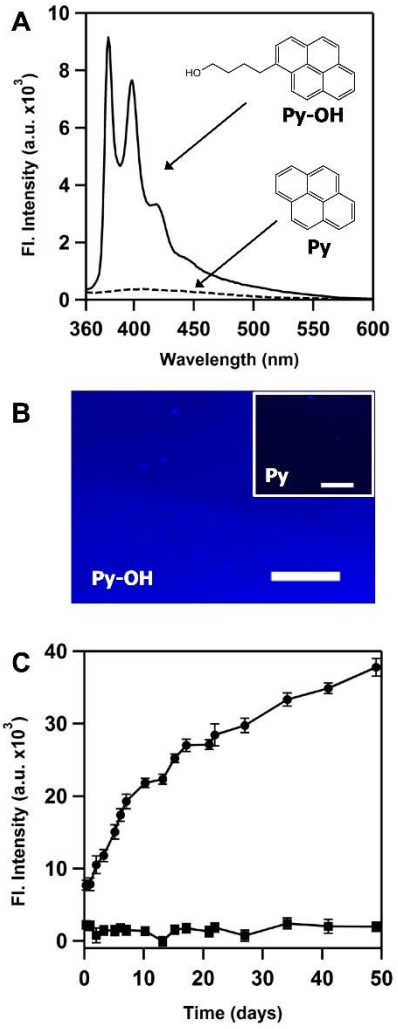

Figure 1. (A) Solid-state fluorescence emission (λ_{ex} = 343 nm) of thin PEI/PVDMA films functionalized with pyrenebutanol (solid line) and the corresponding control experiment performed with non-reactive pyrene (dashed line). (B) Fluorescence micrograph of a pyrenebutanol-functionalized film and (inset) the corresponding pyrene-treated control; both false-colored in blue. Scale bar = 0.25 mm. (C) Release profile for pyrenebutanol-functionalized thin films (circles) and control films treated with non-reactive pyrene (squares) in PBS buffer at 37 °C as monitored by fluorimetry (λ_{ex} = 343 nm, λ_{em} = 380 nm). Error bars represent the standard deviation of measurements obtained on two identically prepared films.

provided by IR spectroscopy measurements of an analogous transformation in the discussion below). The results of studies using non-reactive pyrene suggest that the fluorescence observed in films treated with pyrenebutanol does not arise from the physisorption of this relatively

hydrophobic molecule on the films. We note that, in the pyrenebutanol functionalized film shown in Fig. 1A, we did not observe a broad emission band centered near ~475 nm, characteristic of excited pyrene dimers (excimers),[51] when films were characterized in either the dry or wet state. Although the density of reactive azlactone groups in the PEI/PVDMA films prior to functionalization is not known, this observation suggests that pyrenebutanol groups were immobilized in these films at densities sufficiently low to prevent these self-associative interactions.

Additional experiments demonstrated that the amide/ester bonds resulting from the functionalization of PEI/PVDMA films with primary alcohols could be hydrolyzed under mild conditions to promote the release of covalently-bound molecules. Fig. 1C shows the results of experiments in which PEI/PVDMA coatings containing immobilized pyrenebutanol (fabricated as described above) were incubated in physiologically relevant media (phosphate-buffered saline, PBS; pH = 7.4, 37 °C). These results reveal the fluorescence of the PBS incubation buffer to increase steadily over a period of 50 days (Fig. 1C, circles; these films began to physically delaminate from their substrates after approximately 50 days and were not characterized further in these proof-of-concept studies; squares represent data obtained using control films treated with non-reactive pyrene). These results are consistent with the gradual hydrolysis of the amide/ester linkers in these materials and the subsequent release of pyrenebutanol into solution. It is also possible that this increase in solution fluorescence could arise from the gradual disassembly of these films and the release of fluorescently labeled polymers or oligomers. We consider this possibility to be unlikely in view of the covalently crosslinked nature of these PEI/PVDMA multilayers and the chemical stability of the amide/amide crosslinks that are formed during assembly.[28] Additional support for the labile nature of the amide/ester bonds in these materials is

provided by the results of other experiments described below. We note here that the hydrolysis of these amide/ester bonds releases pyrenebutanol in a manner that is 'traceless' (that is, cleavage of the linker by hydrolysis occurs in a way that does not change the structure or the function of the originally immobilized molecule). Although not investigated further as part of this study, this feature could prove useful for the development of coatings designed to promote the covalent immobilization and subsequent surface-mediated release of active alcohol-functionalized agents (e.g., alcohol-containing small-molecule drugs, etc.).

Modification of Interfacial Properties Using Alcohol- and Thiol-Based Nucleophiles

Past studies demonstrate that the surface energies and wetting behaviors of native (azlactone-containing) PEI/PVDMA films can be permanently modified (through the creation of amide/amide-type bonds) by treatment with primary amines functionalized with hydrophobic or hydrophilic groups.[18-21,24,26,28,42,52] Of particular note in the context of the work reported here, those prior studies reveal that when these covalent modifications are made to multilayers possessing nano- and microscale topographic features, this approach can also be used to design films that are superhydrophobic,[20,24,42,52] or extremely non-wetting to water [superhydrophobic surfaces are defined here as having advancing water contact angles (WCAs) >150°, with low water roll-off angles[53-55]]. The functionalization of nanoporous PEI/PVDMA films ~3.5 μm thick[21] by reaction with *n*-decylamine yielded an increase in WCA from 135.6° (± 1.9°) (Fig. 2A,E; for native, azlactone-functionalized films) to 158.3° (± 1.7°) (Fig. 2B,F; see Materials and Methods and additional past publications[21,52] for details related to the fabrication and characterization of nanoporous PEI/PVDMA multilayers). The images in Fig. 2C-D and H-G reveal that superhydrophobicity can also be achieved by the DBU-catalyzed reaction of residual

azlactones with the hydrophobic alcohol *n*-decanol (WCA = 160.3 ± 1.8°; panel G) and the hydrophobic thiol *n*-decanethiol (WCA = 159.0 ± 1.6°; panel H). These decanol- and decanethiol-functionalized films were uniformly superhydrophobic across the entirety of the material, with properties and behaviors that were both quantitatively and qualitatively similar to those exhibited by decylamine-functionalized films when placed in contact with or immersed in water (Fig. S3).

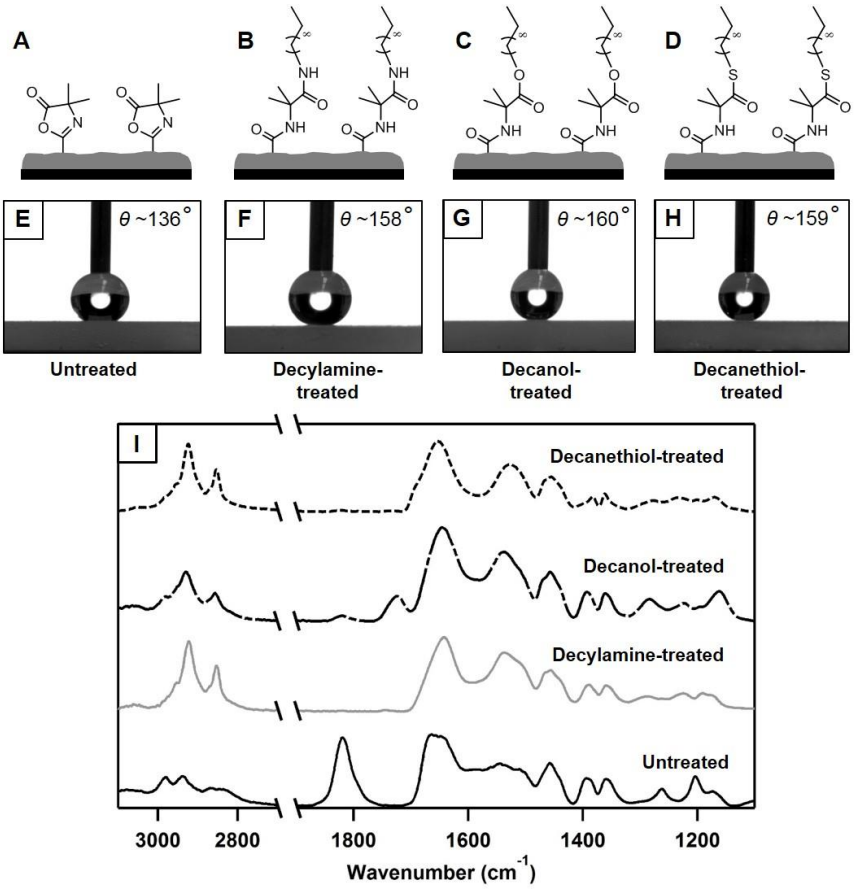

Figure 2. (A-D): Schematic illustrations and chemical structures representing unfunctionalized and functionalized PEI/PVDMA films: (A) an unfunctionalized azlactone-containing film and (B-D) films functionalized with (B) decylamine, (C) decanol, and (D) decanethiol. (E-F) Representative advancing WCA measurements for the corresponding films depicted in (A-D). (I) ATR IR spectra for the unfunctionalized film and decylamine-, decanol- or decanethiol-functionalized films.

Fig. 2I shows representative ATR IR spectra of an untreated (azlactone-containing) PEI/PVDMA film and decylamine-, decanol-, and decanethiol-treated films used in the experiments above. The IR spectrum of the untreated film exhibited a cyclic carbonyl C=O stretch characteristic of residual azlactone groups at 1819 cm^{-1}.[16,23] The two coalescing absorbance bands with peaks at 1666 cm^{-1} and 1646 cm^{-1} correspond to the C=N functionality in the azlactone ring and the C=O stretch of amide bonds that make up the crosslinks of the film, respectively.[16,23] For films treated with decylamine, the peak corresponding to the azlactone functionality at 1819 cm^{-1} was completely consumed, suggesting exhaustive reaction of the azlactone groups with the incoming amine-based nucleophile and consistent with the results of past studies.[16,23,25] For films treated with decanol, the intensity of the azlactone carbonyl stretch at 1819 cm^{-1} was nearly fully consumed, and a carbonyl C=O stretch at 1724 cm^{-1} appeared, consistent with the formation of ester bonds upon the ring-opening of the azlactone groups with this alcohol-based nucleophile. Finally, for films treated with decanethiol, the azlactone peak was also consumed and close inspection of the data reveals a shoulder on the amide C=O stretch (near 1652 cm^{-1}) that we attribute to the C=O carbonyl stretching of thioester functionality. These results, when combined, are consistent with the ring-opening of residual azlactone heterocycles by these alcohol- and thiol- based nucleophiles under these DBU-catalyzed conditions. Control reactions performed using decanol or decanethiol in the absence of catalytic DBU did not proceed significantly, as determined by IR spectroscopy (Fig. S4), suggesting that the alkoxide and thiolate forms of these nucleophiles are required to ring-open the azlactone.

The results of additional experiments demonstrated that, whereas the superhydrophobicity of decylamine-treated PEI/PVDMA films can typically be maintained for long periods in aqueous environments,[20,24] the extremely non-wetting behaviors of decanol- and

decanethiol-treated films could be permanently erased and eliminated by exposure to aqueous analytes that cleave ester and thioester bonds. For these experiments, we used PEI/PVDMA films fabricated on amine-functionalized poly(ethylene terephthalate) (PET) substrates to improve stability at the film/substrate interface and reduce the likelihood of film delamination (see Materials and Methods for additional details).[22,26]

In an initial series of experiments, we characterized the wetting behaviors of decylamine- and decanol-treated films exposed to aqueous base, reasoning that the hydrolysis of ester bonds would reveal hydrophilic carboxylic acid groups (e.g., Fig. 3A) and result in large reductions in WCAs. Fig. 3C shows the results of an experiment in which a large aqueous droplet of 50 mM NaOH was placed onto the surfaces of both decylamine- and decanol-treated films in a humid environment for ~3 hours at room temperature. Inspection of these results reveals a large reduction in the WCA of the decanol-treated film (from ~160° to ~126.9 ± 2.2°; Fig. 3C, gray bars) in the areas of the film treated with aqueous base. In contrast, the WCA of the decylamine-treated films remained largely unaffected under these conditions (Fig. 3C, black bars). These results are also consistent the hydrolysis of the ester bonds of decanol-treated materials. The hydrolyzed regions of the decanol-treated films were rapidly and uniformly wet when contacted with water, whereas surrounding areas that were not treated remained superhydrophobic and were jacketed by a layer of air, as is typical of superhydrophobic surfaces in the Wenzel-Cassie state,[53,54,56] when immersed in water (Fig. S3). This observation suggests new approaches to the chemical patterning of superhydrophobic materials and provides a basis for the design of new surfaces with patterned contrasts in wettability.[27,52,57,58] To demonstrate this approach, we used the selective deposition of small (10 μL) droplets of aqueous base to pattern a small array of hydrophilic spots distributed within a superhydrophobic background (Fig. 3E; small droplets of

colored water show the locations of the hydrophilic spots; a larger droplet reveals the maintenance of superhydrophobicity in surrounding, untreated areas). These arrays of hydrophilic spots could also be used to directly capture and position small samples of water (Fig. 3F) by direct dipping into aqueous solutions without substantial wetting or contamination of the surrounding superhydrophobic surfaces.

Finally, we performed a similar series of experiments using superhydrophobic decanethiol-treated films to determine if these thioester-functionalized films could be induced to undergo changes in structure and wetting behavior in response to a specific chemical stimulus. For these experiments, we used hydrazine as a model nucleophile to attack the thioester and displace hydrophobic decyl chains (Fig. 3B). Fig. 3D shows the results of experiments in which decanethiol-functionalized films were treated with hydrazine over a period of ~11 hours. These results reveal a dramatic reduction in WCA from >150° to ~75.0° (± 6.2°) for decanethiol-functionalized films (gray bars; results using decylamine-functionalized films treated with hydrazine were again stable and did not exhibit changes in contact angle under these conditions; Fig. 3D; black bars). We note here that we also observed a formal loss of superhydrophobicity in decanethiol-functionalized films at shorter reaction times; for example, WCAs decreased to ~134.2° (± 5.3°) after ~5 hours, suggesting that lower exposure times could be used in instances where simple transitions in wetting states are desired. These results are consistent with the hydrazine-mediated cleavage of the hydrophobic thioester groups and the installation of more hydrophilic acylhydrazine groups (Fig. 3B; additional characterization of this transformation by IR spectroscopy is shown in Fig. S5).

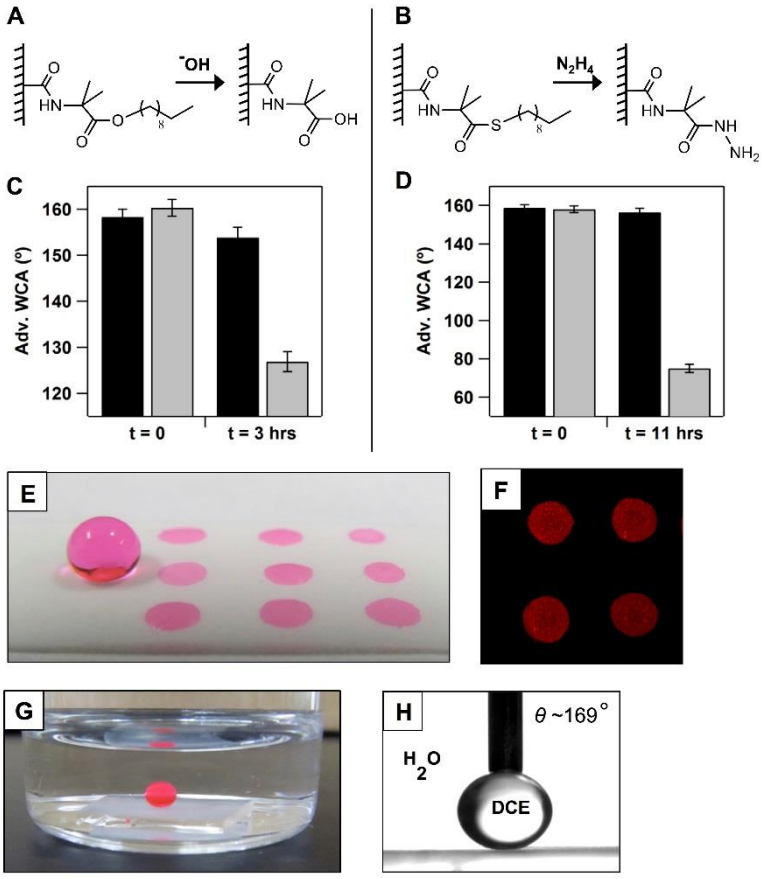

Figure 3. Representative chemical structures of PEI/PVDMA films functionalized with (A) decanol (left), and the result after treatment by hydroxyl ions (right), and (B) films functionalized with decanethiol (left), and the result after treatment with hydrazine (right). (C) Change in the advancing WCA of decanol-functionalized films (gray bars) and decylamine-functionalized films (black bars) after exposure to 50 mM aqueous NaOH. (D) Change in the advancing WCA of decanethiol-functionalized films (gray bars) and decylamine-functionalized films (black bars) after exposure to hydrazine. Errors bars in (C) and (D) represent the standard deviation of measurements obtained on three identical samples. (E) Digital picture of a 3 x 3 array of hydrophilic spots patterned on a decanol-functionalized film by hydrolysis with droplets of aqueous base; a large droplet of water placed nearby beads up on the untreated and still superhydrophobic region surrounding the hydrolyzed spots; see text for complete details. (F) Fluorescence micrograph of a 2 x 2 array of hydrophilic spots prepared the same manner as in (E), after submersion of the film into a solution of aqueous fluorophore (TMR) to load the hydrophilic pattern. (G) Digital image of an oil droplet (dichloroethane, DCE) on the surface of an underwater superoleophobic film (~1 x 1 cm) submerged in a vial underwater. (H) Advancing underwater oil contact angle for the same film as in (G). Droplets in (E) and (G) were colored red to aid visualization.

The inherent nano- and microscale roughness of the superhydrophobic coatings used here and in past reports,[20,21,24,42,52] combined with the degree of hydrophilicity induced by treatment with hydrazine and the cleavage of hydrophobic thioester functionality (Fig. 3B,D), resulted in films that were highly absorbent to water but extremely repellant of oils when placed in aqueous environments (a phenomenon known as underwater superoleophobicity[55,59]). Fig. 3G shows a droplet of a model oil (dichloroethane, stained with a red hydrophobic dye) placed on a hydrazine-treated film submerged in water. As shown in Fig. 3H, this surface exhibits an underwater advancing oil contact angle of 165.8° (± 0.8°), indicating a transition to a robust and extremely oil repellant state (whereas the surface is fully wet by water when exposed to air; not shown). This feature, combined with the ability to chemically pattern regions of hydrophilicity on these substrates (*e.g.*, as described above), could prove useful for the design of surfaces that can capture, manipulate, and guide the transport of oily substances in underwater environments.[56]

Characterization of Reactive Acylhydrazine-Functionalized Multilayers

The ability to functionalize azlactone-containing films using alcohol- and thiol-based nucleophiles substantially expands the range of additional molecules that can be installed and, as described above, introduces new functionality (e.g., chemically labile linkers) that can lead to materials with new and useful behaviors that differ substantially from those designed using primary amine-based nucleophiles. It occurred to us that the introduction of acylhydrazine groups in the work described above—a byproduct of treatment with hydrazine to cleave surface-bound thioester functionality—could also be used as a useful reactive synthon that could further expand the range of functional groups that could be installed in these materials (i.e., by

broadening the pool further, to include the immobilization of aldehyde-containing molecules; Fig. 4A) and, thus, the range of functionality that can be achieved through the installation of acid-labile imine bonds and other chemically reversible groups.

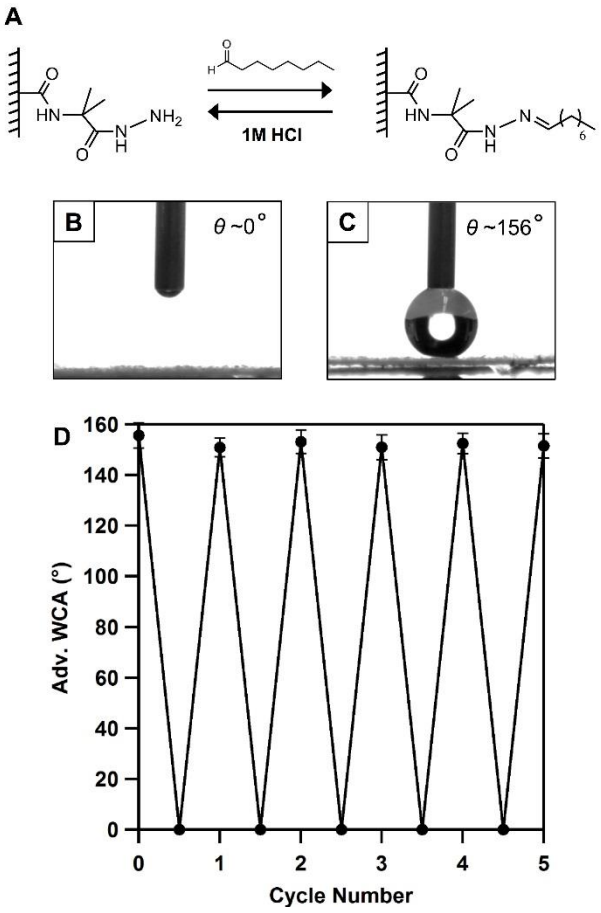

Figure 4. (A) Representative chemical structures of PEI/PVDMA films functionalized with hydrazine (left), and the result after treatment with octyl aldehyde (right). Acylhydrazine groups can be restored by cleavage of the imine bond under acidic conditions (reverse direction; left). (B) Advancing WCA for a hydrophilic, acylhydrazine-functionalized film (A, left) and (C) for a superhydrophobic octyl aldehyde-functionalized film (A, right). (D) Plot showing the reversibility of the process illustrated in (A), as monitored by changes in advancing WCA during iterative treatments in octyl aldehyde and acidic media. Error bars represent the standard deviation of measurements obtained on three identically prepared films.

To explore the feasibility of this approach, we performed experiments using nanoporous PEI/PVDMA multilayers reacted exhaustively with hydrazine (20 mg/mL in methanol, overnight; as determined by IR spectroscopy; Fig. S6). These acylhydrazine-functionalized films were superhydrophilic (they exhibited WCAs of ~0°; Fig. 4B) and were extremely non-wetting to oils when submerged in water, as expected from our observations described above (e.g., Fig. 3G). We treated these acylhydrazine-functionalized coatings with octyl aldehyde to install hydrophobic octyl groups through a rapid and 'click-like' reaction[47,48] that results in the formation of an acid-sensitive imine linker (20 mg/mL in methanol, 1 hour; Fig. 4A; Fig. S6). Characterization of these surfaces after octyl aldehyde treatment revealed these coatings to exhibit robust superhydrophobicity (WCA ~ 156; Fig. 4C) similar to those obtained by treatment with hydrophobic amine-, alcohol-, and thiol-based nucleophiles (e.g., Fig. 2).

The introduction of imine bonds rendered these surfaces sensitive to acidic conditions—for example, exposure to acidic media (1.0 M HCl; 1:1 THF/H_2O) resulted in the cleavage of the imine bonds, the recovery of acylhydrazine functionality on the coatings, and the return of superhydrophilic surface character (WCAs ~0°) and underwater-superoleophobic behavior (Fig. S7; films incubated in otherwise identical conditions in the absence of acid remained superhydrophobic; Fig. S8). Because this acid-catalyzed cleavage process regenerates acylhydrazine functionality, superhydrophobicity could also be restored again by re-treatment with octyl aldehyde. Transitions between superhydrophobicity and superhydrophilicity/ underwater superoleophobicity could be cycled reversibly using this approach at least five times without significant changes in expected extreme wetting behaviors (Fig. 4D).

Summary and Conclusions

We have reported approaches to the chemical modification of covalently crosslinked and physically stable azlactone-functionalized polymer multilayers using alcohol- and thiol-based nucleophiles or by direct treatment with hydrazine followed by reaction with aldehydes. These methods broaden the pool of compounds available for the post-fabrication functionalization of these reactive coatings substantially (e.g., to include molecules functionalized with alcohol, thiol, or aldehyde groups) and provide strategies for the design of thin films and surface coatings with novel amide/ester-, amide/thioester-, and amide/imine-type bonds that are, in contrast to linkages produced by reactions with primary amines, chemically labile.

The results of these studies thus open the door to the design of new environmentally-responsive materials and coatings, including surfaces that can promote the traceless release of covalently-immobilized molecules and coatings that undergo dynamic and predictable changes in extreme wetting behaviors, such as superhydrophobicity, superhydrophilicity, or underwater superoleophobicity, in response to environmental stimuli. The properties and behaviors of these materials could prove useful in emerging applications of special-wetting surfaces, including the design of surfaces that can capture and guide the passive transport of fluids,[27,56] new materials for oil/water separation,[59,60] and in areas such as controlled release,[20,42,61] where controlled and time-dependent changes in extreme wetting behaviors could be used to control the ingress of water into a coating (and, thus, provide control over the rate at which imbedded water-soluble or water-sensitive agents are released).

Overall, the results of this study broaden the range of chemical functionality that can be installed in azlactone-containing multilayers, and thus also expand the range of new functions and properties that can be imparted. The strategies reported here are likely to be general; we

anticipate that these approaches will thus also prove useful for the functionalization of many other classes of azlactone-functionalized polymers, assemblies, and coatings.

Acknowledgments. This work was supported by the National Science Foundation (DMR-1121288), the Office of Naval Research (N00014-16-1-2185), and made use of NSF-supported facilities (DMR-1121288). We thank Dr. Uttam Manna and Michael J. Kratochvil for technical assistance and many helpful discussions. M.C.D.C. acknowledges the Natural Sciences Engineering Research Council of Canada for a graduate fellowship.

References

1. Schonhoff, M. Self-assembled polyelectrolyte multilayers. *Curr. Opin. Colloid Interface Sci.* 2003, *8*, 86-95.

2. Hammond, P. T. Form and function in multilayer assembly: New applications at the nanoscale. *Adv. Mater.* 2004, *16*, 1271-1293.

3. Sukhishvili, S. A. Responsive polymer films and capsules via layer-by-layer assembly. *Curr. Opin. Colloid Interface Sci.* 2005, *10*, 37-44.

4. Tang, Z.; Wang, Y.; Podsiadlo, P.; Kotov, N. A. Biomedical Applications of Layer-by-Layer Assembly: From Biomimetics to Tissue Engineering. *Adv. Mater.* 2006, *18*, 3203-3224.

5. Hammond, P. T. Engineering materials layer-by-layer: Challenges and opportunities in multilayer assembly. *AIChE Journal* 2011, *57*, 2928-2940.

6. Decher, G., Layer-by-Layer Assembly (Putting Molecules to Work). In *Multilayer Thin Films: Sequential Assembly of Nanocomposite Materials, 2nd Edition*, Decher, G.; Schlenoff, J. B., Eds. Wiley-CVH: 2012; pp 1-21.

7. Li, Y.; Wang, X.; Sun, J. Layer-by-layer assembly for rapid fabrication of thick polymeric films. *Chem. Soc. Rev.* 2012, *41*, 5998-6009.

8. Richardson, J. J.; Björnmalm, M.; Caruso, F. Technology-driven layer-by-layer assembly of nanofilms. *Science* 2015, *348*, doi: 10.1126/science.aaa2491.

9. Xiao, F.-X.; Pagliaro, M.; Xu, Y.-J.; Liu, B. Layer-by-layer assembly of versatile nanoarchitectures with diverse dimensionality: a new perspective for rational construction of multilayer assemblies. *Chem. Soc. Rev.* 2016, 45, 3088-3121.

10. Borges, J.; Mano, J. F. Molecular Interactions Driving the Layer-by-Layer Assembly of Multilayers. *Chem. Rev.* 2014, *114*, 8883-8942.

11. Quinn, J. F.; Johnston, A. P. R.; Such, G. K.; Zelikin, A. N.; Caruso, F. Next generation, sequentially assembled ultrathin films: beyond electrostatics. *Chem. Soc. Rev.* 2007, *36*, 707-718.

12. Bergbreiter, D. E.; Liao, K.-S. Covalent layer-by-layer assembly-an effective, forgiving way to construct functional robust ultrathin films and nanocomposites. *Soft Matter* 2009, *5*, 23-28.

13. Rydzek, G.; Schaaf, P.; Voegel, J.-C.; Jierry, L.; Boulmedais, F. Strategies for covalently reticulated polymer multilayers. *Soft Matter* 2012, *8*, 9738-9755.

14. Broderick, A. H.; Lynn, D. M., Covalent layer-by-layer assembly using reactive polymers. In *Functional Polymers by Post-Polymerization Modification*, Wiley-VCH Verlag GmbH & Co. KGaA: 2013; pp 371-406.

15. Buck, M. E.; Lynn, D. M. Azlactone-functionalized polymers as reactive platforms for the design of advanced materials: Progress in the last ten years. *Polym. Chem.* 2012, *3*, 66-80.

16. Buck, M. E.; Zhang, J.; Lynn, D. M. Layer-by-Layer Assembly of Reactive Ultrathin Films Mediated by Click-Type Reactions of Poly(2-Alkenyl Azlactone)s. *Adv. Mater.* 2007, *19*, 3951-3955.

17. Buck, M. E.; Lynn, D. M. Reactive Layer-by-Layer Assembly of Suspended Thin Films and Semipermeable Membranes at Interfaces Created Between Aqueous and Organic Phases. *Adv. Mater.* 2010, *22*, 994-998.

18. Broderick, A. H.; Azarin, S. M.; Buck, M. E.; Palecek, S. P.; Lynn, D. M. Fabrication and Selective Functionalization of Amine-Reactive Polymer Multilayers on Topographically Patterned Microwell Cell Culture Arrays. *Biomacromolecules* 2011, *12*, 1998-2007.

19. Broderick, A. H.; Manna, U.; Lynn, D. M. Covalent Layer-by-Layer Assembly of Water-Permeable and Water-Impermeable Polymer Multilayers on Highly Water-Soluble and Water-Sensitive Substrates. *Chem. Mater.* 2012, *24*, 1786-1795.

20. Manna, U.; Kratochvil, M. J.; Lynn, D. M. Superhydrophobic Polymer Multilayers that Promote the Extended, Long-Term Release of Embedded Water-Soluble Agents. *Adv. Mater*. 2013, *25*, 6405-6409.

21. Manna, U.; Lynn, D. M. Fabrication of Liquid-Infused Surfaces Using Reactive Polymer Multilayers: Principles for Manipulating the Behaviors and Mobilities of Aqueous Fluids on Slippery Liquid Interfaces. *Adv. Mater.* 2015, *27*, 3007-3012.

22. Holden, M. T.; Carter, M. C. D.; Wu, C.-H.; Wolfer, J.; Codner, E.; Sussman, M. R.; Lynn, D. M.; Smith, L. M. Photolithographic Synthesis of High-Density DNA and RNA Arrays on Flexible, Transparent, and Easily Subdivided Plastic Substrates. *Anal. Chem.* 2015, *87*, 11420-11428.

23. Heilmann, S. M.; Rasmussen, J. K.; Krepski, L. R. Chemistry and technology of 2-alkenyl azlactones. *J. Polym. Sci. A Polym. Chem.* 2001, *39*, 3655-3677.

24. Buck, M. E.; Schwartz, S. C.; Lynn, D. M. Superhydrophobic Thin Films Fabricated by Reactive Layer-by-Layer Assembly of Azlactone-Functionalized Polymers. *Chem. Mater.* 2010, *22*, 6319-6327.

25. Buck, M. E.; Lynn, D. M. Free-Standing and Reactive Thin Films Fabricated by Covalent Layer-by-Layer Assembly and Subsequent Lift-Off of Azlactone-Containing Polymer Multilayers. *Langmuir* 2010, *26*, 16134-16140.

26. Broderick, A. H.; Carter, M. C. D.; Lockett, M. R.; Smith, L. M.; Lynn, D. M. Fabrication of Oligonucleotide and Protein Arrays on Rigid and Flexible Substrates Coated with Reactive Polymer Multilayers. *ACS Appl. Mater. Inter.* 2013, *5*, 351-359.

27. Manna, U.; Lynn, D. M. Patterning and Impregnation of Superhydrophobic Surfaces Using Aqueous Solutions. *ACS Appl. Mater. Inter.* 2013, *5*, 7731-7736.

28. Manna, U.; Lynn, D. M. Synthetic Surfaces with Robust and Tunable Underwater Superoleophobicity. *Adv. Funct. Mater.* 2015, *25*, 1672-1681.

29. Cullen, S. P.; Mandel, I. C.; Gopalan, P. Surface-Anchored Poly(2-vinyl-4,4-dimethyl azlactone) Brushes as Templates for Enzyme Immobilization. *Langmuir* 2008, *24*, 13701-13709.

30. Messman, J. M.; Lokitz, B. S.; Pickel, J. M.; Kilbey, S. M., II Highly Tailorable Materials based on 2-Vinyl-4,4-dimethyl Azlactone: (Co)Polymerization, Synthetic Manipulation and Characterization. *Macromolecules* 2009, *42*, 3933-3941.

31. Ho, H. T.; Levere, M. E.; Fournier, D.; Montembault, V.; Pascual, S.; Fontaine, L. Introducing the Azlactone Functionality into Polymers through Controlled Radical Polymerization: Strategies and Recent Developments. *Aust. J. Chem.* 2012, *65*, 970-977.

32. Laquievre, A.; Allaway, N. S.; Lyskawa, J.; Woisel, P.; Lefebvre, J.-M.; Fournier, D. Highly Efficient Ring-Opening Reaction of Azlactone-Based Copolymer Platforms for the Design of Functionalized Materials. *Macromol. Rapid. Commun.* 2012, *33*, 848-855.

33. Lokitz, B. S.; Wei, J.; Hinestrosa, J. P.; Ivanov, I.; Browning, J. F.; Ankner, J. F.; Kilbey, S. M.; Messman, J. M. Manipulating Interfaces through Surface Confinement of Poly(glycidyl methacrylate)-block-poly(vinyldimethylazlactone), a Dually Reactive Block Copolymer. *Macromolecules* 2012, *45*, 6438-6449.

34. Hansen, R. R.; Hinestrosa, J. P.; Shubert, K. R.; Morrell-Falvey, J. L.; Pelletier, D. A.; Messman, J. M.; Kilbey, S. M.; Lokitz, B. S.; Retterer, S. T. Lectin-Functionalized Poly(glycidyl methacrylate)-block-poly(vinyldimethyl azlactone) Surface Scaffolds for High Avidity Microbial Capture. *Biomacromolecules* 2013, *14*, 3742-3748.

35. Quek, J. Y.; Zhu, Y.; Roth, P. J.; Davis, T. P.; Lowe, A. B. RAFT Synthesis and Aqueous Solution Behavior of Novel pH- and Thermo-Responsive (Co)Polymers Derived from Reactive Poly(2-vinyl-4,4-dimethylazlactone) Scaffolds. *Macromolecules* 2013, *46*, 7290-7302.

36. Li, Y.; Duong, H. T. T.; Jones, M. W.; Basuki, J. S.; Hu, J. M.; Boyer, C.; Davis, T. P. Selective Postmodification of Copolymer Backbones Bearing Different Activated Esters with Disparate Reactivities. *ACS Macro Lett.* 2013, *2*, 912-917.

37. Jones, M. W.; Richards, S.-J.; Haddleton, D. M.; Gibson, M. I. Poly(azlactone)s: versatile scaffolds for tandem post-polymerisation modification and glycopolymer synthesis. *Polym. Chem.* 2013, *4*, 717-723.

38. Speetjens, F. W., II; Carter, M. C. D.; Kim, M.; Gopalan, P.; Mahanthappa, M. K.; Lynn, D. M. Post-Fabrication Placement of Arbitrary Chemical Functionality on Microphase-Separated Thin Films of Amine-Reactive Block Copolymers. *ACS Macro Lett.* 2014, *3*, 1178-1182.

39. Schmitt, S. K.; Xie, A. W.; Ghassemi, R. M.; Trebatoski, D. J.; Murphy, W. L.; Gopalan, P. Polyethylene Glycol Coatings on Plastic Substrates for Chemically Defined Stem Cell Culture. *Adv. Healthcare Mater.* 2015, *4*, 1555-1564.

40. Schmitt, S. K.; Trebatoski, D. J.; Krutty, J. D.; Xie, A. W.; Rollins, B.; Murphy, W. L.; Gopalan, P. Peptide Conjugation to a Polymer Coating via Native Chemical Ligation of Azlactones for Cell Culture. *Biomacromolecules* 2016, *17*, 1040-1047.

41. Zhu, Y.; Batchelor, R.; Lowe, A. B.; Roth, P. J. Design of Thermoresponsive Polymers with Aqueous LCST, UCST, or Both: Modification of a Reactive Poly(2-vinyl-4,4-dimethylazlactone) Scaffold. *Macromolecules* 2016, *49*, 672-680.

42. Kratochvil, M. J.; Tal-Gan, Y.; Yang, T.; Blackwell, H. E.; Lynn, D. M. Nanoporous Superhydrophobic Coatings that Promote the Extended Release of Water-Labile Quorum Sensing Inhibitors and Enable Long-Term Modulation of Quorum Sensing in Staphylococcus aureus. *ACS Biomater. Sci. Eng.* 2015, *1*, 1039-1049.

43. Rasmussen, J. K.; Heilmann, S. M.; Palensky, F. J.; Smith, H. K., II; Melancon, K. C. Chemistry of Alkenylazlactones. 2. Reaction with Thiols. *Makromol. Chem., Rapid Communications* 1984, *5*, 67-70.

44. Heilmann, S. M.; Moren, D. M.; Krepski, L. R.; Pathre, S. V.; Rasmussen, J. K.; Stevens, J. The chemistry of 2-alkenyl-5(4H)-oxazolones. VIII - Acid-catalyzed reaction with alcohols. *Tetrahedron* 1998, *54*, 12151-12160.

45. Pereira, A. A.; de Castro, P. P.; de Mello, A. C.; Ferreira, B. R. V.; Eberlin, M. N.; Amarante, G. W. Brønsted acid catalyzed azlactone ring opening by nucleophiles. *Tetrahedron* 2014, *70*, 3271-3275.

46. Heilmann, S. M.; Rasmussen, J. K.; Palensky, F. J.; Smith, H. K., II Chemistry of alkenyl azlactones. I. Radiation-sensitive materials derived from azlactone-containing copolymers. *J. Polym. Sci., Polym. Chem. Ed.* 1984, *22*, 1179-86.

47. Xin, Y.; Yuan, J. Schiff's base as a stimuli-responsive linker in polymer chemistry. *Polym. Chem.* 2012, *3*, 3045-3055.

48. Kool, E. T.; Park, D.-H.; Crisalli, P. Fast Hydrazone Reactants: Electronic and Acid/Base Effects Strongly Influence Rate at Biological pH. *J. Am. Chem. Soc.* 2013, *135*, 17663-17666.

49. Noel, S.; Liberelle, B.; Robitaille, L.; De Crescenzo, G. Quantification of Primary Amine Groups Available for Subsequent Biofunctionalization of Polymer Surfaces. *Bioconjugate Chem.* 2011, *22*, 1690-1699.

50. Sun, B.; Lynn, D. M. Release of DNA from polyelectrolyte multilayers fabricated using 'charge-shifting' cationic polymers: Tunable temporal control and sequential, multi-agent release. *J. Control. Release* 2010, *148*, 91-100.

51. Duhamel, J. New Insights in the Study of Pyrene Excimer Fluorescence to Characterize Macromolecules and their Supramolecular Assemblies in Solution. *Langmuir* 2012, *28*, 6527-6538.

52. Manna, U.; Broderick, A. H.; Lynn, D. M. Chemical Patterning and Physical Refinement of Reactive Superhydrophobic Surfaces. *Adv. Mater.* 2012, *24*, 4291-4295.

53. Feng, L.; Li, S.; Li, Y.; Li, H.; Zhang, L.; Zhai, J.; Song, Y.; Liu, B.; Jiang, L.; Zhu, D. Super-Hydrophobic Surfaces: From Natural to Artificial. *Adv. Mater*. 2002, *14*, 1857-1860.

54. Li, X.-M.; Reinhoudt, D.; Crego-Calama, M. What do we need for a superhydrophobic surface? A review on the recent progress in the preparation of superhydrophobic surfaces. *Chem. Soc. Rev.* 2007, *36*, 1350-1368.

55. Darmanin, T.; Guittard, F. Superhydrophobic and superoleophobic properties in nature. *Mater. Today* 2015, *18*, 273-285.

56. Wen, L.; Tian, Y.; Jiang, L. Bioinspired Super-Wettability from Fundamental Research to Practical Applications. *Angew. Chem. Int. Ed.* 2015, *54*, 3387-3399.

57. Neto, A. I.; Custodio, C. A.; Song, W.; Mano, J. F. High-throughput evaluation of interactions between biomaterials, proteins and cells using patterned superhydrophobic substrates. *Soft Matter* 2011, *7*, 4147-4151.

58. Zahner, D.; Abagat, J.; Svec, F.; Fréchet, J. M. J.; Levkin, P. A. A Facile Approach to Superhydrophilic–Superhydrophobic Patterns in Porous Polymer Films. *Adv. Mater*. 2011, *23*, 3030-3034.

59. Wang, S.; Liu, K.; Yao, X.; Jiang, L. Bioinspired Surfaces with Superwettability: New Insight on Theory, Design, and Applications. *Chem. Rev.* 2015, *115*, 8230-8293.

60. Xue, Z.; Cao, Y.; Liu, N.; Feng, L.; Jiang, L. Special wettable materials for oil/water separation. *J. Mater. Chem. A* 2014, *2*, 2445-2460.

61. Yohe, S. T.; Colson, Y. L.; Grinstaff, M. W. Superhydrophobic Materials for Tunable Drug Release: Using Displacement of Air To Control Delivery Rates. *J. Am. Chem. Soc.* 2012, *134*, 2016-2019.

Supporting Information for Chapter 2

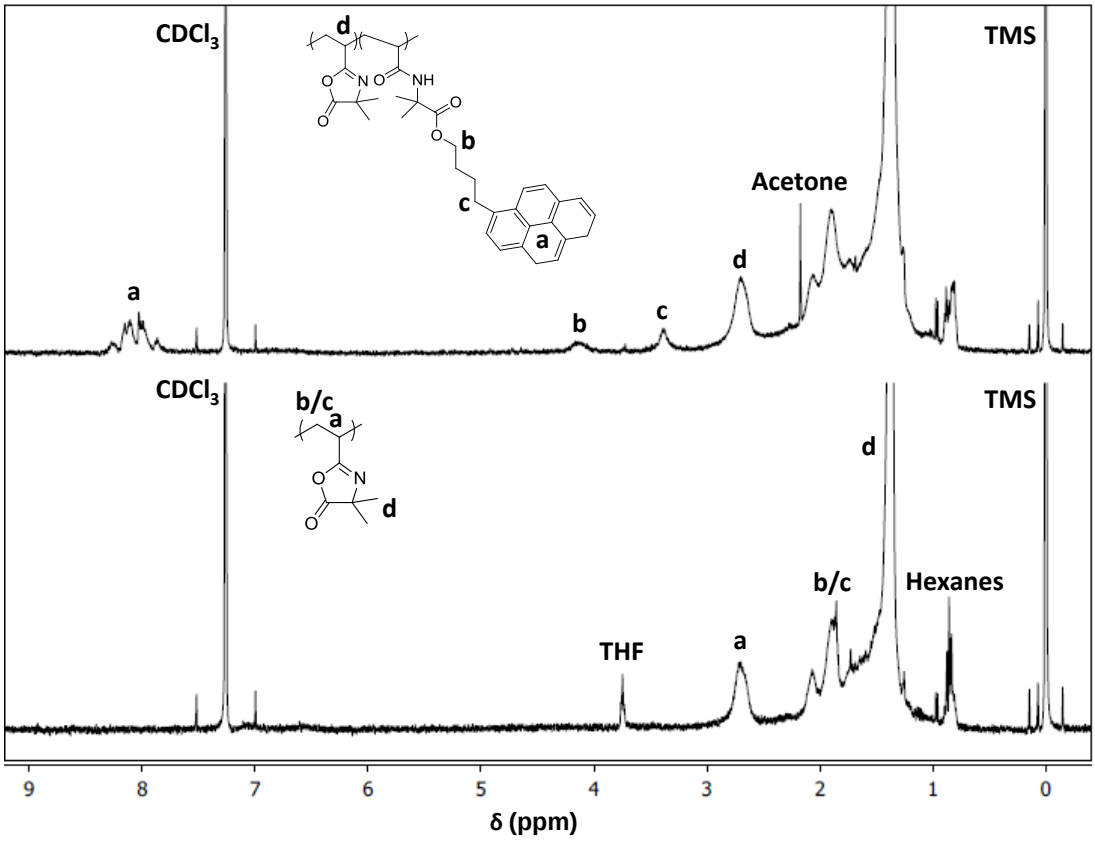

Fig S1. ^{1}H NMR spectrum of PVDMA before (bottom) and after (top) reaction with pyrenebutanol in solution. See Materials and Methods for full synthetic details.

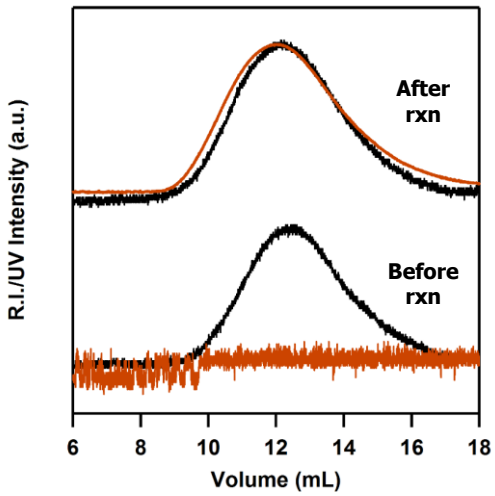

Fig S2. Gel permeation chromatography (GPC) traces for PVDMA before (bottom) and after (top) reaction with pyrenebutanol in solution. The black traces show the response at the refractive index (RI) detector, while the red traces show the response at the UV detector (signal was normalized to the RI peak height). The data indicate that PVDMA is non-fluorescent before reaction with pyrenebutanol, but displays a strong UV absorbance after reaction, owing to the presence of the pyrene moieties.

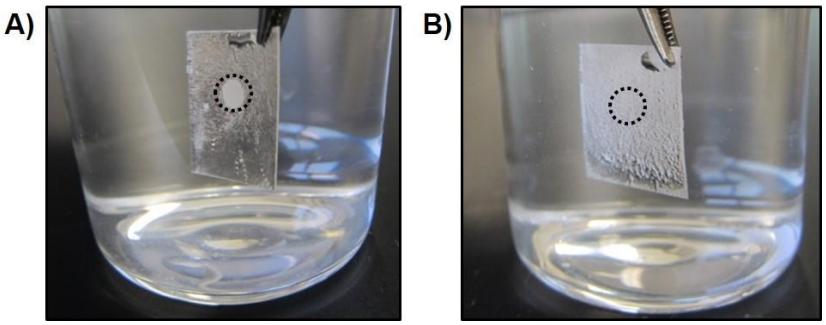

Fig S3. Digital photographs showing (A) decanol-treated and (B) decylamine-treated PEI/PVDMA films (~1 x 1 cm) submerged underwater after treatment with a droplet of 50 mM aqueous NaOH. The approximate location where the droplet of base was placed is denoted in both images by the perforated black circle. Water is observed to wet the location where the NaOH solution was placed on the film in (A) owing to ester hydrolysis and loss of superhydrophobicity in the marked area. The remainder of the film appears shiny, indicative of trapped air and the still-superhydrophobic nature of the surface coating. The decylamine-treated film in (B) does not appear to be wet by water in the location where the NaOH droplet was placed, owing to the stability of the amide bonds.

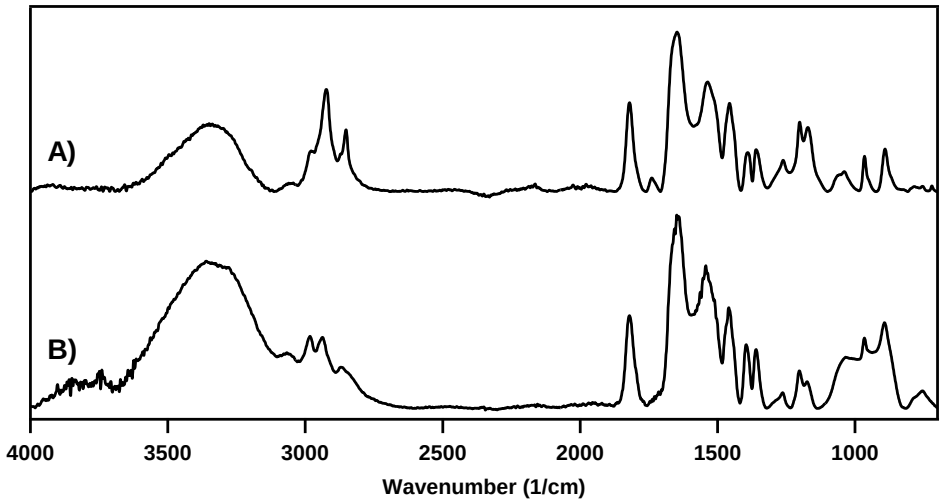

Fig S4. ATR IR spectra of PEI/PVDMA films after treatment with (A) decanethiol and (B) decanol in the absence catalytic DBU. The azlactone carbonyl peak (C=O, 1819 cm^{-1}) is not consumed in either case, suggesting that the thiol and the alcohol do not react with the azlactone in the absence of catalytic base.

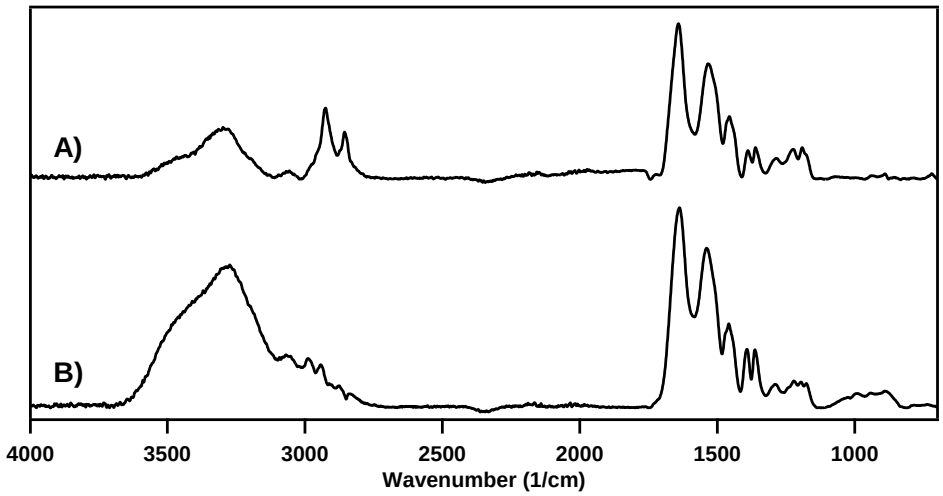

Fig S5. ATR IR spectra of PEI/PVDMA films functionalized with (A) decylamine and (B) decanethiol, after treatment with hydrazine in methanol (20 mg/mL in MeOH, 50 °C overnight). The spectrum of the decylamine-functionalized film in (A) is relatively unchanged (See Fig. 2I in the main text), whereas the coalescence of thioester and amide carbonyl peaks (C=O) near 1650 cm^{-1} has resolved to a single amide stretch, and NHR/NH_2 peak intensities (~3500 cm^{-1}) have diminished. A significant decrease in C-H sp^3 stretching due to the absence of decyl chains is also observed (*c.f.* Fig 2I).

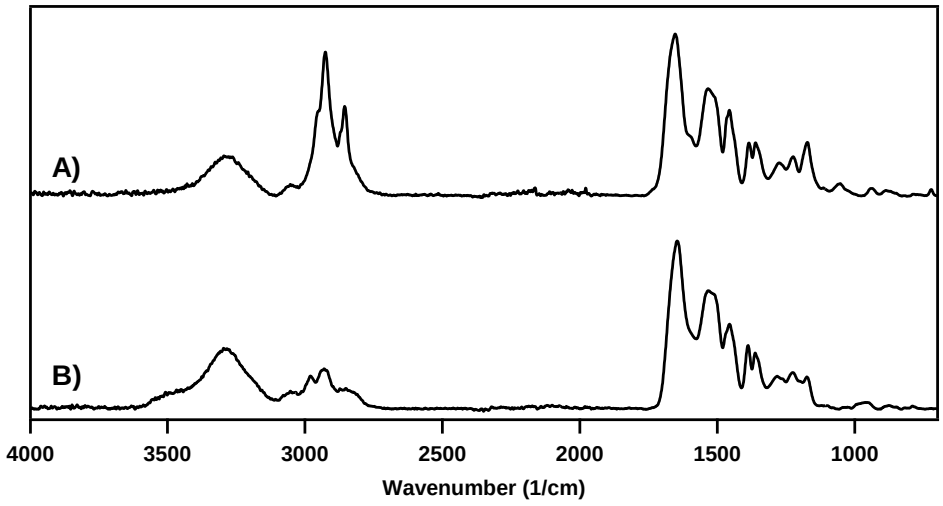

Fig S6. ATR IR spectra of PEI/PVDMA films functionalized with (A) hydrazine and octyl aldehyde and (B) hydrazine only. The spectrum of the hydrazine and octyl aldehyde treated film in (B) shows an increase in C-H sp^3 stretching relative to the spectrum in (B), owing to the presence of newly installed octyl chains. A distinct imine bond stretch (lit. ~1640-1690 cm^{-1}) is not observed, presumably because it is obscured by strong amide carbonyl stretching (C=O, ~1650 cm^{-1}).

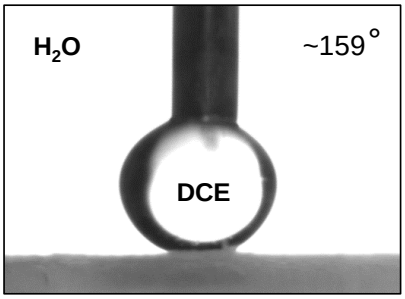

Fig S7. Underwater advancing DCE (oil) contact angle for a underwater superoleophobic PEI/PVDMA film functionalized with hydrazine followed by octyl aldehyde, and after soaking in 1M HCl (1:1 v/v THF:H_2O). See main text Fig. 4 and surrounding discussion for complete details.

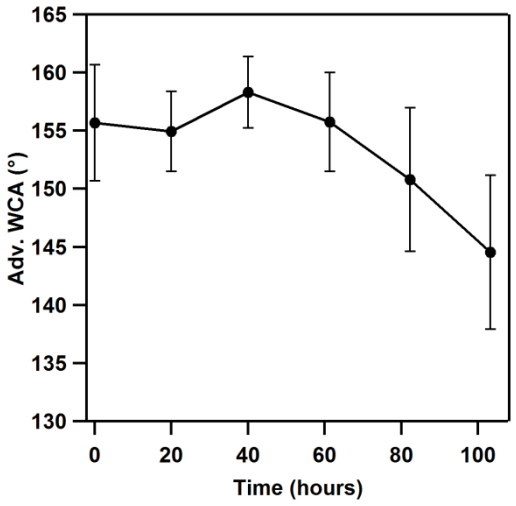

Fig S8. Plot showing the change in advancing WCA over time for PEI/PVDMA films functionalized with hydrazine and octyl aldehyde and incubated in a solution of 1:1 v/v THF:H_2O (without HCl acid). The relative stability of the superhydrophobic state (advancing WCA > 150°) up to ~80 hours in this media stands in contrast to the rapid loss of superhydrophobicity when films are incubated in the presence of acid (1 M HCl in 1:1 v/v THF:H_2O overnight, room temperature).

Chapter 3

Fabrication of Oligonucleotide and Protein Arrays on Rigid and Flexible Substrates Coated with Reactive Polymer Multilayers ‡

‡ Portions of this chapter have previously been published as: Broderick, A.H.; Carter, M.C.D.; Lockett, M.R.; Smith, L.M.; Lynn, D.M. "Fabrication of Oligonucleotide and Protein Arrays on Rigid and Flexible Substrates Coated with Reactive Polymer Multilayers." *ACS Applied Materials and Interfaces*, **2013**, *5*, 351-359. A. Broderick and I fabricated and imaged the films, and analyzed the data.

ABSTRACT: We report a top-down approach to the fabrication of oligonucleotide and protein arrays on surfaces coated with ultrathin, amine-reactive polymer multilayers fabricated by the covalent 'layer-by-layer' (LbL) assembly of polyethyleneimine (PEI) and the amine-reactive, azlactone-functionalized polymer poly(2-vinyl-4,4-dimethylazlactone) (PVDMA). Manual spotting of amine-terminated oligonucleotide probe sequences on planar glass slides coated with PEI/PVDMA multilayers (~35 nm thick) yielded arrays of immobilized probes that hybridized fluorescently labeled complementary sequences with high signal intensities, high signal-to-noise ratios, and high sequence specificity. Treatment of residual azlactone functionality with the non-fouling small-molecule amine D-glucamine resulted in regions between the features of these arrays that resisted adsorption of protein and permitted hybridization in complex media containing up to 10 mg/mL protein. The residual azlactone groups in these films were also exploited to immobilize proteins on film-coated surfaces and fabricate functional arrays of proteins and enzymes. The ability to deposit PEI/PVDMA multilayers on substrates of arbitrary size, shape, and composition permitted the fabrication of arrays of oligonucleotides on the surfaces of multilayer-coated sheets of poly(ethylene terephthalate) and heat-shrinkable polymer film. Arrays fabricated on these flexible plastic substrates can be bent, cut, resized, and manipulated physically in ways that are difficult using more conventional rigid substrates. This approach could thus contribute to the development of new assay formats and new applications of biomolecule arrays. The methods described here are straightforward to implement and do not require access to specialized equipment, and should also be compatible with automated liquid-handling methods used to fabricate higher-density arrays of oligonucleotides and proteins on more traditional surfaces.

Introduction

Spatially addressable arrays of surface-bound biomolecules are powerful tools for basic research and are useful in a broad range of biological and biomedical contexts. DNA microarrays, for example, are now widely used to profile gene expression patterns and identify genetic mutations in massively parallel assays that can dramatically accelerate discovery and the analysis of genetic data.[1-3] Many commercially available DNA microarrays are fabricated by the direct and simultaneous solid-phase synthesis of tens of thousands of different oligonucleotides on a surface – a 'bottom-up' approach that exploits advances in photolithography and other techniques to fabricate arrays containing very high densities of features (e.g., greater than 100,000 elements/cm^2) that facilitate large-scale, whole-genome analyses.[4-8] Other approaches to microarray fabrication are based on methods for the immobilization or 'spotting' of pre-synthesized oligonucleotides on suitably functionalized surfaces.[9,10] These 'top-down' approaches generally lead to lower-density arrays, but they do not require access to specialized or expensive equipment and they can be used by individual groups to prepare 'in house' arrays of smaller collections of oligonucleotides customized to specific research needs. In contrast to 'bottom-up' approaches, these spotting-based methods are also well suited for the preparation of arrays of other types of biomolecules (e.g., proteins and antibodies, etc.)[11,12] that are either difficult or impossible to synthesize in parallel using solid-phase methods.

The usefulness of spotting-based approaches to array fabrication depends upon the properties of the underlying substrate on which a biomolecular probe is deposited. Ideally, these substrates should contain chemical functionality that is suitable for both the immobilization of the biomolecule (in a way that does not significantly alter its structure or activity) and the attachment of other functionality (e.g., a non-fouling motif) that minimizes or prevents non-

specific adsorption of other species between spotted features in downstream assays. Array substrates must also be physically and chemically robust enough to withstand mechanical challenges and exposure to reagents used during washing, hybridization, and characterization. A wide variety of attachment schemes have been developed, including approaches that exploit non-covalent interactions (e.g., electrostatic interactions[1,13] or biotin/streptavidin binding[14,15]) and the formation of covalent bonds (e.g., by reactions between amine-functionalized molecules and surfaces presenting carboxylic acids,[16,17] aldehydes,[18-21] epoxides,[22-24] isothiocyanates,[25,26] and activated esters,[20,26,27] as well as reactions between thiols and maleimide groups[28-31] or disulfides[32,33]). These attachment chemistries have been used to fabricate arrays of oligonucleotides, proteins, antibodies, and other species, most frequently on the surfaces of rigid and planar glass,[1,20] silicon,[30,34] gold,[29,33,35] or carbon-based[36,37] substrates. Each of these approaches brings with it a balance of practical advantages and potential disadvantages in terms of (i) the types of substrates that can be used, and the ease with which they can be prepared, (ii) the short- and long-term stability of the reactive surfaces, and the robustness of the chemical bonds that are formed during fabrication, and (iii) the potential for unwanted cross-reactivity during spotting or subsequent changes in structure of the biomolecular probes (e.g., denaturation, etc.) that can impact the performance of the arrayed species.

The continued development of new materials and reactive interfaces that address these and other important issues could lead to improvements in array performance and facilitate the design of new array and assay formats. Here, we report new approaches to the fabrication of arrays of oligonucleotides and proteins that exploit rapid reactions between amine-functionalized biomolecules and surfaces coated with ultrathin (nanometer-scale) polymer multilayers that present amine-reactive azlactone functionality.

Azlactone groups react rapidly and selectively with primary amines through ring-opening reactions that are water-tolerant and that typically proceed under mild conditions (e.g., at ambient temperatures and without the need for a catalyst; e.g., Equation 1).[38,39] Several groups have demonstrated that polymers bearing azlactone functionality can be used to design thin films and other surfaces that can be further functionalized, post-fabrication, by treatment with primary amine-based nucleophiles to modify interfacial properties (e.g., to change wetting behavior) or introduce chemical or biological functionality (including the immobilization of proteins and active enzymes by reactions between azlactone groups and the primary amine functionality of surface-exposed lysine residues).[39-54] These and other examples illustrating the general utility of azlactone-functionalized materials in the contexts of biocatalysis and biotechnology have been reviewed recently.[54] Of particular relevance to the work reported here, we note that a patent also describes the use of polyethylene surfaces modified with azlactone-containing polymers to immobilize amine-terminated oligonucleotides.[55]

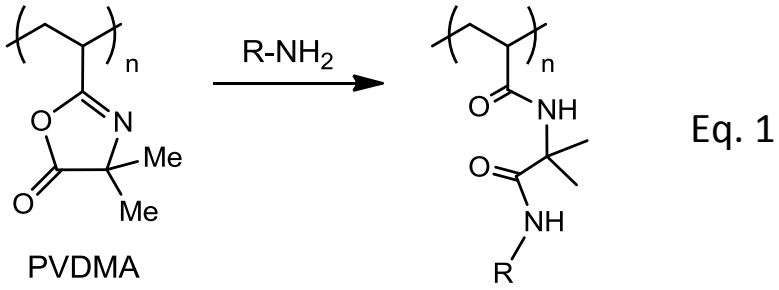

Eq. 1

The work reported here exploits methods developed in our laboratory for the reactive assembly of ultrathin azlactone-containing polymer multilayers (with thicknesses ranging from 10 nm to several hundred nanometers) on surfaces.[51,54] This approach involves the iterative and covalent ‘layer-by-layer’ deposition[56,57] of alternating layers of an azlactone-functionalized polymer [poly(2-vinyl-4,4-dimethylazlactone) (PVDMA; Equation 1)] and a primary amine-

containing polymer [branched polyethyleneimine (PEI)].[51,54] Fast interfacial reactions during film assembly lead to covalently crosslinked PEI/PVDMA multilayers that are stable in a range of aqueous and organic environments and contain residual azlactone functionality that can be used as a reactive handle for the immobilization of small molecules,[51-53,58] polymers,[59,60] peptides, [61] and proteins.[52] Our past studies demonstrate that this approach can be used to deposit conformal films on a broad range of surfaces, including 'hard' materials typically used to fabricate DNA microarrays (e.g., glass and silicon)[51-53,62] as well as soft/flexible materials[59,62] and the surfaces of other topographically and topologically complex objects.[58,63]

We recently reported that PEI/PVDMA films functionalized to present hydroxyl functionality can be used as platforms for the 'bottom-up' fabrication of DNA microarrays using automated methods for *in situ* maskless array synthesis (MAS).[62] This current study sought to investigate surfaces coated with reactive PEI/PVDMA multilayers as platforms for the 'top-down' fabrication of DNA arrays by the direct, spotting-based immobilization of pre-synthesized amine-terminated oligonucleotides. Our results demonstrate that this approach can be used to prepare arrays of oligonucleotide probes that hybridize fluorescently labeled complementary oligonucleotide sequences with high signal intensity, high signal-to-noise ratios, and high sequence specificity, even in complex hybridization media containing high concentrations of bovine serum albumin (BSA). In addition, surfaces coated with these reactive, azlactone-functionalized multilayers were also found to be useful for the fabrication of arrays of immobilized proteins and enzymes. The layer-by-layer approach used here is technically straightforward and inexpensive to implement, and it can be used to fabricate arrays on the surfaces of both conventional substrates (e.g., on film-coated glass slides) and other unconventional substrates, such as flexible plastic substrates and on heat-shrinkable polymer film

that can subsequently be bent, cut, and manipulated in ways that that are difficult using rigid and planar surfaces. These methods could thus facilitate the design of new array formats and new applications of biomolecule arrays.

Materials and Methods

Materials. 2-Vinyl-4,4-dimethylazlactone (VDMA) was a kind gift from Dr. Steven M. Heilmann (3M Corporation, Minneapolis, MN). PVDMA was synthesized by conventional free-radical polymerization of VDMA in the presence of 7% (by weight) of intentionally added cyclic azlactone-functionalized oligomers, as previously described.[53] D-Glucamine was purchased from TCI America (Portland, OR). Amine-terminated oligonucleotide probes and fluorescently labeled target complements were purchased from Integrated DNA Technologies (Coralville, IA). Fluorescein isothiocyanate-labeled bovine serum albumin (FITC-BSA) was purchased from Invitrogen (Carlsbad, CA). Streptavidin was purchased from Promega (Madison, WI). β-Galactosidase (β-Gal) was purchased from Prozyme (Hayward, CA). 2-Nitrophenyl β-D-galactopyranoside (ONPG) was obtained from Sigma Aldrich (Milwaukee, WI). Anti-HA-Biotin, High Affinity (3F10) from rat immunoglobulin G (IgG) was purchased from Roche Applied Science (Indianapolis, IN). Anti-rat IgG Alexa Fluor® 488 Conjugate was purchased from Cell Signaling Technology (Danvers, MA). FITC-streptavidin and glass microscope slides were purchased from Fisher Scientific (Pittsburgh, PA). Thin sheets of poly(ethylene terephthalate) (PET; 0.004 inch thick) were purchased from McMaster Carr (Elmhurst, IL). Heat shrinkable film (RCR International, Elgin IL) was purchased from Menards, Inc. (Madison, WI). Branched poly(ethylene imine) (PEI; MW ~25,000), reagent grade solvents, and all other

chemicals used were purchased from Sigma Aldrich (Milwaukee, WI) or Fisher Scientific (Pittsburgh, PA) and used without further purification unless otherwise noted.

General Considerations. Compressed air used in all drying steps was filtered through a 0.2 μm membrane syringe filter. Fluorescence images of hybridized arrays were acquired using a GeneTAC UC 4×4 scanner (Genomic Solutions) and analyzed using ImageJ (NIH, Bethesda, MD). UV/visible absorbance spectra used to determine the concentration of ortho-nitrophenol (ONP) produced by surface-immobilized β-Gal were recorded using a NanoDrop 2000 Micro-Volume UV/vis spectrophotometer (Thermo Scientific, Fullerton, CA). Absorbance values were recorded at a wavelength of 420 nm. Saline-sodium phosphate-EDTA (SSPE) buffer (pH = 7.4) used in experiments involving oligonucleotides contained 150 mM NaCl, 10 mM Na_2HPO_4, and 1 mM EDTA. A hand-held laboratory grade heat gun (Master Appliance, Racine, WI) was used to shrink arrays fabricated on heat shrinkable film. Digital pictures were acquired using a Canon PowerShot SX130 IS digital camera. Contact angle measurements were made using a Dataphysics OCA 15 Plus contact angle goniometer at ambient temperature with 3.5 μL of 18.2 MΩ Millipore water.

Substrate Preparation and Film Fabrication. Prior to the fabrication of reactive PEI/PVDMA multilayers, glass and PET substrates were prepared as follows. Glass slides were first silanized in a 1% (v/v) solution of (3-amino-propyl)triethoxysilane (APTES) in anhydrous toluene for 1 h. The slides were then rinsed extensively with ethanol and methanol and dried in an oven overnight. PET films were rinsed with methanol, dried under a stream of compressed air, and placed in a solution of PEI (1 mg/mL in methanol) overnight at 37 °C prior to use. Both glass

and PET substrates were cut into strips ~1 cm × 4 cm prior to use in film fabrication experiments. Heat shrinkable film was cut into pieces ~3 cm × 3 cm in size and was used without any further treatment. PEI/PVDMA multilayers were fabricated on glass slides and PET strips using the following general procedure: (i) Substrates were submerged in a solution of PVDMA (20 mM in acetone with respect to the polymer repeat unit) for 20 s; (ii) substrates were removed and immersed in an initial acetone bath for 20 s followed by a second acetone bath for 20 s; (iii) substrates were submerged in a solution of PEI (20 mM in acetone with respect to the polymer repeat unit) for 20 s; and (iv) substrates were removed and rinsed again using the procedure outlined under step (ii). This cycle was repeated four times to fabricate multilayers consisting of 4 PEI/PVDMA layer pairs (referred to hereafter as "bilayers"). A final layer of PVDMA was then deposited (by repeating steps (i) and (ii) of the above procedure) to provide additional reactive azlactone groups on the top surface of the films. Films having this general structure are referred to hereafter as being 4.5 bilayers thick. The resulting multilayers were washed with ~25 mL of acetone and then dried under a stream of compressed air. PEI/PVDMA multilayers were fabricated on heat shrinkable film in an analogous manner, with the exception that PEI was the first polymer deposited, resulting in a film 4 bilayers thick, and the rinse steps (i.e. steps ii and iv) consisted of washing the substrates liberally with a gentle stream of acetone (~10 mL).

Fabrication of Oligonucleotide Arrays. Oligonucleotide arrays were fabricated on azlactone-containing multilayers using a 1-μL syringe mounted above a stage with manual x-, y-, and z-axis control. This approach was used to deposit patterns of small droplets (0.1 μL) of carbonate buffer (0.1 M, pH 10.0) containing one of two different amine-terminated oligonucleotide sequences (1 mM oligonucleotide concentration) on film-coated surfaces. The two sequences

used were 5′-CCA CTG TTG CAA AGT TAT–NH_2-3′ (Probe 1) and 5′-CGC TTC TGT ATC TAT ATT CAT CA-NH_2-3′ (Probe 2). After spotting, substrates were left at room temperature in a humid environment for 30 minutes, washed extensively with SSPE buffer followed by reverse osmosis (RO) water, and then dried under a stream of nitrogen. Arrays on glass slides and PET strips were then treated with a solution of D-glucamine (20 mg/mL in PBS buffer, pH 9.75) for 1 h, rinsed extensively with RO water, and dried (see text). Arrays on heat shrinkable film were not functionalized with glucamine prior to use.

Characterization and Analysis of Oligonucleotide Arrays. Fluorescently labeled complementary oligonucleotide sequences with an exact match to either Probe 1 or Probe 2 (defined above) bearing a 3′-fluorescein (36-FAM) or a 3′-Cy3 (3Cy3Sp) moiety (Complements 1 and 2, respectively) were used in hybridization experiments. Oligonucleotide arrays fabricated on PEI/PVDMA multilayers were hybridized by placing 30 μL of SSPE buffer containing the complementary oligonucleotide(s) (1 μM total oligonucleotide concentration) on the surface, covering the surface with a glass coverslip to ensure that liquid was spread uniformly across the surface, and then incubating the array for 30 min at room temperature in a humid chamber. For experiments designed to evaluate hybridization from complex mixtures containing oligonucleotides and protein, FITC-BSA was added to the hybridization solution to a final concentration of 10 mg/mL. Non-specifically bound complementary oligonucleotides were removed from the surface by rinsing with SSPE buffer. Hybridized arrays were kept wet while fluorescence images were acquired by placing 20 μL of 0.5x SSPE buffer on the surface of the arrays; glass cover slips were applied to provide a uniform layer of buffer over the surface. Excess liquid was removed before imaging. Signal-to-noise (S/N) ratios were calculated by

dividing the background-corrected fluorescence signal by the standard deviation of the background signal.

Heat-Induced Biaxial Shrinking of Film-Coated Heat Shrinkable Film. Oligonucleotide arrays fabricated on multilayer-coated commercial heat shrinkable film were shrunk, either before or after hybridization steps, in the following general manner. Multilayer-coated heat shrinkable film arrays were secured over the open end of a 12 mm diameter straight-edge vial using a rubber band and a curved surface to produce a controlled amount of slack in the shrink wrap over the opening. The array was then exposed to a stream of hot air (measured to be ~180 °C using a thermometer) from a heat gun for ~2 s. Arrays hybridized before shrinking were imaged both prior to and after shrinking; arrays hybridized after shrinking were imaged after heat shrinking.

Fabrication and Characterization of Protein Arrays. Protein arrays containing immobilized streptavidin or FITC-streptavidin were fabricated in a manner analogous to oligonucleotide arrays. Small droplets (0.1 μL) of a 50:50 (v/v) mixture of phosphate buffer (0.1 M, pH 7.4) and glycerol containing protein (1 mg/mL protein concentration) were spotted on film-coated glass slides using a manually controlled spotting device. Protein arrays containing β-Gal and BSA were prepared with larger spots than the other protein arrays (see text) to allow characterization of β-Gal using a colorimetric assay, and, as such, were prepared by manually pipetting 10 μL of the respective protein solution (1 mg/mL, 50:50 (v/v) glycerol/phosphate buffer) onto a film-coated glass substrate. After spotting, all protein arrays were allowed to stand at room temperature in a humid environment for 2 hrs, after which the surfaces were rinsed extensively

with RO water. FITC-streptavidin arrays were imaged without further modification as described above. To characterize the ability of arrayed streptavidin to bind biotinylated substrates, arrays were incubated in a solution of a biotinylated protein [monoclonal Anti-HA High Affinity antibody (clone 3F10), 5 μg/mL in 0.1 M Tris buffer supplemented with 0.1% BSA (Tris-BSA buffer)], rinsed extensively with Tris-BSA buffer, and then incubated with a secondary antibody (Alexa-488 Anti-rat, 4 ng/mL in the same buffer). After the second labeling step, the arrays were rinsed extensively with Tris-BSA buffer and imaged as described above. To characterize the activity of immobilized β-Gal, 20 μL of an ONPG solution (1 mg/mL in 0.1 M sodium phosphate, 1 mM $MgCl_2$, 124 mM mercaptoethanol) was placed on regions reacted with spots of β-Gal and spots of BSA, with the spots of BSA serving as a negative control. Changes in the concentration of ONP over time were monitored by measuring the absorbance of these solutions at 420 nm; absorbance values were converted to concentrations using an extinction coefficient of 4500 $M^{-1}cm^{-1}$.

Results and Discussion

Fabrication of Oligonucleotide Arrays on Film-Coated Glass Substrates

Initial experiments investigating the suitability of PEI/PVDMA films as substrates for the covalent immobilization of single-stranded oligonucleotides were conducted using short (e.g., 18-23 base pair) amine end-modified probe sequences spotted onto film-coated glass slides. We used glass slides for these experiments because glass substrates are used conventionally for the fabrication of DNA arrays using other methods, and because our past studies demonstrate that thin PEI/PVDMA films anchored on APTES-treated glass are stable and compatible with standard DNA hybridization protocols.[62] All experiments described below were performed using

multilayers composed of either 4.0 or 4.5 ‘bilayers’ (or layer pairs) of PEI and PVDMA, with PVDMA deposited as the topmost layer to provide azlactone-functionalized, amine-reactive surfaces suitable for reaction with the end-terminal amines of the DNA probes (see Materials and Methods for additional details). Past reports demonstrated that otherwise identical films fabricated with 4.5 bilayers on reflective silicon substrates were ~35 nm thick, as determined by ellipsometry.[62] These PEI/PVDMA films exhibited relatively high advancing water contact angles (~74°) that prevented the rapid spreading or wicking of small drops of water. Small drops of aqueous solutions (0.1 μL) containing either oligonucleotide Probe 1 or Probe 2 were deposited on these reactive surfaces using a syringe mounted above a stage with manual x-, y-, and z-axis control. After spotting and rinsing, the surfaces of these arrays were treated with solutions containing the amine-functionalized carbohydrate D-glucamine to react with residual unreacted azlactone functionality and immobilize this molecule in the areas between the oligonucleotide spots. Glucamine has been demonstrated in several past studies to serve as an anti-fouling motif[64,65] that can prevent the non-specific adsorption of proteins[52] and fluorescently labeled oligonucleotides[62] when presented on the surfaces of PEI/PVDMA multilayers.

Figure 1A shows a merged fluorescence image of a PEI/PVDMA film patterned with an array of spots containing either Probe 1 or Probe 2, hybridized using a mixture of FAM-modified Complement 1 and Cy3-modified Complement 2 (shown in green and red, respectively) prior to imaging. The presence of bright fluorescent spots reveals that the probes were immobilized successfully and that they are available for the subsequent capture of fluorescent target sequences, suggesting that anchoring occurred substantially through the reaction of azlactone functionality with the terminal primary amines of the probes rather than with other functionality present in the nucleotide bases of these single stranded oligonucleotides (which would prevent

efficient hybridization). These images also reveal that these ultrathin oligonucleotide-functionalized films are able to withstand physical manipulation and all other treatments associated with the fabrication, hybridization, and imaging of the arrays without significant cracking, peeling, or delamination from the underlying glass substrate.

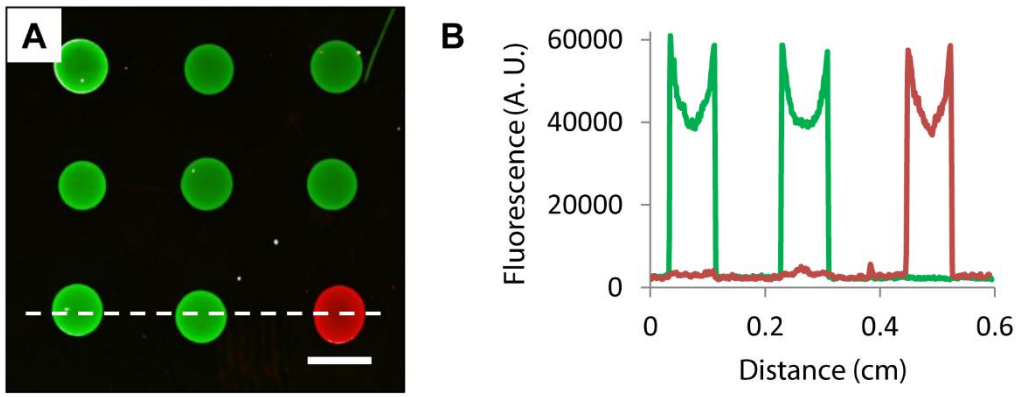

Figure 1: (A) Merged fluorescence micrograph of an oligonucleotide array of Probes 1 and 2 spotted onto a glass slide coated with a PEI/PVDMA film 4.5 bilayers thick. Arrays were hybridized using fluorescein-labeled Complement 1 (green) and Cy3-labeled Complement 2 (red) prior to imaging. Scale bar is 1 mm. (B) Line intensity profiles taken from the bottom row of features of the array in (A) (in a location near the dotted white line) for individual red and green channel images.

The apparent lack of signal overlap in the Probe 1 and Probe 2 spots and the low background signal evident by visual inspection of Figure 1A suggested limited non-specific interactions between the complement strands with the immobilized probes and the glucamine-functionalized areas of the PEI/PVDMA film. These visual observations were confirmed by quantitative analysis of line intensity profiles for one row of features of this array (using the individual, unmerged red and green scanned images; Figure 1B) and calculation of signal intensity and signal-to-noise (S/N) ratios (Table 1). For these calculations, glucamine-treated areas located between array elements and areas in spots containing non-complementary

sequences were used to quantify background signal and S/N ratios.[66] The S/N ratios reported here are similar to those we have reported previously on *in situ* synthesized arrays on standard silanized and multilayer-coated glass surfaces.[62]

Table 1. Characterization of Oligonucleotide Arrays Fabricated on Film-Coated Substrates[a]

	Fluorescence Intensity		Signal-to-Noise	
	FAM	Cy3	FAM	Cy3
Glass	$4.5\times10^4 \pm 5.7\times10^3$	$4.4\times10^4 \pm 6.4\times10^3$	96	63
PET	$2.6\times10^4 \pm 2.3\times10^3$	$4.7\times10^4 \pm 5.4\times10^3$	28	17
Heat-shrink (Prior to Shrinking)	$3.4\times10^4 \pm 5.1\times10^3$	—	13	—
Heat-shrink (After Shrinking)	$4.7\times10^4 \pm 8.8\times10^3$	—	15	—

[a]Oligonucleotide arrays spots containing Probes 1 or 2 were fabricated on glass, PET, or heat-shrinkable polyolefin substrates coated with PEI/PVDMA multilayer films (see text). Average fluorescence signal and average signal-to-noise values were determined after hybridization using fluorescently labeled Complements 1 and 2. See Materials and Methods for additional information regarding determination of background signal and calculation of S/N ratios.

The results of additional experiments demonstrated that the glucamine-functionalized areas of these arrays could resist the adsorption of protein and permit the capture and analysis of complementary oligonucleotide sequences in complex mixtures containing high concentrations of soluble protein (10 mg/mL BSA). To characterize the ability of glucamine-treated regions to prevent adsorption of BSA, we prepared an array of Probes 1 and 2 that was selectively treated with glucamine on only the right half of the array; the left half of this array was not treated with glucamine and, thus, contained residual reactive azlactone functionality (see Materials and

Methods for additional details related to glucamine treatment and array fabrication). Figure 2A shows a merged fluorescence image of this array after hybridization using a solution containing a mixture of FAM-modified Complement 1, Cy3-modified Complement 2, and 10 mg/mL of fluorescein-labeled BSA. The untreated portion of the array (left) exhibited widespread and uniform green fluorescence that rendered signal from the Probe 1 spots more difficult to

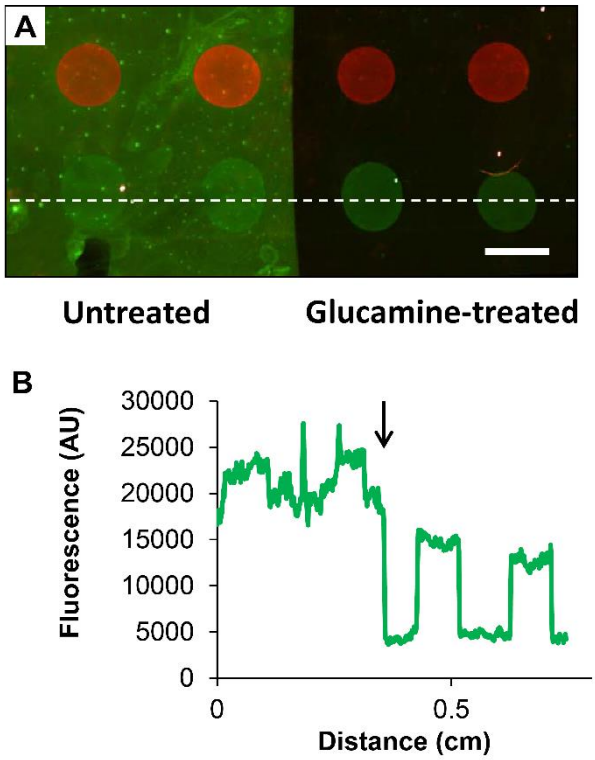

Figure 2: (A) Merged fluorescence micrograph of an oligonucleotide array of Probes 1 and 2 spotted onto a glass slide coated with a PEI/PVDMA film 4.5 bilayers thick. Prior to hybridization, the right half of the array was selectively treated with glucamine to produce a non-fouling surface, while the left half of the array was left untreated (i.e. azlactone-functionalized). The array was hybridized using an aqueous solution containing a mixture of fluorescein-labeled Complement 1 (green), fluorescein-labeled BSA (green), and Cy3-labeled Complement 2 (red) prior to imaging (see text). Scale bar is 1 mm. (B) Line intensity profile taken from the bottom row of features of the array in (A) (in a location near the dotted white line) for the green channel only; the approximate location of the boundary between the glucamine-treated region of the array (right) and untreated region (left) is indicated in this plot by the black arrow.

distinguish against background (see also the line intensity profile of green fluorescence shown on the left side of Figure 2B). This observation is not unexpected, as past results from our group and others have shown that azlactone groups can be used to immobilize proteins on surfaces[39,52,67,68] (e.g., by reaction with surface-exposed lysine groups; we return to a discussion of the utility of this feature for the fabrication of arrays of proteins in the discussion below). In contrast, in the portion of this array that was treated with glucamine (right), red and green spots from Probes 1 and 2 were clearly visible against a dark background, indicating that glucamine treatment substantially prevented protein adsorption in areas between the arrayed spots (see also the line intensity profile shown on the right side of Figure 2B). Further testing will be necessary to explore the range of solution components and more complex environmental conditions under which these surfaces can ultimately be used. However, the results of these current studies demonstrate that glucamine treatment can be used to substantially prevent protein adsorption (i.e., "fouling") that could interfere with oligonucleotide binding and detection at high protein concentrations. With further development, this approach could thus prove useful for analyses where resistance to protein adsorption is important, such as for the capture of RNA from cellular lysates or the characterization of DNA-protein interactions (i.e., transcription factor binding), etc.

Fabrication of Oligonucleotide Arrays on Flexible Plastic Substrates

We next performed a series of experiments to fabricate and characterize oligonucleotide arrays fabricated on PEI/PVDMA multilayers deposited on thin sheets of flexible poly(ethylene terephthalate) (PET). Figure 3A shows a merged fluorescence image of an array of Probes 1 and 2 spotted on a sheet of PET coated with a PEI/PVDMA film 4.5 bilayers thick (the image was acquired after hybridization using a mixture of the fluorescently labeled target complements, as

described above). The image of this plastic-backed array is qualitatively similar to that shown for the glass-backed array shown in Figure 1A, and a plot of line intensity profiles for the two fluorescence channels in the bottom row of features (Figure 3B) confirms sequence-specific binding with minimal non-specific interaction between probes and non-complement sequences. Quantitative comparison of measured fluorescence intensities and calculated S/N ratios (calculated as before for arrays on glass substrates; Table 1) reveals that while the signal intensity is similar for both the coated glass and PET substrates, the S/N ratios are approximately four times lower for the PET-based array. This difference appears to be largely a result of increased background signal intensity.

The reason for the higher background intensity on these plastic-backed arrays, compared to arrays fabricated on film-coated glass, is not clear. It is likely that additional optimization could lead to decreased background signal and improved S/N ratios, however we note that both the qualitative and quantitative results shown in Figure 3 and Table 1 reveal these arrays to permit clear and unambiguous optical differentiation of hybridized spots. In a practical context, any decrease in S/N ratios stemming from the relatively small increases in background intensity observed here could be additionally offset by the potential utility of having flexible, plastic-backed arrays of oligonucleotides that can be manipulated, either during or after fabrication, in ways that are difficult using arrays fabricated on glass.[69] For example, these arrays could be bent, cut with scissors, and readily separated into smaller pieces without observable cracking or peeling of the polymer multilayers (see Figure S1 of the Supporting Information at the end of this chapter).

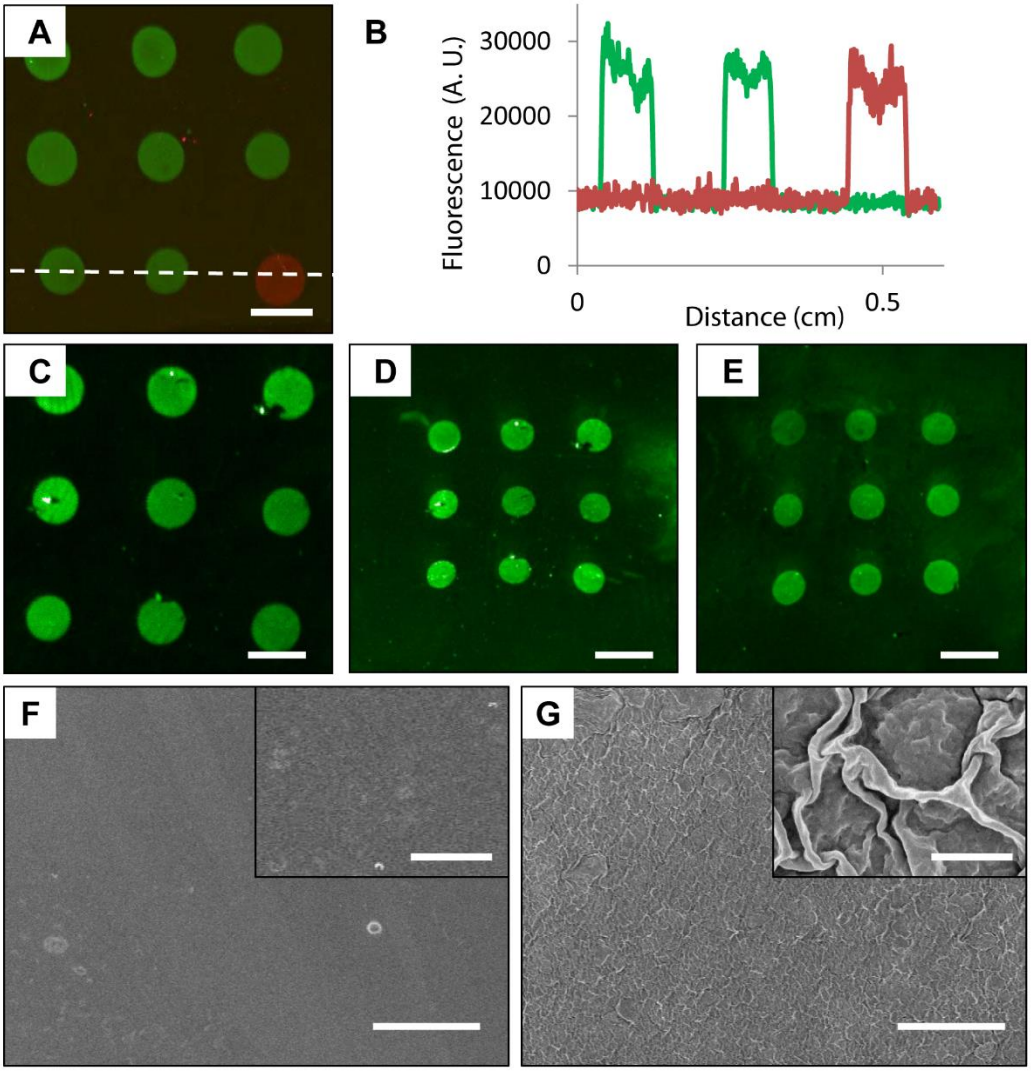

Figure 3: (A) Merged fluorescence micrograph of an oligonucleotide array of Probes 1 and 2 spotted onto a thin flexible PET sheet coated with a PEI/PVDMA film 4.5 bilayers thick. The array was hybridized using fluorescein-labeled Complement 1 (green) and Cy3-labeled Complement 2 (red) prior to imaging. (B) Line intensity profiles taken from the bottom row of features of the array shown in (A) (in a location near the dotted white line) for the individual red and green channels. (C-E) Fluorescence micrographs of arrays containing Probe 1 spotted onto multilayer-coated heat shrinkable film and hybridized prior to imaging. The images in (C) and (D) are of the same substrate (C) before and (D) after heat treatment to shrink the array; the array in (E) was hybridized and imaged after shrinking of an otherwise similar unhybridized array. (F-G) Scanning electron microscopy images of heat shrinkable film coated with PEI/PVDMA films (F) before and (G) after shrinking. Scale bars are (A, C-E) 1 mm, (F-G) 50 μm, and (F-G, inset) 2 μm.

A past patent describes the immobilization of oligonucleotides on chemically modified heat-shrinkable polyethylene film treated with azlactone-containing copolymers to fabricate arrays that can be reduced in size physically (shrunken) by exposure to heat to increase the density of arrayed features.[55] We performed a series of experiments to characterize the layer-by-layer assembly of our PEI/PVDMA multilayers on sheets of unmodified, commercially available polyolefin heat-shrink film and determine the extent to which these covalently crosslinked films (and arrays of oligonucleotides immobilized on them) could withstand exposure to heat and physical forces encountered during subsequent shrinking of the underlying substrate. To our knowledge, the behavior of ultrathin polymer-based multilayers (e.g., films fabricated by layer-by-layer assembly) on heat shrinkable film has not been previously reported, and the thermal properties of covalently crosslinked PEI/PVDMA-based multilayers have not been investigated. It was therefore not clear at the outset of these studies whether these ultrathin PEI/PVDMA films would be physically robust enough to withstand shrinking without cracking and delaminating or whether they would be able to withstand temperatures required to affect shrinking.

Figure 3C shows a fluorescence image of a hybridized array of spots of Probe 1 on PEI/PVDMA-coated heat shrinkable film prior to shrinking. The image of the array shows uniform, well-formed spots with signal intensities and S/N ratios similar to those observed for arrays fabricated on multilayer-coated PET (Table 1). Similar arrays fabricated on these thin polyolefin substrates could also be cut and manually separated into smaller pieces without observable cracking or delamination of the multilayers or the features of the arrays after hybridization (see Figure S1 of the Supporting Information). Treatment of the hybridized array shown in Figure 3C briefly with hot air using a hand-held laboratory heat gun resulted in uniform, biaxial shrinkage of the film to produce, under the conditions used here, an array

approximately two-thirds the size of the original (Figure 3D; see Materials and Methods for additional details of procedures used to heat-treat and shrink these films). Inspection of this image reveals that the shrinking process did not significantly distort the shape or arrangement of the array elements. The amount of shrinking in the vertical and horizontal directions was similar (~64% vs. ~60%, respectively), and the arrayed oligonucleotide spots remained circular in most cases. A comparison of the signal intensity of the array before and after shrinking (Table 1) reveals that despite the higher background signal in the array after shrinking (~11,000 RFU, compared to ~5,000 RFU prior to shrinking), the S/N ratio increases slightly due to a corresponding increase in the average signal intensity of the spots.

Comparison of the fluorescence images of these arrays shown in Figure 3C and 3D before and after shrinking reveals that while several small defects were observed before shrinking, no additional macroscale degradation or delamination of the multilayer film was observed after shrinking. The images in Figure 3F-G show high and low magnification scanning electron microscopy (SEM) images of multilayer-coated heat shrinkable film before (F) and after (G) heat treatment. Before shrinking, the multilayer film coating was smooth and uniform with few distinguishable topographic features. After shrinking of the underlying heat-shrinkable film, however, the cross-linked multilayer coating appeared intact but exhibited a wrinkled morphology. This morphology is similar to that seen in many other examples of wrinkling of thin polymer or metal films induced by the shrinking of an underlying substrate,[70,71] and is thus likely a consequence of compressive forces experienced by the adherent multilayer film as the temperature of the underlying polyolefin film is heated above its glass transition temperature. Characterization by SEM did not reveal significant microscale cracking or peeling or other substantial changes in morphology in these heat-treated multilayers.

We conducted a final experiment to investigate the effect of the induced surface topography, as well as heat treatment, on the integrity and accessibility of the surface-immobilized oligonucleotides after shrinking of the array. Figure 3E shows an array that was fabricated on heat-shrink film (as described above) and shrunken via heat treatment, followed by hybridization using Complement 1. Signal intensities and S/N ratios for this array were 30% and 45% lower, respectively, than those of the array shrunken after hybridization (Figure 3D), suggesting that some probes could have been degraded during heating or rendered less accessible for hybridization during rearrangements that occur in these multilayers upon shrinking. Further optimization of array fabrication and treatment steps (e.g. different heat treatment methods, changes in thickness or post-treatment of the PEI/PVDMA multilayer film coating, or hybridization conditions) could potentially lead to increased signal intensity and/or decreased background signal. However, the results reported here demonstrate that thin multilayered films can be assembled on heat-shrink film and that the films remain stable during functionalization, heat-induced shrinkage, and hybridization steps without substantial film delamination or loss of the ability to hybridize complementary oligonucleotide sequences.

Fabrication of Functional Protein Arrays

As described above, several past studies have demonstrated the utility of azlactone-functionalized polymers and surfaces for the covalent immobilization of proteins.[39,52,67,68] The results shown above in Figure 2 suggest that FITC-labeled BSA can be captured on surfaces coated with reactive PEI/PVDMA multilayers 4.5 bilayers thick. The results of additional experimnts demonstrated that spotting-based methods similar to those described above could be used to fabricate arrays containing individual spots of fluorescently labeled BSA (see Figure S2

of the Supporting Information). On the basis of these results, we performed additional experiments to explore the feasibility of using spotting-based approaches to fabricate immobilized arrays of functional proteins and enzymes on these reactive films. Initial proof of concept experiments were performed using fluorescently labeled streptavidin (FITC-streptavidin). Streptavidin binds strongly to the small molecule biotin,[72] and the immobilization of this protein on surfaces is thus a common first step of strategies used to immobilize other proteins and other agents (e.g., by using streptavidin-functionalized surfaces to capture and present biotinylated target molecules).[73] These experiments were performed by depositing small drops (0.1 μL) of streptavidin in a glycerol/phosphate buffer mixture onto the surfaces of glass slides coated with PEI/PVDMA films, incubating at room temperature for two hours, and then rinsing extensively with deionized water prior to imaging.

Figure 4A shows a fluorescence image of an array of immobilized FITC-streptavidin. Inspection of this image reveals the presence of well-formed, circular green fluorescent spots with no visible streaking, non-uniform intensities (e.g., no substantial 'coffee ring' effect), or other imperfections. These results are generally similar to those observed for arrays of immobilized FITC-BSA (see Figure S2). These results do not establish directly that these proteins are covalently bound to these surfaces by reaction with surface-exposed lysine residues, however we note that these spots remained intact and did not diminish substantially in fluorescence intensity after extensive washing and incubation with surfactant solutions (e.g., see Figure S2), demonstrating that protein is strongly bound to these surfaces.

The results of additional experiments demonstrated that streptavidin was immobilized to film-coated substrates in a form that was intact and able to interact with, capture, and present biotinylated substrates. Arrays used for these experiments were fabricated by depositing small

drops containing unlabeled streptavidin (using procedures identical to those described above for the immobilization of FITC-streptavidin) and then treating the surface of the array with glucamine to consume remaining azlactone functionality and immobilize this non-fouling motif in areas between the spots of the array. Figure 4B shows an image of an array fabricated in this

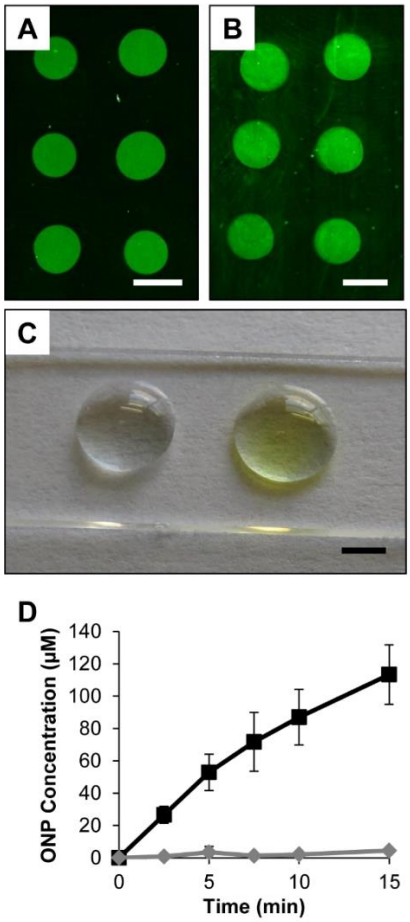

Figure 4: (A-B) Representative fluorescence micrographs of glass substrates coated with PEI/PVDMA films spotted with (A) FITC-labeled streptavidin or (B) unlabeled streptavidin (the image in (B) was treated with anti-HA-biotin and anti-rat IgG Alexa Fluor 488 prior to imaging; see text). (C) Digital photograph of film-coated glass containing spots of immobilized β-galactosidase (right spot) or BSA (left spot) incubated under droplets of ONPG for 10 minutes. (D) Plot of ONP concentration vs. time measured from a droplet incubated on a spot containing immobilized β-galactosidase (black squares) or BSA (grey diamonds). Scale bars are (A-B) 1 mm and (C) 2 mm.

manner after treatment with a biotinylated protein (Anti-HA-Biotin) followed by treatment with a fluorescently labeled secondary antibody (false-colored green) to aid in visualization. Inspection of this image reveals bright green spots clearly visible against the dark background of the array. These results indicate that a substantial fraction of streptavidin deposited during the fabrication of the array was immobilized without denaturation and retained its ability to bind biotinylated substrates. These results also underscore the performance and highlight the general utility of the non-fouling glucamine-functionalized regions of these arrays – features that are particularly important in this specific context because both the biotinylated antibody analyte and the fluorescently labeled secondary antibody used here are protein-based agents that can adsorb non-specifically to a range of other surfaces and thereby complicate analysis.

Finally, to investigate the feasibility of using this multilayer-based approach to design surfaces containing small spots of active enzymes, we also fabricated surfaces containing spots of β-Gal, an enzyme that catalytically cleaves a colorless substrate (in these experiments, ortho-nitrophenyl-β-galactoside, ONPG) to form a highly colored yellow compound (ortho-nitrophenol, ONP) that can be quantified readily in solution using UV-visible spectrophotometry.[74] This provided a convenient readout reflecting the enzymatic activity of β-Gal immobilized on the surfaces of PEI/PVDMA multilayers. Figure 4C shows a digital photograph of two spots of immobilized protein, one containing immobilized β-Gal (right) and one containing immobilized BSA (left, used as a control) incubated under droplets of aqueous ONPG for 10 minutes. The spots shown here are larger (e.g., ~5 mm) than those used for the fabrication of arrays in experiments described above to facilitate visualization and quantification of ONP production in these proof of concept experiments. The visual identification (Figure 4C) of a yellow product and characterization of time-dependent increases in the amount of ONP

(Figure 4D) in the solutions above the spot containing immobilized β-Gal revealed this protein to be immobilized in a form that remains enzymatically active.

Summary and Conclusions

We have reported a top-down approach to fabricate oligonucleotide and protein arrays on surfaces coated with ultrathin amine-reactive polymer multilayers. The reaction of amine-terminated oligonucleotide sequences with azlactone functionality present in PEI/PVDMA multilayers fabricated on planar glass slides yielded arrays of immobilized probes capable of hybridizing fluorescently labeled complementary sequences with high signal intensity, high signal-to-noise ratio, and high sequence specificity. Treatment of residual azlactone functionality in the areas between the probe spots on these arrays with the non-fouling molecule D-glucamine yields regions that resist non-specific adsorption of protein and permitted hybridization of the arrays in complex media containing high concentrations of protein. Our results also demonstrate that the residual azlactone groups in these thin films can be exploited to immobilize proteins on these surfaces and fabricate functional arrays of proteins and enzymes.

Finally, the ability to fabricate these reactive coatings layer-by-layer on substrates of arbitrary size, shape, and composition permitted the design of spotted arrays of oligonucleotide probes on the surfaces of multilayer-coated sheets of poly(ethylene terephthalate) and commercial heat-shrinkable polymer film. Because arrays fabricated on flexible polymer substrates can be bent, cut, resized, and manipulated physically in ways that are difficult using conventional array substrates (e.g., glass), this approach could contribute to the development of new assay formats and non-traditional applications of biomolecule arrays. The surface preparation and spotting methods described here are technically straightforward, easy to

implement on a laboratory scale, and do not require access to specialized equipment. Although manual spotting and arrays with relatively large feature sizes were used to demonstrate proof of concept in this study, this multilayer-based approach should also be compatible with automated liquid-handling methods (e.g., pin-transfer robots, etc.) used routinely to fabricate higher-density arrays of oligonucleotides and proteins on conventional substrates.

Acknowledgments. Support was provided in part by the National Science Foundation (DMR 0520527 and DMR 1121288) through a grant to the Materials Research Science and Engineering Center (MRSEC) and through NSF-supported shared facilities at the University of Wisconsin, and by the National Institutes of Health Protein Capture Reagents Technology Development Program (Contract U54 DK093467). A. H. B. is a NSF Graduate Research Fellow. M. C. D. C. gratefully acknowledges the Natural Sciences and Engineering Research Council of Canada (NSERC) for a graduate fellowship. We thank Dr. Steven M. Heilmann (3M) for providing samples of 2-vinyl-4,4-dimethylazlactone (VDMA), and Jerald Rasmussen (3M) for helpful discussions related to azlactone-functionalized heat shrinkable materials. We thank Thomas Malott, Yuan Yuan, and Dr. Uttam Manna for technical advice and many helpful discussions.

References

(1) Schena, M.; Shalon, D.; Davis, R. W.; Brown, P. O. *Science* **1995**, *270*, 467-470.

(2) Duggan, D. J.; Bittner, M.; Chen, Y. D.; Meltzer, P.; Trent, J. M. *Nat. Genet.* **1999**, *21*, 10-14.

(3) Lockhart, D. J.; Winzeler, E. A. *Nature* **2000**, *405*, 827-836.

(4) Lipshutz, R. J.; Fodor, S. P. A.; Gingeras, T. R.; Lockhart, D. J. *Nat. Genet.* **1999**, *21*, 20-24.

(5) Singh-Gasson, S.; Green, R. D.; Yue, Y. J.; Nelson, C.; Blattner, F.; Sussman, M. R.; Cerrina, F. *Nat. Biotechnol.* **1999**, *17*, 974-978.

(6) Nuwaysir, E. F.; Huang, W.; Albert, T. J.; Singh, J.; Nuwaysir, K.; Pitas, A.; Richmond, T.; Gorski, T.; Berg, J. P.; Ballin, J.; McCormick, M.; Norton, J.; Pollock, T.; Sumwalt, T.; Butcher, L.; Porter, D.; Molla, M.; Hall, C.; Blattner, F.; Sussman, M. R.; Wallace, R. L.; Cerrina, F.; Green, R. D. *Genome Res.* **2002**, *12*, 1749-1755.

(7) LeProust, E. M.; Peck, B. J.; Spirin, K.; McCuen, H. B.; Moore, B.; Namsaraev, E.; Caruthers, M. H. *Nucleic Acids Res* **2010**, *38*, 2522-2540.

(8) Hughes, T. R.; Mao, M.; Jones, A. R.; Burchard, J.; Marton, M. J.; Shannon, K. W.; Lefkowitz, S. M.; Ziman, M.; Schelter, J. M.; Meyer, M. R.; Kobayashi, S.; Davis, C.; Dai, H.; He, Y. D.; Stephaniants, S. B.; Cavet, G.; Walker, W. L.; West, A.; Coffey, E.; Shoemaker, D. D.; Stoughton, R.; Blanchard, A. P.; Friend, S. H.; Linsley, P. S. *Nat Biotechnol* **2001**, *19*, 342-347.

(9) Chrisey, L. A.; Lee, G. U.; Oferrall, C. E. *Nucleic Acids Res.* **1996**, *24*, 3031-3039.

(10) Snijders, A. M.; Nowak, N.; Segraves, R.; Blackwood, S.; Brown, N.; Conroy, J.; Hamilton, G.; Hindle, A. K.; Huey, B.; Kimura, K.; Law, S.; Myambo, K.; Palmer, J.; Ylstra, B.; Yue, J. P.; Gray, J. W.; Jain, A. N.; Pinkel, D.; Albertson, D. G. *Nat. Genet.* **2001**, *29*, 263-264.

(11) MacBeath, G. *Nat. Genet.* **2002**, *32*, 526-532.

(12) Zhu, H.; Snyder, M. *Curr. Opin. Chem. Biol.* **2003**, *7*, 55-63.

(13) Belosludtsev, Y.; Iverson, B.; Lemeshko, S.; Eggers, R.; Wiese, R.; Lee, S.; Powdrill, T.; Hogan, M. *Anal. Biochem.* **2001**, *292*, 250-256.

(14) Gilles, P. N.; Wu, D. J.; Foster, C. B.; Dillon, P. J.; Chanock, S. J. *Nat. Biotechnol.* **1999**, *17*, 365-370.

(15) Rowe, C. A.; Tender, L. M.; Feldstein, M. J.; Golden, J. P.; Scruggs, S. B.; MacCraith, B. D.; Cras, J. J.; Ligler, F. S. *Anal. Chem.* **1999**, *71*, 3846-3852.

(16) Ghosh, S. S.; Musso, G. F. *Nucleic Acids Res.* **1987**, *15*, 5353-5372.

(17) Zammatteo, N.; Jeanmart, L.; Hamels, S.; Courtois, S.; Louette, P.; Hevesi, L.; Remacle, J. *Anal. Biochem.* **2000**, *280*, 143-150.

(18) Schena, M.; Shalon, D.; Heller, R.; Chai, A.; Brown, P. O.; Davis, R. W. *Proc Natl Acad Sci U S A* **1996**, *93*, 10614-10619.

(19) Proudnikov, D.; Timofeev, E.; Mirzabekov, A. *Anal. Biochem.* **1998**, *259*, 34-41.

(20) MacBeath, G.; Schreiber, S. L. *Science* **2000**, *289*, 1760-1763.

(21) Zhu, H.; Bilgin, M.; Bangham, R.; Hall, D.; Casamayor, A.; Bertone, P.; Lan, N.; Jansen, R.; Bidlingmaier, S.; Houfek, T.; Mitchell, T.; Miller, P.; Dean, R. A.; Gerstein, M.; Snyder, M. *Science* **2001**, *293*, 2101-2105.

(22) Lamture, J. B.; Beattie, K. L.; Burke, B. E.; Eggers, M. D.; Ehrlich, D. J.; Fowler, R.; Hollis, M. A.; Kosicki, B. B.; Reich, R. K.; Smith, S. R.; Varma, R. S.; Hogan, M. E. *Nucleic Acids Res.* **1994**, *22*, 2121-2125.

(23) Cohen, G.; Deutsch, J.; Fineberg, J.; Levine, A. *Nucleic Acids Res.* **1997**, *25*, 911-912.

(24) Zhu, H.; Klemic, J. F.; Chang, S.; Bertone, P.; Casamayor, A.; Klemic, K. G.; Smith, D.; Gerstein, M.; Reed, M. A.; Snyder, M. *Nat. Genet.* **2000**, *26*, 283-289.

(25) Guo, Z.; Guilfoyle, R. A.; Thiel, A. J.; Wang, R. F.; Smith, L. M. *Nucleic acids research* **1994**, *22*, 5456-5465.

(26) Beier, M.; Hoheisel, J. D. *Nucleic Acids Res.* **1999**, *27*, 1970-1977.

(27) Benters, R.; Niemeyer, C. M.; Wöhrle, D. *ChemBioChem* **2001**, *2*, 686-694.

(28) Chrisey, L. A.; Lee, G. U.; O'Ferrall, C. E. *Nucleic Acids Res.* **1996**, *24*, 3031-3039.

(29) Brockman, J. M.; Frutos, A. G.; Corn, R. M. *J. Am. Chem. Soc.* **1999**, *121*, 8044-8051.

(30) Strother, T.; Cai, W.; Zhao, X. S.; Hamers, R. J.; Smith, L. M. *J. Am. Chem. Soc.* **2000**, *122*, 1205-1209.

(31) Okamoto, T.; Suzuki, T.; Yamamoto, N. *Nat. Biotechnol.* **2000**, *18*, 438-441.

(32) Rogers, Y. H.; Jiang-Baucom, P.; Huang, Z. J.; Bogdanov, V.; Anderson, S.; Boyce-Jacino, M. T. *Anal. Biochem.* **1999**, *266*, 23-30.

(33) Smith, E. A.; Wanat, M. J.; Cheng, Y. F.; Barreira, S. V. P.; Frutos, A. G.; Corn, R. M. *Langmuir* **2001**, *17*, 2502-2507.

(34) Tengvall, P.; Jansson, E.; Askendal, A.; Thomsen, P.; Gretzer, C. *Colloid Surface B* **2003**, *28*, 261-272.

(35) Peelen, D.; Smith, L. M. *Langmuir* **2005**, *21*, 266-271.

(36) Sun, B.; Colavita, P. E.; Kim, H.; Lockett, M.; Marcus, M. S.; Smith, L. M.; Hamers, R. J. *Langmuir* **2006**, *22*, 9598-9605.

(37) Lockett, M. R.; Weibel, S. C.; Phillips, M. F.; Shortreed, M. R.; Sun, B.; Corn, R. M.; Hamers, R. J.; Cerrina, F.; Smith, L. M. *J. Am. Chem. Soc.* **2008**, *130*, 8611-8613.

(38) Rasmussen, J. K.; Heilmann, S. M.; Krepski, L. R. In *Encyclopedia of Polymer Science and Engineering*; 2nd Edition ed.; Mark, H. F., Kroschwitz, J. I., Eds. 1988; Vol. 11, p 558-571.

(39) Heilmann, S. M.; Rasmussen, J. K.; Krepski, L. R. *J. Polym. Sci., Part A: Polym. Chem.* **2001**, *39*, 3655-3677.

(40) Xie, S. F.; Svec, F.; Frechet, J. M. J. *Biotechnol. Bioeng.* **1999**, *62*, 30-35.

(41) Peterson, D. S.; Rohr, T.; Svec, F.; Frechet, J. M. J. *Anal. Chem.* **2002**, *74*, 4081-4088.

(42) Drtina, G. J.; Haddad, L. C.; Rasmussen, J. K.; Gaddam, B. N.; Williams, M. G.; Moeller, S. J.; Fitzsimons, R. T.; Fansler, D. D.; Buhl, T. L.; Yang, Y. N.; Weller, V. A.; Lee, J. M.; Beauchamp, T. J.; Heilmann, S. M. *React. Funct. Polym.* **2005**, *64*, 13-24.

(43) Heilmann, S. M.; Drtina, G. J.; Haddad, L. C.; Rasmussen, J. K.; Gaddam, B. N.; Liu, J. J.; Fitzsimons, R. T.; Fansler, D. D.; Vyvyan, J. R.; Yang, Y. N.; Beauchamp, T. J. *J. Mol. Catal. B: Enzym.* **2004**, *30*, 33-42.

(44) Fournier, D.; Pascual, S.; Montembault, V.; Haddleton, D. M.; Fontaine, L. *J. Comb. Chem.* **2006**, *8*, 522-530.

(45) Heilmann, S. M.; Drtina, G. J.; Eitzman, P. D.; Haddad, L. C.; Coleman, P. L.; Hyde, F. W.; Johnson, T. W.; Rasmussen, J. K.; Smith, H. K.; Liu, R. J.; Fitzsimons, R. T.; Williams, M. G.; Moeller, S. J.; Nakamura, M. M.; Gibbens, K. J.; Buhl, T. L. *J. Mol. Catal. B: Enzym.* **2007**, *45*, 1-9.

(46) Cullen, S. P.; Mandel, I. C.; Gopalan, P. *Langmuir* **2008**, *24*, 13701-13709.

(47) Lucchesi, C.; Pascual, S.; Dujardin, G.; Fontaine, L. *React. Funct. Polym.* **2008**, *68*, 97-102.

(48) Barringer, J. E.; Messman, J. M.; Banaszek, A. L.; Meyer, H. M.; Kilbey, S. M. *Langmuir* **2009**, *25*, 262-268.

(49) Messman, J. M.; Lokitz, B. S.; Pickel, J. M.; Kilbey, S. M. *Macromolecules* **2009**, *42*, 3933-3941.

(50) Levere, M. E.; Ho, H. T.; Pascual, S.; Fontaine, L. *Polym. Chem.* **2011**, *2*, 2878-2887.

(51) Buck, M. E.; Zhang, J.; Lynn, D. M. *Adv. Mater.* **2007**, *19*, 3951-3955.

(52) Buck, M. E.; Breitbach, A. S.; Belgrade, S. K.; Blackwell, H. E.; Lynn, D. M. *Biomacromolecules* **2009**, *10*, 1564-1574.

(53) Buck, M. E.; Schwartz, S. C.; Lynn, D. M. *Chem. Mater.* **2010**, *22*, 6319-6327.

(54) Buck, M. E.; Lynn, D. M. *Polym. Chem.* **2012**, *3*, 66-80.

(55) Halverson, K. J.; Patil, S. L.; Rasmussen, J. K. US Patent 7189842, 2002

(56) Bergbreiter, D. E.; Liao, K.-s. *Soft Matter* **2009**, *5*, 23-28.

(57) Quinn, J. F.; Johnston, A. P. R.; Such, G. K.; Zelikin, A. N.; Caruso, F. *Chem Soc Rev* **2007**, *36*, 707-718.

(58) Buck, M. E.; Lynn, D. M. *Langmuir* **2010**, *26*, 16134-16140.

(59) Broderick, A. H.; Azarin, S. M.; Buck, M. E.; Palecek, S. P.; Lynn, D. M. *Biomacromolecules* **2011**, *12*, 1998-2007.

(60) Kinsinger, M. I.; Buck, M. E.; Abbott, N. L.; Lynn, D. M. *Langmuir* **2010**, *26*, 10234-10242.

(61) Tocce, E. J.; Broderick, A. H.; Murphy, K. C.; Liliensiek, S. J.; Murphy, C. J.; Lynn, D. M.; Nealey, P. F. *J. Biomed. Mater. Res., Part A* **2012**, *100*, 84-93.

(62) Broderick, A. H.; Lockett, M. R.; Buck, M. E.; Yuan, Y.; Smith, L. M.; Lynn, D. M. *Chem. Mater.* **2011**, *24*, 938-945.

(63) Saurer, E. M.; Flessner, R. M.; Buck, M. E.; Lynn, D. M. *J. Mater. Chem.* **2011**, *21*, 1736-1745.

(64) Ostuni, E.; Chapman, R. G.; Holmlin, R. E.; Takayama, S.; Whitesides, G. M. *Langmuir* **2001**, *17*, 5605-5620.

(65) Orner, B. P.; Derda, R.; Lewis, R. L.; Thomson, J. A.; Kiessling, L. L. *J. Am. Chem. Soc.* **2004**, *126*, 10808-10809.

(66) Lockett, M. R.; Smith, L. M. *Anal. Chem.* **2009**, *81*, 6429-6437.

(67) Xie, S.; Svec, F.; Fréchet, J. M. J. *Biotechnol. Bioeng.* **1999**, *62*, 30-35.

(68) Tripp, J. A.; Stein, J. A.; Svec, F.; Frechet, J. M. J. *Org. Lett.* **2000**, *2*, 195-198.

(69) Heinrich, K. W.; Wolfer, J.; Hong, D.; LeBlanc, M.; Sussman, M. R. *Plant Physiol.* **2012**, *159*, 548-557.

(70) Chen, C.-M.; Yang, S. *Polym. Int.* **2012**, *61*, 1041-1047.

(71) Genzer, J.; Groenewold, J. *Soft Matter* **2006**, *2*, 310-323.

(72) Weber, P. C.; Ohlendorf, D. H.; Wendoloski, J. J.; Salemme, F. R. *Science* **1989**, *243*, 85-88.

(73) Turková, J. *J. Chromatogr., B: Biomed. Sci. Appl.* **1999**, *722*, 11-31.

(74) Miller, J. In *Experiments in Molecular Genetics*; 3 ed.; Cold Spring Harbor Laboratory: 1972, p 352-355.

Supporting Information for Chapter 5

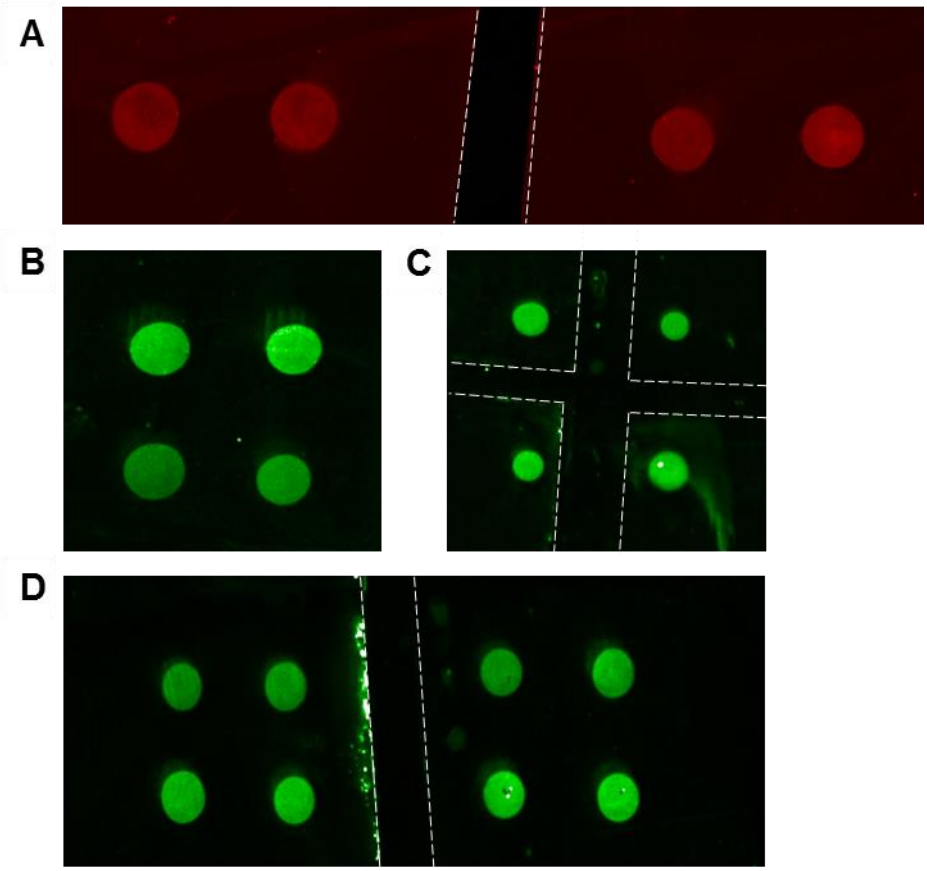

Figure S1: Representative fluorescence micrographs of arrays of oligonucleotide Probe 2 fabricated on a flexible PET substrate (panel A) and oligonucleotide Probe 1 fabricated on flexible heat-shrinkable polymer film substrates (panels B-D). Substrates were fabricated on reactive multilayer-coated substrates using spotting-based methods similar to those described in the main text. The resulting arrays were then bent manually by flexing the substrates end to end multiple times (no creases were formed). Arrays shown in panels A, C and D were then cut manually using scissors and separated into smaller pieces (the substrate in panel B was bent, but not cut). All arrays were then hybridized with either Complement 2 (panel A) or Complement 1 (B-D), using methods described in the main text prior to imaging. White dotted lines indicate locations where the samples were cut; samples were physically separated after cutting, such that areas between the dotted lines in these images are devoid of substrate or film. The spots in these images are ~1 mm in diameter.

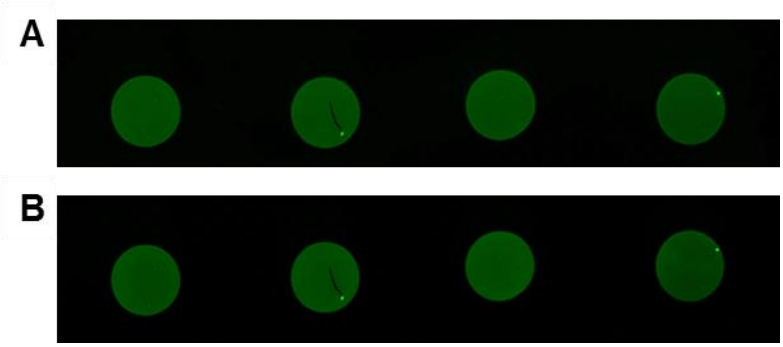

Figure S2: Representative fluorescence micrographs of an array of spots of FITC-labeled bovine serum albumin (BSA) fabricated on glass substrates coated with reactive multilayer films. The array was fabricated manually using spotting-based methods similar to those described in the main text. The image in panel A shows an array of four spots of BSA imaged directly after fabrication (see text). The image in panel B shows an image of the same array after soaking in a solution of the non-ionic surfactant Tween 20 (1% v/v) in water for 30 minutes at room temperature.

Chapter 4

Photolithographic Synthesis of High-Density DNA and RNA Arrays on Flexible, Transparent, and Easily Sub-Divided Plastic Substrates‡

‡ Portions of this chapter have previously been published as: Holden, M.T.; Carter, M.C.D.; Wu, C.-H.; Wolfer, J.; Codner, E.; Sussman, M.R.; Smith, L.M.; Lynn, D.M. "Photolithographic Synthesis of High-Density DNA and RNA Arrays on Flexible, Transparent, and Easily Sub-Divided Plastic Substrates" *Analytical Chemistry* **2015**, *87*, 11420-3089. M.T.H. and M.C.D.C. were co-first authors. M.T.H. performed the MAS synthesis. My contribution was in fabricating the films, operating the laser-cutter, and analyzing the data.

ABSTRACT: The photolithographic fabrication of high-density DNA and RNA arrays on flexible and transparent plas-tic substrates is reported. The substrates are thin sheets of poly(ethylene terephthalate) (PET) coated with crosslinked polymer multilayers that present hydroxyl groups suitable for conventional phosphoramidite-based nucleic acid syn-thesis. We demonstrate that by modifying MAS procedures to accommodate the physical and chemical properties of these materials, it is possible to synthesize plastic-backed oligonucleotide arrays with feature sizes as small as 14 x 14 μm and feature densities in excess of 125 000/cm2, similar to specifications attainable using rigid substrates such as glass or glassy carbon. These plastic-backed arrays are tolerant to a wide range of hybridization temperatures, and improved synthetic procedures are described that enable the fabrication of arrays with sequences up to 50 nucleotides in length. These arrays hybridize with S/N ratios comparable to those fabricated on otherwise identical arrays prepared on glass or glassy carbon. This platform supports the enzymatic synthesis of RNA arrays and proof-of-concept experiments are presented showing that the arrays can be readily sub-divided into smaller arrays (or ‘millichips’) using common labora-tory-scale laser cutting tools. These results expand the utility of oligonucleotide arrays fabricated on plastic substrates and open the door to new potential applications for these important bioanalytical tools.

Introduction

DNA that has been spatially patterned upon a surface is a cornerstone of modern bioanalysis. The development of high-density DNA arrays has been driven largely by their ability to capture complementary nucleic acids from solution with high specificity.[1] This capability has enabled numerous applications including gene expression analysis, genotyping, pathogen detection, enrichment for exome sequencing, and comparative genomic hybridization.[2-7] Recent studies have expanded the range of analytes that can be studied with DNA arrays, through assays such as those examining the sequence preferences of transcription factors or the binding of aptamers and their targets.[8,9] Arrays synthesized using *in situ* methods, such as those produced commercially by Nimblegen, Agilent, or Affymetrix, are also now routinely used as sources for complex oligonucleotide pools for gene synthesis.[10-12] Such arrays are fabricated using phosphoramidite chemistry to build oligonucleotides base-by-base, enabling the synthesis of specific sequences up to ~150 nucleotides in length.[13]

In contrast to 'spotted' or 'top-down' techniques of array production—where pre-synthesized biomolecules are coupled to a surface—*in situ* or 'bottom-up' methods are advantageous in terms of their affordability and versatility. Nonetheless, all *in situ* approaches for DNA synthesis are dependent upon precision optics or highly targeted reagent delivery and have conventionally employed rigid and planar substrates.[14,15] This technical requirement has prevented high-resolution DNA patterning on surfaces with the diverse formats or non-planar geometries often found in miniaturized hybridization devices.[16,17] A conceivable solution to this problem would be to synthesize DNA arrays on flexible substrates that could later be physically manipulated or cut into desired shapes or sizes. Oligonucleotides patterned upon these substrates could, in turn, template the programmable attachment of other species, such as small molecules,

proteins, or even cells, and thereby serve as a universal scaffold for high-resolution biomolecule patterning on arbitrary surfaces.[18]

A proof-of-concept approach to high-density DNA array fabrication has previously been demonstrated on polymer film-coated plastic substrates.[19] That study demonstrated that plastic substrates coated with multilayered polymer films were physically and chemically robust enough to withstand the *in situ* synthesis of short oligonucleotides (~20 bases long), and that these arrays could be hybridized and de-hybridized with fluorescently-labelled complementary sequences. This report extends this work to i) increase the density of features that is possible using this approach, ii) demonstrate that the resulting plastic-backed arrays are stable to a variety of hybridization temperatures, iii) develop improved synthesis conditions for the production of arrays containing longer oligonucleotides, and iv) demonstrate the laser cutting of the PET substrate into smaller sub-sections. These advances are used to synthesize DNA arrays containing two distinct sequences within a single feature and to fabricate the first high-density RNA array on a flexible plastic substrate. We then explore the use of PET-based arrays as a second-generation substrate for millichip fabrication.[20]

Materials and Methods

Glassy Carbon Functionalization

I) Materials: Sigradur G-type glassy carbon surfaces were purchased from HTW (Thierhaupten, Germany). 9-Decen-1-ol was purchased from Sigma-Aldrich (MO, USA).

II) Methods: Glassy carbon surfaces were hydrogen-terminated in a 13.56 MHz inductively coupled hydrogen plasma. Treatment was conducted at 900°C for 20 minutes (H_2 pressure at 50 Torr) and slowly cooled to room temperature while the plasma remained running. 50 µL of 9-

decen-1-ol was immediately placed on the surface, which was then covered with a quartz cover slip. The slides were irradiated with a mercury vapor quartz grid lamp (λ = 254 nm, 0.35 mW/cm^2) for 16 hours under a nitrogen purge. The surfaces were then rinsed with water and ethanol before being dried under a nitrogen stream.

Fabrication and Functionalization of PEI/PVDMA Multilayers

I) Materials: Branched poly(ethylenimine) (PEI; MW ~25,000), acetone (ACS grade), ethyl acetate (>99.5%), dimethylsulfoxide (DMSO, 98%), and azobisisobutyronitrile (AIBN, 98%, recrystallized from methanol) were purchased from Sigma Aldrich (Milwaukee, WI). D-Glucamine (>95.0%) was purchased from TCI Chemicals (Philadelphia, PA). Methanol (MeOH; ACS grade) was purchased from Avantor Performance Materials (Center Valley, PA). Ethanol (EtOH, 200 proof) was obtained from Decon Labs (King of Prussia, PA). 2-Vinyl-4,4-dimethylazlactone (VDMA), a kind gift from Dr. Steven M. Heilmann (3M Corporation, Minneapolis, MN), was fractionally distilled under vacuum (B.P. ~22 °C at ~500 mTorr; clear mobile liquid at room temperature) and then stored with 500 ppm butylated hydroxytoluene (BHT) and 1000 ppm triethylamine at 0 °C prior to use. Poly(2-vinyl-4,4-dimethylazlactone) (PVDMA) was synthesized by free radical polymerization at 60 °C for 24 hours in ethyl acetate (solvent:monomer ratio 3 mL:1 g) initiated by 1.0 mol% AIBN, as described previously.[21] A roll of PET film (thickness = 0.004 inches) was purchased from McMaster Carr (Elmhurst, IL). Water with a resistivity of 18.2 MΩ was obtained from a Millipore filtration system. Compressed air used in drying steps was filtered through a 0.2 μm membrane syringe filter. Chemicals were used without further purification unless otherwise noted above.

II) Methods: Poly(ethylene terephthalate) (PET) substrates were manually cut to the dimensions

of a standard glass microscope slide (25 mm x 35 mm). Prior to the fabrication of PEI/PVDMA multilayers, these substrates were rinsed with EtOH and then placed into a solution of PEI (1 mg/mL in MeOH) overnight at 37 °C, and then rinsed with MeOH and dried in a stream of filtered compressed air. PEI/PVDMA multilayers were fabricated on PET substrates using the following general procedure: (i) substrates were submerged in a solution of PVDMA (20 mM in acetone with respect to the polymer repeat unit) for 30 s; (ii) substrates were removed and immersed in an acetone bath for 10 s with gentle agitation and then rinsed with acetone from a squirt bottle for 10 s; (iii) substrates were submerged in a solution of PEI (20 mM in acetone with respect to the polymer repeat unit) for 30 s; and (iv) substrates were removed and rinsed again using the procedure in step (ii). This cycle was repeated four times to fabricate multilayers consisting of 4 PEI/PVDMA layer pairs (referred to hereafter as 'bilayers'). A final layer of PVDMA was then deposited (using steps (i) and (ii)) on the top surface of the film. Films having this general structure are referred to hereafter as being 4.5 bilayers thick. Films were washed with ~25 mL of acetone and then dried under a stream of compressed air. These films were functionalized with D-glucamine by incubating film-coated substrates in 20 mg/mL solutions in DMSO for 1 hour. These functionalized films were then rinsed copiously with Millipore water and dried under a stream of filtered compressed air.

Maskless Array Synthesis

I) Materials: DCI activator (4,5-dicyanoimidizaole in acetonitrile), 0.1 M Activator 42 (5-[3,5-bis(trifluoromethyl)phenyl]-1H-tetrazole) and all NPPOC (5'-nitrophenylpropyloxycarbonyl) protected phosphoramidites [5'- NPPOC-dAdenosine (tac) 3'-β-cyanoethylphosphoramidite (NPPOC-dA), 5'-NPPOC-dThymidine 3'-β-cyanoethylphosphoramidite (NPPOC-dT), 5'-

NPPOC-dCytidine (ib) 3’-β-cyanoethylphosphoramidite (NPPOC-dC), 5’- NPPOC-dGuanosine (ipac) 3’-β-cyanoethylphosphoramidite (NPPOC-dG)], tetrahydrofuran (THF), 2,6-lutidine, dimethylsulfoxide (DMSO), imidazole, acetonitrile, 1-methylimidazole, ethylenediamine, and ethanol were purchased from Sigma-Aldrich. Anhydrous acetonitrile, diluent (acetonitrile), capping reagent A (THF/Pac_2O), 0.5 M 10-camphorsulfonyl-oxaziridine (CSO), 5'-dimethoxytrityl-2'-deoxythymidine,3'-[(2-cyanoethyl)-(N,N-diisopropyl)]-phosphoramidite (DMT-dT), and deblocking mix (3% dichloroacetic acid in toluene) were purchased from Glen Research (VA, USA). Oxidizer (0.02 M iodine in THF/pyridine/H_2O), 5’-dimethoxytrityl-polyethyleneglycol 2000 phosphoramidite, and all 3’-dimethoxytrityl-5’-cyanoethylphosphoramite 2’-O-methyl or 2’-fluoro ribonucleosides were purchased from ChemGenes (MA, USA). 2-Dimethylaminopyridine was purchased from Tokyo Chemical Industry Co. LTD (Tokyo, Japan). Trap Packs were purchased from BioAutomation (TX, USA).

II) Methods: The array synthesis was conducted on a custom-built maskless array synthesizer (MAS) in a modification to previous techniques for gene synthesis and RNA array fabrication.[22,23] The primary exception is the removal of the capping step from every cycle of the synthesis. Briefly, this yielded synthesis cycles consisting of coupling, oxidation, and deprotection as depicted in Scheme 1. NPPOC-protected pyrimidine phosphoramidites underwent 80-second coupling steps while NPPOC-protected purine phosphoramidites underwent 90-second coupling steps. All 3’-dimethoxytrityl-5’-cyanoethylphosphoramite 2’-O-methyl and 2’-fluoro ribonucleosides underwent 10-minute coupling steps and 5’-dimethoxytrityl-polyethyleneglycol 2000 phosphoramidite underwent two 15-minute coupling steps. 5’-DMT-dT was coupled for 120 seconds. Activator 42 or DCI activator were used as summarized in Supplementary Table 1 (available together with supplemental figures at the end

of this chapter). Where I_2 was used as the oxidizer, oxidation steps (30 x 16 µL pulses on the MAS Expedite solvent delivery system) were conducted for every 3 or 5 couplings of 5'-NPPOC-protected phosphoramidites. When CSO was used as the oxidizer, 4-minute oxidation steps were conducted for every 3 or 5 couplings of 5'-NPPOC protected phosphoramidites and after the coupling of every DMT-protected phosphoramidite. A UV light dose of 3.5 J/cm^2 was used for full removal of the NPPOC on the PET surfaces while a 3.7 J/cm^2 dose was used on glassy carbon surfaces. This UV light dosage was determined in a separate experiment to yield features of the highest signal upon hybridization with a fluorescent complement. A 1.2 J/cm^2 dose was used for partial NPPOC removal on the PET surfaces for the RNA array fabrication. The exposure solvent was 1% (w/v) imidizole in DMSO and was filtered prior to use. Removal of the DMT groups was conducted with 0.36 M DCA in toluene in three 50-second steps. Amidites which were coupled following a step of partial deprotection (5'-DMT-3'-CE-dT for the dual-sequence-feature array and 2'-F-3'-DMT-rC for the RNA array) underwent two coupling steps. In cases where capping was conducted independently of a coupling cycle (between sequence I and II on the dual-sequence-feature array, between DNA and RNA synthesis on the RNA array, and on the 'inverse' image of all the features of the array at the beginning of a synthesis), a capping cycle consisted of three 90-second steps of an equivolume mixture of capping reagent A (THF/Pac_2O) and capping reagent B (0.5% 2-dimethylaminopyridine, 2% (v/v) N-methylimidazole and 10% (v/v) 2,6-lutidine in THF), which was mixed in-house. Capping was carried out in the same way for 60 seconds/NPPOC cycle on the glassy carbon array shown in Figure 4. The synthesis conditions are summarized in Supplementary Table 1. After synthesis, the arrays were deprotected in a 50:50 mixture of ethylenediamine:ethanol for 90 minutes at room temperature before being rinsed in ethanol, water, then rapidly dried under a

nitrogen stream. The nucleic acid sequences for all arrays fabricated are given in Supplementary Table 2.

RNA Array Fabrication

I) Materials: Turbo DNase, 10X Turbo DNase buffer, RNAsecure, 10X phosphate-buffered saline (PBS, pH 7.4), 0.2 µm filtered nuclease free water (not DEPC treated), and 20X SSPE (3.0 M NaCl, 0.2 M NaH_2PO_4, and 0.02 M EDTA at pH 7.4) were purchased from Ambion (TX, USA). Polyethylene glycol 6000, 10% (w/v) sodium dodecyl sulfate (SDS), and diethylpyrocarbonate (DEPC) were purchased from Sigma Aldrich. RiboLock RNase inhibitor, T7 RNA polymerase, and 5X transcription buffer, Gene Frame gaskets, and all adenosine, cytosine, guanosine, and uradine nucleotide triphosphates were purchased from Thermo Scientific (USA).

II) Methods: After array synthesis and chemical deprotection, a Gene Frame gasket was then applied to surround the array features. 50 µL of annealing buffer consisting of 4X SSPE buffer, 1X RNAsecure reagent, and 9% polyethylene glycol 6000 was applied onto the array and incubated at 60 °C for 20 min in a humid chamber, then slowly cooled down to 37 °C overnight. The surface was then rinsed manually at least three times with 1X transcription buffer (40 mM Tris-HCl, pH 7.9, 6 mM $MgCl_2$, 10 mM DTT, 20 mM NaCl, 2 mM spermidine) before exchange with the RNA extension reaction mixture consisting of 40 mM Tris-HCl (pH = 7.9), 6 mM $MgCl_2$, 10 mM DTT, 20 mM NaCl, 2 mM spermidine, 0.5 mM each NTP, 2 U/µl T7 RNA polymerase, and 1 U/µl RiboLock RNase inhibitor. The extension reaction was incubated at 37 °C for ~5 hours in a double humid chamber (a humid chamber within a humid chamber). After extension, the array was rinsed extensively with 1X PBS buffer (pH = 7.4) followed by at least

three rinsing steps of 1X TurboDNase buffer before exchanging the solution on the surface with Turbo DNase at a concentration of 0.1 U/μL in 1X DNase buffer. The mixture was incubated at 37 °C for ~6.5 hrs in a double humid chamber and rinsed in 2% SDS in 1X PBS (pH = 7.4) for 10 minutes and followed by extensive rinsing with water and drying under a nitrogen stream. The array was prevented from drying throughout the steps of enzymatic treatment. Water used for rinses and hybridization buffers was DEPC-treated and subsequently autoclaved.

Array Hybridizations. Fluorescently-labelled oligonucleotides were purchased from Integrated DNA Technologies (IA, USA) and Sigma-Aldrich. Sequences are shown in Supplementary Table 3. Hybridization reactions were conducted by incubating the array for at least 30 minutes with a solution consisting of 1 μM complementary oligonucleotide in 4X SSPE buffer and 0.1% Tween-20 in a humid chamber at 37 °C. The arrays were then transferred to a solution of 0.5X SSPE at room temperature for 15 minutes before further rinsing in 0.5X SSPE. A cover slip was then placed over the gasket to keep the surface wet throughout the imaging process, which was performed with a GeneTac UC 4 x 4 microarray scanner. Arrays synthesized on PET were placed onto a microscope slide to ensure that features remained in the focal plane of the scanner. The arrays shown in Figure 2 of the main text were incubated with the labelled oligonucleotides in a humid chamber at the given temperature, then briefly cooled and incubated at 37 °C for 30 minutes before handling as described above. The arrays that were visualized on an Olympus IX70 microscope (details below) were dried rapidly prior to imaging under a nitrogen stream after the 0.5X SSPE rinse step.

Fabrication of Millichips by Laser Cutting. PET-based arrays were cut by laser using an Epilog Helix 12'' x 24'' laser table (Epilog, Golden CO). The CO_2 laser (45 watts) had a resolution of 30 μm was set to operate at 30% power and a speed of 50%. The laser cutting guidelines were drawn using Adobe Illustrator (line thickness of 0.001") and saved as a PDF file for input to the laser table software.

Fluorescence Microscopy. Fluorescence micrographs were obtained using an Olympus IX70 microscope equipped with a Lumen Dynamics XCite 120PC-Q fluorescence source and a Q Imaging EXi Aqua camera with an objective magnification of 20X coupled with a 1.6X magnification booster at an exposure time of 50 ms (Cy3) and 350 ms (Cy5), respectively. Images were obtained in grey scale using MetaMorph Advanced software, version 7.7.8.0 (Molecular Devices, LLC) and subsequently false-colored using ImageJ software (NIH, Bethesda, MD). Where noted, a GeneTac UC 4 x 4 microarray scanner (Genomic Solutions) was also used to visualize arrays. Acquisition settings are summarized in Supplementary Table 4, while false-color palettes used in image preparation are provided in Supplementary Figure 2.

Results and Discussion

Fabrication of High-Density DNA Arrays on PET

Our approach makes use of thin sheets of poly(ethylene terephthalate) (PET) coated with crosslinked polymer multilayers covalently modified to present hydroxyl functionality suitable for conventional phosphoramidite-based nucleic acid synthesis (Scheme 1).[24-26] We demonstrated recently that this approach, in combination with conventional methods for *in situ* maskless array synthesis, could be used to design functional DNA arrays containing

oligonucleotides ~20 bp long.[19] We note here that the array synthesis exposes substrates to repeated cycles of phosphoramidite chemistry using photolabile protecting groups and UV-light mediated deprotection (an overview of this MAS strategy is depicted in Scheme 1).[27] Further studies (described below) revealed that several procedures and reagents associated with standard array synthesis protocols (*e.g.*, the oxidation step and the acetylation or "capping" step occasionally employed in DNA synthesis, which both involve the use of tetrahydrofuran (THF) as a solvent) can cause the surfaces of film-coated plastic substrates to roughen and promote the delamination of the multilayer film from the underlying PET substrate, ultimately limiting the

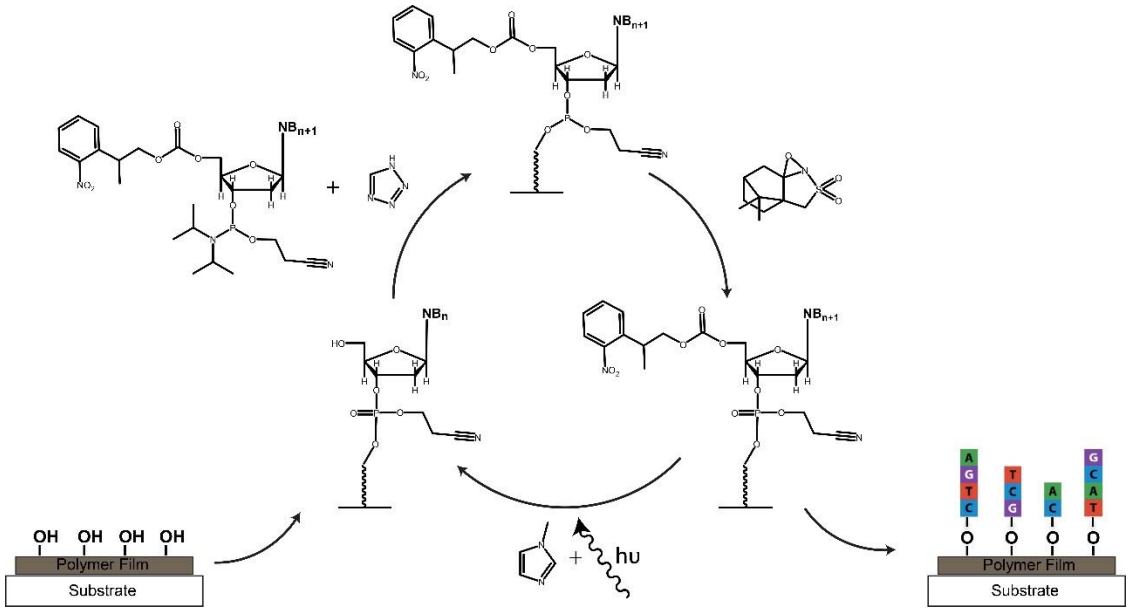

Scheme 1. An overview of nucleic acid array fabrication chemistry used in the maskless array synthesis. Phosphoramidites containing a 5'-nitrophenylpropyloxycarbonyl (5'-NPPOC) are coupled to free hydroxyls on a polymer film-coated plastic substrate using a tetrazole-based activator. Oxidation is carried out once every 3 to 5 cycles utilizing 10-camphorsulfonyl-oxaziridine (CSO) in acetonitrile. A system of digitally controlled micromirrors directs UV light to remove the 5'-NPPOC group in the presence of imidazole to expose a free hydroxyl for the next round of coupling.

length of oligonucleotides that can be synthesized. In this study, we sought to address these issues and develop synthetic protocols that would enable the design of high-density plastic-backed arrays with longer probe sequences and more complex features (*e.g.*, array spots containing two distinct DNA features) and arrays with DNA features suitable for the enzymatic synthesis of RNA arrays. We also sought to determine the smallest feature sizes and highest feature densities that could be achieved using these new methods.

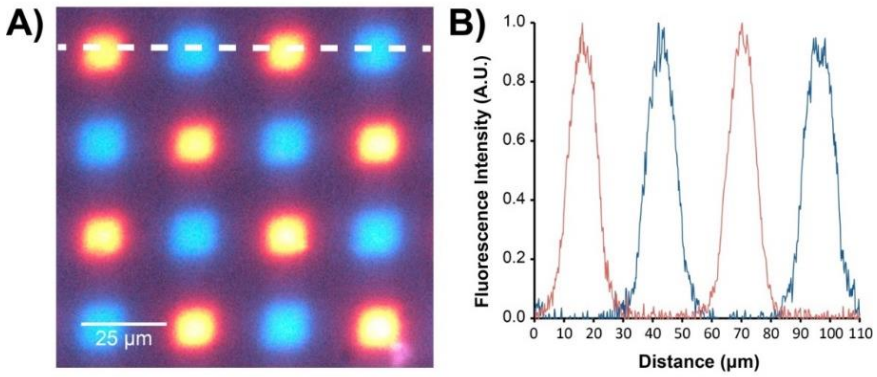

Figure 1. DNA features synthesized from single micromirrors (14 x 14 µm) on polymer-film coated PET. A) Fluorescence micrograph obtained from hybridization of surface-bound DNA to either Cy3 (blue) or Cy5 (red)-labelled oligonucleotides. B) Fluorescence intensity (signal) as measured along the dotted white line shown in (A), from left to right.

Modern DNA arrays used in complex genetic analyses typically contain tens to hundreds of thousands of sequences and thus require that arrays be synthesized with a high feature density.[28] To determine whether it was possible to achieve a DNA feature density on PET surfaces that would be comparable to the density obtainable on conventionally used rigid substrates, we synthesized an array consisting of a checkerboard of two sequences, each ~30 nucleotides long, on polymer film-coated PET substrates. Each feature was synthesized using a single 14 x 14 µm mirror of the DMD so that the area of each feature was as small as the instrumentation could achieve. Features were spaced so that the inter-feature distance between

adjacent sites corresponded to a single mirror on the DMD. This "1-in-2" design (where every other mirror is used to synthesize a feature) corresponds to a feature density of 127,667 features/cm^2. As shown in Figure 1, the hybridization of labelled complementary oligonucleotides produced fluorescence signals of consistent intensity and high specificity. These results are of comparable quality to those obtained from the same design fabricated upon a rigid substrate (Supplementary Figure 2) and correspond to more than an 80-fold increase in feature density over previous reports,[19] suggesting that state-of-the-art genomic analysis experiments could be performed with these flexible DNA arrays.

Array Stability at Different Temperatures

Oligonucleotide hybridization and capture experiments typically use a range of binding temperatures, particularly in applications such as single-nucleotide polymorphism (SNP) genotyping where a high degree of discrimination between the binding of closely related sequences is required. DNA aptamer arrays are subject to similar considerations, as temperature can be used to control analyte binding or influence the formation of secondary structures on the surface.[29] To investigate the stability of the PET arrays fabricated above under different hybridization temperatures, an array was fabricated containing feature sizes from 14 μm to 686 μm and composed of a single sequence of DNA 30 nucleotides long. The array was then incubated overnight at 37, 45, or 60 °C with a fluorescently labelled complementary sequence, cooled to 37 °C (below the T_m of the DNA duplex) to ensure hybridization, and subsequently imaged. Figure 2 shows that there is no discernible physical damage to the surface after such extended incubations at elevated temperature and the ability of the array to bind to the complementary sequence was not negatively affected. The inset in the right panel of Figure 2 depicts the smallest feature size. This feature (measuring 14 x14 μm) is easily discernible,

suggesting that neither large nor small scale degradation is occurring to the oligonucleotides or to the underlying polymer film or plastic substrate. These results compare favorably with previously measured stabilities of arrays made on silanized glass surfaces,[30] and demonstrate that PET-based arrays could be used in a variety of assays where elevated temperatures are required.

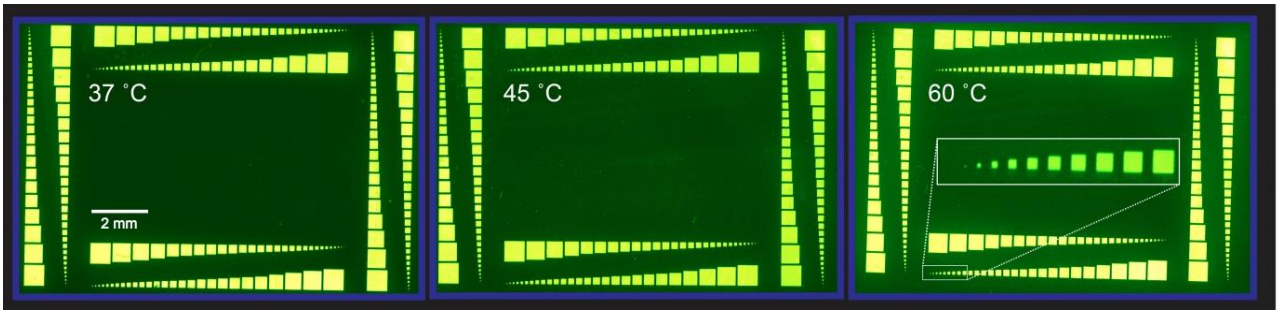

Figure 2. Stability of DNA arrays on polymer-coated PET substrates at various hybridization temperatures. A single array was hybridized at each of the indicated temperatures with a Cy5-labeled complement for 16 hours prior to imaging. After hybridization and imaging at a given temperature, the complement was removed with 8 M urea. The experiments were conducted in order of increasing hybridization temperature. The array layout illustrates that feature quality is consistent across a range of sizes and regions on the surface. Inset of right panel: a magnification of the indicated area, showing that individual features are easily discernible

Improvement of Array Quality Through Oxidizer Optimization

The ability of the polymer-coated PET substrates to withstand the iterative chemical processing steps of array synthesis is an important parameter that governs their utility. The fabrication of arrays containing longer DNA sequences requires a greater number of chemical exposure cycles (the maximum number of cycles is four times the length in nucleotides of the longest feature), thus we examined the suitability of these substrates for the synthesis of arrays with longer sequences. Figure 3 shows fluorescence images after hybridization to the 20 nucleotide termini of a 50 nt long stretch of DNA on a rigid, glassy carbon substrate (3A) and on flexible polymer-coated PET arrays (3B, 3C). Non-complementary control sequences and complementary test sequences were fabricated on the left and right hand sides of the array,

respectively. The different colors for the different arrays are false-colored representations of their intensities. Figure 3D shows the signal intensities acquired from each of the arrays under identical imaging conditions. PET arrays fabricated using the standard iodine oxidation conditions (0.02 M I_2 in THF/pyridine/H_2O, Figure 3B) showed signs of damage to the underlying substrate. This is illustrated by both the high standard deviation of the signal intensities (represented by the error bars in Figure 3D) and the regions of irregular pixel intensity within individual features. This phenomenon was not observed for previous plastic-backed arrays containing shorter sequences that had undergone less cumulative exposure to the tetrahydrofuran (THF).[19]

To reduce damage to the array and improve the synthesis of longer DNA sequences, the use of THF was eliminated entirely by replacing the oxidation solution with 0.5 M camphorsulfonyl oxazaziridine in acetonitrile (CSO, depicted in Scheme 1).[31] Figure 3C shows the resulting improvement in feature uniformity. This is reflected quantitatively in a lower standard deviation without any loss in signal intensity (Figure 3D), although some variation is still evident in the array images. Interestingly, comparison of the signal-to-noise ratio (S/N) across the three conditions implies that there are two modes of surface degradation that occur at high cycle numbers. Figure 3E shows that the S/N values of the three arrays are comparable when the background pixels are selected from a region of the surface where no DNA is synthesized. When the background pixels are selected from regions containing the non-complementary control sequences, the S/N measured on the PET/I_2 array is substantially lower than that obtained on the glassy carbon or PET/CSO arrays (Figure 3F). This implies that the majority of the damage is localized to the regions exposed to UV-light. While this was not studied further, a likely interpretation is that the THF may exacerbate low levels of UV damage

to the multilayered films and suggests that further development may be required for applications requiring even longer sequences.

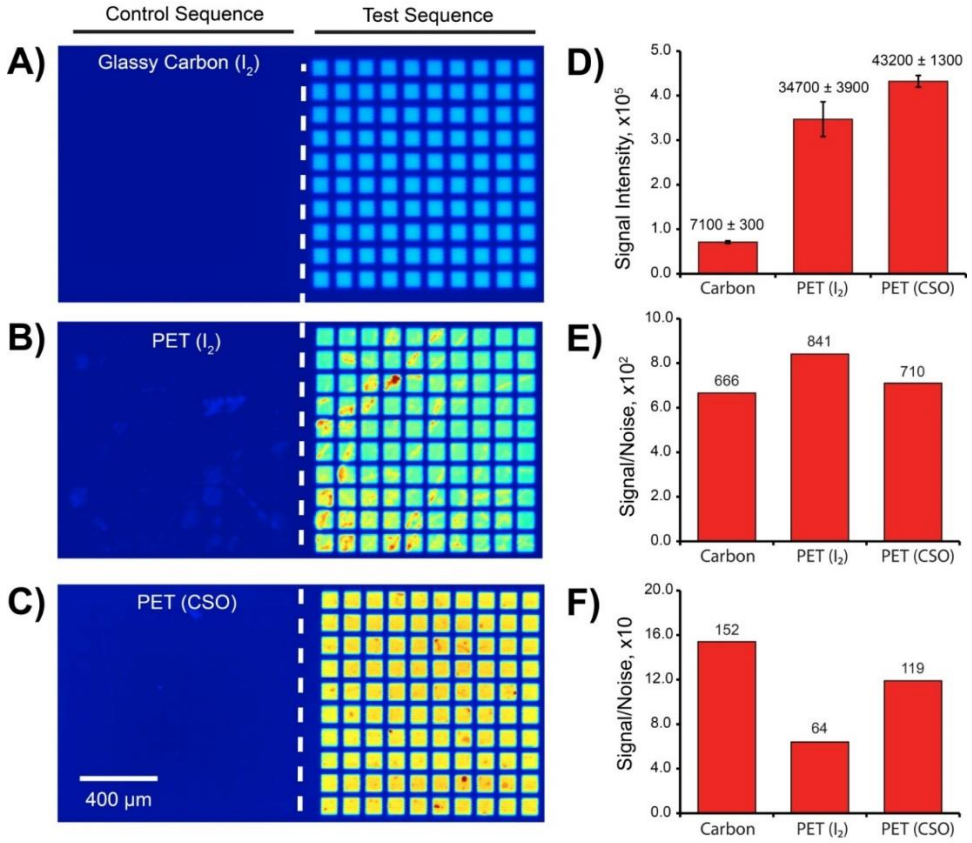

Figure 3. Improved synthesis of longer oligonucleotides. Three arrays consisting of grids containing 100 replicates of 50 nt features were synthesized using different conditions. A)-C) Fluorescence micrographs of arrays hybridized with a Cy5-labelled sequence. The right-hand side contains the test sequences intended to undergo hybridization at their 20 nt termini, while the left-hand side contains the control sequences where no hybridization should occur. A) Hybridization to an array synthesized upon a glassy carbon surface. B) and C) Hybridization to the same array design upon polymer multilayer-coated PET using I_2 (B) or CSO (C) as the oxidizing agent during DNA synthesis. D) Feature intensities detected on each array; the standard deviation is given in the plot. The difference in average feature intensity between the carbon and PET surfaces results from omitting the capping step during the PET array synthesis. E) Signal-to-noise ratio measured against the background of the array surface. F) Signal-to-noise ratio measured against the background of the array region containing the control sequences.

Fabrication of '2-in-1' DNA Arrays

The improved oxidation conditions developed above were then used to fabricate arrays requiring more complex synthesis protocols. First, a '2-in-1' array was synthesized, where a

single feature comprised a mixed population of two different DNA sequences, by using orthogonal deprotection chemistry (Figure 4A). It is notable that such an approach is not possible using an inkjet DNA array synthesizer. A partial dose of UV light was used to remove a fraction of the photolabile 5'-nitrophenylpropyloxycarbonyl (NPPOC) protecting groups early in the synthesis,[32] followed by immediate coupling of a 5'-dimethoxytrityl protected (DMT) phosphoramidite to the resultant deprotected hydroxyl groups to yield features now having both NPPOC and DMT-protected oligonucleotides. The remaining NPPOC groups were then removed by UV light, leaving the DMT group unaffected, and allowing for the light-directed synthesis of a sequence to proceed normally at the exposed sites. At the end of the synthesis of this first strand, designated **sequence I** (21 nt long), the terminal NPPOC was removed to expose a free hydroxyl, which was then capped with phenoxyacetic anhydride to prevent further coupling. The DMT group was then removed with dichloroacetic acid/toluene and the light-directed synthesis of the second strand (**sequence II**, 22 nt long) was conducted to produce a single feature consisting of two distinct DNA sequences with the same 3'-5' polarity. Figures 4B and 4C illustrate that it is possible to alter the hybridization signal intensity by varying the dose of UV light prior to the DMT-phosphoramidite coupling. Each column of the array in Figure 4B received a different UV dose, thus altering the ratio of **sequence I** to **sequence II** in individual features. The profile of hybridization intensities of **sequence I** and **sequence II** across the columns is consistent with the expected NPPOC deprotection behavior.[32] A similar approach has been used previously to fabricate DNA sequences of opposite polarity within a single feature.[33] This '2-in-1' strategy is key to placing both primer and template strands within a feature to carry out enzymatic reactions.

Fabrication of RNA Arrays on PET

One application that is enabled by the improved oxidation and 2-in-1 DNA synthesis strategies described above is the fabrication of high-density arrays of RNA. A recent report from our group details an enzymatic technique for transforming high-density DNA arrays into arrays of RNA on conventional substrates.[23] We evaluated the PET substrates used above to determine their utility in the fabrication of such high-density RNA arrays.

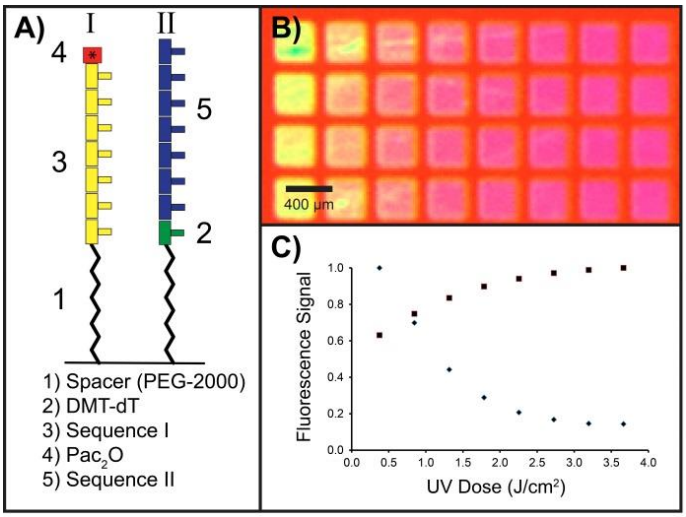

Figure 4. Fabrication of "2-in-1" DNA arrays (containing two sequences per feature) on polymer film-coated PET. A) Scheme depicting the synthesis process to obtain dual-sequence features. Numbers denote the order in which the indicated species was attached to the surface during synthesis. "PEG-2000" indicates polyethylene glycol with a molecular weight of 2 kDa, "DMT-dT" stands for a 5'-dimethoxytrityl protected deoxythymidine phosphoramidite, and "Pac_2O" stands for phenoxyacetic anhydride. The "*" indicates the location of the phenoxyacetyl group that terminates the synthesis of sequence I. B) Fluorescence micrograph of hybridization with Cy5 (purple) and Texas Red (yellow) labelled complements to the features; each column of features received a different UV-dose prior to DMT-dT coupling. C) Fluorescence signal intensity of each sequence and the corresponding light doses used at each column depicted in (B). Diamonds indicate signal intensities of sequence I; squares indicate intensities of sequence II.

To generate the arrays, a partial deprotection step (similar to the one described above) was used to synthesize features containing both template DNA strands (using NPPOC-protected

DNA monomers) and short RNA primer strands (utilizing DMT-protected RNA monomers). The two sequences were then annealed together to yield a DNA:RNA duplex that allowed the RNA primer strands to be extended using T7 RNA polymerase. A subsequent DNase treatment left behind only the RNA sequences, which remained localized to the region of the original template DNA. This technique was implemented here to fabricate an array consisting of three different 32-33 nucleotide long RNA features, which was subsequently hybridized with fluorescently-labelled complementary oligonucleotides. Figure 5 shows the localization of each labelled sequence in its intended location with negligible non-specific adsorption to the background between features.

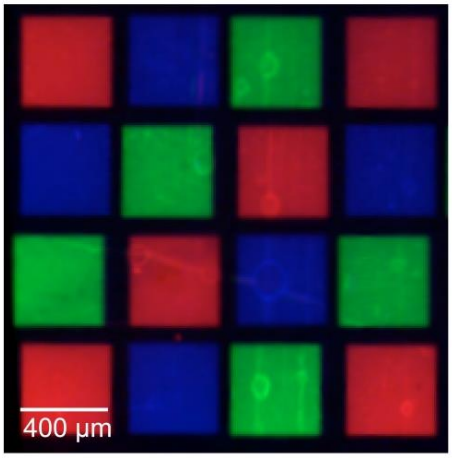

Oligonucleotide Label	*Fluorescence Intensity, x10³*	*S/N*
FAM (Blue)	41.5 ± 1.1	57
Texas Red (Green)	37.0 ± 3.2	106
Cy5 (Red)	19.6 ± 2.4	48

Figure 5. Fluorescence micrograph showing hybridization of three different fluorescently labelled complements to an RNA array fabricated on polymer film-coated PET. The table summarizes the intensity of the fluorescence signals, plus-or-minus one standard deviation and the corresponding signal-to-noise ratio for each of the three sequences.

The signal-to-noise ratios measured here are comparable to those reported for spotted DNA arrays on the same type of substrate.[34] A number of potential applications for RNA arrays, such as the study of RNA binding proteins, aptamers, or the development of new biosensors,

depend critically upon minimizing non-specific interactions between the surface and analytes of interest. The ability to synthesize the arrays on a polymeric surface provides an important new avenue for the control of such interactions. These results also demonstrate the chemical robustness of the multilayered polymer films to the various steps required to effect the transition from DNA to RNA arrays, including the annealing at elevated temperatures and the extended incubation times required for the enzymatic reactions.

Millichip Fabrication by Automated Laser Cutting

An important advantage of the plastic-backed arrays relative to arrays fabricated on glass or glassy carbon substrates is that PET is a soft and flexible material that is readily cut to create smaller individual arrays of arbitrary shape.[19] A previous study explored the fabrication of DNA 'millichips', by synthesizing a DNA array on a pre-scored glass substrate and subsequently physically breaking it into smaller subsections containing arrays that could be used separately.[20] This approach has potential to significantly reduce the cost of DNA array fabrication. To explore the potential of this strategy using our plastic-backed arrays, polymer multilayer-coated PET substrates were cut into squares with dimensions of 2.5 x 2.5 mm using an automated laser cutting tool. The cutting procedure did not deleteriously affect the polymer coatings; delamination, peeling, visual hazing, or other physical changes were not observed by visual inspection (Figure 6A).

A series of DNA arrays was then synthesized (two different DNA probes, ~20 nucleotides long) and cut into individual millichips for hybridization with fluorescently labelled complements (Figure 6B). We observed hybridization intensities comparable to those obtained with PET arrays that were not laser cut (*e.g.* Figure 1) with little non-specific background signal,

indicating that the laser cutting process did not negatively impact array quality. Although the coated PET itself appears bright at the cut edges (Figure 6B), cuts can be made very close to the edge of the arrays (*e.g.* <0.1 mm) without observing damage to the array or the ability of the array to hybridize to complementary oligonucleotides, suggesting that further miniaturization of millichips may be possible. The 2.5 x 2.5 mm millichips used in these proof-of-concept experiments are easy to handle with tweezers and can be readily placed into PCR tubes or 96-well plates for use in experiments.

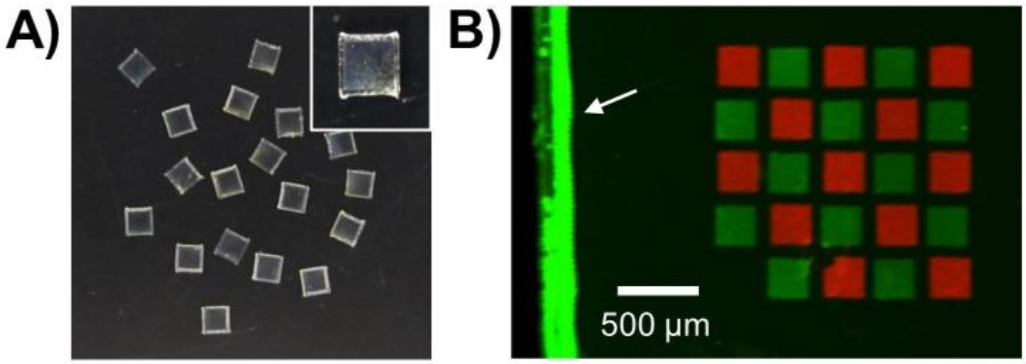

Figure 6. A) Digital photograph of polymer film-coated PET cut using a laser into 2.5 x 2.5 mm millichips. B) Fluorescence micrograph of a DNA millichip array after laser cutting and hybridization with fluorescently labelled complements. The white arrow indicates the edge of the millichip, which appears bright after cutting with the laser.

Conclusions

We describe here the photolithographic fabrication of high-density DNA and RNA arrays on flexible, polymer multilayer-coated plastic substrates. These flexible arrays are compatible with small feature sizes and high feature densities comparable to those of arrays fabricated on rigid substrates such as silanized glass and glassy carbon, and can be imaged and analyzed quantitatively using standard fluorescence imaging techniques. It is shown that the arrays are stable to hybridization at elevated temperatures and are compatible with conditions used for

enzymatic procedures such as the *in situ* synthesis of RNA from DNA oligonucleotides. These flexible and transparent arrays are physically robust, easy to handle, and, because they are fabricated on 'soft' polymer films that can be readily cut using a variety of methods (e.g., scissors or laser cutting tools, etc.), can also be used to create smaller sub-arrays (or "millichips"). We anticipate that numerous 'lab-on-a-chip'-like applications will be enabled by such flexible arrays, including the patterning of oligonucleotides or other molecules in non-planar geometries and the high-throughput production of low-cost millichips for affordable assays with extremely small reagent volumes.

Acknowledgments. This work was supported by the NSF (DMR-1121288, PGRP-0801846); the National Institutes of Health (1R01GM108727, 1R01GM109099, and 5T32GM08349); and the Wisconsin Alumni Research Foundation. The work made use of shared facilities supported by the NSF through the UW-Madison Materials Research Science and Engineering Center (DMR-1121288) and Nanoscale Science and Engineering Center (DMR-0832760). M.C.D.C acknowledges the Natural Sciences and Engineering Research Council of Canada for a graduate fellowship.

References

(1) Pease, A. C.; Solas, D.; Sullivan, E. J.; Cronin, M. T.; Holmes, C. P.; Fodor, S. P. *Proc. Natl. Acad. Sci. U. S. A.* **1994**, *91*, 5022-5026.

(2) Pinkel, D.; Segraves, R.; Sudar, D.; Clark, S.; Poole, I.; Kowbel, D.; Collins, C.; Kuo, W.-L.; Chen, C.; Zhai, Y.; Dairkee, S. H.; Ljung, B.-m.; Gray, J. W.; Albertson, D. G. *Nat. Genet.* **1998**, *20*, 207-211.

(3) Wang, D. G.; Fan, J.-B.; Siao, C.-J.; Berno, A.; Young, P.; Sapolsky, R.; Ghandour, G.; Perkins, N.; Winchester, E.; Spencer, J.; Kruglyak, L.; Stein, L.; Hsie, L.; Topaloglou, T.; Hubbell, E.; Robinson, E.; Mittmann, M.; Morris, M. S.; Shen, N.; Kilburn, D.; Rioux, J.;

Nusbaum, C.; Rozen, S.; Hudson, T. J.; Lipshutz, R.; Chee, M.; Lander, E. S. *Science* **1998**, *280*, 1077-1082.

(4) Eisen, M. B.; Brown, P. O. In *Methods Enzymol.*, Sherman, M. W., Ed.; Academic Press, 1999, pp 179-205.

(5) Call, D. R. *Crit. Rev. Microbiol.* **2005**, *31*, 91-99.

(6) Albert, T. J.; Molla, M. N.; Muzny, D. M.; Nazareth, L.; Wheeler, D.; Song, X.; Richmond, T. A.; Middle, C. M.; Rodesch, M. J.; Packard, C. J.; Weinstock, G. M.; Gibbs, R. A. *Nat. Methods* **2007**, *4*, 903-905.

(7) LaFramboise, T. *Nucleic Acids Res.* **2009**, *37*, 4181-4193.

(8) Katilius, E.; Flores, C.; Woodbury, N. W. *Nucleic Acids Res.* **2007**, *35*, 7626-7635.

(9) Ozers, M. S.; Warren, C. L.; Ansari, A. Z. In *Micro and Nano Technologies in Bioanalysis*, Foote, R. S.; Lee, J. W., Eds.; Humana Press, 2009, pp 637-653.

(10) Kim, C.; Kaysen, J.; Richmond, K.; Rodesch, M.; Binkowski, B.; Chu, L.; Li, M.; Heinrich, K.; Blair, S.; Belshaw, P.; Sussman, M.; Cerrina, F. *Microelectron. Eng.* **2006**, *83*, 1613-1616.

(11) Kosuri, S.; Eroshenko, N.; LeProust, E. M.; Super, M.; Way, J.; Li, J. B.; Church, G. M. *Nat. Biotechnol.* **2010**, *28*, 1295-1299.

(12) Kosuri, S.; Church, G. M. *Nat. Methods* **2014**, *11*, 499-507.

(13) LeProust, E. M.; Peck, B. J.; Spirin, K.; McCuen, H. B.; Moore, B.; Namsaraev, E.; Caruthers, M. H. *Nucleic Acids Res.* **2010**, *38*, 2522-2540.

(14) Fodor, S.; Read, J.; Pirrung, M.; Stryer, L.; Lu, A.; Solas, D. *Science* **1991**, *251*, 767-773.

(15) Hughes, T. R.; Mao, M.; Jones, A. R.; Burchard, J.; Marton, M. J.; Shannon, K. W.; Lefkowitz, S. M.; Ziman, M.; Schelter, J. M.; Meyer, M. R.; Kobayashi, S.; Davis, C.; Dai, H.; He, Y. D.; Stephaniants, S. B.; Cavet, G.; Walker, W. L.; West, A.; Coffey, E.; Shoemaker, D. D.; Stoughton, R.; Blanchard, A. P.; Friend, S. H.; Linsley, P. S. *Nat. Biotechnol.* **2001**, *19*, 342-347.

(16) Wang, L.; Li, P. C. H. *Anal. Chim. Acta* **2011**, *687*, 12-27.

(17) Zopf, A.; Raim, R.; Danzer, M.; Niklas, N.; Spilka, R.; Pröll, J.; Gabriel, C.; Nechansky, A.; Roucka, M. *BioTechniques* **2015**, *58*, 126-133.

(18) Zhang, Z.; Li, S.; Chen, N.; Yang, C.; Wang, Y. *Biomacromolecules* **2013**, *14*, 1174-1180.

(19) Broderick, A. H.; Lockett, M. R.; Buck, M. E.; Yuan, Y.; Smith, L. M.; Lynn, D. M. *Chem. Mater.* **2012**, *24*, 938-945.

(20) Heinrich, K. W.; Wolfer, J.; Hong, D.; LeBlanc, M.; Sussman, M. R. *Plant Phys.* **2012**, *159*, 548-557.

(21) Buck, M. E.; Schwartz, S. C.; Lynn, D. M. *Chem. Mater.* **2010**, *22*, 6319-6327.

(22) Wu, C.-H.; Lockett, M. R.; Smith, L. M. *Angew. Chem., Int. Ed.* **2012**, *51*, 4628-4632.

(23) Wu, C.-H.; Holden, M. T.; Smith, L. M. *Angew. Chem., Int. Ed.* **2014**, *53*, 13514-13517.

(24) Buck, M. E.; Zhang, J.; Lynn, D. M. *Adv. Mater.* **2007**, *19*, 3951-3955.

(25) Fredin, N. J.; Broderick, A. H.; Buck, M. E.; Lynn, D. M. *Biomacromolecules* **2009**, *10*, 994-1003.

(26) Buck, M. E.; Lynn, D. M. *Polym. Chem.* **2012**, *3*, 66-80.

(27) Singh-Gasson, S.; Green, R. D.; Yue, Y.; Nelson, C.; Blattner, F.; Sussman, M. R.; Cerrina, F. *Nat. Biotechnol.* **1999**, *17*, 974-978.

(28) Lipshutz, R. J.; Fodor, S. P. A.; Gingeras, T. R.; Lockhart, D. J. *Nat. Genet.* **1999**, *21*, 20-24.

(29) Goda, T.; Miyahara, Y. *Biosens. Bioelectron.* **2011**, *26*, 3949-3952.

(30) Phillips, M. F.; Lockett, M. R.; Rodesch, M. J.; Shortreed, M. R.; Cerrina, F.; Smith, L. M. *Nucleic Acids Res.* **2008**, *36*, e7.

(31) Ugi, I.; Jacob, P.; Landgraf, B.; Rupp, C.; Lemmen, P.; U.Verfurth. *Nucleosides and Nucleotides* **1988**, *7*, 605.

(32) Chen, S.; Phillips, M. F.; Cerrina, F.; Smith, L. M. *Langmuir* **2009**, *25*, 6570-6575.

(33) Nie, B.; Yang, M.; Fu, W.; Liang, Z. *Analyst* **2015**.

(34) Broderick, A. H.; Carter, M. C. D.; Lockett, M. R.; Smith, L. M.; Lynn, D. M. *ACS Appl. Mater. Interfaces* **2013**, *5*, 351-359.

Supporting Information for Chapter 4

Supplementary Figure 1. False-color LUTs used for the main-text images. ImageJ false-coloring spans the same grayscale values as the GeneTac scanner.

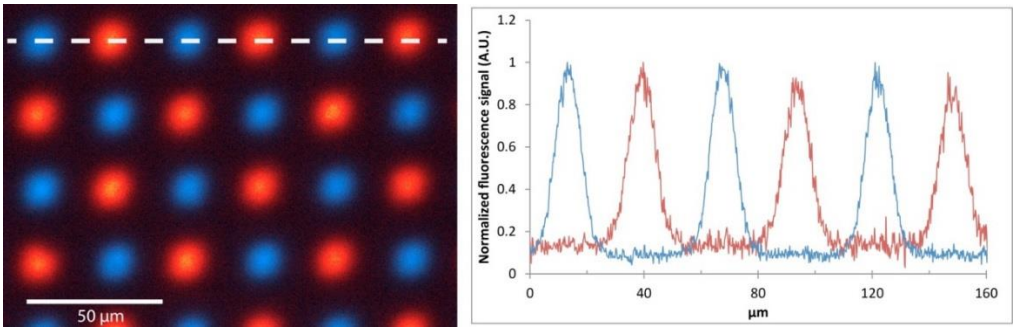

Supplementary Figure 2. Fluorescence image of an array fabricated from single-mirror features on a rigid glass substrate. The design is identical to that of Figure 1 in the main text.

Fig.	Activator	Oxidizer	Oxidation Time	Oxidation Pattern	Capping (Yes/No)
1	Activator 42	CSO in ACN	3 minutes	Every 3 NPPOC-phosphoramidite couplings and every DMT-phosphoramidite coupling	N
2	Activator 42	Iodine/THF/Pyrdine/Water	30 Expedite pulses/NPPOC oxidation cycle	Every 5 NPPOC couplings	N
3A	DCI	Iodine/THF/Pyrdine/Water	30 Expedite pulses/NPPOC oxidation cycle	Every 3 NPPOC-phosphoramidite couplings and every DMT-phosphoramidite coupling	60 sec/NPPOC coupling
3B	DCI	Iodine/THF/Pyrdine/Water	30 Expedite pulses/NPPOC oxidation cycle	Every 3 NPPOC-phosphoramidite couplings and every DMT-phosphoramidite coupling	N
3C	DCI	CSO in ACN	4 minutes	Every 5 NPPOC-phosphoramidite couplings and every DMT-phosphoramidite coupling	N
4B	DCI	CSO in ACN	4 minutes	Every 3 NPPOC-phosphoramidite couplings and every DMT-phosphoramidite coupling	N
5	DCI	CSO in ACN	4 minutes	Every 3 NPPOC-phosphoramidite couplings and every DMT-phosphoramidite coupling	N
6	DCI	Iodine/THF/Pyrdine/Water	30 Expedite pulses/NPPOC oxidation cycle	Every 3 NPPOC-phosphoramidite couplings and every DMT-phosphoramidite coupling	N

Supplementary Table 1: Summary of the synthesis conditions of the arrays shown in the main text.

Figure	Feature	DNA Sequence (3'-5')
1	1	TTTTTTTTTTTAGTCTTGAGTGGACAATC
	2	TTTTTTTTTTTATTGAAACGTTGTCACC
2	1	TTTTTTTTTTTTAGTCTTGAGTGGACAATC
3A-C	Test	TTTTTTTTTTTTCGGCTACTGGACGTTCTCATAGTCTTGAGTGGACAATC
	Control	TTTTTTTTTTTTGAGAACGTCCAGTAGCCGAGATTGTCCACTCAAGACTA
4B	1	T/*PEG2k*/T/TCGGCTACTGGACGTTCTCA
	2	T/*PEG2k*/T*T*TTAGTCTTGAGTGGACAATC
5	1	T/*PEG2k*/T<u>GCCTGTGCCGCTT</u>TTGAGAACGTCCAGTAGCCG
	2	T/*PEG2k*/T<u>GCCTGTGCCGCTT</u>TGATTGTCCACTCAAGACT
	3	T/*PEG2k*/T<u>GCCTGTGCCGCTT</u>TGGTGACAACGTTTCAATA
6	1	TTTTTTTTTTTAGTCTTGAGTGGACAATC
	2	TTTTTTTTTTTCGGCTACTGGACGTTCTCA
		RNA Sequence (5'-3')
5	1	T/*PEG2k*/T<u>*fCmGmGmAfCmAfCmGmGfCmGmAmA*</u>rArArCrUrCrUrUrGrCrArGrGrUrCrArUrCrGrGrC
	2	T/*PEG2k*/T<u>*fCmGmGmAfCmAfCmGmGfCmGmAmA*</u>rArCrUrArArCrArGrGrUrGrArGrUrUrCrUrGrA
	3	T/*PEG2k*/T<u>*fCmGmGmAfCmAfCmGmGfCmGmAmA*</u>rArCrCrArCrUrGrUrUrGrCrArArArGrUrUrArU

Supplementary Table 2. Sequences of DNA and RNA oligonucleotides used to fabricate arrays. *Italic* letters indicate that DMT-protected phosphoramidites were used for coupling, while unformatted letters denotes the use of NPPOC-protected phosphoramidites. <u>Underlined</u> stretches denote the complementary primer and template regions of the RNA array and DNA array, respectively. **Bolded** stretches represent the regions complementary to the hybridization probes used to generate the signals shown in the figures. *fC*, *mG*, and *mA* denote 3'-DMT- 2'-fluoro and 3'-DMT-2'-methoxy ribonucleoside phosphoramidites respectively.

Label	Sequence (5'-3')	Usage
5'-FAM	ATAACTTTGCAACAGTGG	Fig. 5
5'-Texas Red	GCCGATGACCTGCAAGAGT	Fig. 5
3'-Texas Red	GCCGATGACCTGCAAGAGT	Figs. 4B, 6B
3'-Cy3	ATAACTTTGCAACAGTGG	Fig. 1
5'-Cy5	TCAGAACTCACCTGTTAG	Figs. 1,2,3A-3C,4B
5'-FAM	TCAGAACTCACCTGTTAG	Fig. 6B

Supplementary Table 3. Sequences of oligonucleotides used for hybridization to the arrays.

Data analysis and GeneTac image acquisition

Image processing and data analysis were performed using either ImageJ or the native GeneTac software, both of which extract pixel intensities from 16-bit gray-value images. The signal presented in all of the figures of the main text was the background-subtracted and normalized to the highest signal obtained for that particular channel so that the maximum signal was 1 and the minimum was ~0, unless otherwise noted. False-color LUTs utilized for the preparation of each image refer to the standard set availabe in ImageJ or the native GeneTac software and are provided in the table below, which also summarizes the settings used for image acquisition upon the GeneTac scanner.

Figure	**Channel**	**Gain**	**Resolution (µm/pixel)**	**Avg. Pts./Pixel**	**False-color LUT**
2-37	Cy5	28	5	3	Glow-Green
2-45	Cy5	27	5	3	Glow-Green
2-60	Cy5	28	5	3	Glow-Green
2-inset	Cy5	28	1	3	Glow-Green
3a	Cy5	27	5	3	Jet
3b	Cy5	27	5	3	Jet
3c	Cy5	27	5	3	Jet
4b	Cy5	25	5	3	Blue
	TexasRed	46	5	3	Spectrum
5	FITC	50	10	3	Blue
	TexasRed	55	10	3	Green
	Cy5	38	10	3	Red
6	FITC	40	20	2	Green
	TexasRed	40	20	2	Red

Supplementary Table 4: Acquisition parameters for the GeneTac Scanner

Chapter 5

‘Shrink-to-Fit’ Superhydrophobicity: Thermally-Induced Microscale Wrinkling of Thin Hydrophobic Multilayers Fabricated on Flexible Shrink-Wrap Substrates‡

‡ Portions of this chapter have previously been published as: Manna, U.; Carter, M.C.D.; Lynn, D.M. “‘Shrink-to-Fit’ Superhydrophobicity: Thermally-Induced Microscale Wrinkling of Thin Hydrophobic Multilayers Fabricated on Flexible Shrink-Wrap Substrates.” *Advanced Materials* **2013**, *25*, 3085-3089. U.M. and M.C.D.C. were co-first authors. U. Manna and I fabricated the films, performed the physicochemical characterization experiments, and analyzed the data.

The term ‘superhydrophobic’ is used to describe surfaces that are extremely non-wetting (e.g., water contact angles >150°, with low roll-off angles).[1-2] Examples of superhydrophobicity can be found in Nature, and synthetic superhydrophobic surfaces – materials inspired by these examples, but designed to have superior physical, mechanical, or optical properties – have become increasingly important in a variety of contexts, ranging from the design of self-cleaning surfaces to the development of new approaches to water harvesting and oil/water separations.[3-4] Many of these and other applications of superhydrophobic surfaces will either require or benefit from the design of materials that are multi-functional – that is, materials that are extremely non-wetting, but that can also be bent or flexed, integrated into devices with complex geometries, or decorated with additional functionality (e.g., to create hydrophilic domains, etc.).[3-9] Many top-down and bottom-up approaches to the fabrication of superhydrophobic surfaces have been reported,[1-2,10] but the development of robust and multi-functional superhydrophobic materials remains an important challenge.

The non-wetting nature of many superhydrophobic materials is understood to arise from a combination of appropriate surface nano/microstructure and the presence of a low-energy surface coating.[1-2,10] These coatings are often critical to the maintenance of superhydrophobicity, but they are also chemically inert and limit the extent to which these surfaces can be further functionalized. This approach can also introduce other practical limitations because abrasions and scratches in these outer layers (or cracks induced by bending or stretching) can compromise superhydrophobic properties substantially.[11] This latter challenge has been addressed by reports on ‘self-healing’ superhydrophobic surfaces that can restore low-energy barriers after physical insults.[12-14] New superhydrophobic materials that are also ‘internally’ (or three-dimensionally) superhydrophobic[15-17] can also exhibit non-wetting properties after surface layers have been

abraded or removed, and could thus also address issues associated with defects that form upon stretching, bending, or flexing. Examples of these materials have emerged only recently, however, and new methods for the fabrication of flexible superhydrophobic coatings that can be physically manipulated and/or chemically functionalized without loss of function would be useful in a wide variety of fundamental and applied contexts.

Here, we report an approach to the design of flexible superhydrophobic surfaces based on thermally-induced microscale folding and wrinkling of thin, hydrophobic polymer multilayers fabricated on heat-shrinkable polymer films. This approach is straightforward to implement and yields (i) materials that can be bent, cut, and transferred onto other surfaces without loss of superhydrophobicity, and (ii) reactive surfaces that can be further functionalized to impart new properties (e.g., to create superhydrophobic surfaces with patterned domains of hydrophilicity). Because this process exploits biaxial shrinking processes common to commercially available, 'heat-shrink' plastics,[18-20] this approach can also be used to (iii) design materials that 'shrink-to-fit' to create superhydrophobic coatings on complex surfaces, (iv) shrink the dimensions and increase the densities of patterned features, and (v) enable new approaches to the repair of full-thickness surface defects to restore superhydrophobicity to scratched surfaces.

Our approach is based on methods for the 'reactive' layer-by-layer assembly of polymer multilayers using branched poly(ethylenimine) (PEI) and the amine-reactive polymer poly(vinyl-4,4-dimethylazlactone) (PVDMA).[21] These methods yield thin, covalently-crosslinked multilayers that can be functionalized by treatment with amine-functionalized molecules to introduce additional functionality and impart new properties.[22-23] Our past studies demonstrate that thin PEI/PVDMA multilayers (~140 nm thick) have advancing water contact angles (θ) of ~60°, but that the reaction of residual azlactone groups with a hydrophobic primary amine (e.g.,

n-decylamine) can be used to design hydrophobic surfaces (θ = ~100°).[21] We also reported recently that reactive PEI/PVDMA films ~80 μm thick exhibit superhydrophobicity (θ >150°), a property understood to arise from large increases in nano- and microscale roughness during the fabrication of these substantially thicker films.[24]

The work reported here was motivated by our recent observation that thin PEI/PVDMA films (~35 nm thick) fabricated on heat-shrinkable plastic undergo microscale folding and wrinkling when the underlying substrate is shrunken bi-axially by the application of heat.[25] Past studies have demonstrated that combinations of micro- and nanoscale surface features that arise during the shrinking, compression, or swelling of other soft materials can impart permanent or temporary superhydrophobicity.[26-28] On the basis of our past results, we hypothesized that thermally-induced, biaxial shrinking of thin, hydrophobically-modified PEI/PVDMA films could be exploited to create microscale topography sufficient to introduce superhydrophobic properties.

Fig. 1A (gray bars) shows water contact angles for strips of commercially available polyolefin-based shrink-wrap coated with PEI/PVDMA multilayers 3-, 5-, or 7-bilayers thick after treatment with *n*-decylamine to react with remaining azlactone functionality [uncoated shrink-wrap (θ ~85°) is shown as a control; otherwise identical films fabricated on reflective silicon substrates were 33 ±6nm, 55 ±3nm, and 85 ±3nm thick, as determined by ellipsometry]. These results reveal decylamine-treated multilayers to be hydrophobic, with contact angles ranging from ~95° (for films 3-bilayers thick) to ~115° (for films 5- or 7-bilayers thick). These films were then shrunken biaxially (by ~50%) by applying heat from a heat gun (~170 °C for 5 s; see full details in the Experimental Section at the end of this chapter).

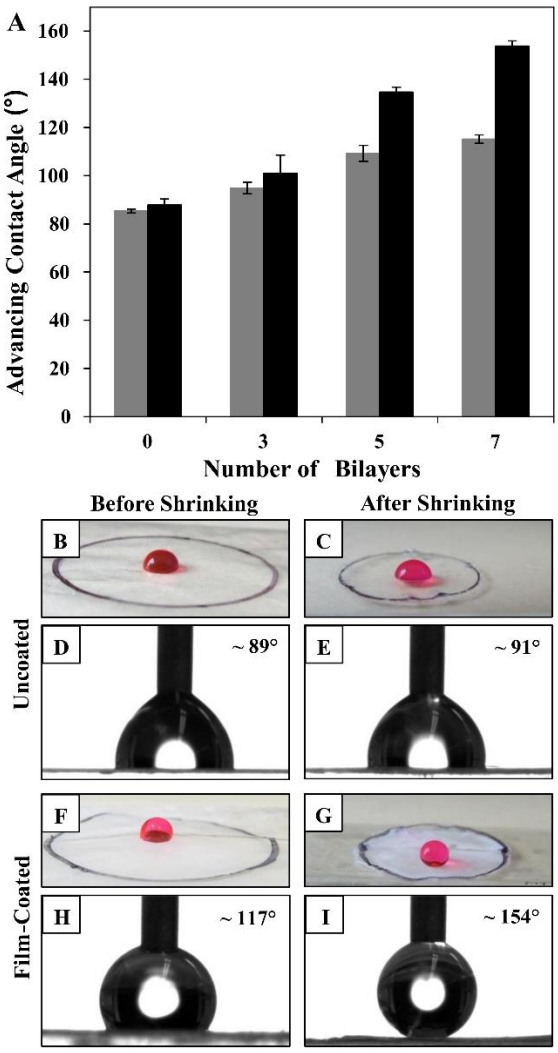

Figure 1. (A) Water contact angles for multilayer-coated shrink-wrap vs the number of PEI/PVMDA bilayers deposited before (gray bars) or after shrinking (black bars). Multilayers were treated with decylamine before use; films were shrunken biaxially by applying heat from a heat gun (~170 °C for 5 s; see Experimental Section). (B-I) Images showing beading and wetting of water and contact angles on uncoated shrink-wrap (B-E) and shrink-wrap coated with PEI/PVDMA multilayers 7-bilayers thick (F-I). Panels B, D, F, H show images of beading and wetting before shrinking; panels C, E, G, I show images after shrinking. In B and F (before shrinking), the circle is 3cm in diameter; in C and G (after shrinking) it is 1.4 cm.

Fig. 1A (black bars) reveals the contact angles of substrates coated with films 5- or 7-bilayers thick to increase substantially after shrinking. In particular, films coated with 7-bilayers exhibited superhydrophobicity (θ = ~154°, with roll-off angles of ~4°); droplets of water placed

on these substrates beaded up (Fig. 1G) and rolled off readily. Fig. 1F-I shows photographs and contact angle measurements made on substrates coated with 7-bilayer films before and after shrinking (images in 1B-E show corresponding results for an uncoated film; the black circles were drawn before heating to indicate the degree of shrinking). These results demonstrate that while the physical properties of (i) 7-bilayer films alone and (ii) shrunken shrink-wrap alone are not sufficient to achieve superhydrophobicity, the heat-induced shrinking of substrates coated with 7-bilayer films drives a transformation that leads to superhydrophobic surfaces. All studies described below were performed using substrates coated with PEI/PVDMA films 7-bilayers thick unless otherwise noted.

Multilayer-coated shrink-wrap was optically transparent before shrinking, but became cloudy and opaque after shrinking; no cracking, delamination, or other large-scale defects were observed in response to the shrinking and re-sizing of the underlying plastic substrates. These superhydrophobic films were flexible and pliable, and no reductions in contact angle were observed after repeated manual bending, folding, or creasing (see Fig. S1 in the Supporting Information at the end of this chapter) or upon storage at ambient conditions for several weeks. Streams of water sprayed forcefully at these films from a ~45° angle rebounded and bounced away on contact (Fig. S1), and samples immersed underwater appeared shiny and reflective as a result of thin pockets of trapped air (Fig. S1). This effect is commonly observed for superhydrophobic materials in the Cassie-Baxter state,[10] and persisted for a period of at least three days of continuous submersion. These results demonstrate that these films are physically robust and maintain superhydrophobicity under a range of conditions; we return to a discussion of physical manipulation and mechanical challenges to these films again below.

Fig. 2 shows SEM images of shrink-wrap coated with 7-bilayers of PEI/PVDMA before

(A-B) and after (C-D) shrinking. Inspection of the morphology of these films before shrinking reveals them to be flat and to exhibit granular nanoscale features (B), but to be devoid of significant microscale structure over large areas (A). Inspection of these films after shrinking, however, reveals microscale wrinkles and folds spread uniformly across the surface (C), with no cracking or peeling over large areas (see also Fig. S2). The image in (D) reveals the surfaces of these wrinkles to be rough and studded with granular features qualitatively similar to those observed before shrinking (B). Uncoated strips of shrink-wrap were featureless both before and after shrinking (E-F).

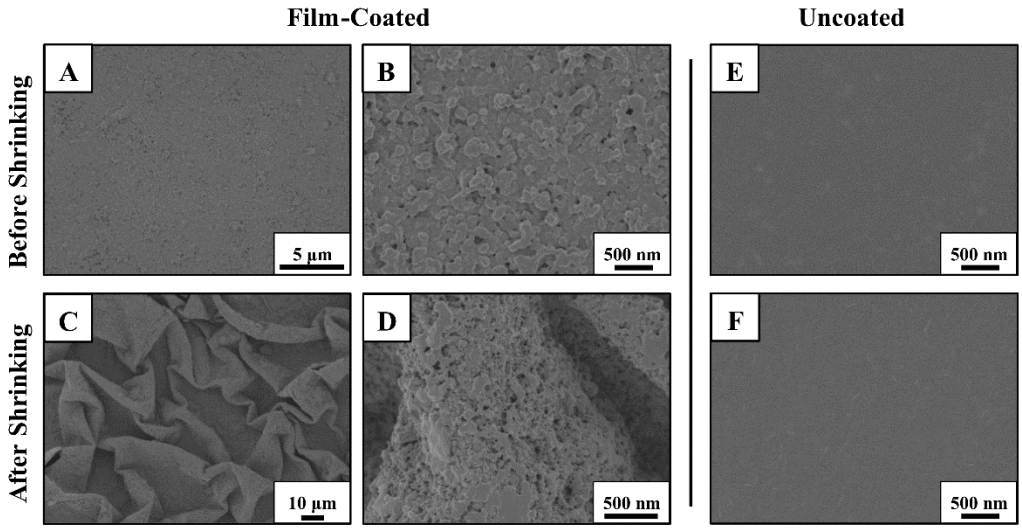

Figure 2. (A-D) SEM images of shrink-wrap coated with decylamine-treated PEI/PVDMA multilayers 7-bilayers thick (A-B) before shrinking and (C-D) after shrinking. Panels E-F show images of uncoated shrink-wrap before and after shrinking.

The folding and wrinkling observed here is consistent with past studies demonstrating that thin polymer- or metal-based films can be induced to fold, buckle, wrinkle, or undergo other changes in microscale topography in response to forces induced by the shrinking, compression, or swelling of an underlying substrate.[19-20,29-30] The evolution of the features in the multilayers investigated here correlates to the large increase in contact angle observed upon shrinking (Fig.

1A) and the onset of superhydrophobicity. Here we note that we also used SEM to characterize the surfaces of shrink-wrap coated with thinner films (3- and 5-bilayers thick; as discussed above) that do not become superhydrophobic after shrinking. These results are included in Fig. S3, and reveal that while these thinner films do also exhibit folds and wrinkles after shrinking, the surfaces of these features do not possess the same degree of nanoscale granularity as thicker, 7-bilayer films. It is not clear from these results whether differences in the sizes or morphologies of the wrinkles in these films could play more dominant roles than these apparent differences in nanoscale topography, but we believe that fruitful combinations of both are likely to be important (i.e., that the dynamic, shrinking-induced introduction of microscale topography to films that are already hydrophobic and exhibit some degree of nanoscale structure leads to appropriate combinations of nano- and microscale features required for superhydrophobicity[31]). It is clear that thinner multilayers do not exhibit superhydrophobicity upon shrinking under the conditions used here.

We next investigated the properties of chemically-patterned multilayers fabricated on heat-shrink substrates. We patterned hydrophilic spots on the surfaces of reactive PEI/PVDMA films by depositing droplets of an aqueous solution of D-glucamine, a carbohydrate-based amine demonstrated to react with the azlactone groups of PEI/PVDMA films in past studies.[16,22] Azlactone groups in areas surrounding these spots were then reacted exhaustively with decylamine. Fig. 3A-B shows droplets of water placed on these chemically patterned hydrophobic/hydrophilic surfaces (A) after fabrication and (B) after shrinking. These images reveal decylamine-treated regions to become superhydrophobic (as described above), but that the glucamine-patterned spots remained hydrophilic after shrinking; droplets of water readily wet those features but did not spread beyond the boundaries dictated by the surrounding

superhydrophobic areas (B). Biaxial shrinkage of the underlying shrink-wrap lead to uniform shrinking of the patterned spots (i.e., these spots were ~50% smaller and closer together, but retained their original shapes), providing a basis for manipulating the sizes and densities of chemical features on patterned superhydrophobic surfaces. These results also illustrate the importance of hydrophobic functionality in attaining superhydrophobicity using this approach – that is, microscale wrinkling of film located in hydrophilic glucamine-treated regions is not sufficient to impart superhydrophobicity. Finally, Fig. 3C shows an untreated (reactive) azlactone-containing film after heat shrinking and Fig. 3D shows the same shrunken film after treatment with decylamine. These images reveal azlactone-containing films to be moderately hydrophobic after shrinking (θ = ~103°), but that superhydrophobicity can also be imparted, *after shrinking*, by subsequent treatment with decylamine (θ = ~153°; with roll-off angles of ~5°). This result indicates that the azlactone functionality in these multilayers can survive temperatures required for heat shrinking and that these reactive groups can be exploited for further post-shrinking chemical modification.

Shrink-wrap can be used to form coatings that 'shrink-to-fit' snugly and conformally around objects with complex shapes. Fig. 3F demonstrates that the films described above can be used to develop shrink-to-fit approaches to the fabrication of superhydrophobic films on curved surfaces. The superhydrophobic coating shown in Fig. 3F was fabricated by wrapping hydrophobic, multilayer-coated shrink-wrap loosely around a glass rod and then shrinking it tightly around the rod (see Experimental Section). We estimate that the substrate in this experiment shrank by ~40%, an amount sufficient to render the outer surface of the film-coated rod superhydrophobic (Fig. 3E shows an image of a control performed using uncoated shrink-wrap). This shrink-to-fit approach is also compatible with methods described above for pre- or

post-shrinking chemical functionalization, but is limited to the fabrication of superhydrophobic coatings on exterior surfaces. We note, however, that the robust and flexible nature of these films also permits them to be bent or rolled into tubes and channels with superhydrophobic interiors suitable for the transport of aqueous solutions.

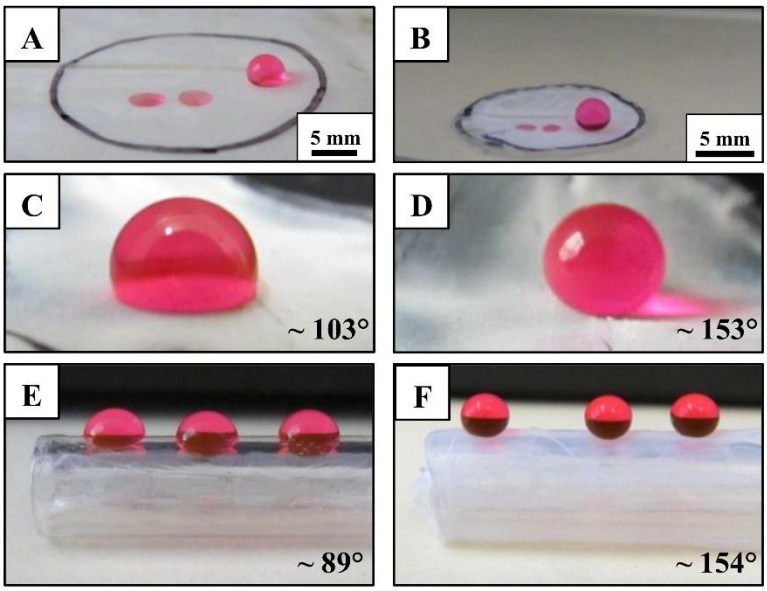

Figure 3. (A-B) Images of shrink-wrap coated with multilayers 7-bilayers thick patterned with hydrophilic spots (diameter ~2.5mm) by deposition of drops of aqueous glucamine before treatment with decylamine. The images show beading and selective wetting of water (A) before and (B) after shrinking. (C) Wetting of a water droplet on a shrunken sample of shrink-wrap coated with reactive, azlactone-containing multilayers. (D) The same sample shown in (C) after treatment with decylamine. (E) Droplets of water placed on the surface of a glass rod coated by shrinking uncoated shrink-wrap around the rod. (F) Droplets of water placed on the surface of a glass rod coated by shrinking shrink-wrap coated with decylamine-treated multilayers around the rod. The volume of the droplets is ~10μL; the diameter of the rod is ~5mm.

Finally, we note that in all of the experiments above, substrates were constrained and prevented from shrinking completely upon heating (e.g., by fixing films over the mouth of a container or shrinking-to-fit around another object; see Experimental Section). This permits additional shrinking by subsequent heat treatments once those constraints are removed. We hypothesized that additional heat-shrinking could be used to repair and restore

superhydrophobicity to films with scratches or other surface defects. To demonstrate proof-of-concept, we made full-thickness scratches in superhydrophobic multilayers by carefully dragging a needle across the surface. Figs. 4A and 4E,G show photographs and SEM images of representative scratches; the image in Fig. 4C demonstrates that these defects compromise the superhydrophobicity of these films (θ = ~123°). Fig. 4B shows an image of the same film shown in Fig. 4A after additional treatment with a heat gun. This image reveals the scratch to be almost completely repaired (by visual inspection), and Fig. 4D demonstrates that heat treatment restores superhydrophobicity in this location (θ = ~154°; with roll-off angles of ~4°) without compromising the superhydrophobicity of surrounding, unscratched regions (θ = ~154°, with roll-off angles of ~4°). These films could be scratched and repaired using this approach at least three times (Fig. S4). Further characterization of films by SEM (Fig. 4F,H) suggested that the 'repair' of these scratches occurred by additional shrinking of the underlying substrate to bring together the edges of the scratches, rather than by thermally-induced flow of the multilayers into the scratched region. This latter possibility is unlikely in view of the covalently crosslinked nature of these films,[21] and heat-treatment of scratched films fabricated on glass substrates did not result in similar repair (Fig. S5).

In conclusion, we have reported an approach to the design of robust and flexible superhydrophobic surfaces based on heat-induced wrinkling of polymer multilayers fabricated on heat-shrinkable polymer films. Biaxial shrinking of thin, crosslinked multilayers that are already hydrophobic and posess some degree of nanoscale structure leads to combinations of nano- and microscale features required to impart superhydrophobicity. The reactive nature of these multilayers also permits them to be patterned with chemical functionality (with hydrophilic groups and potentially other functionality) before or after heat-shrinking. Because this approach

exploits shrinking and re-sizing processes common to heat-shrink plastics, it can be used to design ‘shrink-to-fit’ coatings that can be fixed snugly on complex surfaces, reduce the dimensions and increase the densities of patterned features, and promote heat-activated repair of full-thickness defects, all of which could be useful for advanced applications of superhydrophobic surfaces but are difficult to achieve using conventional methods.

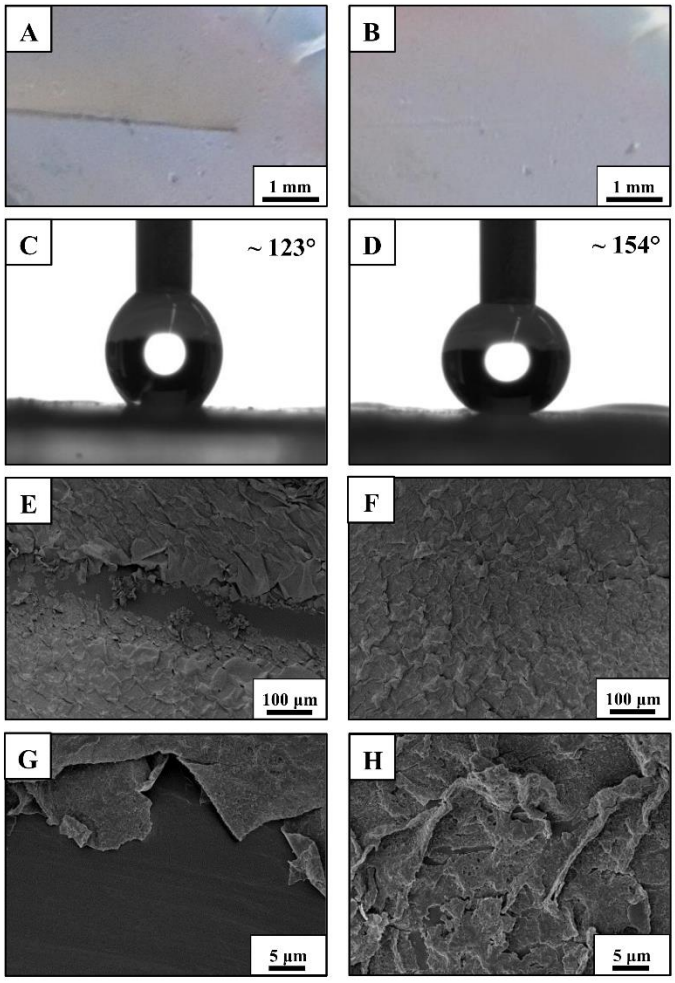

Figure 4. (A) Image of a superhydrophobic, heat-shrunken sample of shrink-wrap coated with decylamine-treated PEI/PVDMA multilayers 7-bilayers thick, showing a portion of the surface scratched to create a full-thickness defect. (B) The same sample shown in (A) after heating with a heat gun. (C-D) Contact angle measurements made by placing droplets of water (C) on the scratch shown in (A), and (D) in the same location on the film shown in (B) after additional heating. (E-H) SEM images of films similar to those shown in (A-B) showing scratched regions (E,G) before and (F,H) after heating. Images in (G) and (H) show high magnification images of the scratched and healed regions shown in (E) and (F), respectively.

Acknowledgements. This work was supported by the NSF through a grant to the Materials Research Science and Engineering Center at UW-Madison (DMR-1121288) and the Office of Naval Research (N00014-07-1-0255) and made use of NSF-supported shared facilities. M.C.D.C. acknowledges the Natural Sciences Engineering Research Council of Canada for a graduate fellowship. We thank Jerald Rasmussen and Adam Broderick for helpful discussions related to heat-shrink materials.

References

[1] L. Feng, S.H. Li, Y.S. Li, H.J. Li, L.J. Zhang, J. Zhai, Y.L. Song, B.Q. Liu, L. Jiang, D.B. Zhu, *Adv. Mater.* **2002,** *14*, 1857.

[2] X.M. Li, D. Reinhoudt, M. Crego-Calama, *Chem. Soc. Rev.* **2007,** *36*, 1350.

[3] X. Zhang, F. Shi, J. Niu, Y.G. Jiang, Z.Q. Wang, *J. Mater. Chem.* **2008,** *18*, 621.

[4] X. Yao, Y. Song, L. Jiang, *Adv. Mater.* **2011,** *23*, 719.

[5] H.Y. Erbil, A.L. Demirel, Y. Avci, O. Mert, *Science* **2003,** *299*, 1377.

[6] W.L. Song, A.C. Lima, J.F. Mano, *Soft Matter* **2010,** *6*, 5868.

[7] S. Lee, W. Kim, K. Yong, *Adv. Mater.* **2011,** *23*, 4398.

[8] F.L. Geyer, E. Ueda, U. Liebel, N. Grau, P.A. Levkin, *Angew. Chem. Int. Ed.* **2011,** *50*, 8424.

[9] I. You, N. Yun, H. Lee, *ChemPhysChem.* **2013,** 10.1002/cphc.201200929.

[10] Y.Y. Yan, N. Gao, W. Barthlott, *Adv. Colloid. Interface Sci.* **2011,** *169*, 80.

[11] T. Verho, C. Bower, P. Andrew, S. Franssila, O. Ikkala, R.H.A. Ras, *Adv. Mater.* **2011,** *23*, 673.

[12] Y. Li, L. Li, J.Q. Sun, *Angew. Chem. Int. Ed.* **2010,** *49*, 6129.

[13] H.X. Wang, Y.H. Xue, J. Ding, L.F. Feng, X.G. Wang, T. Lin, *Angew. Chem. Int. Ed.* **2011,** *50*, 11433.

[14] X.L. Wang, X.J. Liu, F. Zhou, W.M. Liu, *Chem. Commun.* **2011,** *47*, 2324.

[15] P.A. Levkin, F. Svec, J.M. Frechet, *Adv. Funct. Mater.* **2009,** *19*, 1993.

[16] U. Manna, A.H. Broderick, D.M. Lynn, *Adv. Mater.* **2012,** *24*, 4291.

[17] X.T. Zhu, Z.Z. Zhang, G.N. Ren, J. Yang, K. Wang, X.H. Xu, X.H. Men, X.Y. Zhou, *J. Mater. Chem.* **2012,** *22*, 20146.

[18] A. Grimes, D.N. Breslauer, M. Long, J. Pegan, L.P. Lee, M. Khine, *Lab Chip* **2008,** *8*, 170.

[19] H. Yabu, R. Jia, Y. Matsuo, K. Ijiro, S. Yamamoto, F. Nishino, T. Takaki, M. Kuwahara, M. Shimomura, *Adv. Mater.* **2008,** *20*, 4200.

[20] C.C. Fu, A. Grimes, M. Long, C.G.L. Ferri, B.D. Rich, S. Ghosh, S. Ghosh, L.P. Lee, A. Gopinathan, M. Khine, *Adv. Mater.* **2009,** *21*, 4472.

[21] M.E. Buck, J. Zhang, D.M. Lynn, *Adv. Mater.* **2007,** *19*, 3951.

[22] M.E. Buck, A.S. Breitbach, S.K. Belgrade, H.E. Blackwell, D.M. Lynn, *Biomacromolecules* **2009,** *10*, 1564.

[23] M.E. Buck, D.M. Lynn, *ACS Appl. Mater. Interfaces* **2010,** *2*, 1421.

[24] M.E. Buck, S.C. Schwartz, D.M. Lynn, *Chem. Mater.* **2010,** *22*, 6319.

[25] A.H. Broderick, M.C. Carter, M.R. Lockett, L.M. Smith, D.M. Lynn, *ACS Appl. Mater. Interfaces* **2013,** 5, 351.

[26] J. Genzer, K. Efimenko, *Science* **2000,** *290*, 2130.

[27] Y.C. Gan, X.S. Jiang, J. Yin, *Macromolecules* **2012,** *45*, 7520.

[28] Y.H. Kim, Y.M. Lee, J.Y. Lee, M.J. Ko, P.J. Yoo, *Acs Nano* **2012,** *6*, 1082.

[29] L.R. Freschauf, J. McLane, H. Sharma, M. Khine, *Plos One* **2012,** *7*.

[30] L. Ionov, *J. Mater. Chem.* **2012,** *22*, 19366.

[31] P.C. Lin, S. Yang, *Soft Matter* **2009,** *5*, 1011.

Supporting Information for Chapter 5

Experimental Section

Materials. 2-Vinyl-4,4-dimethylazlactone (VDMA) monomer was a kind gift from Dr. Steven M. Heilmann (3M Corporation, Minneapolis, MN). Poly(2-vinyl-4,4-dimethylazlactone) (PVDMA) was synthesized by free-radical polymerization of VDMA in the presence of 7 wt% of intentionally added cyclic azlactone-functionalized oligomer, as described previously.[1] Branched poly(ethylene imine) (BPEI; MW ~25,000), *n*-decylamine (95%), acetone (HPLC grade), and tetrahydrofuran (THF, HPLC grade) were purchased from Sigma Aldrich (Milwaukee, WI). D-Glucamine (>95%) was purchased from TCI America (Portland, OR). Glass microscope slides and phosphate-buffered saline (PBS) were purchased from Fischer Scientific (Pittsburgh, PA). Heat shrinkable film (RCR International, Elgin IL) was purchased from Menards, Inc. (Madison, WI). All chemicals were used as received without further purification unless otherwise noted.

General Considerations. Compressed air used to dry samples was filtered through a 0.2 μm membrane syringe filter. Scanning electron micrographs were acquired using a LEO DSM 1530 scanning electron microscope at an accelerating voltage of 3 kV. Prior to imaging, samples were coated with a thin layer of gold via a gold sputterer operating at 45 mA under a vacuum pressure of 50 mTorr for 40 s. A hand-held laboratory grade heat gun (Master Appliance, Racine, WI) was used to shrink heat shrinkable films. Digital pictures were acquired using a Canon PowerShot SX130 IS digital camera. Contact angle measurements were made using a Dataphysics OCA 15 Plus contact angle goniometer at ambient temperature with 5 μL of 18.2 MΩ Millipore water. The optical thicknesses of films fabricated on silicon were determined using a Gaertner LSE ellipsometer (632.8 nm, incident angle = 70°). Data were processed using

the Gaertner Ellipsometer Measurement Program. Relative thicknesses were calculated assuming an average refractive index of 1.577 for the multilayered films. Thicknesses were determined in at least five different standardized locations on each substrate and are presented as an average (with standard deviation) for each film.

Fabrication of Reactive Polymer Multilayers on Heat-Shrinkable Film. Samples of commercially available, flexible heat-shrinkable polyolefin film (~2.4 cm x 5.5 cm) were cut using scissors and prepared for dipping-based fabrication processes by wrapping them once around a planar glass slide (~1.4 cm x 7.5 cm); the top and bottom edges of the slides were then wrapped tightly with copper wire to secure the film and anchor it to the glass slide. PEI/PVDMA multilayers were then deposited on the heat shrinkable film using the following general procedure: (i) substrates were submerged in a solution of BPEI (20 mM in acetone with respect to the polymer repeat unit) for 20 s; (ii) substrates were removed and immersed in an initial acetone bath for 20 s followed by a second acetone bath for 20 s; (iii) substrates were submerged in a solution of PVDMA (20 mM in acetone with respect to the polymer repeat unit) for 20 s; and (iv) substrates were removed and rinsed again using the procedure outlined under step (ii). This cycle was repeated either 3, 5, or 7 times to fabricate multilayers consisting of 3, 5 or 7 BPEI/PVDMA layer pairs (referred to hereafter as “bilayers”). The copper wire securing the heat shrinkable wrap to the glass slides was then carefully removed, and the multilayer-coated wrap was removed and washed copiously with a stream of acetone (~25 mL, using a laboratory spray bottle) and then dried gently under a stream of filtered compressed air.

Heat-Induced Shrinking of Multilayer-Coated Shrink-Wrap. Prior to shrinking, multilayer films were removed from one side of each multilayer-coated shrink-wrap substrate by laying the sample flat and pressing adhesive tape onto the sample surface; careful peeling of the tape from

the sample removed the underlying multilayers, as determined by visual inspection. Next, the shrink-wrap, with the multilayer-coated side facing up, was placed loosely over the open end of a 12 mm diameter straight-edged vial. A curved surface (a stainless steel ball; diameter = 11 mm) was gently pressed onto the sample to produce a controlled amount of slack in the film. A circular piece of copper wire was then used to secure the shrink-wrap in place by securing the remaining loose/excess shrink-wrap against the outer walls of the vial, and the curved surface was removed. The sample was then exposed to a stream of hot air (~170 °C) using a heat gun for ~5 s, during which time the shrink-wrap contracted and became taut over the opening of the vial. For experiments designed to create heat-activated, 'shrink-to-fit' superhydrophobic surfaces (see text), a loosely-fitting collar of multilayer-coated shrink-wrap film, fixed at the seam using adhesive tape, was placed around the surface of a glass rod (the diameter of the collar was ~ 1.7 times that of the rod); the collar was then exposed to a stream of hot air until it shrank and conformed tightly to the outer surface of the rod by visual inspection.

Functionalization and Chemical Patterning of Multilayer-Coated Shrink-Wrap. PEI/PVDMA multilayers containing residual amine-reactive azlactone groups were chemically functionalized, either before or after heat shrinking (see text), by treatment with solutions of hydrophobic or hydrophilic primary amines. In some cases, samples were functionalized uniformly, and over large areas, by immersing the films in solutions of *n*-decylamine (20 mg/mL in THF) for ~1 hour, as described previously.[2,3] After treatment, films were rinsed with THF and dried under a stream of compressed air. In other cases, multilayers were patterned with small hydrophilic spots by placing small droplets of aqueous solutions of glucamine (3 μL of a 20 mg/mL glucamine solution in PBS buffer, adjusted to pH 9.0) for 1 minute, as previously described.[3] These chemically patterned samples were then immersed in *n*-decylamine, using the

procedure described above, to react with residual azlactone functionality and render the remainder of the surrounding regions of the films hydrophobic.

Heat-Induced Healing of Scratched Superhydrophobic Surfaces. Superhydrophobic surfaces were prepared by heating samples of multilayer-coated shrink-wrap treated with decylamine as described above. Without removing the film from the straight-edge vial on which it was shrunken (see above), a needle was used to make a narrow, visible, full-thickness scratch in the multilayers on the superhydrophobic surface. The scratched film was then exposed to hot air from a heat gun (~170 °C) again for 5 s. Samples were characterized at each step of this experiment using water contact angle measurements, digital photography, and SEM imaging (see text for additional details).

References for Supporting Information

[1] M. E. Buck, S. C. Schwartz, D. M. Lynn, *Chem. Mater.* **2010,** *22*, 6319.

[2] M. E. Buck, A. S. Breitbach, S. K. Belgrade, H. E. Blackwell, D. M. Lynn, *Biomacromolecules* **2009,** *10*, 1564.

[3] U. Manna, A. H. Broderick , D. M. Lynn, *Adv. Mater.* **2012,** *24*, 4291.

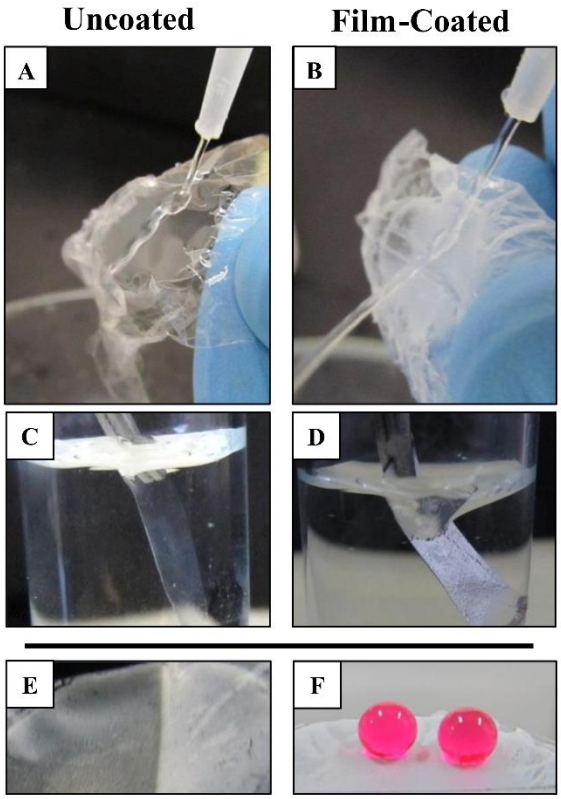

Figure S1. (A-B) Digital photographs showing samples of (A) bare, uncoated and (B) multilayer-coated shrink-wrap after heat shrinking. The sample in panel B was coated with decylamine-treated PEI/PVDMA multilayers 7 bilayers thick prior to shrinking. These images were acquired as water was sprayed forcefully at the surfaces of the films using a laboratory squirt bottle (at an angle of ~45°; the nozzle of the squirt bottle is visible at the top of each image, and the blue objects in these pictures are gloved hands used to support the flexible films during these experiments). In the image in panel B, water was observed to rebound or bounce away from the surface on contact; in the image in panel A, water contacted the surface of the substrate and slid down in an adherent stream. (C-D) Digital photographs of heat-shrunken samples of (C) bare, uncoated shrink-wrap and (D) multilayer-coated shrink-wrap (coated with decylamine-treated PEI/PVDMA multilayers 7 bilayers thick) immersed in a vial of water (forceps used to handle the substrates and keep them submerged are visible near the meniscus). The surface of the film shown in panel D appeared uniformly shiny and reflective over the entirety of its surface as a result of thin pockets of trapped air; this effect was not observed for submerged heat-shrunken samples of bare, uncoated shrink-wrap (panel C). Considerable perturbations of the air/water meniscus observed upon immersion of superhydrophobic surfaces (D) were also not observed in experiments using bare, uncoated substrates (C). (E) Image of a heat-shrunken superhydrophobic film after manually folding and sharply creasing the film; the linear crease is apparent in the middle of the image. (F) Image of the creased film shown in panel E after re-flattening and spreading the film on a flat surface. The red droplet of water on the left was placed directly on the creased part of the film; the droplet on the right was placed on an adjacent region of the film that was not creased.

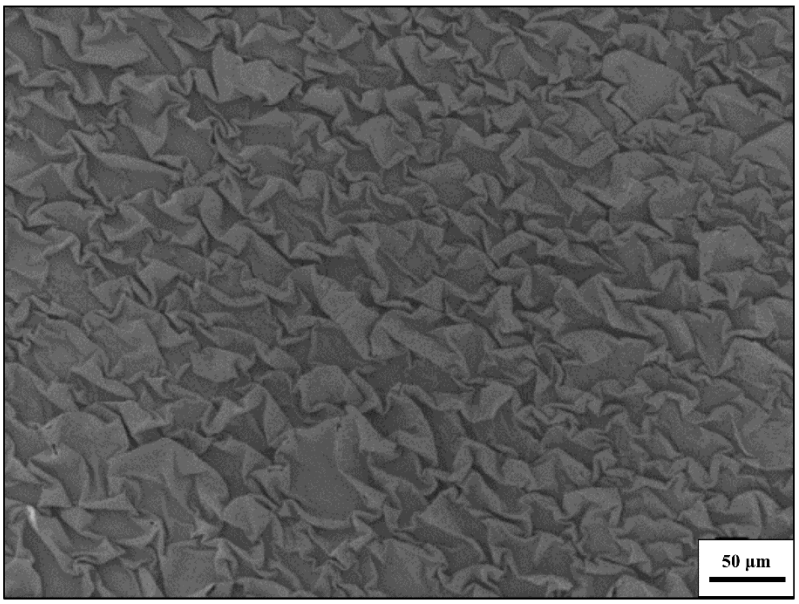

Figure S2. A lower magnification SEM image of the same film shown in Figure 2C (shrink-wrap coated with decylamine-treated PEI/PVDMA multilayers 7 bilayers thick; shown after shrinking) showing the shrinkage-induced folded/wrinkled surface morphology over a larger area.

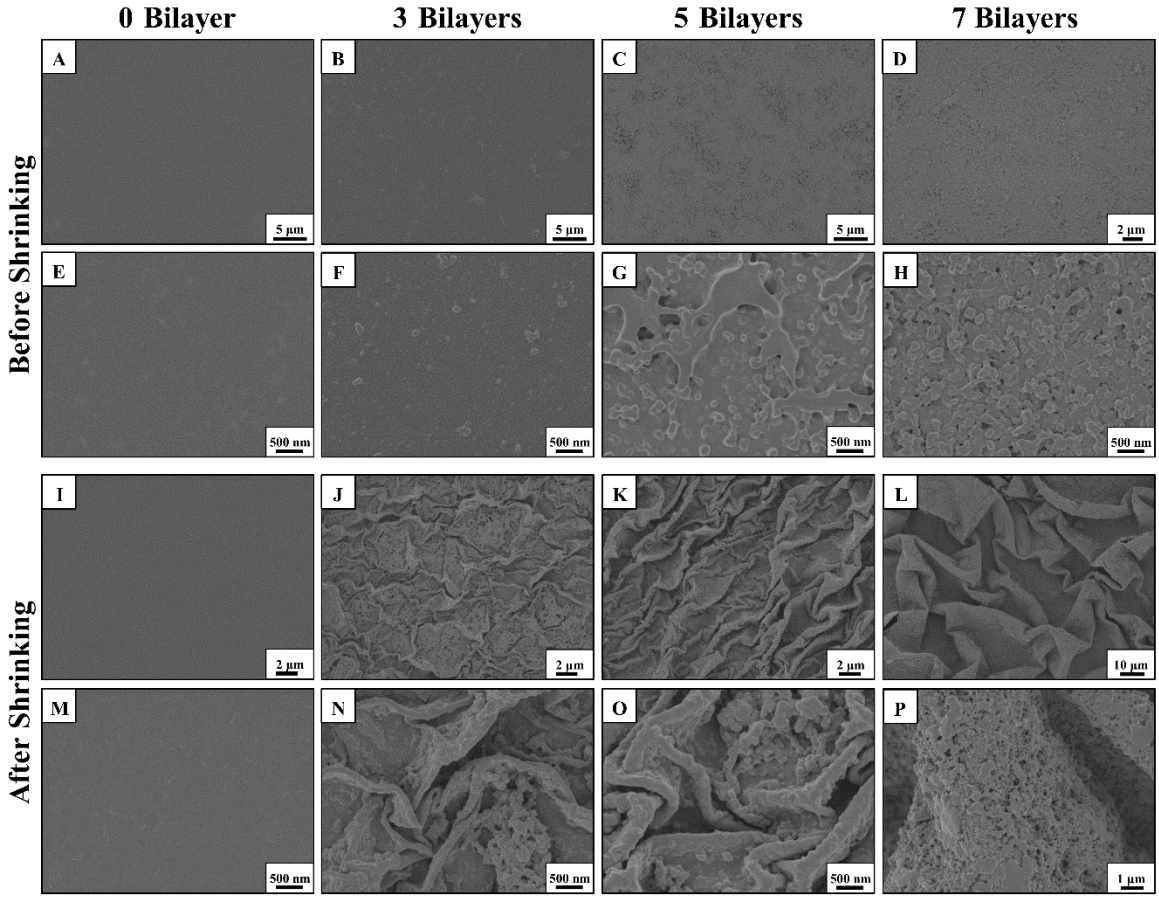

Figure S3. Representative SEM images of flexible shrink-wrap substrates coated with 3, 5, or 7 bilayers of PEI/PVDMA. All multilayers were treated with decylamine prior to analysis (see main text for additional details); the entry marked ‘zero bilayers’ corresponds to uncoated shrink-wrap used as a control. The images show the surface morphologies of these films either before shrinking (A-H) or after heat shrinking (I-P). The images in panels A-D and I-L show representative lower magnification views; the images in panels E-H and M-P show representative higher magnification views of these same films.

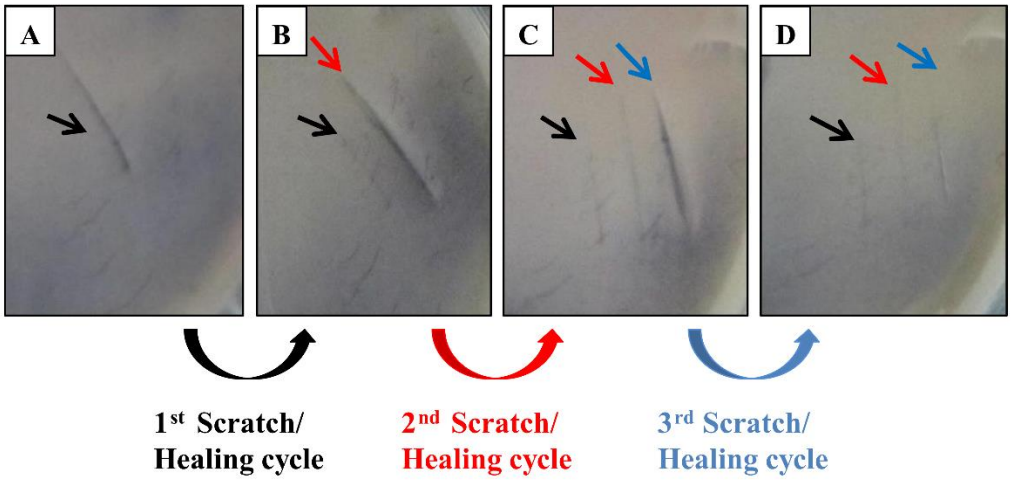

Figure S4. Digital photographs showing the results of multiple 'scratch-and-heal' cycles performed using a single sample of superhydrophobic shrink-wrap. These experiments were conducted in analogy to those shown in panels A-B of Fig. 4 in the main text, using samples of shrink-wrap coated with decylamine-treated PEI/PVDMA multilayers 7 bilayers thick prior to shrinking. After the first scratch-and-heal cycle (shown in A-B), the multilayer film was scratched again in an adjacent location and then subjected to additional brief heating (shown in B-C). This second 'scratch-and-heal' cycle was followed by a third cycle (shown in C-D). In these images, the original locations of the first, second, and third scratches are indicated by black arrows, red arrows, and blue arrows, respectively. Contact angles before scratching were were ~154°, with roll-off angles of ~4°. Contact angles on repaired regions after the 1st, 2nd, and 3rd repair cycles were ~153°, with roll-off angles ranging from ~4–5°.

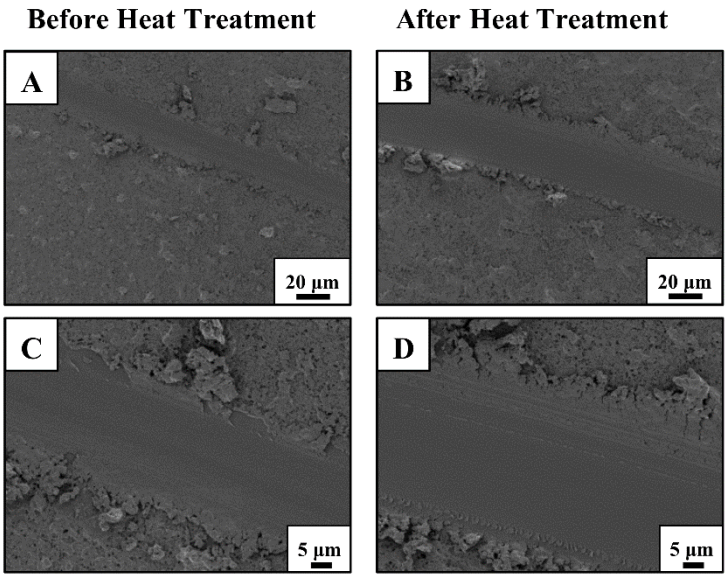

Figure S5. Representative SEM images of glass substrates (standard glass microscope slides) coated with 7 bilayers of PEI/PVDMA. These reactive surfaces were treated with decylamine and then scratched with a needle to create full-thickness defects in the multilayer films. The images in panels A and C show lower and higher magnification views of the scratched regions of these films immediately after scratching. The images in panels B and D show lower and higher magnification views of a similar scratched film after additional heating with a laboratory heat gun (at ~170° C for 2 min). In contrast to samples of scratched multilayers fabricated on flexible shrink-wrap shown in Fig. 4 of the main text, the morphologies of scratched multilayers fabricated on these glass substrates did not change upon additional heat treatment.

Chapter 6

Influence of Partial Side Chain Hydrolysis on the Growth and Morphology of Reactive Polymer Multilayers Fabricated Using Poly(2-Vinyl-4,4-Dimethylazlactone) and Poly(ethyleneimine)‡

‡ Portions of this chapter are being prepared for publication as: Carter, M.C.D.; Wong, M.S.; Lynn, D.M. "Influence of Partial Side Chain Hydrolysis on the Growth and Morphology of Reactive Polymer Multilayers Fabricated Using Poly(2-Vinyl-4,4-Dimethylazlactone) and Poly(ethyleneimine)." M. Wong fabricated many of the films. My contribution was in synthesizing the polymers, fabricating films, performing the physicochemical characterization experiments, and analyzing the data.

Introduction

Polymer-based coatings are widely used to functionalize and define the physicochemical properties of surfaces and interfaces. Layer-by-layer approaches to the fabrication of thin polymer 'multilayers' are particularly useful and versatile in this regard.[1,2] In general, these methods fall into one of two broad categories depending on the type of interactions that drive film growth: (i) aqueous-based approaches that leverage polyvalent weak interactions between mutually interacting polymers (e.g., through ionic interactions, hydrogen bonding, etc.),[2-6] or (ii) reactive/covalent approaches that exploit reactions between polymers containing mutually reactive groups.[7-10] These approaches are inherently versatile, providing control over molecular composition (e.g., through the choice of the constituent polymers), film thickness (e.g., by controlling the number of assembly cycles), and film architecture (e.g., by designing stratified or hierarchical films using multiple different sets of components or building blocks).[2-6,11,12] Although a significant amount of effort has led to the development of a general understanding of the behaviors of layer-by-layer polymer coatings, a number of factors, including the intermixing or interdiffusion of polymer layers[13-16] and other structural reorganizations that can occur during or after film fabrication[1,4,17,18] can influence film morphology and give rise to otherwise unexpected structures and bulk or surface properties. These inherent complexities in layer-by-layer assembly can be useful, and they often result in the unexpected discovery of coatings and interfaces with new features or new types of behaviors that are of interest in many fundamental and applied contexts.[1,4-6,19]

The work reported here was motivated by past studies from our group on the reactive layer-by-layer assembly of poly(2-vinyl-4,4-dimethylazlactone) (PVDMA), a polymer bearing amine-reactive side chain functionality, and poly(ethylenimine) (PEI), a hyperbranched polymer

with primary amine end groups (see, for example, Chapters 2 through 5 of this thesis).[20,21] These past studies demonstrate that interfacial reactions between the azlactone groups in PVDMA and the primary amines in PEI can drive layer-by-layer assembly, and that the resulting multilayers contain residual azlactone groups that can be used for further functionalization and to tailor surface and bulk properties.[10,20] These PEI/PVDMA multilayers are useful in at least three ways: (i) as is typical of most other layer-by-layer assembly processes, these films can be fabricated on a broad range of substrates, including curved and topologically complex substrates,[22-26] (ii) the assemblies that result are stable in chemically complex environments,[25-30] owing to the formation of hydrolytically stable polyacrylamide-type crosslinks, and (iii) these films can be functionalized, and their surface and bulk properties can be manipulated and tuned, by treatment of these azlactone-containing coatings with a broad range of amine-, alcohol-, and thiol-containing nucleophiles.[10,20,21,30] The potential utility of these PEI/PVDMA coatings has been demonstrated in the design of new functional interfaces and membranes, including as platforms for cell culture,[25,31,32] the immobilization and synthesis of microarrays of oligonucleotides and proteins,[27,33,34] the development of new liquid crystal-based chemical sensors,[35-37] and as organic solvent-based alternatives to conventional aqueous layer-by-layer processes for the coating and interfacial modification of water-soluble substrates.[28]

Past work in our group has demonstrated that PEI and PVDMA can also be used to fabricate micrometer thick layer-by-layer films that exhibit nano- and microscale features and substantial nanoscale porosity.[21,38] Those past studies have also demonstrated that these morphologies can impart unique wetting and non-wetting behaviors. For example, when these reactive nanoporous PEI/PVDMA films are functionalized by treatment with hydrophobic amines, the resulting films can become superhydrophobic or extremely non-wetting to aqueous

fluids.[26,28,38-41] In contrast, when these films are functionalized by treatment with hydrophilic amines, the films become superhydrophilic and can be extremely non-wetting to oils and hydrophobic liquids when submerged in water (coatings that exhibit so-called underwater superoleophobicity).[29,30] The reactivity of these materials also permits surface and bulk patterning using a variety of chemical methods; this feature has been exploited fruitfully to design surfaces with patterned contrasts in wettability that can guide and manipulate the transport of aqueous fluids.[42] The bulk, or internal, superhydrophobicity that can be designed into these three-dimensional nanoporous materials has also been exploited to develop new approaches for the chemical protection and long-term release of encapsulated water-soluble agents,[41,43] and to design matrices for the fabrication of slippery liquid-infused porous surfaces (SLIPS) that can prevent fouling by aqueous fluids and pathogenic fungi and bacteria.[44,45]

The rough, nanoporous, and chemically-reactive morphologies and structures that can develop during the fabrication of these PEI/PVDMA films are unique, and have led to novel properties and guiding principles that have enabled new potential applications of these materials. However, while the structures, morphologies, and behaviors of these nanoporous materials have been well characterized, the processes that lead to their development during layer-by-layer assembly, or that can be used to control the extents or the scales on which they occur, remain poorly understood. Past studies have reported specific process parameters, including fabrication procedures and protocols for the synthesis of PVDMA,[29,38,40,42-45] that can lead to the evolution of roughness and porosity, and to morphologies that exhibit the physical properties and functional behaviors described above, but thus far no understanding has emerged regarding molecular-level interactions or other physical processes that influence structure formation during assembly.

The work reported here sought to provide insight into interactions and processes that can lead to the development of micro- and nanoscale structure in PEI/PVDMA-based multilayers, and to elucidate molecular design principles that can be used to control, influence, or tune the morphologies of these materials and their functional properties. In this Chapter, we demonstrate that the presence of hydrolyzed azlactone groups in PVDMA can play a significant role in promoting the generation of porosity and roughness. For example, whereas the layer-by-layer assembly of PVDMA and PEI leads to the linear growth of thin, smooth films that are largely devoid of notable nanoscale features, layer-by-layer assembly using PVDMA synthesized to contain controlled degrees of partial side chain hydrolysis leads to the growth of thick films with substantial nanoscale roughness, porosity, and physicochemical behaviors similar to those reported in past studies. Because the hydrolysis of azlactone functionality leads to the formation of carboxylic acid side chain groups, these results suggest that nanostructure formation may be influenced or driven in part by acid/base ion-pairing interactions with PEI during reactive layer-by-layer assembly. These observations and the results of other related experiments reported here are consistent with this view, and provide a framework for understanding and exploiting the range of competing interactions that can control film growth and lead to changes in film morphology in this reactive layer-by-layer system. Our results provide insights, guiding principles, and new experimental tools that may prove useful in further tuning and tailoring the properties and behaviors of these reactive coatings.

Materials and Methods

Materials. Branched poly(ethyleneimine) (PEI; MW ~25,000), azobisisobutyronitrile (AIBN, recrystallized once from methanol), decylamine (95%+), concentrated hydrochloric acid (HCl,

37%, ACS reagent), tetrahydrofuran (THF, HPLC grade, >99.9%), dichloromethane (DCM, ACS grade), and hexanes (technical grade), were purchased from Sigma-Aldrich (Milwaukee, WI). Inhibitor Removal Resin was purchased from Alfa Aesar (Radnor, PA). 2-Vinyl-4,4-dimethylazlactone (VDMA) was a kind gift from Dr. Steven M. Heilmann (3M Corp., Minneapolis, MN) and was fractionally distilled under in-house vacuum (B.P. ~22 °C at ~500 mTorr; clear mobile liquid at room temperature). The middle distillation fraction was collected as a clear, non-viscous, colorless oil. Butylated hydroxytoluene (BHT, 500 ppm) and triethylamine (NEt_3, 1000 ppm) were added, and the monomer was stored as a crystalline solid at -18 °C in the dark prior to use. Water with a resistivity of 18.2 MΩ•cm was obtained from a Millipore filtration system. Unless otherwise noted, materials were used as received.

General Considerations. ^{1}H NMR spectroscopy of VDMA and **P1** or **P1x** derivatives was performed in $CDCl_3$ using a Bruker Avance-500 spectrometer. A relaxation delay of 10 s was used for the polymers and all spectra were referenced relative to the residual proton peak of $CHCl_3$ (δ 7.26 ppm). Gel permeation chromatography was performed using a Viscotek GPC Max VE2001 equipped with two Polymer Laboratories PolyPore columns (250 mm × 4.6 mm) and a TDA-302 detector array using THF as the eluent at a flow rate of 1 mL/min at 40 °C. The instrument was calibrated using 10 narrow dispersity polystyrene standards with M_n = 0.580−377.4 kg/mol (Agilent Technologies, Santa Clara, CA). Attenuated total reflectance (ATR) IR measurements were obtained using a Bruker Tensor 27 FTIR spectrometer outfitted with a Pike Technologies Diamond ATR stage (Madison, WI). Data were analyzed using Opus Software version 6.5 (Bruker Optik GmbH). Spectra were collected at a resolution of 2 cm^{-1} and are presented as an average of 16 scans. Data were smoothed by applying a nine-point average

and baseline-corrected using a concave rubberband correction (10 iterations, 64 points). Optical thicknesses of films deposited on silicon substrates were determined using a Gaertner LSE ellipsometer (632.8 nm, incident angle = 70°) and data were processed using the Gaertner ellipsometer measurement software. Thicknesses were calculated assuming a refractive index of 1.577, and were determined in at least five different locations for three replicate films. All films were dried under a stream of filtered compressed air prior to thickness measurements. Contact angle measurements were made using a Dataphysics OCA 15 Plus contact angle goniometer at ambient temperature with 4 μL of 18.2 MΩ Millipore water in at least 3 different locations on each film. Scanning electron micrographs were acquired using a LEO-1550 VP field-emission SEM operating with an accelerating voltage of 1 kV. Film samples were coated with a thin layer of gold prior to imaging; polymer and rinse solutions on silicon chips were imaged without gold coating. Digital pictures were acquired using a Canon PowerShot SX130 IS digital camera. Compressed air used to dry samples was filtered through a 0.2 μm membrane syringe filter

Synthesis of Poly(2-Vinyl-4,4-Dimethylazlactone) (PVDMA) [Polymer P1]. The following general procedure yields unhydrolyzed PVDMA when freshly distilled monomer is used. VDMA was first passed through two Pasteur pipet columns of Inhibitor Removal Resin (~3.5 cm height) followed by a Pasteur pipet column of silica gel (~2 cm height) to remove BHT and NEt_3, respectively. VDMA (2.05 g, 14.8 mmol), AIBN (24.37 mg, 0.148 mmol), and ethyl acetate (6.0 mL, dried over $MgSO_4$ and subsequently filtered through a 0.2 μm PTFE syringe filter) were added to an oven-dried 25 mL round-bottomed flask tube, sealed with a rubber septum and parafilm, and sparged with nitrogen for 15 minutes before being placed into an oil bath at 60 °C. After 24 hours, the flask was cooled to room temperature and the mixture was diluted with ~4

mL of DCM and precipitated into ~300 mL of hexanes. The resulting white solid was collected by vacuum filtration and then dried under high vacuum to constant weight to give **P1**. ^{1}H NMR (400.180 MHz, $CDCl_3$, δ ppm): 2.71 (s, 1H), 2.16-1.79 (m, 2H), 1.37 (s, 6H). ATR IR (cm^{-1}): 1818 (C=O azlactone), 1671 (C=N azlactone), 1203 C-O-C (azlactone). See also Figure 1B and Figure S1.

Partial Hydrolysis of PVDMA. Polymer **P1** was partially hydrolyzed to different degrees to yield **P1**x using the following general procedure. A sample of **P1** (~35 mg) was weighed into a threaded 6 mL glass vial with a stir bar and dissolved in 0.75 mL THF to give a clear, non-viscous solution at room temperature. A 0.1 M HCl solution in THF/H_2O was freshly prepared by adding 82.1 μL of concentrated HCl to 9.918 mL of THF using a volumetric pipet (in this solution, [H_2O] = 0.455 mol/L). A pre-determined volume of this solution targeting a specific degree of azlactone hydrolysis was added, with vigorous stirring, to the vial containing the **P1** solution using a volumetric pipet (e.g., for 35.4 mg of **P1**, 27.9 μL of acid solution corresponds to 0.05 molar equivalents of H_2O, with respect to azlactone groups). The mixture turned bright yellow immediately after addition of the acidic solution, and the vial was sealed with a Teflon cap and parafilm and left to stir overnight at room temperature. The yellow color generally dissipated after several hours, but often persisted for samples with higher intended degrees of azlactone hydrolysis (e.g., 20% or greater). The polymer was precipitated into ~15 mL of hexanes at room temperature, the solids were allowed to settle, and the solvent was removed by pipet. The resulting **P1**x derivatives were dried under high vacuum overnight to yield white solids. HPLC grade THF solvent was used for this procedure and was not necessarily anhydrous; the actual degree of hydrolysis was therefore often higher than the targeted degree of hydrolysis.

The final degrees of hydrolysis for **P1x** derivatives were determined using quantitative ^{13}C NMR spectroscopy as described in the next section and are presented in Table 1.

Characterization of Degrees of Hydrolysis of PVDMA by Quantitative ^{13}C NMR Spectroscopy. Quantitative $^{13}C\{^{1}H\}$ NMR spectroscopy was performed using a Bruker Avance3 spectrometer with a liquid He-cooled DCH cryoprobe (the DCH cryoprobe delivers s/n > 10x that of normal coil probes such as the Bruker BBFO+). Samples were dissolved at ~2 wt% in deuterated acetone (acetone-d_6) and all spectra were referenced relative to the residual carbon peak of the carbonyl carbon in acetone-*d*6 (δ206.26 ppm). Acquisition parameters were adapted from the literature[46] and are as follows: PULPROG = zgig30, D1 = 10 s, AQ = 1.1 s, SW = 237 ppm, O1P = 100 ppm, NS = 1024, DS = 4, LB = 1. The combination of the inverse-gated sequence, 30° flip angle, and repetition time = 10 s, together with prior knowledge of T1(^{13}C), permits the acquisition of quantitative data.

Layer-by-Layer Assembly of PEI/P1 and PEI/P1x Coatings. Multilayers of PEI/**P1** or PEI/**P1x** were fabricated on glass or silicon substrates (~1 x 4 cm, five total substrates for each condition; pre-cleaned with methanol and acetone) using the following general procedure reported in past studies for the fabrication of nanoporous PEI/PVDMA films:[30,42,44] (i) substrates were submerged in a solution of PEI (~0.87 mg/mL; 20 mM in acetone with respect to the polymer repeat unit) for 20 s; (ii) substrates were removed and immersed in an initial acetone bath for 20 s, followed by a second acetone bath for 20 s; (iii) substrates were submerged in a solution of **P1** or **P1x** (~2.8 mg/mL; 20 mM in acetone with respect to the polymer repeat unit for **P1**, ~3.1 mg/mL for **P1x**) for 20 s; and (iv) substrates were removed and rinsed again using

the procedure outlined under step (ii). This cycle was repeated 35 times, without changing the rinse solutions to yield films 35 bilayers thick. After fabrication, films were washed copiously with acetone from a spray bottle and then dried under a stream of compressed air. Films were stored in a vacuum desiccator prior to use. To functionalize residual azlactone groups with decylamine, films were incubated overnight in solutions of decylamine (20 mg/mL) in THF at room temperature.[28,38,42,47] After incubation, films were rinsed with THF and then dried under a stream of compressed air.

Characterization of Polymer Aggregates Formed During Film Fabrication. In experiments designed to characterize the presence of polymer aggregates in the polymer dipping solutions and the rinse solutions used for film fabrication, multilayer films were assembled using the above procedure and a model **P1x** polymer containing 22.5 ± 1.4% hydrolyzed side chain groups. After film fabrication, two drops of solution from each polymer solution vial (PEI and **P1x**) were placed onto silicon substrates, the acetone was allowed to evaporate off at room temperature, and the remaining material was imaged by SEM. In separate experiments designed to investigate the effects of polymer solution 'carry-over' and subsequent co-mixing and aggregation of PEI and **P1x** polymers in vials during fabrication, the dipping procedure described above was followed, with the exception that the rinse solutions were replaced with fresh acetone after every rinse step. After film fabrication, a droplet of solution from each polymer solution vial was placed onto a silicon substrate for SEM imaging, as described above.

Results and Discussion

Past work has demonstrated that PEI/PVDMA multilayers can be fabricated in ways that lead to either (i) thin and smooth films that are optically transparent,[25,27,32-34] or (ii) thicker films that are optically opaque and exhibit micro- and nanoscale roughness and substantial internal porosity.[22,26,28-30,38-45,47,48] The approaches used to fabricate these materials have in common protocols that involve the iterative and alternating immersion of substrates into solutions of PEI and PVDMA in acetone, with intervening exposure to acetone rinse solutions. As described above, past studies have identified specific procedures and process parameters that can be used to bias film growth toward the evolution of substantial nanoscale roughness and porosity. For example, the use of (i) PVDMA synthesized in the presence of cyclic oligomers of VDMA[38] and (ii) protocols that do not involve the regular replacement of polymer and rinse solutions during fabrication,[29,40,42-45] have both been used to fabricate nanoporous and topographically complex coatings that exhibit superhydrophobicity, superhydrophilicity, or underwater superoleophilicity when functionalized with appropriate amine-based nucleophiles (e.g., hydrophobic or hydrophilic amines, as discussed below).[26,28-30,38-41,47]

During the course of our studies, however, we occasionally encountered samples of PVDMA, synthesized using previously reported protocols, that either did not lead to substantial roughness or porosity, or lead to films that were porous and rough, but that did not exhibit some anticipated functional properties (e.g., extreme wetting behaviors) after post-fabrication functionalization. Those results prompted additional spectroscopic characterization and comparisons of samples of PVDMA used in those experiments that revealed evidence of variable levels of side chain azlactone hydrolysis in polymers synthesized under otherwise similar conditions (these results are discussed in greater detail below). The ring-opening hydrolysis of

the azlactone side groups in PVDMA yields carboxylic acid functionality, as shown in Scheme 1. For purposes of clarity in the discussion below, we refer from here on to PVDMA as 'polymer **P1**' and denote PVDMA containing specific mole fractions of hydrolyzed side groups, as depicted in Scheme 1, as 'polymers **P1**x', where 'x' denotes a specific mole fraction of hydrolyzed repeat units. Our initial observations from those characterization studies suggested that the presence and variability of hydrolyzed azlactone groups in these polymers could play a role in the evolution of rough and nanoporous morphologies observed in PEI/PVDMA multilayers and motivated the additional series of synthetic and physicochemical characterization studies described below.

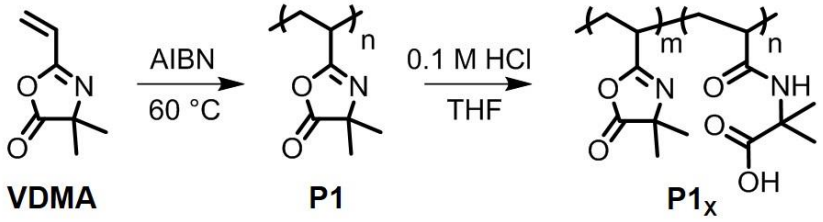

Scheme 1. General scheme showing the polymerization of VDMA to **P1**, and subsequent partial-hydrolysis to yield **P1x** derivatives.

In a first series of experiments, we sought to synthesize samples of **P1** and provide insight into factors that could lead to side chain hydrolysis. To initiate these studies, we prepared samples of **P1** using VDMA monomer that was freshly vacuum distilled (Scheme 1; see Materials and Methods for additional details related to the polymerization of VDMA). The use of freshly distilled monomer yielded **P1** that did not contain hydrolyzed side chain groups[34,49,50] whereas samples of **P1** synthesized using monomer that was not freshly distilled often lead to polymers with varying degrees of side chain hydrolysis (i.e., **P1x**, Scheme 1), as determined by characterization using FTIR. Figure 1 shows the IR spectra of **P1** and a typical sample of **P1x**

polymerized using monomer that was not freshly distilled, similar to that used in past studies to fabricate nanoporous PEI/PVDMA films. The diagnostic azlactone carbonyl (C=O, 1821 cm^{-1}) and azlactone imine (C=N, 1672 cm^{-1}) stretches are present in both spectra.[21,51] However, the spectrum of **P1x** also reveals a carboxylic acid carbonyl (C=O, 1734 cm^{-1}) stretch and an amide bending mode (N-H, 1528 cm^{-1}) characteristic of hydrolyzed side chain groups. Evidence of a ring-opened amide carbonyl peak can also be seen as a shoulder on the C=N peak in the **P1x** spectrum (C=O ~1650 cm^{-1}).[21,51] We did not observe the presence of hydrolyzed VDMA monomer in samples that were not freshly distilled by NMR (data not shown), nor did we detect substantial differences in the water content of freshly distilled VDMA (735 ± 97 ppm) and samples that were not freshly distilled (645 ± 76 ppm) by Karl-Fisher titration.

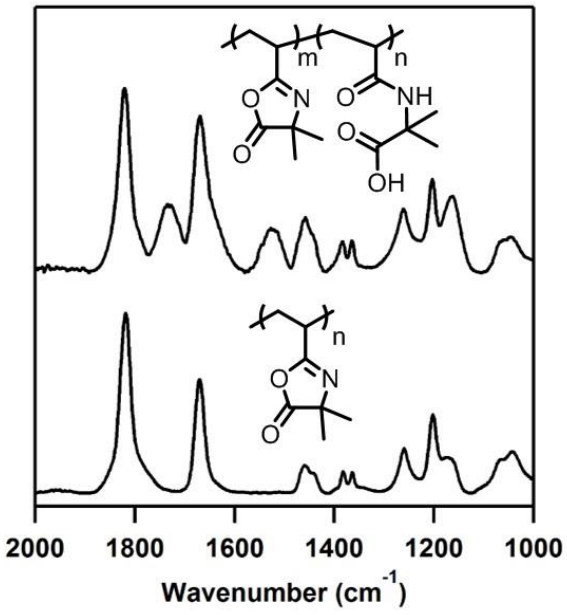

Figure 1. ATR IR spectra for **P1** (bottom) and partially hydrolyzed **P1x** (top). The peaks corresponding to the azlactone carbonyl (C=O, 1818 cm^{-1}) and azlactone imine (C=N, 1671 cm^{-1}) stretches are observed in the spectra of both **P1** and **P1x**. Carboxylic acid carbonyl stretching (C=O, 1734 cm^{-1}) and amide bending (N-H, 1528 cm^{-1}) peaks associated with hydrolyzed azlactone rings are present in the spectrum of **P1x** only.

When combined, these latter results suggest that the hydrolyzed units in samples of **P1x** do not arise from the incorporation of hydrolyzed monomer or the presence of water during polymerization. We speculate that the partial hydrolysis observed in these samples and others used in past studies may be promoted by the presence of other currently unidentified acidic impurities that may exist as a by-product of monomer synthesis[51] or that can form upon the standing and storage of VDMA, or by impurities introduced by the addition of cyclic oligomers of VDMA[38,52] used to prepare PVDMA in some past studies. We note that it is also possible for side chain hydrolysis to occur after polymerization and upon storage by exposure to water, heat, or other acidic species. The further identification of specific impurities that could lead to hydrolysis was not a primary aim of this study.

We also performed a series of initial experiments using the **P1** and the **P1x** polymers characterized above to fabricate PEI/PVDMA multilayers using a protocol used in past studies to fabricate rough and nanoporous coatings.[29,30,40,42-45] In brief, this protocol involves the iterative immersion of substrates into a solution of PEI, two subsequent rinse solutions, then a solution of **P1x**, and finally two additional rinse solutions, to fabricate one PEI/PVDMA 'bilayer' (Figure 2A; this basic cycle was repeated multiple times, as desired, to promote layer-by-layer growth. All solutions were prepared using acetone; see Materials and Methods for full details). Figure 2B shows the increase in optical thickness, as determined by ellipsometry, for PEI/**P1** and PEI/**P1x** films fabricated on reflective silicon substrates as a function of the number of bilayers deposited. These results reveal PEI/**P1** films (filled triangles) to grow relatively slowly and with a linear profile for the deposition of up to 20 bilayers to an average thickness of ~75 nm; this film growth profile is similar to those reported in several past studies on the layer-by-layer assembly of PEI/PVDMA films.[20] In contrast, PEI/**P1x** films (filled circles) increased in thickness much more

rapidly, with a profile that was also roughly linear but with a greater slope, for up to 16 bilayers to an average thickness of ~190 nm under otherwise identical conditions (these films became optically opaque after 16 bilayers were deposited, preventing further analysis of film growth using ellipsometry).

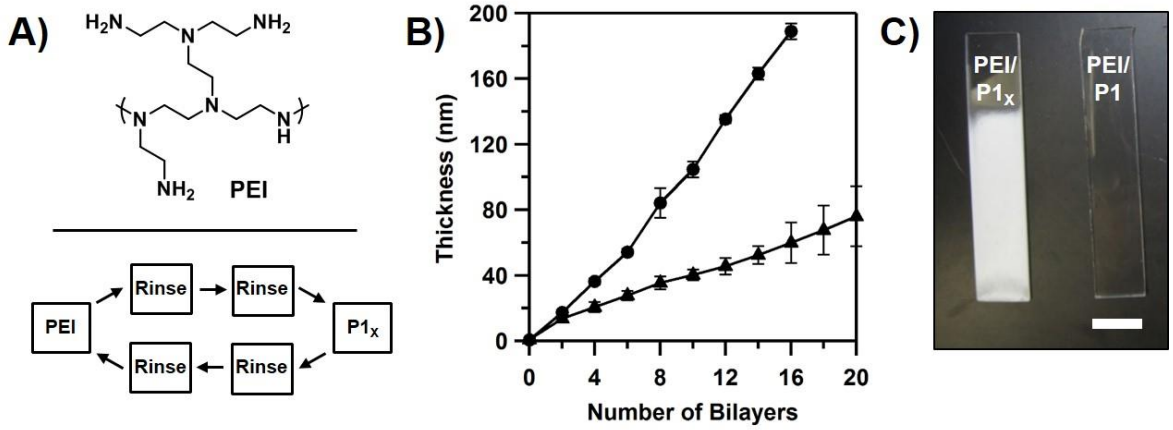

Figure 2. (A) Chemical structure of branched poly(ethylenimine) (top) and schematic showing the process flow of the layer-by-layer approach used to fabricate the films investigated in these studies (bottom). (B) Film growth profiles for PEI/**P1** (filled triangles) and PEI/**P1x** (filled circles) films fabricated on planar silicon substrates, as characterized by ellipsometry. (C) Photos showing the physical appearance of 35 bilayer thick PEI/**P1x** and PEI/**P1** films assembled on glass substrates. Scale bar = 1 cm.

Figure 2C shows digital photographs of PEI/**P1** and PEI/**P1x** films 35 bilayers thick fabricated on glass substrates under otherwise identical conditions. PEI/**P1** films fabricated under these conditions (right) were smooth and optically uniform and transparent; PEI/**P1x** films (left) were optically opaque and exhibited surface roughness that was apparent to the naked eye, similar to rough and nanoporous coatings reported in other past studies.[26,28-30,38-45,47] When combined, these results suggested that the presence of hydrolyzed azlactone functionality in PVDMA could contribute to the evolution of micro- and nanostructures during layer-by-layer assembly. Additional characterization of **P1** and **P1x** by gel permeation chromatography

revealed similar molecular weights and dispersities (see Figure S1), suggesting that the differences shown in Figure 2 do not arise from large differences in these macromolecular parameters.

In all further studies described below, we performed experiments using samples of **P1x** synthesized by the intentional and controlled hydrolysis of **P1** to investigate the influence of hydrolysis and differences in carboxylic acid group content on film growth and morphology.

Table 1. Percentage of Side Chain Hydrolysis (Hydrolysis, %) and [Azlactone]:[Acid] IR Peak Intensity Ratio for **P1x** Copolymers Synthesize in This Study.

Name	Hydrolysis, %[a]	[Azlactone]:[Acid][b]
P1	0	2.67
$P1_A$	13.8 ± 0.9	7.37
$P1_B$	16.7 ± 1.1	4.54
$P1_C$	25.9 ± 1.6	3.57
$P1_D$	35.5 ± 2.1	3.05

[a]Percentage of side chain hydrolysis, as determined by quantitative $^{13}C\{^1H\}$ NMR spectroscopy; [b][Azlactone]:[Acid] ratio calculated from the IR azlactone carbonyl (C=O) peak height (1822 cm^{-1}) divided by the carboxylic acid carbonyl (C=O) peak height (1734 cm^{-1}).

Scheme 1 shows our approach to the synthesis of **P1x** derivatives having different degrees of partial side chain hydrolysis. Treatment of solutions of **P1** in THF with a known amount of water and in the presence of an acid catalyst yielded polymers **$P1_A$**, **$P1_B$**, **$P1_C$**, and **$P1_D$**, as shown in Table 1. (We note here that the addition of water alone to solutions of **P1** in THF, followed by overnight incubation, did not induce any azlactone hydrolysis, as monitored by IR spectroscopy). We determined the percentage of hydrolysis (the mole fraction of carboxylic acid groups) affected under these conditions using quantitative $^{13}C\{^1H\}$ NMR spectroscopy. As shown in Table 1, the percentage of hydrolysis ranged from 13.8% to 35.5% (analysis methods

are described in the Materials and Methods section, and a representative $^{13}C\{^{1}H\}$ NMR spectrum is shown in Figure S2). Figure 3 shows representative IR spectra for these partially hydrolyzed polymers. These results show that as the percentage of hydrolysis increases (from **P1$_A$** to **P1$_D$**), the height of the azlactone carbonyl peak at 1821 cm^{-1} decreases, and the carboxylic acid carbonyl peak at 1734 cm^{-1} increases; the ratio of these two peak heights for polymers **P1$_A$** to **P1$_D$** are given in Table 1. We also note that, as the percentage of hydrolysis increased from **P1$_A$** to **P1$_D$**, evidence of the amide N-H bending mode (1528 cm^{-1}) became more pronounced.

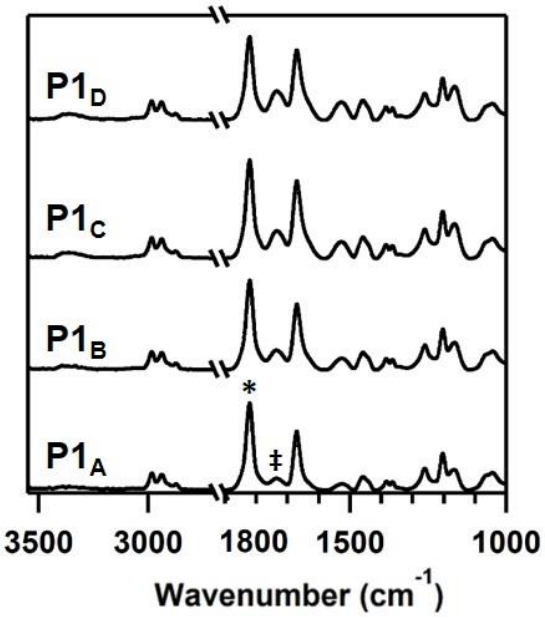

Figure 3. ATR IR spectra for partially hydrolyzed derivatives **P1$_A$**, **P1$_B$**, **P1$_C$**, and **P1$_D$**. The intensity of the azlactone carbonyl [denoted by (*); C=O, 1818 cm^{-1}] peak decreases relative to the intensity of the carboxylic acid carbonyl stretching [denoted by (‡); C=O, 1734 cm^{-1}] with increasing fraction of partial-hydrolysis from **P1$_A$** to **P1$_D$**; this ratio is provided for each polymer in Table 1.

Figure 4A shows digital pictures of PEI/PVDMA multilayers 35 bilayers thick fabricated using **P1$_A$**, **P1$_B$**, **P1$_C$**, and **P1$_D$** and iterative immersion protocols identical to those described above. An image of a control PEI/**P1** film fabricated using pristine PVDMA is also shown for

comparison. All of the films fabricated using the partially hydrolyzed derivatives were optically opaque and appeared rough to the naked eye, similar to the coatings described above using **P1$_X$** and shown in Figure 2C. However, the film fabricated using **P1** (containing 0% hydrolyzed side chains) was again optically clear, visually smooth, and uniform. Figure 4B shows the results of analysis of the advancing water contact angles (θ) of multilayers fabricated using **P1** and polymers **P1$_A$**, **P1$_B$**, **P1$_C$**, or **P1$_D$**. Black bars in Figure 4B show the water contact angles measured on as-fabricated (azlactone-containing) films; grey bars show contact angles measured after the functionalization of those reactive films by treatment with decylamine (20 mg/mL in THF, overnight), a hydrophobic amine used in past studies on the fabrication of nanoporous and superhydrophobic PEI/PVDMA coatings.[30,38,39,41,43,44,47]

Films fabricated using **P1$_A$**, the **P1$_X$** derivative having the lowest amount of hydrolysis, at 13.8%, were the least hydrophobic, with θ = 123.4 ± 1.4°, but became superhydrophobic after decylamine functionalization, θ = 157.7 ± 2.9° (superhydrophobicity is defined here as a surface with a contact angle >150° and a contact angle hysteresis, or roll-off angle, of < 10°).[53,54] In contrast, PEI/**P1$_B$** films (16.7% hydrolyzed) were superhydrophobic both before (θ = 156.2 ± 0.4°) and after (θ = 157.3 ± 0.5°) functionalization. PEI/**P1$_C$** films (25.9% hydrolyzed) exhibited similar wetting behaviors to PEI/**P1$_B$** films (θ = 137.5 ± 2.7° before functionalization, and θ = 152.6 ± 0.2° after functionalization). In contrast, PEI/**P1$_D$** films (35.5% hydrolyzed) did not exhibit superhydrophobicity either before (θ = 130.8 ± 6.1°) or after (θ = 146.0 ± 0.3°) functionalization. Representative images of water droplets contacting these surfaces acquired during these experiments are shown in Figure S3. On the basis of these results, we conclude that (i) the amount of carboxylic acid side chain functionality present in the **P1$_X$** derivatives used to fabricate these materials has a significant influence on the wetting behaviors of these materials,

and (ii) there is an apparent window of carboxylic acid content (between ~17% and ~25%) over which superhydrophobicity can be achieved after treatment with decylamine. Films fabricated using **P1X** derivatives containing higher percentages of hydrolyzed side groups (e.g., **P1**, ~36% hydrolysis) were rough and optically opaque (Figure 4A) but were not superhydrophobic either before or after decylamine functionalization. Moreover, we note that films fabricated using **P1X** derivatives with lower extents of hydrolysis (e.g., **P1A**, ~17% hydrolysis) exhibited superhydrophobicity even prior to functionalization with decylamine.

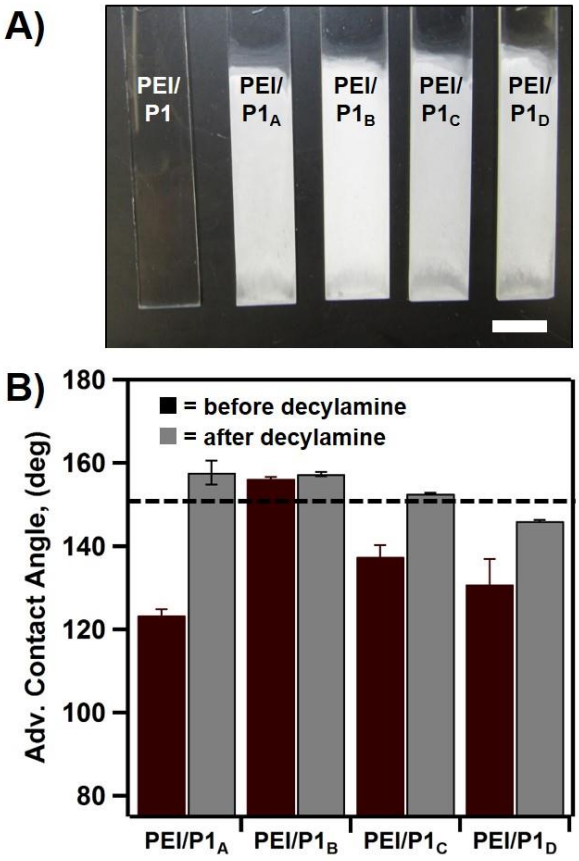

Figure 4. (A) Digital pictures showing the physical appearance of 35 bilayer thick PEI/**P1** and PEI/**P1X** films assembled on glass substrates. Scale bar = 1 cm. (B) Plot showing the advancing water contact angle measured on PEI/**P1X** films fabricated using **P1A**, **P1B**, **P1C**, and **P1D** shown in part A. Water contact angles were measured before (black bars) and after functionalization with decylamine (grey bars; see text). Error bars represent the standard deviation of at least five measurements.

We next sought to characterize potential differences in film morphology exhibited by PEI/PVDMA films fabricated using **P1**, **P1$_A$**, **P1$_B$**, **P1$_C$**, and **P1$_D$**. Figure 5 shows top-down SEM images of the five films shown in Figure 4A. These images reveal PEI/**P1** films to be uniformly smooth and largely featureless (Figure 5A), but that all other films assembled using **P1$_{A\text{-}D}$** exhibited more complex morphologies and many micro- and nanoscale topographic features that were not present in PEI/**P1** films (Figure 5B-E). Further inspection of the images (see also the insets in these images) reveals qualitative differences in film morphologies that vary with the percentages of hydrolysis in the **P1$_X$** derivatives used to fabricate the films. For example, films fabricated using **P1$_A$** and **P1$_B$** (Figure 5B-C), which contain the lowest percentages of hydrolysis (~14% and ~17%, respectively) exhibit complex morphologies composed of surface-exposed nanoscale bumps, particles, and pores that are similar to features reported previously for many nanoporous and topographically rough PEI/PVDMA films that exhibit extreme non-wetting behaviors.[30,38,39] In contrast, inspection of the images in Figure 5D-E reveals films fabricated from polymers with higher percentages of hydrolysis (**P1$_C$** and **P1$_D$**, with ~26% and ~36% hydrolysis, respectively) to have complex morphologies with qualitatively smoother surfaces, or a lack of readily observable hierarchical nanoscale features similar to those shown in Figure 5B-C. These differences in morphology and nanoscale topographic features could account, at least in part, for the lower water contact angles observed for the PEI/**P1$_C$** and PEI/**P1$_D$** films shown in Figure 4B (black bars). Taken together, the SEM images in Figure 5 and the water contact angle results in Figure 4B hint that the apparent influence of side chain hydrolysis on the wetting behaviors of these coatings could arise, at least in part, from the influence of carboxylic acid groups on the nanoscale morphologies that evolve during assembly. We consider it likely that differences in the number of hydrophilic carboxylic acid groups present in the films also plays an

important role in defining the wetting properties of these materials. Ultimately, the wetting behaviors of these materials, as defined by the contact angle measurements reported here, are likely to be a result of the interplay of the influences of both morphology and surface energy.

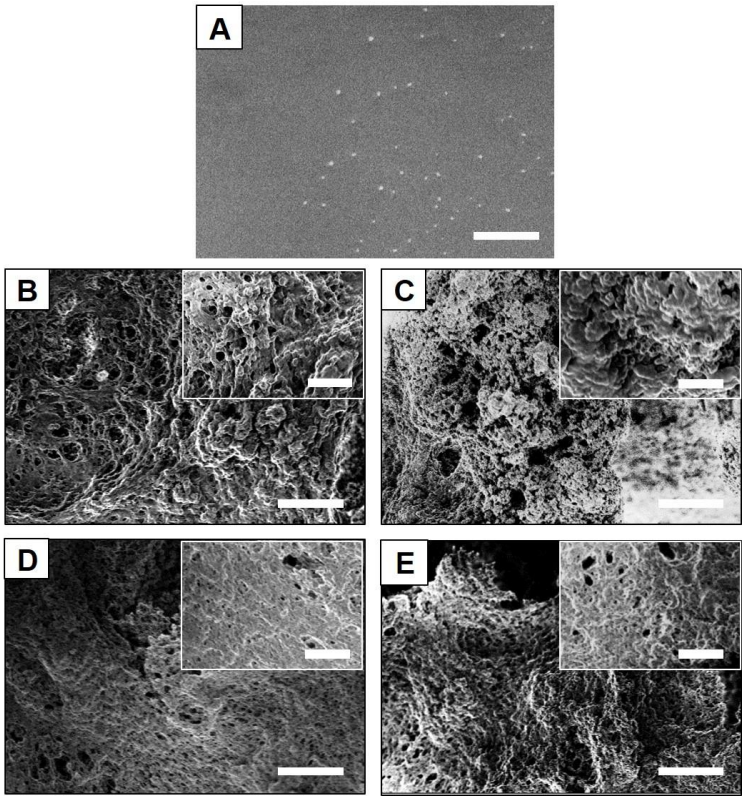

Figure 5. (A-E) SEM images showing the film morphology at the surfaces of 35 bilayer thick PEI/**P1** and PEI/**P1**$_X$ assembled on glass substrates. PEI/**P1** films shown in (A) are largely featureless, while films assembled using (B) **P1**$_A$, (C) **P1**$_B$, (D) **P1**$_C$, and (E) **P1**$_D$ exhibit more complex morphologies with many micro- and nanoscale features. Scale bar = 5 μm; 2 μm insets.

Figure 6 shows ATR IR spectra of PEI/PVDMA films fabricated using **P1**$_A$, **P1**$_B$, **P1**$_C$, and **P1**$_D$ prior to treatment with decylamine. Inspection of these images reveals the presence of unreacted azlactone functionality (e.g., the azlactone carbonyl peak at 1821 cm^{-1}), and that the carboxylic acid carbonyl peak observed in the IR spectra of polymers using **P1**$_A$, **P1**$_B$, **P1**$_C$, and **P1**$_D$ (C=O 1734 cm^{-1}; see Figure 3) is absent. Because PEI contains basic primary, secondary,

and tertiary amine functionality, it is likely that the carboxylic acid groups in these films could be substantially deprotonated and, thus, present in the carboxylate form. We speculate that the absence of a carboxylic acid carbonyl peak in the IR spectra of these films (Figure 6) arises from conversion to carboxylate functionality that exhibits a carbonyl stretch (reported at ~1645 cm^{-1} for cross-linked polymer beads containing hydrolyzed VDMA in the sodium salt form)[51,55] that is obscured by the overlapping amide carbonyl stretch and azlactone imine peaks that are centered at ~1664 cm^{-1}. Although the results shown in Figure 6 are not definitive proof of ion-pairing interactions between the carboxylic acid functionality and the amine functionality in PEI and **P1X** in these films, these results are generally consistent with that possibility. We return again in the discussion below to the potential influence of such ion-pairing interactions on the growth and evolution of nanoscale morphology that occurs during the assembly of these materials.

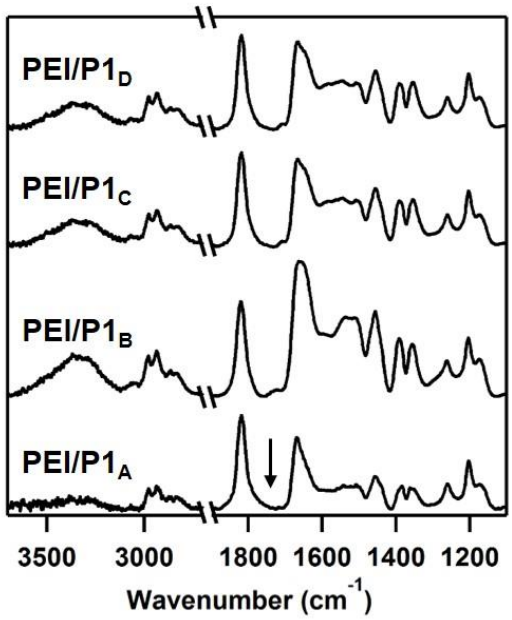

Figure 6. ATR IR spectra for 35 bilayer thick PEI/**P1X** films assembled on glass substrates using partially hydrolyzed derivatives **P1A**, **P1B**, **P1C**, and **P1D**. The black arrow indicates the expected position of the carboxylic acid carbonyl stretching (C=O, 1734 cm^{-1}, based on the IR spectra of the individual polymers prior to assembly; see Figure 1).

We hypothesized that the nanoscale structures and porous morphologies shown above in Figure 5B-C and reported in past studies could arise, during fabrication, from the formation of nanoscale aggregates of PEI and PVDMA either (i) in solution and prior to contact with the surface to be coated (in this scenario, film growth could occur, at least in part, by the deposition of preformed, solution-phase PEI-PVDMA nanostructures), or (ii) upon the deposition of either PEI or PVDMA on the surface of a growing film during individual steps in the fabrication cycle (in this scenario, these features would result from transformations that occur at the surface, or possibly within the bulk, of a growing film as each new polymer 'layer' is deposited). We note that it is also possible that these morphologies could arise during other steps in the fabrication process, including at points during which film-coated substrates are removed from polymer or rinse solutions and transported to new solutions. At these points in the fabrication process, for example, brief exposure to air or physical transformations promoted by the evaporation of acetone could potentially lead to film decomposition or reorganization and the evolution of complex morphologies. Other possibilities may also exist that are not considered here. It is clear from visual inspection and physicochemical characterization of films during fabrication, however, that these morphologies develop and evolve during the fabrication process, and that nanoscale roughness and porosity do not arise as a consequence of transformations that occur after complete film assembly (e.g., upon final drying or upon long-term storage, etc.).

The first of the hypotheses above is supported generally by the observation that both the polymer solutions and primary rinse baths used during fabrication gradually become visually cloudy during fabrication, consistent with the formation of polymer aggregates in these solutions as film fabrication progresses. This phenomenon could arise from carryover of polymer into and between solutions during the iterative transfer of substrates from solution to solution during

fabrication; see Figure 2A. (We note that solutions of PEI and PVDMA alone do not flocculate or yield visible precipitates upon standing on the time scales used for film fabrication). To provide insight into the role that the formation of aggregates in these solutions could potentially play in the evolution of nanostructure in these materials during fabrication, we conducted a series of experiments using acetone solutions of PEI and a model **P1$_x$** polymer containing 22.5% (± 1.4%) hydrolyzed side groups. Characterization of PEI/PVDMA films fabricated using this polymer by ellipsometry, SEM, FTIR, and contact angle measurements revealed the influence of this polymer on film growth and morphology to be similar to that of **P1$_C$**; see discussion below.

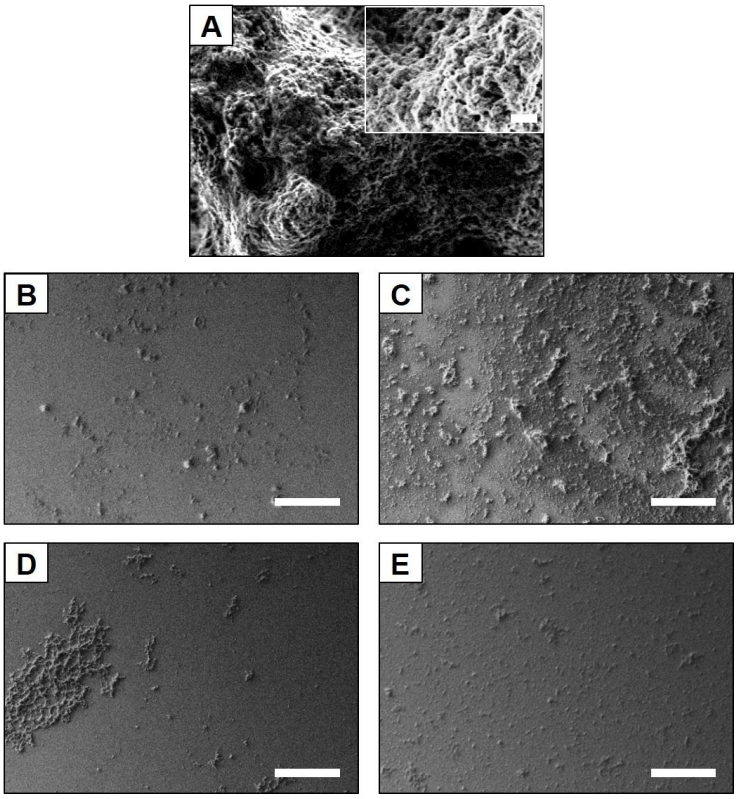

Figure 7. (A) SEM image showing the morphology of a 35 bilayer thick PEI/**P1$_X$** film assembled on a glass substrate using a model **P1$_X$** with 22.5 ± 1.4 percent hydrolysis. (B) and (C) show SEM images of polymer aggregates present in the dried samples of PEI and **P1$_X$** film fabrication solutions, respectively, collected after film assembly. (D) and (E) show SEM images of polymer aggregates present in the first PEI and first **P1$_X$** acetone rinse vials used for film fabrication, respectively, collected after film assembly (see text). Scale bar = 5 μm; 1 μm insets.

Figure 7 shows SEM images of samples of polymer solution (A: PEI solution; B: **P1x** solution) and the rinse baths (C: first rinse vial after immersion in PEI solution; D: first rinse vial after immersion in **P1x** solution) collected after the fabrication of a 35 bilayer PEI/PVDMA film (these solutions were placed on silicon and acetone was evaporated prior to imaging; see Materials and Methods). Inspection of these images reveals the presence of microscale aggregates. Although it is not possible to infer from these results anything regarding the compositions of these aggregates, or the relationship between their sizes when dried and their sizes prior to drying, the aggregates in these images are consistent with the visible presence of aggregates of polymer in these solutions during and after fabrication and, more generally, the possibility that the nanoscale structures in the PEI/PVDMA films discussed above could arise from deposition or reaction of these aggregates onto surfaces during immersion at each step in the film fabrication process.

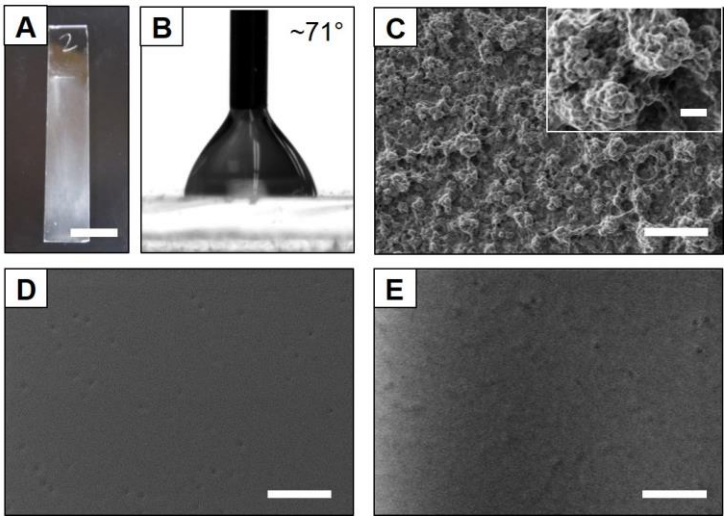

Figure 8. Characterization of a 35 bilayer thick film fabricated using a model **P1x** with 22.5 ± 1.4 percent hydrolysis by changing the acetone rinse solutions after every rinse step (see text). (A) Digital picture showing the physical appearance of the film; scale bar = 1 cm. (B) Water contact angle analysis demonstrating that the film readily wet by water. (C) SEM image showing the morphology at the surface of the film. (D) and (E) show SEM images indicating the absence of polymer aggregates in the PEI and **P1x** film fabrication solutions, respectively, collected after film assembly (see text). Scale bars in (C-E) = 5 μm; 1 μm insets.

The results of additional control experiments in which films were fabricated using a modified rinse procedure suggested that nanoscale structure and morphology can also evolve during fabrication even when polymer aggregates are not substantially present in solution. In this modified procedure, rinse solutions were replaced with fresh acetone during fabrication after every single rinse step to prevent the accumulation and carryover of PEI or **P1**$_X$ during successive immersions (all other fabrication parameters were otherwise identical). The images in Figure 8D and 8E show SEM images of the PEI and **P1**$_X$ solutions used in these experiments. Relative to the images shown in Figure 7, these images reveal the absence of nanoscale or microscale aggregates, demonstrating that this modified rinse protocol was sufficient to prevent polymer carryover and aggregate formation in these solutions. Figure 8C, however, shows an SEM image of a 35-bilayer film fabricated using this modified protocol, and reveals the presence of significant nanoscale structure and texture on the surface of the film. Likewise, Figure 8A shows an image of a film fabricated under similar conditions, and reveals the film to be visually rough and opaque, albeit not as visually rough or as opaque as films shown in Figure 4. When combined, these results demonstrate that micro- and nanoscale features are able to form on the surfaces of growing films during the deposition of PEI or PVDMA in ways that can occur independent of the formation and possible deposition of solution-based polymer aggregates. We note again, however, that films fabricated by this modified are visually different in appearance (Figure 8A), and results shown in Figure 8B also demonstrate the contact angles of these films to be significantly less hydrophobic (θ ~71°) than films made by the more conventional fabrication protocol. On the basis of these preliminary experiments and initial observations, it is thus also possible that the formation and subsequent deposition of polymer aggregates in solution during fabrication could also play a role and lead to a more rapid onset of roughness and porosity.

Additional experiments will be required to probe these possibilities more completely and characterize the factors that influence the formation of nanostructure in these materials under conditions where the potential for the aggregation of PEI and PVDMA in solution is minimized or completely eliminated.

Summary and Conclusions

The work described in this chapter demonstrates that the presence of hydrolyzed azlactone groups in PVDMA can substantially influence the growth of multilayer films fabricated by the reactive layer-by-layer assembly of PEI and PVDMA. Whereas layer-by-layer assembly using unhydrolyzed PVDMA yields thin films that are smooth, transparent, and largely devoid of micro- and nanoscale features, films assembled using partially hydrolyzed PVDMA are thick, and exhibit substantial roughness and nano- and microscale topographic features and porosity. The morphologies and wetting behaviors of PEI/PVDMA films fabricated using PVDMA synthesized to contain defined amounts of hydrolyzed groups are, in general, similar to those of nanoporous and topographically complex PEI/PVDMA coatings reported in past studies, suggesting that partial hydrolysis of azlactone functionality could also have contributed to the evolution of nanostructure in those studies.

Our results also demonstrate that the degree or extent of partial hydrolysis can influence the surface morphologies and interfacial behaviors of these films, and suggest that the carboxylic acid side chain groups that result from azlactone hydrolysis may participate in acid/base interactions and ionic interactions in these materials that could also influence structure formation and film growth. The results of preliminary experiments not discussed in detail here also suggest that the presence of carboxylic acid functionality in partially hydrolyzed PVDMA has the

potential to increase rates of reactions between model amines and azlactones. These insights could shed light on similar processes that drive reactive layer-by-layer assembly and the formation of covalent crosslinks impart physical and chemical stability to PEI/PVDMA multilayers. Although the mechanism for structure formation and the evolution of roughness and porosity during the fabrication of these materials is not yet completely understood, the results reported here provide insight into molecular-level parameters that can influence it or be manipulated to promote changes in the structure and behaviors of PEI/PVDMA coatings (e.g., to fabricate thin and smooth films, to fabricate thick and nanoporous films, or to fabricate thick and nanoporous films that exhibit differences in morphology and wetting behaviors by changes in the extent of side chain hydrolysis or changes to film fabrication protocols). Finally, we note that the potential for ion-pairing interactions between hydrolyzed side chains and the amines in PEI, and the potential for the acid functionality in partially hydrolyzed PVDMA (or the properties of the organic solvents used during assembly) to influence the rates at which, and the extents to which, covalent bonds may form during reactive assembly, could also introduce new tools useful for exerting new levels of control over structure formation in these materials. Overall, the results of these studies provide new insights and guiding principles that may prove useful for further tuning and tailoring the physicochemical behaviors and properties of these reactive coatings, as well as many new exciting avenues for future research in these and other similar poly(vinyl azlactone)/polyamine systems.

Acknowledgments. This work was supported by the NSF through grants to the UW-Madison Materials Research Science and Engineering Center (MRSEC; DMR-1121288) and the UW-Madison Nanoscale Science and Engineering Center (NSEC; DMR-0832760), and by the Office

of Naval Research (N00014-16-1-2185), and made use of NSF-supported facilities (DMR-1121288, DMR-0832760, and CHE-1048642). We thank M. Wong for technical assistance and fabricating polymers films. M.C.D.C. acknowledges the Natural Sciences Engineering Research Council of Canada for a graduate fellowship.

References

(1) Decher, G. Fuzzy nanoassemblies: Toward layered polymeric multicomposites. *Science* **1997,** *277* (5330), 1232.

(2) Schönhoff, M. Self-assembled polyelectrolyte multilayers. *Current Opinion in Colloid & Interface Science* **2003,** *8* (1), 86.

(3) Hammond, P. T. Form and Function in Multilayer Assembly: New Applications at the Nanoscale. *Advanced Materials* **2004,** *16* (15), 1271.

(4) Decher, G. In *Multilayer Thin Films: Sequential Assembly of Nanocomposite Materials, 2nd Edition*; Decher, G.;Schlenoff, J. B., Eds.; Wiley-CVH, 2012.

(5) Xiao, F.-X.; Pagliaro, M.; Xu, Y.-J.; Liu, B. Layer-by-layer assembly of versatile nanoarchitectures with diverse dimensionality: a new perspective for rational construction of multilayer assemblies. *Chemical Society Reviews* **2016**.

(6) Borges, J.; Mano, J. F. Molecular Interactions Driving the Layer-by-Layer Assembly of Multilayers. *Chemical Reviews* **2014,** *114* (18), 8883.

(7) Quinn, J. F.; Johnston, A. P. R.; Such, G. K.; Zelikin, A. N.; Caruso, F. Next generation, sequentially assembled ultrathin films: beyond electrostatics. *Chemical Society Reviews* **2007,** *36* (5), 707.

(8) Bergbreiter, D. E.; Liao, K.-S. Covalent layer-by-layer assembly-an effective, forgiving way to construct functional robust ultrathin films and nanocomposites. *Soft Matter* **2009,** *5* (1), 23.

(9) Rydzek, G.; Schaaf, P.; Voegel, J.-C.; Jierry, L.; Boulmedais, F. Strategies for covalently reticulated polymer multilayers. *Soft Matter* **2012,** *8* (38), 9738.

(10) Broderick, A. H.; Lynn, D. M. In *Functional Polymers by Post-Polymerization Modification*; Wiley-VCH Verlag GmbH & Co. KGaA, **2013**.

(11) Tang, Z.; Wang, Y.; Podsiadlo, P.; Kotov, N. A. Biomedical Applications of Layer-by-Layer Assembly: From Biomimetics to Tissue Engineering. *Advanced Materials* **2006,** *18* (24), 3203.

(12) Hammond, P. T. Engineering materials layer-by-layer: Challenges and opportunities in multilayer assembly. *AIChE Journal* **2011,** *57* (11), 2928.

(13) Wood, K. C.; Chuang, H. F.; Batten, R. D.; Lynn, D. M.; Hammond, P. T. Controlling interlayer diffusion to achieve sustained, multiagent delivery from layer-by-layer thin films. *Proceedings of the National Academy of Sciences* **2006,** *103* (27), 10207.

(14) Zacharia, N. S.; DeLongchamp, D. M.; Modestino, M.; Hammond, P. T. Controlling Diffusion and Exchange in Layer-by-Layer Assemblies. *Macromolecules* **2007,** *40* (5), 1598.

(15) Zacharia, N. S.; Modestino, M.; Hammond, P. T. Factors Influencing the Interdiffusion of Weak Polycations in Multilayers. *Macromolecules* **2007,** *40* (26), 9523.

(16) Gilbert, J. B.; Rubner, M. F.; Cohen, R. E. Depth-profiling X-ray photoelectron spectroscopy (XPS) analysis of interlayer diffusion in polyelectrolyte multilayers. *Proceedings of the National Academy of Sciences* **2013,** *110* (17), 6651.

(17) Nolte, A. J.; Takane, N.; Hindman, E.; Gaynor, W.; Rubner, M. F.; Cohen, R. E. Thin Film Thickness Gradients and Spatial Patterning via Salt Etching of Polyelectrolyte Multilayers. *Macromolecules* **2007,** *40* (15), 5479.

(18) Nolte, A. J.; Treat, N. D.; Cohen, R. E.; Rubner, M. F. Effect of Relative Humidity on the Young's Modulus of Polyelectrolyte Multilayer Films and Related Nonionic Polymers. *Macromolecules* **2008,** *41* (15), 5793.

(19) Richardson, J. J.; Björnmalm, M.; Caruso, F. Technology-driven layer-by-layer assembly of nanofilms. *Science* **2015,** *348* (6233).

(20) Buck, M. E.; Zhang, J.; Lynn, D. M. Layer-by-Layer Assembly of Reactive Ultrathin Films Mediated by Click-Type Reactions of Poly(2-Alkenyl Azlactone)s. *Advanced Materials* **2007,** *19* (22), 3951.

(21) Buck, M. E.; Lynn, D. M. Azlactone-functionalized polymers as reactive platforms for the design of advanced materials: Progress in the last ten years. *Polymer Chemistry* **2012,** *3* (1), 66.

(22) Buck, M. E.; Lynn, D. M. Free-Standing and Reactive Thin Films Fabricated by Covalent Layer-by-Layer Assembly and Subsequent Lift-Off of Azlactone-Containing Polymer Multilayers. *Langmuir* **2010,** *26* (20), 16134.

(23) Buck, M. E.; Lynn, D. M. Functionalization of Fibers Using Azlactone-Containing Polymers: Layer-by-Layer Fabrication of Reactive Thin Films on the Surfaces of Hair and Cellulose-Based Materials. *ACS Applied Materials & Interfaces* **2010,** *2* (5), 1421.

(24) Buck, M. E.; Lynn, D. M. Reactive Layer-by-Layer Assembly of Suspended Thin Films and Semipermeable Membranes at Interfaces Created Between Aqueous and Organic Phases. *Advanced Materials* **2010,** *22* (9), 994.

(25) Broderick, A. H.; Azarin, S. M.; Buck, M. E.; Palecek, S. P.; Lynn, D. M. Fabrication and Selective Functionalization of Amine-Reactive Polymer Multilayers on Topographically Patterned Microwell Cell Culture Arrays. *Biomacromolecules* **2011,** *12* (6), 1998.

(26) Broderick, A. H.; Manna, U.; Lynn, D. M. Covalent Layer-by-Layer Assembly of Water-Permeable and Water-Impermeable Polymer Multilayers on Highly Water-Soluble and Water-Sensitive Substrates. *Chemistry of Materials* **2012,** *24* (10), 1786.

(27) Broderick, A. H.; Lockett, M. R.; Buck, M. E.; Yuan, Y.; Smith, L. M.; Lynn, D. M. In situ Synthesis of Oligonucleotide Arrays on Surfaces Coated with Crosslinked Polymer Multilayers. *Chemistry of Materials* **2012,** *24* (5), 938.

(28) Manna, U.; Broderick, A. H.; Lynn, D. M. Chemical Patterning and Physical Refinement of Reactive Superhydrophobic Surfaces. *Advanced Materials* **2012,** *24* (31), 4291.

(29) Manna, U.; Lynn, D. M. Synthetic Surfaces with Robust and Tunable Underwater Superoleophobicity. *Advanced Functional Materials* **2015,** *25* (11), 1672.

(30) Carter, M. C. D.; Lynn, D. M. Covalently Crosslinked and Physically Stable Polymer Coatings with Chemically Labile and Dynamic Surface Features Fabricated by Treatment of Azlactone-Containing Multilayers with Alcohol-, Thiol-, and Hydrazine-Based Nucleophiles. *Chemistry of Materials* **2016,** *28* (14), 5063.

(31) Buck, M. E.; Breitbach, A. S.; Belgrade, S. K.; Blackwell, H. E.; Lynn, D. M. Chemical Modification of Reactive Multilayered Films Fabricated from Poly(2-alkenyl azlactone)s: Design of Surfaces that Prevent or Promote Mammalian Cell Adhesion and Bacterial Biofilm Growth. *Biomacromolecules* **2009,** *10* (6), 1564.

(32) Fredin, N. J.; Broderick, A. H.; Buck, M. E.; Lynn, D. M. Nanoimprinted Thin Films of Reactive, Azlactone-Containing Polymers: Combining Methods for the Topographic Patterning of Cell Substrates with Opportunities for Facile Post-Fabrication Chemical Functionalization. *Biomacromolecules* **2009,** *10* (4), 994.

(33) Broderick, A. H.; Carter, M. C. D.; Lockett, M. R.; Smith, L. M.; Lynn, D. M. Fabrication of Oligonucleotide and Protein Arrays on Rigid and Flexible Substrates Coated with Reactive Polymer Multilayers. *ACS Applied Materials & Interfaces* **2013,** *5* (2), 351.

(34) Holden, M. T.; Carter, M. C. D.; Wu, C.-H.; Wolfer, J.; Codner, E.; Sussman, M. R.; Lynn, D. M.; Smith, L. M. Photolithographic Synthesis of High-Density DNA and RNA Arrays on Flexible, Transparent, and Easily Subdivided Plastic Substrates. *Analytical Chemistry* **2015,** *87* (22), 11420.

(35) Kinsinger, M. I.; Buck, M. E.; Campos, F.; Lynn, D. M.; Abbott, N. L. Dynamic Ordering Transitions of Liquid Crystals Driven by Interfacial Complexes Formed between Polyanions and Amphiphilic Polyamines. *Langmuir* **2008,** *24* (23), 13231.

(36) Manna, U.; Zayas-Gonzalez, Y. M.; Carlton, R. J.; Caruso, F.; Abbott, N. L.; Lynn, D. M. Liquid Crystal Chemical Sensors That Cells Can Wear. *Angewandte Chemie International Edition* **2013,** *52* (52), 14011.

(37) Guo, X.; Manna, U.; Abbott, N. L.; Lynn, D. M. Covalent Immobilization of Caged Liquid Crystal Microdroplets on Surfaces. *ACS Applied Materials & Interfaces* **2015,** *7* (48), 26892.

(38) Buck, M. E.; Schwartz, S. C.; Lynn, D. M. Superhydrophobic Thin Films Fabricated by Reactive Layer-by-Layer Assembly of Azlactone-Functionalized Polymers. *Chemistry of Materials* **2010,** *22* (23), 6319.

(39) Manna, U.; Lynn, D. M. Restoration of Superhydrophobicity in Crushed Polymer Films by Treatment with Water: Self-Healing and Recovery of Damaged Topographic Features Aided by an Unlikely Source. *Advanced Materials* **2013,** *25* (36), 5104.

(40) Manna, U. M.; Carter, M. C. D.; Lynn, D. M. 'Shrink-to-Fit' Superhydrophobicity: Thermally-Induced Microscale Wrinkling of Thin Hydrophobic Multilayers Fabricated on Flexible Shrink-Wrap Substrates. *Advanced Materials* **2013,** *25* (22), 3085.

(41) Manna, U.; Kratochvil, M. J.; Lynn, D. M. Superhydrophobic Polymer Multilayers that Promote the Extended, Long-Term Release of Embedded Water-Soluble Agents. *Advanced Materials* **2013,** *25* (44), 6405.

(42) Manna, U.; Lynn, D. M. Fabrication of Liquid-Infused Surfaces Using Reactive Polymer Multilayers: Principles for Manipulating the Behaviors and Mobilities of Aqueous Fluids on Slippery Liquid Interfaces. *Advanced Materials* **2015,** *27* (19), 3007.

(43) Kratochvil, M. J.; Tal-Gan, Y.; Yang, T.; Blackwell, H. E.; Lynn, D. M. Nanoporous Superhydrophobic Coatings that Promote the Extended Release of Water-Labile Quorum Sensing Inhibitors and Enable Long-Term Modulation of Quorum Sensing in Staphylococcus aureus. *ACS Biomaterials Science & Engineering* **2015,** *1* (10), 1039.

(44) Kratochvil, M. J.; Welsh, M. A.; Manna, U.; Ortiz, B. J.; Blackwell, H. E.; Lynn, D. M. Slippery Liquid-Infused Porous Surfaces that Prevent Bacterial Surface Fouling and Inhibit Virulence Phenotypes in Surrounding Planktonic Cells. *ACS Infectious Diseases* **2016,** *2* (7), 509.

(45) Manna, U.; Raman, N.; Welsh, M. A.; Zayas-Gonzalez, Y. M.; Blackwell, H. E.; Palecek, S. P.; Lynn, D. M. Slippery Liquid-Infused Porous Surfaces that Prevent Microbial Surface Fouling and Kill Non-Adherent Pathogens in Surrounding Media: A Controlled Release Approach. *Advanced Functional Materials* **2016,** *26* (21), 3599.

(46) Gardner, C. M.; Stöver, H. D. H. Reactive Polyanions Based on Poly(4,4-dimethyl-2-vinyl-2-oxazoline-5-one-co-methacrylic acid). *Macromolecules* **2011,** *44* (18), 7115.

(47) Manna, U.; Lynn, D. M. Patterning and Impregnation of Superhydrophobic Surfaces Using Aqueous Solutions. *ACS Applied Materials & Interfaces* **2013,** *5* (16), 7731.

(48) Kratochvil, M. J.; Carter, M. C. D.; Lynn, D. M. Non-Woven and Amine-Reactive Nanofiber Mats Fabricated by the Electrospinning of Azlactone-Functionalized Polymers. **2016,** *Submitted*.

(49) Appadoo, V.; Carter, M. C. D.; Lynn, D. M. Controlling the Surface-Mediated Release of DNA Using 'Mixed Multilayers'. *Bioengineering & Translational Medicine* **2016**, DOI: 10.1002/btm2.10023.

(50) Carter, M. C. D.; Jennings, J.; Appadoo, V.; Lynn, D. M. Synthesis and Characterization of Backbone Degradable Azlactone-Functionalized Polymers. *Macromolecules* **2016,** *49* (15), 5514.

(51) Heilmann, S. M.; Rasmussen, J. K.; Krepski, L. R. Chemistry and technology of 2-alkenyl azlactones. *Journal of Polymer Science Part A: Polymer Chemistry* **2001,** *39* (21), 3655.

(52) Heilmann, S. M.; Moren, D. M.; Krepski, L. R.; Rasmussen, J. K.; Gaddam, B. N.; Roscoe, S. B.; Lewandowski, K. M.; McIntosh, L. H.; Roberts, R. R.; Fansler, D. D.et al. The Chemistry of 2-Alkenyl-5(4H)-Oxazolones. IX. Acid-Catalyzed Oligomerization. *Journal of Macromolecular Science, Part A* **2003,** *40* (8), 755.

(53) Wang, S.; Liu, K.; Yao, X.; Jiang, L. Bioinspired Surfaces with Superwettability: New Insight on Theory, Design, and Applications. *Chemical Reviews* **2015,** *115* (16), 8230.

(54) Wen, L.; Tian, Y.; Jiang, L. Bioinspired Super-Wettability from Fundamental Research to Practical Applications. *Angewandte Chemie-International Edition* **2015,** *54* (11), 3387.

(55) Rasmussen, J. K.; Heilmann, S. M.; Krepski, L. R.; Jensen, K. M.; Mickelson, J.; Johnson, K. Crosslinked, hydrophilic, azlactone-functional polymeric beads: a two-step approach. *Reactive Polymers* **1992,** *16* (2), 199.

Supporting Information for Chapter 6

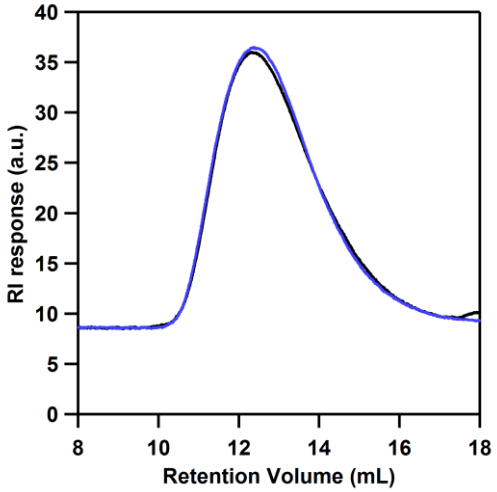

Fig S1. Gel permeation chromatography (GPC) traces for (black) **P1** and (blue) **P1x**. The near overlap in the traces indicate that the molecular weight and dispersity index of each polymer is similar.

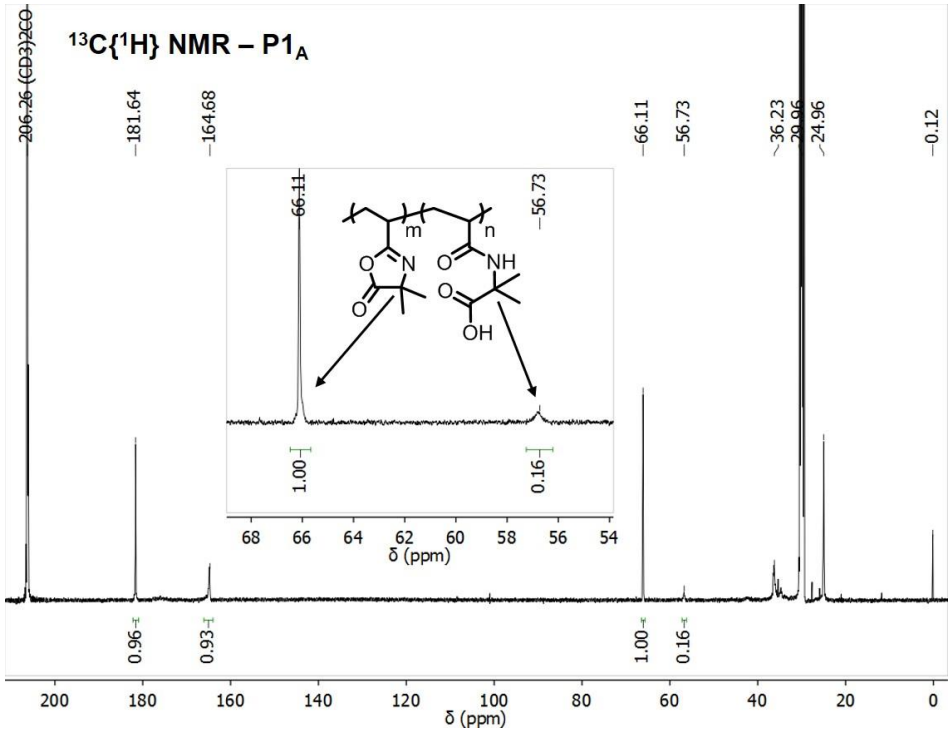

Figure S2. Representative quantitative $^{13}C\{^{1}H\}$ NMR spectrum used to determine the degree of azlactone group hydrolysis in partially hydrolyzed **P1** derivatives. The spectrum for **P1$_A$** is shown as an example.

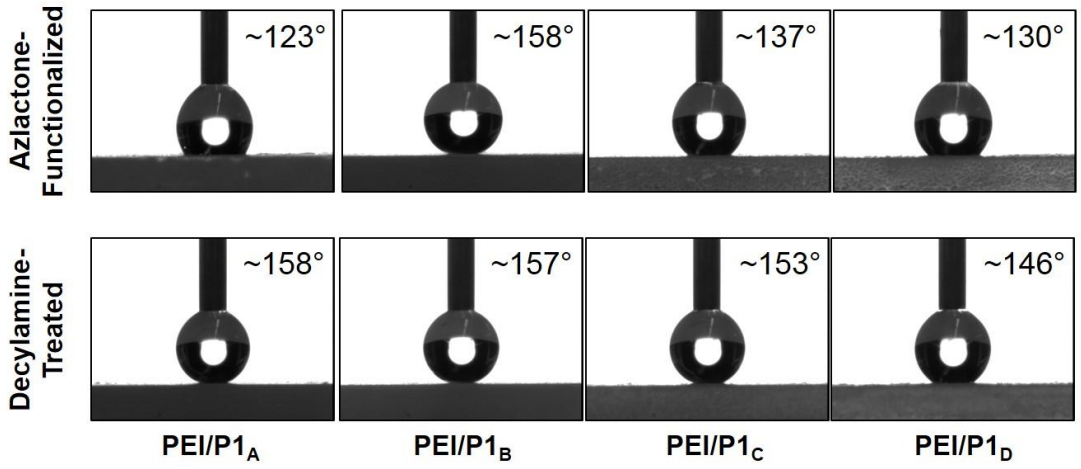

Figure S3. Representative images of advancing water contact angle measurements for 35 bilayer thick PEI/**P1$_X$** films assembled using **P1$_A$**, **P1$_B$**, **P1$_C$**, and **P1$_D$**. These and other related contact angle measurements are combined and presented as averages with standard deviations in Figure 4B of the main text.

Chapter 7

Post-Fabrication Placement of Arbitrary Chemical Functionality on Microphase Separated Thin Films of Amine-Reactive Block Copolymers[‡]

‡ Portions of this chapter have previously been published as: Speetjens, F.W.; Carter, M.C.D.; Kim, M.; Mahanthappa, M.K.; Lynn, D.M. "Post-Fabrication Placement of Arbitrary Chemical Functionality on Microphase Separated Thin Films of Amine-Reactive Block Copolymers." *ACS Macro Letters* **2014**, *3*, 1178-1182. F.W.S. and M.C.D.C. were co-first authors. M. Kim aided with SEM imaging. F.W. Speetjens and I synthesized the block copolymers, fabricated the thin films, performed the physicochemical characterization experiments, and analyzed the data.

ABSTRACT: We report an approach to the post-fabrication placement of chemical functionality on microphase separated thin films of a reactive block copolymer. Our approach makes use of an azlactone-containing block copolymer that microphase separates into domains of perpendicularly-oriented lamellae. These thin films present nanoscale patterns of amine-reactive groups (reactive stripes) that serve as handles for the immobilization of primary amine-containing functionality. We demonstrate that arbitrary chemical functionality can be installed by treatment with aqueous solutions and mild conditions that do not perturb underlying microphase separated patterns dictated by the structure of the reactive block copolymer. This post-fabrication approach provides a basis for the development of modular approaches to the design of microphase separated block copolymer thin films, and access to coatings with patterned chemical domains and surface properties that would be difficult to prepare by the self-assembly and processing of functionally complex block copolymers.

Block copolymers (BCPs) that microphase separate into periodic domains provide powerful opportunities to define the nanoscale structures, bulk properties, and interfacial behaviors of soft materials.[1-3] Due to the molecular length scales at which they microphase separate, BCP thin films that exhibit lamellar or cylindrical morphologies are of particular technological interest and can provide precise, nanoscale control over the placement and patterning of chemical functionality on film-coated surfaces.[4-7] This feature of BCP thin films has been exploited fruitfully to develop new approaches to advanced lithography and create well-defined, periodic patterns of chemical and biological groups on surfaces relevant to the design of nano/biointerfaces, substrates for the directed growth, deposition, or capture of nanoparticles, and other emerging applications.[8-13]

Much is now understood about the influence of polymer structure on the microphase separation of BCPs.[1,5] In principle, one might envision exploiting that understanding to design new BCPs that could direct the periodic placement or presentation of arbitrary functionality on the surface or within the bulk of a substrate-supported film (*e.g.*, in alternating lamellar stripes or as arrays of functional 'spots' created by cylindrical morphologies). Unfortunately, however, the individual blocks of a given BCP cannot simply be 'swapped out' for others without perturbing key parameters that define the morphology of the original copolymer and its behavior in thin films.[1-3,14] In general, it remains difficult to predict the effects of introducing arbitrary and structurally complex chemical features on BCP phase behavior because of the sensitivity of microphase separation to small structural variations.

The bulk microphase separation of a polymer comprised of two chemically distinct blocks (a diblock copolymer) is governed by both the relative volume fraction of each block ($f_A = 1 - f_B$) and the segregation strength ($\chi_{AB}N$) that quantifies the mutual block repulsion energy that drives

structure formation.[1-5] While theoretical and experimental studies have established relationships between the values of these order parameters and observed bulk microphase separation behavior,[1,5] small changes to the structure of one block (*e.g.*, a change in side chain structure) can lead to significant changes in morphology and nano-domain periodicity.[1-5,14,15] The use of BCP thin films in several applied contexts also depends crucially on controlling interfacially confined morphologies and their preferred orientations relative to underlying substrates, both of which depend sensitively on film thickness and the relative surface energies of each block.[4-13,16] For these and other reasons, exerting predictable and universal control over the microphase separation of BCP thin films in a manner that is independent of specific polymer structure and other processing parameters remains a substantial fundamental challenge.

The sensitive dependence of microphase separation on BCP structure makes it difficult to develop modular and general approaches to the design of well-defined BCP interfaces. Although it is now straightforward to synthesize libraries of otherwise identical AB diblocks with B blocks containing different side chain functionality, the thin film phase behaviors of these materials would likely vary widely and be difficult to predict. Even if the interfacial properties of these BCPs permitted uniform film fabrication (*e.g.*, no de-wetting), those films would likely exhibit a range of microphase separated or disordered morphologies (with orientations that vary relative to the substrate) that present B-block functionality in substantially different locations on the surface or in the bulk. Here, we report an approach to the fabrication of reactive microphase separated BCP thin films that side-steps these fundamental issues and permits systematic, post-fabrication installation of arbitrary functionality on well-defined microphase separated coatings.

Our approach makes use of azlactone-containing BCPs that microphase separate into domains of perpendicularly-oriented lamellae. These films present nanoscale patterns of surface-

exposed amine-reactive groups (reactive stripes) that serve as 'handles' for the subsequent immobilization of arbitrary chemical functionality. This post-fabrication approach circumvents problems associated with the influence of polymer structure on BCP phase behavior and affords microphase separated coatings that can be used to vary the features presented by alternating lamellar domains over a broad range of structural and functional space. This strategy thus provides a basis for the development of 'universal' approaches to the interfacial engineering of microphase separated BCP thin films and, thereby, access to coatings with patterned chemical domains and surface properties (*e.g.*, wetting behaviors, binding affinities, *etc*.) that would be difficult to prepare by the self-assembly of functionally complex BCPs. Our results demonstrate proof-of-concept using a model amine-reactive BCP and provide guiding principles for the design of well-defined soft matter interfaces of interest in many fundamental and applied contexts.

We selected diblock copolymers with one block containing azlactone groups for use in this study for several reasons: (i) azlactones react through ring-opening reactions with a broad range of nucleophiles,[17] (ii) reactions with primary amines occur rapidly to produce stable amide bonds under mild conditions, without the need for a catalyst or the generation of by-products,[17] (iii) azlactones are stable under typical BCP thermal processing conditions,[18] and (iv) vinyl azlactones can be copolymerized with other vinyl monomers using living/controlled methods to produce reactive BCPs with a range of side chain functionality.[18-23] Relative to past approaches to the fabrication of oriented thin films of reactive BCPs,[24-27] this approach introduces several practical advantages. While past studies have reported solution-phase characterization of azlactone-functionalized BCPs,[22,23,28,29] investigations of the bulk and thin film phase behaviors of these reactive copolymers are limited.[18] Our results provide insight into the solid-state structures and morphologies of these reactive materials and demonstrate proof-of-concept with respect to

selective functionalization of reactive domains in microphase separated lamellar thin films. In this work, we used a model diblock copolymer synthesized by RAFT polymerization of styrene (S) and 2-vinyl-4,4-dimethylazlactone (VDMA; Figure 1).

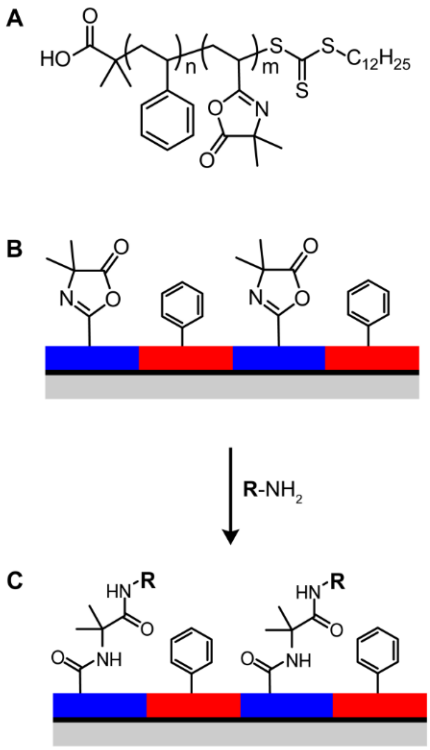

Figure 1. (A) Structure of PS-*b*-PVDMA. (B) Cross-section of a PS-*b*-PVDMA thin film microphase separated into perpendicular lamellae with alternating, surface-exposed stripes of PVDMA segments (blue) and non-reactive PS segments (red). (C) Selective ring-opening of azlactone groups in reactive stripes (blue) by treatment with primary amines permits placement of secondary functionality in defined locations without disrupting the underlying nanoscale morphology.

Polymerization of styrene was performed using *S*-1-dodecyl-*S*'-(α,α′-dimethyl-α″-acetic acid)trithiocarbonate as a chain transfer agent to produce a PS macro-chain transfer agent (M_n = 15.7 kg/mol, $Đ$ = 1.16), followed by chain extension with VDMA to produce PS-*b*-PVDMA (M_n = 33.6 kg/mol, $Đ$ = 1.33) with blocks of roughly equal molecular weights (see Scheme S1A, Figure

S1, and Methods section as the end of this chapter for complete details of synthesis and characterization). DSC revealed a single thermal transition at 111 °C, associated with the T_g of both the PS and PVDMA homopolymer segments (Figure S2); thermogravimetric analysis revealed a mass loss of < 5% at temperatures up to 248 °C (Figure S3). This result permitted characterization of bulk samples of PS-*b*-PVDMA by small angle X-ray scattering (SAXS) at temperatures above the T_g of the material without inducing thermal degradation. SAXS traces acquired at 150 °C (Figure 2, red curve) revealed a sharp principal scattering peak at $q^* = 0.0209$ $Å^{-1}$ with higher order reflections at $q/q^* = \sqrt{4}, \sqrt{9}, \sqrt{16}$, and $\sqrt{25}$ (a high-resolution synchrotron SAXS pattern is provided in Figure S4). Based on the positions of these peaks, coupled with the diminished intensity of the $\sqrt{4}$ peak, we conclude that this copolymer assembles into a bulk lamellar morphology with roughly symmetric volume fractions of each block and a lamellar spacing L_0 = 30.1 nm. We return to Figure 2 and the influence of side chain substitution on the bulk phase behavior of this reactive BCP in the discussion below.

Figure 3 shows a representative SEM image of a thin film of PS-*b*-PVDMA spin-coated and annealed on a silicon substrate coated with a poly(styrene-*r*-methyl methacrylate-*r*-glycidyl methacrylate) crosslinked copolymer mat.[4,30] For this and all other studies below, we used a mat composition with a mole fraction of styrene, F_S, of 0.43 based on ^{1}H NMR. Films of PS-*b*-PVDMA 22 nm thick (0.73 of L_0) were cast on these mats by spin-coating, and samples were then thermally annealed at 160 °C for 4 h at 1 Torr. Figure 3 reveals a microphase separated pattern with characteristics of a perpendicularly-oriented lamellar BCP,[4,8,13,30] as anticipated from the SAXS analyses above (Figure 2, red curve; see also Figure S6 for additional SEM images). The nanodomain periodicity from SEM is also consistent with the domain spacing of the bulk lamellar morphology measured by SAXS (L_0 ~ 30 nm; Figure S5). It is not possible to assign the specific

locations of the S and VDMA blocks solely on the basis of these SEM images. However, we interpret the regions of light and dark contrast in Figure 3 to represent alternating nanoscale stripes of PS and reactive PVDMA blocks. Characterization by infrared reflection absorption spectroscopy confirmed that the azlactone groups of the copolymer remained intact and were not hydrolyzed or degraded by thermal annealing (*e.g.*, as revealed by stretches at 1830, 1679, and 1209 cm^{-1} associated with the C=O, C=N, and C-O-C bonds of the azlactone ring; see Figure S7).

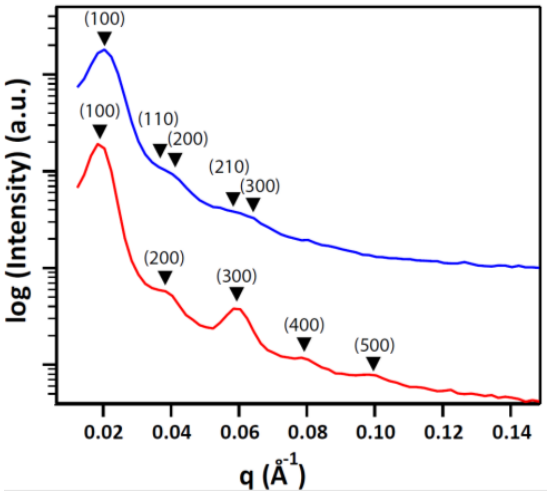

Figure 2. Azimuthally-integrated SAXS patterns for PS-*b*-PVDMA (red) and the product of exhaustive reaction of PS-*b*-PVDMA with dimethylaminopropylamine (blue), after thermal annealing at 150 ºC. The peak markers for PS-*b*-PVDMA correspond to the calculated peak positions of a lamellar morphology, with a principal scattering wavevector $q^* = 0.0209$ $Å^{-1}$. Functionalization with dimethylaminopropylamine causes the resulting block copolymer to microphase separate into hexagonally-packed cylinders with $q^* = 0.0213$ $Å^{-1}$, as indicated by peak markers corresponding to the calculated positions of expected reflections.

Further studies demonstrated that the azlactones in thermally annealed PS-*b*-PVDMA films were surface-accessible and that reactive lamellae could be used to introduce secondary functionality and tailor interfacial properties without compromising underlying phase-separated domains. The images in Figure 4A,C show micrographs of thermally annealed films treated with

aqueous solutions of either (A) a primary amine-functionalized fluorophore (tetramethylrhodamine cadaverine; TMR-cad) or (C) a non-reactive (amine-free) analog (tetramethylrhodamine; TMR) for 20 min at ambient temperature. These images reveal uniform red fluorescence on the film treated with TMR-cad relative to the film treated with TMR. These results reveal non-specific physisorption of TMR to be negligible, suggesting that fluorescence observed in Figure 4A arises solely from the reaction of TMR-cad with the azlactone groups of PVDMA (Figure 1B-C).

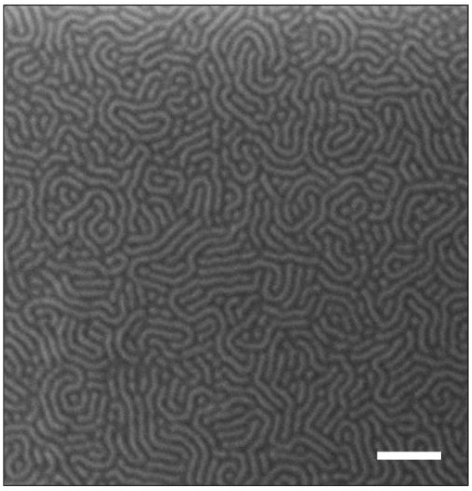

Figure 3. SEM image of a perpendicularly-oriented lamellar thin film obtained by spin-coating and thermal annealing of PS-*b*-PVDMA at 160 °C on a neutral mat composed of poly(styrene-*r*-methyl methacrylate-*r*-glycidyl methacrylate) with a styrene mole fraction of 0.43. Scale = 200 nm. Films exhibited uniformity across the substrate and no indication of dewetting over large areas (See Figure S6 Supporting Information).

We used water as a medium for the experiments above because it is a non-solvent for both PS and PVDMA homopolymers and should, thus, prevent lamellar domain reorientation or disruption that could arise from use of organic solvents. Figure 4B,D shows SEM images of the same films shown in Figure 4A,C after treatment with aqueous solutions of TMR or TMR-cad. The morphologies of the treated films are similar to those of the films prior to treatment (*cf*. Figure 3), leading us to conclude that these mild conditions do not substantially reorganize the underlying

morphology. These images also illustrate how new and complex chemical functionality—here, a large and positively charged fluorophore—can be introduced to a self-assembled BCP film without disturbing the original phase arising from the reactive parent copolymer. Given the absence of observed physisorption, we infer that functionalization occurs selectively on lamellar stripes defined by the PVDMA domains.

The features of this reactive BCP platform are significant in several contexts. First, they enable the selective, post-fabrication placement of new chemical functionality on the surfaces of BCP thin films in domains with shapes, sizes, and characteristic length scales that can be precisely defined by the structure of the reactive parent copolymer. Provided that mild chemical functionalization can be achieved using methods and reagents that do not perturb the film morphology, this approach provides opportunities to create well-defined and functional BCP interfaces in which the chemical functionality of one domain can be varied systematically and orthogonally to all other physical and microstructural features. This approach thus circumvents issues associated with the dependence of BCP phase behavior on chemical structure by using a 'non-invasive' approach to introduce new functionality after the microphase separated morphology has been fixed by vitrification of the glassy PS domains. Finally, we note that this post-fabrication approach to functionalization opens the door to the placement of complex chemical or biological functionality on the surfaces of microphase separated thin films in a manner that would be difficult to achieve by either thermal or solvent annealing of functional BCPs (due to the potentially problematic thermal stabilities of more complex functional groups or the interfacial wetting behaviors of these materials).

The results described above provide opportunities to introduce chemical or biological functionality to reactive lamellar domains using a diverse pool of water-soluble primary amines.

The images in Figure 4E,G show water contact angles (θ) for lamellar PS-*b*-PVDMA films treated with aqueous solutions of either (E) the hydrophobic amine propylamine or (G) the hydrophilic amine dimethylaminopropylamine (SEM images in Figure 4F,H show that morphology is retained after functionalization). These images reveal films treated with propylamine to be hydrophobic (θ_{adv} = 77.0 ± 1.5°); films treated with dimethylaminopropylamine were significantly more hydrophilic (θ_{stat} = 55.8 ± 2.3°). These differences are consistent with differences in the hydrophobicity and hydrophilicity of these amines. These results provide additional support for the reactivity of these microphase separated films with amines of arbitrary structure, and provide principles useful for modifying the interfacial behaviors of BCP thin films. This approach should prove useful for the immobilization and patterning of a range of other chemical and biological functionality. The identification of other solvent systems that do not dissolve PS-*b*-PVDMA or perturb underlying BCP domain structures would also further broaden the range of amines that can be used to functionalize or tune the properties of these materials.

Finally, we return to Figure 2 (blue curve), which depicts the SAXS pattern of a BCP synthesized by solution-phase treatment of PS-*b*-PVDMA with an excess of dimethylaminopropylamine (used to prepare the hydrophilic coatings described above; Figure 4G-H) to install dimethylaminopropyl side chains on the PVDMA block (>95% functionalized; see Figure S8 and Scheme S1B for details). The SAXS trace of this BCP at 150 °C (above the T_g of both homopolymer segments; Figure S9) showed a principal peak at q^* = 0.0213 Å^{-1} (L_0 = 29.5 nm) and higher order reflections at q/q^* = √3, √4, √7, and √9. Based on these relative peak positions, we conclude that this functionalized BCP assembles into hexagonally close-packed cylinders in the bulk, a morphology that differs substantially from the lamellar morphology of the reactive PS-*b*-PVDMA template from which it was synthesized (Figure 2, red curve). While this

difference in morphology is not particularly surprising, it underscores the impact that changes in block structure can have on the resulting microphase separated morphologies of BCPs. This result thus highlights the versatility and potential utility of the post-functionalization approach reported here, as it would likely prove difficult to anneal a pre-synthesized BCP with segments bearing styryl and dimethylamino groups into the lamellar thin films that we fabricated through our post-fabrication functionalization approach.

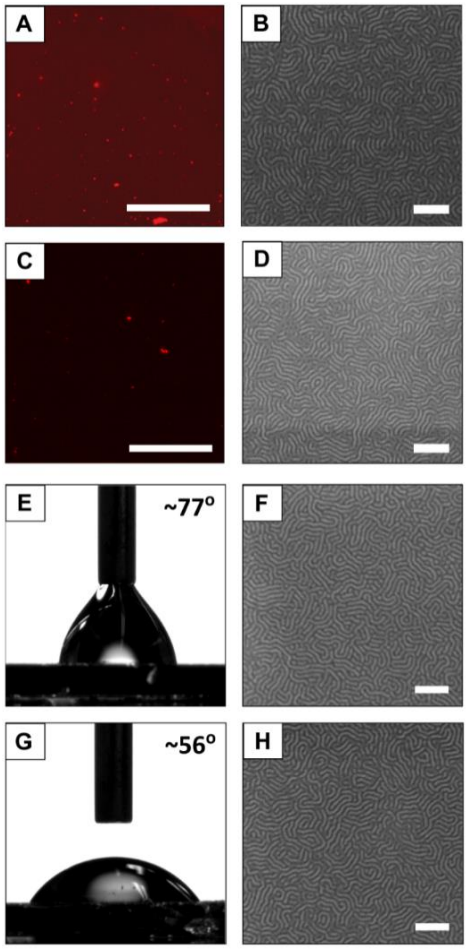

Figure 4. (A-D) Fluorescence micrographs and SEM images of PS-*b*-PVDMA films acquired after treatment with aqueous solutions of (A,B) TMR-cad or (C,D) TMR. The absence of fluorescence in (C) suggests negligible non-specific physisorption and that fluorescence in (A) arises from the reaction of TMR-cad with the azlactone groups in PS-*b*-PVDMA; scale bars in (A) and (C) are 125 μm. (E-H) Advancing (E) and static (G) contact angles and SEM images for thin films after treatment with (E,F) propylamine or (G,H) dimethylaminopropylamine. Scale for SEM images = 200 nm. SEM images show that domain orientation is retained post-functionalization.

Approaches to the design of soft material interfaces that enable precise control over the presentation of chemically- and biologically-relevant functionalities on surfaces provide opportunities to design nano/bio-interfaces for advanced applications. While BCP thin film self-assembly presents a promising path toward these goals, it is intrinsically limited by the fact that copolymer self-assembly and processability are sensitive to the chemical compositions of BCPs. We have described an approach that side-steps this limitation by exploiting the self-assembly of a PS-based diblock copolymer with a second amine-reactive block. This reactive BCP microphase separates into a lamellar thin film morphology, with a preferential perpendicular domain orientation relative to underlying substrates. This morphology provides periodic, nanoscale stripes of azlactone-functionalized segments that can be functionalized, post-fabrication, by treatment with aqueous solutions of primary amines. Because vitreous PS domains cement the film structure, this approach leads to periodic arrays presenting new functionality without disturbing the morphology or domain orientation of the coating. This approach is modular, both in terms of the range of amine-functionalized motifs that can be installed and the variety of vinyl monomers that can be copolymerized with VDMA. We anticipate that this approach can be extended to the design of films that assemble into other reactive morphologies (*e.g.*, perpendicular cylinders, aligned lamellae, or features with domain spacings smaller than those reported here) by judicious choice of polymer structure or careful design of underlying substrates.

Acknowledgments. This work was supported by the NSF through a grant to the Nanoscale Science and Engineering Center at UW-Madison (DMR-0832760) and made use of NSF-supported facilities (DMR-0832760, DMR-1121288 and CHE-1048642). Synchrotron SAXS studies were conducted at Sector 12 of the Advanced Photon Source at Argonne National Laboratory, supported

by the U.S. DOE (Contract #DE–AC02–06CH11357). M.C.D.C. acknowledges the Natural Sciences Engineering Research Council of Canada for a graduate fellowship.

References

(1) Bates, F. S.; Fredrickson, G. H. *Phys. Today* **1999**, *52*, 32.

(2) Lodge, T. P. *Macromol. Chem. Phys.* **2003**, *204*, 265.

(3) Ruzette, A.-V.; Leibler, L. *Nat. Mater.* **2005**, *4*, 19.

(4) Bang, J.; Jeong, U.; Ryu, D. Y.; Russell, T. P.; Hawker, C. J. *Adv. Mater.* **2009**, *21*, 4769.

(5) Marencic, A. P.; Register, R. A. *Annu. Rev. Chem. Biomol. Eng.* **2010**, *1*, 277.

(6) Luo, M.; Epps, T. H. *Macromolecules* **2013**, *46*, 7567.

(7) Hu, H.; Gopinadhan, M.; Osuji, C.O. *Soft Matter* **2014**, *10*, 3867.

(8) Kim, S. O.; Solak, H. H.; Stoykovich, M. P.; Ferrier, N. J.; de Pablo, J. J.; Nealey, P. F. *Nature* **2003**, *424*, 411.

(9) Tang, C. B.; Lennon, E. M.; Fredrickson, G. H.; Kramer, E. J.; Hawker, C. J. *Science* **2008**, *322*, 429.

(10) Peng, Q.; Tseng, Y.-C.; Darling, S. B.; Elam, J. W. *Adv. Mater.* **2010**, *22*, 5129.

(11) Xu, J.; Hong, S. W.; Gu, W.; Lee, K. Y.; Kuo, D. S.; Xiao, S.; Russell, T. P. *Adv. Mater.* **2011**, *23*, 5755.

(12) Killops, K. L.; Gupta, N.; Dimitriou, M. D.; Lynd, N. A.; Jung, H.; Tran, H.; Bang, J.; Campos, L. M. *ACS Macro Letters* **2012**, *1*, 758.

(13) Bates, C. M.; Seshimo, T.; Maher, M. J.; Durand, W. J.; Cushen, J. D.; Dean, L. M.; Blachut, G.; Ellison, C. J.; Willson, C. G. *Science* **2012**, *338*, 775.

(14) Cochran, E. W.; Bates, F. S. *Macromolecules* **2002**, *35*, 7368.

(15) Kennemur, J. G.; Hillmyer, M. A.; Bates, F. S. *Macromolecules* **2012**, *45*, 7228.

(16) Stein, G. E.; Mahadevapuram, N.; Mitra, I. *J. Polym. Sci. Part B: Polym. Phys.* **2015**, *53*, 96-102.

(17) Heilmann, S. M.; Rasmussen, J. K.; Krepski, L. R. *J. Polym. Sci., Part A: Polym. Chem.* **2001**, *39*, 3655.

(18) Lokitz, B.S.; Wei, J.; Hinestrosa, J.P.; Ivanov, I.; Browning, J.F.; Ankner, J.F.; Kilbey, S.M.; Messman, J.M. *Macromolecules* **2012**, *45*, 6438.

(19) Tully, D. C.; Roberts, M. J.; Geierstanger, B. H.; Grubbs, R. B. *Macromolecules* **2003**, *36*, 4302.

(20) Fournier, D.; Pascual, S.; Fontaine, L. *Macromolecules* **2004**, *37*, 330.

(21) Pascual, S.; Blin, T.; Saikia, P. J.; Thomas, M.; Gosselin, P.; Fontaine, L. *J. Polym. Sci., Part A: Polym. Chem.* **2010**, *48*, 5053.

(22) Buck, M. E.; Lynn, D. M. *Polym. Chem.* **2012**, *3*, 66.

(23) Ho, H. T.; Levere, M. E.; Fournier, D.; Montembault, V.; Pascual, S.; Fontaine, L. *Australian Journal of Chemistry* **2012**, *65*, 970.

(24) Shen, L.; Garland, A.; Wang, Y.; Li, Z.; Bielawski, C. W.; Guo, A.; Zhu, X. Y. *Small* **2012**, *8*, 3169.

(25) Stadermann, J.; Riedel, M.; Komber, H.; Simon, F.; Voit, B. *J. Polym. Sci., Part A: Polym. Chem.* **2012**, *50*, 1351.

(26) Zhao, H.; Gu, W.; Kakuchi, R.; Sun, Z.; Sterner, E.; Russell, T. P.; Coughlin, E. B.; Theato, P. *ACS Macro Letters* **2013**, *2*, 966.

(27) Zhao, H.; Gu, W.; Thielke, M. W.; Sterner, E.; Tsai, T.; Russell, T. P.; Coughlin, E. B.; Theato, P. *Macromolecules* **2013**, *46*, 5195.

(28) Quek, J. Y.; Zhu, Y.; Roth, P. J.; Davis, T. P.; Lowe, A. B. *Maromolecules* **2013**, *46*, 7290.

(29) Ho, H. T.; Levere, M. E.; Pascual, S.; Montembault, V.; Casse, N.; Caruso, A.; Fontaine, L. *Polym. Chem.* **2013**, *4*, 675.

(30) Han, E.; Gopalan, P. *Langmuir* **2010**, *26*, 1311.

Supporting Information for Chapter 7

Experimental Section

Materials: Styrene was purchased from Sigma-Aldrich (Milwaukee, WI) and stirred over Brockman Type I basic alumina for 1 h and gravity filtered to remove inhibitors prior to use. 2-Vinyl-4,4-dimethylazlactone (VDMA), a kind gift from Dr. Steven M. Heilmann (3M Corporation, Minneapolis, MN), was passed twice through a short column of inhibitor removal resin (Alfa Aesar) followed by a short column of Silicycle UltraPure silica gel (230-400 mesh) prior to use. *S*-1-Dodecyl-*S*'-(α,α'-dimethyl-α''-acetic acid)trithiocarbonate was synthesized according to a literature procedure and re-crystallized from hexanes prior to use (Lai, J. T.; Filla, D.; Shea, R. *Macromolecules* **2002**, *35*, 6754−6756). Azobisisobutyronitrile (AIBN) was recrystallized from methanol prior to use. Dimethylaminopropylamine (99%) was obtained from Acros Organics (Somerville, NJ). Tetramethylrhodamine (TMR) was obtained from Anaspec (Fremont, CA). Tetramethylrhodamine cadaverine (TMR-cad) was obtained from Invitrogen (Carlsbad, CA). All thin film studies were conducted using undoped (100) silicon wafers (SVM, Santa Clara, CA), with the exception of IRRAS experiments, for which N-type, Sb-doped (100) silicon wafers with a resistivity range of 0.008—0.02 Ω-cm were used (Addison, San Jose, CA). All materials were used as received unless stated otherwise.

General Considerations: ^{1}H NMR spectroscopy was performed in $CDCl_3$ using a Bruker Avance-500 spectrometer and a pulse repetition delay of 12 s. All spectra were referenced relative to tetramethylsilane (TMS). Size exclusion chromatography (SEC) analyses were conducted using a Viscotek GPCMax System equipped with two Polymer Laboratories PolyPore columns (250 mm × 4.6 mm), a differential refractometer, a light scattering module (7° and 90° detection) and a differential viscometer. Tetrahydrofuran was used as the mobile phase at 40 °C with a 0.8 mL/min

flow rate. The instrument was calibrated using 10 narrow dispersity polystyrene standards with M_n = 0.580−377.4 kg/mol (Agilent Technologies Santa Clara, CA). Thermogravimetric analyses (TGA) were performed using a TA instruments Q500 thermogravimetric analyzer. Polymer sample weight loss was measured over the temperature range T = 25-600 °C using a ramp rate of 20 °C/min. Differential scanning calorimetry (DSC) analyses were performed using a TA instruments DSC100 over a temperature range T = 30-175 °C using a heating and a cooling ramp rate of 10 °C/min. The thermal history of each sample was erased in the first cycle by heating to 175 °C and cooling to 40 °C at a cooling ramp rate of 10 °C/min, and all thermal transitions were assigned from the second heating cycle. Attenuated total reflectance (ATR) measurements were obtained using a Bruker Tensor 27 FTIR spectrometer outfitted with a Pike Technologies Diamond ATR stage (Madison, WI.) Data was analyzed using Opus Software version 6.5 (Bruker Optik GmbH). Spectra were collected at a resolution of 2 cm^{-1} and are presented as an average of 32 scans. Data were smoothed by applying a nine-point average and baseline-corrected using a concave rubberband correction (10 iterations, 64 points). Infrared Reflection Absorption Spectroscopy (IRRAS) measurements were made using a Bruker Tensor 70 FTIR spectrometer equipped with a VeeMax II variable angle specular reflectance attachment containing a wire grid polarizer. Spectra were collected with p-polarized light at an incident angle of 65° relative to the normal at a resolution of 2 cm^{-1} and are presented as an average of 2000 scans. Data were collected on polymer thin films spin-coated and annealed on Sb-doped silicon substrates. The background spectrum used to compute the absorbance of the film was the single beam spectrum of a bare Sb-doped silicon substrate. Data were analyzed using Opus Software version 6.5 (Bruker Optik GmbH). A CO_2 atmospheric correction was applied, and the data were smoothed by applying a nine-point average and baseline corrected using a concave rubberband correction (10 iterations,

100 points). Fluorescence micrographs were acquired using an Olympus IX70 microscope equipped with a Lumen Dynamics XCite 120PC-Q fluorescence source and a Q Imaging EXi Aqua camera at 10x magnification and an exposure time of 100 ms. Images were analyzed and false colored using MetaMorph Advanced software, Version 7.7.8.0 (Molecular Devices, LLC). Block copolymer films and random copolymer mat thicknesses were measured using a Gaertner LSE ellipsometer. Top-down scanning electron micrographs of thin film morphologies were acquired using a LEO-1550 VP field-emission SEM operating with an accelerating voltage of 1 kV and processed using the ImageJ software package. Water contact angle measurements were made using a Dataphysics OCA 15 Plus contact angle goniometer at ambient temperature with 4 μL of 18.2 MΩ Millipore water.

Small Angle X-Ray Scattering (SAXS): Synchrotron SAXS measurements were performed at the 12-ID-B beamline at the Advanced Photon Source (Argonne, IL) using a beam energy of 12 keV (λ = 1.034 Å) and a sample to detector distance of 2.027 m, which was calibrated using a silver behenate standard sample with d = 58.38 Å. Two-dimensional SAXS patterns were recorded on a Pilatus 2M detector (25.4 cm x 28.9 cm rectangular area) with a 1475 x 1679 pixel resolution. Prior to SAXS analysis, PS-*b*-PVDMA was loaded into a hermetically sealed aluminum DSC pan and thermally annealed at 130 °C for 1 h. The sample was then heated to 150 °C in a Linkam DSC stage and allowed to equilibrate for 5 min before data collection (exposure time = 1 s). Laboratory SAXS measurements were performed in the Materials Science Center at the University of Wisconsin-Madison. Cu-Kα X-rays generated by a Rigaku Micromax 002+ microfocus source were collimated using a Max-Flux multilayer confocal optic (Osmic, Inc.) followed by passage through three pinholes to collimate and trim the final beam diameter to < 0.5 mm. Samples were mounted in a vacuum chamber on a Linkam temperature-controlled hotstage and thermally

annealed at 150 °C for 10 minutes prior to data collection (exposure time = 20 min). Two-dimensional SAXS patterns were recorded on a Gabriel X-ray detector (150 mm diameter active circular area) using a sample-to-detector distance of 1 meter (calibrated using a silver behenate standard sample with d = 58.38 Å). 2D-SAXS patterns were azimuthally integrated to obtain one-dimensional intensity ($I(q)$) *versus* scattering wavevector (q) plots and analyzed using procedures written for use with Igor Pro (Schmitt, A. K.; Mahanthappa, M. K. Computer Code for Materials Scientists: Igor Pro Procedures for Analyzing Dynamic Light Scattering, Rheology, and Synchrotron X-ray Scattering Data. figShare http://dx.doi.org/10.6084/m9.figshare.644515).

Synthesis of Polystyrene (PS) Homopolymer: S-1-Dodecyl-*S*'-(α,α'-dimethyl-α''-acetic acid)trithiocarbonate (88.2 mg, 0.242 mmol) and freshly purified styrene (20 mL) were added to a 100 mL Schlenk tube and degassed via three freeze-pump-thaw cycles. The solution was placed in a 120 °C oil bath for 13 h. The resulting polymer was precipitated in cold methanol and collected, redissolved in THF, re-precipitated twice more in cold methanol, and freeze-dried from C_6H_6. $M_{n,GPC}$ = 15.7 kg/mol, $Đ$ = 1.16.

Synthesis of Poly(Styrene-block-Vinyl Dimethylazlactone) (PS-b-PVDMA): PS macroinitiator (M_n = 15.7 kg/mol, $Đ$ = 1.16, 1.0159 g, 65 μmol), 2-vinyl-4,4-dimethylazlactone (7.5 mL, 56 mmol), AIBN (7.4 mg, 45 μmol), and C_6H_6 (7.5 mL) were added to a 25 mL Schlenk tube and degassed via three freeze-pump-thaw cycles. The solution was placed in a 60 °C oil bath for 1.25 h. The resulting polymer was precipitated in hexanes and collected, redissolved in THF, re-precipitated in hexanes, and freeze-dried from C_6H_6. $M_{n,\ NMR,\ PS\text{-}b\text{-}PVDMA}$ = 33.6 kg/mol, $Đ$ = 1.33. ^{1}H NMR and ATR-IR characterization is provided in Fig. S8.

Functionalization of PS-b-PVDMA using Dimethylaminopropylamine: PS-*b*-PVDMA (28.32 mg, 0.108 mmol VDMA) was dissolved in 1.5 mL of anhydrous THF in a 6 mL glass vial.

To this solution, dimethylaminopropylamine (20.5 μL, 0.162 mmol) was added. The vial was sealed with a Teflon cap and placed in a 50 °C oil bath overnight. The solution was concentrated using a rotary evaporator and precipitated into ~8 mL of hexanes. The resulting white powder was re-dissolved in ~0.5 mL THF and reprecipitated once more into hexanes. ^{1}H NMR and ATR-IR characterization is provided in Fig. S8.

Preparation of Self-Assembled Thin Films of PS-b-PVDMA: A solution of poly(styrene-*r*-methyl methacrylate-*r*-glycidyl methacrylate) (comprised of 5 mol% glycidyl methacrylate and F_S = 33, 43, or 51 mol% styrene synthesized using a previously reported procedure by Gopalan and co-workers (Han, E.; Gopalan, P. *Langmuir* **2010**, *26*, 1311); see text) in toluene (0.3% *w/w*) was spin-coated at 4000 rpm onto freshly cleaned silicon wafers (piranha acid treated; *caution reacts violently with organic compounds*). The sample was annealed under vacuum at 220 °C for 20 min. After annealing, the sample was sonicated in toluene and then rinsed with fresh toluene to remove un-crosslinked polymer chains, resulting in cross-linked films (or mats) ~5.6 to 6.6 nm thick. A solution of PS-*b*-PVDMA in toluene was then spin-coated on the random copolymer-coated substrate at 4000 rpm. The resulting sample was subsequently annealed at 160 °C for 4 h at 1 Torr. In an initial survey of several different random mat compositions, only films spin-coated at 1% (*w/w*) PS-*b*-PVDMA onto neutral mats with a composition of F_S = 0.43 resulted in perpendicularly-oriented lamellae (see Fig. S5 and S6 and main text for additional results and discussion).

Post-Fabrication Functionalization of Block Copolymer Thin Films by Treatment with Small-Molecule Amines: Solutions of the fluorescent dyes TMR or TMR-cad were prepared at a concentration of ~0.05 mg/mL in Millipore water. 0.5 μL droplets of solution were placed on annealed PS-*b*-PVDMA thin films, as fabricated above, for 20 min at room temperature in a humid

environment. Aqueous solutions of propylamine or dimethylaminopropylamine were prepared at a concentration of 1 mg/mL in Millipore water and the pH was adjusted to 9.0 using small aliquots of 1M HCl and 1M NaOH. Films were placed in 1 mL of the amine-containing solution for 20 min at room temperature. Films were then rinsed liberally with water and dried in a stream of filtered compressed air prior to use.

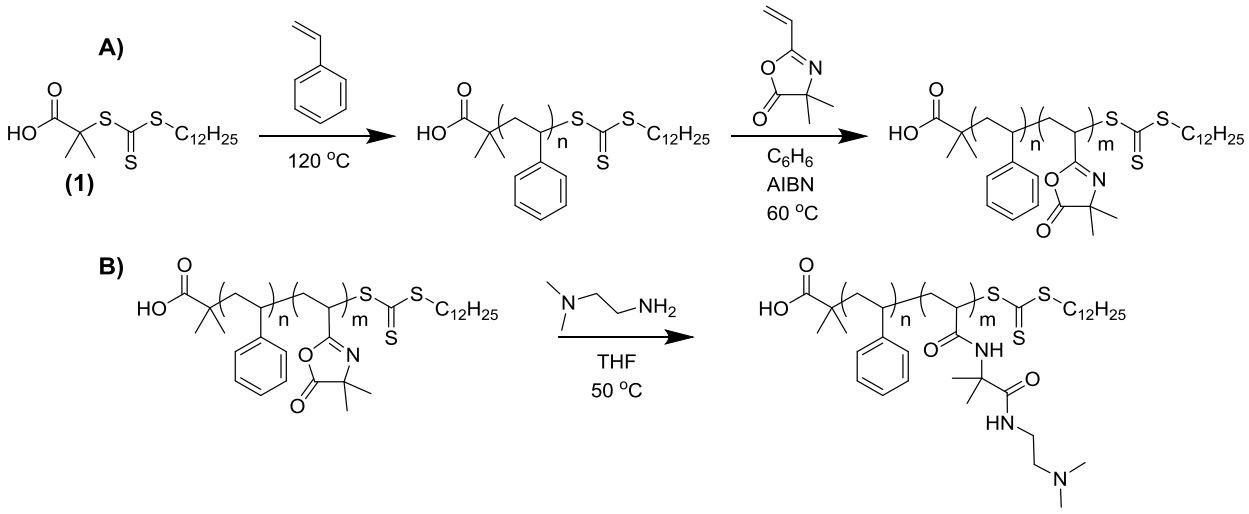

Scheme S1. (A) Synthesis of poly(styrene-*b*-vinyl dimethylazlactone) (PS-*b*-PVDMA) block copolymers *via* the sequential RAFT polymerization of styrene followed by VDMA. (B) Synthesis of a dimethylaminopropyl-functionalized derivative of PS-*b*-PVDMA by reaction of PS-*b*-PVDMA with 1.5 equivalents of dimethylaminopropylamine in THF at 50 °C overnight.

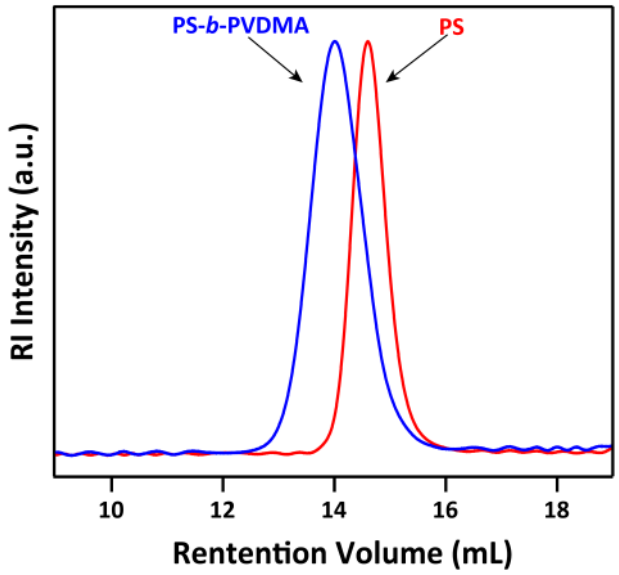

Figure S1. Size exclusion chromatography (SEC) traces for a polystyrene macroinitiator having M_n = 15.7 kg/mol and $Đ$ = 1.17 (red trace) and PS-*b*-PVDMA with $M_{n,}$ = 33.6 kg/mol and $Đ$ = 1.33 (blue trace) obtained from chain extension of the PS macroinitiator.

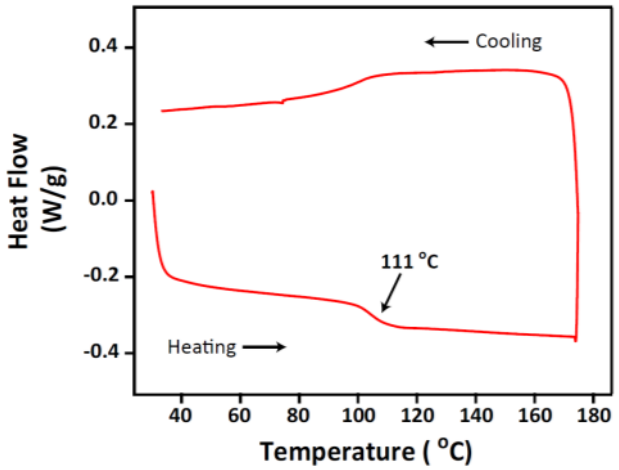

Figure S2. Differential scanning calorimetry (DSC) heating and cooling curves for PS-*b*-PVDMA showing a thermal transition at ~111 ºC, indicating the overlapping T_g's of the PS and PVDMA segments.

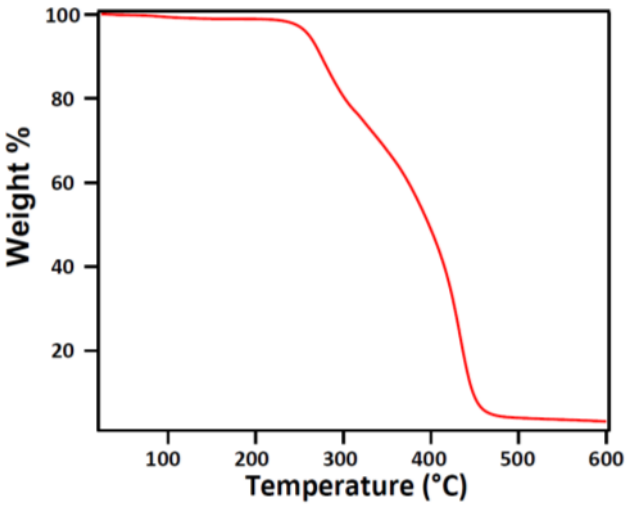

Figure S3. Thermogravimetric analysis of PS-*b*-PVDMA showing a mass loss of less than 5 wt% when heated up to 248 °C a heating rate of 20 °C/min.

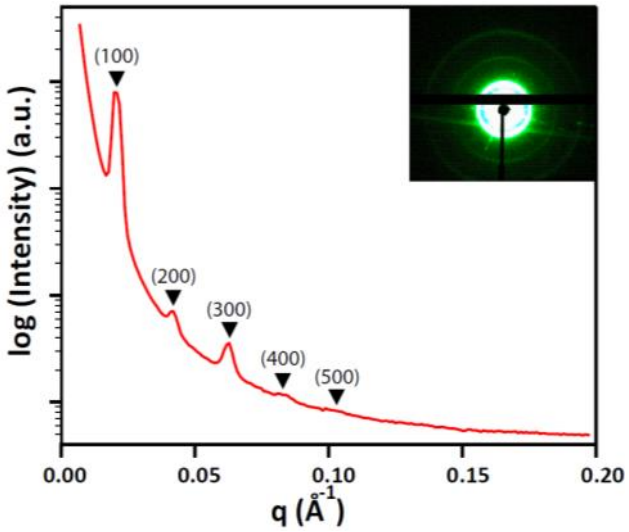

Figure S4. Azimuthally-integrated synchroton SAXS pattern for PS-*b*-PVDMA after thermal annealing at 150 ºC, with markers indicating the calculated peak positions for a lamellar morphology based on the position of the principal scattering wavevector (q^* = 0.0209 Å^{-1}); the inset shows the two-dimensional synchrotron SAXS pattern.

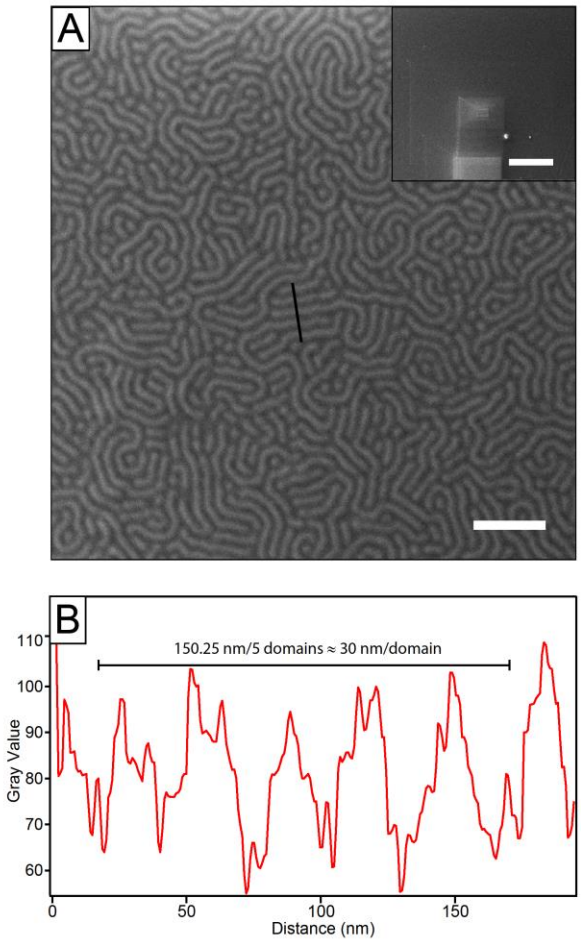

Figure S5. (A) Copy of the SEM image shown in Fig. 3 of the main text. The image shows a perpendicularly-oriented lamellar thin film obtained by spin-coating and subsequent thermal annealing of PS-*b*-PVDMA at 160 °C on an underlying mat composed of poly(styrene-*r*-methyl methacrylate-*r*-glycidyl methacrylate) with a styrene mole fraction of 0.43. Scale bar = 200 nm; inset; scale bar = 5 μm. (B) Grayscale line intensity profile taken along the black line shown in panel A drawn through a region of five well aligned lamellae, indicating an average domain spacing of L_0 ~ 30 nm for the block copolymer thin film. It is difficult to determine L_0 from these data with certainty because the domains are not well aligned over larger distances and contrast between domains is not sharp. However, this approximate value of L_0 is similar to that obtained by SAXS (see Fig. 2, red curve, and surrounding discussion in the main text).

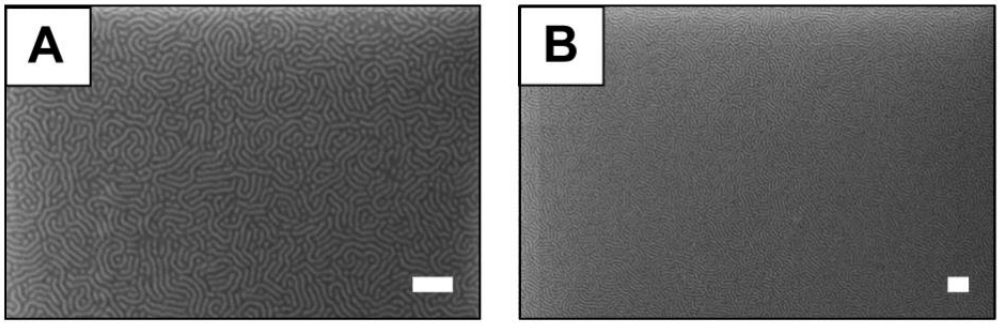

Figure S6. SEM images at different magnifications acquired at different locations on the same sample shown in Fig. 3 of the main text demonstrating that films are uniform across the substrate and that no dewetting occurs. Scale bar = 200 nm in both panels.

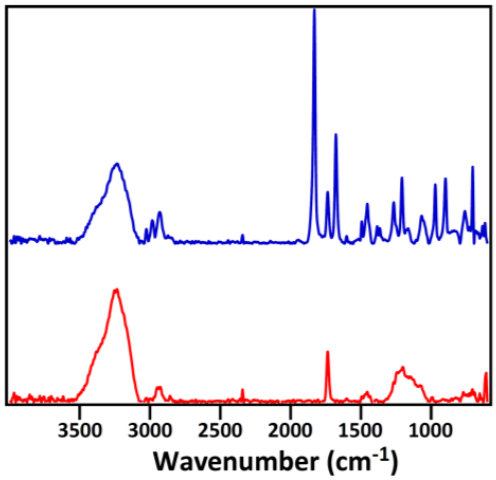

Figure S7. FT-IRRAS spectrum of a poly(styrene-*r*-methyl methacrylate-*r*-glycidyl methacrylate) mat having the composition F_S = 0.43 (red), and the FT-IRRAS spectrum of a sample comprised of an underlying mat at this same composition and an overlying thermally annealed film of PS-*b*-PVDMA (blue) with a film thickness of 0.73 L_0. Peaks at 1830, 1679, and 1209 cm^{-1} correspond to the cyclic C=O, C=N, and C-O-C stretches of the azlactone ring, respectively. All samples used in these experiments were prepared on Sb-doped silicone substrate.

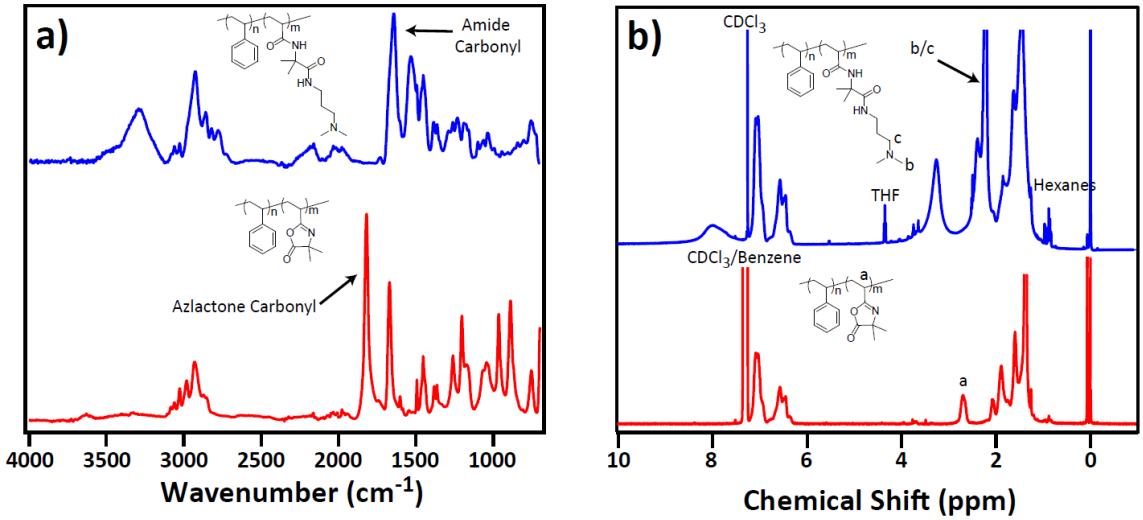

Figure S8. (A) ATR-IR and (B) ^{1}H NMR spectra of PS-*b*-PVDMA (red) and the product of the exhaustive reaction of PS-*b*-PVDMA with dimethylaminopropylamine (blue).

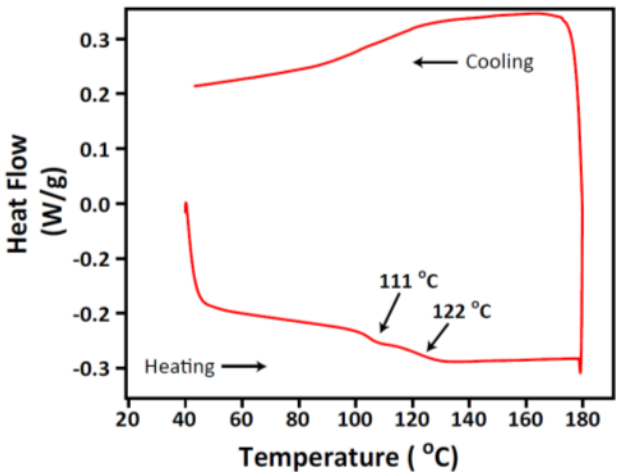

Figure S9. Differential scanning calorimetry (DSC) heating and cooling curves for a derivative of PS-*b*-PVDMA in which the azlactone functionalities were exhaustively reacted with dimethylaminopropylamine. Two thermal transitions are observed, corresponding to the T_g for the PS block (111 °C) and the T_g for the dimethylaminopropylamine-functionalized block (122 °C)

Chapter 8

Self-Assembly and Post-Fabrication Functionalization of Microphase Separated Thin Films of a Reactive Azlactone-Containing Block Copolymer‡

‡ Portions of this chapter have been submitted for publication as: Choi, J.W.; Carter, M.C.D.; Wei, W.; Kanimozi, C.; Speetjens, F.W.; Mahanthappa, M.K.; Lynn, D.M.; Gopalan, P. "Self-Assembly and Post-Fabrication Functionalization of Microphase Separated Thin Films of a Reactive Azlactone-Containing Block Copolymer" **2016**, *Submitted.* J.C. and M.C.D.C. were co-first authors. J. Choi and W. Wei fabricated the thin films, and performed the XPS and ALD. My contribution was in synthesizing the block copolymers, performing the physicochemical characterization, and analyzing the data.

ABSTRACT: We report on the thin film self-assembly and post-fabrication functionalization of cylinder-forming poly(styrene-*block*-2-vinyl-4,4-dimethylazlactone) (PS-*b*-PVDMA) block copolymers (BCPs). Thermal annealing of a lamellar BCP composition, to drive microphase separation in thin-film results in high defect densities and poor long-range order. Using FTIR spectroscopy and ellipsometry, we demonstrate that thermal annealing results in reaction between the azlactone groups and the underlying substrate leading to BCP 'pinning'. We demonstrate that solvent annealing can circumvent these issues and drive high fidelity microphase separation of the BCP in thin film. Solvent annealing approach also permits control over domain orientation; we show that parallel and perpendicularly-oriented cylinders with diameters of 11.7 ± 1.2 nm and a center-to-center distance of 25.2 ± 2.6 nm can be obtained using a BCP with M_n = 29.5 kDa and f_S = 0.75. The PVDMA block in these self-assembled thin film remains available for reaction with primary amine-functionalized nucleophiles. X-ray photoelectron spectroscopy (XPS) depth-profiling reveals that the reaction between azlactone groups and incoming amines occur primarily in the top few nanometers of the reactive domains. Finally, we demonstrate that the azlactone groups in both parallel and perpendicularly-oriented cylindrical films can selectively incorporate trimethylaluminum vapor, which can be subsequently converted into Al_2O_3 nanowires and nanodots with dimensions of 16 nm and 12 nm, respectively.

Introduction

Polymers bearing reactive functional groups can be used as coatings and templates for the post-fabrication installation of new functionality or the modification and patterning of interfacial properties on a range of surfaces and substrates. Polymers containing a variety of different nucleophilic, electrophilic, and "clickable" side chains and endgroups[1-8] have contributed to the development of new reactive surfaces and interfaces of interest in many different contexts, including the immobilization of biomolecules,[9-15] the design of optical and electronic materials,[16-18] and the fabrication of surfaces with unique wetting properties.[19-22] Reactive block copolymers (BCPs), in which one or more blocks are readily amenable to post-fabrication modification,[23] can provide additional opportunities to define interfacial properties and pattern specific surface features. Microphase separation of reactive BCPs and their self-assembly into spherical, cylindrical, and lamellar nanostructured thin films, for example, can provide surface coatings that present spatially-resolved and well-ordered domains of chemical functionality with periodic dimensions over length scales ranging from 10 to 100 nm.[24-29]

When confined to a single domain only, the reactive groups in a BCP can be used to immobilize chemical or biological functionality in regular, ordered arrays at dimensions that are dictated by the BCP morphology and to place specific functionality on alternating domains of a lamellar nanostructure, or on hexagonally arrayed 'dots' within a non-reactive matrix. For example, Zhu and coworkers have used reactive BCPs containing an alkyne-functionalized block to immobilize and array azide-tagged proteins on a self-assembled hexagonal thin film.[30] Theato and others have also investigated photocleavable BCPs as templates to confine reactive functionality within nanopores,[31-34] and the Voit group has explored the synthesis, self-assembly, and potential post-fabrication reactivity of a diverse range of reactive BCPs and their thin film

counterparts.[35-38] These and other related reactive BCP approaches provide opportunities to pattern new functionality at the nanoscale. However, these strategies also require the synthesis of potentially complex BCPs with specific reactive groups, and their subsequent self-assembly into well-defined morphologies.

We recently reported the synthesis and reactivity of self-assembled nanostructures formed from BCPs containing reactive azlactone groups[39]. These reactive BCPs can be synthesized directly by controlled/living radical polymerization of the reactive vinyl monomer 2-vinyl-4,4-dimethylazlactone (VDMA).[40-44] The ring-opening of azlactone groups with functional primary amine proceeds rapidly in quantitative reactions that are both free of by-products and do not require a catalyst, and this approach can therefore be used to design functional materials and interfaces.[4, 10, 12-13, 15, 40, 45-50] Our past work demonstrated that symmetric poly(styrene-*block*-2-vinyl-4,4-dimethylazlactone) (PS-*b*-PVDMA; M_n = 33.6 kg/mol, $Đ$ = 1.33) synthesized by sequential reversible-addition fragmentation chain-transfer (RAFT) polymerization could self-assemble into lamellar thin films with dimensions of L_0 ~ 30 nm (i.e., microdomain feature sizes of ~15 nm), providing access to surfaces that present alternating nanoscale domains of styrene and amine-reactive azlactone groups.[39] That study demonstrated that the reactive domains in those coatings could be functionalized after self-assembly, with amine-containing molecules to modify thin film interfacial properties without the perturbation of the underlying lamellar morphology.

In that previous study, we used a random copolymer mat comprising styrene (S), methyl methacrylate (MMA), and glycidyl methacrylate (GMA) [P(S-*r*-MMA-*r*-GMA)][51] as a non-preferential layer to induce perpendicular domain orientation in lamellar PS-*b*-PVDMA thin films.[39] Although perpendicular domains in PS-*b*-PVDMA were observed by thermal annealing

on those neutral mats, the resulting lamellar thin films lacked long-range order and contained defects (including the presence of possible mixed morphologies of lamellae and so-called perforated lamellae). Those results suggest that self-assembly into equilibrium, microphase-separated morphologies could be hindered by chemical interactions between the reactive azlactone rings and the underlying non-preferential layers induced by thermal annealing. The development of methods and processing steps for the elaboration of long-range, defect-free morphologies in both the bulk and thin film regime will ultimately be required to exploit these reactive PS-*b*-PVDMA templates for the design of new functional nanostructured materials.

Here, we sought to investigate, characterize, and compare the self-assembly and post-fabrication functionalization of a cylinder-forming PS-*b*-PVDMA BCP thin films prepared by both thermal and solvent annealing. Using IR spectroscopy and ellipsometry, we show that thermal annealing induces 'pinning' of the reactive PVDMA domains in thin films fabricated on bare silicon substrates, preventing development of defect-free and long-range self-assembled morphologies. Solvent annealing, however, prevents undesirable interactions and yields nanoscale patterns of both perpendicular and parallel cylinders of high fidelity with long-range order and low defect density. Characterization of the reactivity and post-fabrication modification of the azlactone groups in self-assembled cylindrical BCP thin films using X-ray photoelectron spectroscopy (XPS) revealed that the azlactone groups are not completely consumed during post-fabrication treatment, and that reactions in cylindrical PS-*b*-PVDMA BCPs occur primarily in the top 4 nm of the film. Finally, we demonstrate the selective infusion of $AlMe_3$ vapor into the PVDMA domains of parallel and perpendicular cylindrical thin films and subsequent transformation to give aluminum oxide (ALO) nanowires and nanodots, introducing a new

approach to the fabrication of hard masks of potential widespread utility in nanolithography applications.

Materials and Methods

Materials. Styrene (99.9%), 2,2'-azobis(isobutyronitrile) (AIBN, recrystallized from CH_3OH), hexanes (technical grade), 3-iodobenzylamine hydrochloride (97%), trimethylaluminum (packaged for use in deposition systems), and toluene (ACS grade, >99.5%) were purchased from Sigma-Aldrich (Milwaukee, WI). Inhibitor Removal Resin was purchased from Alfa Aesar (Radnor, PA). 2-Vinyl-4,4-dimethylazlactone (VDMA) was a gift from Dr. Steven M. Heilmann (3M Corp., St. Paul, MN). *S*-1-Dodecyl-*S*'-(α,α'-dimethyl-α''-acetic acid)trithiocarbonate was synthesized according to a literature procedure,[52] stored at 0 °C, and recrystallized from hexanes prior to use. Toluene was passed through a short column of Brockman Type I basic alumina (~10% *m/v*) prior to use as a polymerization solvent. Materials were used as received unless otherwise stated.

General Considerations. ^{1}H NMR spectroscopy was performed in $CDCl_3$ using a Bruker Avance-400 or a Bruker Avance-500 spectrometer with a pulse repetition delay of 16 sec. Spectra were referenced relative to the residual proton peak of $CHCl_3$ (δ 7.26 ppm). Size exclusion chromatography (SEC) analyses were performed using a Viscotek GPC Max VE2001 equipped with two Polymer Laboratories PolyPore columns (250 mm × 4.6 mm), and a TDA-302 detector array, using THF as the eluent at a flow rate of 1 mL/min at 40 °C. The instrument was calibrated using 10 narrow dispersity polystyrene standards with M_n = 0.580−377.4 kg/mol (Agilent Technologies Santa Clara, CA). Attenuated total reflectance (ATR) IR measurements

were obtained using a Bruker Tensor 27 FTIR spectrometer outfitted with a Pike Technologies Diamond ATR stage (Madison, WI). Data were analyzed using Opus Software v. 6.5 (Bruker Optik GmbH). Spectra were collected at a resolution of 2 cm^{-1} and are presented as an average of 16 scans. Data were smoothed by applying a nine-point average and baseline-corrected using a concave rubberband correction (10 iterations, 64 points). Scanning electron microscope (SEM) images were acquired using a LEO-1550 field-emission SEM at an accelerating voltage of 1 to 2 kV.

Representative RAFT Synthesis of Poly(styrene-*block*-2-vinyl-4,4-dimethylazlactone) (PS-*b*-PVDMA-1) BCPs. *Synthesis of Polystyrene (PS) Homopolymer:* Styrene was stirred over Brockman Type I basic alumina for 30 min and gravity filtered through Whatman #1 filter paper. Freshly purified styrene (15 mL, 131 mmol) and the RAFT agent *S*-1-dodecyl-*S*'-(α,α'-dimethyl-α''-acetic acid) trithiocarbonate (65.8 mg, 0.180 mmol) were added to an oven-dried 25 mL Schlenk tube and degassed *via* three freeze-pump-thaw cycles. The solution was placed in a 120 °C oil bath for 10 h, after which it was rapidly cooled in liquid nitrogen to stop the reaction. The resulting polymer was precipitated in ~400 mL of cold methanol and collected, redissolved in ~15 mL of THF, re-precipitated twice more in cold methanol, and freeze-dried from benzene. $M_{n,GPC}$ = 21.7 kg/mol, $Đ$ = 1.13. *Synthesis of PS-b-PVDMA-1:* 2-Vinyl-4,4-dimethylazlactone (VDMA) was passed twice through a short column of Inhibitor Removal Resin followed by a short column of silica gel to remove inhibitor and triethylamine base, respectively. PS macroinitiator (2.00 g, 0.0192 mmol), VDMA (1.14 g, 8.17 mmol), AIBN (1.52 mg, 0.00926 mmol), and toluene (6.7 mL) were added to an oven-dried 25 mL Schlenk tube and degassed *via* three freeze-pump-thaw cycles. Assuming ~80% VDMA monomer conversion, these reagent

quantities target the final molecular weight of the VDMA block to be 9.85 kg/mol with a corresponding volume fraction of f_{VDMA} = 0.30 in the final block copolymer based on the known homopolymer segment densities of ρ(PS) = 1.02 g/cm^3 and ρ(PVDMA) = 1.08 g/cm^3. The solution was stirred in a 70 °C oil bath for 24 h, after which the tube was rapidly cooled by immersion in liquid nitrogen. The resulting solution was diluted with ~3 mL of THF, precipitated in ~250 mL of cold hexanes and collected, redissolved in ~10 mL of THF, re-precipitated in cold hexanes, and freeze-dried from benzene to yield a white powder. Quantitative ^{1}H NMR analysis of molecular weight compared to the PS macro-RAFT agent revealed that $M_{n,NMR,VDMA}$ = 7.80 kg/mol with $Đ$ = 1.20 (against PS standards) and f_S = 0.75. ^{1}H NMR (400.182 MHz, $CDCl_3$, δ ppm): 1.26-2.17 (*m*, 5H, (-C<u>H</u>$_2$-C<u>H</u>)-(C<u>H</u>$_2$-CH-) and *s*, 6H, -$(CH_3)_2$), 2.70 (*s*, 1H, azlactone, (-CH$_2$-C<u>H</u>-)), 6.29-6.83 (*m*, 2H, aromatic), 6.85-7.23 (*m*, 3H, aromatic). ATR IR (cm^{-1}): C-H *sp*^{2} 3024 cm^{-1}, C-H *sp*^{3} 2920 cm^{-1}, C=O azlactone 1819 cm^{-1}, C=N azlactone 1670 cm^{-1}, C-O-C azlactone 1200 cm^{-1}. Note that FTIR analyses indicate that the azlactone ring was not hydrolyzed during polymerization or polymer isolation by the presence of adventitious water; ring-opening gives rise to peaks corresponding to NH stretching ~3200 cm^{-1}, C=O amide stretching ~1650 cm^{-1}, NH bending ~1540 cm^{-1}, and C=O carboxylic acid stretching ~1730 cm^{-1}, which are absent.[40] PS-*b*-PVDMA-2 ($M_{n,GPC,S}$ = 12.9 kg/mol; $M_{n,NMR,VDMA}$ = 5.34 kg/mol; $Đ$ = 1.18; f_S = 0.72) and PS-*b*-PVDMA-3 ($M_{n,GPC,S}$ = 9.25 kg/mol; $M_{n,NMR,VDMA}$ = 3.70 kg/mol; $Đ$ = 1.20; f_S = 0.73) were synthesized by analogous methods and exhibited similar spectral characteristics.

RAFT Synthesis of Poly(2-vinyl-4,4-dimethylazlactone) (PVDMA). Freshly distilled VDMA (2 g, 14.3 mmol), AIBN (1.6 mg, 9.48 μmol), RAFT chain-transfer agent 2-cyano-2-propylbenzodithioate (10.5 mg, 47.5 μmol), and anhydrous toluene (8 mL) were added to an

oven-dried 25 mL Schleck tube and degassed *via* three freeze-pump-thaw cycles. The flask was backfilled with argon and stirred in a 60 °C oil bath for 6 h. The resulting polymer was precipitated in ~200 mL of hexanes and collected, redissolved in ~5 mL of THF, re-precipitated in ~200 mL of cold hexanes, and dried overnight under high vacuum. $M_{n,GPC}$ = 39.7 kg/mol; $Đ$ = 1.1.

Small Angle X-Ray Scattering (SAXS). Temperature-dependent laboratory source SAXS measurements were performed in the Materials Science Center at the University of Wisconsin—Madison for PS-*b*-PVDMA-2 and PS-*b*-PVDMA-3. Analyses were performed using Cu-Kα X-rays generated by a Rigaku Micromax 002+ microfocus source coupled with a Max-Flux multilayer confocal optic (Osmic, Inc.), which were collimated by three pinholes to trim the final beam diameter to ≤ 0.5 mm. Samples were mounted in a vacuum chamber on a Linkam hot-stage and equilibrated at 150 °C for 15 min prior to data collection (typical exposure times ~20 min). Two-dimensional SAXS patterns were recorded on a Gabriel X-ray detector (150 mm diameter active circular area) using a sample-to-detector distance of 2 meters (calibrated using a silver behenate standard sample with d = 58.38 Å). 2D SAXS patterns were azimuthally–integrated using the DataSqueeze software package (figShare http://dx.doi.org/10.6084/m9.figshare.644515) to obtain one-dimensional scattering profiles.

Synchrotron SAXS measurements were performed for PS-*b*-PVDMA-1 at the 12-ID-B beamline at the Advanced Photon Source (Argonne, IL) using a beam energy of 14 keV (λ = 0.886 Å) and a sample to detector distance of 1.99 m, as calibrated using a silver behenate standard.. Two-dimensional SAXS patterns were recorded on a Pilatus 2M detector (25.4 cm x 28.9 cm rectangular area) with a 1475 x 1679 pixel resolution. Prior to SAXS analysis, samples were loaded into a hermetically sealed aluminum DSC pan and thermally annealed at 150 °C for

10 hours at 1 Torr to induce block copolymer ordering, followed by cooling to 22 °C. SAXS data was collected at 25 °C (exposure time = 1 sec). 2D-SAXS patterns were azimuthally integrated to obtain one-dimensional intensity ($I(q)$) *versus* scattering wavevector (q) plots and analyzed using freely available procedures in Igor Pro (Wavemetrics, Inc.).[53]

Fabrication and Self-Assembly of PS-*b*-PVDMA Thin Films. Silicon wafers were cleaned using piranha solution (7:3 H_2SO_4 : 30% H_2O_2; *caution! strongly oxidizing solution!*) at 75 °C for 20 min and then washed copiously with deionized water prior to drying under a stream of compressed air. PS-*b*-PVDMA-1 was dissolved in toluene at (0.8 wt%), filtered through a 0.2 μm syringe filter, and then spin-coated onto silicon wafers to give thin films (~24 nm thick, as determined by ellipsometry; Rudolph Research Auto EL). Thermal annealing was conducted at 150 °C for 4 h under vacuum (80 Torr). Solvent vapor annealing was performed by placing film coated substrates into a sealed 350 mL glass jar containing 15 mL of toluene for pre-determined periods of time.

Polarization Modulation Infrared Reflection-Adsorption Spectroscopy (PM-IRRAS) Analysis of Thin Films. Solutions of PVDMA homopolymer (0.8 wt% in toluene) were spin-coated onto gold substrates (~1000 Å thick, Model TA134, EMF Corporation, Ithaca, NY) coated with a thin layer of silicon dioxide (SiO_2, >10 nm) to give PVDMA homopolymer films ~28 nm thick. For PM-IRRAS measurements, samples were placed at an incident angle of 83° in a Nicolet Magna-IR 860 FTIR spectrophotometer (Thermo Fisher Scientific, Waltham, MA) equipped with a PEM-90 photoelastic modulator (Hinds Instruments, Hillsboro, OR), a SSD-100 synchronous sampling demodulator (GWC Technologies, Madison, WI), and a liquid nitrogen

cooled mercury–cadmium–telluride (MCT) detector. An aperture value of 20 in the OMNIC software settings was selected, which sets the IR beam spot size to 4.75 mm. The photoelastic modulation was set to 1600 cm^{-1} and 500 scans were obtained for each sample at a resolution of 8 cm^{-1}. Obtained differential reflectance IR spectra were normalized and converted to absorbance spectra using the OMNIC software package.

X-Ray Photoelectron Spectroscopy (XPS) Analysis of PS-*b*-PVDMA Thin Films. Solvent annealed PS-*b*-PVDMA thin films were immersed for 1 h at room temperature in a solution of 3-iodobenzylamine (5 mg/mL in ethanol) after which they were removed, rinsed with ethanol, and dried under a stream of compressed nitrogen gas. XPS analysis was performed using a Thermo Scientific Model K-Alpha XPS instrument using monochromatic Al Kα radiation (1486.7 eV). The instrument was outfitted with a hemispherical electron energy analyzer equipped with a 128 multichannel detector system. Survey spectra and high-resolution spectra were acquired using analyzer pass energies of 200 eV and 50 eV, respectively. The X-ray spot size was 400 μm for single point analysis. Depth-profiling was performed using Argon clusters (4000 eV) for etching, and data were collected every 30 sec using the 'snap capture' function and subsequently analyzed using Avantage XPS software package. Peak fitting was performed using Gaussian/Lorentzian peak shapes and a Shirley/Smart-type background correction.

Sequential Infiltration Synthesis (SIS) Using Cylindrical PS-*b*-PVDMA Thin Films. SIS experiments were performed using a MSL-110-NT tube furnace (MTI Co., Richmond, CA) using nitrogen as a carrier gas at 40 sccm at a chamber base pressure of ~500 mTorr. BCP thin film samples were loaded into the tube furnace at 85 °C and subjected to three repeated cycles of

trimethylaluminum for 2 s and water vapor for 0.1 s. Any remaining organic materials were subsequently removed by exposure to O_2 plasma (50 W, 10 mTorr, 10 sccm) for 20 sec.

Results and Discussion

PS-b-PVDMA Thin Film Self-Assembly: Thermal and Solvent Annealing

Our approach to the fabrication of reactive nanoscale patterns exploits the self-assembly of amine-reactive, azlactone-containing BCPs. We previously reported the self-assembly of a nearly symmetric PS-*b*-PVDMA BCP (M_n = 33.6 kg/mol, $Đ$ = 1.33, f_S = 0.48) into lamellar thin films, and demonstrated that their thermal annealing on a random copolymer neutral mat yielded perpendicularly-ordered domains with relatively high defect densities and poor long-range order.[39] Here, we report on the self-assembly of a cylinder-forming PS-*b*-PVDMA BCP in both the bulk and thin film regime with the goals of (i) expanding the range of morphologies and reactive surface patterns accessible using PS-*b*-PVDMA, and (ii) exploring the potential for solvent annealing methods to access microphase separated thin films and to minimize interactions that can prevent long-range ordering in reactive PS-*b*-PVDMA films self-assembled by thermal annealing.

We synthesized a series of PS-*b*-PVDMA BCPs using sequential reversible-addition fragmentation chain-transfer (RAFT) polymerization[39, 43] targeting minority volume fractions of VDMA expected to lead to self-assembled hexagonal or cylindrical morphologies. Figure 1A shows a high-resolution synchrotron small-angle X-ray scattering (SAXS) 1D intensity profile for a bulk sample of PS-*b*-PVDMA-1 (M_n = 33.6 kg/mol, $Đ$ = 1.33; f_S = 0.75) acquired at 25 °C after extended thermal annealing (at 150 °C, 10 hours, 1 Torr). The primary scattering peak at q^* = 0.0265 Å^{-1}, together with the presence of higher-ordered scattering peaks at $\sqrt{3}q^*$ (11), $\sqrt{7}q^*$

(21), and $\sqrt{9}q^*$ (30), indicates that this BCP self-assembles into a hexagonally-packed cylindrical morphology in the bulk, with a d-spacing of 23.7 nm and a cylinder center-to-center distance of 27.4 nm (based on the location of q^*). We also synthesized BCPs of lower molecular weights and similar compositions to determine whether smaller domain spacings were accessible in this cylinder-forming system. PS-*b*-PVDMA-2 (M_n = 18.2 kg/mol, $Đ$ = 1.18; f_S = 0.72) self-assembled into a cylindrical morphology with a domain spacing of 19.1 nm, whereas PS-*b*-PVDMA-3 (M_n = 12.9 kg/mol, $Đ$ = 1.20; f_S = 0.73) was disordered by lab-source SAXS analysis. Based on these results, we conclude that there is a molecular weight-dependent order-to-disorder transition between 18.2 < M_n < 12.9 kDa, and that sub-20 nm domain spacing are accessible. With further development, these materials could thus be useful in nanolithography applications; we return to this point in the discussion below. For all of the proof of concept studies reported below, we used PS-*b*-PVDMA-1 as a model BCP and refer to this polymer from here on simply as 'PS-*b*-PVDMA' for brevity.

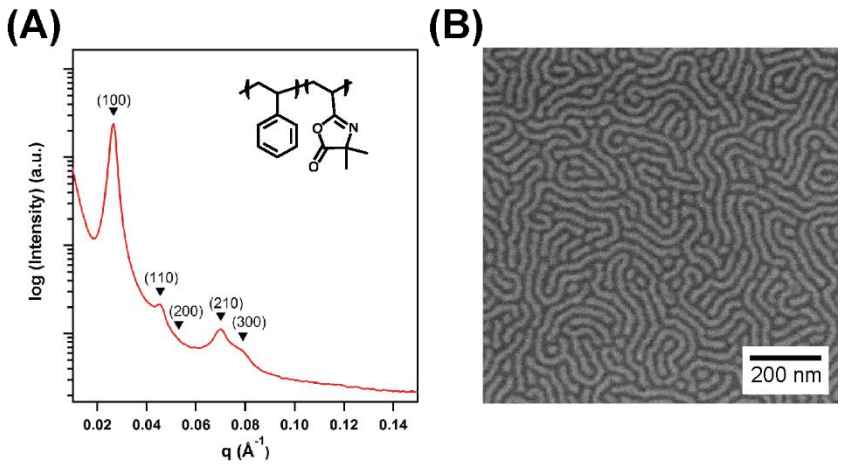

Figure 1. (A) Azimuthally-integrated room temperature SAXS pattern for PS-*b*-PVDMA after thermal annealing at 150 °C. The peak markers for PS-*b*-PVDMA correspond to the calculated peak positions of a cylindrical morphology, with a principal scattering vector, q^* = 0.0265 Å^{-1}. (B) SEM image of a perpendicularly-oriented cylindrical thin film obtained by spin-coating and thermal annealing of PS-*b*-PVDMA at 150 °C for 4 h on a silicon substrate.

Figure 1B shows a top-down SEM image of a thin film of PS-*b*-PVDMA on a silicon substrate after thermal annealing at 150 °C for 4 h. This image reveals characteristic dark circular domains in a matrix of lighter contrast consistent with a 2D–hexagonal self-assembled morphology in which the cylinders are oriented parallel to the substrate. Based on this image and the composition of the polymer, we conclude that the dark domains correspond to the PVDMA block, with diameters of 12.0 ± 1.9 nm and a cylinder center-to-center distance of 29.6 ± 1.8 nm. This increase in apparent center-to-center distance in the thin film regime (as compared to the value measured in the bulk material by SAXS; see Figure 1A) is likely due to surface reconstruction that can occur due to domain pinning. Discontinuities in the morphology, as well as relatively small grain sizes and a mixed morphology consisting of PS dots (light areas), can be observed throughout the film (Figure 1B). This morphology is qualitatively similar to that of samples of symmetric (lamellae-forming) PS-*b*-PVDMA BCPs self-assembled in previous studies by thermal annealing on non-preferential P(S-*r*-MMA-*r*-GMA) random copolymer mats[39] (i.e., these samples share a lack of long-range order and high defect density), suggesting incomplete self-assembly. Based on these SEM images and the reactive nature of the azlactone group, we hypothesized that the PVDMA blocks could react with the underlying silicon substrate or neutral mat used in past studies during thermal annealing in ways that could inhibit complete self-assembly.

The ring-opening of azlactone groups during thermal annealing could prevent the formation of an equilibrium structure in multiple ways. For example, (i) the volumetric expansion of the PVDMA block and (ii) changes in the interaction parameter between the PS and PVDMA domains, as well as (iii) physical or chemical interactions that could ‘pin’ the PVDMA domains to the substrate and reduce mobility leading to the formation or trapping of defects. To

provide insight into whether the azlactone functionality in PS-*b*-PVDMA could undergo physicochemical changes during thermal annealing that could change the nature of interactions with an underlying silicon substrate, we spin-coated a PVDMA homopolymer ($M_{n,GPC}$ = 39.7 kg/mol; $Đ$ = 1.1) from toluene (0.8 wt%) onto a silicon oxide-coated (~10 nm) gold substrate and characterized chemical changes in the azlactone functional group under both thermal annealing and solvent annealing conditions using IR spectroscopy. Figure 2A shows polarization modulated internal reflectance-absorption infrared (PM-IRRAS) spectra of an as-spun PVDMA homopolymer thin film, as well as spectra for samples obtained after thermal annealing at 160 °C for 4 h and toluene vapor solvent annealing (see Materials and Methods for complete details).

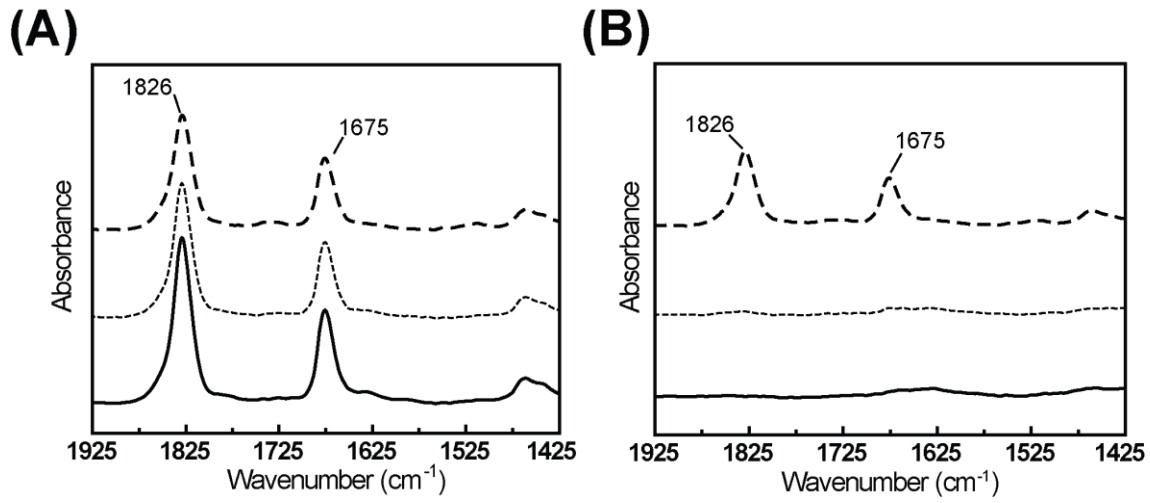

Figure 2. PM-IRRAS spectra obtained using PVDMA thin films spin-coated onto silicon oxide-coated gold substrates. (A) Films as-spun: no treatment (solid trace), after solvent annealing in toluene vapor (dotted trace), and after thermal annealing at 160 °C for 4 h (dashed trace). (B) Films after washing with THF: as-spun film (solid trace), solvent annealed film (dotted trace), and thermally annealed film (dashed trace). The azlactone carbonyl (C=O) and azlactone cyclic imine stretch (C=N) are observed at ~1826 and ~1675 cm^{-1}, respectively (see text).

Inspection of these results reveals that the azlactone functionality in PVDMA remains largely intact after both thermal and solvent annealing (C=O azlactone stretch, ~1826 cm^{-1}; C=N

azlactone stretch, ~1675 cm^{-1}) and that prominent signature peaks characteristic of azlactone ring-opening are undetected (C=O amide stretch, ~1650 cm^{-1}; NH bend, ~1540 cm^{-1}).[4, 40] Figure 2B shows IR spectra of these three samples after immersing and washing with THF solvent to remove any free PVDMA. Both the as-spun (untreated and un-annealed) and the solvent annealed samples were devoid of any residual PVDMA polymer. In contrast, the IR spectrum of the thermally annealed sample reveals the presence of residual PVDMA on the silicon substrate (as determined by peaks at ~1826 cm^{-1} and ~1675 cm^{-1}). These results suggest that thermal annealing induces strong interactions between the polymer and the substrate. Although our present results do not rule out other potential contributions, these interactions could occur through a small number of azlactone groups ring-opening by reaction with surface-hydroxyl groups present at the polymer/substrate interface. Such reactions could effectively 'pin' the polymer to the substrate, thereby reducing chain mobility and hindering formation of defect-free and long-range self-assembled morphologies.[51, 54] Ellipsometric film thickness measurements furnish further evidence in support of this hypothesis. Film thickness after thermal annealing measured ~28 nm; after washing with THF, the thicknesses decreased to ~25 nm, confirming that the polymer film had not been removed from the surface. In contrast, samples that were solvent annealed and then washed with THF were completely removed from the substrate, in agreement with the IR data. Although the IR spectra in Figure 2A and B for the thermally annealed thin films do not reveal peaks diagnostic of azlactone ring-opening reactions, our concern over the potential for these reactions and the visual differences between the thermally annealed and solvent annealed samples (*vide supra*; Figure 1B *c.f.* Figure 3 below) motivated the selection and further characterization of solvent vapor annealing approaches in all subsequent studies.

Characterization of PS-b-PVDMA Thin Film During Solvent Annealing and the Evolution of Self-Assembled Morphologies

We used solvent vapor annealing techniques to obtain cylinder-forming PS-*b*-PVDMA thin films using toluene. Toluene was chosen as the solvent for these studies because it is a good solvent for the PS block (δ_{tol} - δ_{PS} = 0.3 $MPa^{1/2}$).[55-57] However, the kinetics of self-assembly is a function of chain length, and it may take hours to drive higher degree of ordering. During solvent annealing, one block preferentially swells with solvent, thus reducing the glass transition temperature (T_g) and lowering the effective interaction parameter between the blocks to promote microphase separation and self-assembly.[56-58] A primary advantage of solvent annealing relative to thermal annealing is that the microdomain orientation (parallel *or* perpendicular with respect to the substrate) can be controlled by judicious choice of solvent and annealing time, obviating the need to regulate interfacial energies by employing non-preferential layers at the interfaces (e.g., substrate/BCP thin film and BCP thin film/air interfaces).

Figure 3 shows SEM images of the time-based evolution of microphase separated morphologies in a 28 nm thick PS-*b*-PVDMA film upon exposure to toluene vapor (see Materials and Methods for complete solvent annealing details). Inspection of these images reveals that, from 15 min to 3 h (Figure 3A-D), film morphology evolves from one that lacks any long-range orientational order to well-ordered VDMA cylinders that are perpendicularly-oriented with respect to the substrate. Figure 3D reveals a PVDMA cylinder diameter of 11.7 ± 1.2 nm and a cylinder center-to-center distance of 25.2 ± 2.6 nm. This center-to-center distance is slightly smaller than that obtained by SAXS measurements on the bulk BCP (see Figure 1A) and likely a result of surface reconstruction during solvent annealing. With extended annealing over 3 to 18 h (Figure 3D, E), the VDMA cylinders gradually transitioned from a perpendicular to a

parallel orientation with respect to the substrate, and further prolonged exposure (e.g., 24 h or more; Figure 3F) resulted in a featureless film. The results of these experiments underscore the utility of solvent annealing as a method for controlling the microdomain orientation and achieving defect-free and well-ordered thin film morphologies in reactive PS-*b*-PVDMA BCPs.

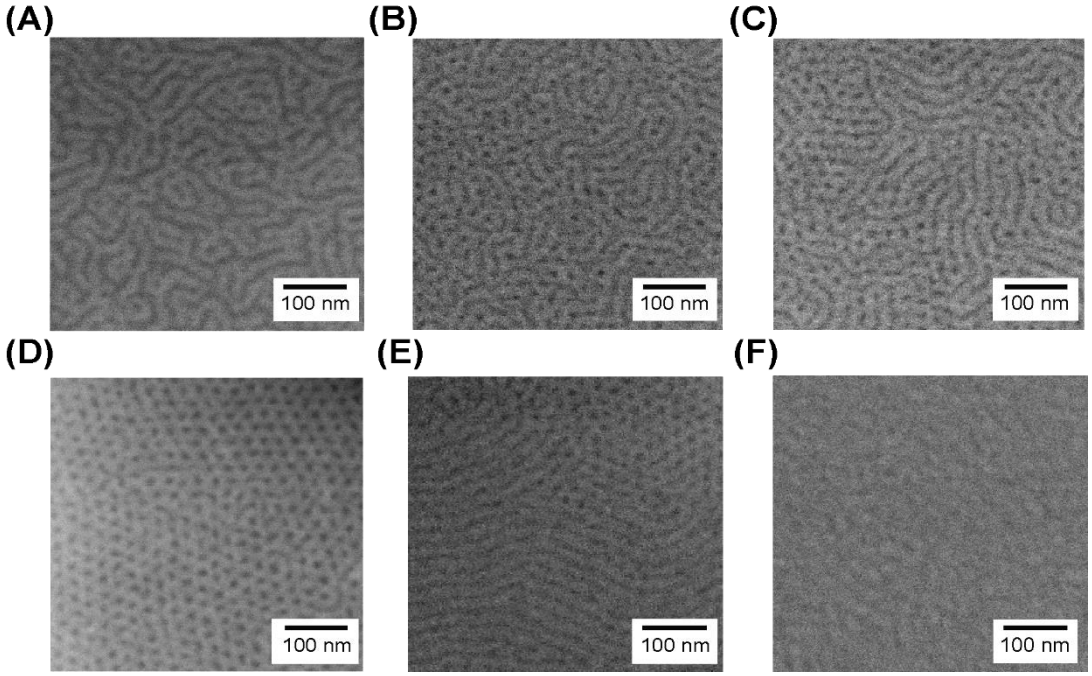

Figure 3. SEM images showing the evolution of microstructure in spin-coated and solvent annealed thin films of cylinder-forming PS-*b*-PVDMA on silicone substrate. Samples were annealed in toluene vapor for (a) 15 min, (b) 1 hour, (c) 2 hours, (d) 3 hours, (e) 18 hours, and (f) 24 hours.

Characterization of Thin Film Reactivity Using XPS

We selected 3-iodobenzylamine as a model compound to characterize the accessibility and reactivity of azlactone groups in perpendicularly-oriented cylindrical thin films of PS-*b*-PVDMA because it contains an iodine atom that should facilitate analysis by X-ray photoelectron scattering (XPS) spectroscopy. Figure 4A shows an SEM image of a perpendicularly-ordered film (i.e., as in Figure 3B) after incubation with a solution of

iodobenzylamine in ethanol (5 mg/mL, 1 hour, room temperature) and confirms that the self-assembled morphology has not been disrupted or otherwise lost under these post-fabrication treatment conditions (ethanol is a non-solvent for PS-*b*-PVDMA). Figure 4C shows the results of XPS analysis of thin films before (black) and after (red) treatment with iodobenzylamine. The absence of iodine peaks in the spectrum of the unfunctionalized sample, coupled with the appearance of iodine $3d_{3/2}$ (630 eV) and iodine $3d_{5/2}$ (620 eV) peaks in the iodobenzylamine-treated sample, confirms that iodobenzylamine has been incorporated into the thin film.

From the reaction stoichiometry, the ratio of nitrogen to iodine atoms, N:I, is expected to be 2:1. However, Figure 4D shows a summary of the XPS analyses and reveals that the observed ratio is closer to 3:1, suggesting that the reaction of azlactone groups with iodobenzylamine does not go to completion under these conditions. This result is not entirely surprising given the poor solubility of the PVDMA in the ethanolic reaction solvent used here. Characterization of these iodobenzylamine-treated samples in XPS depth-profiling experiments suggested that reactions between azlactones and the incoming amine occurred primarily at the surface and in the top-most regions of the thin films. Figure 4E shows a plot of atomic abundance against etch time and depth into the film; the intensity of the iodine signal decreases rapidly after etching ~4 nm into the film (signal multiplied by a factor of 10). This result, combined with the data shown in Figure 4D suggests that functionalization of the VDMA groups is largely confined to the film/solvent interface under the conditions used here. It is possible that the extent of functionalization and the penetration depth of the reaction could be improved or modulated by investigating other solvent choices, or mixtures of solvents. Our results, however, demonstrate that it is possible to selectively functionalize the surfaces of these films and produce gradients of functionality in specific domains of these reactive materials (presumably based on the poor

solubility and slow diffusion of the amine-containing compound into the cylindrical VDMA domains).

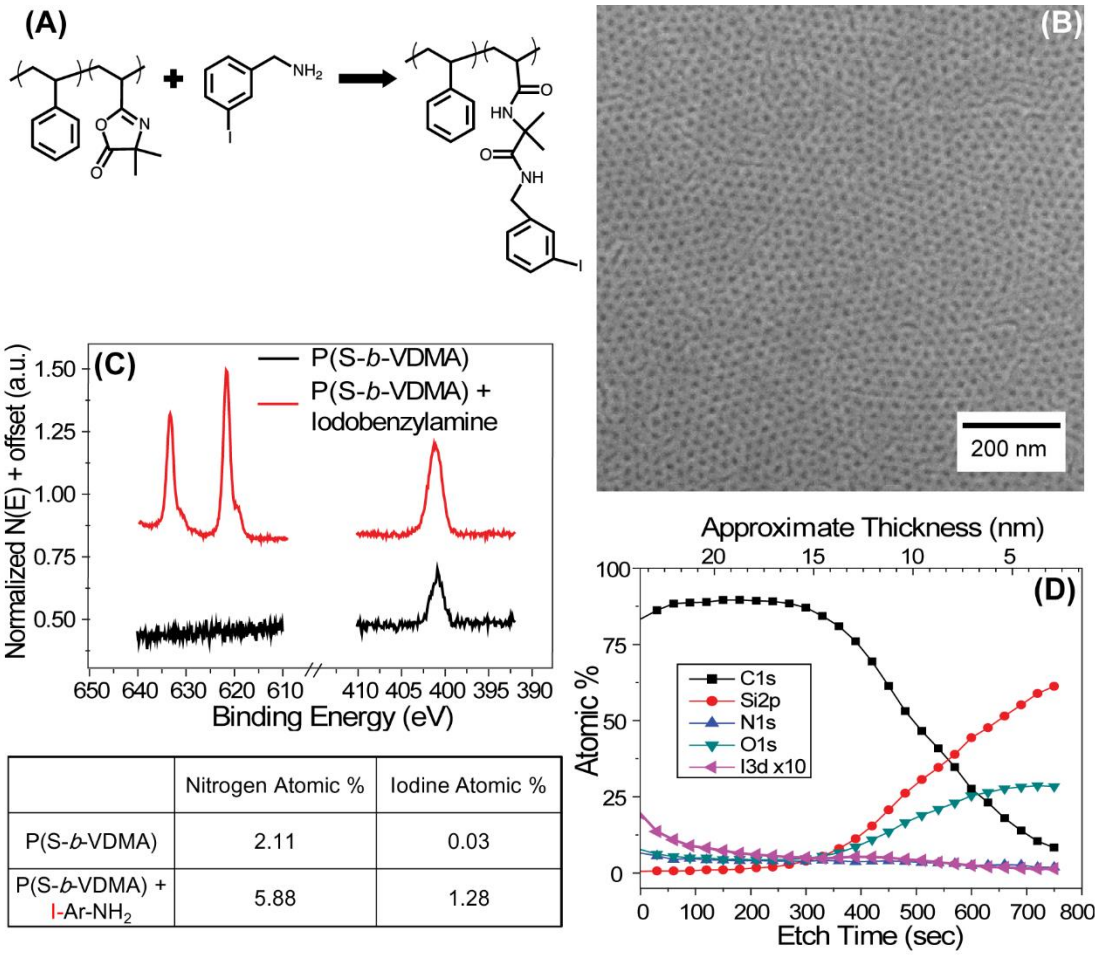

	Nitrogen Atomic %	Iodine Atomic %
P(S-*b*-VDMA)	2.11	0.03
P(S-*b*-VDMA) + I-Ar-NH_2	5.88	1.28

Figure 4. (A) Scheme showing the ring-opening of azlactone groups in the PVDMA block of PS-*b*-PVDMA by iodobenzylamine. (B) Top-down SEM image of perpendicularly-oriented PS-*b*-PVDMA after iodobenzylamine coupling. (C) Table summarizing the XPS-derived nitrogen and iodine atomic percentage before and after PS-*b*-PVDMA thin-film functionalization with iodobenzylamine along with the spectra. (D) XPS depth profiling results showing the relative atomic percentage of nitrogen, iodine, oxygen, carbon, and silicon as a function of etch depth into the film. Depth-profiling was performed using argon gas clusters with an energy of 4000 eV and data was collected every 30 s. The iodine signal has been multiplied by a factor of 10.

Fabrication of Lithographic Hard Masks by Sequential Infiltration Synthesis

To demonstrate the utility of self-assembled PS-*b*-PVDMA thin films beyond solution phase interfacial functionalization, we used vapor phase infiltration to create nanostructured hard masks for potential applications in BCP lithography. Past studies have shown that trimethylaluminum (TMA) vapor can be selectively infused into specific domains of self-assembled poly(styrene-*block*-methyl methacrylate) (PS-*b*-PMMA)[59-61] and poly(*t*-butyl styrene-*block*-2-vinylpyridine) (P*t*BS-*b*-P2VP)[62] thin films promoted by MMA or 2VP chelation interactions, and that, depending on the thin film morphology used, the subsequent transformation of infused TMA can yield arrays of aluminum oxide (ALO) nanowires or nanodots. This process, known collectively as sequential infiltration synthesis (SIS), is useful for the fabrication of new metal-containing nanostructures and has been investigated for the design of hard masks useful for advanced lithography.[59-63] Overall, the success of this approach is dependent on many factors, including the affinity of the pendant side-chain groups in the BCP thin film for TMA and other SIS precursors. For example, if the total degree of incorporation of metal vapor is low, then the resulting nanostructures may incompletely mimic the template, contain defects, or fail to form contiguous arrays. We reasoned that the azlactone heterocycle present in PS-*b*-PVDMA, which contains two polar groups capable of binding to metal species (i.e., a carbonyl and an imine), could be used to host TMA and provide new platforms for the development of inorganic nanostructures by SIS. This view of microphase separated films of PS-*b*-PVDMA regards the azlactone groups in PVDMA-rich domains as potential sinks for the infusion and chelation of TMA, rather than as reactive domains for the covalent immobilization of amine-based functionality, as in the examples described above.

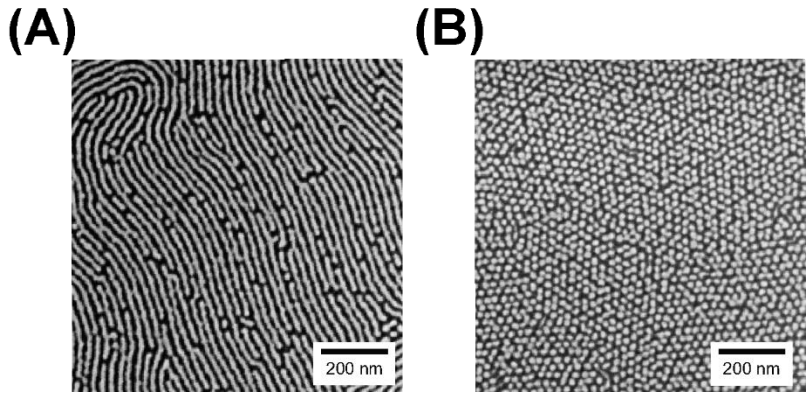

Figure 5. SEM images of alumina nanostructures obtained from sequential infiltration synthesis using trimethylaluminum vapors in cylinder-forming PS-*b*-PVDMA thin films (A) oriented parallel and (B) oriented perpendicular to the substrate. The microstructure of the film in (A) was obtained by solvent annealing in toluene for 15 h, while the microstructure of the film in (B) was obtained by solvent annealing in toluene for 4 h. Both samples were etched with O_2 plasma to remove organic residue before imaging the alumina nanostructures.

To explore the feasibility of this approach and demonstrate proof of concept, we performed an initial series of experiments in which parallel and perpendicular cylindrical PS-*b*-PVDMA films were exposed to cycles of TMA vapor and then treated with O_2 plasma to remove remaining organic material and reveal the alumina features (see Materials and Methods for complete details). Figure 5A shows top-down SEM images of well-defined alumina nanowires resulting from SIS using a template film composed of parallel cylinders. Figure 5B shows alumina nanodots resulting from experiments using a perpendicularly-oriented template. Inspection of these images reveals inorganic ALO-based nanostructures that are densely packed, relatively defect-free, and that mimic the original pattern present in the BCP thin films. In both cases, the feature sizes of these nanostructures are slightly larger than the domain sizes in the native solvent-annealed template films (alumina cylinders and dots ~17.0 ± 1.4 nm in diameter; as compared to ~11.7 ± 1.2 nm). The difference observed here could potentially arise from greater incorporation of the TMA vapor precursor mediated by the azlactone groups in PS-*b*-

PVDMA relative to the functionalities in other polymers. Additional studies will be required to fully understand the nature of the molecular interactions that lead to the infusion of TMA into these materials, including the extent to which the ring-opening of the pendant azlactone groups (to yield carboxylic acid functionality) could also influence the extent of TMA infusion during SIS. Our current results do, however, suggest the potential utility of this PS-*b*-PVDMA platform for future applications in hard-mask nanolithography and for the directed self-assembly of metallic nanostructures.

Conclusions

Approaches to the 'bottom-up' design of nanostructured soft materials and interfaces present unique opportunities to control the spatial organization and presentation of chemical and biological functionalities for next-generation applications in materials science. We have described a platform for the self-assembly and post-fabrication modification of a reactive BCP thin film that microphase separates into both parallel and perpendicular cylinders. Our approach exploits poly(styrene-*block*-2-vinyl-4,4-dimethylazlactone) (PS-*b*-PVDMA) BCPs that contain the amine-reactive azlactone functional group and can self-assemble in cylindrical thin films with ~12 nm feature sizes.

We have reported methods for the solvent annealing of BCP thin films with toluene that side-step issues associated with the pinning of polymer chains encountered using thermal annealing, ultimately leading to defect-free morphologies over large areas. These parallel and perpendicular morphologies present alternating nanoscale lines or dots of reactive azlactone functionality, respectively, which can be exploited to immobilize amine-containing functionalities. Using a model amine-containing compound, we show by XPS and depth-

profiling analyses that ring-opening reactions with azlactones are confined primarily to the uppermost ~ 4 nm of a thin film, suggesting opportunities to pattern diverse functionality selectively at the thin film/air interface. In addition, using vapor phase infiltration of a metal precursor, we converted the VDMA domains to alumina nanowires and nanodots, demonstrating the utility of self-assembled PS-*b*-PVDMA thin films in generating nanometer-sized hard masks for potential applications in advanced lithography. Our work resolves challenges associated with the self-assembly of reactive BCP thin films, and highlights both the diversity of azlactone-containing thin film morphologies that can be accessed using PS-*b*-PVDMA BCPs as well as myriad possibilities for post-fabrication functionalization of thin films with organic and inorganic moieties as a route to create new functional nanostructured surfaces.

Acknowledgments. This work was supported by the U.S. National Science Foundation Nanoscale Science and Engineering Center at UW–Madison (DMR–0832760) and made use of NSF–supported facilities (DMR–0832760, DMR–1121288 and CHE–1048642). J.C and P.G acknowledge NSF-CMMI grant 1462771 for support. We acknowledge support from the staff and the use of equipment at the Materials Science Center, Wisconsin Center for Microelectronics, and Soft Materials Lab. We thank Xudong Wang and Zhaodong Li for allowing us to conduct the SIS process on their atomic layer deposition system. We thank Dominic Perroni for organizing synchrotron SAXS studies conducted at Sector 12 of the Advanced Photon Source, a U.S. Department of Energy (DOE) Office of Science User Facility operated for the DOE Office of Science by Argonne National Laboratory under Contract No. DE-AC02-06CH11357. M.C.D.C. acknowledges the Natural Sciences Engineering Research Council of Canada for a graduate fellowship.

References

1. Boaen, N. K.; Hillmyer, M. A. Post-polymerization functionalization of polyolefins. *Chem. Soc. Rev.* **2005**, *34*, 267-275.

2. Fournier, D.; Hoogenboom, R.; Schubert, U. S. Clicking polymers: a straightforward approach to novel macromolecular architectures. *Chem. Soc. Rev.* **2007**, *36*, 1369-1380.

3. Golas, P. L.; Matyjaszewski, K. Marrying click chemistry with polymerization: expanding the scope of polymeric materials. *Chem. Soc. Rev.* **2010**, *39*, 1338-1354.

4. Buck, M. E.; Lynn, D. M. Azlactone-functionalized polymers as reactive platforms for the design of advanced materials: Progress in the last ten years. *Polym. Chem.* **2012**, *3*, 66-80.

5. Theato, P.; Klok, H.-A.; Editors, *Functional Polymers by Post-Polymerization Modification: Concepts, Guidelines, and Applications*. Wiley-VCH Verlag GmbH & Co. KGaA: **2013**; p 414 pp.

6. Günay, K. A.; Theato, P.; Klok, H.-A. Standing on the shoulders of Hermann Staudinger: Post-polymerization modification from past to present. *J. Polym. Sci., Part A: Polym. Chem.* **2013**, *51*, 1-28.

7. Tempelaar, S.; Mespouille, L.; Coulembier, O.; Dubois, P.; Dove, A. P. Synthesis and post-polymerisation modifications of aliphatic poly(carbonate)s prepared by ring-opening polymerisation. *Chem. Soc. Rev.* **2013**, *42*, 1312-1336.

8. Xi, W.; Scott, T. F.; Kloxin, C. J.; Bowman, C. N. Click Chemistry in Materials Science. *Adv. Funct. Mater.* **2014**, *24*, 2572-2590.

9. Feng, C. L.; Zhang, Z.; Förch, R.; Knoll, W.; Vancso, G. J.; Schönherr, H. Reactive Thin Polymer Films as Platforms for the Immobilization of Biomolecules. *Biomacromolecules* **2005**, *6*, 3243-3251.

10. Cullen, S. P.; Mandel, I. C.; Gopalan, P. Surface-Anchored Poly(2-vinyl-4,4-dimethyl azlactone) Brushes as Templates for Enzyme Immobilization. *Langmuir* **2008**, *24*, 13701-13709.

11. Tran, H.; Killops, K. L.; Campos, L. M. Advancements and challenges of patterning biomolecules with sub-50 nm features. *Soft Matter* **2013**, *9*, 6578-6586.

12. Broderick, A. H.; Carter, M. C. D.; Lockett, M. R.; Smith, L. M.; Lynn, D. M. Fabrication of Oligonucleotide and Protein Arrays on Rigid and Flexible Substrates Coated with Reactive Polymer Multilayers. *ACS Appl. Mater. Interfaces* **2013**, *5*, 351-359.

13. Hansen, R. R.; Hinestrosa, J. P.; Shubert, K. R.; Morrell-Falvey, J. L.; Pelletier, D. A.; Messman, J. M.; Kilbey, S. M.; Lokitz, B. S.; Retterer, S. T. Lectin-Functionalized Poly(glycidyl methacrylate)-block-poly(vinyldimethyl azlactone) Surface Scaffolds for High Avidity Microbial Capture. *Biomacromolecules* **2013**, *14*, 3742-3748.

14. Lahann, J.; Balcells, M.; Lu, H.; Rodon, T.; Jensen, K. F.; Langer, R. Reactive Polymer Coatings: A First Step toward Surface Engineering of Microfluidic Devices. *Anal. Chem.* **2003**, *75*, 2117-2122.

15. Schmitt, S. K.; Trebatoski, D. J.; Krutty, J. D.; Xie, A. W.; Rollins, B.; Murphy, W. L.; Gopalan, P. Peptide Conjugation to a Polymer Coating via Native Chemical Ligation of Azlactones for Cell Culture. *Biomacromolecules* **2016**, *17*, 1040-1047.

16. Dorr, M.; Zentel, R.; Dietrich, R.; Meerholz, K.; Brauchle, C.; Wichern, J.; Zippel, S.; Boldt, P. Reactions on Vinyl Isocyanate/Maleimide Copolymers: NLO-functionalized Polymers with High Glass Transitions for Nonlinear Optical Applications. *Macromolecules* **1998**, *31*, 1454-1465.

17. Priimagi, A.; Vapaavuori, J.; Rodriguez, F. J.; Faul, C. F. J.; Heino, M. T.; Ikkala, O.; Kauranen, M.; Kaivola, M. Hydrogen-Bonded Polymer−Azobenzene Complexes: Enhanced Photoinduced Birefringence with High Temporal Stability through Interplay of Intermolecular Interactions. *Chem. Mater.* **2008**, *20*, 6358-6363.

18. Valkama, S.; Hartikainen, J.; Torkkeli, M.; Serimaa, R.; Ruokolainen, J.; Rissanen, K.; ten Brinke, G.; Ikkala, O. Self-organized nanostructures of poly(4-vinylpyridine), polyaniline and polyamides due to metal complexation. *Macromol. Symp.* **2002**, *186*, 87-92.

19. Buck, M. E.; Schwartz, S. C.; Lynn, D. M. Superhydrophobic Thin Films Fabricated by Reactive Layer-by-Layer Assembly of Azlactone-Functionalized Polymers. *Chem. Mater.* **2010**, *22*, 6319-6327.

20. Zahner, D.; Abagat, J.; Svec, F.; Fréchet, J. M. J.; Levkin, P. A. A Facile Approach to Superhydrophilic–Superhydrophobic Patterns in Porous Polymer Films. *Adv. Mater.* **2011**, *23*, 3030-3034.

21. Feng, W.; Li, L.; Yang, C.; Welle, A.; Trapp, O.; Levkin, P. A. UV-Induced Tetrazole-Thiol Reaction for Polymer Conjugation and Surface Functionalization. *Angew. Chem., Int. Ed.* **2015**, *54*, 8732-8735.

22. Manna, U.; Lynn, D. M. Fabrication of Liquid-Infused Surfaces Using Reactive Polymer Multilayers: Principles for Manipulating the Behaviors and Mobilities of Aqueous Fluids on Slippery Liquid Interfaces. *Adv. Mater.* **2015**, *27*, 3007-3012.

23. Romulus, J.; Henssler, J. T.; Weck, M. Postpolymerization Modification of Block Copolymers. *Macromolecules* **2014**, *47*, 5437-5449.

24. Segalman, R. A. Patterning with block copolymer thin films. *Mater. Sci. Eng., R.* **2005**, *48*, 191-226.
25. Marencic, A. P.; Register, R. A. Controlling Order in Block Copolymer Thin Films for Nanopatterning Applications. *Annu. Rev. Chem. Biomol. Eng.* **2010**, *1*, 277-297.

26. Schacher, F. H.; Rupar, P. A.; Manners, I. Functional block copolymers: nanostructured materials with emerging applications. *Angew. Chem., Int. Ed. Engl.* **2012**, *51*, 7898-7921.

27. Kao, J.; Thorkelsson, K.; Bai, P.; Rancatore, B. J.; Xu, T. Toward functional nanocomposites: taking the best of nanoparticles, polymers, and small molecules. *Chem. Soc. Rev.* **2013**, *42*, 2654-2678.

28. Hu, H.; Gopinadhan, M.; Osuji, C. O. Directed self-assembly of block copolymers: a tutorial review of strategies for enabling nanotechnology with soft matter. *Soft Matter* **2014**, *10*, 3867-3889.

29. Epps, I. I. I. T. H.; O'Reilly, R. K. Block copolymers: controlling nanostructure to generate functional materials - synthesis, characterization, and engineering. *Chem. Sci.* **2016**, *7*, 1674-1689.

30. Lei, S.; Garland, A.; Yini, W.; Zicheng, L.; Bielawski, C. W.; Guo, A.; Zhu, X. Y. Two Dimensional Nanoarrays of Individual Protein Molecules. *Small* **2012**, *8*, 3169-3174.

31. Schumers, J.-M.; Vlad, A.; Huynen, I.; Gohy, J.-F.; Fustin, C.-A. Functionalized Nanoporous Thin Films From Photocleavable Block Copolymers. *Macromol. Rapid Commun.* **2012**, *33*, 199-205.

32. Zhao, H.; Gu, W.; Kakuchi, R.; Sun, Z.; Sterner, E.; Russell, T. P.; Coughlin, E. B.; Theato, P. Photocleavable Triblock Copolymers Featuring an Activated Ester Middle Block: "One-Step" Synthesis and Application as Locally Reactive Nanoporous Thin Films. *ACS Macro Lett.* **2013**, *2*, 966-969.

33. Zhao, H.; Gu, W.; Thielke, M. W.; Sterner, E.; Tsai, T.; Russell, T. P.; Coughlin, E. B.; Theato, P. Functionalized Nanoporous Thin Films and Fibers from Photocleavable Block Copolymers Featuring Activated Esters. *Macromolecules* **2013**, *46*, 5195-5201.

34. Gamys, C. G.; Schumers, J.-M.; Mugemana, C.; Fustin, C.-A.; Gohy, J.-F. Pore-Functionalized Nanoporous Materials Derived from Block Copolymers. *Macromol. Rapid Commun.* **2013**, *34*, 962-982.

35. Messerschmidt, M.; Millaruelo, M.; Choinska, R.; Jehnichen, D.; Voit, B. Thin Film Nanostructures Prepared via Self-Assembly of Partly Labile Protected Block Copolymers for Hybrid Patterning Strategies. *Macromolecules* **2009**, *42*, 156-163.

36. Riedel, M.; Stadermann, J.; Komber, H.; Simon, F.; Voit, B. Synthesis, post-modification and self-assembled thin films of pentafluorostyrene containing block copolymers. *Eur. Polym. J.* **2011**, *47*, 675-684.

37. Stadermann, J.; Riedel, M.; Komber, H.; Simon, F.; Voit, B. Functionalized block copolymers for preparation of reactive self-assembled surface patterns. *J. Polym. Sci., Part A: Polym. Chem.* **2012**, *50*, 1351-1361.

38. Stadermann, J.; Riedel, M.; Voit, B. Nanostructured Films of Block Copolymers Functionalized With Photolabile Protected Amino Groups. *Macromol. Chem. Phys.* **2013**, *214*, 263-271.

39. Speetjens, F. W., II; Carter, M. C. D.; Kim, M.; Gopalan, P.; Mahanthappa, M. K.; Lynn, D. M. Post-Fabrication Placement of Arbitrary Chemical Functionality on Microphase-Separated Thin Films of Amine-Reactive Block Copolymers. *ACS Macro Letters* **2014**, *3*, 1178-1182.

40. Heilmann, S. M.; Rasmussen, J. K.; Krepski, L. R. Chemistry and technology of 2-alkenyl azlactones. *J. Polym. Sci., Part A: Polym. Chem.* **2001**, *39*, 3655-3677.

41. Tully, D. C.; Roberts, M. J.; Geierstanger, B. H. Synthesis of Reactive Poly(vinyl oxazolones) via Nitroxide-Mediated "Living" Free Radical Polymerization. *Macromolecules* **2003**, *36*, 4302-4308.

42. Fournier, D.; Pascual, S.; Fontaine, L. Copper-mediated living radical polymerization of 2-vinyl-4,4-dimethyl-5-oxazolone. *Macromolecules* **2004**, *37*, 330-335.

43. Pascual, S.; Blin, T.; Saikia, P. J.; Thomas, M.; Gosselin, P.; Fontaine, L. Block Copolymers Based on 2-Vinyl-4,4-dimethyl-5-oxazolone by RAFT Polymerization: Experimental and Computational Studies. *J. Polym. Sci., Part A: Polym. Chem.* **2010**, *48*, 5053-5062.

44. Ho, H. T.; Levere, M. E.; Fournier, D.; Montembault, V.; Pascual, S.; Fontaine, L. Introducing the Azlactone Functionality into Polymers through Controlled Radical Polymerization: Strategies and Recent Developments. *Aust. J. Chem.* **2012**, *65*, 970-977.

45. Messman, J. M.; Lokitz, B. S.; Pickel, J. M.; Kilbey, S. M., II Highly Tailorable Materials based on 2-Vinyl-4,4-dimethyl Azlactone: (Co)Polymerization, Synthetic Manipulation and Characterization. *Macromolecules* **2009**, *42*, 3933-3941.

46. Laquievre, A.; Allaway, N. S.; Lyskawa, J.; Woisel, P.; Lefebvre, J.-M.; Fournier, D. Highly Efficient Ring-Opening Reaction of Azlactone-Based Copolymer Platforms for the Design of Functionalized Materials. *Macromol. Rapid Commun.* **2012**, *33*, 848-855.

47. Manna, U.; Zayas-Gonzalez, Y. M.; Carlton, R. J.; Caruso, F.; Abbott, N. L.; Lynn, D. M. Liquid Crystal Chemical Sensors That Cells Can Wear. *Angew. Chem., Int. Ed.* **2013**, *52*, 14011-14015.

48. Ho, H. T.; Levere, M. E.; Pascual, S.; Montembault, V.; Casse, N.; Caruso, A.; Fontaine, L. Thermoresponsive block copolymers containing reactive azlactone groups and their bioconjugation with lysozyme. *Polym. Chem.* **2013**, *4*, 675-685.

49. Jones, M. W.; Richards, S.-J.; Haddleton, D. M.; Gibson, M. I. Poly(azlactone)s: versatile scaffolds for tandem post-polymerisation modification and glycopolymer synthesis. *Polym. Chem.* **2013**, *4*, 717-723.

50. Carter, M. C. D.; Lynn, D. M. Covalently Crosslinked and Physically Stable Polymer Coatings with Chemically Labile and Dynamic Surface Features Fabricated by Treatment of Azlactone-Containing Multilayers with Alcohol-, Thiol-, and Hydrazine-Based Nucleophiles. *Chem. Mater.* **2016**, *28*, 5063-5072.

51. Han, E.; Gopalan, P. Cross-Linked Random Copolymer Mats As Ultrathin Nonpreferential Layers for Block Copolymer Self-Assembly. *Langmuir* **2010**, *26*, 1311-1315.

52. Lai, J. T.; Filla, D.; Shea, R. Functional Polymers from Novel Carboxyl-Terminated Trithiocarbonates as Highly Efficient RAFT Agents. *Macromolecules* **2002**, *35*, 6754-6756.

53. Schmitt, A. K.; Mahanthappa, M. K. Igor Pro Procedures for Analyzing Dynamic Light Scattering, Rheology, and Synchrotron X-ray Scattering Data. **figShare** http://dx.doi.org/10.6084/m9.figshare.644515.

54. Zdyrko, B.; Klep, V.; Luzinov, I. Synthesis and Surface Morphology of High-Density Poly(ethylene glycol) Grafted Layers. *Langmuir* **2003**, *19*, 10179-10187.

55. Hansen, C. M. Hansen Solubility Parameters-A User's Handbook. *Boca Raton, FL: CRC Press* **2007**.

56. Jung, Y. S.; Ross, C. A. Orientation-controlled self-assembled nanolithography using a polystyrene−polydimethylsiloxane block copolymer. *Nano Lett.* **2007**, *7*, 2046-2050.

57. Jung, Y. S.; Ross, C. A. Solvent-Vapor-Induced Tunability of Self-Assembled Block Copolymer Patterns. *Adv. Mater.* **2009**, *21*, 2540-2545.

58. Sinturel, C.; Vayer, M.; Morris, M.; Hillmyer, M. A. Solvent vapor annealing of block polymer thin films. *Macromolecules* **2013**, *46*, 5399-5415.

59. Peng, Q.; Tseng, Y. C.; Darling, S. B.; Elam, J. W. Nanoscopic patterned materials with tunable dimensions via atomic layer deposition on block copolymers. *Adv. Mater.* **2010**, *22*, 5129-5133.

60. Peng, Q.; Tseng, Y.-C.; Darling, S. B.; Elam, J. W. A route to nanoscopic materials via sequential infiltration synthesis on block copolymer templates. *ACS Nano* **2011**, *5*, 4600-4606.

61. Ruiz, R.; Wan, L.; Lille, J.; Patel, K. C.; Dobisz, E.; Johnston, D. E.; Kisslinger, K.; Black, C. T. Image quality and pattern transfer in directed self assembly with block-selective atomic layer deposition. *J. Vac. Sci. Technol., B: Microelectron. Nanometer Struct.* **2012**, *30*, 06F202.

62. Choi, J. W.; Li, Z.; Black, C. T.; Sweat, D. P.; Wang, X.; Gopalan, P. Patterning at the 10 nanometer length scale using a strongly segregating block copolymer thin film and vapor phase infiltration of inorganic precursors. *Nanoscale* **2016**, *DOI: 10.1039/C6NR01409G*.

63. Padbury, R. P.; Jur, J. S. Temperature-Dependent Infiltration of Polymers during Sequential Exposures to Trimethylaluminum. *Langmuir* **2013**, *30*, 9228-9238.

Chapter 9

A Reactive Platform Approach for the Rapid Synthesis and Discovery of High χ/Low N Block Polymers[‡]

‡ Portions of this chapter have previously been published as: Carter, M.C.D.; Jennings, J.; Speetjens, F.W.; Mahanthappa, M.K.; Lynn, D.M. A Reactive Platform Approach for the Rapid Synthesis and Discovery of High χ/Low N Block Polymers." *Macromolecules* **2016**, *DOI: 10.1021/acs.macromol.6b01268*. J. Jennings acquired the SAXS data for the humidity experiments. F. Speetjens helped design the experiments. My contribution was in synthesizing the block polymers and derivatives, performing the physiochemical characterization experiments and SAXS measurements, and analyzing the data.

ABSTRACT: We report a reactive polymer platform for the rapid discovery of strongly segregated diblock polymers that microphase separate into well–defined morphologies with sub–5 nm features. Our strategy employs reactive poly(styrene–*block*–2–vinyl–4,4–dimethylazlactone) (SV) polymers with low degrees of polymerization (*N*), in which the V blocks undergo selective and quantitative reactions with functional primary amines, to identify new poly(acrylamides) that are highly immiscible with poly(styrene) and induce block polymer self–assembly. Using a combination of optical birefringence and small–angle X–ray scattering (SAXS), we characterize a library of 17 block polymers produced by amine functionalization of four parent SV diblocks synthesized by sequential RAFT polymerizations. We demonstrate that V block functionalization with hydroxy– and methoxy–functional amines yields diblocks that order into lamellar mesophases with half–pitches as small as 3.8 nm. Thus, this azlactone-based reactive molecular platform enables combinatorial generation of polymer libraries with diverse side chain structures that may be rapidly screened to identify new high χ/low *N* systems for self–assembly at ever decreasing length scales.

Introduction

Block polymers offer unique, "bottom up" opportunities for manipulation of the structures and properties of polymeric materials, as a consequence of their microphase separation into well–defined morphologies with periodically placed chemical functionalities at the ~10–100 nm length scale. By tailoring the molecular weight, polymer composition, and structures of the constituent homopolymer segments, the morphologies and feature sizes formed by ordered linear diblock polymers may be readily tuned.[1, 2] The precise chemical structures of the constituent homopolymer segments govern the magnitude of the pairwise effective interaction parameter (χ_{eff}) in a diblock polymer, which quantifies the energetic repulsions between the homopolymer segments. In strongly segregated melts, the observed self–assembly length scale follows the functional dependence $d \sim \chi_{eff}^{1/6}N^{2/3}$ subject to the mean–field constraint $(\chi_{eff}N) \geq 10.5$ necessary for microphase separation, where N is the segment density-normalized degree of polymerization.[3-6] The nanoscale morphologies of block polymers have been recently used as templates for inorganic nanomaterials,[7-16] to fabricate nanoporous membranes,[17-19] and to design new nano/biointerfaces[20-22] that would be difficult to construct by other methods.

Successful utilization of diblock copolymers in nanotemplating applications hinges on the discovery of new monomer pairs, block sequences, and polymer architectures that enable supramolecular self–assembly at the sub–10 nm length scale.[7, 13, 23, 24] Sinturel *et al.* recently reviewed this topic and noted that one solution to this challenge lies in discovering "high χ_{eff}/low N" microphase separated block polymers.[6] While polyolefin, polydiene, and polyacrylate block copolymers are known to exhibit relatively small pairwise χ_{eff} values, their modification with silicon,[13, 25, 26] fluorine,[27, 28] or metal species[29, 30] is known to increase significantly the magnitude of χ_{eff} at a constant degree of polymerization (N). Thus, these materials adopt segregated

morphologies with smaller microdomain spacings than their parent compounds. However, microelectronic device fabrication applications would ideally utilize "all organic" high χ_{eff}/low N block polymers to achieve sub–10 nm patterning,[13, 24] which somewhat limits the value of some of the aforementioned chemical modification strategies.[6, 24] Thus, a methodology for rapidly discovering new high χ_{eff}/low N block polymers would furnish important lead compounds that form sub–10 nm structures, which could be optimized by the stepwise synthesis and characterization of individual constructs to quantify the specific χ_{eff} values.

Herein, we report a reactive polymer template approach for the parallel synthesis of a new family of all organic, polystyrene (PS)–based diblock polymers. This parallel synthesis strategy allows the rapid identification of new high χ_{eff}/low N block polymers and underlying molecular motifs that increase the segment incompatibility to drive their thermodynamic self-assembly at reduced length scales. We recently reported the synthesis of high molecular weight poly(styrene–*block*–2–vinyl–4,4–dimethylazlactone) (SV) diblock polymers that microphase separate into vertically–oriented lamellae in thin films, which can be functionalized after film fabrication to alter the chemical functionalities and interfacial properties of the film surface.[31] Building on this earlier report, we demonstrate that low molecular weight SV diblocks that are melt–disordered may be readily functionalized with amine-containing nucleophiles to generate a library of block polymers. Using a combination of polarized light microscopy and small–angle X–ray scattering (SAXS) to quickly screen this library, we identify new high χ_{eff}/low N ordered block polymers with degrees of polymerization as low as N = 30 with lamellar half–pitches as small as 3.8 nm. We further identify one specific block polymer system in which the domain spacing may be readily manipulated using controlled relative humidity environments.

Materials and Methods

Materials. Styrene (99.9%), benzylamine (99%), ethanolamine (>98%), 2,2'–azobis(isobutyronitrile) (AIBN, recrystallized from methanol), trimethylsilylamine (>98%), hexanes (technical grade), and toluene (ACS grade, >99.5%) were purchased from Sigma–Aldrich (Milwaukee, WI). 2–Methoxyethylamine was purchased from TCI America (Portland, OR). 1–Amino–4–butanol (98%), and dimethylaminopropylamine (99%) were purchased from Acros Organics (Morris Plains, NJ). Inhibitor Removal Resin was purchased from Alfa Aesar (Radnor, PA). 2–Vinyl–4,4–dimethylazlactone (VDMA) was a gift from Dr. Steven M. Heilmann (3M Corp., St. Paul, MN). *S*–1–Dodecyl–*S*'–(α,α'–dimethyl–α''–acetic acid)trithiocarbonate was synthesized according to a literature procedure,[32] stored at 0 °C, and recrystallized from hexanes prior to use. Toluene was passed through a short column of Brockman Type I basic alumina (~10 *m*/*v*) prior to use as a polymerization solvent. All other materials were used as received unless otherwise stated.

General Considerations. ^{1}H NMR spectroscopy was performed in $CDCl_3$ using a Bruker Avance–500 spectrometer, using a pulse repetition delay of 16 s. All spectra were referenced relative to the residual proton peak of $CHCl_3$ (δ7.26 ppm). Size exclusion chromatography (SEC) analyses were performed using a Viscotek GPC Max VE2001 equipped with two Polymer Laboratories PolyPore columns (250 mm × 4.6 mm), a TDA–302 tetradetector array (7° and 90° light scattering, four capillary differential viscometer, and UV-Vis diode array), using THF as the eluent at a flow rate of 1 mL/min at 40 °C. SEC measurements were calibrated using 10 narrow dispersity polystyrene standards with M_n = 0.580−377.4 kg/mol (Agilent Technologies Santa Clara, CA). Thermogravimetric analyses (TGA) were performed using a TA instruments

Q500 thermogravimetric analyzer. Polymer sample weight loss was measured over the temperature range T = 25–600 °C using a ramp rate of 20 °C/min. Differential scanning calorimetry (DSC) was performed using a TA Instruments DSC100 between T = 30–200 °C using a heating and cooling ramp rate of 10 °C/min. The thermal history of each sample was erased in the first cycle by heating to 200 °C and cooling to 30 °C at 10 °C/min, and all thermal transitions were assigned from the second heating cycle. Attenuated total reflectance (ATR) measurements were obtained using a Bruker Tensor 27 FTIR spectrometer outfitted with a Pike Technologies Diamond ATR stage (Madison, WI.) Data were analyzed using Opus Software v. 6.5 (Bruker Optik GmbH). Spectral data were collected at a resolution of 2 cm^{-1} and are presented as an average of 32 scans; spectra were smoothed by applying a nine–point average and baseline–corrected with a concave rubberband correction (10 iterations, 64 points). Optical birefringence analyses were performed using an Olympus BX60 microscope equipped with crossed polarizers at ambient temperature. Samples were rotated through 360° under the microscope, and images of the films were captured using a digital camera (Olympus C–2040 Zoom) mounted on the microscope set to an *f*–stop of 2.8 with an exposure time of 1/125 sec at 4X magnification using an objective lens.

Small Angle X–Ray Scattering (SAXS). Temperature-dependent lab source SAXS measurements were performed using Cu–Kα X–rays generated by a Rigaku Micromax 002+ microfocus source coupled with a multilayer confocal optic, followed by passage through three pinhole collimators to trim the final beam diameter to ≤ 0.5 mm. Samples were mounted in a vacuum chamber on a Linkam thermal hot–stage and annealed at a desired temperature for 15 min prior to data collection (typical exposure times ~20 min). Two–dimensional SAXS patterns

were recorded on a Gabriel X–ray detector (150 mm diameter active circular area) using a sample–to–detector distance of either 1 m or 55 cm (calibrated using a silver behenate standard with d = 58.38 Å). Ambient temperature SAXS measurements were made using a Bruker D8 Discover diffractometer, with Cu–K_α X–rays produced from a micro X–ray source with a Montel mirror that were passed through a 0.5 mm pinhole to collimate the beam. Samples were prepared by incubation in a controlled relative humidity chamber (*vide infra*) and sealed between two pieces of Kapton tape to mitigate water loss. Two–dimensional scattering patterns were collected on a VANTEC–500 detector (140 mm in diameter) for ~5 min using a 36 cm sample–to–detector distance (calibrated with a silver behenate). 2D–SAXS patterns were azimuthally integrated using the Datasqueeze software package in order to obtain one–dimensional scattering profiles.

Synchrotron SAXS measurements were performed at the 12–ID–B beamline at the Advanced Photon Source (Argonne, IL) using a beam energy of 14 keV (λ = 0.886 Å) and a sample to detector distance of 1.99 m, which was calibrated using silver behenate. 2D–SAXS patterns were recorded at 25 °C on a Pilatus 2M detector (25.4 cm x 28.9 cm rectangular area) with a 1475 x 1679 pixel resolution with a 1 s exposure time. 2D–WAXS measurements were simultaneously recorded, with a sample to detector distance of 0.455 m using a Pilatus 300K detector (8.4 cm x 10.7 cm rectangular area) with a 487 x 619 pixel resolution. All synchrotron SAXS/WAXS samples were loaded into hermetically sealed aluminum DSC pans and thermally annealed at 150 °C for 10 h at 1 Torr prior to analysis. SAXS patterns were recorded at elevated temperatures by heating the samples in a Linkam DSC stage, with a 5 min thermal equilibration time prior to data collection. 2D–SAXS patterns were azimuthally integrated to obtain one–dimensional intensity ($I(q)$) *versus* scattering wavevector (q) plots and analyzed using freely available procedures in Igor Pro (Wavemetrics, Inc.).[33]

Representative Synthesis of Polystyrene (PS) Macro–RAFT Agents. Poly(styrene) macro-RAFT chain transfer agents were synthesized by the following general procedure, which represents the first step in the synthesis of diblock **SV-2k**. Styrene was stirred over Brockman Type I basic alumina (~20 *m*/*v*) for 45 min and gravity filtered through Whatman #1 filter paper. Styrene (15.0 mL, 131 mmol) and *S*–1–dodecyl–*S*'–(α,α'–dimethyl–α''–acetic acid)trithiocarbonate (327 mg, 0.895 mmol) were added to an oven–dried 25 mL Schlenk tube and degassed via three freeze–pump–thaw cycles. The yellow solution was stirred in a 120 °C oil bath for 3.5 h, after which the tube was immersed in liquid nitrogen. The resulting polymer was precipitated in cold methanol (~300 mL), collected, redissolved in THF (~10 mL), reprecipitated twice more in cold methanol, and freeze–dried from benzene. Yield 0.800 g. $M_{n,SEC}$ = 2.02 kg/mol. M_w/M_n = 1.11 (against PS Standards).

Representative Synthesis of Poly(styrene–*block*–2–vinyl–4,4–dimethylazlactone) (SV) Block Copolymers. The synthesis of SV diblock copolymers was generally conducted according to the following procedure, which describes the second step of the synthesis of **SV–2k**. 2–Vinyl–4,4–dimethylazlactone (VDMA) was passed twice through a short column of Inhibitor Removal Resin followed by a short column of silica gel, in order to remove inhibitor and stabilizing triethylamine base, respectively. PS macroinitiator (0.780 g, 0.386 mmol, M_n = 2.02 kg/mol), VDMA (0.648 g, 4.66 mmol), AIBN (6.43 mg, 0.0392 mmol), and toluene (~2.0 mL) were added to an oven–dried 25 mL Schlenk tube and degassed *via* three freeze–pump–thaw cycles. Assuming 85% VDMA monomer conversion, these reagent quantities target the final molecular weight of the VDMA block to be 1.43 kg/mol with a corresponding volume fraction f_{VDMA} = 0.40 (f_S = 0.60) in the final block polymer based on the known homopolymer segment

densities.[31] The reaction was stirred in a 70 °C oil bath for 24 h, after which the tube was immersed in liquid nitrogen. The resulting solution was diluted with THF (~3 mL), precipitated in cold hexanes (~200 mL) and collected, redissolved in THF (~6 mL), re–precipitated in cold hexanes (~200 mL), and freeze–dried from benzene to yield a light yellow powder. Quantitative ^{1}H NMR analysis of molecular weight compared to PS Macro-RAFT agent reveals that $M_{n,NMR,VDMA}$ = 1.46 kg/mol with $Đ$ = 1.17 (from SEC using PS Standards). ^{1}H NMR and FTIR spectra for all SV copolymers are shown in Figures S1 and S2, respectively. (Supporting Information can be found at the end of this chapter).

Functionalization of SV Block Copolymers by Reaction with Primary Amines. In a typical polymer modification reaction, ~100 mg **SV** was dissolved in anhydrous THF (2.25 mL) in a 6 mL glass vial. To this light yellow solution, 1.5 mol equiv. of amine relative to VDMA monomer units was added. The vial was sealed with a Teflon cap and stirred at 50 °C in an oil bath overnight. The resulting colorless solution was precipitated into hexanes (~15 mL) at ambient temperature and centrifuged. The supernatant liquid was removed and the resulting white powder was dried for ~15 min under ambient conditions prior to its re-dissolution in THF (0.5 mL) and reprecipitation into hexanes. The final polymer sample was isolated by centrifugation, after which it was collected and dried *in vacuo*. Note that during the VDMA ring-opening reaction with the 1° amine, the trithiocarbonate RAFT endgroup was cleaved to yield a terminal thiol. Representative ^{1}H NMR and FTIR spectra and DSC heating curves for the side chain–functionalized copolymers are shown in Figures S4–S6.

Optical Birefringence Characterization of Polymer Films. Polymer films were prepared for imaging by bright–field and polarized light microscopy by spreading ~10 mg of each dry, powdered sample onto a standard microscope glass slide. Two standard glass coverslips were used as spacers to set a constant film thickness (~0.18 mm), and a second glass slide was placed on top of the polymer sample. Samples were then annealed at 160 °C for 6 hours at 1 Torr and cooled to yield a uniform polymer film prior to imaging at ambient temperature.

Influence of Humidity on Microdomain Spacing. A solution of **SV–4k–2OH** in THF (70 mg/mL) was prepared, and four aliquots (0.5 mL each) were drop–cast onto plasma oxidized silicon wafers (2 x 2 cm). The solvent was allowed to evaporate for 6 h at ambient temperature, after which the samples were dried and annealed in a vacuum oven at 150 °C for 10 h at 1 Torr. The samples were then placed into separate glass jars with screw–top lids, which contained test tubes filled with 5 mL of a given saturated aqueous salt solution. Salt solutions of LiCl, K_2CO_3, NaCl and pure MilliQ H_2O provided controlled relative humidity environments of approximately 23.4, 48.7, 75.8, and 100 %RH, respectively, at ambient temperature. These exact %RH values inside each chamber were directly measured by insertion of a Fisher Scientific Traceable Hygrometer Thermometer Dew Point 11–661–7A probe through a hole in the chamber lid. Upon sealing each chamber with Parafilm^{TM}, samples were allowed to anneal overnight at ambient temperature. Annealed samples were immediately characterized by room-temperature SAXS by removing the polymer film from its silicon substrate and sealing it between two pieces of Kapton tape. To characterize the reversibility of water uptake by the samples and its effect on the observed domain spacings, the Kapton sandwich was opened and samples were dried under vacuum overnight at ambient temperature, prior to subjecting them SAXS analysis.

Results and Discussion

Our approach to discovering new high χ/low N ordered block polymers relies upon post–synthetic functionalization of low molecular weight diblock polymer 'templates' containing poly(styrene) and amine-reactive azlactone–functionalized blocks (Scheme 1). We used sequential reversible addition-fragmentation chain-transfer (RAFT) polymerization to synthesize four low molecular weight poly(styrene–*block*–2–vinyl–4,4–dimethylazlactone) (**SV**) diblock polymers with styrene blocks having $M_{n,S}$ = 2–5 kg/mol.[31, 34] To maximize the probability of observing microphase separation at the smallest possible length scales, we sought access to a series of side chain–functionalized **SV** diblocks with nearly symmetric volume compositions, whereby microphase separation is expected to occur at the minimum value $(\chi_{eff}N)_{ODT}$ = 10.5 predicted by mean-field theory.[3] Based on the expectation that side chain functionalization of the azlactone with a 1° amine would result in volumetric expansion of the V block,[31] our syntheses targeted **SV** diblocks with VDMA volume fractions f_{VDMA} ~ 0.40 with $N \leq 100$ that might transform into nearly symmetric, self-assembled diblock polymers upon amine functionalization.

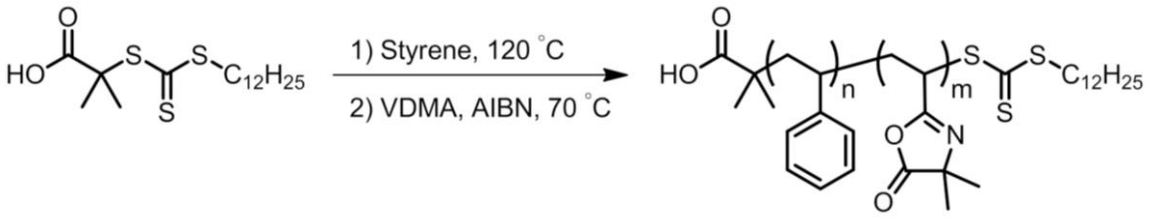

Scheme 1. Sequential reversible–addition fragmentation chain-transfer (RAFT) polymerization synthesis of the poly(styrene–*block*–2–vinyl–4,4–dimethylazlactone) (**SV**) reactive diblock copolymers used in this study.

The molecular characteristics of each reactive diblock are given in Table 1, which shows that the segment density-normalized degree of polymerization for each of these samples ranges from 33 $\leq N \leq$ 78 with dispersities $Đ = M_w/M_n \leq 1.17$ from SEC analyses. Preliminary SAXS analyses indicated that all of these low N samples were disordered, even after thermal annealing at T = 150 °C, above the highest glass transition temperature observed by DSC analysis (see Figures S3 and S6; Supporting Information can be found at the end of this chapter).

Table 1. Molecular Parameters and Bulk Morphologies for SV Block Polymers.

Sample	S Block $M_{n,SEC}$ (kg/mol)[a]	V Block $M_{n,NMR}$ (kg/mol) [b]	N [c]	f_S[c]	$Đ$[a]
SV-2k	2.02	1.46	33.4	0.59	1.17
SV-3k	3.05	2.20	48.7	0.59	1.16
SV-4k	4.36	2.91	69.7	0.61	1.16
SV-5k	4.96	3.18	78.0	0.62	1.17

[a]Determined by SEC analysis against poly(styrene) standards. [b]Determined by quantitative ^{1}H NMR spectroscopy using $M_{n,SEC}$ for the PS block. [c]Calculated from the homopolymer densities ρ(PS) = 1.06 g/cm^3 and ρ(PVDMA) = 1.08 g/cm^3, at 25 °C using a 185 Å^3 reference volume.

The reactive V blocks of the **SV** diblocks were post-synthetically functionalized to install hydrophilic and hydrophobic side chains by azlactone ring–opening reactions[35, 36] with the 1° amines depicted in Figure 1. The selection of these specific amines was guided by various molecular design hypotheses. **Benz** was selected because its apparent similarity to the aromatic side chain of the S blocks might provide insights into the chemical dissimilarity of the S domains and the 'amide/amide' linkages arising from azlactone ring–opening in the V blocks. Incorporation of silicon-containing functionalities into block polymers containing poly(styrene) is typically observed to increase immiscibility with poly(styrene),[25, 37, 38] thus motivating **TMS**

side-chain functionalization. **DMAP**, **2OH**, and **4OH** side chains were chosen to assess the extent to which terminal polar groups such as 3° amines and 1° alcohols[39, 40] increase χ_{eff} to induce block polymer self-assembly. In order to tease apart the possible role of hydrogen bonding interactions in driving possible microphase separation in **2OH** and **4OH**, we also investigated **2OMe** in which the free hydroxyl functionality is capped with a methyl group. ^{1}H NMR and FTIR ATR spectroscopic analyses indicate that reactive functionalization of each of the four **SV** diblocks with these 1° amines proceeded to > 95% completion (see Figures S4–S5). We refer to these side chain–functionalized diblocks using the convention **SV-Xk-YYY** wherein X = 2–5 and refers to the length of the S block in kg/mol, and YYY refers to the approximate side chain functionality derived from polymer modification with the 1° amines depicted in Figure 1. By this parallel and combinatorial synthesis strategy, we produced a total of 17 diblock polymer homologs.

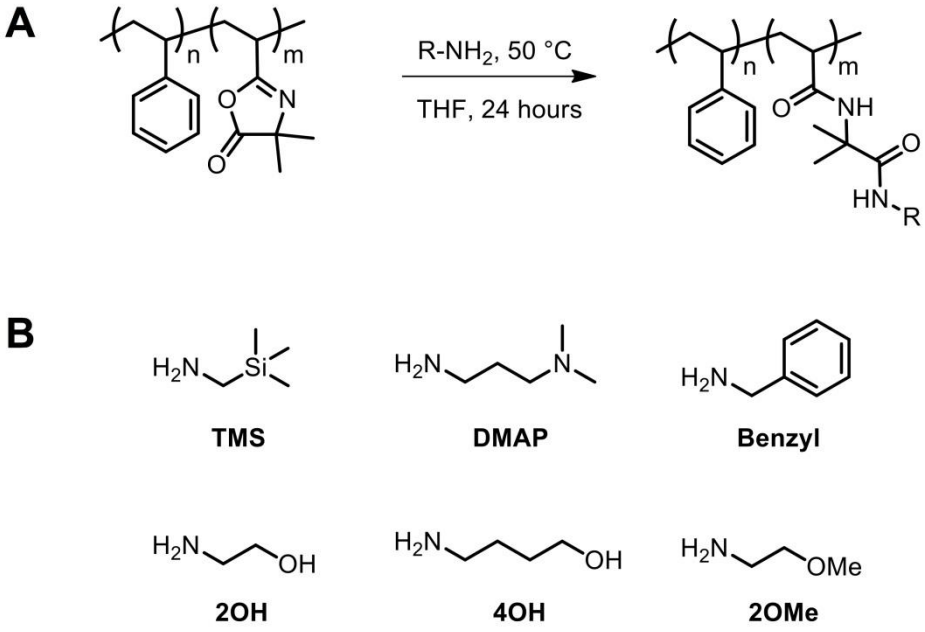

Figure 1. (A) General scheme and reaction conditions used for functionalization of the PVDMA blocks of SV copolymers using nucleophilic primary amines. (B) Structures of the different primary amines used for side chain functionalization

Table 2. Results of Optical Birefringence and SAXS Analyses of SV Diblock Copolymers.

	Parent SV Diblock		
	SV-2k	**SV-3k**	**SV-4k**
Functional Amine			
TMS	*n.d.*[a]	*n.d.*	Non-birefringent[b] DIS[c]
DMAP	*n.d.*	*n.d.*	Non-birefringent DIS
Benz	*n.d.*	*n.d.*	Non-birefringent DIS
2OH	Birefringent LAM (L_0 =7.6 nm)	Birefringent LAM (L_0 = 10.3 nm)	Birefringent LAM (L_0 =12.5 nm)
4OH	*n.d.*	Birefringent LAM (L_0 =10.3 nm)	Birefringent LAM (L_0 =12.1) nm
2OMe	Non-birefringent	Non-birefringent DIS	Birefringent LAM (L_0 =9.8 nm)

[a] *n.d.* = not determined. [b] Birefringence data was acquired at ambient temperature after thermal annealing at 160 °C. [c] DIS = disordered polymer melt, LAM = lamellar morphology with domain spacing listed in parenthesis, as determined by SAXS analysis at 180 °C using ($L_0 = 2\pi/q^*$).

While combinatorial production of new AB diblock systems removes one bottleneck from the process of discovering new high χ/low N materials for nanotemplating, we also sought to quickly evaluate which of these new diblocks microphase separate and to focus our attention on the most promising systems. Consequently, we screened our polymer library using optical birefringence as a qualitative means of identifying side chain functionalities that induce molecular weight–dependent microphase separation. Ordered block polymer morphologies with non-cubic symmetries typically exhibit strong optical birefringence when viewed between cross-polarizers, whereas disordered copolymers are optically isotropic and thus appear dark.[41] Thin films of the side chain–functionalized **SV** diblocks were cast and annealed on planar glass substrates at 160 °C, above the glass transition temperatures of all of the constituent homopolymer segments (see Figure S6). Figure 2 shows representative bright-field and polarized light microscopy images from **SV–4k** and its 2-hydroxyethyl side chain derivative **SV–4k–2OH**.

The lack of birefringence in **SV-4k** strongly suggests that it is disordered, which is consistent with our preliminary SAXS analyses (Figure S3). However, the strong optical birefringence of **SV–4k–2OH** shown in Figures 2C and 2D indicates that exhaustive functionalization of **SV-4k** with ethanolamine increases the chemical dissimilarity of the V segment enough to drive its demixing from the poly(styrene) segment. Birefringence data for other **SV** derivatives is shown in Figure S7.

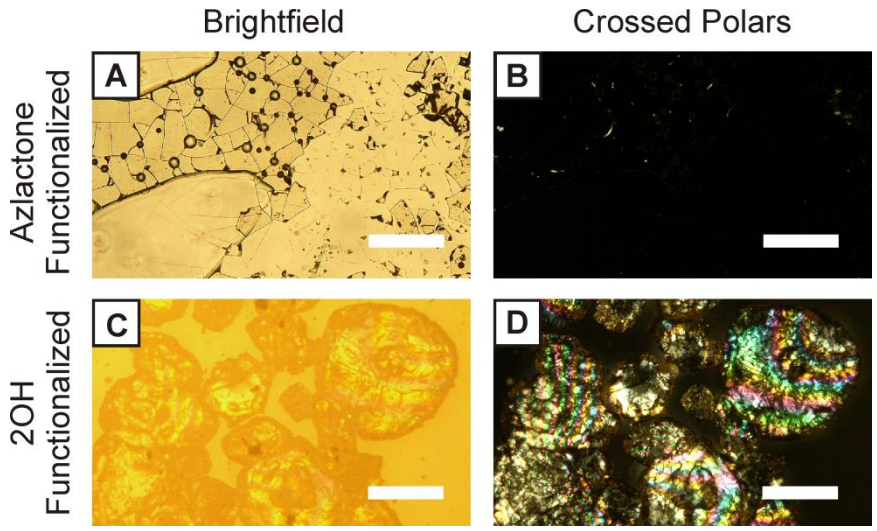

Figure 2. Representative results of bright–field (A,C) and polarized light (B,D) microscopy analyses used to determine the influence of side chain structure on the morphologies of side chain–functionalized **SV** diblock polymers. Ambient temperature images acquired for polymer **SV–4k** and its **SV–4k–2OH** derivative are shown as representative examples (see Figure S7 for complete set of results), after thermally annealing at 160 °C for 6 h. Scale bars represent 0.5 mm. SV diblocks, we deduce that the relative chemical incompatibility with poly(styrene) in this series of functional polymers increases as **2OMe** < **4OH** < **2OH**.

The complete results of the optical birefringence screening experiments on annealed diblock thin films given in Table 2 reveal the influence of V block side chain structure on the extent to which these diblocks thermodynamically self-assemble. Derivatization of **SV-4k** with **TMS**, **DMAP**, and **Benz** did not result in any observed optical birefringence, and thus these

polymers apparently remained disordered. We did not further characterize the related derivatives arising from functionalization of **SV-3k** and **SV-2k**, since the lack of any ordered morphology in **SV-4k** implies that the lower molecular weight analogs will also be disordered. We also did not pursue further investigations of the phase behaviors of polymers derived from **SV–5k**, since our primary goal was to identify new high χ/low N block polymers with currently inaccessible domain spacings. However, **SV–4k** functionalized with any of **2OMe, 2OH**, or **4OH**, exhibited strong birefringence. From the data presented in Table 2, we note that **SV–4k**–**2OMe** presents an ordered morphology and that its lower molecular weight analogs do not. **SV–3k-4OH** and **SV–2k-2OH** are the lowest molecular weight samples studied here with **4OH** and **2OH** side chains that present ordered morphologies, respectively (Figure S7; Table 2). Given the molecular weight dependence of the self-assembly behaviors of these families of differently functionalized

We subjected the aforementioned optically birefringent block polymer samples to SAXS analyses to identify their underlying ordered morphologies and microdomain spacings. Figure 3 depicts azimuthally-integrated lab source SAXS patterns obtained at 180 °C (above the T_g of both blocks) for the SV block polymers that microphase separate upon side chain functionalization; the associated domain spacings (L_0) derived from the positions of the principal scattering peak are given in Table 2. **SV–4k–2OH**, **SV–4k–4OH**, and **SV–4k–2OMe**, derived from the **SV–4k** parent polymer, all exhibit self–assembled lamellar morphologies, with L_0 = 12.5 nm, 12.1 nm, and 9.8 nm, respectively (Figure 3A). The extinction of the $q^*\sqrt{4}$ peak in the SAXS pattern for **SV–4k–2OH** implies that this polymer is compositionally symmetric (f_S ~ 0.5). This observation concurs with our expectation that side chain functionalization increases the volume of the V block (*vide supra*). The systematic decrease in domain spacing at constant backbone degree of polymerization for the **SV-4k** series also implies that the chains are less

stretched in **SV–4k–2OMe** than in **SV–4k–2OH**. This last result supports our preliminary deduction that χ_{eff} increases along the series **2OMe** < **4OH** < **2OH**. SAXS analyses of **SV–4k-TMS**, **SV–4k-DMAP**, and **SV–4k-Benz** also corroborate the conclusions of our optical birefringence studies: these materials exhibit only correlation-hole scattering associated with a disordered diblock polymer (see Figure S8).[42] In the case of **SV–3k**, SAXS analyses again confirm that **SV–3k–2OH** and **SV–3k–4OH** microphase separate into lamellar mesophases with L_0 = 10.3 nm, whereas **SV–3k–2OMe** is disordered. Thus, terminal –OH groups in the side chain lead to a larger χ_{eff} with poly(styrene) that drives copolymer self-assembly at lower overall molecular weights and reduced length scales. Finally, a SAXS pattern for **SV–2k–2OH** demonstrates its microphase separation into lamellae with L_0 = 7.6 nm. This principal domain spacing translates into a lamellar half-pitch of 3.8 nm, which is amongst the smallest reported feature sizes that are accessible from block polymer self-assembly.[43-47]

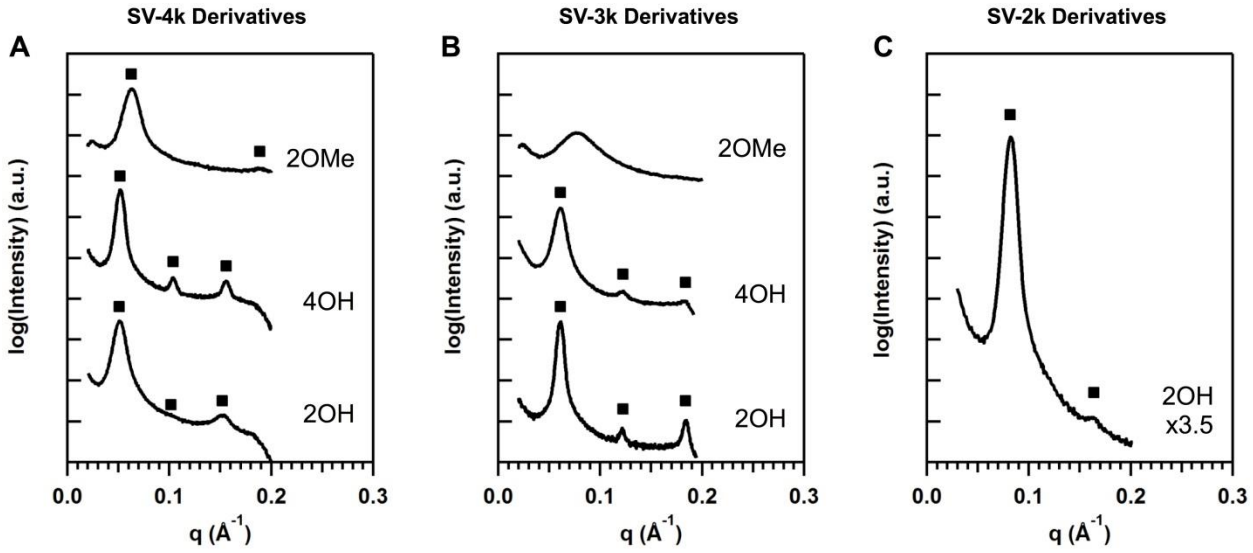

Figure 3. (A) Azimuthally–integrated lab source SAXS patterns for (A) **SV–4k**, (B) **SV–3k** and (C) **SV–2k** derivatives acquired at 180 °C. Peak markers indicate the calculated peak positions associated with a lamellar morphology based on the principal scattering peak position (q^*) for each sample, from which the microdomain spacings, L_0, listed in Table 2 are calculated.

We note that it is unlikely that the specific combination of side chains found in the **SV–2k–2OH** polymer would have been targeted *a priori* or identified as a potentially useful lead compound in the absence our combinatorial synthesis approach. As such, the identification of **SV–2k–2OH** as a high χ/low N monomer system establishes the utility of our reactive polymer screening strategy for the accelerated discovery of new polymer systems that form decreasingly small feature sizes. In this broader context, our parallel synthesis and preliminary characterization experiments also revealed a few other surprising molecular structure–property relationships. For example, reports on the microphase separation of high χ, silicon-containing block polymers [where the silicon atom (or atoms) is present in the side chain][25, 38] sharply contrast our observation that **SV-4k-TMS** does not microphase separate. Additionally, our results reveal that **SV-4k-DMAP** apparently does not microphase separate, even though one might anticipate block polymer ordering given that structurally related PS-b-P2VP[48] and PS-b-P4VP[49] (P2VP = poly(2-vinylpryidine); P4VP = poly(4-vinylpyridine)) diblocks exhibit relatively large effective interaction parameters $\chi > 0.15$. The fact that microphase separation cannot be simply predicted from the chemical constitution of the side chains further highlights the need for facile methods for identifying high χ/low N monomer pairs.

High-resolution synchrotron SAXS analyses confirm the accuracy of our lab–source SAXS results (Figure S9) for the following derivatives: polymer **SV–2k–2OH** (lamellae, L_0 = 7.63 nm), polymer **SV–4k–2OMe** (lamellae, L_0 = 9.80 nm), and polymer **SV–3k–2OMe** (disordered). Simultaneous synchrotron wide–angle X–ray scattering (WAXS) experiments also affirm the absence of any crystallinity in these block polymers (see Figure S10) in a manner consistent with our DSC analyses.

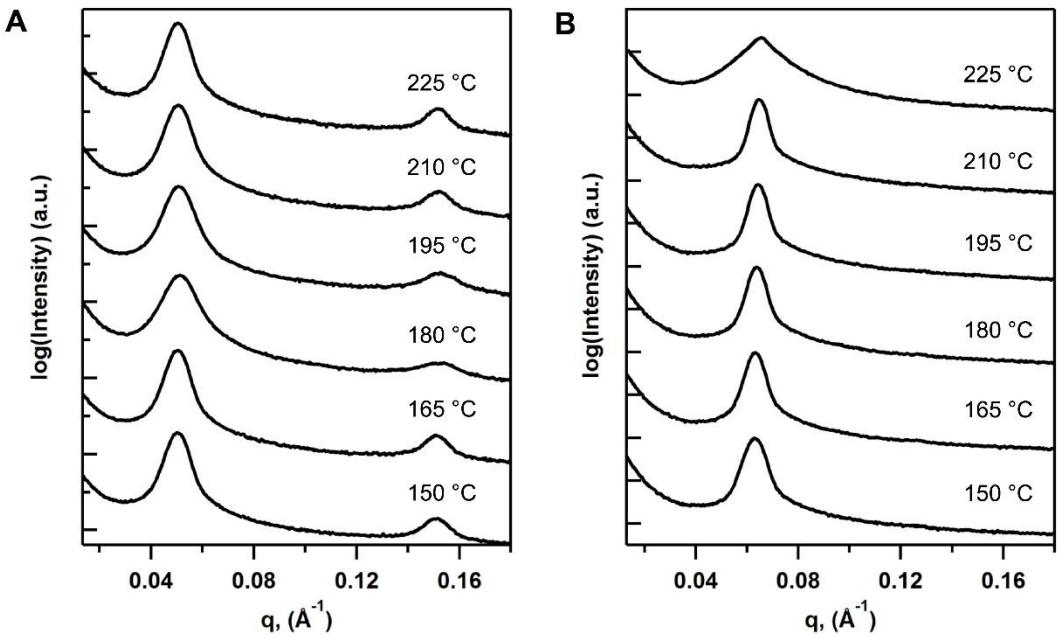

Figure 4. Azimuthally–integrated, lab source temperature-dependent SAXS analysis of (A) **SV-4k-2OH** and (B) **SV-4k-2OMe** measured at 15 °C increments from 150 °C to 225 °C. **SV-4k-2OH** displays Bragg peaks at q^* and $3q^*$ at all temperatures. **SV-4k-2OMe** exhibits an order-to-disorder transition temperature with 210 °C ≤ T_{ODT} ≤ 225 °C, evidenced by disappearance of the sharp scattering peaks and the evolution of broad, low-intensity correlation-hole scattering at 225 °C.

The proximity of **SV–4k–2OMe** and **SV–2k–2OH** to the critical molecular weight required for microphase separation suggested the possibility that we could access the order-disorder transitions for these self-assembled materials. Thermogravimetry indicated that both of these polymers remained stable with less than 5% total weight loss up to 250 °C (Figure S11). Figure 4 shows temperature-dependent SAXS patterns for **SV–4k–2OMe**, which indicate "melting" of the supramolecular lamellar mesophase at an order-disorder transition temperature 210 ≤ T_{ODT} ≤ 225 °C, while no such disordering transition is observed for **SV–4k–2OH**. This observation again implies that the effective interaction parameter between poly(styrene) and **2OMe** is smaller than with **2OH**. The strong propensity for **2OH** to demix from poly(styrene) is likely driven by a combination of: (i) the higher polarity of the **2OH**–derived side chain, and (ii)

intra- and inter-molecular hydrogen bonding interactions amongst the terminal hydroxyl and amide groups of the side chains.

In the course of our quantitative morphological studies of the domain spacings of **SV–4k–2OH**, we observed that solvent annealing this polymer from tetrahydrofuran (THF) yielded significantly larger domain spacings than those of thermally annealed samples. We hypothesized that adventitious water in the THF was swelling the hydrophilic **2OH**–functionalized polymer segments. We further recognized the opportunity to exploit this moisture-induced swelling behavior as a means of manipulating the observed domain spacing of this ordered diblock polymer, by analogy with previous reports on PEO-containing block polymers.[50-52] We prepared a series of micrometer-thick films of lamellae-forming **SV–4k–2OH** drop cast from THF by the above thermal annealing protocol. These polymer films were then subjected to ambient temperature annealing in controlled relative humidity environments, the effects of which were monitored by SAXS to assess the influence of moisture on the observed L_0. Figure 5A shows that L_0 for the lamellar morphology increased with increasing relative humidity (RH), from 12.5 nm at 0% RH (vacuum annealed) to 14.9 nm at 100% RH, evidenced by shifting of the primary scattering peak toward lower *q*-values. Furthermore, the appearance of the √4 peak and the concomitant disappearance of the √9 peak above 48.7 % RH imply that the homopolymer-rich microdomains swell unevenly, with the polar block absorbing water to swell while the S block remains vitreous. Inspection of Figure 5B reveals that L_0 dilates linearly as a function of humidity up to ~75 %RH, whereas L_0 increases much more rapidly at higher relative humidities. Thus, humidification of the annealing environment enables fine tuning of the obtained feature sizes **SV–4k–2OH** with a dynamic range of ~2.5 nm, or 20% of the initial accessible feature size.

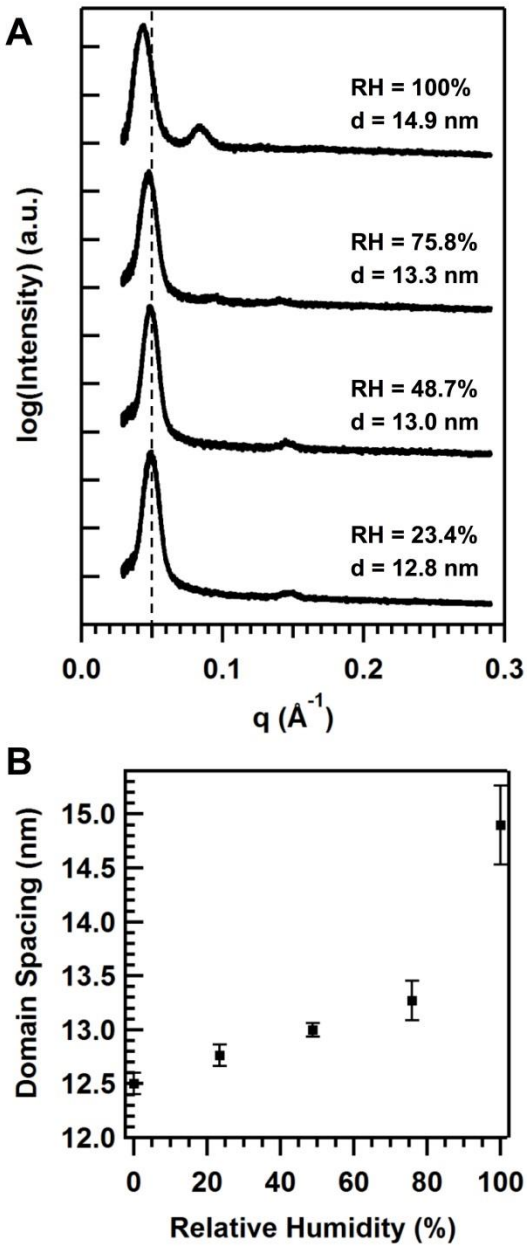

Figure 5. (A) Azimuthally–integrated SAXS patterns acquired at ambient temperature for **SV–4k–2OH** samples annealed in variable relative humidity (%RH) environments, indicating that the observed domain spacing increases with increasing %RH. (B) Relationship between observed domain spacing and %RH, wherein the 0% RH data point corresponds to the **SV–4k–2OH** thermally annealed at 160 °C under vacuum. Error bars represent the standard deviation of the average domain spacing calculated from the location of the principal scattering peak, *q**, and any observed higher order reflections.

Lamellar phases of **SV–4k–2OH** with domain spacings tuned by exposure to controlled humidity environments retain their dilated dimensions even after brief handling in dry air (e.g., after removal from a controlled humidity environment and during SAXS sample preparation). However, the humidity–induced domain swelling can be completely reversed to return L_0 to its original value by high vacuum annealing of the humidified materials. SAXS studies revealed the recovery of a symmetric lamellar nanostructure, with the expected decrease in L_0 when a RH–conditioned sample of polymer **SV–4k–2OH** was thoroughly dried (Figure S12). Our results suggest the possibility of tuning the feature sizes of these responsive materials by controlled exposure to other polar compounds, including less volatile or non–volatile compounds that could be used to "dial in" small changes in the nanoscale dimensions of self–assembled block polymer morphologies.

Conclusion

High χ/low N block polymers that self–assemble into well–defined morphologies provide opportunities to define the properties of soft materials at ever decreasing length scales. Intrinsic physicochemical limitations of well-known block polymers have motivated the search for new, highly incompatible polymer pairs that thermodynamically self-assemble at the sub-10 nm length scale for nanotemplating applications. We have described a rapid synthesis and screening approach for discovering new, non-obvious, low molecular weight block polymers that order into bulk lamellar morphologies comprising sub–5 nm domains. Our approach depends upon facile functionalization of low molecular weight, reactive styrenic block polymers derived from 2–vinyl–4,4-dimethylazlactone. This route to entirely organic block polymers enables combinatorial generation of polymer libraries having a diversity of side chain structures that can

be screened to identify new and useful monomer combinations that drive self–assembly at small length scales. Furthermore, our methodology enables qualitative evaluation of the relative magnitudes of the effective interaction parameters χ_{eff} between various monomer pairs, so that attention may be focused on the monomers of greatest interest for a given application. For example, we identified a non-obvious high χ/low N polymer that spontaneously forms a polymer nanotemplate with 3.8 nm features—one of the smallest reported to date. In contrast to many other high χ copolymers containing silicon or fluorine, these entirely organic block polymers have modest glass transition temperatures that may facilitate thermal processing. We anticipate that this general approach can be extended to other classes of technologically useful block polymers, including those that contain selectively degradable blocks useful in lithographic surface patterning and other reactive block polymer segments. Thus, this approach will provide new leads and insights into new structural motifs that drive macromolecular self-assembly at ever smaller length scales.

Acknowledgments. This work was supported by the U.S. National Science Foundation Nanoscale Science and Engineering Center at UW–Madison (DMR–0832760) and made use of NSF–supported facilities (DMR–0832760, DMR–1121288 and CHE–1048642). We thank Dominic Perroni for organizing synchrotron SAXS studies conducted at Sector 12 of the Advanced Photon Source, a U.S. Department of Energy (DOE) Office of Science User Facility operated for the DOE Office of Science by Argonne National Laboratory under Contract No. DE-AC02-06CH11357. We thank Xiaoguang Wang for assistance with birefringence imaging experiments and Prof. Padma Gopalan and Dr. Justin Kennemur for many helpful discussions.

M.C.D.C. acknowledges the Natural Sciences Engineering Research Council of Canada for a graduate fellowship.

References

1. Abetz, V.; Simon, P. F. W., Phase Behaviour and Morphologies of Block Copolymers. *Advances in Polymer Science* **2005,** *190* (Block Copolymers II), 125-212.

2. Bates, F. S.; Hillmyer, M. A.; Lodge, T. P.; Bates, C. M.; Delaney, K. T.; Fredrickson, G. H., Multiblock Polymers: Panacea or Pandora's Box? *Science* **2012,** *336* (6080), 434-440.

3. Leibler, L., Theory of Microphase Separation in Block Copolymers. *Macromolecules* **1980,** *13* (6), 1602-1617.

4. Matsen, M. W., Effect of Architecture on the Phase Behavior of AB-Type Block Copolymer Melts. *Macromolecules* **2012,** *45* (4), 2161-2165.

5. Bates, F. S.; Fredrickson, G. H., Block copolymer thermodynamics: theory and experiment. *Annual Review of Physical Chemistry* **1990,** *41*, 525-57.

6. Sinturel, C.; Bates, F. S.; Hillmyer, M. A., High Chi-Low N Block Polymers: How Far Can We Go? *ACS Macro Letters* **2015,** *4* (9), 1044-1050.

7. Bang, J.; Jeong, U.; Ryu, D. Y.; Russell, T. P.; Hawker, C. J., Block Copolymer Nanolithography: Translation of Molecular Level Control to Nanoscale Patterns. *Advanced Materials* **2009,** *21* (47), 4769-4792.

8. Marencic, A. P.; Register, R. A., Controlling Order in Block Copolymer Thin Films for Nanopatterning Applications. *Annual Review of Chemical and Biomolecular Engineering* **2010,** *1* (1), 277-297.

9. Kim, H.-C.; Park, S.-M.; Hinsberg, W. D., Block Copolymer Based Nanostructures: Materials, Processes, and Applications to Electronics. *Chemical Reviews* **2010,** *110* (1), 146-177.

10. Orilall, M. C.; Wiesner, U., Block copolymer based composition and morphology control in nanostructured hybrid materials for energy conversion and storage: solar cells, batteries, and fuel cells. *Chemical Society Reviews* **2011,** *40* (2), 520-535.

11. Hsueh, H.-Y.; Huang, Y.-C.; Ho, R.-M.; Lai, C.-H.; Makida, T.; Hasegawa, H., Nanoporous Gyroid Nickel from Block Copolymer Templates via Electroless Plating. *Advanced Materials* **2011,** *23* (27), 3041-3046.

12. Cummins, C.; Gangnaik, A.; Kelly, R. A.; Borah, D.; O'Connell, J.; Petkov, N.; Georgiev, Y. M.; Holmes, J. D.; Morris, M. A., Aligned silicon nanofins via the directed self-assembly of PS-b-P4VP block copolymer and metal oxide enhanced pattern transfer. *Nanoscale* **2015,** *7* (15), 6712-6721.

13. Bates, C. M.; Seshimo, T.; Maher, M. J.; Durand, W. J.; Cushen, J. D.; Dean, L. M.; Blachut, G.; Ellison, C. J.; Willson, C. G., Polarity-Switching Top Coats Enable Orientation of Sub–10-nm Block Copolymer Domains. *Science* **2012,** *338* (6108), 775-779.

14. Ruiz, R.; Kang, H.; Detcheverry, F. A.; Dobisz, E.; Kercher, D. S.; Albrecht, T. R.; de Pablo, J. J.; Nealey, P. F., Density Multiplication and Improved Lithography by Directed Block Copolymer Assembly. *Science* **2008,** *321* (5891), 936-939.

15. Bosworth, J. K.; Paik, M. Y.; Ruiz, R.; Schwartz, E. L.; Huang, J. Q.; Ko, A. W.; Smilgies, D.-M.; Black, C. T.; Ober, C. K., Control of Self-Assembly of Lithographically Patternable Block Copolymer Films. *ACS Nano* **2008,** *2* (7), 1396-1402.

16. Zhang, J.; Clark, M. B.; Wu, C.; Li, M.; Trefonas, P.; Hustad, P. D., Orientation Control in Thin Films of a High-χ Block Copolymer with a Surface Active Embedded Neutral Layer. *Nano Letters* **2016,** *16* (1), 728-735.

17. Olson, D. A.; Chen, L.; Hillmyer, M. A., Templating Nanoporous Polymers with Ordered Block Copolymers. *Chemistry of Materials* **2008,** *20* (3), 869-890.

18. Jackson, E. A.; Hillmyer, M. A., Nanoporous Membranes Derived from Block Copolymers: From Drug Delivery to Water Filtration. *ACS Nano* **2010,** *4* (7), 3548-3553.

19. Gopinadhan, M.; Deshmukh, P.; Choo, Y.; Majewski, P. W.; Bakajin, O.; Elimelech, M.; Kasi, R. M.; Osuji, C. O., Thermally Switchable Aligned Nanopores by Magnetic-Field Directed Self-Assembly of Block Copolymers. *Advanced Materials* **2014,** *26* (30), 5148-5154.

20. Killops, K. L.; Gupta, N.; Dimitriou, M. D.; Lynd, N. A.; Jung, H.; Tran, H.; Bang, J.; Campos, L. M., Nanopatterning Biomolecules by Block Copolymer Self-Assembly. *ACS Macro Letters* **2012,** *1* (6), 758-763.

21. Tran, H.; Killops, K. L.; Campos, L. M., Advancements and challenges of patterning biomolecules with sub-50 nm features. *Soft Matter* **2013,** *9* (29), 6578-6586.

22. Malmström, J.; Travas-Sejdic, J., Block copolymers for protein ordering. *Journal of Applied Polymer Science* **2014,** *131* (14), 40360-40372.

23. Jeong, S.-J.; Kim, J. Y.; Kim, B. H.; Moon, H.-S.; Kim, S. O., Directed self-assembly of block copolymers for next generation nanolithography. *Materials Today* **2013,** *16* (12), 468-476.

24. Bates, C. M.; Maher, M. J.; Janes, D. W.; Ellison, C. J.; Willson, C. G., Block Copolymer Lithography. *Macromolecules* **2014,** *47* (1), 2-12.

25. Durand, W. J.; Blachut, G.; Maher, M. J.; Sirard, S.; Tein, S.; Carlson, M. C.; Asano, Y.; Zhou, S. X.; Lane, A. P.; Bates, C. M.; Ellison, C. J.; Willson, C. G., Design of high-χ block copolymers for lithography. *Journal of Polymer Science Part A: Polymer Chemistry* **2015,** *53* (2), 344-352.

26. Tavakkoli K. G., A.; Gotrik, K. W.; Hannon, A. F.; Alexander-Katz, A.; Ross, C. A.; Berggren, K. K., Templating Three-Dimensional Self-Assembled Structures in Bilayer Block Copolymer Films. *Science* **2012,** *336* (6086), 1294-1298.

27. Ren, Y.; Lodge, T. P.; Hillmyer, M. A., Effect of Selective Perfluoroalkylation on the Segregation Strength of Polystyrene−1,2-Polybutadiene Block Copolymers. *Macromolecules* **2002,** *35* (10), 3889-3894.

28. Davidock, D. A.; Hillmyer, M. A.; Lodge, T. P., Mapping Large Regions of Diblock Copolymer Phase Space by Selective Chemical Modification. *Macromolecules* **2004,** *37* (2), 397-407.

29. Maher, M. J.; Mori, K.; Sirard, S. M.; Dinhobl, A. M.; Bates, C. M.; Gurer, E.; Blachut, G.; Lane, A. P.; Durand, W. J.; Carlson, M. C.; Strahan, J. R.; Ellison, C. J.; Willson, C. G., Pattern Transfer of Sub-10 nm Features via Tin-Containing Block Copolymers. *ACS Macro Letters* **2016,** *5* (3), 391-395.

30. Kim, S. H.; Misner, M. J.; Yang, L.; Gang, O.; Ocko, B. M.; Russell, T. P., Salt Complexation in Block Copolymer Thin Films. *Macromolecules* **2006,** *39* (24), 8473-8479.

31. Speetjens, F. W., II; Carter, M. C. D.; Kim, M.; Gopalan, P.; Mahanthappa, M. K.; Lynn, D. M., Post-Fabrication Placement of Arbitrary Chemical Functionality on Microphase-Separated Thin Films of Amine-Reactive Block Copolymers. *ACS Macro Letters* **2014,** *3* (11), 1178-1182.

32. Lai, J. T.; Filla, D.; Shea, R., Functional Polymers from Novel Carboxyl-Terminated Trithiocarbonates as Highly Efficient RAFT Agents. *Macromolecules* **2002,** *35* (18), 6754-6756.

33. Schmitt, A. K.; Mahanthappa, M. K., Igor Pro Procedures for Analyzing Dynamic Light Scattering, Rheology, and Synchrotron X-ray Scattering Data. figShare http://dx.doi.org/10.6084/m9.figshare.644515.

34. Pascual, S.; Blin, T.; Saikia, P. J.; Thomas, M.; Gosselin, P.; Fontaine, L., Block Copolymers Based on 2-Vinyl-4,4-dimethyl-5-oxazolone by RAFT Polymerization: Experimental and Computational Studies. *Journal of Polymer Science, Part A: Polymer Chemistry* **2010,** *48* (22), 5053-5062.

35. Heilmann, S. M.; Rasmussen, J. K.; Krepski, L. R., Chemistry and technology of 2-alkenyl azlactones. *Journal of Polymer Science, Part A: Polymer Chemistry* **2001,** *39* (21), 3655-3677.

36. Buck, M. E.; Lynn, D. M., Azlactone-functionalized polymers as reactive platforms for the design of advanced materials: Progress in the last ten years. *Polymer Chemistry* **2012,** *3* (1), 66-80.

37. Son, J. G.; Gotrik, K. W.; Ross, C. A., High-Aspect-Ratio Perpendicular Orientation of PS-b-PDMS Thin Films under Solvent Annealing. *ACS Macro Letters* **2012,** *1* (11), 1279-1284.

38. Maher, M. J.; Rettner, C. T.; Bates, C. M.; Blachut, G.; Carlson, M. C.; Durand, W. J.; Ellison, C. J.; Sanders, D. P.; Cheng, J. Y.; Willson, C. G., Directed Self-Assembly of Silicon-Containing Block Copolymer Thin Films. *ACS Applied Materials & Interfaces* **2015,** *7* (5), 3323-3328.

39. Senshu, K.; Yamashita, S.; Ito, M.; Hirao, A.; Nakahama, S., Surface Characterization of 2-Hydroxyethyl Methacrylate/Styrene Block Copolymers by Transmission Electron Microscopy Observation and Contact Angle Measurement. *Langmuir* **1995,** *11* (6), 2293-2300.

40. Schmidt, V.; Borsali, R.; Giacomelli, C., Nanostructure of polystyrene-b-poly(2-hydroxyethyl methacrylate) and derivatives with phosphonic diacid groups. *Journal of the Brazilian Chemical Society* **2012,** *23*, 747-752.

41. Balsara, N. P.; Perahia, D.; Safinya, C. R.; Tirrell, M.; Lodge, T. P., Birefringence detection of the order-to-disorder transition in block copolymer liquids. *Macromolecules* **1992,** *25* (15), 3896-3901.

42. Bates, F. S., Measurement of the correlation hole in homogeneous block copolymer melts. *Macromolecules* **1985,** *18* (3), 525-528.

43. Cushen, J. D.; Otsuka, I.; Bates, C. M.; Halila, S.; Fort, S.; Rochas, C.; Easley, J. A.; Rausch, E. L.; Thio, A.; Borsali, R.; Willson, C. G.; Ellison, C. J., Oligosaccharide/Silicon-Containing Block Copolymers with 5 nm Features for Lithographic Applications. *ACS Nano* **2012,** *6* (4), 3424-3433.

44. Kennemur, J. G.; Yao, L.; Bates, F. S.; Hillmyer, M. A., Sub-5 nm Domains in Ordered Poly(cyclohexylethylene)-block-poly(methyl methacrylate) Block Polymers for Lithography. *Macromolecules* **2014,** *47* (4), 1411-1418.

45. Sweat, D. P.; Kim, M.; Larson, S. R.; Choi, J. W.; Choo, Y.; Osuji, C. O.; Gopalan, P., Rational Design of a Block Copolymer with a High Interaction Parameter. *Macromolecules* **2014,** *47* (19), 6687-6696.

46. van Genabeek, B.; de Waal, B. F. M.; Gosens, M. M. J.; Pitet, L. M.; Palmans, A. R. A.; Meijer, E. W., Synthesis and Self-Assembly of Discrete Dimethylsiloxane–Lactic Acid Diblock Co-oligomers: The Dononacontamer and Its Shorter Homologues. *Journal of the American Chemical Society* **2016,** *138* (12), 4210-4218.

47. Thomas, T. S.; Hwang, W.; Sita, L. R., End-Group-Functionalized Poly(α-olefinates) as Non-Polar Building Blocks: Self-Assembly of Sugar–Polyolefin Hybrid Conjugates. *Angewandte Chemie International Edition* **2016,** *55* (15), 4683-4687.

48. Schulz, M. F.; Khandpur, A. K.; Bates, F. S.; Almdal, K.; Mortensen, K.; Hajduk, D. A.; Gruner, S. M., Phase Behavior of Polystyrene−Poly(2-vinylpyridine) Diblock Copolymers. *Macromolecules* **1996,** *29* (8), 2857-2867.

49. Zha, W.; Han, C. D.; Lee, D. H.; Han, S. H.; Kim, J. K.; Kang, J. H.; Park, C., Origin of the Difference in Order−Disorder Transition Temperature between Polystyrene-block-poly(2-vinylpyridine) and Polystyrene-block-poly(4-vinylpyridine) Copolymers. *Macromolecules* **2007,** *40* (6), 2109-2119.

50. Chavis, M. A.; Smilgies, D.-M.; Wiesner, U. B.; Ober, C. K., Widely Tunable Morphologies in Block Copolymer Thin Films Through Solvent Vapor Annealing Using Mixtures of Selective Solvents. *Advanced Functional Materials* **2015,** *25* (20), 3057-3065.

51. Bang, J.; Kim, B. J.; Stein, G. E.; Russell, T. P.; Li, X.; Wang, J.; Kramer, E. J.; Hawker, C. J., Effect of Humidity on the Ordering of PEO-Based Copolymer Thin Films. *Macromolecules* **2007,** *40* (19), 7019-7025.

52. Park, M. J.; Nedoma, A. J.; Geissler, P. L.; Balsara, N. P.; Jackson, A.; Cookson, D., Humidity-Induced Phase Transitions in Ion-Containing Block Copolymer Membranes. *Macromolecules* **2008,** *41* (6), 2271-2277.

Supporting Information for Chapter 9

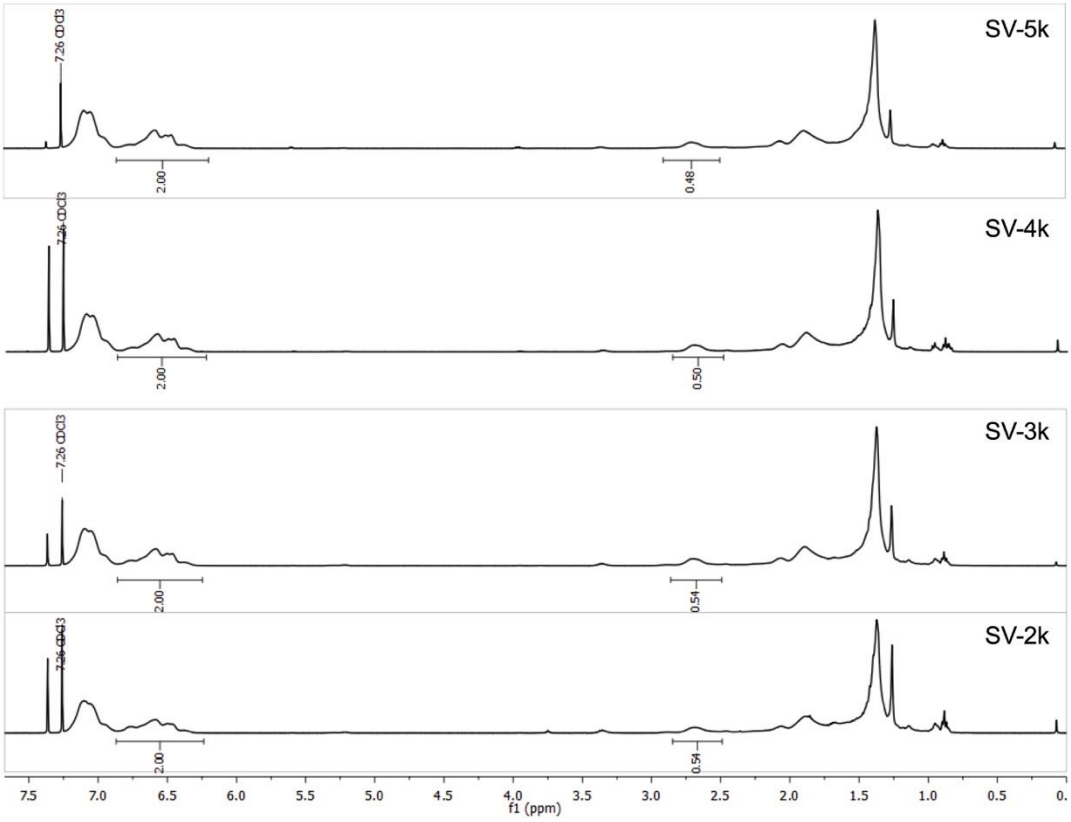

Figure S1. ^{1}H NMR spectra for **SV** block polymers, recorded in $CDCl_3$ and referenced to the residual protiated solvent peak. The the S block $M_{n,SEC}$ was determined by SEC analysis (see Table 1), from which $M_{n,NMR}$ of the VDMA block was determined by quantitative ^{1}H NMR using the ratio of intergral of the styrenic aromatic protons (2H, δ 6.23-6.84 ppm) and the backbone C<u>H</u> of VDMA (1H, δ 2.70 ppm).

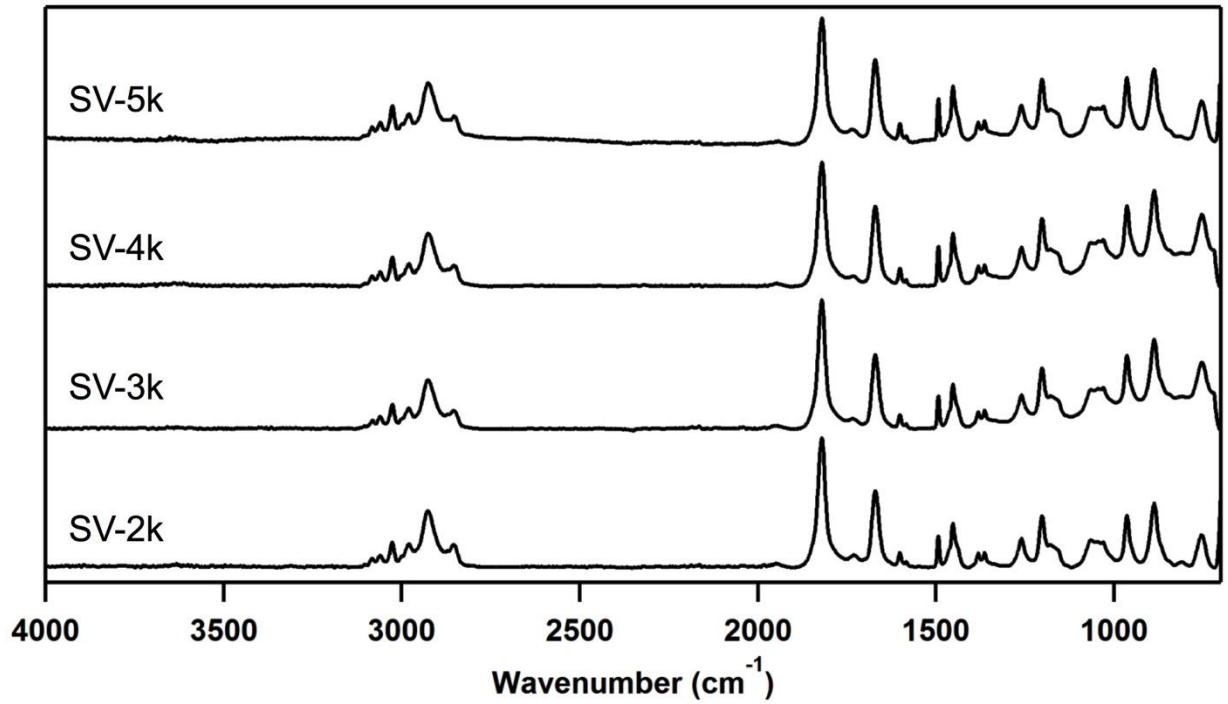

Figure S2. ATR FTIR spectra of **SV** block polymers. Peaks at 1830, 1679, and 1209 cm^{-1} correspond to the cyclic C=O, C=N, and C-O-C stretches of the azlactone ring, respectively. The azlactone ring is not hydrolyzed during the polymerization or polymer isolation by the presence of adventitious water (ring-opening gives rise to peaks corresponding to NH stretching ~3200 cm^{-1}, NH bending ~1540 cm^{-1}, and C=O stretching ~1730 cm^{-1}, which are absent). Note that the small peak at ~1730 cm^{-1} corresponds to the C=O stretch of RAFT agent carboxylic acid functionality.

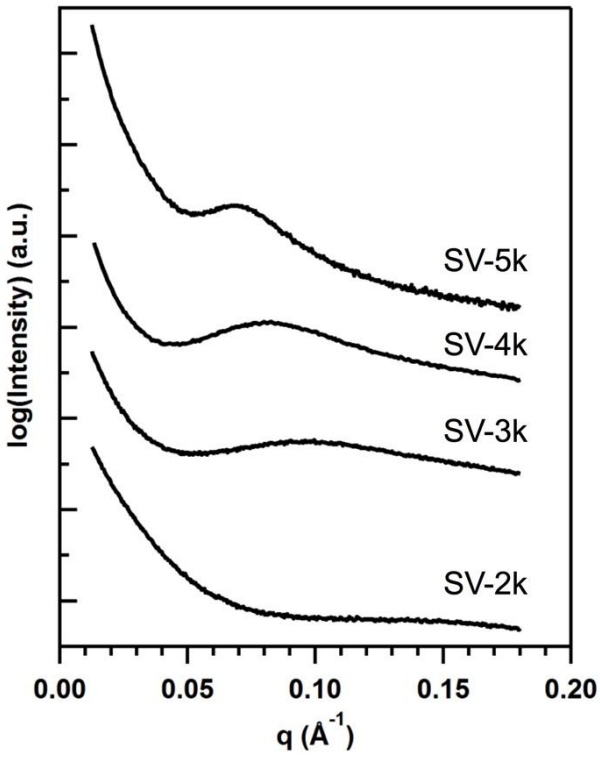

Figure S3. Azimuthally-integrated SAXS patterns acquired at 150 ºC for **SV** block polymers after thermal annealing (at the same temperature) indicate that all of these polymers exhibit a single, broad correlation-hole scattering peak associated with a disordered block polymer.

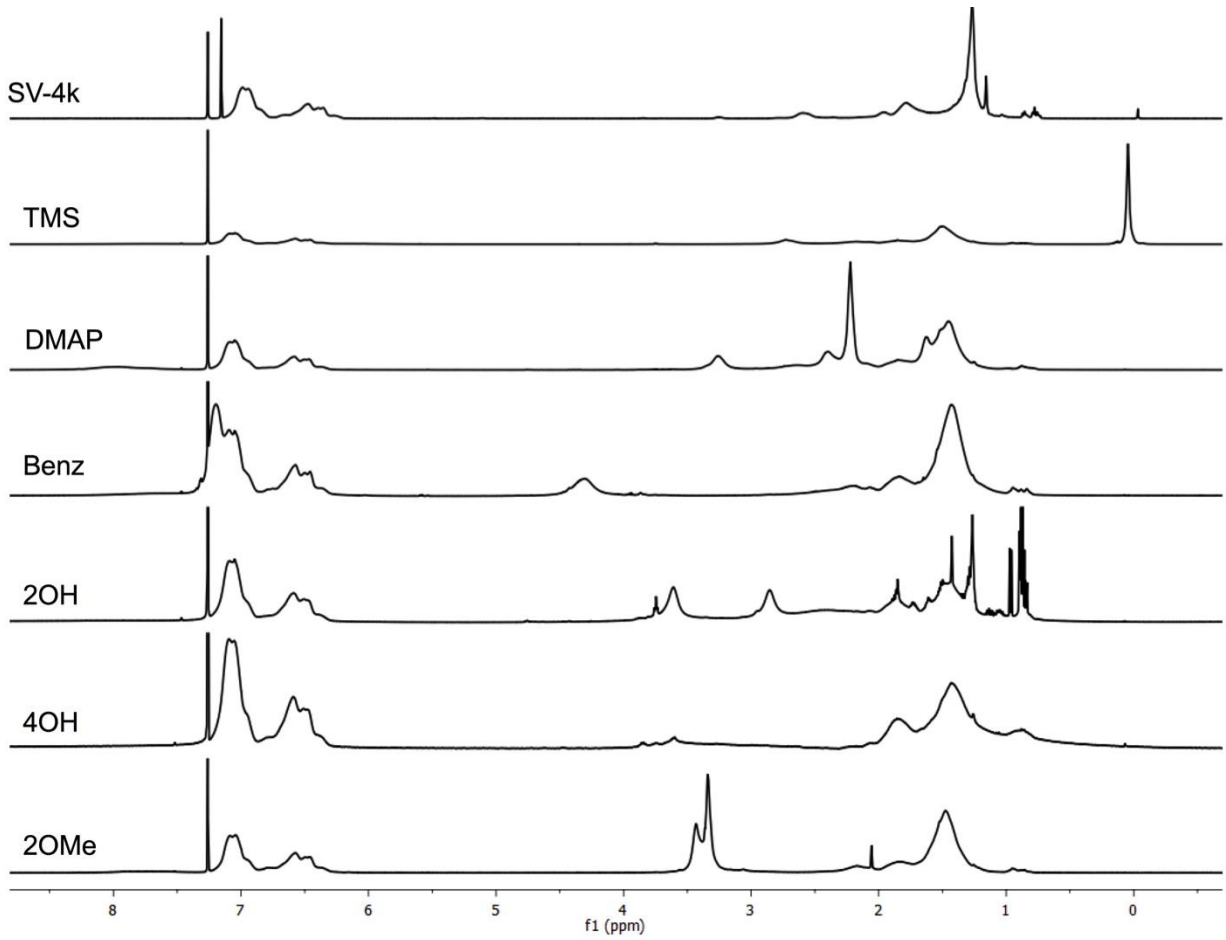

Figure S4. Representative ^{1}H NMR spectra for side chain-functionalized **SV-4k** block polymer, recorded in $CDCl_3$ and referenced to the residual protiated solvent peak. In all cases, the backbone C<u>H</u> signal of VDMA (1H, δ 2.70 ppm) is absent after functionalization, suggesting > 95% efficient ring-opening with the amine. The RAFT agent signal at δ 3.35 ppm also vanishes after functionalization, indicating cleavage of the trithiocarbonate group by aminolysis.

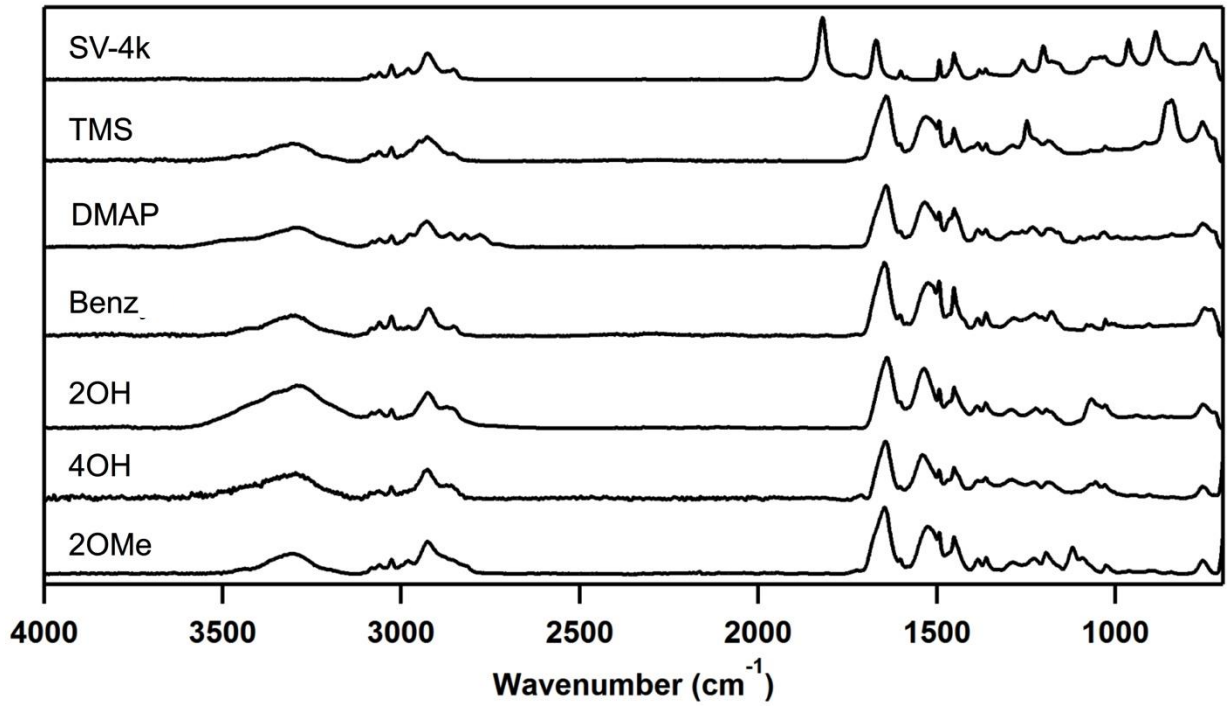

Figure S5. ATR FTIR spectra for **SV-4k** block polymer side chain-functionalized derivatives. In all cases, the stretches corresponding to azlactone ring at (1830 cm^{-1} C=O, 1679 cm^{-1} C=N, and 1209 cm^{-1} C-O-C) are absent after functionalization, suggesting > 95% efficient ring-opening with the amine, consistent with quantitative ^{1}H NMR analyses (see Figure S4).

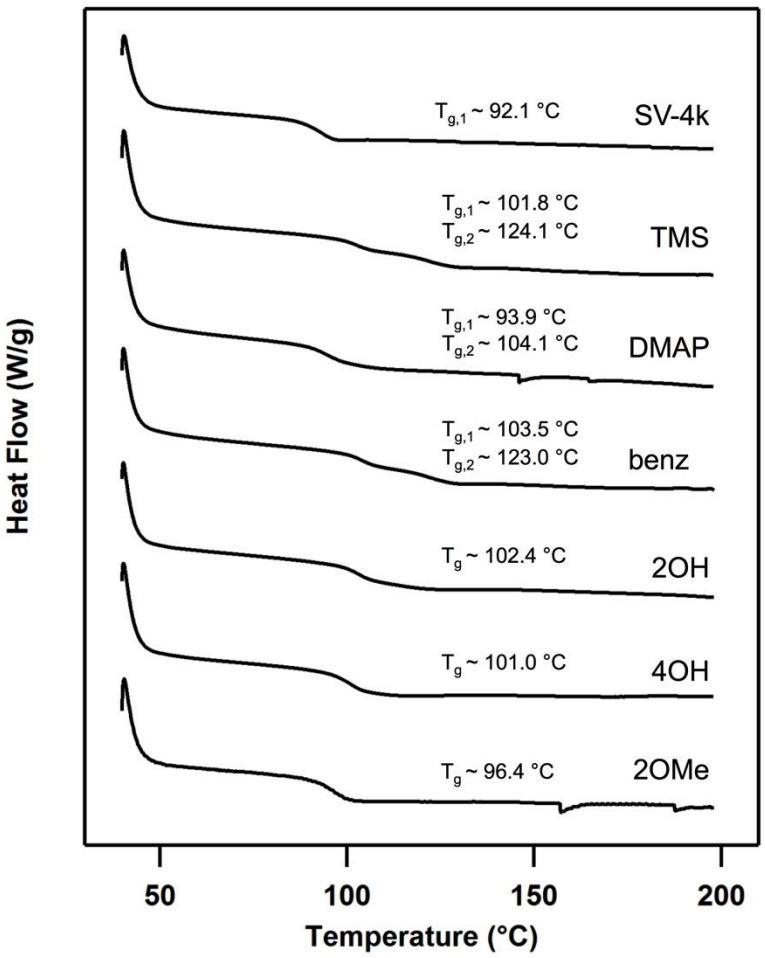

Figure S6. Differential scanning calorimetry (DSC) heating curves for **SV-4k** and its side chain-functionalized derivatives. The azlactone-functionalized parent **SV-4k** block polymer exhibits a single thermal transition at ~92.1 ºC, representing the overlapping glass transition temperature (T_g) of the PS and PVDMA segments. Other block polymer derivatives exhibit either one or two T_g's, depending on the identity and T_g of the derivatized VDMA block. Note that the occurrence of two T_g's is not necessarily indicative of block polymer microphase separation (see Lodge, T. P; Wood. E. R.; Haley, J.C. *J. Polym. Sci. Part B: Polym. Phys.* **2006**, *44*, 756.).

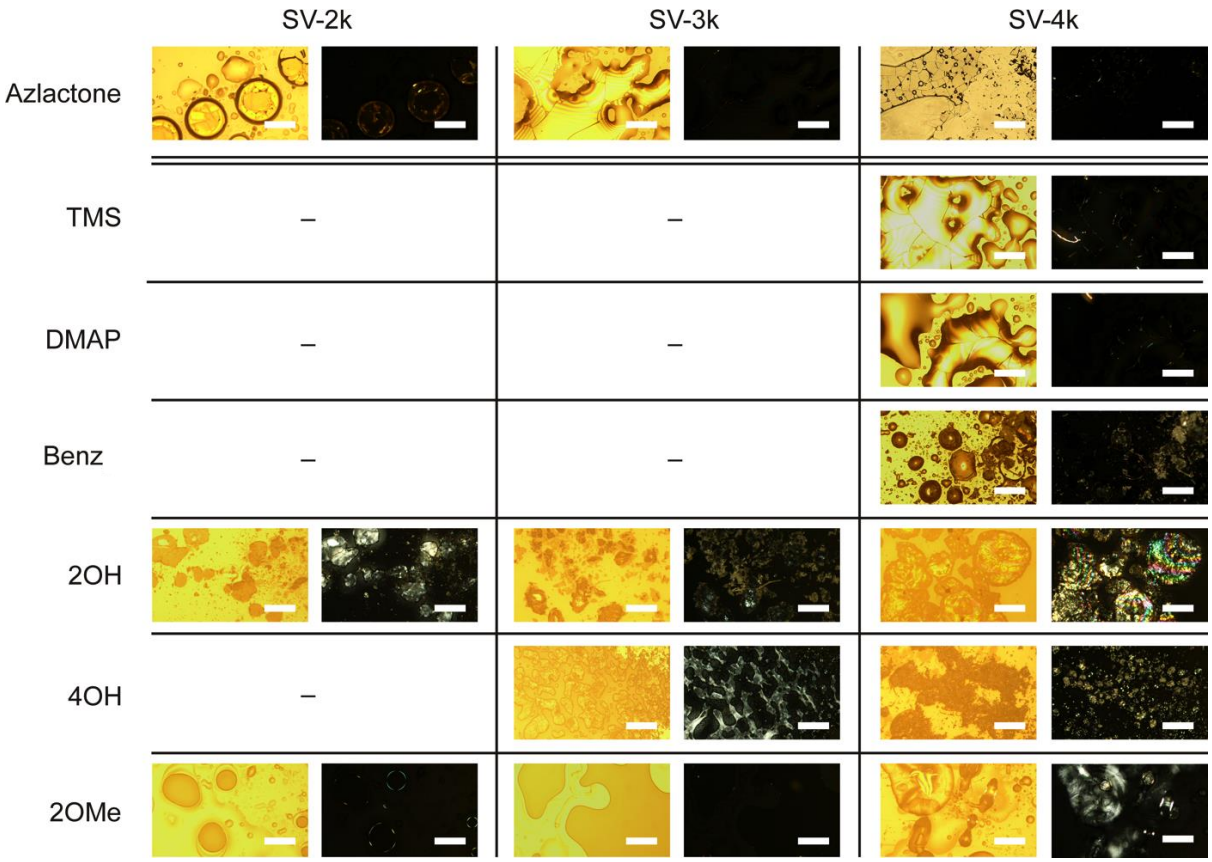

Figure S7. Optical micrographs (left columns) and images obtained under crossed polarizers (right columns) for **SV-2k**, **SV-3k**, and **SV-4k** block polymers and their side chain-functionalized derivatives. Azlactone-functionalized parent **SV** block polymers are disordered, as suggested by their lack of birefringence (dark images), whereas bright images displaying brilliant colors (*e.g.* **SV-4k-2OH** and others) indicate optical birefringence and suggest nanoscale ordering of these block polymer. Block polymer films (~0.18 mm thick) were prepared by thermal annealing at 160 °C for 6 h at 1 Torr prior to imaging at ambient temperature. Scale bar is 0.5 mm.

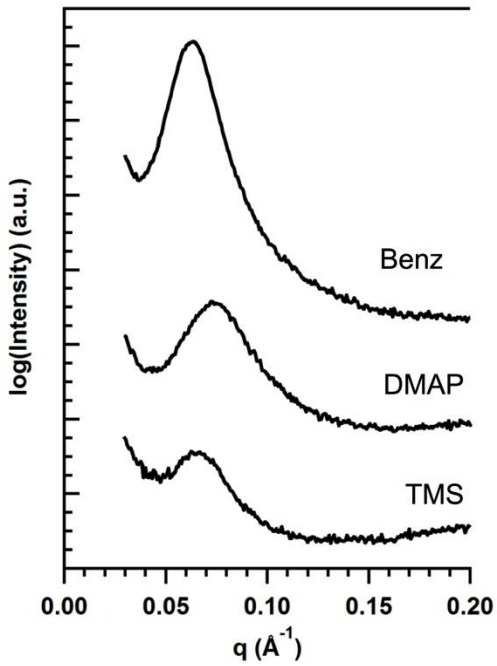

Figure S8. Azimuthally-integrated SAXS patterns for **SV** block polymer derivatives **Benz**, **DMAP**, and **TMS** acquired at 180 ºC after thermal annealing at the same temperature. The broad, correlation-hole scattering associated with each of these samples is indicative of a lack of any microphase separation in these samples.

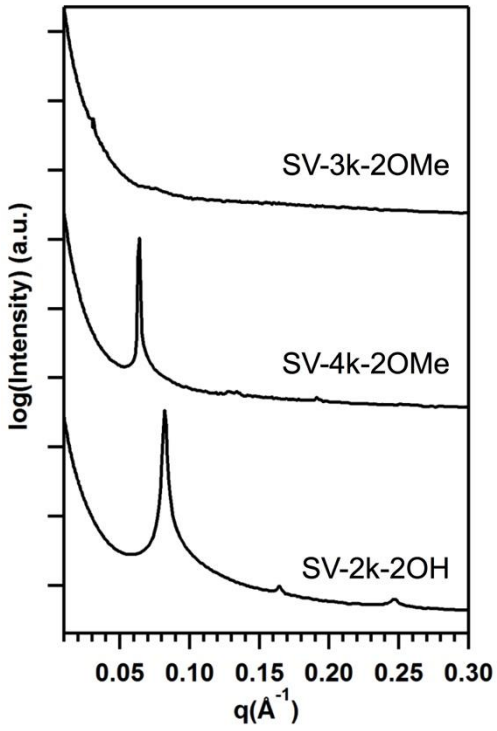

Figure S9. High-resolution, azimuthally-integrated synchrotron SAXS pattern for selected block polymer derivatives presented in Figure 3. Polymers **SV-2k-2OH** and **SV-4k-2OMe** form lamellar mesophases with L_0 = 7.63 nm and 9.80 nm, respectively, in agreement by the values determined by lab source measurements (see Table 2). Synchrotron SAXS confirms that polymer **SV-3k-OMe** is disordered. Samples were thermally annealed in DSC pans and annealed at 150 ºC for 10 h at 1 Torr prior to data acquisition at ambient temperature.

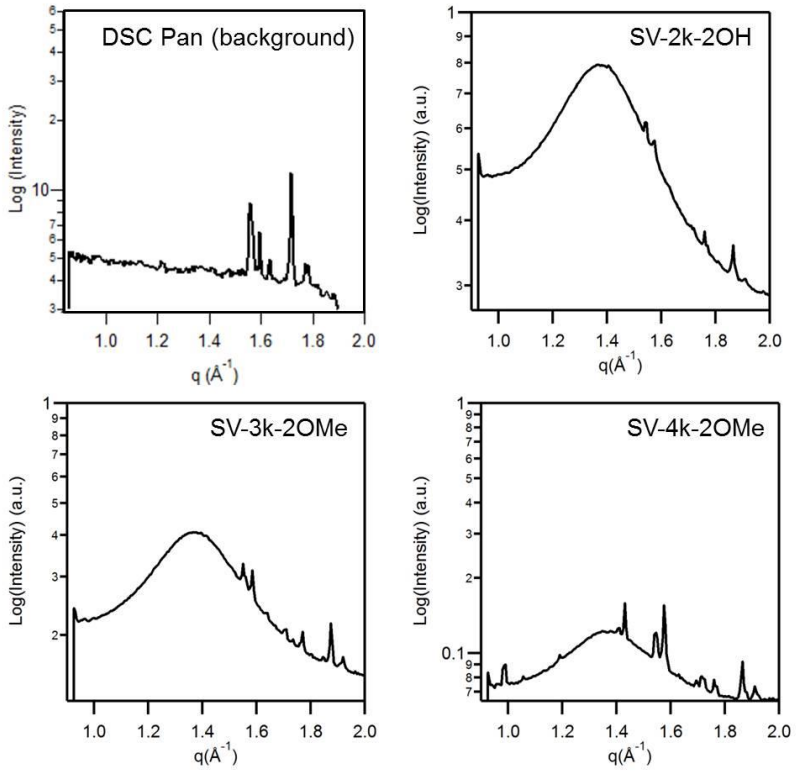

Figure S10. High-resolution, azimuthally-integrated synchrotron WAXS patterns for block polymer derivatives presented in Figure S9 with the same sample history. The top left diffractogram presents the background scattering arising from an empty aluminum DSC pan, indicating that the sharp peaks in all panels correspond to parasitic scattering arising from the encapsulating DSC pans.

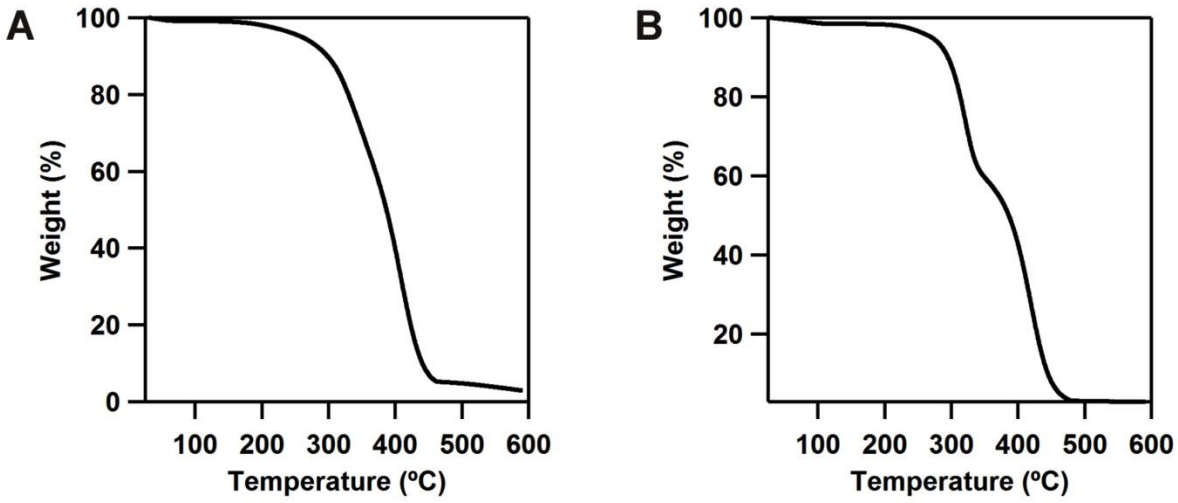

Figure S11. Thermogravimetric analysis (TGA) of (A) **SV-4k-2OH** and (B) **SV-4k-2OMe**, demonstrating a mass loss of less than 5 wt% upon heating to 260 °C and 271 °C, respectively, at a ramp rate of 20 °C/min.

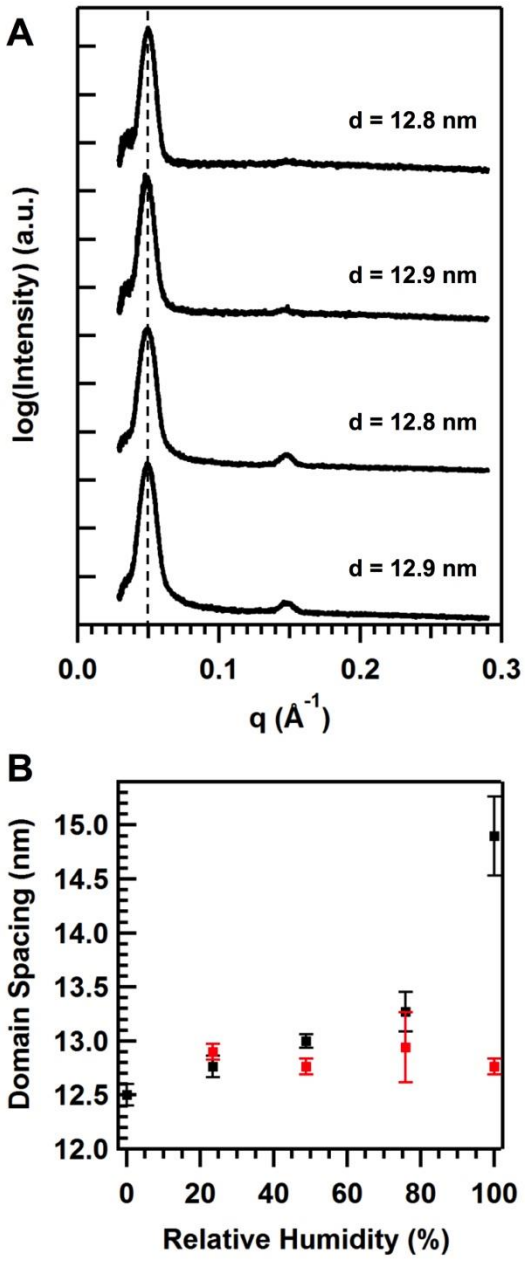

Figure S12. (A) Ambient temperature azimuthally-integrated SAXS patterns for **SV-4k-2OH** samples annealed in various humid environments and subsequently dried *in vacuo* overnight (see Figure 4 and corresponding discussion in main text). (B) Relationship between domain spacing and %RH for humidified films before (*black*) and after (*red*) vacuum annealing. The calculated domain spacings in (B) (*red*) closely match the pre-RH state, suggesting that humidity-induced domain swelling may be reversed by vacuum annealing. Domain spacings were calculated by a regression analysis of the SAXS data against the anticipated reflection positions based on the principal scattering peak q^*, and are reported as an average value. Error bars represent the standard deviation of the average values obtained from the regression.

Chapter 10

Synthesis and Characterization of Backbone Degradable Azlactone-Functionalized Polymers‡

‡ Portions of this chapter have previously been published as: Carter, M.C.D.; Jennings, J.; Appadoo, V.; Lynn, D.M. "Synthesis and Characterization of Backbone Degradable Azlactone-Functionalized Polymers" *Macromolecules* **2016**, *49*, 5514-5526. V. Appadoo fabricated the LbL thin film and performed the DNA transfection experiments. J. Jennings and synthesized the polymers, capsules, and gels, performed the physicochemical characterization experiments, and analyzed the data.

ABSTRACT: We report the design of reactive and degradable copolymers that contain both azlactone side chain functionality and hydrolyzable backbone ester groups. Copolymerization of the vinyl monomer 2-vinyl-4,4-dimethylazlactone (VDMA) and the cyclic ketene acetal 2-methylene-1,3-dioxepane (MDO) using conventional or reversible-deactivation radical polymerization techniques yielded copolymers and block copolymers that exhibit amine-reactivity associated with poly(vinyl azlactone)s but also hydrolytic degradability associated with conventional polyesters. Our results demonstrate that control over monomer feed ratios and other parameters can be used to tune both copolymer composition (e.g., the number/ratio of azlactone and ester repeat units) and the physical properties of the resulting materials (e.g., glass transition temperatures and ability to self-assemble into nanoscale structures). Post-fabrication functionalization of reactive azlactone groups in MDO-*co*-VDMA copolymers by treatment with primary amines proceeds rapidly and quantitatively, and can be achieved without disruption or degradation of backbone ester groups. These azlactone-functionalized copolymers are thus well suited for use as templates for the design of new degradable polymers and as building blocks for the design of covalently and ionically-crosslinked macromolecular thin films, capsules, and gels that degrade in aqueous environments.

Introduction

Polymers with reactive side chains are useful tools for the design of new classes of soft materials. Depending on the nature of their reactivity, for example, reactive polymers can provide access to functional polymers and other types of assemblies that would be difficult, impractical, or impossible to synthesize directly using other methods.[1-7] Many different types of side chain reactive polymers have been developed for these purposes, with those accessible by the free radical polymerization of vinyl monomers providing arguably the most comprehensive and broad suite of side chain reactivity (e.g., polymers bearing reactive nucleophilic, electrophilic, and click-chemistry groups, etc.).[2-4,6-10] Although this approach to the design of reactive polymers is particularly flexible, the classes of polymers that result all possess carbon-carbon backbones—a feature that confers structural stability to the resulting materials, but which can serve as a barrier to the use of these reactive materials in applications where degradability, erosion, or structural transience are desired.

The work reported here was motivated broadly by the utility of reactive polymers bearing azlactone functionality—a class of side chain reactive materials that reacts rapidly and efficiently with primary amine, alcohol, and thiol-based nucleophiles[9,11]—and the potential to exploit the unique properties of these materials in biomedical and biotechnological contexts (or in other applications where degradation or physical erosion would be useful). As a first step toward the design of azlactone-containing polymers with chemically degradable backbones, we report here on the synthesis and physicochemical characterization of a series of azlactone-functionalized vinyl polymers and block polymers containing backbone ester functionality. Our approach is based on the free radical copolymerization of 2-vinyl-4,4-dimethylazlactone (VDMA) with 2-methylene-1,3-dioxepane (MDO; Scheme 1).

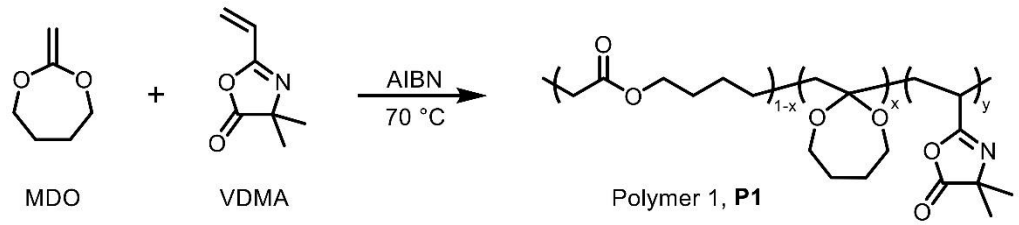

Scheme 1. General scheme showing the polymerization of MDO and VDMA

MDO is a cyclic ketene acetal with an exocyclic double bond that can polymerize during free radical polymerization by one of two principal mechanisms: (i) through ring-opening, which yields polymers containing backbone ester bonds, and (ii) by conventional vinyl addition, which yields polymers bearing acetal-functionalized side chains (Scheme 1).[12-14] The use of MDO as a co-monomer during the radical polymerization of other vinyl monomers has thus been used in past studies as a strategy for the design of vinyl polymers containing chemically degradable backbone linkages.[12,15-27] This general approach has also been used to synthesize degradable vinyl polymers bearing reactive side chain functionality (including polymers bearing epoxide[24,25] and azide groups[26,27]) by copolymerization with, or derivatization of, appropriately functionalized vinyl monomers. The results of these past studies illustrate the broader potential of this copolymerization approach, but also highlight the diversity of parameters and variables—including the impacts of monomer reactivity ratios and the relative ratio of vinyl addition *vs.* ring-opening of MDO, each of which can vary widely as monomer pairs or reaction conditions are manipulated—that govern the range of polymer microstructures and, thus, polymer properties that can be attained.[12]

We sought to explore the feasibility of using this MDO co-monomer approach to design vinyl polymers bearing both amine-reactive, azlactone-containing side chains and degradable backbone ester functionality. We demonstrate here that MDO and VDMA can be co-polymerized to synthesize poly(MDO-*co*-VDMA) copolymers having a broad range of backbone

ester content—spanning from polymers that are predominantly VDMA-based with few backbone ester units, to polyester-like materials containing a minority of azlactone-functionalized side chains—by varying monomer feed ratios. These reactive azlactone-containing copolymers can be functionalized by treatment with primary amine-based nucleophiles to synthesize new side chain-functionalized materials without substantial degradation of backbone ester linkages, providing access to new ester-containing polymers that can be induced to degrade hydrolytically upon exposure to aqueous media. The introduction of backbone ester functionality into VDMA-based materials creates new opportunities to exploit the unique reactivity of the electrophilic azlactone functionality and design functional polymers and macromolecular assemblies that erode or degrade in aqueous environments.

Materials and Methods

Materials. Styrene, benzylamine (99%), propargylamine (99%), ethanolamine (>98%), branched poly(ethylenimine) (PEI, M_n ~ 25 kDa), fluorescein-labelled dextran (FITC-dextran, average molecular weight = 2000 kDa), azobisisobutyronitrile (AIBN, recrystallized from methanol), potassium *tert*-butoxide (95%+), acetone (technical grade), hexanes (technical grade), toluene (ACS grade, >99.5%), tetrahydrofuran (THF, HPLC grade, >99.9%), 3-(trimethylsilyl)-1-propanesulfonic acid sodium salt (97%), α-cyano-4-hydroxycinnamic acid (CHCA, 99%), deuterated water (D_2O, 99%), and deuterated chloroform ($CDCl_3$, 99%) were purchased from Sigma-Aldrich (Milwaukee, WI). 2-Bromo-1,1-dimethoxyethane (95%+) was purchased from Matrix Scientific (Columbia, SC). Aliquat® 336, 1,4-butanediol (99%), and Inhibitor Removal Resin were purchased from Alfa Aesar (Radnor, PA). Dimethylaminopropylamine (99%) and ethylenediaminetetraacetic acid trisodium salt (EDTA, 98%) were purchased from Acros

Organics (Morris Plains, NJ). Tris(2-aminoethyl)amine (TREN, 96%) was purchased from TCI (Portland, OR). Tetramethylrhodamine (TMR) was obtained from Anaspec (Fremont, CA). Tetramethylrhodamine cadaverine (TMR-cad) was obtained from Invitrogen (Carlsbad, CA). 2-Vinyl-4,4-dimethylazlactone (VDMA), a kind gift from Dr. Steven M. Heilmann (3M Corp., Minneapolis, MN), was fractionally distilled under vacuum (B.P. ~22 °C at ~500 mTorr; clear mobile liquid at room temperature) and then stored with 500 ppm butylated hydroxytoluene (BHT) and 1000 ppm triethylamine at 0 °C prior to use. Poly(vinyl-4,4-dimethylazlactone) (PVDMA) homopolymer used to fabricate non-degradable microcapsules was synthesized as previously described.[28] The reversible-addition fragmentation chain-transfer (RAFT) agent *S*-1-dodecyl-*S*'-(α,α'-dimethyl-α''-acetic acid)trithiocarbonate was synthesized according to a literature procedure[29] stored at 0 °C, and re-crystallized from hexanes prior to use. Toluene was passed through a short column of Brockman Type I basic alumina (~10 m/v%) prior to use as a polymerization solvent. Anhydrous THF was obtained from a Pure Process Technology solvent purification system (Nashua, NH). Deuterated phosphate-buffered saline (PBS, pD = 7.4) and acetate buffer (pD = 5.0), both with an ionic strength of 154 mM, were obtained by freeze drying and re-dissolving each (non-deuterated) buffer in D_2O; the pD was calculated from the expression pD = pH + 0.4 and was adjusted by addition of small amounts of either NaOD or DCl in D_2O. Plasmid DNA [pEGFP-N1, encoding enhanced green fluorescent protein (EGFP), 4.7 kb, >95% supercoiled] was obtained from Elim Biopharmaceuticals, Inc. (San Francisco, CA). Lipofectamine 2000 was purchased from Invitrogen (Carlsbad, CA). Silicon wafers (n-type) were obtained from Silicon Inc. (Glenshaw, PA). Water with a resistivity of 18.2 MΩ was obtained from a Millipore filtration system. Materials were used as received unless otherwise stated.

General Considerations. ^{1}H NMR spectroscopy was performed using a Bruker Avance-500 spectrometer and a pulse repetition delay of 16 sec. All spectra were referenced relative to the residual proton or carbon peak of $CHCl_3$ (δ7.26 ppm, δ77.16 ppm) or the residual proton peak of D_2O (δ4.79 ppm). Size exclusion chromatography (SEC) analyses for **Polymer 1** (*i.e.*, **P1**$_x$) were performed using a Viscotek GPC Max VE2001 equipped with two Polymer Laboratories PolyPore columns (250 mm × 4.6 mm) and a TDA-302 detector array, using THF as the eluent at a flow rate of 1 mL/min at 40 °C. SEC analyses for **Polymer 1** derivatives (*i.e.*, **P1**$_x$**-DMAP** and **P1**$_x$**-benz**) and for the PS macroRAFT agent, **BCP1**, and **BCP1-Deg** were performed using a Waters L9 515 344M GPC equipped with two Styragel HT6E columns (300 mm × 7.8 mm), a Waters 515 HPLC pump, a 7726i manual injector, and a 2410 RI detector using filtered THF (containing 0.1 M NEt_3) as the eluent at a flow rate of 1 mL/min at 40 °C. The SEC instruments were both calibrated using 10 narrow dispersity polystyrene standards with M_n = 0.580−377.4 kg/mol (Agilent Technologies, Santa Clara, CA). Differential scanning calorimetry (DSC) for **P1**$_x$ was performed using a TA Instruments DSC100 over a temperature range of T = 10-150 °C (***x*** = 10, 30, 50, 70) or T = -50-60 °C (***x*** = 90) using a heating and cooling rate of 10 °C/min. The thermal history of each sample was erased in the first cycle by heating to 150 °C and cooling to 10 °C (***x*** = 10, 30, 50, 70) or by heating to 60 °C and cooling to -50 °C (***x*** = 90) at a rate of 10 °C/min. All thermal transitions were assigned from the third heating cycle. Attenuated total reflectance (ATR) IR measurements were obtained using a Bruker Tensor 27 FTIR spectrometer outfitted with a Pike Technologies Diamond ATR stage (Madison, WI) and data were analyzed using Opus Software (version 6.5, Bruker Optik GmbH). Spectra were collected at a resolution of 2 cm^{-1} and are presented as an average of 16 scans. Data were smoothed by applying a nine-point average and baseline-corrected using a concave rubberband correction (10 iterations, 64

points). Matrix-assisted laser desorption ionization time-of-flight (MALDI-ToF) mass spectrometry experiments were performed using a Bruker Microflex LRF, over the mass range 1000-30000 kDa, operating at ~80% laser power and measurements are reported as an average of 10 laser pulses. Samples were prepared for analysis by co-spotting equal volumes of saturated solutions of α-cyano-4-hydroxycinnamic acid (CHCA) and polymer in THF. Layer-by-layer film thicknesses were measured using a Gaertner LSE ellipsometer, assuming a refractive index of 1.57; three measurements were obtained on each film and data are reported as an average with standard deviation. Fluorescence micrographs were obtained using an Olympus IX70 microscope equipped with a Lumen Dynamics XCite 120PC-Q fluorescence source and a Q Imaging EXi Aqua camera with an objective magnification of 4X for gels and COS-7 cells, and a 60X oil immersion lens for particles and capsules. A RFP filter set was used for TMR and a GFP filter set was used for GFP (COS-7 cells) and fluorescein (FITC-dextran). Images were obtained in grey scale and false-colored using MetaMorph Advanced software, version 7.7.8.0 (Molecular Devices, LLC). Digital images were acquired using a Canon PowerShot SX130 IS digital camera.

Small-Angle X-Ray Scattering (SAXS). Laboratory SAXS measurements were performed in the Materials Science Center at the University of Wisconsin-Madison. Constant temperature scans were performed using Cu-Kα X-rays generated by a Rigaku Micromax 002+ microfocus source and collimated through a Max-Flux multilayer confocal optic (Osmic, Inc.), followed by passage through three pinholes to collimate and trim the final beam diameter to < 0.5 mm. Samples were annealed at 150 °C for 4 hours at 1 Torr before they were mounted in a vacuum chamber on a Linkam temperature-controlled hot-stage and equilibrated at room temperature for

15 min prior to data collection (exposure time = 20 min). Two-dimensional XRD patterns were recorded on a Gabriel X-ray detector (150 mm diameter active circular area) using a sample-to-detector distance of 1 m or 55 cm (calibrated using a silver behenate standard sample with d = 58.38 Å). 2D SAXS patterns were azimuthally integrated using the DataSqueeze software package to obtain one-dimensional scattering profiles.

Synthesis of 2-Methylene-1,3-Dioxepane (MDO). The synthesis was carried out in two steps according to a modified literature procedure, as follows.[13,30] *2-Bromo-1,3-dioxepane.* In a typical synthesis, 1,4-butanediol (11.4 g, 126.7 mmol), 2-bromo-1,1-dimethoxyethane (21.4 g, 126.7 mmol) and *p*-toluenesulfonic acid (239.3 mg, 1.26 mmol) were added to an oven-dried 100 mL round-bottom flask outfitted with a short-path distillation apparatus and receiving flask. The mixture was stirred at 85 °C for 3 days, over which time ~90% of the theoretical mass of methanol byproduct was collected. The crude mixture was fractionally distilled at 250 mTorr to yield 16.29 g (66.0%) of the desired product, 2-bromo-1,3-dioxepane. Colorless mobile liquid, B.P. 82-85 °C at 250 mTorr. ^{1}H NMR (500.022 MHz, $CDCl_3$, δ ppm): 1.61-1.77 (m, 4H, -OCH_2-$C\underline{H}_2$-$C\underline{H}_2$-CH_2O-), 4.31 (d, 2H, *J* = 5.34 Hz, -CH-$C\underline{H}_2$-Br), 3.60-3.68 (m, 2H, -$OC\underline{H}_2$-CH_2-CH_2-CH_2O-), 3.87-3.96 (m, 2H, -OCH_2-CH_2-CH_2-$C\underline{H}_2O$-), 4.87 (t, 1H, *J* = 5.34 Hz, -C<u>H</u>-CH_2Br). *2-Methylene-1,3-dioxepane (MDO).* The synthesis was carried out according to a modified literature procedure, as follows.[13,30] In a typical synthesis, 2-bromo-1,3-dioxepane (21.69 g, 111.2 mmol), Aliquat® 336 (902.3 mg, 2.23 mmol, 0.02 equiv.) and 100 mL anhydrous THF were added to a 250 mL oven dried round-bottom flask and placed under nitrogen. This colorless solution was vigorously stirred in a dry ice/*i*PrOH bath while potassium *tert*-butoxide (24.85 g, 221.4 mmol, 2.0 equiv.) was added portion-wise over the course of ~45 mins. The now colloidal,

light-orange mixture was allowed to react for 1.25 hrs on dry ice/*i*PrOH, and then warmed to room temperature and stirred for an additional 1 hr, over which time the mixture turned light brown. 70 mL of ether was added, and the mixture was stirred vigorously and then vacuum filtered through Whatman #1 filter paper. The filtered off-white solids were collected and washed with ether (3 x 70 mL). The ether extracts were collected and rotovapped down to a slurry containing off-white solids. The slurry was vacuum filtered through Whatman #1 filter paper, concentrated, and then filtered again through a glass wool plug in a Pasteur pipet with the aid of an additional ~5 mL of ether. This light yellow solution was fractionally distilled at ~24 Torr (using a water aspirator) to yield 6.61 g (52.1%) of the desired product, 2-methylene-1,3-dioxepane (MDO). Colorless mobile liquid, B.P. 42-43 °C at ~24 Torr. ^{1}H NMR (500.022 MHz, $CDCl_3$, δ ppm): 1.75 (m, 4H, -OCH_2-$C\underline{H}_2$-$C\underline{H}_2$-CH_2O-), 3.45 (s, 2H, -C=$C\underline{H}_2$), 3.92 (m, 4H, -$OC\underline{H}_2$-CH_2-CH_2-$C\underline{H}_2O$-). ^{13}C NMR (125.74 MHz, $CDCl_3$): 29.0 (-OCH_2-$\underline{C}H_2$-$\underline{C}H_2$-CH_2O-), 67.4 (-$O\underline{C}H_2$-CH_2-CH_2-$\underline{C}H_2O$-), 70.4 (-C=$\underline{C}H_2$), 164.0 (-$\underline{C}$=CH_2).

Synthesis of Poly(MDO-VDMA) [Polymer 1; P1$_x$]. The synthesis of MDO-VDMA copolymers, referred to hereafter using the notation **P1$_x$**, where ***x*** is the mole fraction of MDO in the feed, was conducted in the following general manner, using the synthesis of **P1$_{50}$** as a representative example. VDMA was passed twice through a short column of Inhibitor Removal Resin followed by a short column of silica gel to remove inhibitor and triethylamine base, respectively. VDMA (0.921 g, 6.62 mmol), MDO (0.758 g, 6.64 mmol), AIBN (21.3 mg, 0.130 mmol), and toluene (5.0 mL) were added to an oven-dried 10 mL round-bottom flask and the stirred colorless solution was sparged with nitrogen for 15 min before being placed into an oil bath at 70 °C. After 24 hours, the flask was cooled to room temperature and the mixture was

diluted with ~2 mL DCM and then precipitated into ~200 mL of 8:1 (v/v) hexanes:*i*PrOH. The resulting white solid was collected by vacuum filtration, redissolved in ~ 5 mL DCM, re-precipitated once more into hexanes:*i*PrOH and then dried under high vacuum overnight. $M_{n,GPC}$ = 18.1 kDa with $Đ$ = 3.0. ^{1}H NMR and ATR IR spectra are given in Fig S1 and Fig S2, respectively, and DSC traces are given in Fig S3 (Supporting Information can be found at the end of this chapter). Molecular weights and dispersities for all copolymers are given in Table 1 of the main text. **P1$_{10}$**, **P1$_{30}$**, **P1$_{50}$**, and **P1$_{70}$** are white solids at room temperature; **P1$_{90}$** is a viscous white paste.

Side-Chain Functionalization of P1$_x$ by Reaction with Primary Amines. In a typical functionalization reaction, ~50 mg of copolymer **P1$_x$** was dissolved in 0.75 mL of anhydrous THF in a 6 mL glass vial. To this colorless solution, 1.0 mol equiv. of a primary amine was added (w.r.t. moles of VDMA; for **P1$_{50}$**, wt. fraction VDMA = 0.73). The chemical structures of the primary amines used in this study are given in Scheme 2 of the main text. The vial was sealed with a Teflon cap and stirred overnight at room temperature. The resulting colorless solution was precipitated into ~6 mL of hexanes at room temperature and centrifuged. The supernatant was removed and the resulting white powder was dried under high vacuum overnight. The resulting polymers are denoted as **P1$_x$-sidechain**, where the side-chains are dimethylaminopropylamine (**DMAP)**, ethanolamine (**OH**), benzylamine (**benz**), and propargylamine (**prop**).

Characterization of the Degradation of P1$_{50}$-DMAP in Aqueous Media. A sample of **P1$_{50}$-DMAP** (~10 mg; synthesized as described above) was dissolved in either 1.0 mL of deuterated PBS (pD = 7.4) or deuterated acetate buffer (pD = 5.0). 3-(Trimethylsilyl)-1-propanesulfonic

acid sodium salt (~0.5 mg) was added as an internal standard, and this solution was transferred to an NMR tube. ^{1}H NMR measurements (32 scans) were taken at 30 min intervals over ~15 hours at room temperature using a T1 relaxation delay of 10 sec. The change in the integration ratio of the methylene protons adjacent to the backbone ester functionality (4.03 ppm) relative to the internal standard was monitored and used to determine the extent of ester hydrolysis. NMR data analysis was performed using MestReNova software (Version 10.0.2). Samples were subsequently freeze-dried for ATR IR analysis.

Synthesis of [Poly(S-*block*-(MDO-*co*-VDMA)], BCP1. *Synthesis of Polystyrene (PS) Homopolymer:* Styrene was stirred over Brockman Type I basic alumina for 30 min and gravity filtered through Whatman #2 filter paper. Freshly purified styrene (15 mL, 131 mmol) and the RAFT agent *S*-1-dodecyl-*S*'-(α,α'-dimethyl-α''-acetic acid)trithiocarbonate (12 mM) were added to an oven-dried 25 mL Schlenk tube and degassed via three freeze-pump-thaw cycles. The solution was placed in a 120 °C oil bath for 10 h, after which it was cooled in liquid nitrogen. The resulting polymer was precipitated in ~400 mL cold methanol and collected, redissolved in ~15 mL THF, re-precipitated twice more in cold methanol, and freeze-dried from benzene. $M_{n,GPC}$ = 21.7 kg/mol, $Đ$ = 1.13. *Synthesis of BCP1:* VDMA was passed twice through a short column of inhibitor removal resin followed by a short column of silica gel to remove inhibitor and triethylamine base, respectively. PS macroinitiator (0.485 g, 0.224 mmol), VDMA (0.359 g, 2.58 mmol), MDO (0.125 g, 1.10 mmol), AIBN (0.37 mg, 0.00223 mmol), and toluene (1.5 mL) were added to an oven-dried 25 mL Schlenk tube and degassed *via* three freeze-pump-thaw cycles. The solution was stirred in a 70 °C oil bath for 24 hours, after which it was cooled in liquid nitrogen. The resulting solution was diluted with ~3 mL THF, precipitated in ~200 mL

cold hexanes, collected, and freeze-dried from benzene to yield a light yellow powder. M_{nNMR} = 33.8 kDa, with $Đ$ = 1.57. ^{1}H NMR and ATR IR spectra are shown in Fig S8AB.

Side-Chain Functionalization of BCP1 by Reaction with Primary Amines. In a typical functionalization reaction, ~25 mg of block copolymer was dissolved in 0.5 mL of anhydrous THF in a 6 mL glass vial. To this colorless solution, 1.0 mol equiv. of amine (w.r.t. moles of VDMA) was added. The vial was sealed with a Teflon cap and stirred for 30 min at room temperature. The resulting colorless solution was precipitated into ~6 mL hexanes at room temperature and centrifuged. The supernatant was removed and the resulting white powder was dried under high vacuum.

Characterization of the Degradation of BCP1. A sample of **BCP1** (~30 mg) was dispersed in a mixture of 3.0 mL of THF and 3.0 mL of 0.1 M NaOH in methanol and stirred at 50 °C overnight. The mixture was filtered and then rotovapped down to an off-white solid. ATR IR analysis revealed the disappearance of backbone ester groups (C=O ester, 1740 cm^{-1}) and the hydrolysis of azlactone side-chains (C=O azlactone, 1821 cm^{-1} absent) and the appearance of C=O carboxylate stretching (1650 cm^{-1}); see Fig 3C. The remaining solids were triturated with THF (containing 0.1 M NEt_3) and filtered for subsequent GPC analysis.

Fabrication of Multilayer-Coated Microparticles and Hollow Microcapsules using $P1_{70}$. Multilayer-coated microparticles and hollow capsules were prepared in analogy to previous reports.[31] Spherical calcium carbonate cores loaded with FITC-dextran and with diameters ranging from ~5-10 μm (as determined by optical microscopy) were suspended in 1.0 mL of

acetone in microcentrifuge tubes. Films were fabricated layer-by-layer by iteratively depositing solutions of branched PEI (20 mM in acetone) and fluorescently labelled **P1$_{70}$** (5.0 mg/mL; ~1 mol% TMR-cad added to the polymer in acetone and allowed to react for 5 min at room temperature to install fluorescent labels) onto the spherical particles as follows. The first polymer layer was deposited by centrifuging the particle solution, followed by removal of the acetone and addition of 1.0 mL of PEI solution. The particle suspension was shaken manually for ~15 sec and then centrifuged for 10 sec at 3000 rpm. The supernatant was removed and the particles were rinsed twice by resuspension and shaking in ~1 mL of acetone and subsequent centrifugation. The second polymer layer was deposited by adding 1.0 mL of **P1$_{70}$** solution to the suspension of particles and manually shaking for ~15 sec. The particles were then rinsed twice with ~1 mL of acetone, as above. This process was repeated to deposit 4.5 layer pairs ("bilayers") of PEI/**P1$_{70}$**, such that the terminal layer was **P1$_{70}$**. Next, coated particles were placed into ~1 mL of a solution of dimethylaminopropylamine in THF (40 mM) and the residual azlactone groups were allowed to react for 10 min at room temperature. The particles were then centrifuged, washed with THF, and redispersed in PBS buffer for imaging. To generate hollow capsules, a suspension of microparticles was centrifuged and the supernatant PBS buffer was removed. EDTA solution (1.0 mL; 0.40 M in MilliQ water) was added to the tube and the particles were resuspended prior to imaging. To characterize degradation, capsules were centrifuged and the EDTA solution was replaced with PBS solution (pH 7.4); a 90 μL aliquot of the suspension was removed, 10 μL of 10 M $KOH_{(aq)}$ was added (such that the final concentration of base was 1 M), and this solution was incubated at 50 °C for 2 hrs. To fabricate non-degradable (control) capsules, PVDMA (20 mM) was used instead of of **P1$_{70}$** and the procedure outlined above was followed.

Synthesis of Degradable Gels using P1$_{50}$-DMAP. Two methods were used to synthesize degradable gels from **P1$_{50}$**. *Method 1:* **P1$_{50}$** (~25 mg) was dissolved in 200 μL of THF and the cross-linker tris(2-aminoethyl)amine (TREN; 0.5 equiv. w.r.t. VDMA) was added to induce gelation and cross-linking. The as-formed gel was then incubated overnight in a solution of dimethylaminopropylamine in THF (20 mM) and subsequently rinsed with THF. *Method 2:* **P1$_{50}$** (~25 mg) was dissolved in 200 μL THF and 8.75 μL of dimethylaminopropylamine (0.5 equiv. w.r.t. VDMA) was added. The solution was stirred for 10 min and then 38.3 μL of TREN solution (20 μL TREN in 0.5 mL THF; 0.5 equiv. TREN w.r.t. VDMA) was added with vigorous stirring to induce cross-linking and gelation. For experiments designed to characterize gel degradation *via* ester bond hydrolysis, gels were placed in PBS buffer (pH 7.4) and allowed to stand at room temperature overnight. The resulting solutions were freeze-dried to recover degraded polymer for ATR IR analysis. For experiments designed to further functionalize reactive gels, gels were manually split into two pieces and each portion was soaked in a solution of either TMR-cad or TMR (0.02 mg/mL in acetone) for 15 min. Gels were then rinsed and soaked in fresh acetone overnight to remove any unreacted or adsorbed dye molecules prior to imaging by fluorescence microscopy. For both Methods 1 and 2, ATR IR analysis was performed after the addition of each amine (see Fig S10).

Fabrication and Erosion of DNA-Containing Polyelectrolyte Multilayers using P1$_{30}$-DMAP. Multilayer films composed of **P1$_{30}$-DMAP** (synthesized as above) and DNA (both in sodium acetate buffer, pH = 5.0) were fabricated on silicon substrates (0.5 cm x 3.5 cm) using a manual dipping procedure[32,33] as follows: 1) substrates were submerged in a solution of **P1$_{30}$-DMAP** (1.16 mg/mL, filtered through a 0.2 μm membrane syringe filter) for 5 min, 2) substrates were

removed and immersed in 100 mM sodium acetate buffer (pH = 5.0) for 1 min followed by a second rinse in a fresh solution of the same buffer for 1 min, 3) substrates were submerged in a solution of DNA (750 μg/mL) for 5 min, and 4) substrates were rinsed in the manner described in step 2. This cycle was repeated until the desired number of polymer/DNA layers (or 'bilayers') was reached. All films were fabricated under ambient conditions at room temperature. In experiments used to characterize film growth profiles by ellipsometry, films were dried after every cycle using filtered compressed air. Experiments designed to characterize film erosion and DNA release profiles were performed in triplicate as follows. Film-coated substrates were placed into plastic cuvettes and 1.0 mL of PBS buffer (pH 7.4, 154 mM) was added. The samples were incubated at 37 °C and, at pre-determined intervals, films were removed from solution and dried under a stream of filtered air. Film thicknesses were measured by ellipsometry and the quantity of DNA released into solution was determined by UV/Vis absorbance measurements. Films were then transferred to fresh PBS solutions for further incubation.

Cell Transfection Assays. COS-7 cells were grown in 96-well plates at an initial seeding density of 12,000 cells/well in 200 μL of growth medium (90% Dulbecco's modified Eagle's medium, 10% fetal bovine serum, penicillin 100 units/mL, streptomycin 100 mg/μL). Cells were grown for 24 h, at which time 15 μL of a Lipofectamine 2000/plasmid mixture (see below) were added directly to each well. Experiments were performed in triplicate in accordance with the general protocol provided by the manufacturer. The Lipofectamine 2000/plasmid mixture was composed of 50 μL of a DNA solution collected at a given each time point during release experiments (see above) and 25 μL of Lipofectamine 2000 reagent (24 μL stock diluted into 976

μL of Opti-MEM). Fluorescence images used to characterize relative levels of gene expression in cells were acquired after 48 hr.

Results and Discussion

Synthesis and Characterization of MDO-co-VDMA Copolymers

Our approach to the design of degradable azlactone-functionalized polymers is based on the free radical copolymerization of the amine-reactive vinyl monomer 2-vinyl-4,4-dimethylazlactone (VDMA) and the cyclic ketene acetal 2-methylene-1,3-dioxepane (MDO) using AIBN as an initiator. We synthesized a series of poly(MDO-*co*-VDMA) polymers with different compositions by varying the mole fraction of MDO in the feed. Scheme 1 shows the polymerization scheme and conditions used to obtain these copolymers, hereafter denoted **P1**$_x$, where ***x*** is the mole fraction of MDO in the feed. We varied the feed fraction from 0.10 to 0.90 MDO, and the resulting molecular weights (M_n), dispersity indices ($Đ$), compositions (by ^{1}H NMR), and glass transition temperatures (T_g) of **P1**$_x$ (where ***x*** = 10, 30, 50, 70, 90) are summarized in Table 1. All **P1**$_x$ polymers had number average molecular weights of

Table 1. Molecular weight (M_n by GPC, relative to polystyrene standards), dispersity ($Đ$), feed fraction of monomer (f), molar composition (F), and glass transition temperatures (T_g), for Polymer 1 (**P1**$_x$) copolymers synthesized in this study.

Name	$M_{n,GPC}$ (kDa)	$Đ$	f_{MDO}	F_{ester}	F_{acetal}	f_{VDMA}	F_{VDMA}	Ratio Ester:Acetal	T_g (°C)
$P1_{10}$	20.3	3.3	10	0.019	0.051	90	0.93	0.37	86.7
$P1_{30}$	22.7	2.4	30	0.047	0.098	70	0.86	0.48	78.9
$P1_{50}$	18.1	3.0	50	0.11	0.15	50	0.73	0.73	54.9
$P1_{70}$	22.2	2.4	70	0.25	0.25	30	0.51	1.0	44.3
$P1_{90}$	16.7	2.1	90	0.49	0.22	10	0.29	2.2	19.9

approximately 20 kDa (M_n by GPC, relative to PS standards) and $Đ$ values between 2.0-3.0. Characterization by ^{1}H NMR and IR spectroscopy confirmed that the azlactone groups remained intact after polymerization (e.g., they were not hydrolyzed by the presence of adventitious water, or otherwise chemically degraded during polymerization; Fig 1AB and Fig S1-S2).

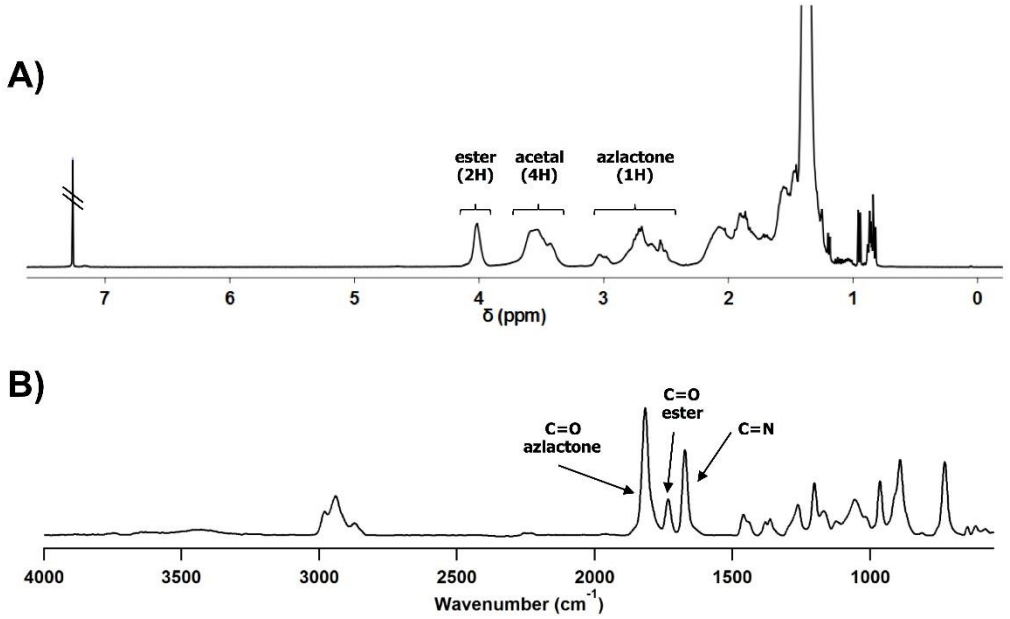

Figure 1. (A) ^{1}H NMR spectrum for **P1$_{50}$**, showing the locations of the ester, acetal, and azlactone proton peaks used for determination of polymer composition (see Table 1). (B) ATR IR spectrum for **P1$_{50}$** showing the locations of the bands corresponding to the azlactone carbonyl (C=O), azlactone imine (C=N), and backbone ester carbonyl (C=O) groups. A complete set of ^{1}H NMR and IR spectra for all **P1$_x$** polymers is given in Figs S1 and S2.

As anticipated, when lower feed fractions of MDO were used, polymers contained a majority of VDMA. **P1$_{10}$** and **P1$_{30}$**, for example, contained 93 and 86% VDMA, respectively, and had relatively high glass transition temperatures (T_g ~ 86.7 and 78.9 °C, respectively; **T**able 1) similar to the homopolymer of VDMA [poly(2-vinyl-4,4-dimethylazlactone), PVDMA, T_g ~ 92 °C].[11] When the molar feed fractions of MDO and VDMA were set equal, as in **P1$_{50}$**, the copolymer contained 73% VDMA, and higher feed fractions of MDO continued to decrease the number of VDMA units incorporated into the polymer and lower the glass transition temperature

(Table 1). **P1$_{70}$** and **P1$_{90}$** were composed of 51% and 29% VDMA, respectively, demonstrating the ability to incorporate a mole fraction of MDO in excess of 70% when the feed fraction of VDMA is 0.10. Thus, while **P1$_{10}$** is effectively a homopolymer of VDMA containing a small number of degradable ester groups, **P1$_{90}$** is essentially a polyester with a small fraction of amine-reactive azlactone groups. **P1$_{90}$** is an amorphous gel at room temperature (T_g ~19.9 °C), whereas all other **P1$_x$** polymers are white powders under ambient conditions. In all cases, we observed that, under these polymerization conditions, MDO repeat units in **P1$_x$** polymers had short, ester-containing side-chain branches resulting from [1,7]-H and [1,4]-H transfer,[14,34,35] as evidenced by a triplet at 0.88 ppm in the ^{1}H NMR spectra (assigned to terminal methyl groups of the branches; Fig S1). These transfer mechanisms are well-documented for the radical (co)polymerization of MDO during radical ring-opening and propagation.[14,34,35] The presence of branching can prevent crystallinity in polymers containing MDO;[12] the absence of any melting transition temperatures (T_m) in DSC traces confirmed this outcome for all **P1$_x$** polymers investigated here (e.g., Fig S3).

Past studies of the radical copolymerization of MDO and other vinyl monomers have established that MDO tends to polymerize in both the ring-opened and ring-closed form, leading to the incorporation of both ester and acetal units, respectively, into a vinyl polymer backbone (e.g., see **Equation 1**).[12] We observed both of these groups by ^{1}H NMR (Fig 1A) and by ^{13}C NMR spectroscopy (Fig S1 and S4, respectively), and we used ^{1}H NMR to calculate the ratio of the number of ester to acetal repeat units (Table 1; see also Fig S1). Inspection of the data in Table 1 shows that the ratio of ester to acetal units increased as the mole fraction of MDO in the feed increased. For example, in **P1$_{10}$**, there were approximately 0.27 ester groups for every acetal, but for **P1$_{50}$** the number of ester groups increased to approximately 0.73 per acetal unit. When the feed fraction of MDO was greater than 0.5 (e.g., for **P1$_{70}$**), the ester to acetal ratio

reached unity, and for a large excess of MDO relative to VDMA (e.g., **P1$_{90}$**) there were 2.2 ester groups for every acetal in the backbone. Because the presence of acetal groups in the polymer backbone did not detrimentally affect the amine reactivity or hydrolytic degradability of these copolymers (see following discussion), we did not seek to control the degree of incorporation of the acetal group as part of this study.

Finally, we note that for all **P1$_x$** compositions investigated, the total quantity of MDO monomer incorporated into the polymer chain in both the ester and acetal form was lower than the amount present in the feed, a result that has been widely observed in radical copolymerizations of MDO with other vinyl monomers.[12] The cross-propagation reactivity of MDO toward other vinyl monomers tends to be low, and although determination of reactivity ratios of MDO and VDMA in this system was not a goal of this study, we note that we did obtain greater incorporation of MDO (relative to VDMA) as compared to past studies of the copolymerization of MDO with other common monomers, such as methyl methacrylate (MMA),[36] methyl acrylate (MA),[16] and styrene (S).[37]

Post-Fabrication Functionalization of MDO-co-VDMA Copolymers

MDO-co-VDMA polymers represent an amine-reactive platform for the synthesis of a wide range of other side-chain functionalized and degradable copolymers. We used **P1$_{50}$** as a model polymer to characterize the post-fabrication modification of the azlactone groups in these materials by reaction with primary amine-containing compounds. Many past studies have exploited the rapid reactivity of azlactone-functionalized polymers with primary amines to synthesize new side-chain functionalized polymers and materials,[9,11,38-51] in part because the reaction between these electrophiles and primary amines is rapid, byproduct free, and does not

require a catalyst.[9,11] We functionalized **P1$_{50}$** with four different model amines containing four representative types of functional groups: tertiary amine (dimethylaminopropylamine; **DMAP**), alcohol (ethanolamine; **OH**), aromatic (benzylamine; **benz**), and alkyne (propargylamine; **prop**) side-chain groups were investigated as part as this study (Scheme 2; 1 equiv. amine, room temperature). Characterization of the resulting side-chain functionalized polymers by ^{1}H NMR and IR spectroscopy revealed that the ring-opening of the azlactone group could be achieved without any substantial aminolysis of backbone ester linkages that would lead to degradation of molecular weight (**Fig S5** and **S6**).

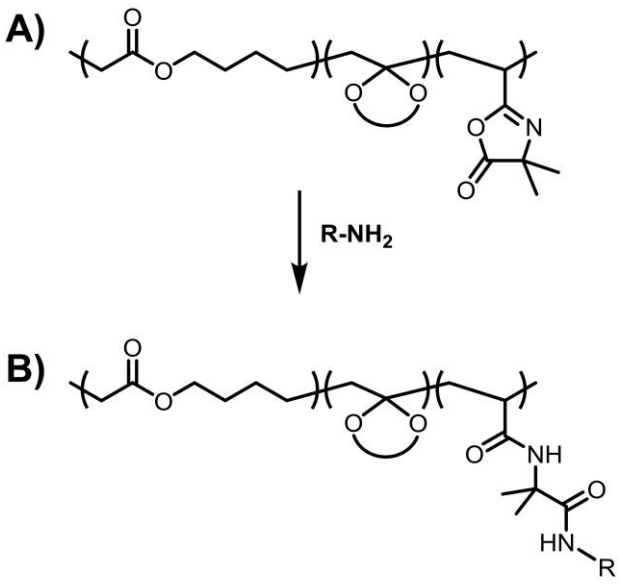

P1$_{50}$-DMAP, R = -$CH_2CH_2CH_2N(CH_3)_2$
P1$_{50}$-OH, R = -CH_2CH_2-OH
P1$_{50}$-benz, R = -CH_2-Ph
P1$_{50}$-prop, R = -CH_2-C≡CH

Scheme 2. General scheme showing the functionalization of the azlactone rings in **P1$_{50}$** by reaction with primary amine-containing compounds (the 7-membered dioxepane ring has been abbreviated for clarity). The names and chemical structures of derivatives prepared using this approach are also shown. ^{1}H NMR and IR spectra for all **P1$_x$** derivatives are given in Figs S5 and S6.

Characterization of **P1$_{50}$-DMAP** and **P1$_{50}$-benz** derivatives by GPC revealed unimodal peaks at retention times comparable to that of the reactive **P1$_{50}$** template (Fig S7A; derivatives **P1$_{50}$-OH** and **P1$_{50}$-prop** were insoluble in GPC solvents used for these studies). MALDI time-of-flight mass spectrometry also revealed an increase in the molecular weights (mass-to-charge ratios) of all polymer derivatives relative to the **P1$_{50}$** parent template, a result consistent with the addition of side-chain functionality and the absence of significant backbone degradation (Fig S7B). The ability to selectively functionalize the azlactones is a useful property of these reactive polyester materials and is likely facilitated by the greater electrophilicity of the heterocyclic azlactone ring as compared to the backbone ester carbonyl (the azlactone carbonyl is ~10 ppm more downfield in the ^{13}C NMR spectrum; Fig S4).

The side-chain functionalized polymers described above are polyesters, and should thus be capable of undergoing degradation by backbone hydrolysis under a variety of conditions. Fig 2A demonstrates that the backbone ester bonds of **P1$_{50}$-DMAP** hydrolyze when this tertiary amine-functionalized polyester is dissolved in aqueous media (with a half-life of approximately 8.0 hours at pD = 7.4 in deuterated PBS buffer; roughly 75% of these backbone groups have hydrolyzed after approximately 15 hours). These results also reveal that minimal degradation occurs over the same time period at pD = 5.0 (deuterated acetate buffer), consistent with the generally slower rate of acid-catalyzed hydrolysis of esters relative to base-catalyzed hydrolysis. Fig 2B shows ATR IR spectra before and after incubation under both conditions, and reveals that the ester stretch (at ~1730 cm^{-1}) is substantially reduced after approximately 15 hours at pD = 7.4, but largely unchanged at pD = 5.0. Past studies demonstrate that a variety of other non-water-soluble copolymers of MDO and other vinyl monomers (e.g., S, MMA, MA, VAc, VBr, NIPAm, etc.) can degrade or undergo mass loss under a variety of different conditions.[15-22,25,27,35]

The ability to control the number of ester repeat units in these **P1**$_x$ copolymers, combined with the ability to install a broad range of side chain functionality without degrading backbone ester groups, could prove useful for the design of new functional and degradable polymers. We return to this approach and a discussion of the properties of water-soluble and hydrolytically degradable **P1**$_x$**-DMAP** in the sections below.

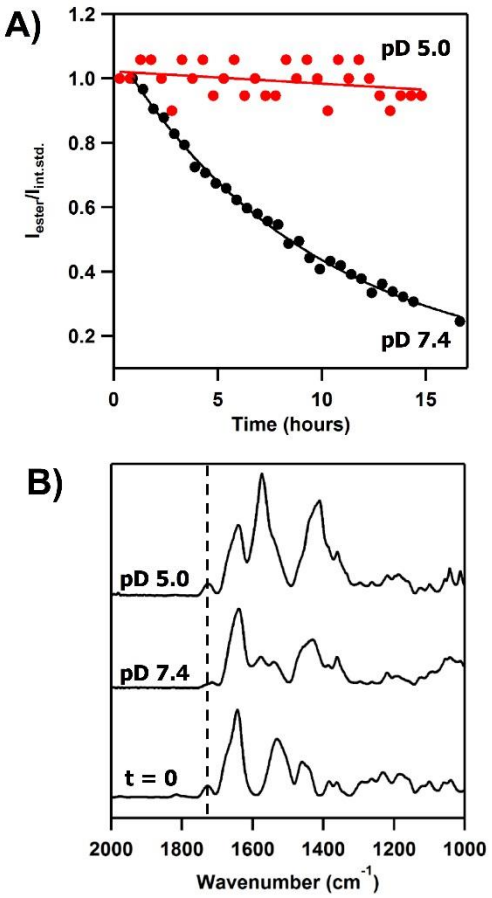

Figure 2. (A) Hydrolysis of the ester bonds in the backbone of **P1$_{50}$-DMAP** as monitored by ^{1}H NMR spectroscopy. Samples of polymer were dissolved in deuterated aqueous buffers (PBS, pD = 7.4 or acetate, pD = 5.0) and the integration of the protons adjacent to the ester bond (4.03 ppm) was monitored relative to an internal standard. Ester bonds exhibited a half-life decay of ~~8.0 hrs at pD = 7.4 (black curve), but were relatively stable at pD = 5.0 (red line). (B) ATR IR spectra showing a decrease in the intensity of the ester carbonyl stretch (C=O, ~1730 cm^{-1}) after incubation in pD = 7.4 buffer for ~18 hrs; the intensity remained relatively unchanged after incubation at pD = 5.0 for the same time period.

RAFT Synthesis and Self-Assembly of Poly[S-block-(MDO-co-VDMA)]

We next performed a series of studies to demonstrate that reversible-deactivation radical polymerization techniques could be used to synthesize block copolymer (BCP) architectures containing degradable MDO/VDMA blocks. Fig 3A shows the results of chain extension of a polystyrene (PS) macroRAFT block (21.7 kDa, $Đ$ = 1.13) with MDO and VDMA (30:70 mol:mol) to obtain poly[S-*b*-(MDO-*co*-VDMA)]), hereafter denoted **BCP1** ($M_{n,NMR}$ = 33.8 kDa, $Đ$ = 1.57). ^{1}H NMR spectroscopy compositional analysis revealed that the non-styrene block of **BCP1** contained a majority of VDMA units, with a ratio of 0.75:0.08:0.17 VDMA:ester:acetal (Fig S8A), a composition similar to that of copolymer **P1$_{30}$** (i.e., a copolymer synthesized using the same monomer feed ratio; see Table 1). Fig 3B shows the results of characterization of **BCP1** by GPC and demonstrates (i) that polymer molecular weight increased after chain extension and (ii) that the molecular weight distribution of **BCP1** was roughly unimodal, with a dispersity of $Đ$ = 1.57 (PS, black trace; **BCP1**, blue trace). The increase in dispersity after chain extension could result from a combination of the trithiocarbonate RAFT agent used here (which controls the polymerization of VDMA well, but is not ideal for the controlled polymerization of MDO, typically requiring the use of xanthate RAFT agents[52]) and the prevalence of main-chain branching within MDO units by [1,7]-H and [1,4]-H transfer rearrangements (as discussed above).[14,34,35]

Treatment of amine-reactive **BCP1** with dimethylaminopropylamine (1 equiv. amine, room temperature) yielded **BCP1-DMAP**, thus confirming the reactivity and accessibility of azlactone groups in **BCP1** and providing access to new side-chain functionalized BCPs (full details are provided in the Materials and Methods; characterization by ^{1}H NMR and IR spectroscopy are provided in Fig S8). Additional experiments in which **BCP1** was exposed to

solutions of NaOH in methanol/THF at elevated temperature also demonstrated that the MDO/VDMA block of this BCP was hydrolytically degradable (see Materials and Methods). GPC analysis of this degraded product, denoted **BCP1-Deg**, revealed a single peak of lower molecular weight (Fig 3B, red trace) at a retention time comparable to that of the initial PS block; analysis by IR spectroscopy confirmed the disappearance of the backbone ester peak and the appearance of carbonyl carboxylate stretching (~1652 cm^{-1}, Fig 3C).

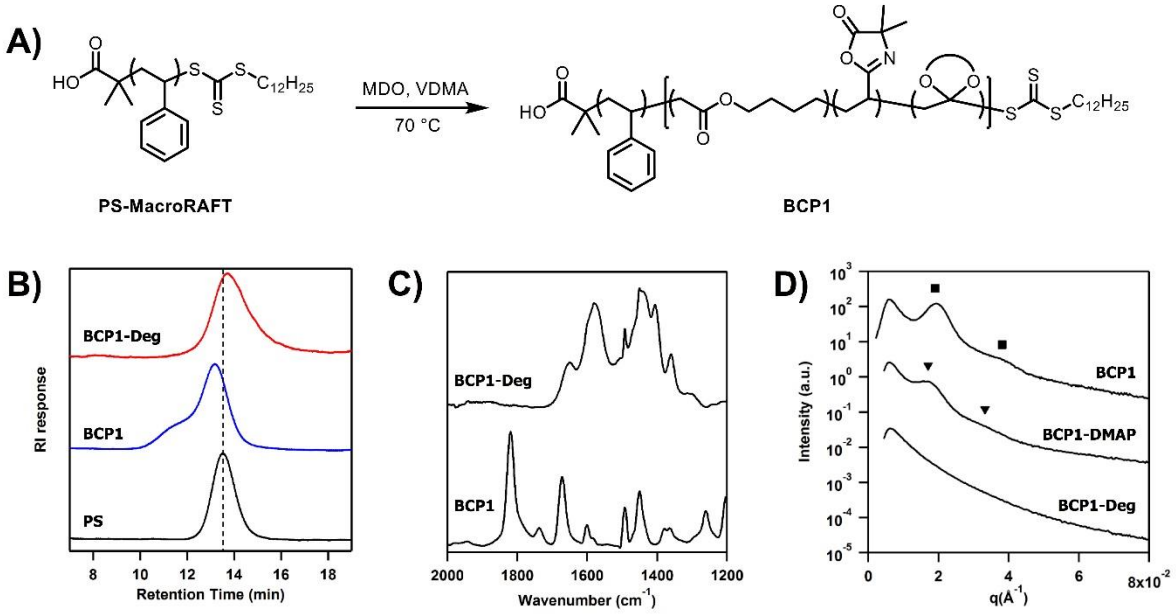

Figure 3. (A) Synthesis of P[S-*b*-(MDO-*co*-VDMA)], **BCP1**, by sequential reversible-addition fragmentation chain transfer (RAFT) polymerization; the 7-membered dioxepane ring has been abbreviated for clarity. (B) GPC traces showing chain extension of the poly(styrene) MacroRAFT agent (black) to the block copolymer **BCP1** (blue), and subsequent degradation under basic conditions to **BCP1-Deg** (red, see text for complete details). The molecular weight of **BCP1** increased after chain extension, and degradation caused a substantial decrease in molecular weight (vertical dotted line, guide only). (C) ATR IR spectra for **BCP1** (bottom) and **BCP1-Deg** (top). The ester carbonyl stretch (C=O, ~1730 cm^{-1}) present in the spectrum of **BCP1** is absent in **BCP1-Deg**, suggesting that ester bond hydrolysis has occurred. (D) Azimuthally-integrated small-angle X-ray scattering (SAXS) patterns for **BCP1**, **BCP1-DMAP**, and **BCP1-Deg**, after thermal annealing at 150 °C. Peak markers indicate the calculated peak positions of a lamellar morphology based on the location of the principal scattering wavevector, q^*, for **BCP1** and **BCP1-DMAP**; the domain spacings were calculated to be 32.1 and 34.8 nm, respectively. The plot of **BCP1-Deg** is featureless, suggesting that the polymer is disordered after degradation.

Depending on their structures, many BCPs can microphase separate into periodic nanoscale morphologies.[53,54] Past work from our group has shown that the azlactone-containing BCP PS-*b*-PVDMA (a non-degradable BCP composed of PS and a second block consisting exclusively of VDMA units) can self-assemble into lamellar morphologies in both the bulk and when cast as thin films[50] to yield surfaces that present alternating nanoscale domains of styrene and amine-reactive azlactone groups that could be functionalized and chemically patterned by treatment with small-molecule amines.[50] Additional characterization of bulk samples of **BCP1** by small-angle x-ray scattering (SAXS) revealed that this reactive and degradable BCP can also self-assemble into a lamellar morphology (Fig 3D). Based on the position of the principal scattering peak at $q^* = 0.01955$ Å^{-1} and a higher order reflection at $q/q^* = \sqrt{4}$, we conclude that this polymer self-assembles into a bulk lamellar morphology with an $L_0 = 32.1$ nm. In contrast to PS-*b*-PVDMA BCPs reported in earlier studies,[50,55-57] the reactive block of **BCP1** is degradable owing to the incorporation of MDO. Fig 3D also shows the SAXS trace for a bulk sample of **BCP1-Deg** and does not reveal any reflections, consistent with hydrolytic degradation and transformation into a non-BCP, PS-like material that can no longer self-assemble into a lamellar morphology. Finally, the SAXS plot for a bulk sample of the **BCP1-DMAP** derivative described above is also shown in Fig 3D; a principal scattering peak at $q^* = 0.01804$ Å^{-1} and higher order reflection at $q/q^* = \sqrt{4}$ are observed, corresponding to a lamellar morphology with $L_0 = 34.8$ nm. The domain spacing of this **BCP1** derivative is larger than for the reactive **BCP1** template (32.1 nm), likely owing to the conjugation of additional side-chain functionality and a corresponding increase in the volume fraction of the MDO/VDMA block.[50] The ability to manipulate BCP volume fractions, and thus the length scales of self-assembly in nanostructured morphologies by simple functionalization of a common reactive BCP template with different primary amines,

combined with the degradable properties of these materials, could prove useful for applications in BCP self-assembly,[53] patterning and lithography,[54] and the development of methods for the discovery of new degradable block copolymers. In the following sections, we provide several examples that demonstrate the potential utility of these reactive and degradable MDO-co-VMDA copolymers and their functionalized derivatives.

Fabrication of Reactive and Degradable Covalently Cross-Linked Multilayer Microcapsules

Past studies demonstrate that the reactivity of the azlactone groups in PVDMA homopolymers can be used to fabricate a range of functional soft materials by 'reactive' or 'covalent' layer-by-layer assembly with other polymers containing primary amines (e.g., branched polyethylenimine, PEI).[9,38,58] This reactive layer-by-layer approach yields reactive polymer multilayers that can be further functionalized by treatment with primary amines to design interfaces of potential utility in many biomedical and biotechnological contexts.[9,28,41,44,58,59] The use of PVDMA, however, leads to covalently cross-linked coatings and other multilayer structures that are physically stable and do not degrade in aqueous environments.[44,59,60] We performed a series of experiments to determine whether the amine-reactive and degradable **P1**$_x$ polymers described above could be used to fabricate chemically reactive and cross-linked, but also degradable, polymer multilayers using this reactive layer-by-layer approach.

To explore feasibility and demonstrate proof of concept, we fabricated hollow multilayer microcapsules using a previously described sacrificial core template approach.[31] We iteratively deposited layers of PEI and the degradable polymer **P1$_{70}$** [containing ~25% ester and ~51% azlactone repeat units, as well as a small fraction of fluorescently labelled side chains

(tetramethylrhodamine cadaverine; TMR-cad) to facilitate characterization by fluorescence microscopy],[43] onto spherical $CaCO_3$ cores containing fluorescently-labeled dextran (FITC-dextran, avg. MW = 2000 kDa).[31] During assembly, interfacial reactions between primary amines in PEI and the amine-reactive azlactone groups in **P1$_{70}$** drove layer-by-layer film growth, resulting in multilayered coatings on the surfaces of the $CaCO_3$ particles. In these experiments, the particles were coated with 4.5 layer pairs (or "bilayers") of PEI/**P1$_{70}$** (terminated with a layer of **P1$_{70}$**) and then treated with dimethylaminopropylamine (**DMAP**, 40 mM in THF) to react exhaustively with the remaining residual azlactones in the multilayers and install cationic functionality on the walls of the capsules.[61] Hollow PEI/**P1$_{70}$** multilayer capsules filled with FITC-labelled dextran were subsequently obtained by treatment with EDTA to dissolve out the $CaCO_3$ cores. Otherwise identical control capsules were also fabricated using PEI and the homopolymer PVDMA. A series of fluorescence and brightfield images of the fabrication process is given in Fig S9.

Fig 4A-D shows representative fluorescence micrographs of the FITC-dextran loaded PEI/**P1$_{70}$** (**A** and **C**) PEI/PVDMA (**B** and **D**) capsules dispersed in PBS buffer at pH 7.4. Inspection of these images reveals fabrication using both **P1$_{70}$** and PVDMA to lead to intact hollow capsules (red) containing dissolved FITC-dextran (green) that does not diffuse out of the capsules under these conditions. Fig 4E-H shows representative fluorescence micrographs of PEI/**P1$_{70}$** (E and G) and PEI/PVDMA (F and H) capsules after treatment with aqueous base (1 M KOH, 50 °C, 2 hr). These images reveal capsules fabricated using **P1$_{70}$** to have degraded under these conditions, as determined by the appearance of broken capsule walls and the presence of other polymeric debris, and the loss of encapsulated FITC-dextran. In contrast, capsules fabricated using PVDMA remained intact and spherical, and retained encapsulated FITC-

dextran, suggesting that capsules fabricated using this non-degradable reactive polymer do not degrade significantly under these conditions. These results could prove useful for the design of new classes of functionalized polymer capsules with tailored degradation and release rates[62] (e.g., by changing the mol% of ester bonds in **P1**$_x$) and more broadly, for the design of other covalently cross-linked and chemically functionalized thin films, coatings, or biointerfaces that degrade upon exposure to aqueous environments.

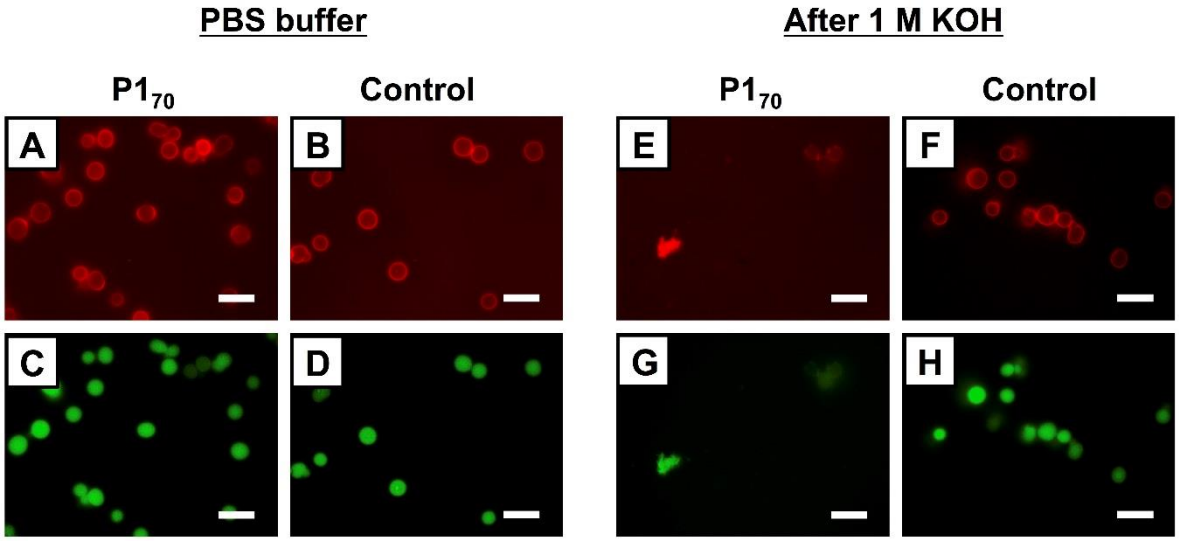

Figure 4. Fluorescence microscopy images of hollow multilayer microcapsules fabricated using PEI and **P1$_{70}$** (labeled '**P1$_{70}$**'), or PEI and non-degradable PVDMA (labeled 'Control'). Capsules were loaded with fluorescein-labelled dextran (FITC-dextran; false-colored green) and azlactone-containing polymers were labelled with TMR (false-colored red). (A,C) **P1$_{70}$** capsules and (B,D) control capsules dispersed in PBS buffer at pH 7.4. (E,G) **P1$_{70}$** capsules and (G,H) control samples after incubation in basic conditions (1 M KOH, 50 °C, 2 hrs). After treatment with base, **P1$_{70}$** capsules degraded and the encapsulated FITC-dextran was released. Control capsules were not degradable under the same conditions and continued to encapsulate FITC-dextran. Scale bars are 20 μm. Supplemental brightfield and fluorescence micrographs of microparticles and capsules are given in Fig S9.

Synthesis and Characterization of Covalently Cross-Linked and Degradable Gels

We conducted a series of experiments to explore the feasibility of using our reactive and degradable **P1**$_x$ copolymers as macromolecular precursors for the synthesis of reactive and degradable gels. We used two different approaches to fabricate cross-linked and reactive solid materials, based on the reactive covalent cross-linking of **P1**$_x$ and **P1**$_x$ derivatives by multifunctional amines. In a first approach, **P1$_{50}$** was dissolved in THF and directly cross-linked by addition of a sub-stoichiometric amount of tri-functional tris(2-aminoethyl)amine (TREN; 0.5 equiv. of primary amines w.r.t azlactone groups in **P1$_{50}$**) to yield a non-flowing gel. In a second approach, **P1$_{50}$** was first partially functionalized by treatment with a sub-stoichiometric amount of **DMAP** and then cross-linked into a gel by addition of TREN. In both cases, chemical cross-linking was followed by ATR IR spectroscopy (Fig S10AB). Fig 5A shows a schematic representation of this second approach and the digital images in Fig 5BC show the results of polymer cross-linking.

The resulting gel shown in Fig 5C was hydrophilic and absorbed water owing to the partial functionalization with **DMAP**, and the gel completely disintegrated upon incubation in PBS buffer overnight (Fig 5D). Inspection of ATR IR spectra of the gel before (Fig 5E, bottom) and the materials recovered after degradation (Fig 5E, top) reveals that the ester functionality (~1730 cm^{-1}) present after cross-linking was completely consumed, consistent with a mechanism of gel disassembly driven by backbone ester hydrolysis. Closer inspection of these spectra reveals that the gel contained residual azlactone functionality that was not consumed during cross-linking (Fig 5E, bottom, arrow, ~1820 cm^{-1}). Subsequent experiments demonstrated that

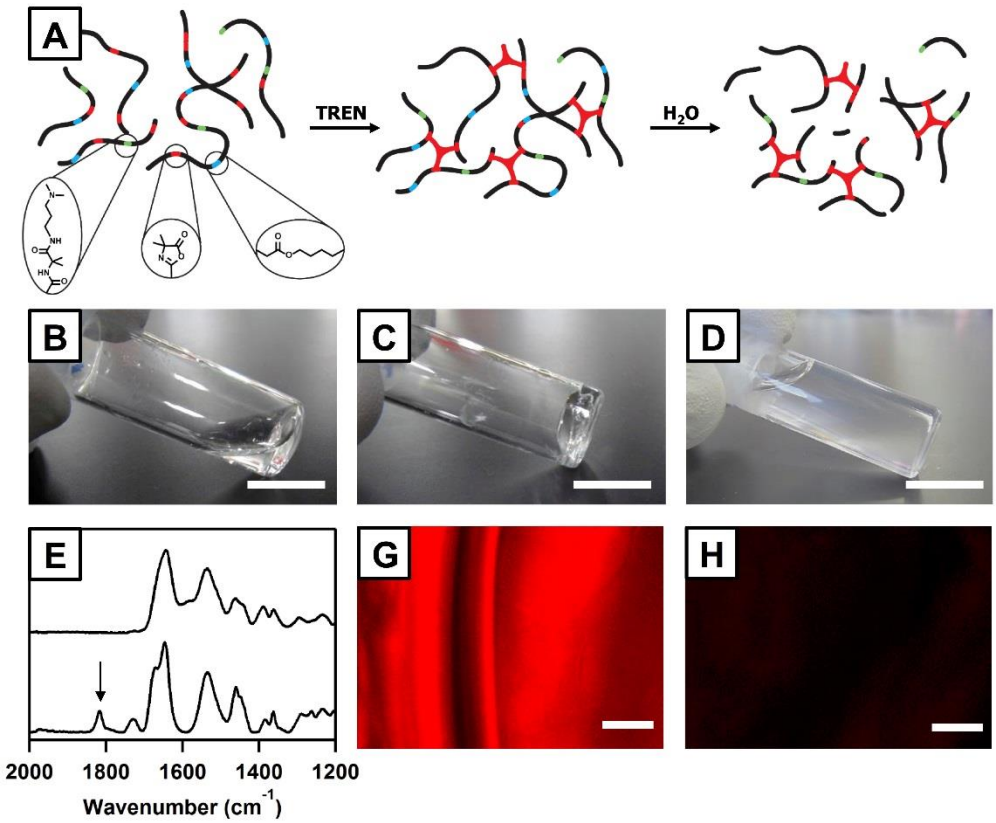

Figure 5. Synthesis and characterization of polymer hydrogels fabricated from **P1$_{50}$** using the second approach described in the main text. (A) Schematic showing the fabrication and subsequent degradation of polymer gels starting from partially functionalized **P1$_{50}$**, followed by cross-linking with the trifunctional amine (TREN), and subsequent gel degradation and disassembly in an aqueous environment. (B-D) Digital images corresponding to the steps shown above in (A). (E) ATR IR spectrum (bottom) for the as-prepared gel shown in (C), revealing that it contains a significant number of unreacted azlactone groups after cross-linking (black arrow), and the spectrum (top) of the products of gel degradation, obtained by freeze-drying the degraded sample shown in (D). Panels (G) and (H) show fluorescence images of the gel obtained in (C) after treatment with the amine-containing fluorophore tetramethylrhodamine cadaverine [TMR-cad, (G)] and non-reactive tetramethylrhodamine [TMR, (H)]. Scale bars are ~1.2 cm in (B-D) and 0.125 mm in (G) and (H).

this residual functionality present after cross-linking could be used to further functionalize gels by additional treatment with amine-containing nucleophiles. Fig 5G shows a sample of gel treated with a solution of the amine-containing fluorophore tetramethylrhodamine cadaverine (TMR-cad) and reveals red fluorescence across large areas of the gel. Fig 5H shows an image of

an otherwise identical gel treated with the non-reactive fluorophore tetramethylrhodamine (TMR). When combined, these images suggest that the red fluorescence in Fig 5G was the result of covalent immobilization, and not the result of physisorption of the fluorophore or non-specific internalization within the gel matrix. These results provide opportunities to design new types of degradable polymer gels functionalized with a range of primary amine-containing chemical and biological agents.

Fabrication of Degradable DNA-Containing Multilayers Using Cationic P1$_x$-DMAP

Finally, we note that degradable and water-soluble cationic polymers are of potential utility in a broad range of applications, including for use as vehicles for the delivery of negatively charged DNA to mammalian cells.[63] We performed a final series of experiments to determine whether the degradable and cationic **P1$_{30}$-DMAP** derivative described above could be used to fabricate polyelectrolyte multilayers containing DNA by conventional electrostatically-driven aqueous layer-by-layer assembly (as has been demonstrated in several past studies[64,65] using other types of hydrolytically degradable polyamines). Fig 6A shows the ellipsometric growth profile for films (~200 nm thick) composed of eight bilayers of **P1$_{30}$-DMAP** and plasmid DNA encoding for green fluorescent protein (GFP) fabricated on planar silicon substrates (see Materials and Methods for complete details). We selected **P1$_{30}$-DMAP** for use in these experiments because **P1$_x$-DMAP** polymers with $\boldsymbol{x} > 30$ have fewer tertiary-amine side-chains and resulted in lower quantities of DNA incorporated into multilayer films (data not shown). The results shown in Fig 6A are consistent with layer-by-layer film growth. Fig 6B shows a plot of DNA released into solution when these **P1$_x$-DMAP**/DNA films were incubated in PBS buffer

(pH 7.4, 37 °C), and demonstrates that DNA was released over a period of 25 days with a release profile that was approximately linear. This result is consistent with a process of film erosion and

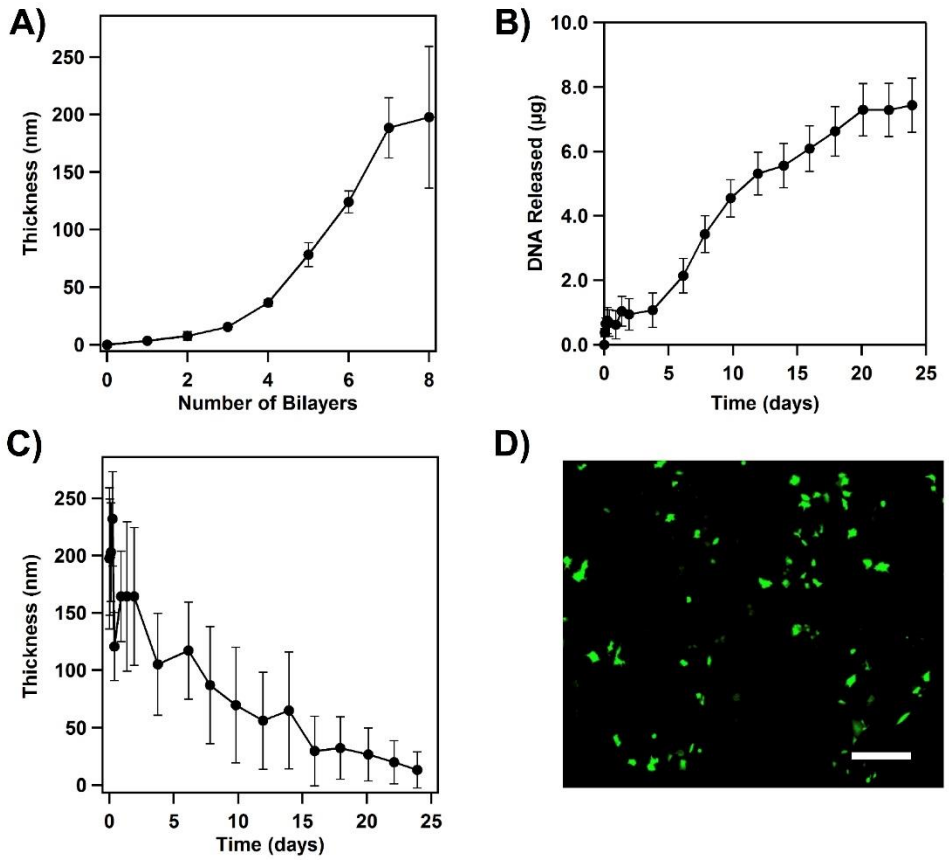

Figure 6. Characterization of layer-by-layer film growth and the release of DNA from multilayers assembled using **P1$_{30}$-DMAP** and plasmid DNA encoding for the expression of GFP. (A) Film growth on planar silicon substrates as characterized by ellipsometry. (B) Plot showing the release of DNA from substrates coated with **P1$_{30}$-DMAP**/DNA films. Films were incubated in PBS buffer (pH 7.4, 37 °C) and the amount of DNA released into solution was characterized by measuring UV/vis absorbance. (C) Plot showing the decrease in film thickness versus time for the film incubated in PBS and characterized in (B); films were periodically removed from PBS and thicknesses were characterized by ellipsometry. (D) Representative fluorescence microscopy image showing COS-7 cells expressing GFP collected during the erosion of the film incubated in PBS and characterized in (B,C); released DNA used in this experiment was collected between days 4 and 6 of incubation; scale bar = 300 µm. All data in (A-C) are presented as the average and standard deviation of three identically prepared films.

disassembly that is driven by the gradual hydrolysis of MDO-derived backbone ester groups. Physical erosion and disassembly of these films was confirmed by a gradual decrease in film thickness over this same 25-day period (Fig 6C). The degradation and linear release behaviors observed here differ from those observed in past studies using degradable polyamine/DNA films fabricated using other cationic polyesters [e.g., poly(*β*-aminoesters), for which film erosion and release generally proceed over periods of hours to days[32,33,65]], and thus open the door to applications in which the gradual and sustained surface-mediated release of DNA would be useful. Finally, Fig 6D shows a representative fluorescence micrograph of mammalian cells treated with DNA released in this experiment,[32] demonstrating that DNA was released from these degradable **P1$_x$-DMAP**/DNA coatings in a form that is intact and able to promote transgene expression in mammalian cells.

Summary and Conclusions

We have reported the synthesis and physicochemical characterization of reactive and degradable copolymers that contain azlactone side chains and hydrolyzable backbone ester units. Copolymerization of the vinyl monomer 2-vinyl-4,4-dimethylazlactone (VDMA) and the cyclic ketene acetal 2-methylene-1,3-dioxepane (MDO) using conventional or reversible-deactivation radical polymerization techniques afforded copolymers and block copolymers that exhibit the amine-reactivity associated with poly(vinyl azlactone)s but also the hydrolytic degradability typical of conventional polyesters. Our results demonstrate that control over monomer feed ratios and other parameters can be used to tune both copolymer composition (e.g., the number and ratio of azlactone and ester repeat units incorporated) and the physical properties of the resulting materials (e.g., glass transition temperatures, their ability to self-assemble into nanoscale

structures, etc.). Post-fabrication functionalization of the azlactone groups in MDO-*co*-VDMA copolymers with primary amine-containing compounds proceeded rapidly, quantitatively, and under mild conditions, and could be achieved without the disruption or degradation of the ester groups in the polymer backbones. These amine-reactive polymer templates are thus well suited for the synthesis of new types of degradable copolymers containing a broad range of different chemical functionality (including the potential to introduce new and more diverse functionality to these materials by treatment with other types of alcohol- and thiol-based nucleophiles). Finally, we demonstrated the utility of these azlactone-functionalized degradable polymers and their functionalized derivatives for the fabrication and assembly of covalently and ionically-crosslinked macromolecular thin films, capsules, and gels. The incorporation of ester functionality into VDMA-based materials creates opportunities to leverage the reactivity of azlactone-functionalized polymers to design new polymers and assemblies that degrade in aqueous environments.

Acknowledgments. This work was supported by the NSF through grants to the UW-Madison Materials Research Science and Engineering Center (MRSEC; DMR-1121288) and the UW-Madison Nanoscale Science and Engineering Center (NSEC; DMR-0832760), and made use of NSF-supported facilities (DMR-1121288, DMR-0832760, and CHE-1048642). The Bruker Microflex LRF mass spectrometer was purchased using funds donated by Prof. Paul J. Bender. We thank Joshua Fishman for help with MDO synthesis and many helpful discussions related to degradable polymers, Xuanrong Guo for assistance with microcapsule fabrication, and Dr. Martha Vestling for assistance with MALDI-ToF analysis. V.A. acknowledges the American Heart Association for a graduate fellowship and the UW-Madison Biotechnology Center for a

Morgridge Biotechnology Fellowship. M.C.D.C. acknowledges the Natural Sciences Engineering Research Council of Canada for a graduate fellowship.

References

1. Boaen, N. K.; Hillmyer, M. A. Post-polymerization functionalization of polyolefins. *Chem. Soc. Rev.* **2005,** *34*, 267-275.

2. Fournier, D.; Hoogenboom, R.; Schubert, U. S. Clicking polymers: A straightforward approach to novel macromolecular architectures. *Chem. Soc. Rev.* **2007,** *36*, 1369-1380.

3. Gauthier, M. A.; Gibson, M. I.; Klok, H.-A. Synthesis of functional polymers by post-polymerization modification. *Angew. Chem. Int. Ed.* **2009,** *48*, 48-58.

4. Golas, P. L.; Matyjaszewski, K. Marrying click chemistry with polymerization: Expanding the scope of polymeric materials. *Chem. Soc. Rev.* **2010,** *39*, 1338-1354.

5. Tempelaar, S.; Mespouille, L.; Coulembier, O.; Dubois, P.; Dove, A. P. Synthesis and post-polymerisation modifications of aliphatic poly(carbonate)s prepared by ring-opening polymerisation. *Chem. Soc. Rev.* **2013,** *42*, 1312-1336.

6. Theato, P.; Klok, H.-A.; Editors, *Functional Polymers by Post-Polymerization Modification: Concepts, Guidelines, and Applications*. Wiley-VCH Verlag GmbH & Co. KGaA: **2013**; p 414 pp.

7. Romulus, J.; Henssler, J. T.; Weck, M. Postpolymerization Modification of Block Copolymers. *Macromolecules* **2014,** *47*, 5437-5449.

8. Gibson, M. I.; Froehlich, E.; Klok, H.-A. Postpolymerization Modification of Poly(Pentafluorophenyl methacrylate): Synthesis of a Diverse Water-Soluble Polymer Library. *J. Polym. Sci., Part A: Polym. Chem.* **2009,** *47*, 4332-4345.

9. Buck, M. E.; Lynn, D. M. Azlactone-functionalized polymers as reactive platforms for the design of advanced materials: Progress in the last ten years. *Polym. Chem.* **2012,** *3*, 66-80.

10. Günay, K. A.; Theato, P.; Klok, H.-A. Standing on the shoulders of Hermann Staudinger: Post-polymerization modification from past to present. *J. Polym. Sci., Part A: Polym. Chem.* **2013,** *51*, 1-28.

11. Heilmann, S. M.; Rasmussen, J. K.; Krepski, L. R. Chemistry and technology of 2-alkenyl azlactones. *J. Polym. Sci., Part A: Polym. Chem.* **2001,** *39*, 3655-3677.

12. Agarwal, S. Chemistry, chances and limitations of the radical ring-opening polymerization of cyclic ketene acetals for the synthesis of degradable polyesters. *Polym. Chem.* **2010,** *1*, 953-964.

13. Bailey, W. J.; Ni, Z.; Wu, S.-R. Synthesis of poly-ϵ-caprolactone via a free radical mechanism. Free radical ring-opening polymerization of 2-methylene-1,3-dioxepane. *J. Polym. Sci., Part A: Polym. Chem.* **1982,** *20*, 3021-3030.

14. Jin, S.; Gonsalves, K. E. A study of the mechanism of the free-radical ring-opening polymerization of 2-methylene-1,3-dioxepane. *Macromolecules* **1997,** *30*, 3104-3106.

15. Jin, S.; Gonsalves, K. E. Synthesis and Characterization of Functionalized Poly(ε-caprolactone) Copolymers by Free-Radical Polymerization. *Macromolecules* **1998,** *31*, 1010-1015.

16. Sun, L. F.; Zhuo, R. X.; Liu, Z. L. Synthesis and enzymatic degradation of 2-methylene-1,3-dioxepane and methyl acrylate copolymers. *J. Polym. Sci., Part A: Polym. Chem.* **2003,** *41*, 2898-2904.

17. Borkar, S.; Sen, A.; Shallenberger, J. R. Alternating polyester/fluoroalkene copolymers: Combining high hydrophobicity with degradability. *J. Polym. Sci., Part A: Polym. Chem.* **2006,** *44*, 1225-1232.

18. Xu, J.; Liu, Z.-L.; Zhuo, R.-X. Synthesis and biodegradability evaluation of 2-methylene-1,3-dioxepane and styrene copolymers. *J. Appl. Polym. Sci.* **2007,** *103*, 1146-1151.

19. Galperin, A.; Long, T. J.; Ratner, B. D. Degradable, Thermo-Sensitive Poly(N-isopropyl acrylamide)-Based Scaffolds with Controlled Porosity for Tissue Engineering Applications. *Biomacromolecules* **2010,** *11*, 2583-2592.

20. Undin, J.; Illanes, T.; Finne-Wistrand, A.; Albertsson, A.-C. Random introduction of degradable linkages into functional vinyl polymers by radical ring-opening polymerization, tailored for soft tissue engineering. *Polym. Chem.* **2012,** *3*, 1260-1266.

21. Zhang, Y.; Zheng, M.; Kissel, T.; Agarwal, S. Design and Biophysical Characterization of Bioresponsive Degradable Poly(dimethylaminoethyl methacrylate) Based Polymers for In Vitro DNA Transfection. *Biomacromolecules* **2012,** *13*, 313-322.

22. Hedir, G. G.; Bell, C. A.; Ieong, N. S.; Chapman, E.; Collins, I. R.; O'Reilly, R. K.; Dove, A. P. Functional Degradable Polymers by Xanthate-Mediated Polymerization. *Macromolecules* **2014,** *47*, 2847-2852.

23. Delplace, V.; Tardy, A.; Harrisson, S.; Mura, S.; Gigmes, D.; Guillaneuf, Y.; Nicolas, J. Degradable and Comb-Like PEG-Based Copolymers by Nitroxide-Mediated Radical Ring-Opening Polymerization. *Biomacromolecules* **2013,** *14*, 3769-3779.

24. Undin, J.; Finne-Wistrand, A.; Albertsson, A.-C. Copolymerization of 2-Methylene-1,3-dioxepane and Glycidyl Methacrylate, a Well-Defined and Efficient Process for Achieving Functionalized Polyesters for Covalent Binding of Bioactive Molecules. *Biomacromolecules* **2013,** *14*, 2095-2102.

25. Undin, J.; Finne-Wistrand, A.; Albertsson, A.-C. Adjustable Degradation Properties and Biocompatibility of Amorphous and Functional Poly(ester-acrylate)-Based Materials. *Biomacromolecules* **2014,** *15*, 2800-2807.

26. Hedir, G. G.; Pitto-Barry, A.; Dove, A. P.; O'Reilly, R. K. Amphiphilic block copolymer self-assemblies of poly(NVP)-b-poly(MDO-co-vinyl esters): Tunable dimensions and functionalities. *J. Polym. Sci., Part A: Polym. Chem.* **2015,** *53*, 2699-2710.

27. Hedir, G. G.; Bell, C. A.; O'Reilly, R. K.; Dove, A. P. Functional Degradable Polymers by Radical Ring-Opening Copolymerization of MDO and Vinyl Bromobutanoate: Synthesis, Degradability and Post-Polymerization Modification. *Biomacromolecules* **2015,** *16*, 2049-2058.

28. Holden, M. T.; Carter, M. C. D.; Wu, C.-H.; Wolfer, J.; Codner, E.; Sussman, M. R.; Lynn, D. M.; Smith, L. M. Photolithographic Synthesis of High-Density DNA and RNA Arrays on Flexible, Transparent, and Easily Subdivided Plastic Substrates. *Anal. Chem.* **2015,** *87*, 11420-11428.

29. Lai, J. T.; Filla, D.; Shea, R. Functional Polymers from Novel Carboxyl-Terminated Trithiocarbonates as Highly Efficient RAFT Agents. *Macromolecules* **2002,** *35*, 6754-6756.

30. Plikk, P.; Tyson, T.; Finne-Wistrand, A.; Albertsson, A.-C. Mapping the characteristics of the radical ring-opening polymerization of a cyclic ketene acetal towards the creation of a functionalized polyester. *J. Polym. Sci., Part A: Polym. Chem.* **2009,** *47*, 4587-4601.

31. Saurer, E. M.; Flessner, R. M.; Buck, M. E.; Lynn, D. M. Fabrication of covalently crosslinked and amine-reactive microcapsules by reactive layer-by-layer assembly of azlactone-containing polymer multilayers on sacrificial microparticle templates. *J. Mater. Chem.* **2011,** *21*, 1736-1745.

32. Zhang, J.; Chua, L. S.; Lynn, D. M. Multilayered Thin Films that Sustain the Release of Functional DNA under Physiological Conditions. *Langmuir* **2004,** *20*, 8015-8021.

33. Jewell, C. M.; Zhang, J.; Fredin, N. J.; Wolff, M. R.; Hacker, T. A.; Lynn, D. M. Release of Plasmid DNA from Intravascular Stents Coated with Ultrathin Multilayered Polyelectrolyte Films. *Biomacromolecules* **2006,** *7*, 2483-2491.

34. Agarwal, S. Microstructural characterisation and properties evaluation of poly(methyl methacrylate-co-ester)s. *Polym. J.* **2007,** *39*, 163-174.

35. Agarwal, S.; Kumar, R.; Kissel, T.; Reul, R. Synthesis of Degradable Materials Based on Caprolactone and Vinyl Acetate Units Using Radical Chemistry. *Polym. J.* **2009,** *41*, 650-660.

36. Roberts, G. E.; Coote, M. L.; Heuts, J. P. A.; Morris, L. M.; Davis, T. P. Radical Ring-Opening Copolymerization of 2-Methylene 1,3-Dioxepane and Methyl Methacrylate: Experiments Originally Designed To Probe the Origin of the Penultimate Unit Effect. *Macromolecules* **1999,** *32*, 1332-1340.

37. Morris, L. M.; Davis, T. P.; Chaplin, R. P. An assessment of the copolymerization reaction between styrene and 2-methylene-1,3-dioxepane. *Polymer* **2001,** *42*, 495-500.

38. Buck, M. E.; Zhang, J.; Lynn, D. M. Layer-by-Layer Assembly of Reactive Ultrathin Films Mediated by Click-Type Reactions of Poly(2-Alkenyl Azlactone)s. *Adv. Mater.* **2007,** *19*, 3951-3955.

39. Cullen, S. P.; Mandel, I. C.; Gopalan, P. Surface-Anchored Poly(2-vinyl-4,4-dimethyl azlactone) Brushes as Templates for Enzyme Immobilization. *Langmuir* **2008,** *24*, 13701-13709.

40. Messman, J. M.; Lokitz, B. S.; Pickel, J. M.; Kilbey, S. M., II Highly Tailorable Materials based on 2-Vinyl-4,4-dimethyl Azlactone: (Co)Polymerization, Synthetic Manipulation and Characterization. *Macromolecules* **2009,** *42*, 3933-3941.

41. Buck, M. E.; Breitbach, A. S.; Belgrade, S. K.; Blackwell, H. E.; Lynn, D. M. Chemical Modification of Reactive Multilayered Films Fabricated from Poly(2-alkenyl azlactone)s: Design of Surfaces that Prevent or Promote Mammalian Cell Adhesion and Bacterial Biofilm Growth. *Biomacromolecules* **2009,** *10*, 1564-1574.

42. Sun, B.; Liu, X.; Buck, M. E.; Lynn, D. M. Azlactone-functionalized polymers as reactive templates for parallel polymer synthesis: synthesis and screening of a small library of cationic polymers in the context of DNA delivery. *Chem. Commun.* **2010,** *46*, 2016-2018.

43. Buck, M. E.; Lynn, D. M. Functionalization of Fibers Using Azlactone-Containing Polymers: Layer-by-Layer Fabrication of Reactive Thin Films on the Surfaces of Hair and Cellulose-Based Materials. *ACS Appl. Mater. Inter.* **2010,** *2*, 1421-1429.

44. Broderick, A. H.; Azarin, S. M.; Buck, M. E.; Palecek, S. P.; Lynn, D. M. Fabrication and Selective Functionalization of Amine-Reactive Polymer Multilayers on Topographically Patterned Microwell Cell Culture Arrays. *Biomacromolecules* **2011,** *12*, 1998-2007.

45. Laquievre, A.; Allaway, N. S.; Lyskawa, J.; Woisel, P.; Lefebvre, J.-M.; Fournier, D. Highly Efficient Ring-Opening Reaction of Azlactone-Based Copolymer Platforms for the Design of Functionalized Materials. *Macromol. Rapid Commun.* **2012,** *33*, 848-855.

46. Hansen, R. R.; Hinestrosa, J. P.; Shubert, K. R.; Morrell-Falvey, J. L.; Pelletier, D. A.; Messman, J. M.; Kilbey, S. M.; Lokitz, B. S.; Retterer, S. T. Lectin-Functionalized Poly(glycidyl methacrylate)-block-poly(vinyldimethyl azlactone) Surface Scaffolds for High Avidity Microbial Capture. *Biomacromolecules* **2013,** *14*, 3742-3748.

47. Jones, M. W.; Richards, S.-J.; Haddleton, D. M.; Gibson, M. I. Poly(azlactone)s: Versatile scaffolds for tandem post-polymerisation modification and glycopolymer synthesis. *Polym. Chem.* **2013,** *4*, 717-723.

48. Hien The, H.; Levere, M. E.; Pascual, S.; Montembault, V.; Casse, N.; Caruso, A.; Fontaine, L. Thermoresponsive block copolymers containing reactive azlactone groups and their bioconjugation with lysozyme. *Polym. Chem.* **2013,** *4*, 675-685.

49. Li, Y.; Duong, H. T. T.; Jones, M. W.; Basuki, J. S.; Hu, J. M.; Boyer, C.; Davis, T. P. Selective Postmodification of Copolymer Backbones Bearing Different Activated Esters with Disparate Reactivities. *ACS Macro Lett.* **2013,** *2*, 912-917.

50. Speetjens, F. W., II; Carter, M. C. D.; Kim, M.; Gopalan, P.; Mahanthappa, M. K.; Lynn, D. M. Post-Fabrication Placement of Arbitrary Chemical Functionality on Microphase-Separated Thin Films of Amine-Reactive Block Copolymers. *ACS Macro Lett.* **2014,** *3*, 1178-1182.

51. Zhu, Y.; Batchelor, R.; Lowe, A. B.; Roth, P. J. Design of Thermoresponsive Polymers with Aqueous LCST, UCST, or Both: Modification of a Reactive Poly(2-vinyl-4,4-dimethylazlactone) Scaffold. *Macromolecules* **2016,** *49*, 672-680.

52. Bell, C. A.; Hedir, G. G.; O'Reilly, R. K.; Dove, A. P. Controlling the synthesis of degradable vinyl polymers by xanthate-mediated polymerization. *Polym. Chem.* **2015,** *6*, 7447-7454.

53. Lodge, T. P. Block Copolymers: Past Successes and Future Challenges. *Macromol. Chem. Phys.* **2003,** *204*, 265-273.

54. Marencic, A. P.; Register, R. A. Controlling Order in Block Copolymer Thin Films for Nanopatterning Applications. *Annual Review of Chemical and Biomolecular Engineering* **2010,** *1*, 277-297.

55. Tully, D. C.; Roberts, M. J.; Geierstanger, B. H.; Grubbs, R. B. Synthesis of reactive poly(vinyl oxazolones) via nitroxide-mediated "living" free radical polymerization. *Macromolecules* **2003,** *36*, 4302-4308.

56. Fournier, D.; Pascual, S.; Fontaine, L. Copper-mediated living radical polymerization of 2-vinyl-4,4-dimethyl-5-oxazolone. *Macromolecules* **2004,** *37*, 330-335.

57. Pascual, S.; Blin, T.; Saikia, P. J.; Thomas, M.; Gosselin, P.; Fontaine, L. Block Copolymers Based on 2-Vinyl-4,4-dimethyl-5-oxazolone by RAFT Polymerization: Experimental and Computational Studies. *J. Polym. Sci., Part A: Polym. Chem.* **2010,** *48*, 5053-5062.

58. Broderick, A. H.; Lynn, D. M., Covalent layer-by-layer assembly using reactive polymers. In *Functional Polymers by Post-Polymerization Modification*, Wiley-VCH Verlag GmbH & Co. KGaA: **2013**; pp 371-406.

59. Kratochvil, M. J.; Tal-Gan, Y.; Yang, T.; Blackwell, H. E.; Lynn, D. M. Nanoporous Superhydrophobic Coatings that Promote the Extended Release of Water-Labile Quorum Sensing Inhibitors and Enable Long-Term Modulation of Quorum Sensing in Staphylococcus aureus. *ACS Biomater. Sci. Eng.* **2015,** *1*, 1039-1049.

60. Manna, U.; Lynn, D. M. Synthetic Surfaces with Robust and Tunable Underwater Superoleophobicity. *Adv. Funct. Mater.* **2015,** *25*, 1672-1681.

61. Manna, U.; Zayas-Gonzalez, Y. M.; Carlton, R. J.; Caruso, F.; Abbott, N. L.; Lynn, D. M. Liquid Crystal Chemical Sensors That Cells Can Wear. *Angew. Chem. Int. Ed.* **2013,** *52*, 14011-14015.

62. Becker, A. L.; Johnston, A. P. R.; Caruso, F. Layer-By-Layer-Assembled Capsules and Films for Therapeutic Delivery. *Small* **2010,** *6*, 1836-1852.

63. Pack, D. W.; Hoffman, A. S.; Pun, S.; Stayton, P. S. Design and development of polymers for gene delivery. *Nat. Rev. Drug Discov.* **2005,** *4*, 581-593.

64. Jewell, C. M.; Lynn, D. M. Multilayered polyelectrolyte assemblies as platforms for the delivery of DNA and other nucleic acid-based therapeutics. *Adv. Drug Deliv. Rev.* **2008,** *60*, 979-999.

65. Lynn, D. M., Polyelectrolyte Multilayer Coatings for the Release and Transfer of Plasmid DNA. In *Layer-by-Layer Films for Biomedical Applications*, Wiley-VCH Verlag GmbH & Co. KGaA: 2015; pp 171-194.

Supporting Information for Chapter 10

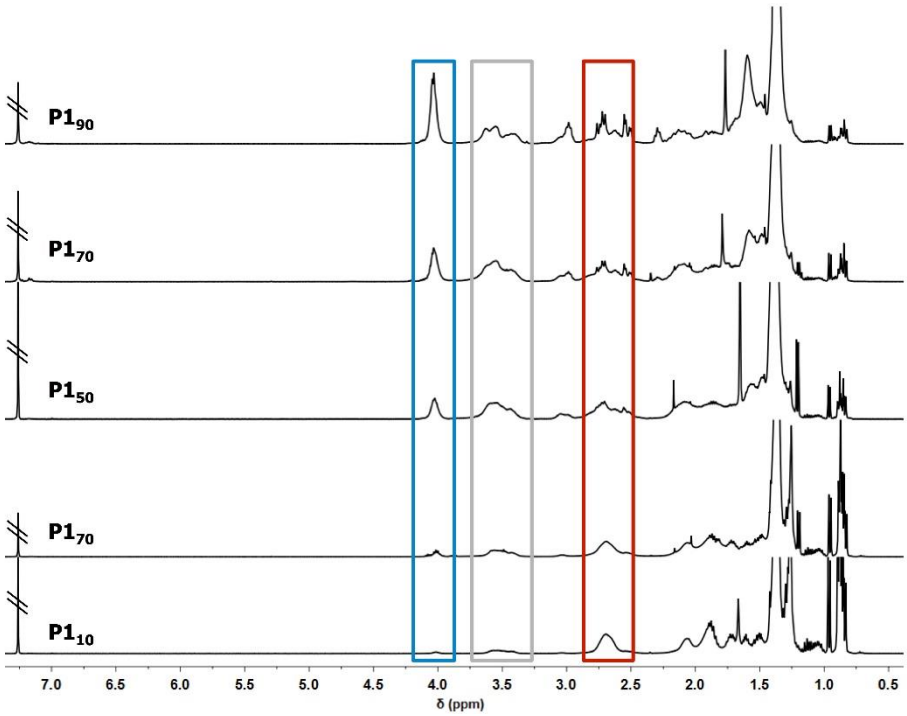

Fig S1. ^{1}H NMR spectra for **P1**$_{x}$ polymers, where ***x*** is the mole fraction of MDO in the feed. The azlactone backbone proton peak (1H, 2.70 ppm) decreases in intensity relative to the acetal (4H, 3.30-3.80 ppm) and backbone ester (2H, 4.03 ppm) peaks when ***x*** is increased from 0.10 to 0.90, indicating greater incorporation of acetal and ester groups from MDO into the polymer. Peak integration values were used to calculate the final polymer compositions; see Table 1 in the main text.

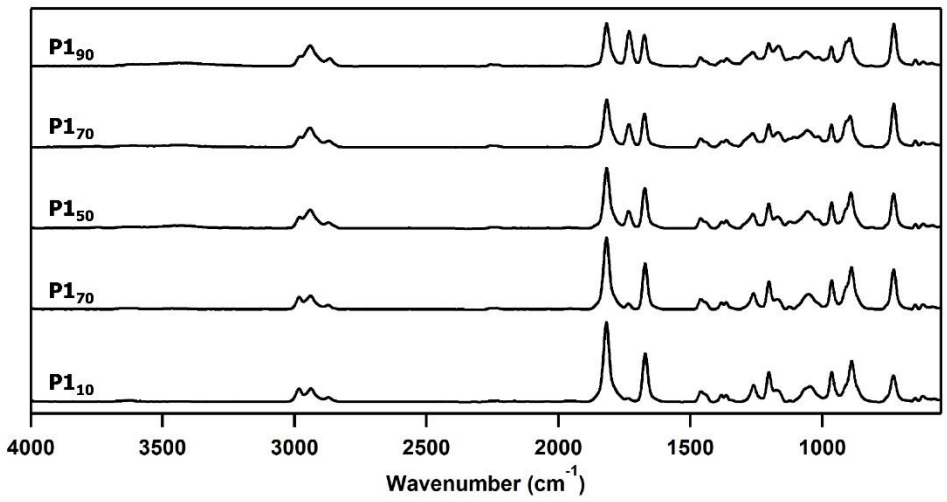

Fig S2. ATR IR spectra for **P1**$_x$ polymers. The intensities of the azlactone carbonyl stretch (C=O, ~1820 cm^{-1}) and cyclic imine stretch (C=N, ~1673 cm^{-1}) decrease relative to the intensity of the backbone ester carbonyl stretch (~1734 cm^{-1}) as ***x*** is increased from 0.10 to 0.90, indicating greater incorporation of MDO into the polymers. No evidence of unintended azlactone ring-opening by hydrolysis is observed by IR: strong peaks which would correspond to amide carbonyl stretching (C=O, ~1650 cm^{-1}) and amide N-H bending (~1530 cm^{-1}) are absent.

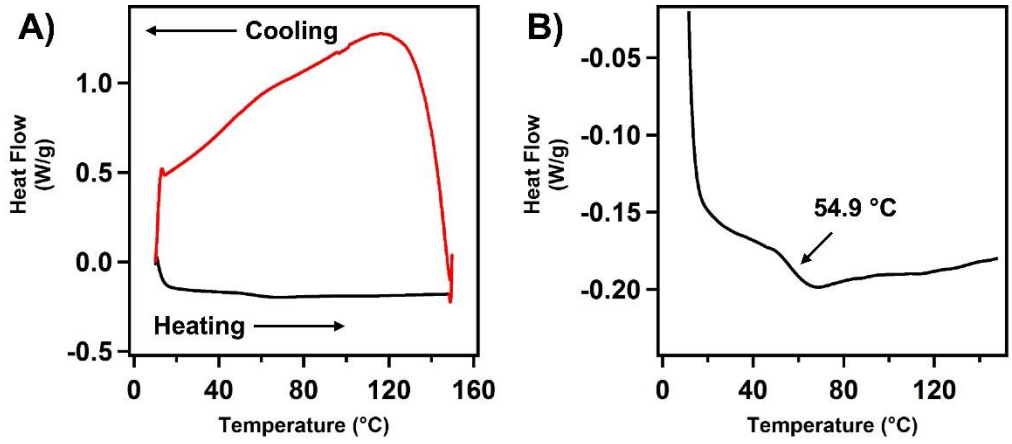

Fig S3. (A) Differential scanning calorimetry (DSC) heating (black) and cooling (red) curves for **P1**$_{50}$. (B) Enlarged view of the thermal transition at 54.9 °C, indicating the glass transition temperature (T_g) of the polymer. Other **P1**$_x$ derivatives displayed similar heating and cooling traces with a single T_g. See Table 1 of the main text for complete thermal data on **P1**$_x$ polymers.

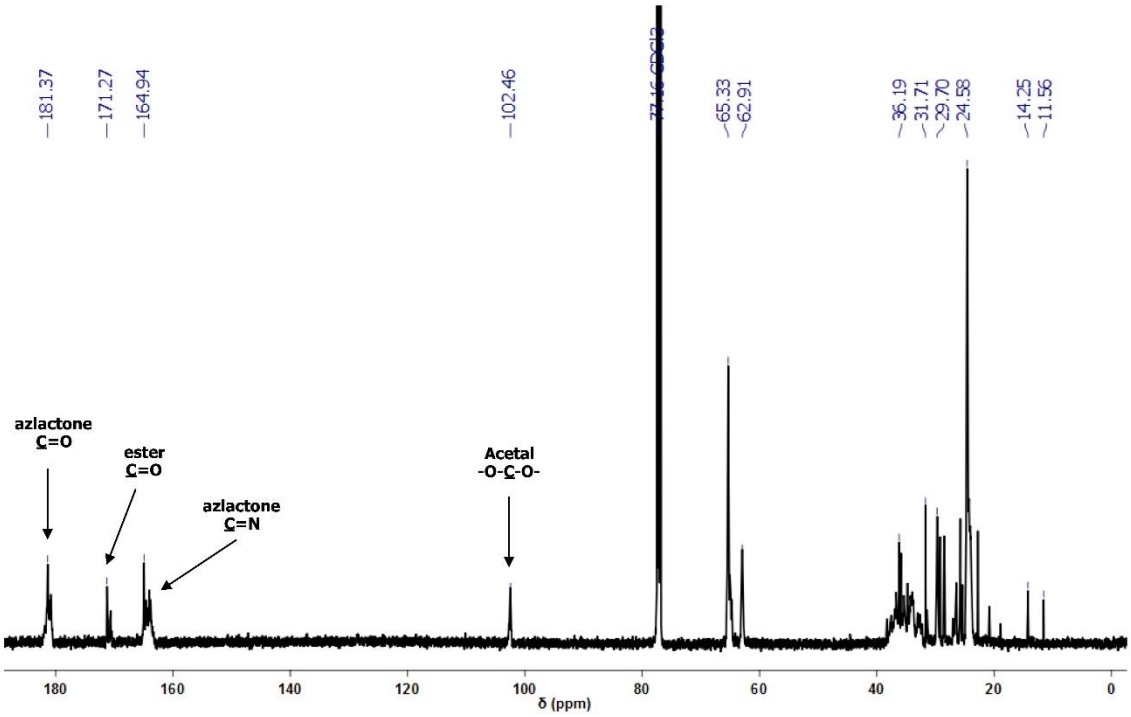

Fig S4. ^{13}C NMR spectrum of **P1$_{50}$**. Peaks corresponding to the azlactone ring, backbone ester, and acetal groups are labeled.

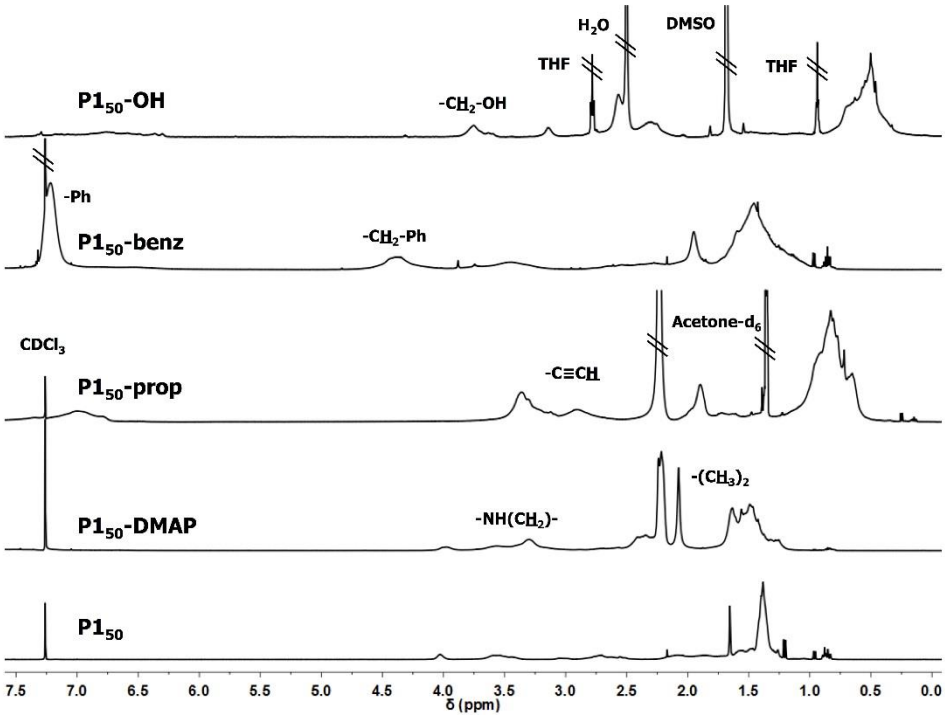

Fig S5. ^{1}H NMR spectra for **P1$_{50}$** derivatives synthesized in this study. All spectra were obtained by dissolution of the polymer derivatives in $CDCl_3$ with the exception of **P1$_{50}$-OH**, which was dissolved in deuterated DMSO. Peaks of note are labeled directly in each spectrum above.

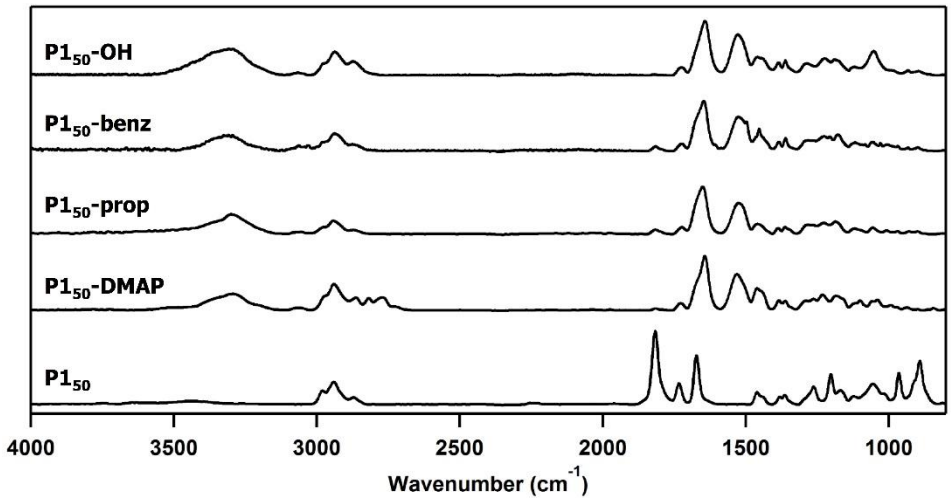

Fig S6. ATR IR spectra for **P1$_{50}$** derivatives synthesized in this study. Complete or near-complete reduction of the azlactone carbonyl stretch (C=O, ~1820 cm^{-1}) and cyclic imine stretch (C=N, ~1673 cm^{-1}), coupled with the appearance of amide carbonyl stretching (C=O, ~1650 cm^{-1}) and amide N-H bending (~1530 cm^{-1}) after the reaction with primary amines is observed. The backbone ester carbonyl stretch (~1734 cm^{-1}) is still present after reaction, suggesting that no substantial aminolysis of the backbone occurred.

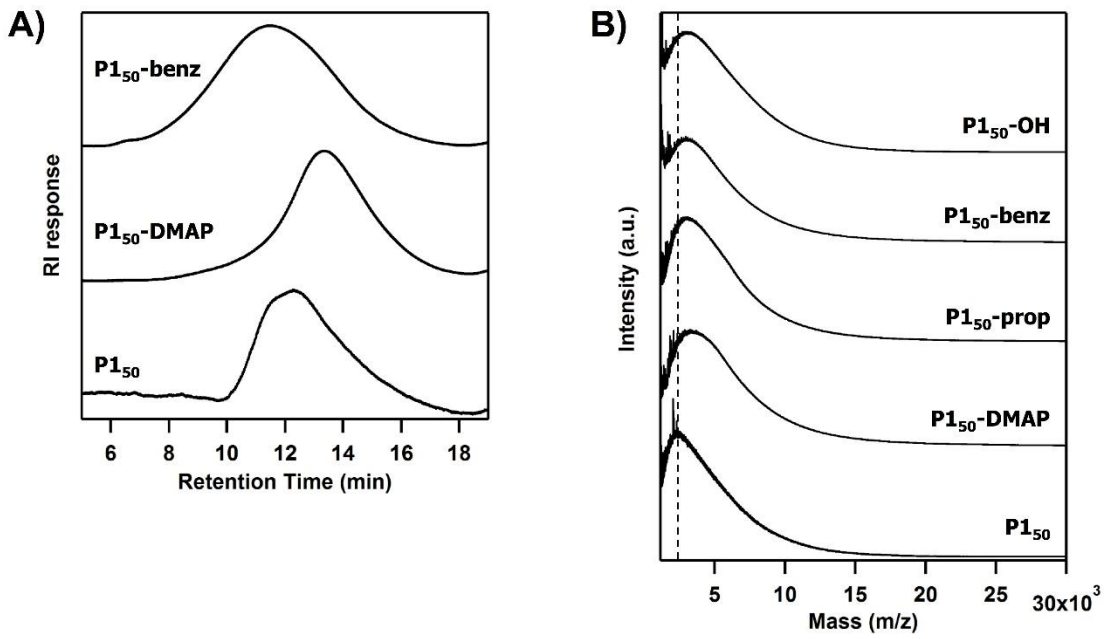

Fig S7. (A) SEC/GPC traces for selected **P1$_{50}$** derivatives synthesized in this study. **P1$_{50}$-benz** and **P1$_{50}$-DMAP** were soluble in the GPC eluent (THF with 0.1 M NEt_3), while **P1$_{50}$-prop** and **P1$_{50}$-OH** were not. The observation of unimodal peaks at retention times similar to that of the original parent polymer (**P1$_{50}$**) suggest that backbone hydrolysis did not occur during functionalization. (B) MALDI-ToF mass spectra for **P1$_{50}$** derivatives. All derivatives exhibited peak maxima at mass-to-charge (*m/z*) ratios greater than that of the reactive parent polymer (**P1$_{50}$**), supporting the conclusion that functionalization with primary amines leads to a mass increase without significant disruption of the ester bond-containing backbone, which would decrease the overall molecular weight and *m/z* ratio (vertical dashed line included to guide the eye).

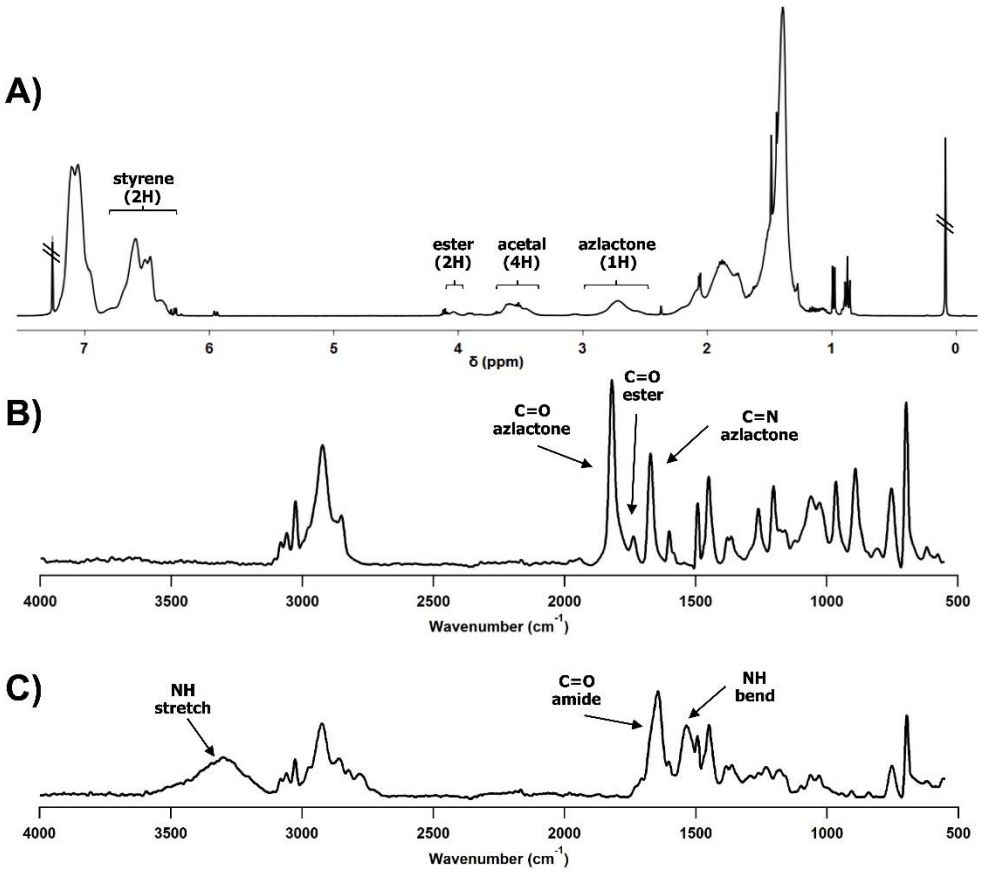

Fig S8. (A) ^{1}H NMR spectrum for reactive block copolymer **BCP1**. Peaks corresponding to styrene, ester, acetal, and azlactone protons are labelled. (B) ATR IR spectrum for **BCP1**, with peaks correspnding to the azlactone carbonyl stretch (C=O, ~1820 cm^{-1}), cyclic imine stretch (C=N, ~1673 cm^{-1}), and backbone ester stretch (C=O, ~1734 cm^{-1}) labelled. (C) ATR IR spectrum for block copolymer derivative **BCP1-DMAP**. The absence of azlactone ring stretches, coupled with the appearance of an amide carbonyl stretch (C=O, ~1650 cm^{-1}) and amide N-H bend (~1530 cm^{-1}) are consistent with complete conversion of the azlactone ring. The backbone ester carbonyl stretch (~1734 cm^{-1}) is still present after reaction (but is partially obscured by the strong amide carbonyl peak), suggesting that minimal backbone disruption has occurred. See also **Fig 3B** of the main text.

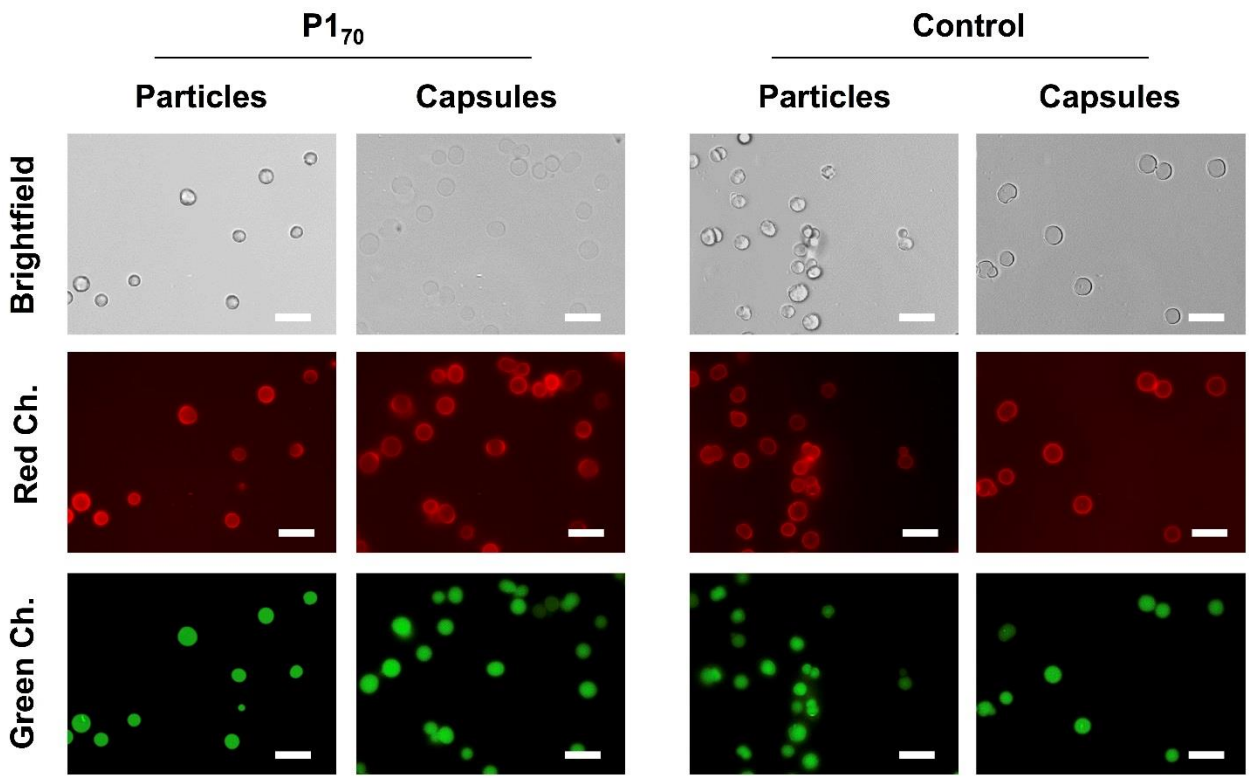

Fig S9. Representative brightfield and fluorescence micrographs of film-coated microparticles and hollow multilayer capsules fabricated using PEI and **P1$_{70}$** or PEI and non-degradable PVDMA (as a control). Capsules contain FITC-dextran (false-colored green) and a small number of azlactone groups in **P1$_{70}$** and PVDMA were labelled with TMR (false-colored red) to aid visualization. Brightfield images reveal changes in optical appearance after removal of the calcium carbonate cores (see main text) to yield hollow capsules and, together when combined with the fluorescence images, show that FITC-dextran remains confined within the capsules after dissolution of the core. Scale bars are 20 μm.

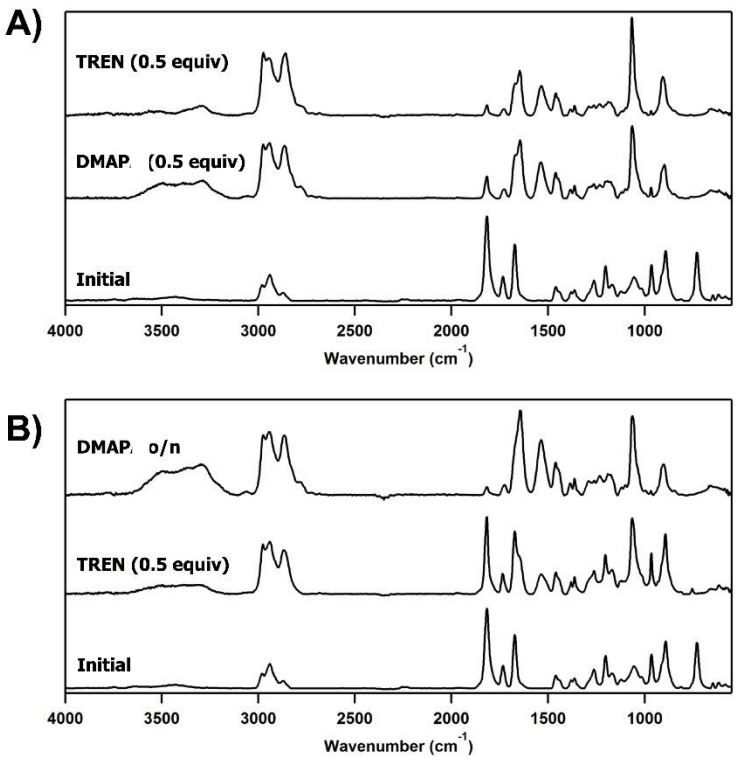

Fig S10. ATR IR spectra polymer hydrogels fabricated using the two methods described in the main text. (A) Method 1: the polymer was dissolved in THF (Initial, lower) and then 0.5 equiv. of amine were added (DMAP, middle), resulting in partial reaction with the azlactone groups as evidenced by a decrease in the intensity of the azlactone carbonyl stretch (C=O, ~1820 cm^{-1}). Next, 0.5 equiv. of trifunctional cross-linking agent was added (TREN, top) to form the gel. (B) Method 2: the polymer was dissolved in THF (Initial, lower) and then cross-linked to form the gel using TREN. A small reduction in azlactone carbonyl stretching intensity was observed, coupled with the appearance of an amide carbonyl stretch (C=O, ~1650 cm^{-1}) and amide N-H bend (~1530 cm^{-1}). A decrease in polymer chain mobility upon gelation presumably results in relatively low overall total azlactone group consumption with TREN (*c.f.* a mono-functional amine, e.g., Fig S10A). Next, the gel was functionalized with a further 0.5 equiv. of a primary amine-containing compound (DMAP, top). The backbone ester carbonyl stretch (~1734 cm^{-1}) was not consumed during these processes, suggesting that minimal backbone disruption occurred.

Chapter 11

Controlling the Surface-Mediated Release of DNA Using 'Mixed Multilayers'‡

‡ Portions of this chapter have previously been published as: Appadoo, V.; Carter, M.C.D.; Lynn, D.M. "Controlling the Surface-Mediated Release of DNA Using 'Mixed Multilayers'" *Bioengineering & Translational Medicine* **2016,** DOI: 10.1002/btm2.10023. V. Appadoo performed all of the LbL thin film and transfection experiments. My contribution was in synthesizing the polymers and analyzing the data.

ABSTRACT: We report the design of erodible ‘mixed multilayer’ coatings fabricated using plasmid DNA and combinations of both hydrolytically degradable and charge-shifting cationic polymer building blocks. Films fabricated layer-by-layer using combinations of a model poly(β-amino ester) (polymer 1) and a model charge-shifting polymer (polymer 2) exhibited DNA release profiles that were substantially different than those assembled using DNA and either polymer 1 or polymer 2 alone. In addition, the order in which layers of these two cationic polymers were deposited during assembly had a profound impact on DNA release profiles when these materials were incubated in physiological buffer. Mixed multilayers ~225 nm thick fabricated by depositing layers of polymer 1/DNA onto films composed of polymer 2/DNA released DNA into solution over ~60 days, with multi-phase release profiles intermediate to and exhibiting some general features of polymer 1/DNA or polymer 2/DNA films (e.g., a period of rapid release, followed by a more extended phase). In sharp contrast, ‘inverted’ mixed multilayers fabricated by depositing layers of polymer 2/DNA onto films composed of polymer 1/DNA exhibited release profiles that were almost completely linear over ~60-80 days. These and other results are consistent with substantial interdiffusion and commingling (or mixing) among the individual components of these compound materials. Our results reveal this mixing to lead to new, unanticipated, and useful release profiles and provide guidance for the design of polymer-based coatings for the local, surface-mediated delivery of DNA from the surfaces of topologically complex interventional devices, such as intravascular stents, with predictable long-term release profiles.

Introduction

Thin films and coatings that promote the transfer of DNA to cells are important in a range of fundamental and applied contexts extending from the development of new research tools to the design of new platforms for the local delivery of DNA from implants and interventional devices.[1-6] These goals define fundamental challenges related to the integration of DNA with synthetic materials, the engineering of molecular assemblies with properties and behaviors governed by changes in weak interactions, and responsiveness to stimuli that are both complex and, in many cases, specific to the needs of a particular application. For example, while many applications may benefit from the rapid release of DNA from a surface (e.g., film-coated microneedles for the delivery of DNA vaccines),[7-9] others are likely to benefit from the gradual or sustained release of DNA over periods of days, weeks, or months (e.g., gene-eluting intravascular stents).[1,10,11] While many different materials can be used to immobilize DNA on surfaces,[1-3,6,12-17] the mechanisms and design rules that govern the assembly and disassembly of these materials—and the extents to which they influence the rates at which DNA is released and the forms in which it can be made available to cells—are poorly understood. The design of polymer-based coatings that can be tuned to provide spatiotemporal control over the release of DNA remains an important goal as well as an obstacle to the development of new gene-based therapies.

The work reported here takes steps toward addressing these challenges through (i) the design of ionically crosslinked polymer coatings (called ‘polyelectrolyte multilayers’) that erode in aqueous environments and promote the surface-mediated release of DNA, and (ii) the development of new insights into the assembly of these materials that provide control over the rates at which these assemblies erode, disintegrate, and release DNA into surrounding media.

Our approach is based on methods for the layer-by-layer assembly[13,14] of oppositely charged polymers on surfaces—a strategy that has been used in many past studies for the fabrication of thin, DNA-containing coatings.[5] Past studies have demonstrated that layer-by-layer assembly can be used to fabricate polyelectrolyte multilayers (e.g., ~200 nm thick) using plasmid DNA and a variety of different natural and synthetic cationic polymers.[5] When the cationic components of these assemblies contain structural features that can degrade or trigger changes in ionic interactions that stabilize the films, this approach provides a platform for the design of thin polymer films that erode and release their incorporated DNA 'layers'. Many different cationic polymers have been developed for this purpose, with the extent to which DNA can be released rapidly, gradually, or selectively (e.g., in the presence of specific chemical triggers) dependent upon the types of chemical functionality incorporated into the polymer backbones or side chains.[5,17]

When combined with other practical advantages of layer-by-layer assembly,[18,19] including control over film thickness, DNA loading and composition,[5,20] and the relative ease with which these methods can be used to fabricate conformal films on topologically complex objects (including the surfaces of common medical interventional devices),[21-23] this 'multilayered' approach has the potential to be broadly useful for the development of new strategies for the localized delivery of DNA *in vitro* and *in vivo*.[24,25] However, while layer-by-layer assembly has been used widely in the basic research community to design coatings for the delivery or contact transfer of DNA,[5,25] there are currently no applications of these tools used in clinical practice. Potentially transformative applications continue to emerge,[7,26] but successful translation to clinical practice will require sustained efforts to understand the physicochemical properties and behaviors of these materials and the development of innovative new approaches to

guide their design for specific applications.

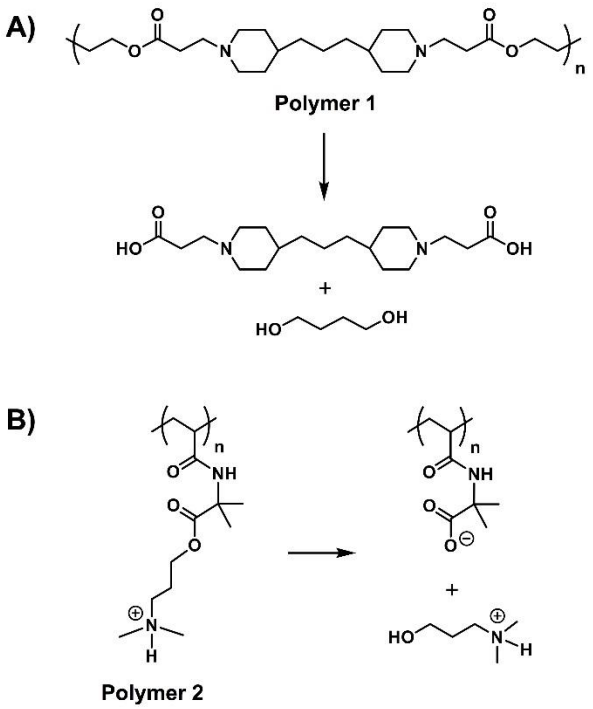

Figure 1. General scheme showing the structures of (A) polymer **1**, a hydrolytically degradable poly(*β*-aminoester), and (B) polymer **2**, a charge-shifting cationic polymer. The products resulting from backbone or side chain hydrolysis are also shown.

The work reported here exploits two advances that have been used in past studies to promote and provide control over the disruption of polyelectrolyte multilayers. Our group has reported extensively on the utility of a class of hydrolytically degradable polyamines called poly(β-amino ester)s (Figure 1A) as building blocks for the assembly of erodible plasmid DNA-containing coatings.[22,23,27] In this approach, film disassembly is driven, at least in part, by gradual backbone ester hydrolysis,[28] and the release of DNA generally occurs over short periods (e.g., over a period of several days upon exposure to physiologically relevant media[23,27]). As an alternative to the use of hydrolytically degradable polyamines, we[29-31] and others[32-35] have also

reported on the design of cationic ‘charge-shifting’ polymers. These polymers are not backbone degradable, but instead contain hydrolyzable ester-based side chains (Figure 1B) that lead to changes in polymer net charge that can, in turn, lead to the disruption of ionic assemblies (e.g., by becoming less positively charged over time). In contrast to approaches based on the incorporation of poly(β-amino ester)s, this approach leads to thin polymer coatings that can erode and promote the surface-mediated release of plasmid DNA for prolonged periods (e.g., over periods of up to several months).[29,31]

In this study, we sought to explore the behaviors of ‘mixed’ multilayers fabricated using DNA and combinations of both poly(β-amino ester)s and charge-shifting cationic polymers. This work was broadly motivated by the hypothesis that films fabricated using combinations of these two different materials could open the door to new designs and film compositions that exhibit unique and useful release profiles that cannot be attained using coatings constructed from either type of polymer alone (e.g., coatings that permit the staged or sequential release of DNA, or release profiles with other useful features that can be tuned, accentuated, or eliminated by varying film composition and structure).

The results reported here demonstrate that changes in the nominal structures and compositions of coatings fabricated using combinations of poly(β-amino ester)s and charge-shifting cationic polymers lead to large changes in the behaviors (e.g., the release profiles) of these materials when exposed to physiologically relevant media. In particular, we find that the order in which layers of these two polymers are deposited (e.g., whether DNA and poly(β-amino ester) layers are deposited before layers of DNA and charge-shifting polymers, or *vice versa*) has profound effects on release behaviour, leading, in some cases, to films that can promote the extended release of one or more plasmid DNA constructs with linear release profiles that are

difficult to obtain using other polyelectrolyte multilayer systems. Our results are consistent with processes of interdiffusion and mixing that occur among polymer layers during the assembly or erosion of these materials, and provide guidance useful for the design of conformal thin-film coatings that can promote the release of DNA from surfaces at constant rates for up to 80 days. These methods expand the range of DNA release profiles that can be accessed using a limited pool of layer-by-layer building blocks and are, in principle, substrate independent and amenable to the immobilization and subsequent long-term release of DNA from the surfaces of interventional devices such as intravascular stents.

Materials and Methods

Materials. Diazabicycloundec-7-ene (DBU, 98%), concentrated hydrochloric acid (HCl, 37%, ACS reagent), azobisisobutyronitrile (AIBN, recrystallized from methanol), tetrahydrofuran (THF, HPLC grade), dichloromethane (DCM, ACS grade), hexanes (technical grade), 4,4′-trimethylenedipiperidine (97%), sodium poly(4-styrenesulfonate) (SPS, M_w = 70,000), and ethyl acetate (ACS grade, >99.5%) were purchased from Sigma-Aldrich (Milwaukee, WI). 3-Dimethylamino-1-propanol (99%) was purchased from Acros Organics (Morris Plains, NJ). 1,4-Butanediol diacrylate was purchased from Alfa Aesar (Ward Hill, MA). Anhydrous THF was obtained from a Pure Process Technology solvent purification system (Nashua, NH). Linear poly(ethyleneimine) (LPEI, MW = 25000) was obtained from Polysciences, Inc. (Warrington, PA). Inhibitor Removal Resin was purchased from Alfa Aesar (Radnor, PA). 2-Vinyl-4,4-dimethylazlactone (VDMA), a kind gift from Dr. Steven M. Heilmann (3M Corp., Minneapolis, MN) was fractionally distilled under vacuum (B.P. ~22 °C at ~500 mTorr; clear mobile liquid at room temperature) and then stored with 500 ppm butylated hydroxytoluene (BHT) and 1000

ppm triethylamine at 0 °C prior to use. Polymer **1** (M_n = 23.3 kDa, $Đ$ = 2.39) was synthesized as previously described.[36] Phosphate-buffered saline (PBS, pH = 7.4, ionic strength = 154 mM) was prepared by dilution of commercially available concentrate (EM Science, Gibbstown, NJ). Plasmid DNA [pEGFP-N1 (encoding enhanced green fluorescent protein; EGFP) and pDsRed2-N1 (encoding red fluorescent protein; RFP; pRFP) (4.7 kb), >95% supercoiled] was obtained from Elim Biopharmaceuticals, Inc. (San Francisco, CA). Dulbecco's modified Eagle's medium (DMEM), fetal bovine serum (FBS; 10%), penicillin (100 units/mL), streptomycin (100 μg/mL), Opti-MEM reduced serum medium, trypsin-EDTA (0.25%), and Lipofectamine 2000 were purchased from Invitrogen (Carlsbad, CA). COS-7 cells were obtained from the American Type Culture Collection (Manassas, VA). Expired stainless steel stents used for SEM studies (Abbott Vascular, Abbott Park, IL; Medtronic, Shoreview, MN) were obtained from the Cardiovascular Physiology Core Facility at the University of Wisconsin-Madison. All stents had nominal diameters ranging from 2 to 5 mm and lengths ranging from 8 to 30 mm. Stent expansion was performed using a standard inflation device with deionized water as the expansion fluid. All buffers and polymer solutions were filtered through a 0.2 μm membrane syringe filter prior to use unless noted otherwise. Test-grade n-type silicon wafers were purchased from Silicon Inc. (Glenshaw, PA). Water with a resistivity of 18.2 MΩ was obtained from a Millipore filtration system. Materials were used as received unless otherwise noted.

General Considerations. ^{1}H NMR spectroscopy was performed in $CDCl_3$ or D_2O using a Bruker Avance-400 or Bruker Avance-500 spectrometer and a pulse repetition delay of 10 s. All spectra were referenced relative to the residual proton peak of $CHCl_3$ (δ 7.26 ppm) or D_2O (δ 4.79 ppm). Size exclusion chromatography (SEC) analyses for polymer **1** were performed using

a Waters L9 515 344M GPC equipped with two Styragel HT6E columns (300 mm x 7.8 mm), a Waters 515 HPLC pump, a Waters 7726i manual injector, and a Waters 2410 RI detector, using THF with 0.1 M NEt_3 as the eluent at a flow rate of 1 mL/min at 40 °C. SEC analyses for poly(2-vinyl-4,4-dimethylazlactone) (PVDMA) were performed using a Viscotek GPC Max VE2001 equipped with two Polymer Laboratories PolyPore columns (250 mm × 4.6 mm) and a TDA-302 detector array using THF as the eluent at a flow rate of 1 mL/min at 40 °C. The SEC instruments were both calibrated using 10 narrow dispersity polystyrene standards with M_n = 0.580−377.4 kg/mol (Agilent Technologies, Santa Clara, CA). Attenuated total reflectance (ATR) IR measurements were obtained using a Bruker Tensor 27 FTIR spectrometer outfitted with a Pike Technologies Diamond ATR stage (Madison, WI). Data were analyzed using Opus Software version 6.5 (Bruker Optik GmbH). Spectra were collected at a resolution of 2 cm^{-1} and are presented as an average of 16 scans. Data were smoothed by applying a nine-point average and baseline-corrected using a concave rubberband correction (10 iterations, 64 points). Optical thicknesses of films deposited on silicon substrates were determined using a Gaertner LSE ellipsometer (632.8 nm, incident angle = 70°) and data were processed using the Gaertner ellipsometer measurement software. Thicknesses were calculated using a pre-determined refractive index for each location measured on the film, and were determined in at least five different locations for three replicate films. All films were dried under a stream of filtered compressed air prior to thickness measurements. Scanning electron micrographs were acquired using a LEO-1550 VP field-emission SEM operating with an accelerating voltage of 1-3 kV. Samples were coated with a thin layer of gold prior to imaging. UV/Vis absorbance values for solutions used to characterize DNA release profiles were recorded on a Beckman Coulter DU520 UV/Vis spectrophotometer (Fullerton, CA). Fluorescence microscopy images used to evaluate

EGFP or RFP expression in transfection experiments were acquired using an Olympus IX70 microscope equipped with a Lumen Dynamics XCite 120PC-Q fluorescence source and a Q Imaging EXi Aqua camera. Images were analyzed and false-colored using MetaMorph Advanced software, Version 7.7.8.0 (Molecular Devices, LLC).

Synthesis of Poly(2-vinyl-4,4-dimethylazlactone) (PVDMA). 2-Vinyl-4,4-dimethylazlactone was passed twice through a short column of Inhibitor Removal Resin followed by a short column of silica gel to remove inhibitor and triethylamine base, respectively. VDMA (2.06 g, 14.8 mmol), AIBN (24.32 mg, 0.148 mmol), and ethyl acetate (6.0 mL, dried twice over $MgSO_4$) were added to an oven-dried 25 mL round-bottomed flask tube and sparged with nitrogen for 15 minutes before being placed into an oil bath at 60 °C. After 24 hours, the flask was cooled to room temperature and the mixture was diluted with ~4 mL of DCM and precipitated into ~150 mL of hexanes. The resulting white solid was collected by vacuum filtration, redissolved in DCM, re-precipitated twice more in hexanes, and then dried under high vacuum overnight. M_n = 47.6 kDa; $Đ$ = 3.64. ^{1}H NMR (400.180 MHz, $CDCl_3$, δ ppm): 2.71 (s, 1H), 2.16-1.79 (m, 2H), 1.37 (s, 6H). ATR IR (cm^{-1}): 1818 (C=O azlactone), 1671 (C=N azlactone), 1203 C-O-C (azlactone); peaks at ~3200 cm^{-1} (NH stretch) and ~1540 cm^{-1} (NH bend) absent, indicating no unintended azlactone hydrolysis by adventitious water.

Synthesis of Charge-Shifting Polymer 2. Charge-shifting polymer **2** was synthesized based on a modified literature procedure,[29,31] as follows. Briefly, PVMDA (0.512 g, 3.68 mmol), 3-dimethylamino-1-propanol (1.3 equiv. with respect to the azlactone groups of PVDMA, 557.4 µL, 4.78 mmol) and DBU (55.1 µL, 0.368 mmol, 0.1 equiv. with respect to the azlactone groups

of PVDMA) were dissolved in 8.0 mL of anhydrous THF in a 15 mL glass vial. The vial was sealed with a Teflon cap and parafilm and stirred at 65 °C overnight. The resulting light yellow solution was concentrated under reduced pressure to ~5 mL total volume and precipitated into 100 mL of 1:1 (v/v) hexanes/acetone containing 307 µL of concentrated $HCl_{(aq)}$ (1 equiv. w.r.t. VDMA). The resulting sticky white solid was isolated by centrifugation, dried in air, dissolved in ~8 mL MeOH, and precipitated into 150 mL of 1:1 (v/v) hexanes/acetone containing 307 µL of concentrated $HCl_{(aq)}$ (37%). This process was repeated a total of six times to remove the excess unreacted alcohol (as monitored by ^{1}H NMR in D_2O) to yield the product as a slightly sticky white solid after drying under high vacuum overnight. ^{1}H NMR (500.022 MHz, 1.0 mL D_2O and 10 µL DCl, δ ppm): 4.35 (s, 2H, -CH_2-CH_2-C$\underline{H}_2$-COC(O)-), 3.28 (s, 2H, -CH_2-C$\underline{H}_2$-CH_2-COC(O)-), 2.93 (s, 6H, -N(C$\underline{H}_3$)$_2$)-CH_2-), 2.16 (s, 2H, CH_2-C$\underline{H}_2$-CH_2- COC(O)-), 1.52 [m, 3H, -COC(O)-C(C$\underline{H}_3$))$_2$, and 6H, (-C$\underline{H}_2$C$\underline{H}$-)]. ATR-IR (cm^{-1}): 3350 (NH stretch), 1732 (C=O ester), 1658 (C=O amide), 1151 (C-O-C ether).

Preparation of Polyelectrolyte Solutions. Solutions of LPEI and SPS used for the fabrication of LPEI/SPS base layers[27] were prepared at a concentration of 20 mM (w.r.t. the molecular weight of the polymer repeat unit) in aqueous solutions containing 10 mM NaCl. LPEI solutions also contained 5 mM HCl to aid polymer solubility. Solutions of polymers **1** and **2** were prepared at a concentration of 5 mM (w.r.t the molecular weight of the polymer repeat unit) in 100 mM sodium acetate buffer (pH = 5.0). All polymer solutions were filtered through a 0.2 µm nylon syringe filter prior to use. Solutions of plasmid DNA were prepared at concentrations ranging from 0.7-1.0 mg/mL in 100 mM sodium acetate buffer (pH = 5.0) and were not filtered prior to use.

Fabrication of Polyelectrolyte Multilayers. Prior to use, silicon substrates (0.5 × 3.5 cm) were rinsed with acetone, ethanol, and deionized water and then dried under a stream of filtered compressed air. Stainless steel stents were used as received. Films designed to contain polymer **1** in the bottommost layers (e.g., Films 1, 4, and 7; see Figure 2) were first pre-coated with a multilayer film composed of 10 bilayers of LPEI and SPS (terminated with SPS), as previously described using an automated dipping robot (Riegler & Kirstein GmbH, Potsdam, Germany).[23] Films designed to contain polymer **2** in the bottom-most layers (see Figure 2) were deposited directly onto the substrates without any precursor layers. Films were deposited on bare or pre-coated substrates manually using the following general protocol: 1) substrates were submerged in a solution of polymer **1** or polymer **2** for 5 min, 2) substrates were removed and immersed in either 100 mM sodium acetate buffer at pH = 5.0 (after the deposition of polymer **1**) or water (after the deposition of polymer **2**) for 1 min followed by a second similar rinse for 1 min, 3) substrates were submerged in a solution of DNA for 5 min, and 4) substrates were rinsed in the manner described above. This cycle was repeated until the desired number of polymer/DNA layers (or 'bilayers') was reached. We describe films fabricated in this manner using the notation $(X/DNA)_n$, where "X" refers to the polymer used and "n" denotes the number of polyamine/DNA bilayers deposited. The nominal structures of films and 'mixed multilayer' architectures investigated in this study are depicted in Figure 2. For experiments aimed at characterizing film growth profiles by ellipsometry, films were dried after every two cycles using filtered compressed air prior to characterization. Films to be used in erosion experiments were either used immediately or dried under a stream of filtered compressed air and stored in a vacuum desiccator until use. All films were fabricated at ambient room temperature. Films fabricated on stents and used in erosion studies were coated on both the inner and outer portions

of the stent in the unexpanded state. Following film fabrication, stents were expanded by mounting them onto catheter balloon deployment systems. The catheter balloons were inflated to expand the stents and then deflated and removed. Stents used for SEM imaging studies were mounted and crimped onto catheter balloons prior to coating with multilayered films.

Characterization of Film Erosion and DNA Release Profiles. Experiments designed to characterize film erosion and DNA release profiles were performed in the following general manner.[27] Film-coated substrates were placed into a plastic cuvette and 1.0 mL of PBS solution was added to cover the film-coated portion of the substrate. The samples were incubated at 37 °C and transferred to fresh PBS solutions at predetermined intervals. UV/Vis absorbance readings were made directly on the incubation solutions and measurements were used to determine the amount of DNA released (λ = 260 nm).

Cell Transfection Assays. COS-7 cells were grown in 96-well plates for 24 hours at an initial seeding density of 12,000 cells/well in 200 μL of growth medium (90% DMEM, 10% FBS, penicillin 100 units/mL, streptomycin 100 μg/μL). After 24 hours, 10 μL of a Lipofectamine 2000/DNA plasmid mixture was added directly to each well according to the general protocol provided by the manufacturer (experiments were performed in triplicate). The Lipofectamine 2000/DNA plasmid mixtures used contained 25 μL of DNA solution collected at a given time point during a release experiment and 25 μL of Lipofectamine 2000 reagent (24 μL stock diluted into 976 μL of water). Fluorescence images used to qualitatively characterize levels of gene expression were acquired after 48 hours.

Results

*Fabrication of Mixed Multilayers: Deposition of Degradable Polymer **1**/DNA Layers on Charge-Shifting Polymer **2**/DNA Films*

We performed an initial series of experiments to characterize the fabrication and film growth profiles of 'mixed multilayers' assembled using a combination of poly(β-amino ester) **1** and charge-shifting polymer **2** as cationic film components together with a plasmid DNA construct encoding EGFP as an anionic building block. For these experiments, we fabricated films having the general structure represented by Film 3 shown in Figure 2 by depositing eight bilayers of polymer **1** and DNA onto a multilayer film composed of eight bilayers of polymer **2** and DNA (e.g., a film having the nominal structure (polymer **2**/pEGFP)$_8$(polymer **1**/pEGFP)$_8$; see Materials and Methods for additional details of film fabrication procedures). Figure 3A (closed triangles) shows a plot of film thickness versus the number of polymer and DNA layers deposited on a planar silicon substrate during fabrication. Inspection of these results reveals film growth to occur in a linear manner that is characteristic of the iterative, layer-by-layer growth of control films fabricated exclusively from pEGFP and either polymer **1** [i.e., (polymer **1**/pEGFP)$_{16}$, Film 1 in Figure 2; closed squares in Figure 3)][27] or polymer **2** [i.e., (polymer **2**/pEGFP)$_{16}$, Film 2 in Figure 2; closed circles in Figure 3)][29] to an optical film thickness of ~225 nm. These results demonstrate that 'hydrolytically degradable' bilayers of polymer **1**/pEGFP can be deposited directly on the surfaces of 'charge shifting' films fabricated from polymer **2** and DNA without any significant changes in film growth profiles (e.g., without a change in slope or a transition from linear to a phase reflecting so-called exponential growth,[37-40] etc.).

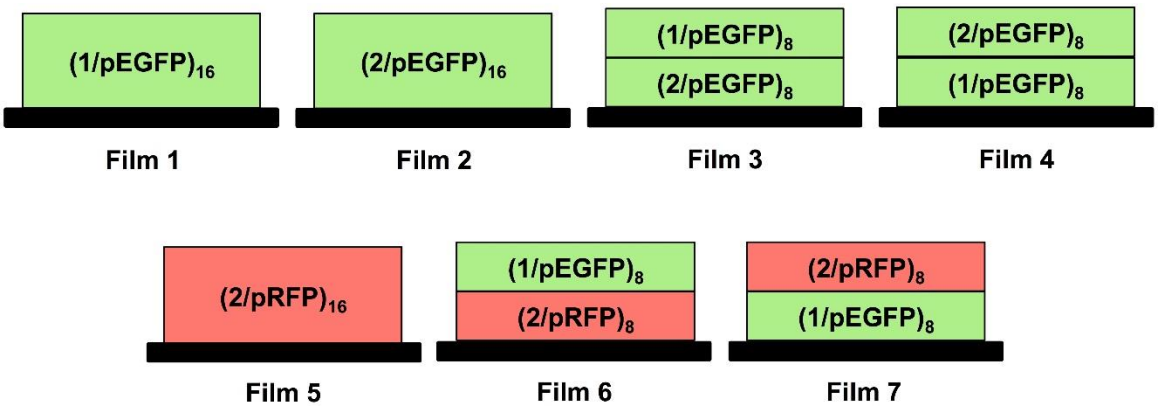

Figure 2. Schematic representations of the polyelectrolyte multilayer film architectures investigated in this study. Polymer **1** and polymer **2** are denoted here as '**1**' and '**2**', respectively. Plasmid DNA encoding green fluorescent protein and red fluorescent protein are denoted 'pEGFP' and 'pRFP', respectively, and sets of layers fabricated using these two plasmids are colored green or red coded for additional emphasis. Subscripts indicate the number of bilayers of cationic polymer and DNA were deposited.

*Release Profiles of Mixed (Polymer **2**/DNA)–(Polymer **1**/DNA) Multilayers in Aqueous Buffer*

We characterized the release profiles of mixed (polymer **2**/pEGFP)$_8$(polymer **1**/pEGFP)$_8$ multilayers in physiologically relevant media by incubating them in PBS buffer at 37 °C and characterizing the release of pEGFP into solution over time. Figure 3B (closed triangles) shows the release of DNA from these Film 3-coated silicon substrates in comparison to the release of DNA from control substrates coated with either (polymer **1**/pEGFP)$_{16}$ films (Film 1; closed squares) or (polymer **2**/pEGFP)$_{16}$ films (Film 2; closed circles). Inspection of these results reveals substrates coated with Film 1 to release DNA into solution rapidly (e.g., over ~1-2 days), consistent with the behaviors of these hydrolytically degradable coatings reported in past studies.[23,27] In contrast, substrates coated with Film 2 exhibited prolonged release profiles, with an extended 'lag' phase of ~2-3 weeks, followed by the onset of release extended up to ~60 days under these conditions; this behavior is also consistent with those of past studies of films fabricated using DNA and charge-shifting polymer **2**.[29,31] Substrates coated with Film 3 [so-

called ‘mixed’ (polymer **2**/pEGFP)$_8$(polymer **1**/pEGFP)$_8$ multilayers] exhibited release profiles that were intermediate to those two extremes. As shown in Figure 3, Film 3 (closed triangles) also released DNA over an extended period of ~60 days. These films did not exhibit a delayed ‘lag’ phase typical of the Film 2 architecture or release a substantial percentage of their DNA over the first 1-2 days of immersion in physiological media.

Fabrication and Characterization of Mixed Multilayers on Intravascular Stents

Panels A-B of Figure 4 show SEM images of bare metal stainless steel intravascular stents coated with mixed Film 3 multilayers after hand crimping onto a deflated balloon assembly (A) and after inflation of the balloon to re-expand the stent (B). These images reveal the surfaces of the stents to be coated with a uniform and conformal polymer/DNA film that did not crack, peel, or delaminate substantially from the surface of the stent over large areas when subjected to mechanical forces associated with crimping or balloon expansion. Figure 4C shows a selected portion of a film from a small region of a coating that did partially delaminate from the stent surface; cross-sectional analysis of this and other related images (see Figure S1; Supporting Information can be found at the end of this chapter) reveals these mixed Film 3 stent coatings to be ~240 (±70) nm thick, a value that is in general agreement with optical thicknesses measured using ellipsometry for films fabricated on silicon substrates (Figure 3A). These Film 3-coated stents also released pEGFP gradually over extended periods of ~60 days when incubated in PBS buffer at 37 °C (Figure S2), with an overall release profile that was similar to that shown in Figure 3B for Film 3-coated silicon substrates (and intermediate to those exhibited by control stents coated with Film 1 or Film 2).

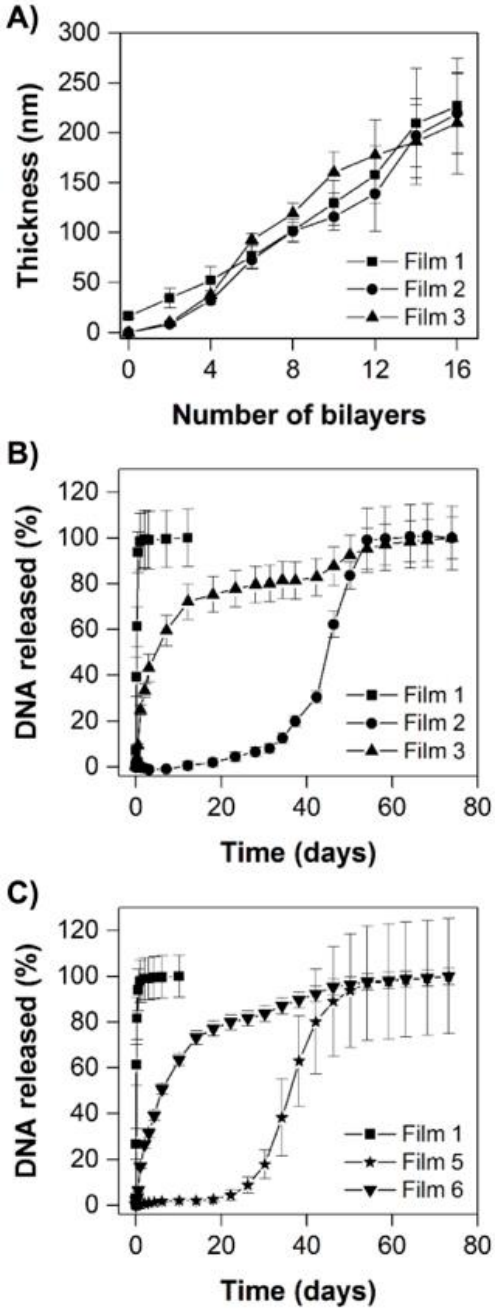

Figure 3. (A) Plot of film thickness versus the number of polymer/DNA layers deposited on silicon substrates as determined by ellipsometry during the growth of Films 1, 2, and 3 (see Figure 2 for additional details of the compositions of these films). (B) Plot showing the release of DNA from substrates coated with Films 1, 2, and 3. (C) Plot showing the release of DNA from substrates coated with Films 1, 5, and 6. (B-C) Films were incubated in PBS buffer (pH 7.4, 37 °C) and the amount of DNA released into solution was measured by UV/Vis absorbance. In each case, data are presented as the average and standard deviation of measurements obtained on three identically prepared films.

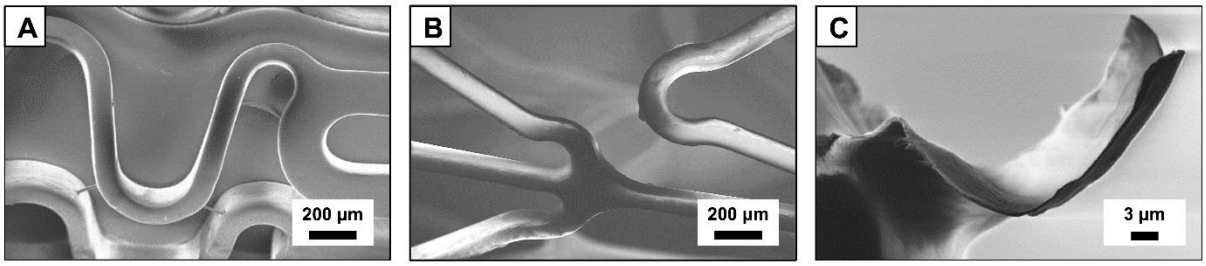

Figure 4. Scanning electron microscopy images showing intravascular stents coated with Film 3 (see Figure 2 for additional details of the compositions of these films). (A) Film-coated stent crimped on a catheter balloon prior to expansion. (B) Film-coated stent after expansion and removal of the catheter balloon. (C) High-magnification image showing a region the film that was partially delaminated from the stent surface; images such as those in (C) were used to characterize film thickness, see Fig. S1.

Characterization of Mixed Multilayers Fabricated Using Two Plasmid Constructs

To provide additional insight into the release profiles of the Film 3 structures described above, we fabricated films having the structure shown in Film 6 of Figure 2 [i.e., (polymer **2**/pRFP)$_8$(polymer **1**/pEGFP)$_8$] using polymer **1**, polymer **2**, and two different plasmid DNA constructs encoding either EGFP or RFP. These films were fabricated in a manner identical to that used to fabricate Film 3, with the exception that pRFP was used to fabricate the bottommost portion of the films (i.e., the (polymer **2**/pRFP) bilayers). Silicon substrates coated with Film 6 exhibited DNA release profiles nearly identical to those of substrates coated with Film 3 [(see Figure 3C, closed triangles; the release profile of substrates coated with control films fabricated using polymer **2** and the pRFP plasmid (Film 5; Figure 3, closed stars) is shown for comparison, and is similar to that of substrates coated with polymer **2** and the pEGFP plasmid; Figure 3B)]. These results demonstrate that this second pRFP plasmid, which is similar in size to the pEGFP plasmid (4.7 kb), does not have a significant impact on the erosion and DNA release profiles of these mixed multilayer films (coatings with the Film 6 structure were ~250 nm thick, as determined by ellipsometry, and were thus also similar in thickness to the Film 3 coatings).

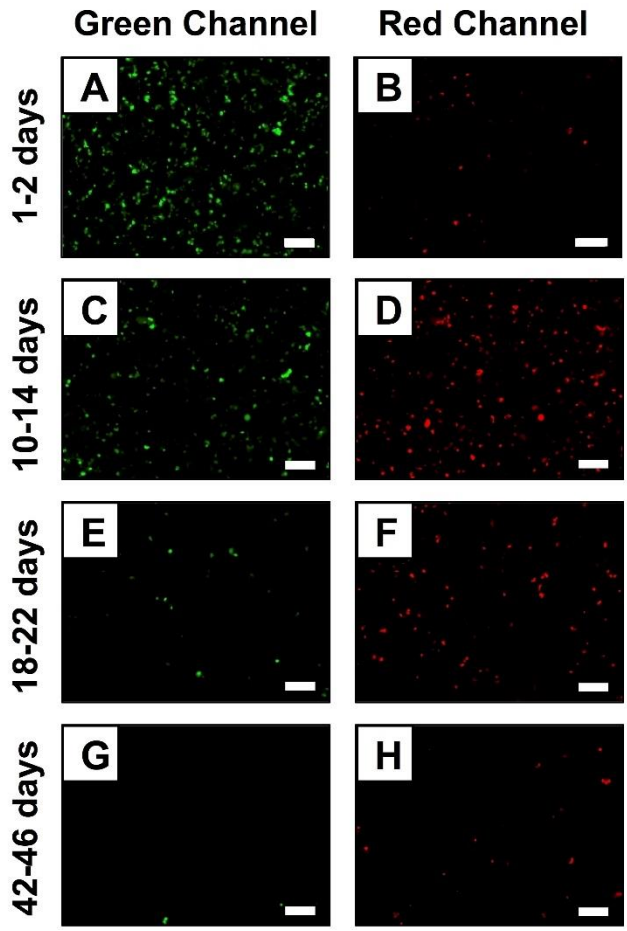

Figure 5. Representative fluorescence microscopy images showing COS-7 cells expressing GFP (green channel) and RFP (red channel) after treatment with samples of DNA collected during the erosion of substrates coated with Film 6 (see Figure 2 for additional details of the compositions of these films; see main text and Materials and Methods for additional details for these transfection experiments). The relative levels of GFP and RFP expression observed correspond qualitatively to the amount of each plasmid released from the film during the following time periods: (A-B) 1-2 days, (C-D) 10-14 days, (E-F) 18-22 days, and (G-H) 42-46 days. Scale bar = 250 μm. A complete set of images for all time points measured is provided in Figure S1.

To determine whether the structures of these mixed multilayers could be used to provide differential control over the release of the pEGFP and pRFP plasmid constructs (e.g., whether both plasmids were released simultaneously or in a manner that was sequential or ‘staged’), we collected samples of DNA released over defined intervals during the course of the film erosion

experiments described above and used them to transfect mammalian COS-7 cells (using a commercial lipid as a delivery agent; see Materials and Methods and past studies[27,29-31,41] for additional details of this experimental design). These studies were not aimed at quantifying relative levels of transgene expression, but rather to provide a qualitative, expression-based indicator of the presence or absence of either plasmid in the degradation milieu at any time interval.[30,31,41] We note here that films fabricated using fluorescently labeled plasmids were not used for these studies on the basis of past studies demonstrating that that approach is not reliable for the characterization of DNA in experiments requiring long incubation times (e.g., over 60 days).[31] The results of studies using Film 6 coatings are summarized in Figure 5 for samples of DNA collected over four time periods early (over 1-2 days of incubation; A-B), mid-way (over 10-14 days or 18-22 days; C-D and E-F, respectively) or late (over 42-46 days; G-H) in the release experiment (a complete set of results for samples collected over other intermittent time periods during this experiment can be found in Figure S3). Inspection of these results and those shown in Figure S3 reveals that EGFP is expressed almost exclusively in samples collected during the first ~48 hours, and that both EGFP and RFP are expressed simultaneously at subsequent time points. We return to these observations again in the discussion below.

Characterization of 'Inverted' Mixed Multilayers: Long-Term Linear Release of DNA

Finally, we performed a series of experiments to characterize the behaviors of mixed multilayers having nominal structures that were the 'inverse' of those characterized above—that is, films having the structure of Film 4 in Figure 2, in which eight bilayers of polymer **2** and DNA were deposited onto a multilayer film composed of eight bilayers of polymer **1** and DNA [i.e., (polymer **1**/pEGFP)$_8$(polymer **2**/pEGFP)$_8$ films; the opposite of the procedure used to

fabricate Film 3]. These films were fabricated on silicon substrates pre-coated with a thin multilayer film (~20 nm thick) composed of 10 bilayers of LPEI and SPS to facilitate the adsorption of polymer **1**/DNA layers, as described in past studies.[23,27] Figure 6A shows a plot of film thickness versus the number of polymer/DNA layers deposited, as determined by ellipsometry. These results reveal these 'inverted' mixed multilayers to grow in a linear manner and to final thicknesses (~250 nm) similar to those exhibited by mixed Film 3 films (Figure 3A).

Additional characterization of these inverted mixed Film 4 multilayers revealed stark and substantial differences in DNA release profiles, compared to the behaviors of Film 3 multilayers, when these films were incubated in PBS at 37 °C. Substrates coated with Film 4 multilayers also released DNA over a period of ~60-70 days (Figure 6B), but, in contrast to Film 3 multilayers (Figure 3B), exhibited nearly completely linear release profiles over that time period. Figure 6C shows the release profile of inverted mixed-polymer/mixed-plasmid multilayers having the structure of Film 7 in Figure 2 [i.e., (polymer **1**/pEGFP)$_8$(polymer **2**/pRFP)$_8$]. These results also reveal both plasmid constructs to be released at a constant rate over a period of ~70-80 days. These linear release profiles are very different from those exhibited by either (polymer **1**/DNA)-type films[23,27] or (polymer **2**/DNA)-type films[29,31] reported in past studies, or the mixed Film 3-type and Film 6-type multilayers reported above (Figure 3B-C). We performed cell transfection experiments similar to those described above and shown in Figure 5 using aliquots of erosion milieu collected during the erosion of the Film 7 coatings used to generate the results shown in Figure 6C. Unfortunately, the concentrations of DNA in samples collected during these long-term, linear release experiments were sufficiently low to prevent meaningful conclusions regarding any potential differences in the rates of release of the pEGFP and pRFP plasmids from these inverted multilayer coatings.

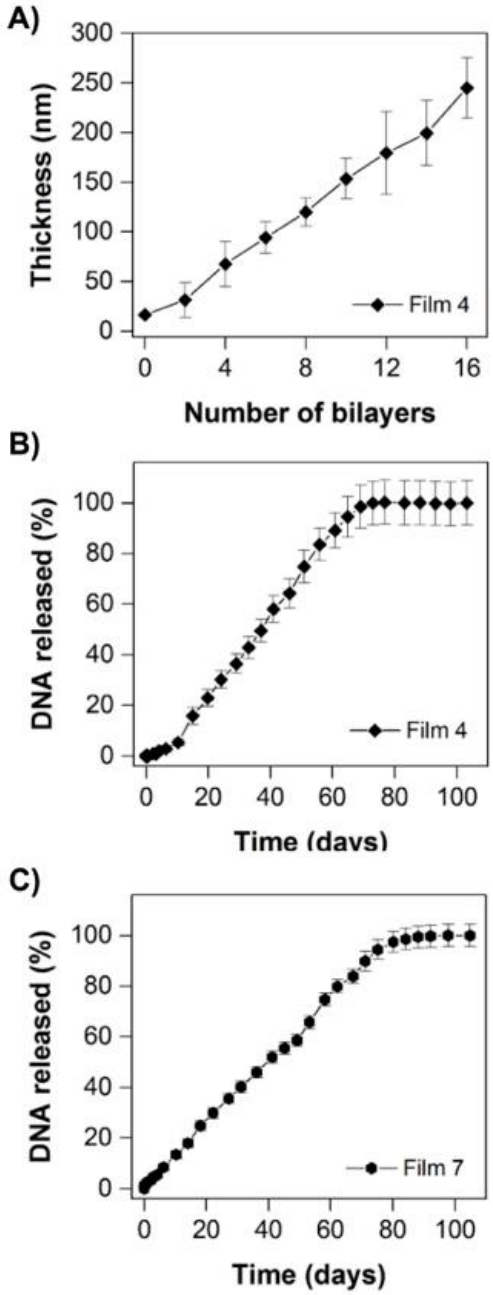

Figure 6. (A) Plot of film thickness versus the number of polymer/DNA layers deposited on silicon substrates as determined by ellipsometry during the growth of Film 4. (B) Plot showing the release of DNA from substrates coated with Film 4. (C) Plot showing the release of DNA from substrates coated with Film 7. (B-C) Films were incubated in PBS buffer (pH 7.4, 37 °C) and the amount of DNA released was measured by UV/Vis absorbance. In panels (A) and (C), data are presented as the average and standard deviation of multiple measurements made using three identically prepared films. In panel (B), data are presented as the average and standard deviation of multiple measurements made using two identically prepared films.

Discussion

The iterative and step-wise nature of the layer-by-layer assembly process used to fabricate the films investigated here provides a straightforward and practical framework for the design of thin films composed of multiple different layers of multiple different components (e.g., simply by varying the number of 'layers' of each component deposited during assembly).[18,19,42,43] This approach provides control over the relative loading of DNA that is incorporated into a film[17,27] and—provided that significant polymer interdiffusion and structural reorganization do not occur during or after assembly—can be used to design films with hierarchical nanoscale structures.[18,19] This general approach has thus been used in past studies to design DNA-containing multilayers that promote either the simultaneous,[44] staged/offset,[41] or sequential release[30,31] or cellular expression[45] of multiple different plasmid DNA constructs, with the types of DNA release profiles and other film behaviors that can be achieved generally depending heavily upon the structures of the cationic polymers that are used[5,20,24,25] and the presence (or absence) of intervening 'barrier' layers[30,45] that can prevent interdiffusion and mixing among layers.

Our group has reported extensively on the behaviors of multilayers fabricated using plasmid DNA and either poly(β-amino ester)s (including polymer **1**)[5,23,27,44] or charge-shifting polymers (including polymer **2**)[5,29,31] as cationic building blocks, and on the influence of polymer structure and film architecture on the DNA release profiles of those materials.[5,17,20,25] The results of this current study demonstrate that this relatively limited pool of cationic materials can be used in combination to design conformal polymeric coatings that release DNA with new, useful, and unanticipated release profiles that cannot be attained using either type of polymer alone. The results shown in Figures 3B-C and 6B-C, for example, demonstrate that 'mixed multilayer' films

fabricated using combinations of hydrolytically degradable and charge-shifting polymer/DNA bilayers erode and release DNA in ways that differ substantially from those fabricated from polymer **1** or polymer **2** alone. Importantly, those results also reveal that the order in which the individual polymer layers in these films are deposited during assembly has a substantial influence on their subsequent DNA release profiles.

The deposition of hydrolytically degradable polymer **1**/DNA layers on top of charge-shifting polymer **2**/DNA films (mixed Film 3 or Film 6 multilayers; Figure 2) leads to films with multi-phase release profiles that are intermediate to those exhibited by polymer **1**/DNA and polymer **2**/DNA films, but that have elements that are otherwise common to both (e.g., an overall extended release profile similar to that of polymer **2**/DNA films, but an early-stage release phase that is more reflective of the behavior of polymer **1**/DNA films). It is possible to interpret the profiles of these mixed Film 3 multilayers (Figure 3B-C) as being, to some extent, linear combinations of those exhibited by polymer **1**/DNA and polymer **2**/DNA films (e.g., a rapid, burst release of DNA characteristic of polymer **1**/DNA films, followed by an extended phase of release more typical of polymer **2**/DNA films). The results of experiments using otherwise identical films fabricated using pEGFP and pRFP plasmids (mixed Film 6 multilayers), however, suggest that these films do not simply consist of discrete 'stacks' of polymer **1**/DNA and polymer **2**/DNA bilayers (as represented schematically in Figure 2) that erode and behave independently of each other.

The EGFP and RFP expression results shown in Figure 5 and Figure S3, for example, suggest that pEGFP, which was deposited last during assembly, is released first (over a period of ~48 hours), but that both pEGFP and pRFP are subsequently released simultaneously for prolonged periods after that initial burst phase. Those results, combined with the release profiles

shown in Figure 3B-C, suggest that significant intermixing of individual polymer/DNA layers occurs in these materials, either (i) during layer-by-layer assembly or (ii) after they are exposed to physiologically relevant media. Interlayer diffusion and the 'mixing' of layers is well known to occur in many different polyelectrolyte multilayer systems,[18,19,46-49] and can be eliminated (or reduced/controlled)[47-49] to design hierarchical films that can 'stage' the release of multiple agents by incorporating intermittent barrier layers during assembly,[30,45,47] as noted above. It is likely that that same approach could be adopted here to design hierarchical films that promote the release of multiple plasmids with non-overlapping release profiles. Although not investigated as part of this current study, our results suggest that the overall release profiles of these mixed Film 3-type multilayers could also be tuned further, and over a broader range, by manipulating the relative numbers of polymer **1**/DNA and polymer **2**/DNA bilayers that are deposited during assembly (films constructed using eight bilayers of each type of polymer/DNA pair were used in all experiments in this study to explore feasibility and establish proof of concept).

Our results also suggest that the internal structures of these mixed multilayer assemblies—and thus their subsequent DNA release profiles—can be manipulated broadly and in useful ways simply by varying the order in which polymer **1**/DNA and polymer **2**/DNA bilayers are deposited during assembly. In contrast to the behaviors of mixed Film 3 multilayers, the deposition of charge-shifting polymer **2**/DNA layers on top of hydrolytically degradable polymer **1**/DNA films ('inverted' mixed Film 4 or Film 7 multilayers; Figure 2) leads to films that exhibit linear release profiles for periods of up to ~80 days (Figure 6B-C). These films do not exhibit multiple phases of release or other features that reflect linear combinations of the behaviors of fast-releasing polymer **1**/DNA[23,27] and slow-releasing polymer **2**/DNA[29,31] films. These results were unanticipated at the outset of these studies and, when combined, suggest (i)

that interdiffusion also occurs in these ‘inverted’ (slow on top/fast on bottom) films, and (ii) that the extents and degrees of intermixing in these ‘inverted’ films are likely to differ substantially from those that occur in Film 3-type (fast on top/slow on bottom) films.

Our current results suggest that the order in which polymer **1**/DNA and polymer **2**/DNA layers are deposited does not impact film growth profiles or thickness substantially (Figures 3A and 6A). We note also that the growth profiles exhibited by both of these types of films are linear in nature, and show no hints of ‘exponential-type’ growth that is often associated with substantial diffusion of polyelectrolytes into and out of a multilayer during assembly (and that can lead to much thicker, but more compositionally homogeneous, films).[37-40] Additional physicochemical characterization, including characterization of potential changes in film morphology that could occur during these ‘change of polymer’ assembly processes, will be required to characterize the locations and dynamics of the polymers in these assemblies and understand the factors that contribute to the large differences in DNA release profiles reported here more completely. The results of this study do, however, provide guidance useful for the design of thin films that promote the extended, surface-mediated release of DNA with linear release profiles that have been difficult to achieve using multilayers fabricated from other cationic polymer building blocks. The ability to fabricate these mixed multilayers on the surfaces of topologically complex objects, including clinical interventional devices such as intravascular stents (Figure 4), without substantial changes in DNA release profiles (Figure S2) suggests opportunities to further explore and exploit the potential utility of these new materials in many different applied biomedical and translational contexts.

Summary and Conclusions

We have reported the fabrication and characterization of polymer-based 'mixed' multilayer coatings fabricated using plasmid DNA and combinations of both hydrolytically degradable and charge-shifting cationic polymer building blocks. Our results reveal (i) that films fabricated using combinations of polymers **1** and **2** exhibit DNA release profiles that are substantially different from films fabricated using DNA and either polymer **1** or polymer **2** alone, and (ii) that the order in which these two cationic polymers are deposited during assembly has a substantial impact on DNA release profiles when these materials are incubated in physiologically relevant media.

Mixed multilayers fabricated by depositing layers of polymer **1** and DNA onto multilayers composed of polymer **2** and DNA (Film 3-type coatings) released functional plasmid DNA into solution over a period of ~60 days, with multi-phase release profiles that were intermediate to those of polymer **1**/DNA or polymer **2**/DNA films (i.e., a period of rapid release, followed by a second and more sustained period of release). In contrast, 'inverted' mixed multilayers fabricated by depositing layers of polymer **2** and DNA onto multilayers composed of polymer **1** and DNA (Film 4-type coatings) yielded coatings with DNA release profiles that were almost completely linear over periods ranging from ~60-80 days. These results are consistent with substantial polymer layer interdiffusion in both types of mixed multilayer films, and suggest that the extent of intermixing in the 'inverted' mixed multilayers differs substantially from that present in Film 3-type films. Additional support for the occurrence of layer interdiffusion in these materials was provided by the results of cell transfection experiments using DNA released from mixed multilayers fabricated using two different plasmid DNA constructs.

Thus, in addition to being ‘mixed’ by virtue of being composed of two different classes of cationic polymers that can promote film disruption by two completely different mechanisms, the multilayers reported here can also be regarded as being ‘mixed’ by virtue of substantial commingling and nanoscale mixing of their individual components that occurs either during assembly or after introduction to physiological media. Our results reveal this commingling of components to lead to new, useful, and unanticipated DNA release profiles, and expand the range of release profiles that can be accessed using a limited pool of layer-by-layer building blocks. Overall, the results of this study provide new approaches and guidance useful for the design of polymer-based coatings that promote the surface-mediated release of DNA with predictable release profiles, and suggest opportunities to design new classes of coatings for the localized and long-term surface-mediated delivery of DNA from topologically complex clinical interventional devices, including intravascular stents.

Acknowledgments. Financial support was provided by the National Institutes of Health (R01 EB006820) and the College of Engineering at UW-Madison and made use of NSF-supported facilities (DMR-1121288). V.A. acknowledges the American Heart Association for a graduate fellowship and the UW-Madison Biotechnology Center for a Morgridge Biotechnology Fellowship. M.C.D.C. acknowledges the Natural Sciences Engineering Research Council of Canada for a graduate fellowship.

References

1. Klugherz BD, Jones PL, Cui X, et al. Gene delivery from a DNA controlled-release stent in porcine coronary arteries. *Nat. Biotechnol.* Nov 2000;18(11):1181-1184.

2. Bielinska AU, Yen A, Wu HL, et al. Application of membrane-based dendrimer/DNA complexes for solid phase transfection in vitro and in vivo. *Biomaterials.* 2000;21(9):877-887.

3. Segura T, Shea LD. Surface-tethered DNA complexes for enhanced gene delivery. *Bioconjugate Chem.* 2002;13(3):621-629.

4. Klugherz BD, Song C, DeFelice S, et al. Gene Delivery to Pig Coronary Arteries from Stents Carrying Antibody-Tethered Adenovirus. *Hum. Gene Ther.* 2004;13(3):443-454.

5. Jewell CM, Lynn DM. Multilayered polyelectrolyte assemblies as platforms for the delivery of DNA and other nucleic acid-based therapeutics. *Adv. Drug Delivery Rev.* 2008;60(9):979-999.

6. Zelikin AN. Drug Releasing Polymer Thin Films: New Era of Surface-Mediated Drug Delivery. *ACS Nano.* 2010;4(5):2494-2509.

7. DeMuth PC, Min Y, Huang B, et al. Polymer multilayer tattooing for enhanced DNA vaccination. *Nat. Mater.* 2013;12(4):367-376.

8. Gill HS, Prausnitz MR. Coated microneedles for transdermal delivery. *J. Control. Release.* 2007;117:227-237.

9. Prausnitz MR, Mikszta JA, Cormier M, Andrianov AK. Microneedle-based vaccines. *Curr. Top. Microbiol. Immunol.* 2009;333:369-393.

10. Fishbein I, Chorny M, Levy RJ. Site-specific gene therapy for cardiovascular disease. *Curr Opin Drug Disc.* Mar 2010;13(2):203-213.

11. Fishbein I, Stachelek SJ, Connolly JM, Wilensky RL, Alferiev I, Levy RJ. Site specific gene delivery in the cardiovascular system. *J. Control. Release.* Dec 5 2005;109(1-3):37-48.

12. Segura T, Volk MJ, Shea LD. Substrate-mediated DNA delivery: role of the cationic polymer structure and extent of modification. *J. Control. Release.* 2003;93(1):69-84.

13. Bengali Z, Pannier AK, Segura T, et al. Gene delivery through cell culture substrate adsorbed DNA complexes. *Biotech. Bioeng.* 2005;90(3):290-302.

14. Bengali Z, Shea LD. Gene delivery by immobilization to cell-adhesive substrates. *Mrs Bull.* 2005;30(9):659-662.

15. Park IK, Von Recum HA, Jiang SY, Pun SH. Supramolecular assembly of cyclodextrin-based nanoparticles on solid surfaces for gene delivery. *Langmuir.* 2006;22(20):8478-8484.

16. Blocker KM, Kiick KL, Sullivan MO. Surface Immobilization of Plasmid DNA with a Cell-Responsive Tether for Substrate-Mediated Gene Delivery. *Langmuir.* 2011;27(6):2739-2746.

17. Jewell CM, Lynn DM. Surface-mediated delivery of DNA: Cationic polymers take charge. *Curr. Opin. Coll. Inter. Sci.* 2008;13(6):395-402.

18. Decher G, Schlenoff JB. *Multilayer Thin Films: Sequential Assembly of Nanocomposite Materials - Volume 1.* Vol 1. Weinheim, Germany: Wiley-VCH; 2012.

19. Decher G, Schlenoff JB. *Multilayer Thin Films: Sequential Assembly of Nanocomposite Materials - Volume 2.* Vol 2. Weinheim, Germany: Wiley-VCH; 2012.

20. Lynn DM. Peeling back the layers: controlled erosion and triggered disassembly of multilayered polyelectrolyte thin films. *Adv. Mater.* 2007;19(23):4118-4130.

21. Monge C, Almodovar J, Boudou T, Picart C. Spatio-temporal Control of LbL Films for Biomedical Applications: From 2D to 3D. *Adv. Healthcare Mater.* 2015;4(6):811-830.

22. Bechler SL, Si Y, Yu Y, Ren J, Liu B, Lynn DM. Reduction of intimal hyperplasia in injured rat arteries promoted by catheter balloons coated with polyelectrolyte multilayers that contain plasmid DNA encoding PKCδ. *Biomaterials.* 2013;34(1):226-236.

23. Jewell CM, Zhang J, Fredin NJ, Wolff MR, Hacker TA, Lynn DM. Release of Plasmid DNA from Intravascular Stents Coated with Ultrathin Multilayered Polyelectrolyte Films. *Biomacromolecules.* 2006;7(9):2483-2491.

24. Lynn DM. A "Multilayered" Approach to the Delivery of DNA: Exploiting the Structure of Polyelectrolyte Multilayers to Promote Surface-Mediated Cell Transfection and Multi-Agent Delivery. *Multilayer Thin Films*: Wiley-VCH Verlag GmbH & Co. KGaA; 2012:731-748.

25. Lynn DM. Polyelectrolyte Multilayer Coatings for the Release and Transfer of Plasmid DNA. *Layer-by-Layer Films for Biomedical Applications*: Wiley-VCH Verlag GmbH & Co. KGaA; 2015:171-194.

26. DeMuth PC, Su X, Samuel RE, Hammond PT, Irvine DJ. Nano-Layered Microneedles for Transcutaneous Delivery of Polymer Nanoparticles and Plasmid DNA. *Adv. Mater.* 2010;22(43):4851-4856.

27. Zhang J, Chua LS, Lynn DM. Multilayered Thin Films that Sustain the Release of Functional DNA under Physiological Conditions. *Langmuir*. 2004;20(19):8015-8021.

28. Zhang J, Fredin NJ, Lynn DM. Erosion of multilayered films fabricated from degradable polyamines: characterization and evidence in support of a mechanism that involves polymer hydrolysis. *J. Polym. Sci., Part A: Polym. Chem.* 2006;44(17):5161-5173.

29. Zhang J, Lynn DM. Ultrathin multilayered films assembled from "charge-shifting" cationic polymers: extended, long-term release of plasmid DNA from surfaces. *Adv. Mater.* 2007;19(23):4218-4223.

30. Liu X, Zhang J, Lynn DM. Ultrathin multilayered films that promote the release of two DNA constructs with separate and distinct release profiles. *Adv. Mater.* 2008;20(21):4148-4153.

31. Sun B, Lynn DM. Release of DNA from polyelectrolyte multilayers fabricated using charge-shifting' cationic polymers: Tunable temporal control and sequential, multi-agent release. *J. Control. Release.* 2010;148(1):91-100.

32. Funhoff AM, van Nostrum CF, Janssen APCA, Fens MHAM, Crommelin DJA, Hennink WE. Polymer side-chain degradation as a tool to control the destabilization of polyplexes. *Pharm. Res.* 2004;21(1):170-176.

33. Luten J, Akeroyd N, Funhoff A, Lok MC, Talsma H, Hennink WE. Methacrylamide Polymers with Hydrolysis-Sensitive Cationic Side Groups as Degradable Gene Carriers. *Bioconjugate Chem.* 2006;17(4):1077-1084.

34. Jiang X, Lok MC, Hennink WE. Degradable-brushed poly(hydroxyethylmethacrylate)-poly(2-(dimethylamino)ethyl methacrylate) synthesized via ATRP and click chemistry for gene delivery. *Bioconjugate Chem.* 2007;18(6):2077-2084.

35. Luten J, van Nostrum CF, De Smedt SC, Hennink WE. Biodegradable polymers as non-viral carriers for plasmid DNA delivery. *J. Control. Release.* 2008;126(2):97-110.

36. Lynn DM, Langer R. Degradable Poly(β-amino esters): Synthesis, Characterization, and Self-Assembly with Plasmid DNA. *J. Am. Chem. Soc.* 2000;122(44):10761-10768.

37. Picart C, Mutterer J, Richert L, et al. Molecular basis for the explanation of the exponential growth of polyelectrolyte multilayers. *Proc. Natl. Acad. Sci. U. S. A.* 2002;99(20):12531-12535.

38. Boulmedais F, Ball V, Schwinte P, Frisch B, Schaaf P, Voegel JC. Buildup of exponentially growing multilayer polypeptide films with internal secondary structure. *Langmuir.* 2003;19(2):440-445.

39. Richert L, Boulmedais F, Lavalle P, et al. Improvement of stability and cell adhesion properties of polyelectrolyte multilayer films by chemical cross-linking. *Biomacromolecules.* 2004;5(2):284-294.

40. Lavalle P, Vivet V, Jessel N, et al. Direct evidence for vertical diffusion and exchange processes of polyanions and polycations in polyelectrolyte multilayer films. *Macromolecules.* 2004;37(3):1159-1162.

41. Zhang J, Montanez SI, Jewell CM, Lynn DM. Multilayered films fabricated from plasmid DNA and a side-chain functionalized poly(beta-amino ester): surface-type erosion and sequential release of multiple plasmid constructs from surfaces. *Langmuir.* 2007;23(22):11139-11146.

42. Boudou T, Crouzier T, Ren K, Blin G, Picart C. Multiple Functionalities of Polyelectrolyte Multilayer Films: New Biomedical Applications. *Adv. Mater.* 2010;22(4):441-467.

43. Tang ZY, Wang Y, Podsiadlo P, Kotov NA. Biomedical applications of layer-by-layer assembly: From biomimetics to tissue engineering. *Adv. Mater.* 2006;18(24):3203-3224.

44. Jewell CM, Zhang J, Fredin NJ, Lynn DM. Multilayered Polyelectrolyte Films Promote the Direct and Localized Delivery of DNA to Cells. *J. Control. Release.* 2005;106:214-223.

45. Jessel N, Oulad-Abdelghani M, Meyer F, et al. Multiple and time-scheduled in situ DNA delivery mediated by beta-cyclodextrin embedded in a polyelectrolyte multilayer. *Proc. Natl. Acad. Sci. U. S. A.*;103(23):8618-8621.

46. Porcel C, Lavalle P, Ball V, et al. From Exponential to Linear Growth in Polyelectrolyte Multilayers. *Langmuir.* 2006;22(9):4376-4383.

47. Wood KC, Chuang HF, Batten RD, Lynn DM, Hammond PT. Controlling interlayer diffusion to achieve sustained, multiagent delivery from layer-by-layer thin films. *Proc. Natl. Acad. Sci. U. S. A.* 2006;103(27):10207-10212.

48. Zacharia NS, DeLongchamp DM, Modestino M, Hammond PT. Controlling Diffusion and Exchange in Layer-by-Layer Assemblies. *Macromolecules.* 2007;40(5):1598-1603.

49. Zacharia NS, Modestino M, Hammond PT. Factors Influencing the Interdiffusion of Weak Polycations in Multilayers. *Macromolecules.* 2007;40(26):9523-9528.

Supporting Information for Chapter 11

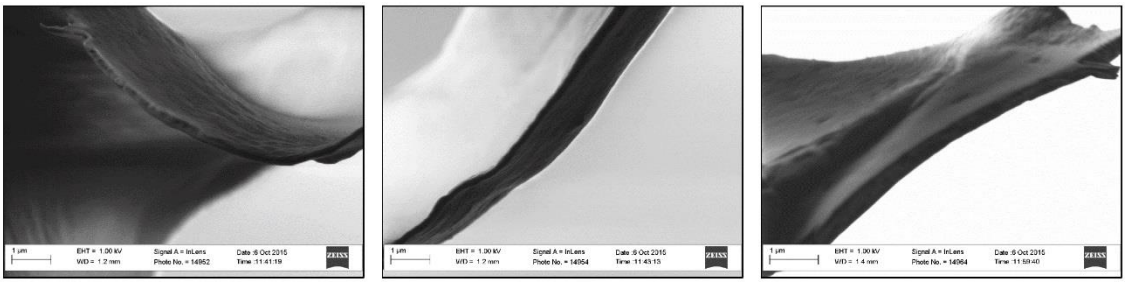

Figure S1. Additional representative scanning electron microscopy images showing intravascular stents coated with Film 3 in regions where the multilayer film was delaminated from the substrate. These images were used, in addition to the image shown in Figure 4C of the main text, to estimate film thickness (~240 nm ± 70 nm).

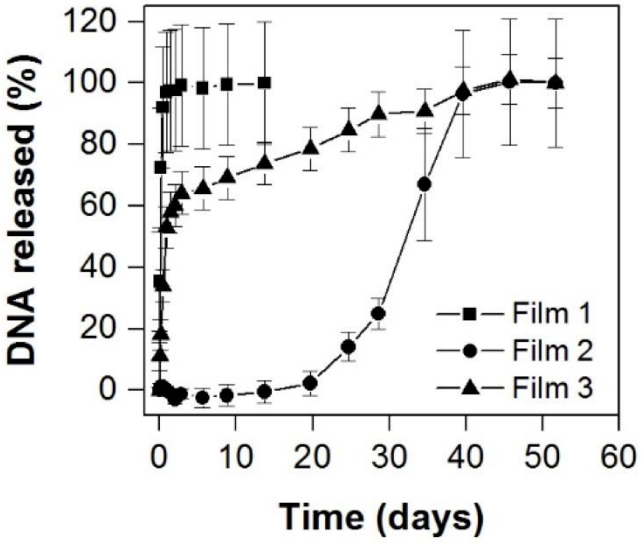

Figure S2. Plot showing the release of DNA from stainless steel stents coated with Films 1, 2, and 3. Films were incubated in PBS buffer (pH 7.4, 37 °C) and the amount of DNA released into solution was measured by UV/Vis absorbance. Data are presented as the average and standard deviation of three identically prepared film-coated stents.

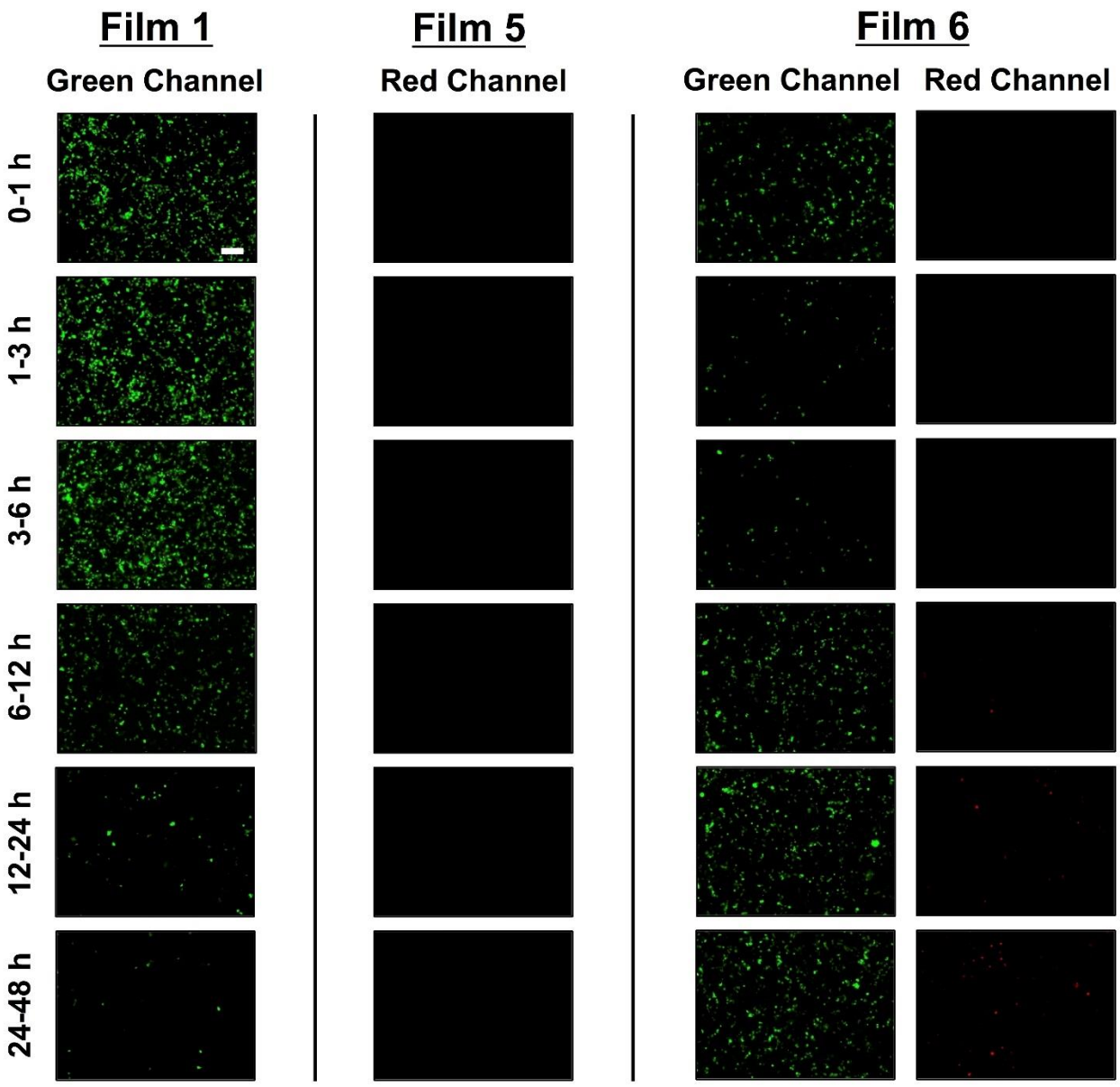

Figure S3-A. *Part of a three-part figure; see companion images in Figures S3-B and S3-C for results arising from this extended-release experiment at different time points.* Representative fluorescence microscopy images showing COS-7 cells expressing GFP (green channel) and RFP (red channel) after treatment with samples of DNA collected during the erosion of substrates coated with Film 6 (additional results for samples collected during the erosion of substrates coated with Film 1 and Film 5 are also shown for comparison). The relative levels of GFP and RFP expression observed correspond qualitatively to the amount of each plasmid released from the film during the following time periods: 0-1 hour, 1-3 hours, 3-6 hours, 6-12 hours, 12-24 hours, and 24-48 hours. Scale bar = 250 μm.

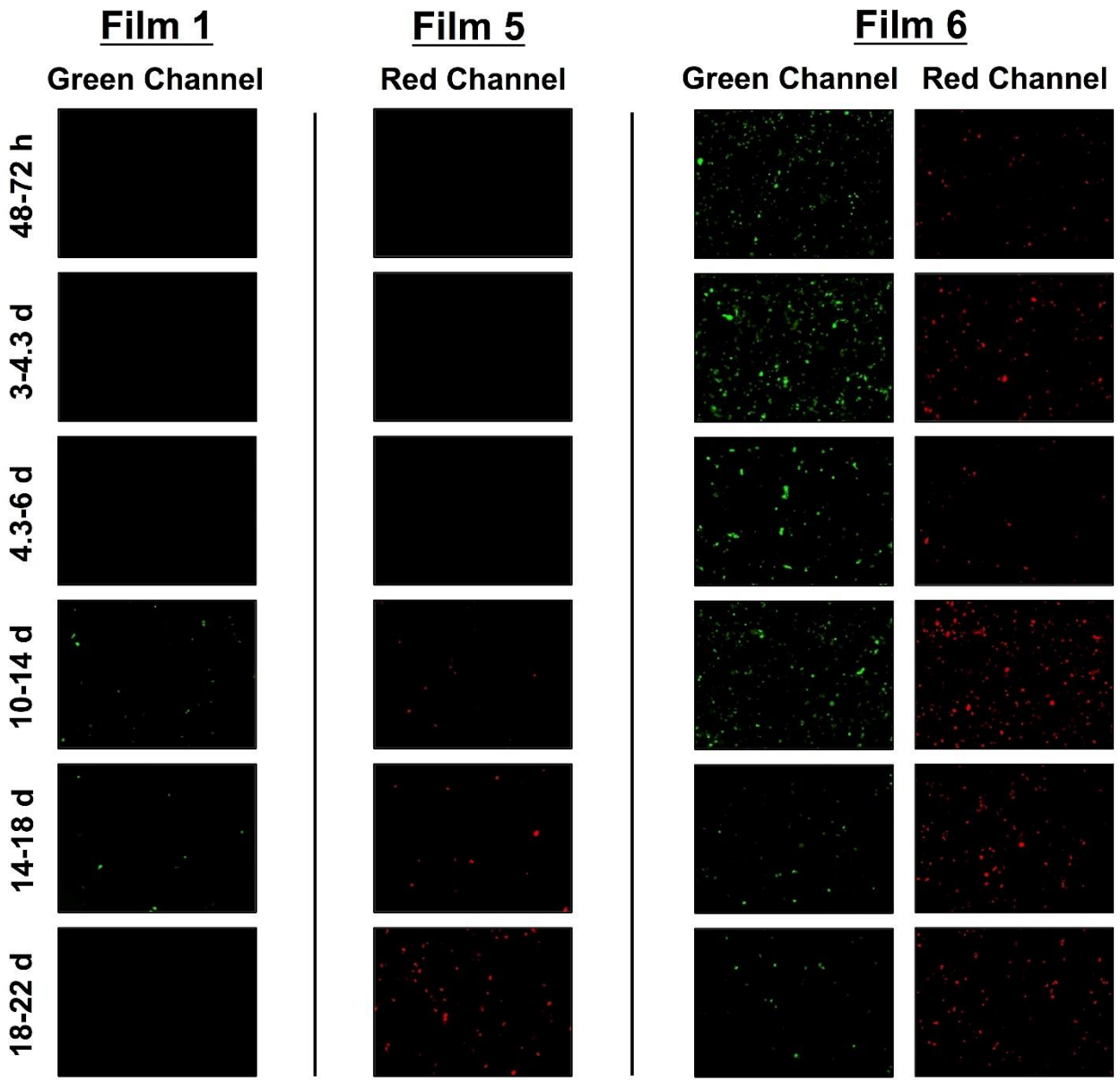

Figure S3-B. *Part of a three-part figure; see companion images in Figures S3-A and S3-C for results arising from this extended-release experiment at different time points.* Representative fluorescence microscopy images showing COS-7 cells expressing GFP (green channel) and RFP (red channel) after treatment with samples of DNA collected during the erosion of substrates coated with Film 6 (additional results for samples collected during the erosion of substrates coated with Film 1 and Film 5 are also shown for comparison). The relative levels of GFP and RFP expression observed correspond qualitatively to the amount of each plasmid released from the film during the following time periods: 48-72 hours, 3-4.3 days, 4.3-6 days, 10-14 days, 14-18 days, and 18-22 days. Scale bar = 250 μm.

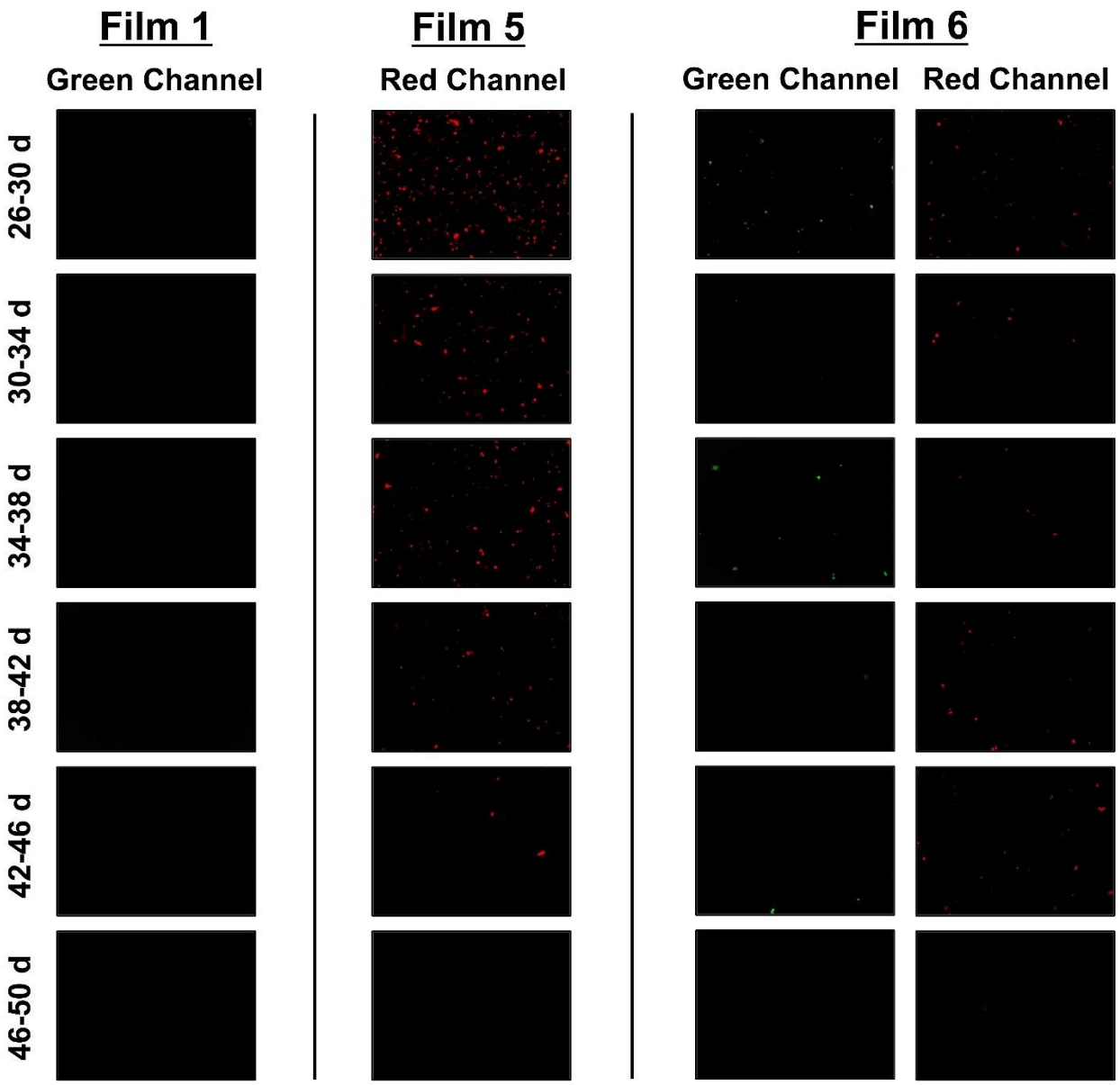

Figure S3-C. *Part of a three-part figure; see companion images in Figures S3-A and S3-B for results arising from this extended-release experiment at different time points.* Representative fluorescence microscopy images showing COS-7 cells expressing GFP (green channel) and RFP (red channel) after treatment with samples of DNA collected during the erosion of substrates coated with Film 6 (additional results for samples collected during the erosion of substrates coated with Film 1 and Film 5 are also shown for comparison). The relative levels of GFP and RFP expression observed correspond qualitatively to the amount of each plasmid released from the film during the following time periods: 26-30 days, 30-34 days, 34-38 days, 38-42 days, 42-46 days, and 46-50 days. Scale bar = 250 μm.

Chapter 12

Non-Woven and Amine-Reactive Nanofiber Mats Fabricated by the Electrospinning of Azlactone-Functionalized Polymers‡

‡ Portions of this chapter have been submitted for publication as: Kratochvil, M.J.; Carter, M.C.D.; Lynn, D.M. "Non-Woven and Amine-Reactive Nanofiber Mats Fabricated by the Electrospinning of Azlactone-Functionalized Polymers" **2016**, *Submitted.* M. Kratochvil performed the electrospinning and related experiments. My contribution was in synthesizing the polymers, performing the SEM imaging and analyzing the data.

ABSTRACT: We report the design of amine-reactive polymer nanofibers and non-woven reactive nanofibrous mats fabricated by the electrospinning of azlactone-functionalized polymers. We demonstrate that randomly oriented mats fabricated using a model random copolymer of methyl methacrylate and 2-vinyl-4,4-dimethylazlactone contain intact and reactive azlactone groups that can be used to introduce new functionality and modulate important interfacial properties of these materials (e.g., wetting behaviors) by post-fabrication treatment with primary amine-based nucleophiles. The facile nature of the azlactone chemistry used here permits post-fabrication functionalization under mild conditions without introducing substantial changes to nanofiber or mat morphologies. This approach enables the macroscale or microscale patterning of new functionality on mat-coated surfaces by treatment with bulk solutions or using methods such as microcontact printing. Our results also demonstrate (i) that these reactive nanofiber mats can be transferred or printed onto secondary surfaces by pressing them into contact with other amine-functionalized objects, and (ii) that this approach can be used to design and pattern hydrophobic mats that can serve as a basis for the design of slippery liquid-infused porous materials (SLIPS). The approaches described here enable the introduction of new properties to electrospun polymer nanofibers after nanofiber fabrication and, as such, reduce the need to design new functional polymers to design nanofibers with desired properties or surface functionality. The azlactone-based chemistry used here broadens the scope of reactions that can be used to functionalize the properties of polymer nanofibers, and is likely to prove general. The strategies reported here can be used to design new azlactone-functionalized copolymers, or be used in combination with other azlactone-reactive nucleophiles (e.g., alcohols or thiols) to design nanofibers and nanofiber-based coatings with new physical properties, surface features, and behaviors of interest and potential utility in a broad range of fundamental and applied contexts.

Introduction

The electrospinning of polymer solutions provides a useful and practical approach to the fabrication of non-woven meshes and 'mats' of polymer-based nanofibers. This approach is compatible with the use of both natural and synthetic polymers, and typically yields meshes and nanoporous coatings with very high surface areas owing to the nanometer-scale dimensions and random alignment of the individual fibers that comprise these materials.[1, 2] These features, combined with the ability to tune the physical properties and morphologies of the fibers and meshes by control over polymer composition and electrospinning process variables (e.g., solution concentration, flow rate, etc.), render these methods useful for the design of porous polymer scaffolds and fiber-based coatings of utility in many different contexts, ranging from chemical sensing and catalysis[3-7] to tissue engineering[8-12] and the controlled release or delivery of therapeutic agents.[9, 13, 14]

For some potential applications (e.g., controlled release), electrospinning provides useful means to encapsulate or load small molecules or other agents within fibers by using polymer solutions that contain those agents during fabrication.[13] Many other potential applications of electrospun materials (e.g., catalysis[3-7] and tissue engineering[8-12]), however, can benefit considerably from the presentation of defined chemical or biological functionality on the surfaces of the individual fibers in these materials. Many different functional polymers have been investigated for these purposes,[15] with the degrees or densities with which desired functionality can be displayed on the surface of an electrospun fiber depending heavily upon the structures and physicochemical properties of the polymers, the properties of the solvents that are used, and other electrospinning process variables.

The work reported here was motivated by recent reports on the electrospinning of

chemically reactive polymers and the potential of this approach to lead to reactive nanofibers and reactive polymer meshes that can be functionalized—after fabrication—to introduce new functionality, tune interfacial properties, or pattern features on these materials in ways that would be difficult to achieve by the direct electrospinning of functionalized polymers.[15] Past studies have demonstrated, for example, that electrospun fibers fabricated using reactive polymers can be functionalized using copper-catalyzed azide alkyne cycloaddition (CuAAC),[16-24] strain-promoted azide alkyne cycloaddition (SPAAC),[25-27] thiol-ene conjugation,[23, 28, 29] oxime ligation,[27] Diels-Alder addition,[30] and nucleophilic attack on activated esters,[31, 32] to produce functional mats and meshes containing immobilized dyes,[19, 21, 25-27, 30-32] biological agents,[16, 22-24, 27, 30, 31] and nanoparticles.[25, 30] While each of these reactive approaches is useful for the modification of nanofiber surfaces, the nature of the chemical reactivity used and the nature of any residual reaction byproducts associated with functionalization reactions can place constraints on the environments in which those materials can subsequently be used. For example, residual metal impurities arising from copper-catalyzed click reactions could be problematic in many biological applications;[33] similarly, approaches based on the nucleophilic substitution of activated pentafluorophenyl esters generate byproducts that may be difficult to remove[34, 35] without disturbing fiber or mat morphologies.

To address these and other related practical issues, Becker and coworkers have demonstrated in a series of recent reports that copper-free click reactions can be used to functionalize the surfaces of electrospun nanofibers via SPAAC.[25-27] That approach used poly(γ-benzyl-L-glutamate)[25] or copolymers of ε-caprolactone and 1,3,8-trioxaspiro[4.6]-9-undecanone[27] end-functionalized with a highly strained cyclooctyne group, thus eliminating the need for metal catalysts to promote subsequent nanofiber functionalization. The Becker group

has also reported approaches to the conjugation of bioactive peptides and model fluorescent compounds to modified poly(ester-urea)s using a range of 'clickable' groups, including alkenes that can participate in photo-initiated thiol-ene radical addition reactions.[23] Guo et al. have also reported photo-initiated thiol-ene radical addition-based approaches and used Michael addition-based thiol-ene reactions to affect the byproduct-free functionalization and crosslinking of poly((3-mercaptopropyl)methylsiloxane)-based nanofibers.[28] The continued development of new reactive strategies for the functionalization of nanofibers that permit rapid, efficient, and byproduct-free 'click-type' functionalization, while maintaining broad substrate scope, will create new opportunities to design reactive meshes and mat-coated surfaces that can be modified, patterned, or customized after fabrication and thereby open the door to new potential applications of these non-woven materials.

Here, we report the fabrication, characterization, and modification of chemically reactive polymer nanofibers and non-woven electrospun mats functionalized with amine-reactive azlactone groups. Our approach is based on the electrospinning of organic solutions of a model random copolymer of methyl methacrylate (MMA) and 2-vinyl-4,4-dimethylazlactone (VDMA) (Figure 1A). We demonstrate (i) that the nanofibers comprising electrospun mats of poly[MMA-*co*-VDMA] retain their electrophilic azlactone functionality (Figure 1C), and (ii) that these reactive mats can be functionalized or patterned, post-fabrication, either by direct solution treatment or by micro-contact printing with a range of primary amine-functionalized nucleophiles (Figure 1D) to install new surface features and modify interfacial properties (e.g., wetting behaviors) without promoting changes in underlying nanoporous mat morphologies. These functionalization reactions proceed under mild conditions and without the need for a catalyst or the creation of reaction byproducts that would otherwise need to be removed or

extracted after functionalization.[36, 37] Finally, we demonstrate that the reactivity of these azlactone-functionalized mats also permits them to be 'contact transferred' to create new reactive nanofiber coatings on other objects by pressing them into contact with other amine-functionalized surfaces. The 'click-like' nature of the azlactone chemistry used here[36, 37] creates opportunities to design, fabricate, and tune the properties of functional polymer nanofibers and electrospun polymer mats. This reactive approach to post-polymerization functionalization also obviates the need to synthesize individual functional polymers to design electrospun materials with specifically tailored surface functionality. We anticipate that this combination of features will prove useful for the design, patterning, and parallel functionalization and screening of functional nanofibers and mats of interest and potential utility in a broad range of fundamental and applied contexts.

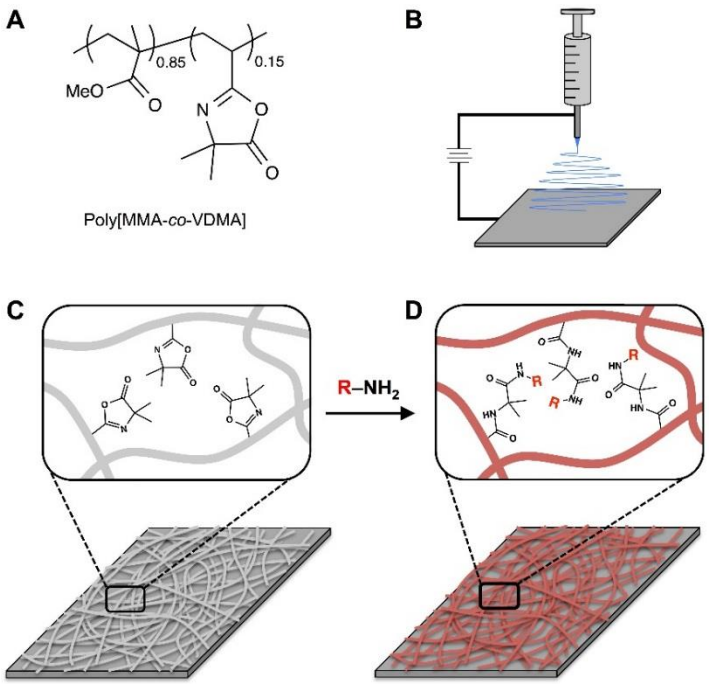

Figure 1: (A) Chemical structure of the poly[MMA-co-VDMA] copolymer used in this study. (B) Schematic illustration depicting the electrospinning process. (C, D) Schematic illustrations showing (C) an azlactone-containing electrospun mat of nanofibers before functionalization, and (D) after functionalization with a generic primary amine.

Materials and Methods

Materials. Acetone (ACS grade), branched poly(ethyleneimine) (PEI; MW ~25,000), *n*-decylamine (95%), acetic anhydride (>99%), triethylamine (≥99.5%), dimethylformamide (DMF, ACS grade), hexanes (ACS grade), propylamine (95%), and deuterated chloroform ($CDCl_3$, 99%) were purchased from Sigma-Aldrich (Milwaukee, WI). Methanol (Semiconductor Grade) was purchased from VWR (West Chester, PA). Isopropyl alcohol (ACS grade) was purchased from Macron (Center Valley, PA). 6-Amino-1-hexanol (97%) was purchased from Alfa Aesar (Ward Hill, MA). Tetramethylrhodamine cadaverine (TMR-Cad) was purchased from Invitrogen (Eugene, OR). Glycerol (ACS grade) was purchased from Fisher Chemicals (Fair Lawn, NJ). Minimum Essential Medium (MEM) and fetal bovine serum were purchased from Gibco (Grand Island, NY). Lake water was collected from Lake Mendota (Madison, WI). Poly(methyl methacrylate-co-2-vinyl-4,4-dimethylazlactone) [poly(MMA-co-VDMA)] with a molar feed composition of 80:20 MMA:VDMA, was a gift from Dr. Steven Heilmann (3M Corporation, Minneapolis, MN). Thin sheets of poly(ethylene terephthalate) (PET; 0.004 in. thick) were purchased from McMaster Carr (Elmhurst, IL). Commercially available Reynolds Wrap aluminum foil was obtained from Reynolds Consumer Products (Lake Forest, IL). Deionized water (18 MΩ) was used unless otherwise noted. All reagents and materials were used as received without further purification unless otherwise noted.

General Considerations. ^{1}H NMR spectroscopy was performed using a Bruker Avance-400 spectrometer and a pulse repetition delay of 10 sec. All spectra were referenced relative to the residual proton peak of $CHCl_3$ (δ7.26 ppm). Gel permeation chromatography was performed using a Viscotek GPC Max VE2001 equipped with two Polymer Laboratories PolyPore columns

(250 mm × 4.6 mm) and a TDA-302 detector array using THF as the eluent at a flow rate of 1 mL/min at 40 °C. The instrument was calibrated using 10 narrow dispersity polystyrene standards with M_n = 0.580−377.4 kg/mol (Agilent Technologies, Santa Clara, CA). Fluorescence microscopy images were acquired using an Olympus IX70 microscope and analyzed using the Metavue version V7.7.8.0 software package (Molecular Devices, LLC). Contact angle measurements were made using a Dataphysics OCA 15 Plus instrument with an automatic liquid dispenser at ambient temperature. Advancing and receding contact angles were measured using 5 μL droplets of deionized water (18.2 MΩ). Top-down scanning electron micrographs were acquired using a LEO-1550 VP field-emission SEM operating with an accelerating voltage of 2.00 kV. Images were acquired using the secondary electron (SE2) detector. Samples were coated prior to imaging with a thin layer of gold using a Hummer Junior Sputtering system (Technics) operating at 10 mA under a vacuum pressure of 70 mTorr for 120 s prior to imaging. Fiber diameters were measured using the ImageJ version 1.49r software package. Digital pictures were acquired using a Canon PowerShot SX130 IS digital camera. Attenuated total reflectance (ATR) IR measurements were collected using a Bruker Tensor 27 FTIR spectrometer outfitted with a Pike Technologies (Fitchburg, WI) Diamond ATR stage and analyzed using the Opus software version 6.5.92 (Bruker Optik GmbH). Spectra were collected at a resolution of 2 cm^{-1} and are presented as an average of 16 scans. Data were smoothed and baseline-corrected using the instrument software. Compressed air was filtered through a 0.2 μm syringe tip filter. Deionized water with a resistance of 18.2 MΩ was used for all aqueous solutions unless otherwise noted.

Preparation and Purification of poly[MMA-co-VDMA]. Initial IR analysis of stored samples of poly[MMA-co-VDMA] revealed the presence of hydrolyzed azlactone groups (carboxylic acid C=O stretch ~1730 cm^{-1}). Azlactone groups were recyclized following an adopted literature procedure.[38] The polymer was dispersed in acetic anhydride (1:3 *m/v*) and heated to 100 °C in an oil bath. To this light yellow solution, triethylamine (1.5 equiv. with respect to carboxylic acid groups) was added dropwise with vigorous stirring. The solution immediately turned red, and was allowed to stir for 2 hr, after which it is concentrated under reduced pressure to approximately half the original volume and precipitated into ~300 mL of 3:1 (v/v) hexanes:iPrOH. The resulting off-white solid was collected by vacuum filtration, redissolved in ~80 mL of THF, and reprecipitated twice more to yield a white solid that was dried under high vacuum overnight. $M_{n,GPC}$ = 41.2 kDa (relative to polystyrene standards); $Đ$ = 2.4. ATR IR (cm^{-1}): 2985 & 2951 (C-H sp^3 stretch), 1818 (C=O, VDMA), 1725 (C=O, MMA), 1672 (C=N, VDMA), 1238 (C-O-C, MMA), and 1145 (C-O-C, VDMA). ^{1}H NMR (400.182 MHz, $CDCl_3$, δ ppm): 0.75-1.06 (m, (-CH_2-CH_2($C\underline{H}_3$)-, MMA), 1.37 (s, –C($C\underline{H}_3$)$_2$, VDMA), 1.53–2.31 (m, -$C\underline{H}_2$CH-, MMA & VDMA), 2.32–2.70 (m, -$CH_2C\underline{H}$-, VDMA), 3.60 (m,–O$C\underline{H}_3$, MMA). Quantitative ^{1}H NMR analysis of the azlactone backbone proton and the MMA terminal methyl group revealed a molar composition of 1.0:5.58 VDMA:MMA.

Electrospinning of Reactive Nanofibers. A 170 mg/mL polymer solution was prepared by dissolving poly[MMA-*co*-VDMA] in a 1:1 mixture (v/v) of acetone and DMF. Electrospinning was performed using a custom-built electrospinning device with a digital syringe pump (Harvard Bioscience Company) at a flow rate of 0.2 mL/hr through a 20G blunt needle at a distance of 15 cm with a voltage of ~20 kV. Fibers were collected for 1 hr (i.e., 0.2 mL of polymer solution)

onto a grounded 10 cm x 10 cm segment of aluminum foil (e.g., see schematic shown in Figure 1B). After fabrication, nanofiber mats were stored in a vacuum desiccator until further use. For the electrospinning of solutions of poly[MMA-co-VDMA] functionalized by pre-treatment with decylamine, 0.5 mol equiv. of decylamine (with respect to the number of azlactone groups) was added to the poly[MMA-co-VDMA] polymer solution (170 mg/mL of polymer in a 1:1 mixture of acetone and DMF, as described above). The resulting solution was allowed to stir overnight at room temperature and was then used directly for electrospinning, as described above, without further processing or purification.

Post-Fabrication Functionalization of Reactive Fiber Mats. Functionalization of reactive fiber mats was conducted by placing small segments (~0.8 cm x 2 cm) of the material into solutions of primary amines for defined periods of times (typically overnight). Solution concentrations of decylamine and propylamine (25 mM in hexanes), and 6-amino-1-hexanol (5 mM in hexanes with 4 vol% isopropanol) used in the experiments ensured an excess of the primary amine-containing compound relative to the anticipated number of azlactone groups in the reactive fibers). Solutions of TMR-Cad used in functionalization experiments were 20 μM in 1:1 (v/v) hexanes/iPrOH. After functionalization, materials were briefly rinsed in hexanes, allowed to air dry, and then stored under vacuum prior to further use.

Contact Transfer of Nanofiber Mats. PET substrates were cut into ~1.5 cm x 4 cm strips, rinsed with methanol, dried under a stream of compressed air, and placed in a solution of PEI (1 mg/mL in methanol) overnight prior to use to produce amine-functionalized PET, as previously described.[39] Substrates were then rinsed with fresh methanol and air-dried using compressed air.

Strips of aluminum foil coated with electrospun poly[MMA-co-VDMA] mats were placed directly onto the amine-functionalized PET and pressed together between two glass slides (held together by binder clips) for at least 2 h. For transfer to the surfaces of glass pipettes, pipettes were soaked in an aqueous solution 1 mg/mL of PEI in methanol overnight to allow PEI to adsorb to the glass surface. Strips of aluminum foil coated with electrospun poly[MMA-co-VDMA] were placed onto the surface of the glass and pressed into close contact for 2 h by tightly wrapping a strip of thin foam around the pipette. After transfer, the original mat-coated master strips were carefully removed from contact with the receiving surface. The receiving surfaces were then functionalized with decylamine as described above.

Fabrication of Oil-Infused Nanofiber Mats. Strips of decylamine treated poly[MMA-co-VDMA] (either on aluminum foil substrates, or mats transferred to PET substrates, as described above) were infused with oil by depositing an excess of silicone oil (~10 μL) and allowing the oil to spread out across the entirety of the surface. The resulting surfaces were characterized by placing a 10 μL droplet of water on oil-infused samples held at a 10º incline. Strips of poly[MMA-co-VDMA] patterned with both decylamine- and propylamine-functionalized regions (see text) were prepared by partially submerging substrates coated with reactive mats in a solution of propylamine in hexanes for 1 hr, followed by fully submerging them in a decylamine solution in hexanes overnight.

Reactive Micro-Contact Printing of Functionalized Patterns on Reactive Nanofiber Mats. A poly(dimethylsiloxane) (PDMS) stamp [Sylgard 184 silicone elastomer kit (Dow Corning, Midland, MI); prepared by following manufacturer's instructions] with repeating 50-μm square

features was dabbed into a small volume of 30 μM TMR-Cad in PBS (pH = 9.5). The stamp was then pressed against reactive poly[MMA-co-VDMA] mats previously contact-transferred to amine-functionalized PET substrates as described above for 20 min. After functionalization, the patterned strip was placed in a solution of decylamine in hexanes (25 mM) to functionalize any unreacted azlactone groups. The samples were then briefly rinsed using hexanes and allowed to air dry before imaging or use in other experiments.

Results and Discussion

Fabrication, Characterization, and Functionalization of Azlactone-Functionalized Nanofibers

We selected a poly[MMA-*co*-VDMA] random copolymer (molar ratio of 85:15 MMA:VDMA, as determined by ^{1}H NMR spectroscopy, see Materials and Methods) as a model amine-reactive polymer for all experiments described below because (i) MMA has been used in past studies on electrospinning,[2, 40] and (ii) initial screening experiments demonstrated that this copolymer composition provided nanofibers with physical characteristics and levels of reactive azlactone functionality (Figure 2A) sufficient for these proof of concept studies. Nanofibers and non-woven mats were fabricated by electrospinning solutions of poly[MMA-co-VDMA] in 1:1 (v/v) acetone/DMF onto grounded aluminum foil (e.g., Figure 1B; see Materials and Methods for additional details of electrospinning process parameters used in these experiments). Figure 2E-F shows representative low and high magnification SEM images of the resulting poly[MMA-co-VDMA] nanofiber mats. The images reveal these materials to be comprised of networks of relatively smooth and randomly aligned nanofibers with average diameters of approximately 430 nm (± 150 nm) and only occasional instances of beaded fiber morphologies (see also Table 1; additional characterization of the size distributions of these and all other nanofibers used in this

study are included in Figure S1 of the Supporting Information, available at the end of this chapter). Characterization of these poly[MMA-co-VDMA] mats by FTIR-ATR revealed a peak at ~1828 cm^{-1} (Figure 2M, black curve) that is diagnostic of the azlactone carbonyl group reported for other VDMA-based polymers,[36, 41-44] demonstrating that these reactive groups can survive electrospinning and remain intact under the conditions used here.

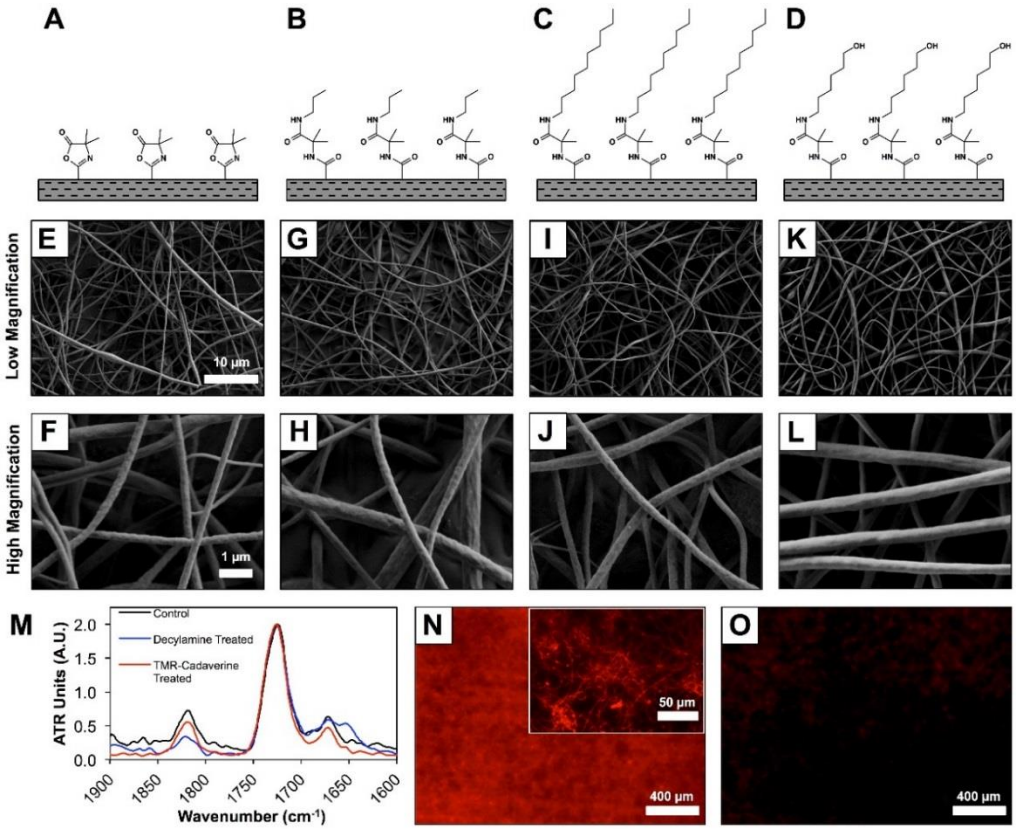

Figure 2: (A-D) Schematic illustrations depicting poly[MMA-co-VDMA] nanofiber surface chemistry (A) before amine treatment, showing unreacted azlactone-functionality, and after treatment with (B) propylamine, (C) decylamine, and (D) 6-amino-1-hexanol. These reactions result in ring opening of the azlactone and the formation of an amide/amide-based linker. (E-L) Low and high magnification SEM images of nanofibers, (E,F) before functionalization, and after amine treatment with (G,H) propylamine, (I,J) decylamine, and (K,L) 6-amino-1-hexanol. (M) Plot of IR absorbance of unreacted, azlactone-functionalized nanofibers (black), and after fibers after treatment with TMR-Cad (red) or decylamine (blue); all curves are normalized to the carbonyl peak of MMA (see text for details). (N,O) Fluorescence microscopy image of (N) TMR-Cad treated nanofibers (with high magnification inset), and (O) image of nanofibers treated with decylamine first, followed by TMR-Cad treatment (see text).

Table 1: Average Sizes of Functionalized Poly(MMA-co-VDMA) Fibers[a]

Treatment	Average Diameter (nm)	Standard Deviation (nm)
No Treatment	430	150
Decylamine	490	160
Propylamine	410	130
6-Amino-1-hexanol	440	140
TMR-Cadaverine	440	130

[a]Determined by SEM; diameters are reported as an averages of measurements made on 200 fibers.

To characterize the reactivity of the azlactone functionality present in these poly[MMA-co-VDMA] mats and determine whether these groups were present on the surfaces of the nanofibers in locations accessible for ring-opening with primary amines, we treated nanofiber-coated substrates with the primary amine-containing fluorophore TMR-Cad (in 1:1 (v/v) hexanes/isopropanol) for 20 min at room temperature. Characterization by FTIR revealed a small decrease in the azlactone carbonyl stretch (Figure 2M, red curve) relative to untreated samples (black curve; all IR spectra in Figure 2 are normalized to the carbonyl stretch of MMA repeat units to facilitate comparisons). Further characterization of these TMR-Cad-treated mats by fluorescence microscopy revealed bright and uniform red fluorescence across the samples and associated with the individual fibers of these coatings (Figure 2N; samples characterized by fluorescence microscopy were also treated with decylamine, a model non-fluorescent primary amine-based nucleophile, to permit rigorous washing with aqueous media prior to analysis; see Materials and Methods and discussion below for additional details and characterization of

decylamine-treated mats). The results in Table 1 and the SEM images shown in Figure S1 demonstrate that treatment with TMR-Cad under these conditions did not substantially alter the average diameters or the overall morphologies of the mats.

These results, when combined, are consistent with the covalent immobilization of TMR-Cad on the surfaces of the fibers mediated by ring-opening reactions with surface-accessible azlactone groups. Further support for this view was provided by the results of experiments performed using decylamine-treated mats (Figure 2C). Figure 2I-J shows representative SEM images of poly[MMA-co-VDMA] mats after treatment with an excess of decylamine in hexanes for ~8 hours, conditions that we anticipated to be sufficient to promote exhaustive ring-opening with any surface-accessible azlactone groups. These results, and those shown in Table 1 and Figure S1, again reveal that functionalization and these more extended solvent exposure periods do not lead to large changes in nanofiber diameters or non-woven mat morphologies. Inspection of the IR spectrum of these decylamine-treated mats (Figure 2M, blue curve) also reveals a reduction in the azlactone carbonyl peak. We note that the reduction in this peak is greater than that observed after treatment with TMR-Cad (red curve), likely a result, at least in part, of the substantially longer reaction times used in these decylamine-based experiments (e.g., ~8 h v. 20 min). The fact that the azlactone carbonyl peak does not completely disappear in these decylamine-based experiments could reflect incomplete surface functionalization. However, we note that this outcome is also consistent with the likelihood that these nanofibers contain some azlactone functionality that may be buried or otherwise inaccessible for reactions with primary amine groups under the treatment conditions used here.

Figure 2O shows a fluorescence microscopy image of a mat that was treated exhaustively with decylamine and then subsequently treated with a solution of TMR-Cad for 20 min (using

conditions identical to those described above), and reveals very little fiber-associated fluorescence. These results, when combined with those described above, suggest that the red fluorescence observed in Figure 2N arises from the covalent immobilization of TMR-Cad on the surfaces of these fibers (by reaction with surface-accessible azlactone groups), and is not a result of physisorption of the fluorophore. Overall, we conclude from these experiments that electrospun mats of poly[MMA-co-VDMA] contain accessible amine-reactive azlactone functionality that can be used to functionalize the surfaces of individual nanofibers under mild conditions. The results of experiments described below demonstrate that this approach can be used to impart new interfacial properties to surfaces coated with these materials.

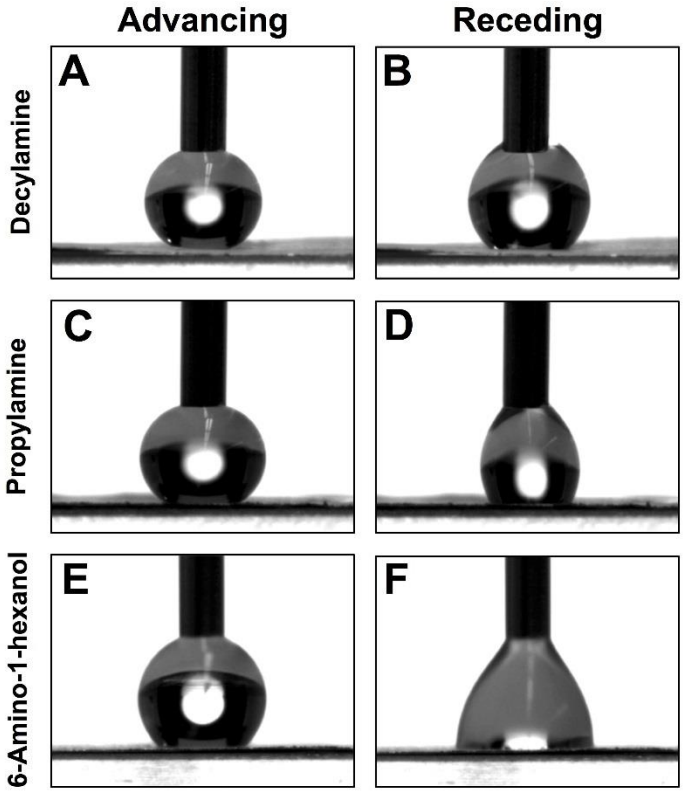

Figure 3: Representative images showing the advancing and receding water contact angles of poly[MMA-co-VDMA] nanofiber mats following treatment with (A-B) decylamine, (C-D) propylamine, and (E-F) 6-amino-1-hexanol.

Modulation of Interfacial Properties by Treatment with Hydrophobic and Hydrophilic Amines

Characterization of the water contact angles of decylamine-treated poly[MMA-co-VDMA] nanofiber mats revealed these materials to be hydrophobic, with an advancing water contact angle (θ_{adv}) of 149º (± 1°) and a contact angle hysteresis (θ_{hys}) of ~8º (± 1°) (e.g., see Table 2 and Figure 3A-B). Table 2 and Figure 3 also show values of θ_{adv} and θ_{hys} for otherwise identical poly[MMA-co-VDMA] mats treated, post-fabrication, with propylamine (a shorter alkylamine) and 6-amino-1-hexanol (a more hydrophilic alkylamine containing a terminal hydroxyl group; panels G-H and K-L of Figure 2 and results included in Figures S1 and S2 show additional physicochemical characterization of these alkylamine-functionalized fibers). Propylamine-functionalized mats (e.g., Figure 2B) exhibited values of θ_{adv} that were similar to those of decylamine-treated mats (147° ± 3°), but with a value of θ_{hys} that was significantly higher (19° ± 3°). In contrast, surfaces coated with poly[MMA-co-VDMA] mats treated with more hydrophilic 6-amino-1-hexanol (Figure 2D) were substantially less hydrophobic (θ_{adv} = 115º ± 7°; θ_{hys} = 41º ± 8°).

Table 2: Water Contact Angles of Amine-Functionalized Poly(MMA-co-VDMA) Mats

Treatment	θ_{Adv} (º)	θ_{Hys} (º)
Decylamine	149 ± 1	8 ± 1
Propylamine	147 ± 3	19 ± 3
6-Amino-1-hexanol	115 ± 7	41 ± 8

The SEM images of these functionalized mats, shown in Figure 2, demonstrate that these large changes in wetting behaviors arise from differences in the structures of the amines used to

functionalize the films, and not from large changes in the microstructures or morphologies of the fibers or the mats during functionalization. Although our current results do not permit conclusions regarding the density of reactive azlactone groups present on the surfaces of these nanofibers, the results shown in Table 2 and Figure 3 demonstrate that the density of these groups is sufficient to yield large changes in wetting behaviors upon ring-opening with simple hydrophilic and hydrophobic amines. The ability to modulate wetting behaviors and other interfacial properties of these nanofiber mats by the post-fabrication treatment of a common (or 'universal') reactive coating with amine-based nucleophiles—under mild solution conditions and without introducing substantial changes to nanofiber morphologies—introduces new opportunities for the modification, patterning, or customization of these materials for a range of potential applications.

Contact Transfer of Reactive Nanofibers onto Amine-Functionalized Substrates

The results of additional experiments demonstrated that these azlactone-functionalized mats could also be used to promote the 'contact transfer' of reactive nanofibers to secondary surfaces by pressing them into contact with other amine-functionalized surfaces (e.g., as shown schematically in Figure 4A-C). We performed a series of experiments using thin strips of aluminum foil coated with native (azlactone-containing) poly[MMA-co-VDMA] nanofiber mats and either (i) thin strips of unmodified poly(ethylene terephthalate) (PET) or (ii) strips of PET that were chemically modified to display primary amine groups on the surface (see Materials and Methods for details). Figure 4E shows the result of an experiment in which a mat-coated substrate was pressed into contact with an amine-functionalized PET substrate for two hours. The right side of this image shows the mat-coated 'master' substrate used in this experiment after

removal from the PET substrate shown on the left side of the image. Inspection of this image reveals a rectangular area on the PET substrate that is the same shape and size as the master substrate and coated uniformly with white nanofibers, consistent with the transfer of the reactive nanofibers to the amine-functionalized surface. Further inspection of these two surfaces reveals that a substantial portion of the reactive mat remained on the surface of the master substrate, and that only a thin layer of reactive nanofibers was transferred to the amine-functionalized surface (as characterized by visual inspection, and as shown schematically in Figure 4A-C; these mat-coated master substrates containing residual nanofibers could be used multiple times to affect the transfer of additional 'daughter' films on amine-functionalized surfaces; data not shown).

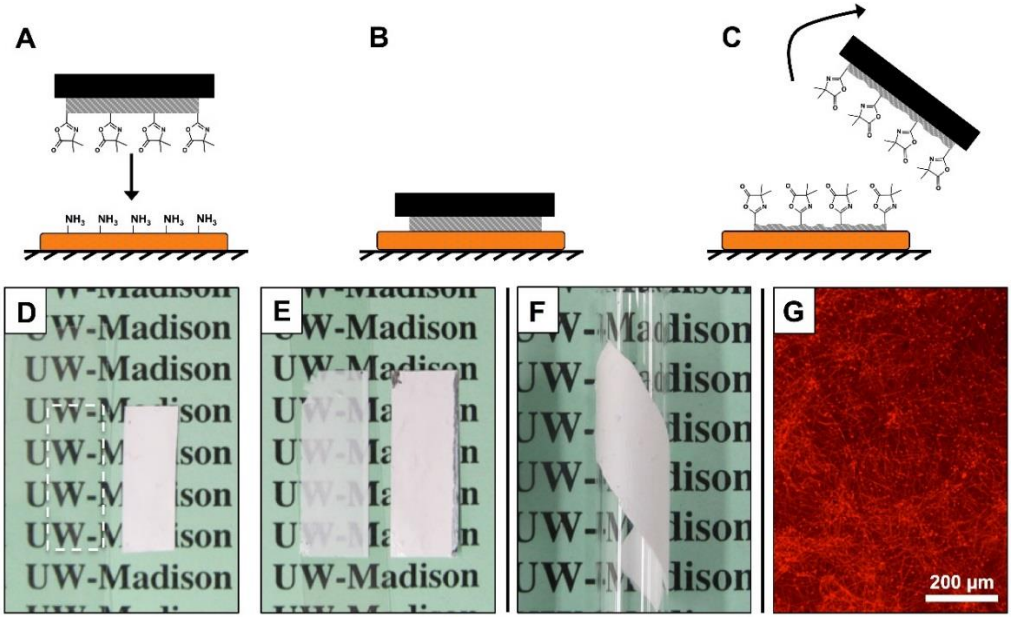

Figure 4: (A-C) Schematic illustration depicting the reactive transfer of poly[MMA-co-VDMA] nanofibrous mats to secondary, amine-functionalized surfaces. (A) An azlactone-functionalized nanofiber master substrate is placed onto an amine-functionalized substrate. (B) The two substrates are pressed together. (C) The master substrate is then removed, leaving a portion of transferred nanofibers on the secondary surface. (D-E) Images showing the result of reactive transfer of poly[MMA-co-VDMA] nanofibers to (D) native PET; dashed white box indicates the area where the master substrate was placed during transfer, and (E) amine-functionalized PET. (F) Image showing transfer of nanofibers to the curved surface of a PEI-functionalized glass tube. (G) Fluorescence microscopy image of a transferred nanofiber mat after treatment with TMR-Cad.

Figure 4D shows the results of an otherwise identical control experiment performed using a mat-coated master substrate (right) and a strip of unmodified PET (left; no amine functionalization). Under these conditions, we observed virtually no transfer of nanofibers to the PET (the dotted white rectangle in panel D indicates the area in which the mat-coated surface was pressed into contact with the PET substrate). Mats transferred to amine-functionalized PET remained in place after treatment with decylamine and subsequent rinsing with water, whereas any nanofibers adhered to unmodified PET substrates were readily removed under these conditions. These results, when combined, are consistent with the reactive transfer of nanofibers to the amine-treated surfaces shown in Figure 1E. Additional experiments suggested that this approach could also be used to promote the contact transfer of these mats to amine-modified glass substrates, including transfer onto curved surfaces (Figure 4F shows the results of contact transfer to the outer surface of a glass tube; see Materials and Methods for additional details).

Finally, Figure 4G shows an image of a transferred reactive ‘daughter’ film on the surface of an amine-treated PET substrate after treatment with TMR-Cad. Inspection of this image reveals bright red fluorescence associated with individual fibers, demonstrating that the nanofibers that comprise these contact-transferred films contain a sufficient amount of residual, unreacted azlactone groups to permit further chemical functionalization after transfer to secondary surfaces. Below, we demonstrate that this reactive contact transfer approach, combined with the ability to functionalize and tune the interfacial properties of these poly[MMA-co-VDMA] mats by treatment with primary amines, can be exploited to design and chemically pattern new types of oil-infused antifouling surfaces.

Infusion of Oil into Hydrophobic Contact-Transferred Mats Yields Slippery Antifouling Surfaces

Slippery liquid-infused porous surfaces (SLIPS) are a relatively new and promising class of antifouling materials with potential utility in a broad range of commercial, industrial, and clinical contexts.[45-49] These materials are typically fabricated by the infusion of a viscous oil into a porous or textured surface to yield 'slippery' coatings that allow water or other fluids to slide off their surfaces at relatively low tilt angles (e.g., >10º). Shiratori and coworkers recently demonstrated that electrospun mats fabricated using a highly fluorinated polymer [poly(vinylidene fluoride-co-hexafluoropropylene)] could be used as a matrix for the infusion of a liquid perfluoropolyether to design transparent 'omniphobic' surfaces that were slippery to both aqueous and organic fluids.[50] Initial experiments demonstrated that our porous and hydrophobic decylamine-treated poly[MMA-co-VDMA] nanofiber mats could be infused with a model oil (silicone oil) to produce slippery surfaces that were antifouling to a range of hydrophilic liquids, including water, glycerol, and serum-containing mammalian cell culture medium (Figure S3). Droplets of water placed on these oil-infused mats slid freely, with velocities of 2.9 (± 0.8) mm/s, when the mats were tilted at an angle of 10°. Droplets did not slide (at tilt angles of 10°) on otherwise identical oil-infused mats that were functionalized using propylamine (Figure S3). This difference is consistent with the results of past studies on oil-infused porous polymer multilayers,[51] and underscores the importance of achieving appropriate chemical compatibility between the porous matrix and the infused oil to achieve slippery character. As described below, this observation also provides opportunities to pattern the surfaces of these mats to design oil-infused surfaces that can manipulate the behaviors and mobilities of aqueous droplets.

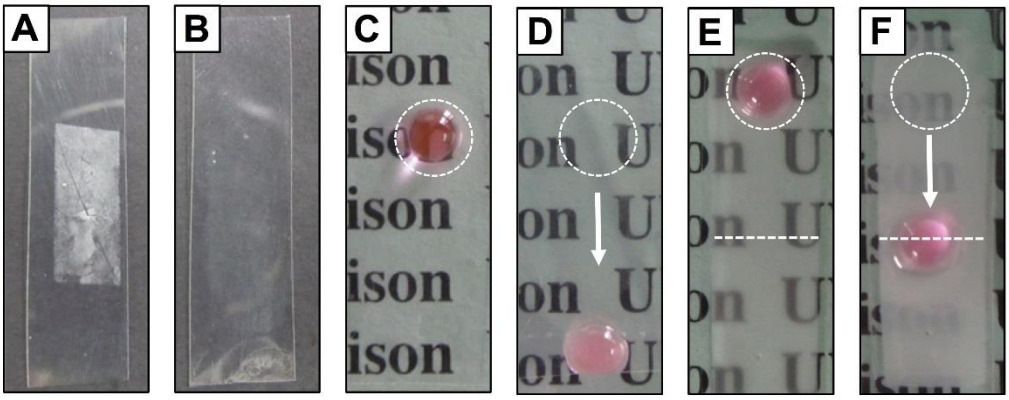

Figure 5: (A-B) Images of a mat of nanofibers transferred to amine-functionalized PET (A) and after the infusion of silicone oil (B; the nanofiber material becomes nearly transparent following oil-infusion). (C-D) Image of a droplet of water (red dye added to aid visualization) placed on a decylamine-treated, silicone oil-infused mat (C) at 0º and (D) at a 10º incline. At an angle of 10º, the water droplet quickly slides across the surface. The white-dashed circle indicates the initial position of the water droplet. (E-F) Images of a water droplet on an oil-infused substrate that was functionalized both with decylamine (above the dashed line) and propylamine (below the dashed line). When the substrate was lifted from (E) a 0º incline to (F) a 10º incline, the water droplet slid across the decylamine-treated region until it reached the propylamine-treated region.

We conducted a subsequent series of experiments using thin poly[MMA-co-VDMA] mats that were contact-transferred onto amine-functionalized PET substrates as described above. Figure 5A-B shows images of a decylamine-treated, contact-transferred mat (A) before and (B) after the infusion of silicone oil. Inspection of these images reveals the optically opaque mat to become nearly transparent after oil infusion. As shown in Figure 5B-C, droplets of water placed on the surfaces of these oil-infused mats slid down readily when the substrates were held at tilt angles of 10°. Figure 5D-E shows the result of a similar experiment conducted using a slippery surface prepared by the infusion of silicone oil into a contact-transferred mat that was subsequently spatially patterned by treatment with (i) decylamine on the top-most portion of the film and (ii) propylamine on the bottom-most portion of the film prior to infusion with silicone oil (the dotted white lines in these images indicate the approximate location of the border

between these two patterned regions). Inspection of these images reveals droplets of water to slide down the top-most, decylamine-treated portion of the coating when the substrate is tilted at 10°, but that sliding is arrested once the droplet contacts the propylamine-treated portion of the material under these conditions (droplet mobility could be recovered on these propylamine-treated surfaces when substrates were tilted at angles substantially greater than 10°). These results are similar to the results described above, and shown in Figure S3, for the behaviors of aqueous droplets on propylamine-functionalized poly[MMA-co-VDMA] mats, and are also consistent with those of past studies on porous polymer multilayers patterned with 'slippery' decylamine-functionalized and 'sticky' propylamine-functionalized regions.[51]

Electrospinning of Reactive Decylamine-Functionalized Poly[MMA-co-VDMA] Nanofibers

The results above demonstrate that nanofiber mats fabricated by the electrospinning of solutions of poly[MMA-co-VDMA] can be used as reactive platforms for the immobilization of new chemical functionality. One practical issue associated with mats fabricated by the direct electrospinning of solutions of poly[MMA-co-VDMA], however, is that functionalization of the resulting mats is limited, in general, to the use of solvents that do not dissolve poly[MMA-co-VDMA] or otherwise promote substantial changes in nanofiber morphology during functionalization steps. In this context, we found polar-protic solvents, such as water, ethanol, and methanol to be particularly problematic. For example, submersion of poly[MMA-co-VDMA] mats in water for as little as 20 minutes resulted in large changes in physical morphology, and exposure to water for two hours resulted in substantial amounts of the mats detaching or dislodging from their underlying substrates (Figures S4 and S5). This sensitivity to aqueous solvents also precluded the use of conventional microcontact printing techniques to

pattern microscale regions of functionality on these reactive mats (e.g., using PDMS stamps that minimize the volume of aqueous solutions needed during functionalization; see additional discussion below).

The reasons for this physical and functional instability are not completely understood, but this behavior places some practical limits on the types of functionality that can be installed on these materials (e.g., many hydrophilic or biologically relevant amines that are soluble only in polar-protic solvents could be difficult to immobilize without perturbing nanofiber and mat morphologies). We note, however, that the decylamine-functionalized mats described above do not exhibit such solvent instability, and can be rinsed, washed, or submerged in aqueous solutions for prolonged periods without promoting substantial changes in film morphology (e.g., as discussed above and shown in panels N-O of Figure 2). On the basis of these observations, we reasoned that the partial conjugation of decylamine to poly[MMA-co-VDMA] prior to electrospinning, to produce a more hydrophobic, amine-reactive terpolymer structure (Figure 6A; denoted poly[MMA-co-VDMA]$_{Dec}$), might lead to reactive mats with improved physical stability to polar-protic solvents and expand the pool of agents, reagents, and conditions available or useful for post-fabrication functionalization.

To test this hypothesis, we fabricated electrospun mats using solutions of poly[MMA-co-VDMA]$_{Dec}$) prepared by adding 0.5 molar equivalents of decylamine (with respect to the azlactone subunits; see Materials and Methods for additional details; the IR spectrum of this polymer, shown in Figure 6B, reveals a decrease in the azlactone carbonyl peak at ~1828 cm^{-1} relative to poly[MMA-co-VDMA]). Electrospun mats fabricated from acetone/DMF solutions of more hydrophobic poly[MMA-co-VDMA]$_{Dec}$ exhibited fiber and mat morphologies and size distributions (Figure S6) similar to those of poly[MMA-co-VDMA] mats shown in Figure 2E-F,

but were significantly more stable toward exposure to aqueous media and mixtures of polar-protic solvents (Figure S4 and S5). As an example, Figure 6C shows a fluorescence micrograph of a poly[MMA-co-VDMA]$_{Dec}$ mat on an amine-functionalized PET substrate after microcontact printing using a soft PDMS stamp patterned with an array of square posts (50 μm x 50 μm) inked with an aqueous solution of TMR-Cad (in PBS, pH = 9.5; see Materials and Methods for additional details of microcontact printing protocols). Inspection of this image reveals an array of red fluorescent squares on the mat that is similar to the pattern of the stamp. This result and the fidelity of pattern transfer contrasts sharply to the results of otherwise identical experiments performed using poly[MMA-co-VDMA] mats, which exhibited irregular and non-uniform regions of fluorescence distributed over large areas and visual evidence of larger scale changes in mat morphology (see Figure S7).

As noted above, the ability to functionalize these fibers and mats using aqueous or other polar-protic solvents should broaden the pool of available amine-based nucleophiles (including many technologically-relevant biological motifs) that can be used to functionalize or pattern the surfaces of these materials. In that context, we also note that while the poly[MMA-co-VDMA] copolymer used here is sufficient to provide useful proof of concept, VDMA can also be copolymerized with a broad range of other vinyl monomers to produce other amine-reactive copolymers.[43, 44, 52-61] This azlactone-based approach to the design of reactive electrospun fibers is therefore likely to be general. The investigation of other comonomers, the manipulation of comonomer ratios, and changes to other structural and electrospinning processing parameters, for example, are likely to lead to amine-reactive nanofibers and reactive mats with a much broader range of physicochemical properties and functional behaviors than those based on the poly[MMA-co-VDMA] copolymer reported here.

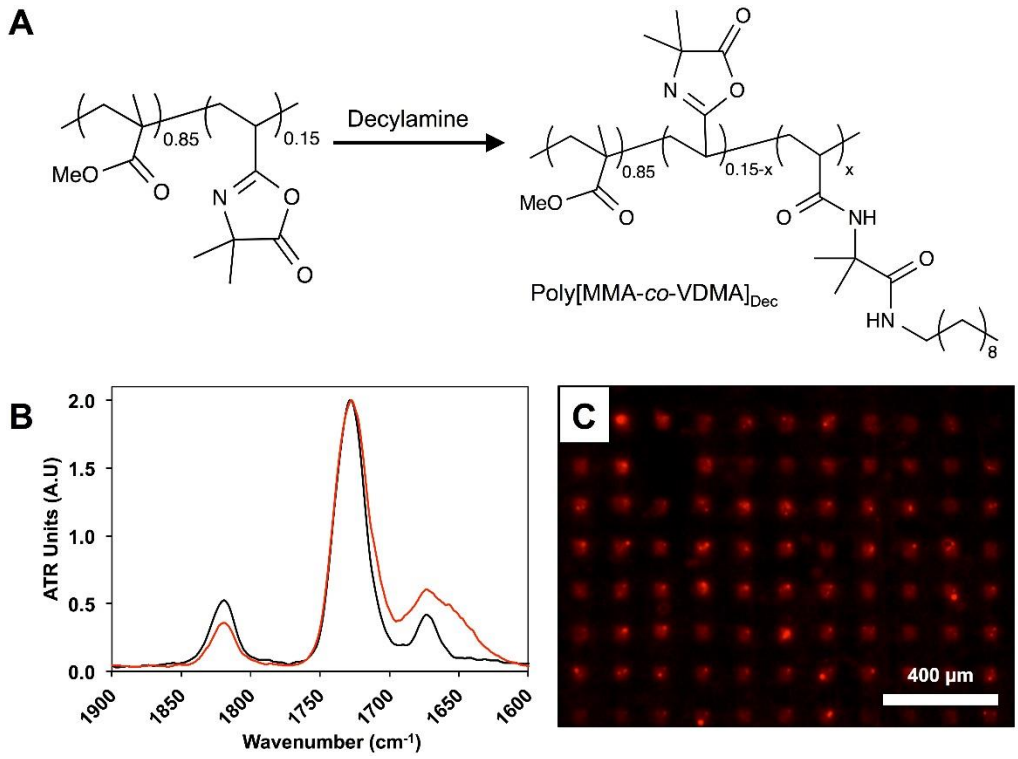

Figure 6: (A) Schematic showing the reaction of poly[MMA-co-VDMA] with decylamine to yield the terpolymer poly[MMA-co-VDMA]$_{Dec}$. (B) Plot showing IR absorbance for P[MMA-co-VDMA] (black) and P[MMA-co-VDMA]$_{Dec}$ (red); both spectra are normalized to the carbonyl MMA peak. The decreased intensity of the azlactone carbonyl C=O stretch (~1828 cm^{-1}) is indicative of the reaction of decylamine and the formation of the terpolymer. (C) Fluorescence microscopy image of a reactive P[MMA-co-VDMA]$_{Dec}$ mat microcontact-functionalized with an aqueous solution of TMR-Cad using a PDMS stamp patterned with a 50 µm square features (see text).

Summary and Conclusions

We have reported the characterization of amine-reactive polymer nanofibers and non-woven reactive nanofiber mats fabricated by the electrospinning of azlactone-functionalized polymers. Our results demonstrate that nanofibers and mats electrospun from solutions of the model copolymer poly(MMA-co-VDMA) contain intact and surface-accessible azlactone groups, and that these reactive groups can be used to introduce additional functionality and modulate important interfacial properties of these materials (e.g., wetting behaviors), after

fabrication, by simple treatment with solutions containing primary amine functionalized nucleophiles. The facile and 'click-like' nature of the azlactone chemistry used here permits post-fabrication functionalization under mild reaction conditions and can be achieved without introducing substantial changes to nanofiber or mat morphologies. This general approach also enables the macroscale or microscale patterning of new functionality using methods such as microcontact printing; conversely, our results demonstrate that these azlactone-functionalized nanofiber mats themselves can be transferred or printed onto secondary surfaces by pressing them into contact with other amine-functionalized surfaces. Finally, our results demonstrate that functionalization with hydrophobic amines, such as *n*-decylamine, can increase the physical stability of these materials upon exposure to aqueous liquids, and yields hydrophobic porous mats that can be used as scaffolds for the design of new slippery liquid-infused coatings.

The strategies and materials reported here enable the modification, patterning, and introduction of new functional properties to electrospun polymer nanofibers and nanofiber-based coatings after nanofiber fabrication. As such, these materials obviate the need to design and synthesize new functional polymers to fabricate new electrospun materials with desired properties or specifically tailored surface functionality. The azlactone-based chemistry used here broadens the scope of approaches that can be used to functionalize the properties of polymer nanofibers. Although we used a model poly(MMA-co-VDMA) copolymer here to demonstrate proof of concept and explore feasibility, we anticipate that this approach can be used to design other azlactone-functionalized vinyl polymers, or used in combination with other nucleophiles (e.g., hydroxyl- or thiol-functionalized nucleophiles[58]) to design nanofibers and nanofiber-based coatings with functional behaviors and physical properties of interest and potential utility in a broad range of fundamental and applied contexts.

Acknowledgments. Financial support for this work was provided by the Office of Naval Research (N00014-16-1-2185) and the NSF (through a grant to the UW-Madison Materials Research Science and Engineering Center; MRSEC; DMR-1121288), and made use of NSF-supported facilities (DMR-1121288). We acknowledge the support of the Wisconsin Institutes of Discovery and the Vice Chancellor for Research and Graduate Education at the University of Wisconsin—Madison. M. J. K. acknowledges the UW-Madison Biotechnology Center for a Morgridge Biotechnology Fellowship. M. C. D. C. acknowledges the Natural Sciences Engineering Research Council of Canada for a graduate fellowship.

References

1. Li, D.; Xia, Y. N., Electrospinning of nanofibers: Reinventing the wheel? *Advanced Materials* **2004,** *16* (14), 1151-1170.

2. Greiner, A.; Wendorff, J. H., Electrospinning: A fascinating method for the preparation of ultrathin fibres. *Angewandte Chemie-International Edition* **2007,** *46* (30), 5670-5703.

3. Guo, L. P.; Bai, J.; Li, C. P.; Meng, Q. R.; Liang, H. O.; Sun, W. Y.; Li, H. Q.; Liu, H., A novel catalyst containing palladium nanoparticles supported on PVP composite nanofiber films: Synthesis, characterization and efficient catalysis. *Applied Surface Science* **2013,** *283*, 107-114.

4. Demir, M. M.; Ugur, G.; Gulgun, M. A.; Menceloglu, Y. Z., Glycidyl-methacrylate-based electrospun mats and catalytic silver nanoparticles. *Macromolecular Chemistry and Physics* **2008,** *209* (5), 508-515.

5. Tong, Y.; Lu, X. F.; Sun, W. N.; Nie, G. D.; Yang, L.; Wang, C., Electrospun polyacrylonitrile nanofibers supported Ag/Pd nanoparticles for hydrogen generation from the hydrolysis of ammonia borane. *Journal of Power Sources* **2014,** *261*, 221-226.

6. Formo, E.; Lee, E.; Campbell, D.; Xia, Y. N., Functionalization of electrospun TiO2 nanofibers with Pt nanoparticles and nanowires for catalytic applications. *Nano Letters* **2008,** *8* (2), 668-672.

7. Lu, X. F.; Wang, C.; Wei, Y., One-Dimensional Composite Nanomaterials: Synthesis by Electrospinning and Their Applications. *Small* **2009,** *5* (21), 2349-2370.

8. Li, W. J.; Laurencin, C. T.; Caterson, E. J.; Tuan, R. S.; Ko, F. K., Electrospun nanofibrous structure: A novel scaffold for tissue engineering. *Journal of Biomedical Materials Research* **2002,** *60* (4), 613-621.

9. Sill, T. J.; von Recum, H. A., Electrospinning: Applications in drug delivery and tissue engineering. *Biomaterials* **2008,** *29* (13), 1989-2006.

10. Matthews, J. A.; Wnek, G. E.; Simpson, D. G.; Bowlin, G. L., Electrospinning of collagen nanofibers. *Biomacromolecules* **2002,** *3* (2), 232-238.

11. Yoshimoto, H.; Shin, Y. M.; Terai, H.; Vacanti, J. P., A biodegradable nanofiber scaffold by electrospinning and its potential for bone tissue engineering. *Biomaterials* **2003,** *24* (12), 2077-2082.

12. Pham, Q. P.; Sharma, U.; Mikos, A. G., Electrospinning of polymeric nanofibers for tissue engineering applications: A review. *Tissue Engineering* **2006,** *12* (5), 1197-1211.

13. Chou, S. F.; Carson, D.; Woodrow, K. A., Current strategies for sustaining drug release from electrospun nanofibers. *Journal of Controlled Release* **2015,** *220*, 584-591.

14. Kim, K.; Luu, Y. K.; Chang, C.; Fang, D. F.; Hsiao, B. S.; Chu, B.; Hadjiargyrou, M., Incorporation and controlled release of a hydrophilic antibiotic using poly(lactide-co-glycolide)-based electrospun nanofibrous scaffolds. *Journal of Controlled Release* **2004,** *98* (1), 47-56.

15. Kalaoglu-Altan, O. I.; Sanyal, R.; Sanyal, A., Reactive and 'clickable' electrospun polymeric nanofibers. *Polymer Chemistry* **2015,** *6* (18), 3372-3381.

16. Shi, Q.; Chen, X. S.; Lu, T. C.; Jing, X. B., The immobilization of proteins on biodegradable polymer fibers via click chemistry. *Biomaterials* **2008,** *29* (8), 1118-1126.

17. Fu, G. D.; Xu, L. Q.; Yao, F.; Zhang, K.; Wang, X. F.; Zhu, M. F.; Nie, S. Z., Smart Nanofibers from Combined Living Radical Polymerization, "Click Chemistry" and Electrospinning. *Acs Applied Materials & Interfaces* **2009,** *1* (2), 239-243.

18. Fu, G. D.; Xu, L. Q.; Yao, F.; Li, G. L.; Kang, E. T., Smart Nanofibers with a Photoresponsive Surface for Controlled Release. *Acs Applied Materials & Interfaces* **2009,** *1* (11), 2424-2427.

19. Chang, Z. J.; Fang, Y.; Zhang, Q. H.; Chen, D. J., "Click" Chemistry for Facile Immobilization of Iron Phthalocyanines onto Electrospun Nanofiber Surface. *Chemistry Letters* **2009,** *38* (12), 1144-1145.

20. Chang, Z. J.; Xu, Y.; Zhao, X.; Zhang, Q. H.; Chen, D. J., Grafting Poly(methyl methacrylate) onto Polyimide Nanofibers via "Click" Reaction. *Acs Applied Materials & Interfaces* **2009,** *1* (12), 2804-2811.

21. Lancuski, A.; Fort, S.; Bossard, F., Electrospun Azido-PCL Nanofibers for Enhanced Surface Functionalization by Click Chemistry. *Acs Applied Materials & Interfaces* **2012,** *4* (12), 6499-6504.

22. Lancuski, A.; Bossard, F.; Fort, S., Carbohydrate-Decorated PCL Fibers for Specific Protein Adhesion. *Biomacromolecules* **2013,** *14* (6), 1877-1884.

23. Lin, F.; Yu, J. Y.; Tang, W.; Zheng, J. K.; Xie, S. B.; Becker, M. L., Postelectrospinning "Click" Modification of Degradable Amino Acid-Based Poly(ester urea) Nanofibers. *Macromolecules* **2013,** *46* (24), 9515-9525.

24. Qian, Y. C.; Ren, N.; Huang, X. J.; Chen, C.; Yu, A. G.; Xu, Z. K., Glycosylation of Polyphosphazene Nanofibrous Membrane by Click Chemistry for Protein Recognition. *Macromolecular Chemistry and Physics* **2013,** *214* (16), 1852-1858.

25. Zheng, J. K.; Liu, K. Y.; Reneker, D. H.; Becker, M. L., Post-Assembly Derivatization of Electrospun Nanofibers via Strain-Promoted Azide Alkyne Cycloaddition. *Journal of the American Chemical Society* **2012,** *134* (41), 17274-17277.

26. Zheng, J. K.; Xie, S. B.; Lin, F.; Hua, G.; Yu, T. Y.; Reneker, D. H.; Becker, M. L., 4-Dibenzocyclooctynol (DIBO) as an initiator for poly(epsilon-caprolactone): copper-free clickable polymer and nanofiber-based scaffolds. *Polymer Chemistry* **2013,** *4* (7), 2215-2218.

27. Zheng, J. K.; Hua, G.; Yu, J. Y.; Lin, F.; Wade, M. B.; Reneker, D. H.; Becker, M. L., Post-Electrospinning "Triclick" Functionalization of Degradable Polymer Nanofibers. *Acs Macro Letters* **2015,** *4* (2), 207-213.

28. Yang, H.; Zhang, Q.; Lin, B. P.; Fu, G. D.; Zhang, X. Q.; Guo, L. X., Thermo-sensitive electrospun fibers prepared by a sequential thiol-ene click chemistry approach. *Journal of Polymer Science Part a-Polymer Chemistry* **2012,** *50* (20), 4182-4190.

29. Thielke, M. W.; Bruckner, E. P.; Wong, D. L.; Theato, P., Thiol-ene modification of electrospun polybutadiene fibers crosslinked by UV irradiation. *Polymer* **2014,** *55* (22), 5596-5599.

30. Kalaoglu-Altan, O. I.; Sanyal, R.; Sanyal, A., "Clickable" Polymeric Nanofibers through Hydrophilic Hydrophobic Balance: Fabrication of Robust Biomolecular Immobilization Platforms. *Biomacromolecules* **2015,** *16* (5), 1590-1597.

31. Gentsch, R.; Pippig, F.; Nilles, K.; Theato, P.; Kikkeri, R.; Maglinao, M.; Lepenies, B.; Seeberger, P. H.; Borner, H. G., Modular Approach toward Bioactive Fiber Meshes Carrying Oligosaccharides. *Macromolecules* **2010,** *43* (22), 9239-9247.

32. Zhao, H.; Gu, W. Y.; Thielke, M. W.; Sterner, E.; Tsai, T. H.; Russell, T. P.; Coughlin, E. B.; Theato, P., Functionalized Nanoporous Thin Films and Fibers from Photocleavable Block Copolymers Featuring Activated Esters. *Macromolecules* **2013,** *46* (13), 5195-5201.

33. Jewett, J. C.; Bertozzi, C. R., Cu-free click cycloaddition reactions in chemical biology. *Chemical Society Reviews* **2010,** *39* (4), 1272-1279.

34. El-Faham, A.; Albericio, F., Peptide Coupling Reagents, More than a Letter Soup. *Chemical Reviews* **2011,** *111* (11), 6557-6602.

35. Das, A.; Theato, P., Activated Ester Containing Polymers: Opportunities and Challenges for the Design of Functional Macromolecules. *Chemical Reviews* **2016,** *116* (3), 1434-1495.

36. Heilmann, S. M.; Rasmussen, J. K.; Krepski, L. R., Chemistry and technology of 2-alkenyl azlactones. *Journal of Polymer Science Part A: Polymer Chemistry* **2001,** *39* (21), 3655-3677.

37. Buck, M. E.; Lynn, D. M., Azlactone-functionalized polymers as reactive platforms for the design of advanced materials: Progress in the last ten years. *Polymer Chemistry* **2012,** *3* (1), 66-80.

38. Rasmussen, J. K.; Heilmann, S. M.; Krepski, L. R.; Jensen, K. M.; Mickelson, J.; Johnson, K. Z.; Coleman, P. L.; Milbrath, D. S.; Walker, M. M., Cross-Linked, Hydrophilic, Azlactone-Functionalized Polymeric Beads - A 2-Step Approach. *Reactive Polymers* **1992,** *16* (2), 199-212.

39. Broderick, A. H.; Carter, M. C. D.; Lockett, M. R.; Smith, L. M.; Lynn, D. M., Fabrication of Oligonucleotide and Protein Arrays on Rigid and Flexible Substrates Coated with Reactive Polymer Multilayers. *Acs Applied Materials & Interfaces* **2013,** *5* (2), 351-359.

40. Gupta, P.; Elkins, C.; Long, T. E.; Wilkes, G. L., Electrospinning of linear homopolymers of poly(methyl methacrylate): exploring relationships between fiber formation, viscosity, molecular weight and concentration in a good solvent. *Polymer* **2005,** *46* (13), 4799-4810.

41. Buck, M. E.; Zhang, J.; Lynn, D. M., Layer-by-layer assembly of reactive ultrathin films mediated by click-type reactions of poly(2-alkenyl azlactone)s. *Advanced Materials* **2007,** *19* (22), 3951-3955.

42. Xie, S. F.; Svec, F.; Frechet, J. M. J., Design of reactive porous polymer supports for high throughput bioreactors: Poly(2-vinyl-4,4-dimethylazlactone-co-acrylamide-co-ethyl dimethacrylate) monoliths. *Biotechnology and Bioengineering* **1999,** *62* (1), 30-35.

43. Laquievre, A.; Allaway, N. S.; Lyskawa, J.; Woisel, P.; Lefebvre, J. M.; Fournier, D., Highly Efficient Ring-Opening Reaction of Azlactone-Based Copolymer Platforms for the Design of Functionalized Materials. *Macromolecular Rapid Communications* **2012,** *33* (9), 848-855.

44. Messman, J. M.; Lokitz, B. S.; Pickel, J. M.; Kilbey, S. M., Highly Tailorable Materials based on 2-Vinyl-4,4-dimethyl Azlactone: (Co)Polymerization, Synthetic Manipulation and Characterization. *Macromolecules* **2009,** *42* (12), 3933-3941.

45. Cao, M. Y.; Guo, D. W.; Yu, C. M.; Li, K.; Liu, M. J.; Jiang, L., Water-Repellent Properties of Superhydrophobic and Lubricant-Infused "Slippery" Surfaces: A Brief Study on the Functions and Applications. *Acs Applied Materials & Interfaces* **2016,** *8* (6), 3615-3623.

46. Wong, T. S.; Kang, S. H.; Tang, S. K. Y.; Smythe, E. J.; Hatton, B. D.; Grinthal, A.; Aizenberg, J., Bioinspired self-repairing slippery surfaces with pressure-stable omniphobicity. *Nature* **2011,** *477* (7365), 443-447.

47. Epstein, A. K.; Wong, T. S.; Belisle, R. A.; Boggs, E. M.; Aizenberg, J., Liquid-infused structured surfaces with exceptional anti-biofouling performance. *Proceedings of the National Academy of Sciences of the United States of America* **2012,** *109* (33), 13182-13187.

48. Kim, P.; Wong, T. S.; Alvarenga, J.; Kreder, M. J.; Adorno-Martinez, W. E.; Aizenberg, J., Liquid-Infused Nanostructured Surfaces with Extreme Anti-Ice and Anti-Frost Performance. *Acs Nano* **2012,** *6* (8), 6569-6577.

49. Wilson, P. W.; Lu, W. Z.; Xu, H. J.; Kim, P.; Kreder, M. J.; Alvarenga, J.; Aizenberg, J., Inhibition of ice nucleation by slippery liquid-infused porous surfaces (SLIPS). *Physical Chemistry Chemical Physics* **2013,** *15* (2), 581-585.

50. Abe, J.; Tenjimbayashi, M.; Shiratori, S., Electrospun nanofiber SLIPS exhibiting high total transparency and scattering. *Rsc Advances* **2016,** *6* (44), 38018-38023.

51. Manna, U.; Lynn, D. M., Fabrication of Liquid-Infused Surfaces Using Reactive Polymer Multilayers: Principles for Manipulating the Behaviors and Mobilities of Aqueous Fluids on Slippery Liquid Interfaces. *Advanced Materials* **2015,** *27* (19), 3007-3012.

52. Gardner, C. M.; Brown, C. E.; Stover, H. D. H., Synthesis and properties of water-soluble azlactone copolymers. *Journal of Polymer Science Part a-Polymer Chemistry* **2012,** *50* (22), 4674-4685.

53. Ho, H. T.; Levere, M. E.; Fournier, D.; Montembault, V.; Pascual, S.; Fontaine, L., Introducing the Azlactone Functionality into Polymers through Controlled Radical Polymerization: Strategies and Recent Developments. *Australian Journal of Chemistry* **2012,** *65* (8), 970-977.

54. Quek, J. Y.; Zhu, Y. C.; Roth, P. J.; Davis, T. P.; Lowe, A. B., RAFT Synthesis and Aqueous Solution Behavior of Novel pH- and Thermo-Responsive (Co)Polymers Derived from Reactive Poly(2-vinyl-4,4-dimethylazlactone) Scaffolds. *Macromolecules* **2013,** *46* (18), 7290-7302.

55. Fournier, D.; Pascual, S.; Montembault, V.; Haddleton, D. M.; Fontaine, L., Well-defined azlactone-functionalized (Co)polymers on a solid support: Synthesis via supported living radical polymerization and application as nucleophile scavengers. *Journal of Combinatorial Chemistry* **2006,** *8* (4), 522-530.

56. Xie, S.; Svec, F.; Fréchet, J. M., Design of reactive porous polymer supports for high throughput bioreactors: Poly (2-vinyl-4, 4-dimethylazlactone-co-acrylamide-co-ethylene dimethacrylate) monoliths. *Biotechnology and bioengineering* **1999,** *62* (1), 30-35.

57. Lokitz, B. S.; Wei, J. F.; Hinestrosa, J. P.; Ivanov, I.; Browning, J. F.; Ankner, J. F.; Kilbey, S. M.; Messman, J. M., Manipulating Interfaces through Surface Confinement of Poly(glycidyl methacrylate)-block-poly(vinyldimethylazlactone), a Dually Reactive Block Copolymer. *Macromolecules* **2012,** *45* (16), 6438-6449.

58. Carter, M. C.; Lynn, D. M., Covalently Crosslinked and Physically Stable Polymer Coatings with Chemically Labile and Dynamic Surface Features Fabricated by Treatment of Azlactone-Containing Multilayers with Alcohol-, Thiol-, and Hydrazine-Based Nucleophiles. *Chemistry of Materials* **2016,** *28* (14), 5063-5072.

59. Schmitt, S. K.; Xie, A. W.; Ghassemi, R. M.; Trebatoski, D. J.; Murphy, W. L.; Gopalan, P., Polyethylene Glycol Coatings on Plastic Substrates for Chemically Defined Stem Cell Culture. *Advanced Healthcare Materials* **2015,** *4* (10), 1555-1564.

60. Ho, H. T.; Levere, M. E.; Pascual, S.; Montembault, V.; Casse, N.; Caruso, A.; Fontaine, L., Thermoresponsive block copolymers containing reactive azlactone groups and their bioconjugation with lysozyme. *Polymer Chemistry* **2013,** *4* (3), 675-685.

61. Li, Y.; Duong, H. T. T.; Jones, M. W.; Basuki, J. S.; Hu, J. M.; Boyer, C.; Davis, T. P., Selective Postmodification of Copolymer Backbones Bearing Different Activated Esters with Disparate Reactivities. *Acs Macro Letters* **2013,** *2* (10), 912-917.

Supporting Information for Chapter 12

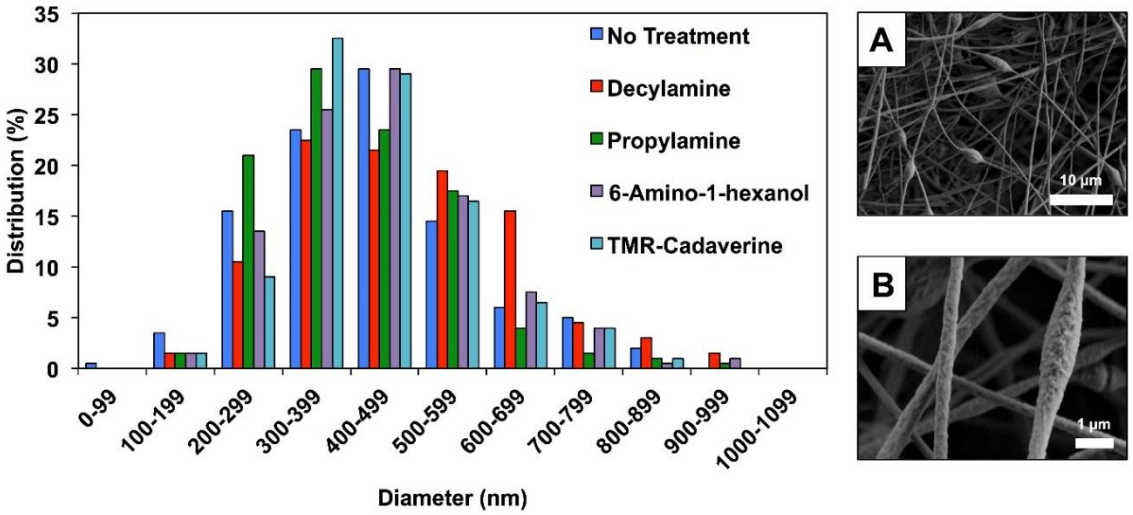

Figure S1: Histogram of fiber diameters of poly[MMA-co-VDMA] nanofibers before or after treatment with the indicated primary amines (n = 200 for each set of measurements) showing that the distribution of fiber diameters is nearly the same for each amine treatment and no substantial morphological changes occur to the fibers as a result of the amine treatments. (A) Low and (B) high magnification SEM images of TMR-Cad treated nanofibers

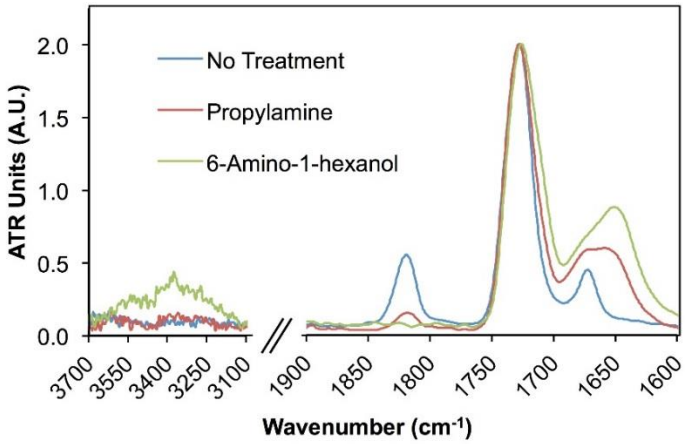

Figure S2: Plot showing the IR spectra of poly[MMA-co-VDMA] nanofibers before treatment (blue), and after treatment with the primary amines propylamine (red) and 6-amino-1-hexanol (green). Plots are normalized to the MMA C=O carbonyl stretch (see main text). The decrease in azlactone C=O carbonyl peak intensity (~1828 cm^{-1}) indicates ring-opening of the azlactone groups with the incoming primary amines. The broad absorbance from ~3100-3700 cm^{-1} for 6-amino-1-hexanol treated nanofibers is consistent with OH-stretching and the installation of hydroxyl functionality.

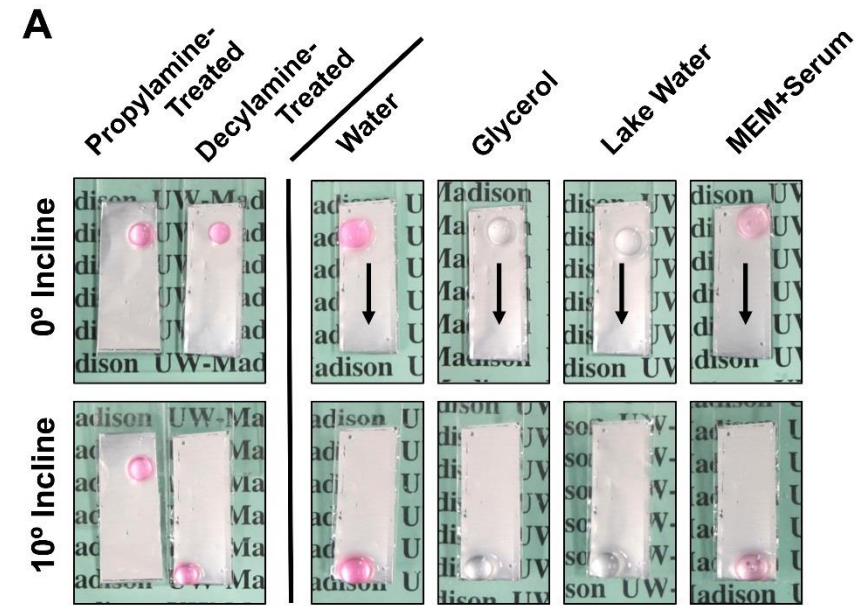

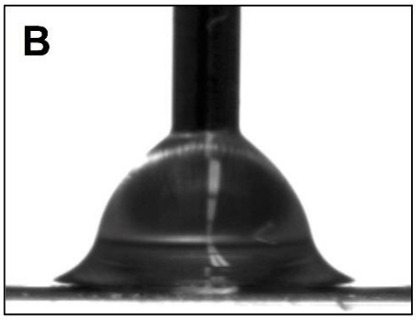

C: Velocities and Contact Angles of Water Droplets on SLIPS

Velocity (mm/s)	2.9 ± 0.8
θ_{Adv}(º)	83.8 ± 2.4
θ_{Hyst}(º)	8.9 ± 4.0

Figure S3: (A) Images of liquid droplets placed on oil-infused nanofiber materials. A water droplet (dyed red to aid visualization) placed on an oil-infused propylamine-treated nanofiber mat remains pinned to the substrate when the substrate is inclined to 10º. Conversely, a droplet placed on an oil-infused decylamine-treated nanofiber mat slides to the edge of the substrate at the same 10º incline. Droplets of glycerol, lake water, and serum-containing cell culture media (MEM) placed on an oil-infused decylamine-treated nanofiber mat all slide freely to the bottom of the substrate when the substrate is place at a 10º incline. (B) An image of the advancing contact angle of a water droplet place on oil-infused decylamine-treated SLIPS mats. (C) Table showing the velocities and contact angles of water droplets on decylamine-treated SLIPS.

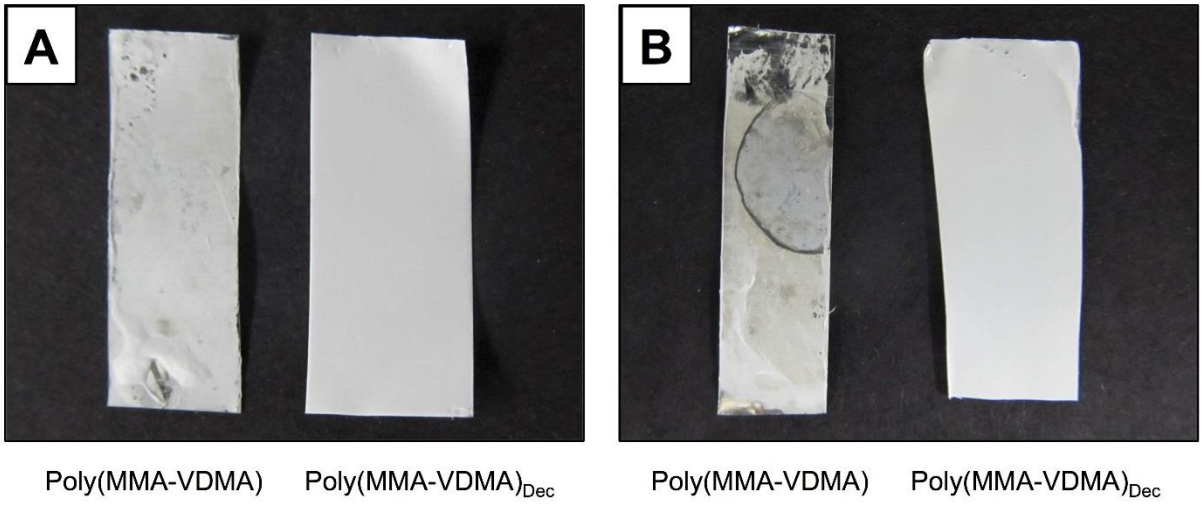

Figure S4: (A-B) Images of poly[MMA-co-VDMA] and poly[MMA-co-VDMA]$_{Dec}$ nanofiber mats after incubation in PBS (pH = 9.5) for (A) 20 min and (B) 2 hr. The poly[MMA-co-VDMA] mats are increasingly disrupted by treatment with the aqueous solution over the course of the two incubation periods, whereas the poly[MMA-co-VDMA]$_{Dec}$ materials remain practically unadulterated by these treatment (by visual inspection).

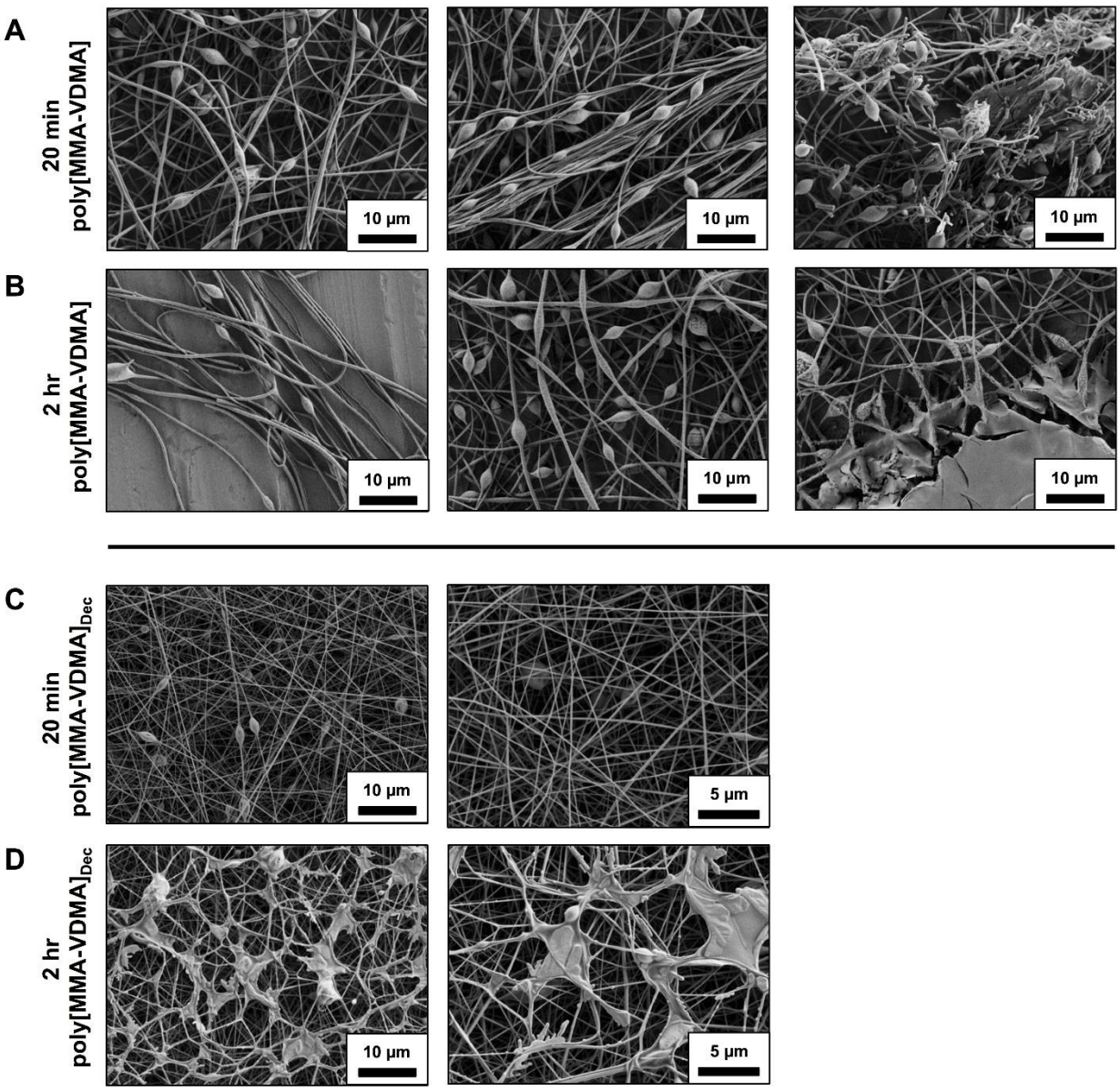

Figure S5: (A-D) Representative SEM images of (A-B) poly[MMA-co-VDMA] and (C-D) poly[MMA-co-VDMA]$_{Dec}$ nanofiber mats after incubation in PBS (pH = 9.5) for (A,C) 20 min and (B,D) 2 hr. Images of poly[MMA-co-VDMA] mats treated under these conditions reveal beaded fiber morphologies, areas of locally aligned fibers, and regions of disrupted fibers after exposure for 20 min (A), and substantial removal of fibers and the formation of other skin-like surface features after 2 hr (B) that are not evident prior to treatment with water (e.g., see images in Figure 2 of the main text for comparison). In comparison, poly[MMA-co-VDMA]$_{Dec}$ mats (C-D) are substantially less disrupted under these conditions (see also companion photographs shown in Figure S4).

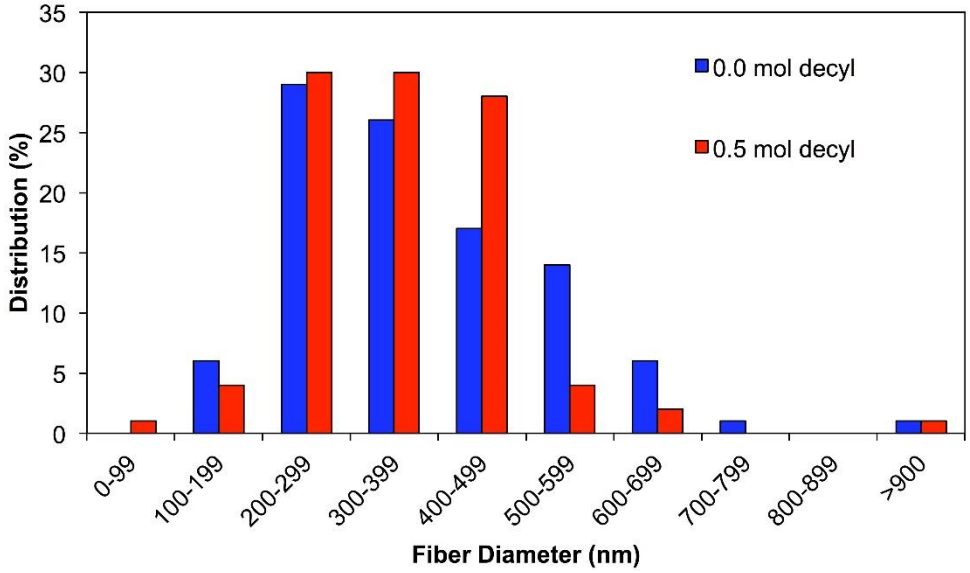

Figure S6: Histogram of fiber diameters for poly[MMA-co-VDMA] (blue bars) and poly[MMA-co-VDMA]$_{Dec}$ nanofibers (red bars). n = 200 measurements for each condition. The distribution of electrospun nanofiber diameters is similar for both polymer systems.

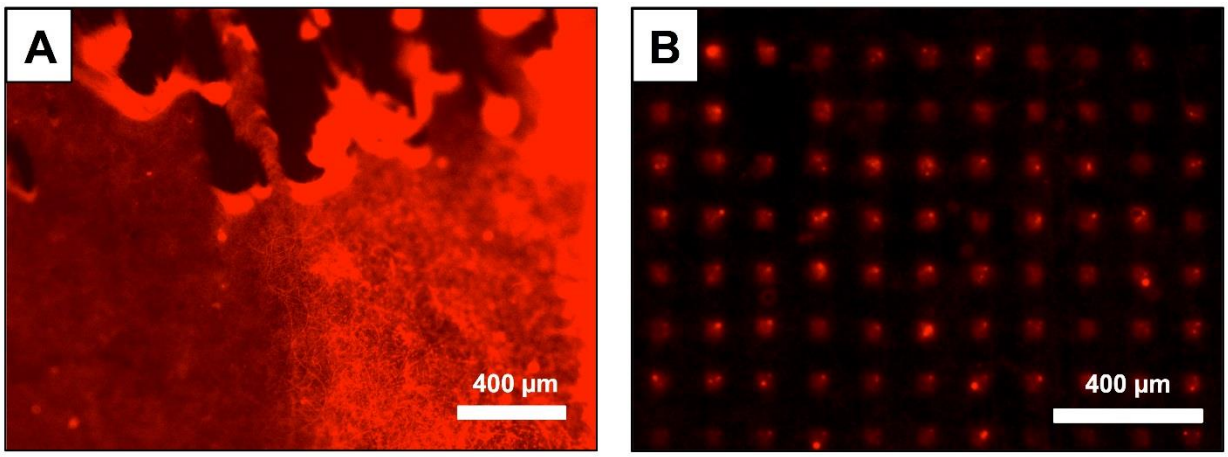

Figure S7: (A-B) Fluorescence microscopy images of (A) poly[MMA-co-VDMA] and (B) poly[MMA-co-VDMA]$_{Dec}$ mats after microcontact printing functionalization with aqueous TMR-Cad (see main text for additional detail of these experiments). The image in (A) reveals irregular and non-uniform regions of fluorescence distributed over large areas and evidence of larger scale changes in mat morphology for the poly[MMA-co-VDMA] mat. The image in (B) is identical to the image shown in Figure 6 of the main text and is included here to facilitate comparisons.

Chapter 13

Synthetic Mimics of Bacterial Lipid A Trigger Optical Transitions in Liquid Crystal Microdroplets at Ultralow Picogram-per-Milliliter Concentrations ‡

‡ Portions of this chapter have previously been published as Carter, M.C.D.; Miller, D.S.; Jennings, J.; Wang, X.; Mahanthappa, M.K.; Abbott, N.L.; Lynn, D.M. "Synthetic Mimics of Bacterial Lipid A Trigger Optical Transitions in Liquid Crystal Microdroplets at Ultralow Picogram-per-Milliliter Concentrations." *Langmuir*, **2015**, *31*, 12850-12855. M.C.D.C. and D.S.M. were co-first authors. D. Miller and X. Wang performed the LC droplet analysis experiments. J. Jennings and I performed the SAXS experiments. My contribution was also in synthesizing the six-tailed amphiphiles, performing the physicochemical characterization experiments, and analyzing the data.

ABSTRACT: We report synthetic six-tailed mimics of the bacterial glycolipid Lipid A that trigger changes in the internal ordering of water-dispersed liquid crystal (LC) microdroplets at ultralow (picogram-per-milliliter) concentrations. These molecules represent the first class of synthetic amphiphiles to mimic the ability of Lipid A and bacterial endotoxins to trigger optical responses in LC droplets at these ultralow concentrations. This behavior stands in contrast to all previously reported synthetic surfactants and lipids, which require near-complete monolayer coverage at the LC droplet surface to trigger ordering transitions. Surface-pressure measurements and SAXS experiments reveal these six-tailed synthetic amphiphiles to mimic key aspects of the self-assembly of Lipid A at aqueous interfaces and in solution. These and other results suggest that these amphiphiles trigger orientational transitions at ultralow concentrations through a unique mechanism that is similar to that of Lipid A and involves formation of inverted self-associated nanostructures at topological defects in the LC droplets.

Introduction

Materials that exhibit macroscopic and easily transduced changes in properties in response to specific molecular stimuli offer unique opportunities to design new classes of sensors and actuators. In this context, supramolecular materials—which derive their structures and properties from weak, non-covalent interactions—are particularly promising because the ordering of these assemblies is easily perturbed by molecular interactions, and the dynamics of reorganization induced by stimuli can be fast.[1-5] In particular, recent studies have demonstrated that a variety of molecular species and assemblies—ranging from simple synthetic surfactants to polyelectrolyte assemblies and protein-receptor complexes—can trigger ordering transitions in thin films and water-dispersed microdroplets of thermotropic liquid crystals (LCs) in ways that can be readily observed and quantified using light.[6-17] These ordering transitions are sensitive to even very small changes in the structures or concentrations of environmental analytes, and thus provide a basis for the design of exceedingly sensitive LC-based sensors.

Of particular relevance to the work reported here, we recently reported that bacterial endotoxins and their six-tailed glycolipid component Lipid A (Figure 1A) can trigger ordering transitions in micrometer-size droplets of LC at remarkably low concentrations (*e.g.*, 1 pg/mL in water; from the so-called 'bipolar' to the 'radial' state, see Figure 1D-I and additional discussion below).[9,18] In contrast, all one- and two-tailed synthetic surfactants and other biological lipids investigated to date trigger ordering transitions in the 10-100 μg/mL range—concentrations that lead to near-complete monolayer coverage of the LC droplets and are five to six orders of magnitude *higher* than those at which Lipid A elicits a response.[8,9,18] The results of past studies suggest that Lipid A promotes optical transitions in LC droplets at such ultra-low concentrations through a fundamentally new mechanism that involves the formation of inverted self-associated

nanostructures at topological defects in the LC.[9,18] The study reported here was motivated by the goal of providing insight into the origins of this ultra-sensitive and specific response of LC microdroplets to Lipid A by exploring designs of synthetic amphiphiles (*e.g.*, Figure 1B) inspired by salient structural features of Lipid A.[19,20]

The design of the synthetic amphiphiles reported here was guided by the hypothesis that the sensitivity of LC droplets to Lipid A arises principally from the multiplicity of tails present in this natural lipid. The six tails of Lipid A, for example, render it more hydrophobic than one- and two-tailed amphiphiles and endow it with other properties (*e.g.*, negative spontaneous curvature resulting from a large ratio of tail volume to head group area) that promote the formation of inverted self-associated structures.[21,22] We note that past studies have reported structurally complex mimics of Lipid A designed to preserve elements of the function of this amphiphile in biological contexts.[19] In contrast, the work reported here sought to explore the design of simple synthetic amphiphiles that mimic aspects of the structure of Lipid A that govern its behavior at liquid/liquid interfaces and trigger ordering transitions in LC droplets, with the goals of (i) providing insights into molecular mechanisms through which LC microdroplets respond to Lipid A, and (ii) expanding the potential significance of the ultrasensitive response of LC microdroplets to Lipid A by incorporating functionality into synthetic mimics that could enable additional stimuli-responsive properties.

Results and Discussion

To design synthetic mimics of Lipid A, we adopted an approach based on the ring-opening of 1,2-epoxyalkanes by primary amines (Figure 1C) for the following reasons: (i) these reactions are robust and proceed in a single step, (ii) this scheme provides ready access to

amphiphiles possessing many aliphatic tails, (iii) both head group structure and the number, length, and structure of hydrophobic tails can be varied systematically, and (iv) each ring-opening reaction affords a hydroxyl group that can be further transformed, if desired, to modify the structures, properties, and phase behaviors of the resulting amphiphiles. This synthetic approach has been used in recent studies to design cationic lipid-like molecules for nucleic acid delivery,[23-26] but reports on the behaviors of this class of amphiphile in aqueous solution and at aqueous/organic interfaces are limited.

We synthesized five six-tailed amphiphiles with aliphatic tail lengths ranging from 6 to 16 carbons by the reaction of tris(2-aminoethyl)amine with a series of 1,2-epoxyalkanes (amphiphiles $\mathbf{1_6}$ to $\mathbf{1_{16}}$; Figure 1C).[23] In the notation used here, the subscript indicates the number of carbons in each aliphatic tail, such that amphiphile $\mathbf{1_{10}}$ consists of a head group containing 4 tertiary amines to which 6 aliphatic tails, each 10 carbons in length, are bound. All compounds were purified by flash chromatography; structure and purity were confirmed by NMR and mass spectrometry (see Supporting Information at the end of this Chapter). In a first set of studies, we characterized the ability of amphiphile $\mathbf{1_{10}}$ to trigger ordering transitions in micrometer-sized droplets of a nematic LC [4'-pentyl-4-cyanobiphenyl (5CB)] using a protocol reported previously to characterize interactions between Lipid A and bacterial endotoxin in LC-in-water emulsions.[9,18] For these experiments, an aqueous dispersion of LC droplets (~5,000 droplets/μL) in a 'bipolar' configuration was added to a solution of $\mathbf{1_{10}}$ to achieve a final concentration of 1000 pg/mL (in the 'bipolar' configuration, the LC is aligned tangentially to the droplet surface, resulting in two topological defects at opposite poles; see Figure 1D,G).[17] Changes in droplet configurations were then determined using polarized light microscopy (see Supporting Information for details). An amphiphile concentration of 1000 pg/mL was selected as an upper

limit for these studies because it corresponds to a concentration 3 orders of magnitude below that required to trigger ordering transitions in LC droplets using conventional surfactants and lipids.[8,9]

Following the addition of amphiphile **1$_{10}$**, we observed all LC droplets to transition from the initial bipolar state (Figure 1D,G) to either a 'radial' configuration (in which the director of the LC is aligned normal to the droplet surface, resulting in a single defect at the center of the droplet; Figure 1F,I) or an 'escaped radial' configuration (Figure 1E,H).[17] In the escaped radial configuration, a single defect similar to that observed in radial droplets is located near, but not in, the geometric center of a droplet (Figure 1E). This configuration has an optical appearance (Figure 1H) that can also be readily distinguished from that of a bipolar droplet when viewed between crossed polarizers.

We further quantified the response to amphiphile **1$_{10}$** in larger populations of LC droplets using flow cytometry. This analytical approach can be used to quantify the percentage of radial droplets in mixtures containing bipolar and radial droplets based on differences in the scattering of light and is significantly faster than methods based on optical microscopy.[27] We characterized the dependence of changes in LC droplet configurations at 5 different concentrations of amphiphile **1$_{10}$** (ranging from 10 to 10,000 pg/mL). We note here that our analysis of scatter plots obtained using flow cytometry (in light scattering mode) enabled us to differentiate between either (i) bipolar or (ii) radial and escaped radial droplets combined (see Supporting Information and Figure S1 for details). Accordingly, we report in Figure 2A the percentage of droplets transformed from the bipolar configuration relative to all droplets characterized. This analysis reveals **1$_{10}$** to trigger ordering transitions in droplets of 5CB at concentrations as low as 100 pg/mL, but not at 10 pg/mL (Figure 2A).

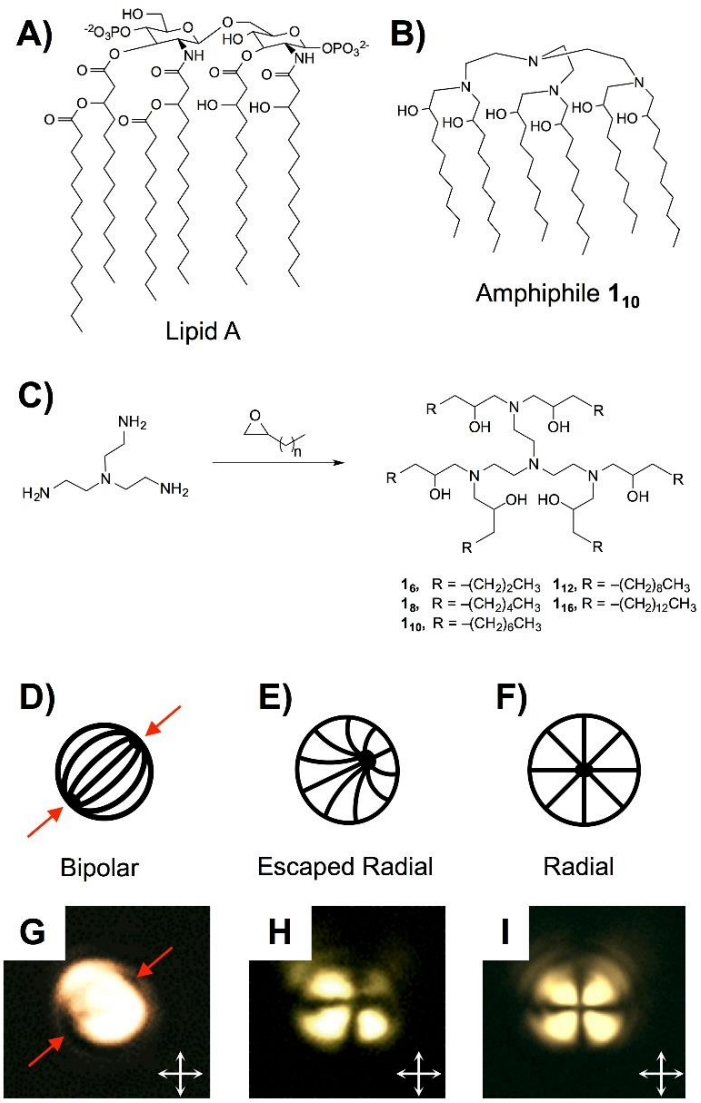

Figure 1. (A,B) Structures of Lipid A and amphiphile **1**$_{10}$. (C) Scheme used to synthesize six-tailed Lipid A mimics. (D-F) Director profiles for LC droplets in (D) bipolar, (E) escaped radial, and (F) radial configurations. (G-I) Polarized light micrographs of microdroplets of 5CB (diameters of ~5 μm) prior to (G) and after (H and I) exposure to amphiphile **1**$_{10}$ (see text). Red arrows in D and G point to topological defects in the bipolar droplets; white arrows (G-I) indicate orientation of crossed polarizers.

Although the threshold concentration required to trigger complete conversion of the bipolar LC droplets using amphiphile **1**$_{10}$ is an order of magnitude higher than that of Lipid A, we note that it is 4 orders of magnitude lower than the concentrations at which conventional

surfactants trigger these transitions.[9] As noted above, past studies using conventional one- and two-tailed amphiphiles have established that ordering transitions in LC droplets require near-complete monolayer coverage of amphiphiles over the droplet surface.[9] At a concentration of 100 pg/mL, however, we calculate the maximum areal density of **1$_{10}$** at the interface of the LC droplets in the experiments above (assuming complete adsorption onto the ~3.9×10^6 droplets in the dispersion) to be 5,000 nm^2/molecule, or only ~10^{-4} of monolayer coverage. Similar to Lipid A, this interfacial concentration of amphiphile **1$_{10}$** is orders of magnitude below that required to trigger changes in the configurations of the LC droplets via formation of a monolayer at the aqueous/LC interface. These results support our conclusion that the structure of this six-tailed amphiphile allows it to drive ordering transitions in LC droplets through a novel mechanism that is similar to that of Lipid A (see additional discussion below).

Past studies of ordering transitions in LC droplets using endotoxin and Lipid A have led to the hypothesis that these natural six-tailed amphiphiles promote changes in the configurations of LC droplets (from bipolar to radial) through a mechanism involving the formation of inverted self-associated lipid nanostructures at topological defects in the LC droplets (Figure 1D, red arrows; these defects correspond to regions of high strain where LC order is reduced).[9,18] This mechanism differs substantially from that involving one- and two-tailed surfactants (described above). The tendency of an amphiphile to adopt inverted self-assembled nanostructures is dependent, in part, on the ratio of head group area to molecular volume (the so-called 'packing parameter').[22,28] Because amphiphile **1$_{10}$** has the same number and approximate tail length as Lipid A, the molecular volumes of the two should be similar. To determine if amphiphile **1$_{10}$** possesses a molecular area comparable to Lipid A, and thus a comparable packing parameter, we characterized their interfacial molecular areas by measuring Langmuir isotherms at air/water

interfaces. A comparison of the isotherms of these two species (Figure 2B) reveals the mean molecular area of **1**$_{10}$ and Lipid A to be ~175 Å^2 and ~150 Å^2, respectively, suggesting that like Lipid A, amphiphile **1**$_{10}$ can assume a packing geometry consistent with formation of inverted self-associated nanostructures. We note here, however, that there are also some significant differences between the two isotherms in Figure 2B, including evidence of phase transitions at intermediate surface pressures for Lipid A that are not apparent for amphiphile **1**$_{10}$.

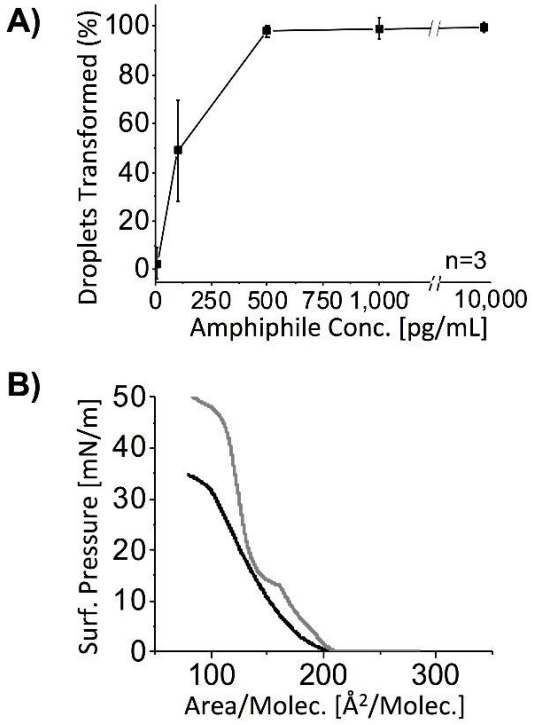

Figure 2: (A) Percentage of droplets transformed from the bipolar state *v.* concentration of amphiphile **1**$_{10}$. (B) Langmuir isotherms measured during compression of monolayers of amphiphile **1**$_{10}$ (black) or Lipid A (grey) at air/water interfaces at 25 °C.

To explore other potential similarities in the fundamental self-assembly behaviors of amphiphile **1**$_{10}$ and Lipid A that could provide insight into the results described above, we used

small angle X-ray scattering (SAXS) to characterize the nanostructures formed by these amphiphiles in bulk solution (*i.e.*, in water or aqueous buffer, and not in the presence of LC droplets). Pure amphiphile $\mathbf{1}_{10}$ did not form lyotropic liquid crystalline phases in water or in phosphate-buffered saline that we could observe by SAXS. We note, however, that Lipid A possesses negatively charged phosphate functionality in its head group (Figure 1A) that is expected to influence self-assembly. Acidification of solutions of amphiphile $\mathbf{1_{10}}$ (0.133 wt % in 1.0 M aqueous H_2SO_4) to protonate the amines in the head group and promote formation of a multi-tailed, cationic analogue of Lipid A led to the immediate precipitation of lyotropic liquid crystalline particles. SAXS profiles for amphiphile $\mathbf{1}_{10}$ exhibited an unusual peak pattern under these conditions, including 4 high intensity peaks located at $q^*\sqrt{3}$, $q^*\sqrt{4}$, $q^*\sqrt{5}$, and $q^*\sqrt{6}$ (where $q^* = 0.1258$ Å^{-1}) (Figure 3). These scattering maxima are tentatively ascribed to the (111), (200), (210) and (211) reflections of a micellar cubic phase with $P4_232$ symmetry (space group #208) with a unit cell dimension d = 50 Å. The persistence of this lyotropic phase in the presence of excess acid solution strongly suggests that amphiphile $\mathbf{1}_{10}$ forms an inverse phase. This result is similar in some important ways to the previously reported lyotropic liquid crystalline phase behaviour of Lipid A, which also forms inverse cubic phases at high water content.[21,22,29,30] We note in this context that past SAXS studies have investigated the bulk solution phase behaviours of Lipid A using conditions different from the strongly acidic conditions used here,[21,22] and that more explicit comparisons between the self-assembly behaviors of Lipid A and amphiphile $\mathbf{1}_{10}$ should thus be made with caution. Nevertheless, the results shown in Figure 3 demonstrate that amphiphile $\mathbf{1}_{10}$ can form inverse phases in aqueous solution, and provide support for the proposition that amphiphile $\mathbf{1_{10}}$, like Lipid A, can trigger transitions of LC droplets at ultra-low concentrations *via* the formation of inverted nanostructures at defects in the LC droplets.

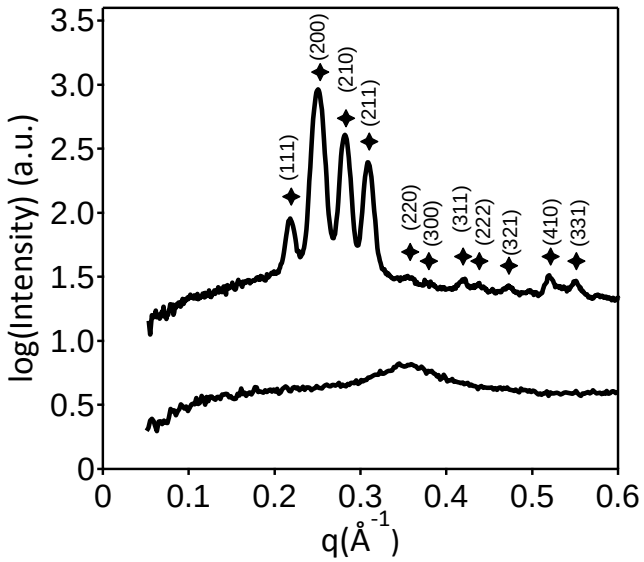

Figure 3: SAXS patterns for amphiphile $\mathbf{1_{10}}$ (*upper*) and amphiphile $\mathbf{1_6}$ (*lower*) in 1M aqueous H_2SO_4 at 22 °C. Peak markers correspond to positions of expected reflections for a cubic morphology with $P4_232$ symmetry with unit cell dimension d = 50 Å (q^*= 0.126 Å^{-1}).

Experiments performed using amphiphiles $\mathbf{1_6}$, $\mathbf{1_8}$, $\mathbf{1_{12}}$, and $\mathbf{1_{16}}$ revealed the impact of tail length on the interfacial behavior of this class of six-tailed amphiphiles at aqueous/LC interfaces. As shown in Figure 4A, amphiphiles $\mathbf{1_8}$ and $\mathbf{1_{12}}$, possessing aliphatic tails 8 and 12 carbons in length, were also able to trigger LC droplets (at concentrations of 500 pg/mL). In contrast, species with tails 6 or 16 carbons in length ($\mathbf{1_6}$ and $\mathbf{1_{16}}$) did not. The apparent insensitivity of LC droplets to the presence of amphiphile $\mathbf{1_{16}}$ is likely a result of the sparing water solubility of this amphiphile under the conditions used here. We speculate that the inability of amphiphile $\mathbf{1_6}$ to trigger ordering transitions in LC droplets arises from the influence of its shorter tail length on self-assembly. Langmuir isotherms revealed molecular areas at air/water interfaces to decrease significantly with decreasing tail length (from ~175 Å^2 for amphiphile $\mathbf{1_{10}}$ to ~105 Å^2 for amphiphile $\mathbf{1_6}$; see Figure S2). In addition, SAXS characterization of amphiphile $\mathbf{1_6}$ in 1.0 M H_2SO_4 indicates that it does not self-assemble into the inverse cubic lyotropic phase observed

with amphiphile **1**$_{10}$ (Figure 3) under the conditions investigated here. Our results suggest that a critical amphiphile tail length is required to drive self-assembly into nanostructures that trigger ordering transitions in LC droplets.

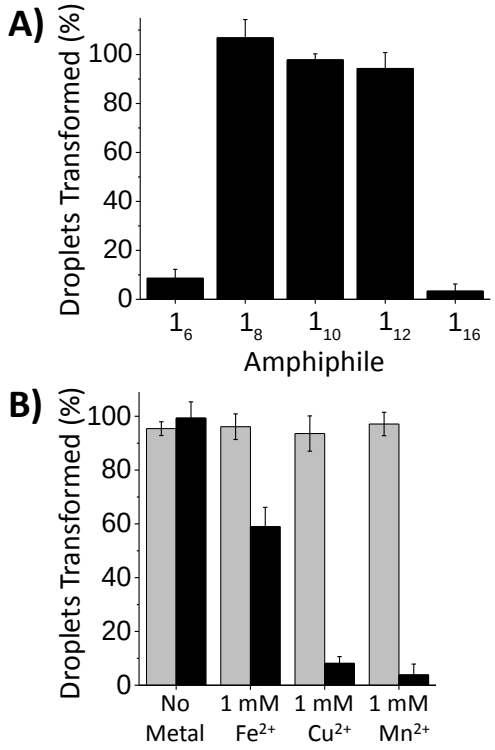

Figure 4: (A) Percent of LC droplets transformed as a function of amphiphile tail length using amphiphiles **1**$_6$–**1**$_{16}$ ([**1**]=500 pg/mL). (B) Percent of LC droplets transformed in solutions of amphiphile **1**$_{10}$ (black) or Lipid A (grey) in the presence or absence of $FeSO_4$, $CuSO_4$, or $MnCl_2$ ([M^{2+}] = 1 mM, [**1**$_{10}$] = 500 pg/mL).

Amphiphiles **1**$_8$, **1**$_{10}$, and **1**$_{12}$ mimic the ability of Lipid A to trigger ordering transitions in LC droplets at exceedingly low concentrations. We note, however, that these amphiphiles have a head group functionality that differs substantially from the disaccharide-based head group of Lipid A, and that could endow these synthetic structures with the potential to respond to

environmental stimuli in ways that Lipid A does not (*e.g.*, to changes in pH or the chelation of multivalent metal ions, *etc.*). To explore the potential utility of this new structural feature, we performed a final series of proof-of-concept experiments to determine whether the ability of amphiphile **1$_{10}$** to trigger configurational transitions in LC droplets could be modulated by the presence of divalent metal ions in the aqueous phase (using flow cytometry to quantify changes in droplet configurations, as described above). As shown in Figure 4B (grey bars), the responses of LC droplets to Lipid A remained insensitive to the addition of three divalent metal ions (Fe^{2+}, Cu^{2+}, Mn^{2+}; [M^{2+}] = 1 mM, [**1$_{10}$**] = 500 pg/mL; pH = 7.2) under these conditions. However, as shown in Figure 4B (black bars), the responses of LC droplets to amphiphile **1$_{10}$** were strongly suppressed (to extents that varied with the identity of the metal ion used). This stimuli-responsive behavior is consistent with chelation of the metal ions by the polyamine head group of **1$_{10}$** and subsequent associated changes in self-assembly. Additional studies will be necessary to characterize the sensitivity of these six-tailed amphiphiles to the presence of ions and understand their impacts on self-assembly and the apparent selectivity (*e.g.,* Fe^{2+} relative to Cu^{2+} or Mn^{2+}) shown in Figure 4B. The results of these initial experiments, however, suggest potential opportunities to use amphiphile **1$_{10}$** in combination with LC droplets to report the presence of specific ions in aqueous environments. More broadly, the nature of the polyamine head group in these synthetic amphiphiles could also enable the design of amphiphile/LC droplet systems that respond to changes in a broader range of environmental stimuli (pH, ionic strength, *etc.*).

Summary and Conclusions

In summary, the synthetic amphiphiles reported here mimic key features of the structure, interfacial behaviors, and self-assembly of Lipid A and provide insight into the origins of the

ultra-sensitive response of LC droplets to Lipid A. We anticipate that the materials and guiding principles reported here will enable the design of colloidal LC droplet systems that respond with exquisite sensitivity to chemical and biological stimuli and open the door to new applications of this emerging class of responsive soft matter.

Acknowledgments. This work was supported by the NSF (DMR-1121288, CHE-9974839, CHE-1048642), the ARO (W911NF-11-1-0251 and W911NF-14-1-0140), and the NIH (CA108467 and CA105730), and made use of and made use of NSF-supported facilities. M.C.D.C acknowledges the Natural Sciences and Engineering Research Council of Canada for a graduate fellowship.

References

1. Badjic, J. D.; Nelson, A.; Cantrill, S. J.; Turnbull, W. B.; Stoddart, J. F., Multivalency and cooperativity in supramolecular chemistry. *Acc. Chem. Res.* **2005,** *38*, 723-732.

2. Woltman, S. J.; Jay, G. D.; Crawford, G. P., Liquid-crystal materials find a new order in biomedical applications. *Nat. Mater.* **2007,** *6*, 929-938.

3. Aida, T.; Meijer, E. W.; Stupp, S. I., Functional Supramolecular Polymers. *Science* **2012,** *335*, 813-817.

4. Yan, X.; Wang, F.; Zheng, B.; Huang, F., Stimuli-responsive supramolecular polymeric materials. *Chem. Soc. Rev.* **2012,** *41*, 6042-6065.

5. Zhuang, J.; Gordon, M. R.; Ventura, J.; Li, L.; Thayumanavan, S., Multi-stimuli responsive macromolecules and their assemblies. *Chem. Soc. Rev.* **2013,** *42*, 7421-7435.

6. Brake, J. M.; Daschner, M. K.; Luk, Y. Y.; Abbott, N. L., Biomolecular interactions at phospholipid-decorated surfaces of liquid crystals. *Science* **2003,** *302*, 2094-2097.

7. Price, A. D.; Schwartz, D. K., DNA Hybridization-Induced Reorientation of Liquid Crystal Anchoring at the Nematic Liquid Crystal/Aqueous Interface. *J. Am. Chem. Soc.* **2008,** *130*, 8188-8194.

8. Gupta, J. K.; Sivakumar, S.; Caruso, F.; Abbott, N. L., Size-Dependent Ordering of Liquid Crystals Observed in Polymeric Capsules with Micrometer and Smaller Diameter. *Angew. Chem. Intl. Ed.* **2009,** *48*, 1652-1655.

9. Lin, I. H.; Miller, D. S.; Bertics, P. J.; Murphy, C. J.; de Pablo, J. J.; Abbott, N. L., Endotoxin-induced structural transformations in liquid crystalline droplets. *Science* **2011,** *332*, 1297-300.

10. Alino, V. J.; Pang, J.; Yang, K. L., Liquid Crystal Droplets as a Hosting and Sensing Platform for Developing Immunoassays. *Langmuir* **2011,** *27*, 11784-11789.

11. McUmber, A. C.; Noonan, P. S.; Schwartz, D. K., Surfactant-DNA interactions at the liquid crystal-aqueous interface. *Soft Matter* **2012,** *8*, 4335-4342.

12. Alino, V. J.; Sim, P. H.; Choy, W. T.; Fraser, A.; Yang, K.-L., Detecting Proteins in Microfluidic Channels Decorated with Liquid Crystal Sensing Dots. *Langmuir* **2012,** *28*, 17571-17577.

13. Bera, T.; Fang, J., Polyelectrolyte-coated liquid crystal droplets for detecting charged macromolecules. *J. Mater. Chem.* **2012,** *22*, 6807-6812.

14. Kim, J.; Khan, M.; Park, S. Y., Glucose Sensor using Liquid-Crystal Droplets Made by Microfluidics. *ACS Appl. Mater. Inter.* **2013,** *5*, 13135-13139.

15. Noonan, P. S.; Roberts, R. H.; Schwartz, D. K., Liquid Crystal Reorientation Induced by Aptamer Conformational Changes. *J. Am. Chem. Soc.* **2013,** *135*, 5183-5189.

16. Chang, C.-Y.; Chen, C.-H., Oligopeptide-decorated liquid crystal droplets for detecting proteases. *Chem. Commun.* **2014,** *50*, 12162-12165.

17. Miller, D. S.; Wang, X.; Abbott, N. L., Design of Functional Materials Based on Liquid Crystalline Droplets. *Chem. Mater.* **2014,** *26*, 496-506.

18. Miller, D. S.; Abbott, N. L., Influence of droplet size, pH and ionic strength on endotoxin-triggered ordering transitions in liquid crystalline droplets. *Soft Matter* **2013,** *9*, 374-382.

19. Molinaro, A.; Holst, O.; Di Lorenzo, F.; Callaghan, M.; Nurisso, A.; D'Errico, G.; Zamyatina, A.; Peri, F.; Berisio, R.; Jerala, R.; Jimenez-Barbero, J.; Silipo, A.; Martin-Santamaria, S., Chemistry of Lipid A: At the Heart of Innate Immunity. *Chem. Eur. J.* **2015,** *21*, 500-519.

20. Matsuura, M., Structural modifications of bacterial lipopolysaccharide that facilitate Gram-negative bacteria evasion of host innate immunity. *Front. Immunol.* **2013,** *4*, 1-9.

21. Brandenburg, K.; Koch, M. H. J.; Seydel, U., Phase-Diagram of Lipid-A from Samonella-Minnesota and Escherichia-coli Rough Mutant Lipopolysaccharide. *J. Struct. Biol.* **1990,** *105*, 11-21.

22. Brandenburg, K.; Seydel, U.; Schromm, A. B.; Loppnow, H.; Koch, M. H. J.; Rietschel, E. T., Conformation of lipid A, the endotoxic center of bacterial lipopolysaccharide. *J. Endotoxin Res.* **1996,** *3*, 173-178.

23. Love, K. T.; Mahon, K. P.; Levins, C. G.; Whitehead, K. A.; Querbes, W.; Dorkin, J. R.; Qin, J.; Cantley, W.; Qin, L. L.; Racie, T.; Frank-Kamenetsky, M.; Yip, K. N.; Alvarez, R.; Sah, D. W. Y.; de Fougerolles, A.; Fitzgerald, K.; Koteliansky, V.; Akinc, A.; Langer, R.; Anderson, D. G., Lipid-like materials for low-dose, in vivo gene silencing. *Proc. Natl. Acad. Sci. U. S. A.* **2010,** *107*, 1864-1869.

24. Sun, S.; Wang, M.; Knupp, S. A.; Soto-Feliciano, Y.; Hu, X.; Kaplan, D. L.; Langer, R.; Anderson, D. G.; Xu, Q. B., Combinatorial Library of Lipidoids for In Vitro DNA Delivery. *Bioconjugate Chem.* **2012,** *23*, 135-140.

25. Zhang, Y. L.; Pelet, J. M.; Heller, D. A.; Dong, Y. Z.; Chen, D. L.; Gu, Z.; Joseph, B. J.; Wallas, J.; Anderson, D. G., Lipid-Modified Aminoglycoside Derivatives for In Vivo siRNA Delivery. *Adv. Mater.* **2013,** *25*, 4641-4645.

26. Sun, S.; Wang, M.; Alberti, K. A.; Choy, A.; Xu, Q. B., DOPE facilitates quaternized lipidoids (QLDs) for in vitro DNA delivery. *Nanomed. Nanotechnol.* **2013,** *9*, 849-854.

27. Miller, D. S.; Wang, X.; Buchen, J.; Lavrentovich, O. D.; Abbott, N. L., Analysis of the Internal Configurations of Droplets of Liquid Crystal Using Flow Cytometry. *Anal. Chem.* **2013,** *85*, 10296-10303.

28. Israelachvili, J. N., *Intermolecular and Surface Forces: Revised Third Edition*. 3rd ed.; 2011.

29. Seydel, U.; Brandenburg, K.; Koch, M. H. J.; Rietschel, E. T., Supramolecular Structure of Lipopolysaccharide and Free Lipid-a under Physiological Conditions as Determined by Synchrotron Small-Angle X-Ray-Diffraction. *Eur. J. Biochem.* **1989,** *186*, 325-332.

30. Brandenburg, K.; Koch, M. H. J.; Seydel, U., Phase-Diagram of Deep Rough Mutant Lipopolysaccharide from Salmonella-Minnesota R595. *J. Struct. Biol.* **1992,** *108*, 93-106.

Supporting Information for Chapter 13

Materials and General Considerations. Tris(2-aminoethyl)amine (TREN, 96%) was purchased from Acros Organics (Morris Plains, NJ). 1,2-Epoxyhexane (>96%) and 1,2-epoxyhexadecane (>80%) were purchased from TCI America (Philadelphia, PA); 1,2-epoxyoctane (99%), 1,2-epoxydecane (97%) and 1,2-epoxydodecane (95%) were purchased from Alfa Aesar (Radnor, PA). Lipid A from *Escherichia coli F583* (Rd mutant, 1800 Da), sodium dodecyl sulfate (SDS), triethylamine (TEA), sulfuric acid (H_2SO_4) and phosphate-buffered saline (PBS) pouches (used to make PBS buffer as the sheath fluid for flow cytometry), dichloromethane (HPLC grade, >99.8%), chloroform ($CHCl_3$; HPLC grade, >99.8%), aqueous ammonium hydroxide solution (ACS grade, 28-30%), deuterated chloroform ($CDCl_3$, 99.8%) and deuterated methanol (MeOD, 99.8%) were purchased from Sigma-Aldrich (Milwaukee, WI). Methanol (MeOH; ACS grade) was purchased from Avantor Performance Materials (Center Valley, PA). 4'-Pentyl-4-cyanobiphenyl (5CB) was obtained from EM Sciences (New York, NY). EndoTrap® Red Equilibration Buffer [10 mM Na_2HPO_4/NaH_2PO_4, 80 mM NaCl, pH 7.2; certified to contain a concentration of endotoxin of less than 0.02 EU/mL (2 pg/ mL)] was purchased from Hyglos GmbH (Regensburg, Germany). Iron (II) sulfate ($FeSO_4$), copper (II) sulfate ($CuSO_4$), and manganese (II) chloride ($MnCl_2$) were purchased from Sigma-Aldrich ($FeSO_4$ and $CuSO_4$) and Fisher Scientific ($MnCl_2$; Pittsburgh, PA). Neptune pipette tips (no detectable endotoxin) were purchased from Continental Lab Product, Inc. (San Diego, CA). Fisher's Finest PremiumGrade cover glass, Wheaton glass 20 mL scintillation vials, 1.5 mL FisherBrand micro-centrifuge tubes, 12 x 75 mm disposable glass culture tubes, and a 10 µL glass Hamilton blunt-tipped syringe were obtained from Fisher Scientific. Quartz capillary tubes (1.5 mm diameter) used for SAXS experiments were obtained from Hampton Research (Aliso Viejo, CA). Deionization of a

distilled water source was performed with a Milli-Q system (Millipore, Bedford, MA) to give water with a resistivity of 18.2 MΩ cm (referred to as Milli-Q water below). SilicaFlash P60 silica gel (230-400 mesh) was purchased from Silicycle (Quebec City, QC). Silica gel TLC plates were purchased from Sigma-Aldrich (Milwaukee, WI); spots were visualized using iodine and anisaldehyde stains. ^{1}H and ^{13}C NMR spectra were recorded on a Bruker Avance III 500 spectrometer. NMR chemical shift values are given in ppm and are referenced to the residual protons of $CDCl_3$ (δ 7.26, 77.2) or deuterated methanol (δ 3.31). Mass spectrometry was performed on a Waters LCT electrospray ionization time-of-flight mass spectrometer using 10 mM NH_4OAc/CH_3CN in methanol at a flow rate of 40 uL/min. Unless otherwise noted, materials were used as received without further purification.

Synthesis of Six-Tailed Amphiphiles. Amphiphiles $\mathbf{1_6}$ – $\mathbf{1_{16}}$ were synthesized using the following general procedure. TREN (1.0 eq) and an epoxide having the desired aliphatic chain length (6.6 eq) were weighed into a 6 mL glass vial equipped with a magnetic stir bar. The vial was briefly purged with nitrogen and then sealed with a Teflon-lined cap and Parafilm, and placed into an oil bath at 90 °C for 4 days. Crude reaction products were diluted by approximately half with DCM and then purified by flash chromatography on silica gel using gradient elution from 100% DCM to 75:22:3 DCM/MeOH/$NH_4OH_{(aq)}$. (In 100% DCM: $R_{f\ (1,2\text{-epoxydecane})} = 0.54$; $R_{f\ (\mathbf{1_{10}})} \sim 0$. In 75:22:3 DCM/MeOH/$NH_4OH_{(aq)}$: $R_{f\ (1,2\text{-epoxydecane})} = 1.00$; $R_{f\ (\mathbf{1_{10}})} = 0.95$). Solvent was evaporated under reduced pressure and purified amphiphiles were dried under high vacuum overnight. Representative ^{1}H and ^{13}C NMR spectra for each amphiphile are given below.

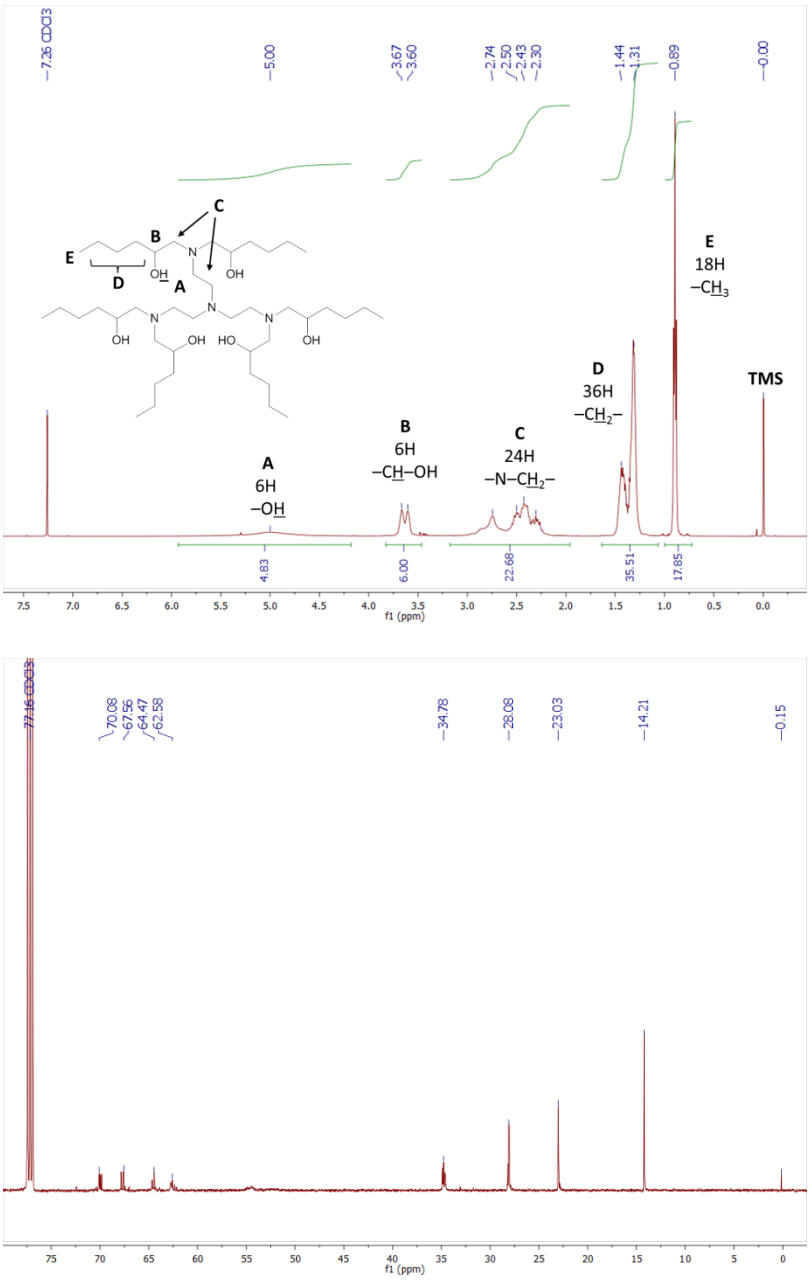

Amphiphile 1$_6$: Yield: 90.7%, viscous yellow oil. ^{1}H NMR (500.022 MHz, $CDCl_3$): δ 0.89 (t, J = 6.92 Hz, 18H), 1.22-1.53 (m, 36H), 2.08-3.04 (m, 24H), 3.65 (d, J = 30.63 Hz, 6H), 5.00 (s, 6H). ^{13}C NMR (125.74 MHz, $CDCl_3$): 14.21, 23.03, 28.08, 34.78 (m), 62.58 (m), 64.57 (m), 67.56 (m), 70.08 (m). MS (ESI+) found: $[M+H]^+$ 747.6; $[M+2H]^{2+}$ 374.3

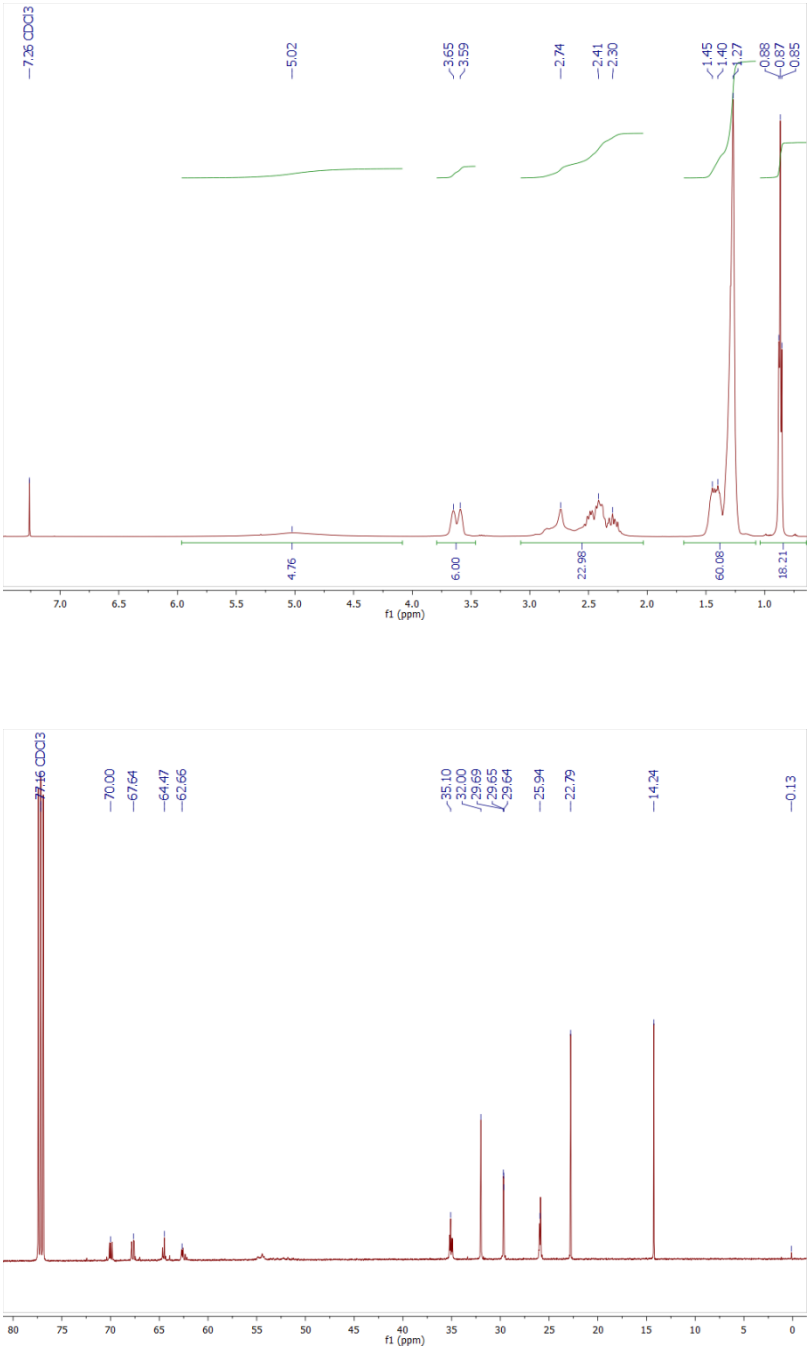

Amphiphile 1$_8$: Yield: 91.0%, viscous yellow oil. ^{1}H NMR (500.022 MHz, $CDCl_3$): δ 0.87 (t, J = 6.60 Hz, 18H), 1.10-1.60 (m, 60H), 2.06-3.05 (m, 24H), 3.63 (d, J = 28.83 Hz, 6H), 5.02 (s, 6H). ^{13}C NMR (125.74 MHz, $CDCl_3$): 14.24, 22.79, 25.94 (m), 29.64 (m), 32.00, 35.10 (m), 62.66 (m), 64.47 (m), 67.64 (m), 70.00 (m). MS (ESI+) found: $[M+H]^+$ 915.9; $[M+2H]^{2+}$ 458.5

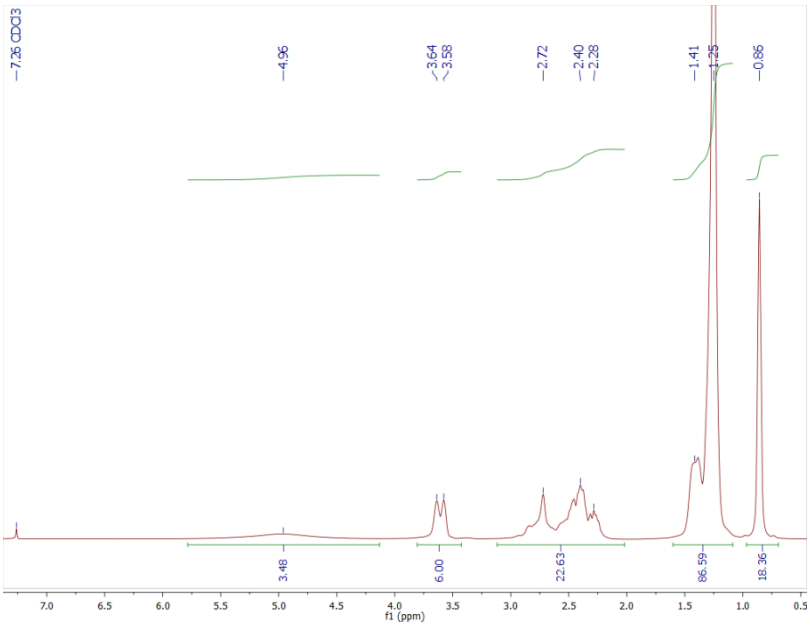

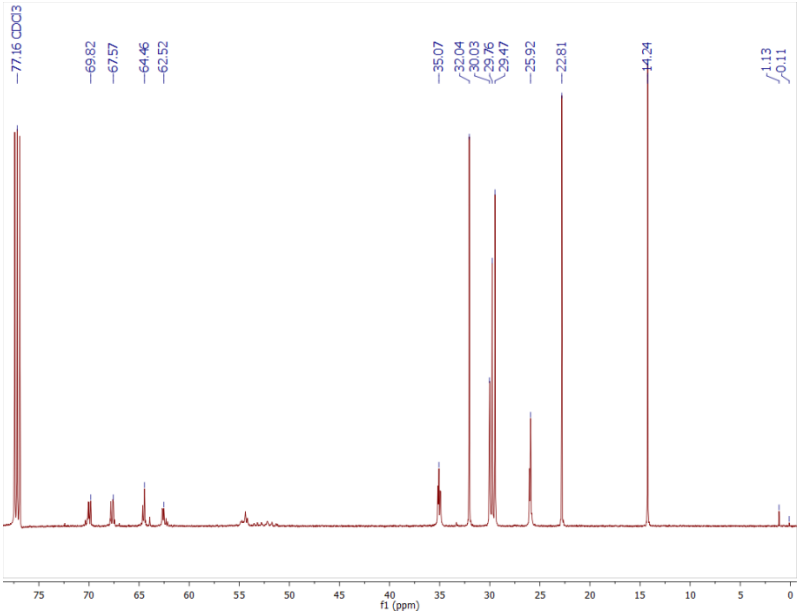

Amphiphile 1$_{10}$: Yield: 88.2%, viscous yellow oil. ^{1}H NMR (500.022 MHz, $CDCl_3$): δ 0.87 (t, J = 6.80 Hz, 18H), 1.05-1.57 (m, 84H) 2.16-3.05 (m, 24H), 3.62 (d, J = 28.95 Hz, 6H), 4.99 (s, 6H). ^{13}C NMR (125.74 MHz, $CDCl_3$): 14.24, 22.841, 25.92 (m), 29.47, 29.76, 30.03, 32.04, 35.07 (m), 65.52 (m), 67.57 (m), 67.57 (m) 69.82 (m). MS (ESI+) found: $[M+H]^+$ 1084.2; $[M+2H]^{2+}$ 542.6

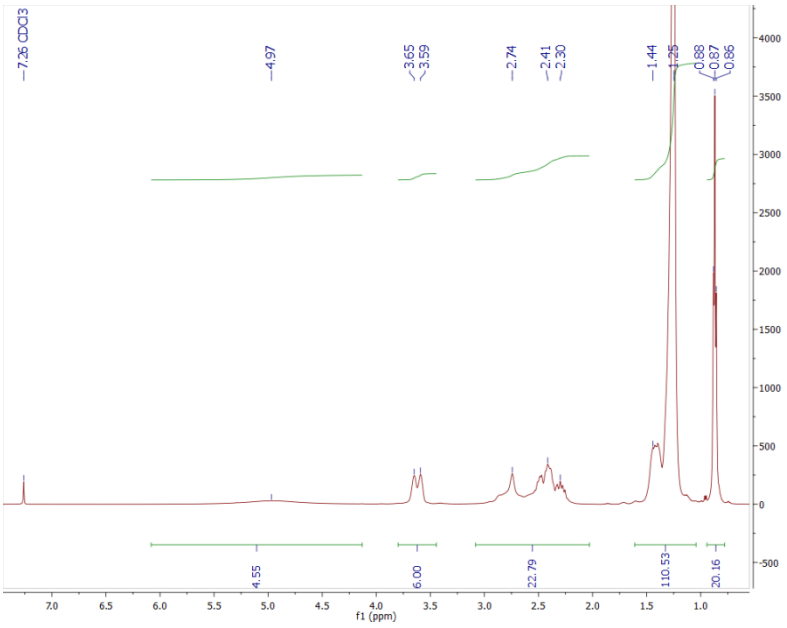

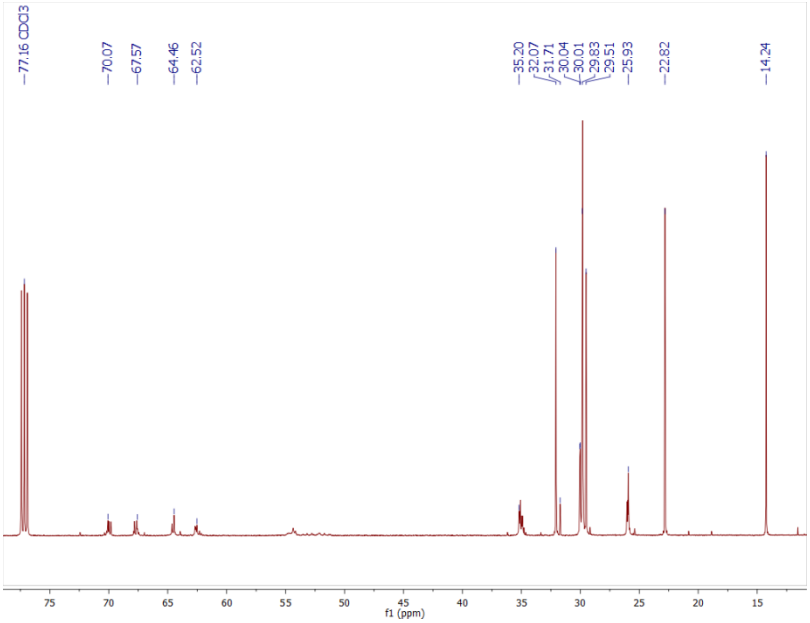

Amphiphile 1$_{12}$: Yield: 95.3%, viscous yellow oil. ^{1}H NMR (500.022 MHz, $CDCl_3$): δ 0.87 (t, J = 6.66 Hz, 18H), 1.08-1.56 (m, 108H) 2.15-3.00 (m, 24H), 3.58 (d, J = 29.19 Hz, 6H), 4.97 (s, 6H). ^{13}C NMR (125.74 MHz, $CDCl_3$): 14.24, 22.82, 25.93 (m), 29.51, 29.83, 30.03 (d, J = 3.77 Hz), 31.71, 32.0, 35.20 (m), 62.52 (m), 64.46 (m), 67.57 (m), 70.07 (m). MS (ESI+) found: $[M+H]^+$ 1252.0; $[M+2H]^{2+}$ 626.5

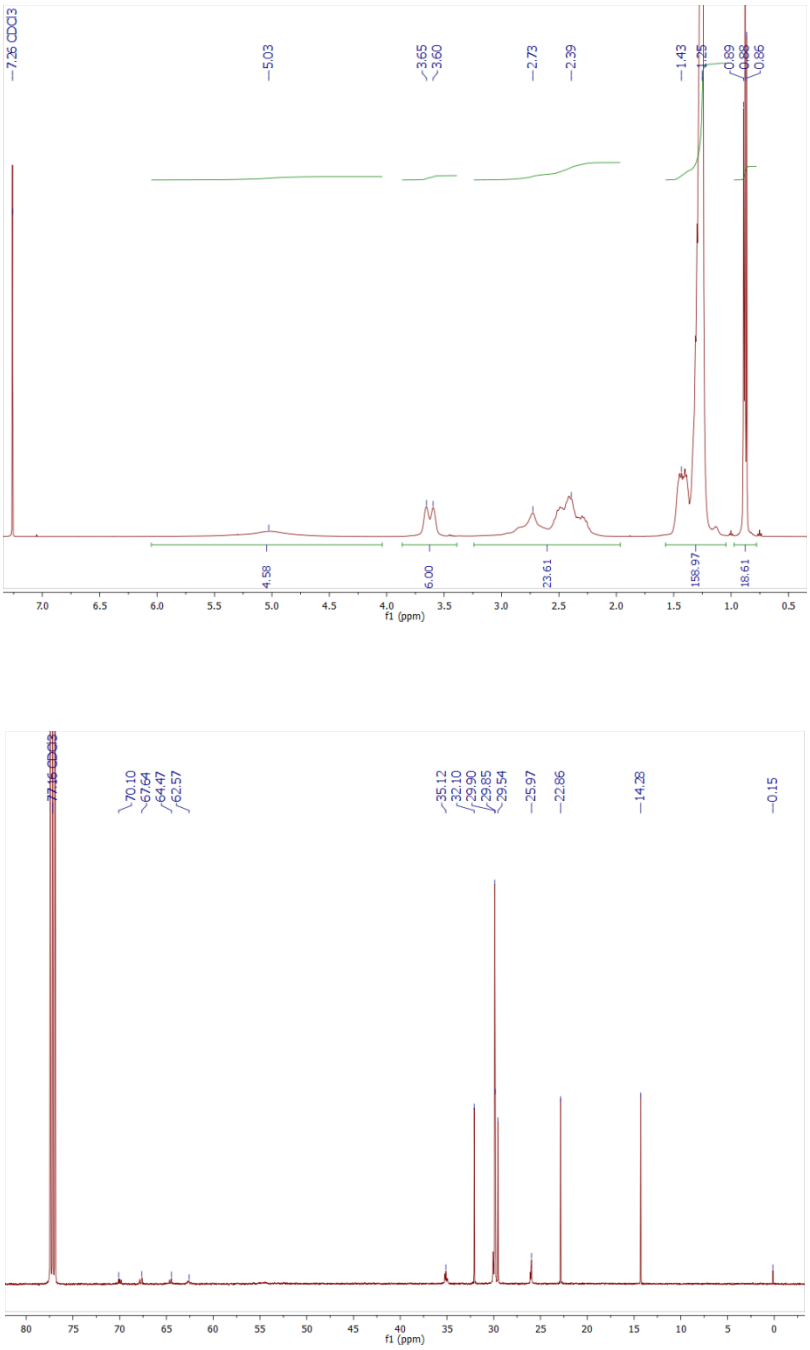

Amphiphile 1_{16}: Yield: 81.0%, light brown paste. ^{1}H NMR (500.022 MHz, $CDCl_3$): δ 0.88 (t, J = 6.96 Hz, 18H), 1.06-1.54 (m, 156H) 2.12-3.19 (m, 24H), 3.63 (d, J = 29.15 Hz, 6H), 5.03 (s, 6H). ^{13}C NMR (125.74 MHz, $CDCl_3$): 14.14, 22.71, 25.82 (m) 29.40, 29.70 (m), 31.95, 34.98 (m), 62.48 (m), 64.32 (m), 67.50 (m), 69.96 (m). MS (ESI+) found: $[M+H]^+$ 1588.9; $[M+2H]^{2+}$ 794.4

Preparation of Aqueous Dispersions of Lipid A. Powdered Lipid A (1 mg) was dissolved in 1 mL of a 10 µM solution of SDS in EndoTrap® Red Equilibration Buffer [also containing 0.2% (v/v) TEA] at room temperature. The resulting solution was then subjected to two cycles of sonication for 5 s using a Branson Sonifier 250 (Emerson Electric Company, St. Louis, MO) and vortex mixing at 2,500 rpm for 1 minute. Following mixing, the 1 mg/mL stock solution was divided into 80 µL aliquots and stored -80 °C for future use. Serial dilutions were performed by first removing an 80 µL aliquot of 1 mg/mL Lipid A from the freezer and allowing the solution to warm to room temperature. This stock was then vortexed at 2,500 rpm for 30 s, and serial dilutions were performed to reach final desired concentrations.

Preparation of Aqueous Dispersions of Synthetic Amphiphiles. The desired amphiphile (~1 mg) was weighed into a 12 x 75 mm disposable glass culture tube and a desired volume of a 10 µM solution of SDS in EndoTrap® Red Equilibration Buffer [also containing 0.2% (v/v) TEA] was added at room temperature to reach a final concentration of 1 mg/mL. The resulting dispersion was then subjected to two cycles of vortex mixing at 3,000 rpm for 30 s followed by sonication for 15 min in a water bath at 55 °C, and serial dilutions were performed to reach final desired concentrations.

Preparation of LC Emulsions and Dilution into Aqueous Dispersions of Amphiphiles. LC-in-water emulsions were formed by adding 6 µL of 5CB to the bottom of a 12 x 75 mm disposable glass culture tube using a 10 µL blunt-tipped syringe. Then, 3 mL of a 10 µM solution of SDS in EndoTrap® Red Equilibration Buffer was added to the tube, and the mixture was vortexed for 30 s at 3,000 rpm. A concentration of 10 µM SDS was selected because it led to

reproducible emulsions without influencing the configuration of the 5CB droplets. The emulsions were allowed to incubate for 1 hour prior to dilution to allow measurable coalescence to arrest. As described in past studies,[1] this emulsification procedure resulted in relatively polydisperse emulsions with droplet sizes ranging between 1 and 20 μm in diameter. Finally, 70 μL aliquots of the stock emulsions were diluted into 700 μL of aqueous dispersions of either Lipid A or the desired amphiphile, and the emulsion was allowed to incubate for at least 3 hours prior to characterization by light scattering by flow cytometry (a 3 hour incubation was found to be optimal for the ordering transitions induced by the amphiphiles to reach completion; see below for additional details). We measured this emulsion-to-sample volume ratio to result in an average droplet concentration of 5,600 ± 1,000 LC droplets/μL.

Characterization of LC Emulsions by Flow Cytometry. Frequency histograms of the intensity of forward light scattering (FSC) were obtained for LC emulsions using a BD Accuri C6 flow cytometer (Ann Arbor, MI). FSC was measured at a detection angle of 0° ± 15°; all flow cytometry measurements were performed at room temperature. Emulsions were pumped through the flow cytometer at a flow rate of 14 μL/min and histograms were constructed from data collected from the measurement of 5,000 LC droplets.

Calculation of the Percentage of Radial Droplets Contained in a LC Emulsion from Frequency Histograms of FSC. The percentage of radial droplets contained in a LC emulsion was quantified according to our previously reported procedure.[2, 3] Briefly, for a given emulsion, the number of light scattering events measured between 30,000 a.u. and 60,000 a.u. was compared to the number of events measured within this region for an emulsion of LC droplets

dispersed in 100 ng/mL Lipid A (positive control), because this concentration of Lipid A was found to lead to a pure population of radial droplets. The following equation was used to calculate the percentage of radial LC droplets contained in an emulsion from the peak occurring between 30,000 a.u. and 60,000 a.u in frequency histograms of FSC values:

$$\text{Percent Radial} = \frac{\sum_{FSC=30,000}^{60,000} Count|_{emulsion} - \sum_{FSC=30,000}^{60,000} Count|_{10\mu MSDS}}{\sum_{FSC=30,000}^{60,000} Count|_{\frac{100ng}{mL}} - \sum_{FSC=30,000}^{60,000} Count|_{10\mu MSDS}} \times 100\% \qquad (1)$$

In Equation 1, the area below the peak measured for an emulsion of LC droplets dispersed in a 10 μM aqueous solution of SDS (negative control) is subtracted from the integrated area under each peak as a baseline. Then, the percentage of the corrected area under each peak relative to the area under the corrected peak measured for the positive control is calculated.

Optical Characterization of LC Emulsions by Polarized Light Microscopy. LC emulsions were characterized by polarized light microscopy according to previously published methods.[4] Briefly, a 40 μL volume of LC emulsion was dispensed onto a glass coverslip, and the configurations of the LC within the emulsion droplets were determined by observation of the droplets using an Olympus IX71 inverted microscope (Center Valley, PA) with an objective magnification power of 100x (oil-immersion lens). Polarized light micrographs of the LC emulsions were collected with a Hamamatsu 1394 ORCAER CCD camera (Bridgewater, NJ) connected to a computer and controlled through SimplePCI imaging software (Compix, Inc., Cranberry Twp., NJ). We characterized LC droplets that were located at least 50 μm above the surface of the coverslip and translating with velocities greater than 1 μm/s to avoid observation of LC droplets interacting with the surfaces of the coverslips.[5] Because the droplets were

diffusing (translating and rotating), radial droplets exhibited an optical appearance that was invariant with time when viewed between crossed polarizers, whereas bipolar droplets had a distinct, time-varying optical appearance.[4] Multiple images of each droplet were taken to determine the time-dependent optical appearances of the droplets, and thus the director configurations.

Characterization of the Interactions of LC Droplets with Amphiphiles in the presence of Divalent Metal Ions. LC-in-water emulsions containing the desired concentrations of amphiphiles were prepared as described above with the following modification. Solutions of metal ions were prepared in 10 μM SDS in EndoTrap® Red Equilibration Buffer [also containing 0.2% (v/v) TEA] by direct dissolution at room temperature. Solutions containing 500 pg/mL amphiphile and 1 mM metal ion were obtained by mixing 750 μL of 1 ng/mL amphiphile and 750 μL of 2 mM metal ion solutions.

Measurement of Langmuir Isotherms. Langmuir films of Lipid A or synthetic amphiphiles were prepared on a Nima 602A film balance (Coventry, England) equipped with a filter paper Wilhelmy plate for surface pressure measurements. The sub-phase was Milli-Q water and was maintained at a temperature of 25.0 ± 0.1 °C by circulating water at a constant temperature beneath the trough. Surface pressure/area isotherms (Langmuir isotherms) were measured by spreading a solution of Lipid A (1 mg/mL in $CHCl_3$/MeOH/water (96.6/3/0.4 %v/v)) or amphiphile **1$_n$** (1 mg/mL in $CHCl_3$) onto the air/water interface, allowing the solvent to evaporate for 20 minutes, and compressing the barriers at a rate of 35 cm^2/min. Isotherms for all amphiphiles are given in Fig. S1 below.

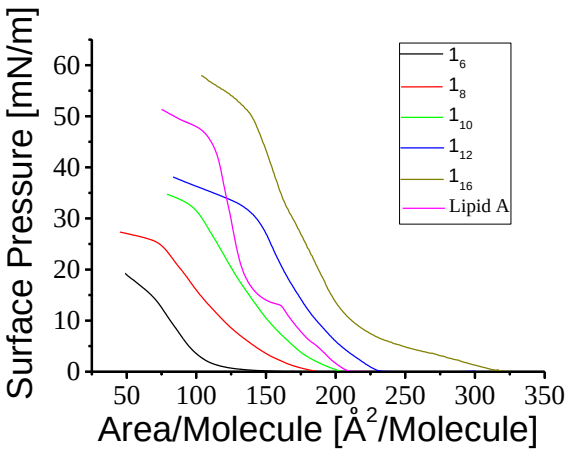

Figure S1. Langmuir isotherms measured for synthetic amphiphiles and Lipid A at an air-water interface at 25 °C. The estimated areas for each molecule, in Å^2, are follows: **1$_6$**: 105, **1$_8$**: 145, **1$_{10}$**: 175, **1$_{16}$**: 200, **1$_{16}$**: 225, Lipid A: 150.

Small-Angle X-Ray Scattering (SAXS). SAXS measurements were performed in the Materials Science Center at the University of Wisconsin-Madison using a Bruker D8 Discover diffractometer. Amphiphile **1$_6$** and **1$_{10}$** (~15 mg) were weighed into a glass vial to which 20 mL of 1 M H_2SO_4 was added such that the final concentration of amphiphile was 0.133 wt%. The solid, gel-like samples were subjected to repeated vortex mixing and sonication at room temperature before being transferred to a quartz capillary tube. After addition of 1 M H_2SO_4, the tube was sealed with Parafilm and the samples were allowed to equilibrate in a humid environment at room temperature overnight prior to analysis by SAXS. Analysis of a sample of **1$_{10}$** incubated in 1 M H_2SO_4 for 1 week by ^{1}H NMR and mass spectrometry revealed no chemical degradation (Figure S2). SAXS analysis was performed with Cu-K_α X-rays produced from a micro x-ray source with a Montel mirror passed through a 0.5 mm pinhole to collimate the beam. Each sample was irradiated for 5 min at room temperature. Two-dimensional scattering patterns were collected on a VANTEC-500 detector (140 mm in diameter, at a sample-to-detector

distance of 22.26 cm) calibrated with a silver behenate standard (d = 58.38 Å). The resulting 2D SAXS patterns were azimuthally integrated using the DataSqueeze software package to obtain one-dimensional scattering profiles. Cubic diffraction lines were fit to peaks in the one-dimensional profile using the DataSqueeze software package and procedures written for use with Igor Pro. [6]

Frequency histograms of forward light scattering (FSC) intensities measured for dispersions of bipolar and radial droplets and mixtures of radial and escaped radial droplets. Recently, we showed that measurement of low angle light scattering [so-called forward scattering (FSC)] in the flow focusing device of a flow cytometer can be used distinguish between LC droplets in a bipolar or radial configuration.[2] However, light scattering measurements for dispersions of escaped radial LC droplets, a configuration of 5CB droplets that persists at long times after interaction with amphiphiles (see main text), have not been reported to be independently distinguishable using this approach. We note here that the distinct light scattering from bipolar droplets and radial droplets, the latter of which closely resemble escaped radial droplets (see Figure 1D-I of the main text), stems from differences in the rotational symmetry of the refractive index environments of the droplet configurations.[2] Specifically, radial droplets possess a centrosymmetric refractive index environment, and thus scatter light as isotropic oil droplets. In contrast, bipolar droplets possess a rotationally-dependent refractive index environment, which leads to broadening of the distribution of FSC intensities measured by flow cytometry. Based on these previous results for bipolar and radial LC droplets and the nearly centrosymmetric refractive index environment of escaped radial droplets (see Figure 1E,H of the main text), we reasoned that the light scattering from escaped radial droplets would be similar to

that from radial droplets. Consistent with our hypothesis, frequency histograms of FSC intensities for 5CB droplets dispersed in 500 pg/mL solutions of amphiphile **1$_{10}$** (see Figure 1 of the main text and surrounding discussion) were similar to those measured for a dispersion of droplets entirely in the radial configuration as a result of interaction with Lipid A (100 ng/mL Lipid A; Figure S3). From this result, we conclude that radial and escaped radial configurations of LC droplets lead to similar distributions of FSC intensities that cannot be distinguished from each other, but both of which are readily distinguishable, alone or in combination, from distributions measured for bipolar droplets (Figure S3).

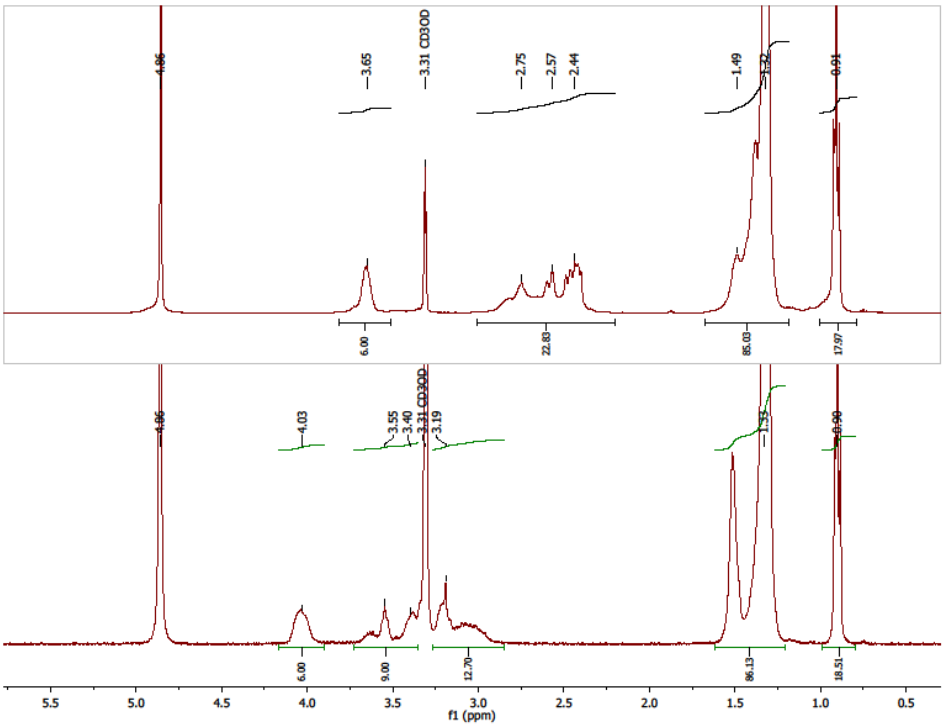

Figure S2. ^{1}H NMR spectrum (top) of untreated amphiphile **1$_{10}$** and (bottom) amphiphile **1$_{10}$** after incubation in 1 M H_2SO_4 for one week; both spectra were obtained in deuterated methanol (CD_3OD, δ 3.31 ppm). Mass spectrometry analysis (EI, positive ion mode) of the acid-treated amphiphile in 10 mM NH_4OAc/CH_3CN gave $[M^{2+}OAc^{-}]$ = 1144 and $[M^{3+}OAc^{-}]$ = 527.5, further suggesting the amphiphile was not chemically degraded by treatment in H_2SO_4 under these conditions.

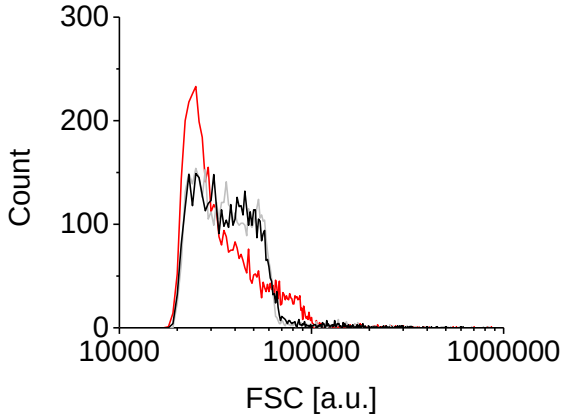

Figure S3. Frequency histogram of the intensity of forward light scattering (FSC) events generated by flowing droplets of nematic 5CB microdroplets dispersed in 10 µM aqueous solutions of SDS to which no lipid (red), 100 ng/mL of Lipid A (grey), or 500 pg/mL of amphiphile $\mathbf{1_{10}}$ (black) were added. The droplets dispersed in 10 µM SDS without added lipid were bipolar, whereas those dispersed in 100 ng/mL Lipid A were radial, and those dispersed in 500 pg/mL amphiphile $\mathbf{1_{10}}$ were a combination of escaped radial and radial. The concentration of droplets was ~5,000 droplets/µL and the histograms were constructed from an analysis of 5,000 droplets.

References for Supporting Information

(1) Miller, D. S.; Abbott, N. L. Influence of Droplet Size, pH and Ionic Strength on Endotoxin-Triggered Ordering Transitions in Liquid Crystalline Droplets. *Soft Matter* **2013**, *9*, 374-382.

(2) Miller, D. S.; Wang, X.; Buchen, J.; Lavrentovich, O. D.; Abbott, N. L. Analysis of the Internal Configurations of Droplets of Liquid Crystal Using Flow Cytometry. *Analytical Chemistry* **2013**, *85*, 10296-10303.

(3) Tan, L. N.; Wiepz, G. J.; Miller, D. S.; Shusta, E. V.; Abbott, N. L. Liquid Crystal Droplet-Based Amplification of Microvesicles that are Shed by Mammalian Cells. *Analyst* **2014**, *139*, 2386-2396.

(4) Miller, D. S.; Carlton, R. J.; Mushenheim, P. C.; Abbott, N. L. Introduction to Optical Methods for Characterizing Liquid Crystals at Interfaces. *Langmuir* **2013**, *29*, 3154-3169.

(5) Kinsinger, M. I.; Buck, M. E.; Abbott, N. L.; Lynn, D. M. Immobilization of Polymer-Decorated Liquid Crystal Droplets on Chemically Tailored Surfaces. *Langmuir* **2010**, *26*, 10234-10242.

(6) Schmitt, A. K.; Mahanthappa, M. K. Igor Pro Procedures for Analyzing Dynamic Light Scattering, Rheology, and Synchrotron X-ray Scattering Data. figShare http://dx.doi.org/10.6084/m9.figshare.644515.

Chapter 14

Characterization of Lyotropic Liquid Crystalline Assemblies of Synthetic Six-Tailed Amphiphiles‡

‡ Portions of this chapter are being prepared for publication as: Jennings, J.; Carter, M.C.D.; Son, C.Y.; Demapan, D.; Lynn, D.M.; Mahanthappa, M.K. "Characterization of Lyotropic Liquid Crystalline Assemblies of Synthetic Six-Tailed Amphiphiles." J. Jennings and I synthesized the amphiphiles, performed the physicochemical characterization experiments, and analyzed the data. C. Son and D. Demapan are performing ongoing molecular simulations experiments

ABSTRACT: We report on the self-assembly behaviors and physiochemical properties of a class of synthetic six-tailed amphiphiles inspired by the six-tailed bacterial lipid Lipid A. These synthetic amphiphiles are obtained in one step from the ring-opening reaction of (1,2)-epoxyalkanes and tris(2-aminoethyl)amine and, like Lipid A, they display complex self-assembly behaviors in aqueous environments, forming rare inverse discontinuous cubic and lamellar lyotropic liquid crystals (LLCs). Small-angle X-ray scattering (SAXS) studies suggest that both the protonation state of the head group and the amphiphile tail length determine the amphiphile conformation and the resulting supramolecular LLC morphologies. We also investigate the environment- and temperature-responsive properties of these LLC phases, underscoring their stimuli-responsive behavioral similarities to Lipid A. The guiding principles arising from these fundamental studies provide means to understand the molecular parameters that govern LLC self-assembly in this class of synthetic six-tailed amphiphiles. The results of this study should enable the use of this new class of modular synthetic materials for the design of new amphiphile-based and nanostructured soft materials.

Introduction

Synthetic assemblies inspired by the complex and often unique properties of naturally-occurring biological systems are useful tools for the design of new functional materials. Cell membranes, for example, are assemblies of biological amphiphiles and other components that collectively enable selective transport, permit intracellular communication, and provide structural flexibility.[1,2] Insights from previous studies of these membranes and the self-assembly behavior of their phospholipid components have led to new design approaches for bio-inspired synthetic membranes and interfaces, with unique properties, behaviors, and functions distinct from those of natural systems.[3-7] The work reported here was motivated broadly by the observation that naturally-occurring lipids with a multiplicity of tails often display unique self-assembly behaviors,[8-11] and the general hypothesis that the design of synthetic amphiphiles inspired by this structural feature could lead to diverse lipid self-assembled structures.

Amphiphilic molecules tend to self-assemble in the presence of water into lyotropic liquid crystals (LLCs), comprising well-organized, discrete, and nanostructured hydrophilic and hydrophobic domains with periodic long-range order.[12] The morphologies of these LLCs depend upon the water concentration-dependent structures and properties of the constituent amphiphiles, which induce the formation of lamellar, hexagonally-packed cylinders, and bicontinuous and discontinuous cubic structures.[13,14] These LLC phases are generally categorized according to the hydrophobic-hydrophilic interfacial curvature exhibited: Type I or normal phases have positive curvature interfaces, while negative curvature structures are classified as Type II or inverse phases. Supramolecular Type II inverse phases are particularly useful because they may be stable over a wide range of conditions and often persist in excess aqueous media.[15] This combination of

features has made inverse phases attractive for use in applications ranging from drug and gene delivery[16-20] to ion-conducting membranes,[21,22] and as membranes for molecular separations.[23,24]

The work reported here was motivated by the self-assembly and complex physical behaviors of a class of naturally-occurring multi-tailed bacterial glycolipids, known as Lipid A. Lipid A anchors the antigen-containing polysaccharide domain of lipopolysaccharides (LPS) to the outer membrane of Gram-negative bacteria, and is known to self-assemble into inverse Type II LLC phases.[8,9,25] Although variations exist across bacterial species, Lipid A generally bears six saturated aliphatic tails connected to a phosphate-containing head-group.[11] This unique structure results in diverse and rich LLC phase behaviors that vary widely under different aqueous conditions (e.g., upon changes in pH, temperature, or ionic strength).[8,26-28] Many investigations of the phase behavior of Lipid A have established structure-property relationships between the number and the length of the lipid tails, as well as the number of negatively-charged phosphate groups in the head group, and its propensity to form inverse cubic, hexagonal, and lamellar phases.[10,26,29] While the complex self-assembly behavior of Lipid A and the variety of structures that it can form may potentially provide a useful palette for the design of new materials, this lipid can also be toxic, difficult to obtain in large quantities, and is potentially chemically unstable owing to the presence of phosphate groups and ester bond-linked tails. The availability of synthetic lipids that mimic or recapitulate many of the unique behaviors of this biological lipid could open the door to the design of nanostructured materials with superior and readily tuned physicochemical properties.

Here, we report on the physicochemical properties and LLC self-assembly behaviors of a class of six-tailed synthetic amphiphiles generally inspired by the structure of Lipid A. This work builds from a recent report from our group demonstrating that synthetic six-tailed amphiphiles

synthesized from the ring-opening reaction of (1,2)-epoxyalkanes with the polyamine head group tris(2-aminoethyl)amine (TREN) self-assemble into inverse cubic LLC phases.[30] Similar to Lipid A, these synthetic amphiphiles have a large tail volume to head group area ratio which drives self-assembly into a variety of negative curvature LLC phases. However, in contrast to Lipid A, these synthetic and chemically stable amphiphiles may be synthesized in large quantities, thus enabling opportunities to manipulate the amphiphile tail length without changing head group chemistry. We demonstrate that varying the tail length and charge-compensating counterions associated with the lipidic headgroup in a homologous series of these amphiphiles provides access to both lamellar and new inverse discontinuous cubic phases. Using small angle X-ray scattering (SAXS) analyses we also investigate media- and temperature-dependent transitions between these LLC phases, highlighting the stimuli-responsive properties of synthetic six-tailed lipids and their behavioral similarities to Lipid A. Our results provide a framework for understanding key parameters that govern the molecular conformations that drive self-assembly in this class of multi-tailed lipids. The results of this study also open the door to future applications for bulk, thin film, and particle-based LLC assemblies using synthetic six-tailed amphiphiles that would be otherwise difficult to fabricate using conventional or biologically-derived lipids.

Materials and Methods

Tris(2-aminoethyl)amine (TREN, 96%) and *meta*-chloroperoxybenzoic acid (*m*CPBA, 70-75%) were purchased from Acros Organics (Morris Plains, NJ). (1,2)-Epoxyoctane (99%), 1,2-epoxydecane (97%), (1,2)-epoxydodecane (95%), and 1-undecene (97%) were purchased from Alfa Aesar (Radnor, PA). 1-Nonene was purchased from TCI America (Philadelphia, PA).

Concentrated sulfuric acid (H_2SO_4, ACS grade, 95-98%), concentrated hydrochloric acid (HCl, ACS grade 37%), concentrated nitric acid (HNO_3, 70%), concentrated phosphoric acid (H_3PO_4, 85 wt%), dichloromethane (DCM, HPLC grade, >99.8%), chloroform ($CHCl_3$, HPLC grade, >99.8%), aqueous ammonium hydroxide solution (ACS grade, 28-30%), and deuterated chloroform ($CDCl_3$, 99.8%) were purchased from Sigma-Aldrich (Milwaukee, WI). Methanol (MeOH; ACS grade) was purchased from Avantor Performance Materials (Center Valley, PA). SilicaFlash P60 silica gel (230-400 mesh) was purchased from Silicycle (Quebec City, QC). Anhydrous THF was obtained from a Pure Process Technology solvent purification system (Nashua, NH). Deionization of a distilled water source was performed with a Milli-Q system (Millipore, Bedford, MA) to give water with a resistivity of 18.2 MΩ•cm (referred to as Milli-Q water below). Silica gel TLC plates were purchased from Sigma-Aldrich (Milwaukee, WI) and spots were visualized using iodine and anisaldehyde stains.

General Considerations. ^{1}H and ^{13}C NMR spectra were recorded at ambient temperature on a Bruker Avance III 500 or a Varian INOVA 500 spectrometer. NMR chemical shift values are given in ppm and are referenced to the residual protons of $CDCl_3$ (δ 7.26 ppm for ^{1}H NMR spectra, 77.2 ppm for ^{13}C NMR). Sonication was accomplished using a Branson 2510 water bath sonicator operating at ambient temperature. Mass spectrometry was performed using a Waters LCT electrospray ionization time-of-flight mass spectrometer using 10 mM NH_4OAc/CH_3CN in methanol at a flow rate of 40 μL/min. Elemental analysis (C, H, N, S) was conducted at Atlantic Microlab, Inc. (Norcross, GA, USA). Unless otherwise noted, materials were used as received without further purification. Attenuated total reflectance (ATR) IR measurements were obtained using a Bruker Tensor 27 FTIR spectrometer outfitted with a Pike Technologies Diamond ATR

stage (Madison, WI) and data were analyzed using Opus Software (version 6.5, Bruker Optik GmbH). Spectra were collected at a resolution of 2 cm^{-1} and are presented as an average of 16 scans. Data were smoothed by applying a nine-point average and baseline-corrected using a concave rubberband correction (10 iterations, 64 points).

Synthesis of Odd-Numbered (1,2)-Epoxyalkanes. (1,2)-Epoxyalkanes of odd-numbered tail lengths (e.g., n = 9 or 11) were synthesized by the following modification of a literature procedure.[31] The appropriate alkene (1-nonene or 1-undecene; ~110 mM, 1.0 eq) was dissolved in 300 mL DCM in a 500 mL flask that was stirred in an ice/H_2O bath. *m*CPBA (1.25 eq) was added portionwise as a solid over the course of ~1 hr. After warming to room temperature, the resulting clear solution was stirred overnight. The mixture was then concentrated to approximately half of its original volume under reduced pressure, transferred to a separatory funnel, and washed with 3 x 40 mL saturated $NaHCO_3$, 1 x 40 mL 10% NaOH, and then 3 x 40 mL saturated NaCl (*aq*). The colorless organic phase was dried over solid Na_2SO_4, gravity filtered, and the solvent was removed under reduced pressure to afford the desired product as a clear, colorless oil. (1,2)-Epoxynonane: ^{1}H NMR (500.022 MHz, $CDCl_3$, 22 °C): δ 0.88 (t, 3H), 1.28 (m, 8H), 1.39-1.56 (m, 4H), 2.46 (m, 1H), 2.74 (m, 1H), 2.90 (m, 1H). (1,2)-Epoxyundecane: ^{1}H NMR (500.022 MHz, $CDCl_3$, 22 °C): δ 0.88 (t, 3H), 1.26 (m, 12H), 1.38-1.56 (m, 4H), 2.46 (m, 1H), 2.74 (m, 1H), 2.90 (m, 1H).

Synthesis of Six-Tailed Amphiphiles. Amphiphiles $\mathbf{1_{10}}$ and $\mathbf{1_{12}}$ were synthesized and purified as described previously.[30] Amphiphiles $\mathbf{1_9}$ and $\mathbf{1_{11}}$ were obtained from the ring-opening reaction of TREN with the appropriate (1,2)-epoxyalkane synthesized above. Briefly, TREN (1.0 eq) and the

desired (1,2)-epoxyalkane (6.6 eq) were weighed into a sealed 6 mL glass vial and stirred at 90 °C for 4 days. Purification of the resulting reaction mixture by gradient elution flash chromatography gave the desired products, which exhibited similar spectral characteristics to amphiphiles previously described.[30]

Preparation of Lyotropic Liquid Crystals. Amphiphiles (~20 mg) were weighed into a 24 mL glass vial, and 15 mL of a desired acidic solution was added such that the final concentration of amphiphile was 0.133 wt%. These dispersions were vortex mixed for 30 s, sonicated in a water bath for 30 s, and then annealed at 90 °C in an oil bath for 2 h. After cooling to room temperature, the physical consistencies of the amphiphiles in acidic dispersions ranged from viscous oils to stiff gel-like materials (see text for details). These materials were manually transferred to quartz capillary tubes or Kapton tubes containing the supernatant solution (i.e., acidic media) prior to SAXS analyses.

Compositional Analysis of Protonated Amphiphiles. Following amphiphile protonation by strong acids, the excess acid solution was decanted to isolate the resulting lyotropic liquid crystalline, oily, or gel-like material, which was weighed in a clean sample vial. Samples were centrifuged at 4000 rpm for 5 minutes to promote the expulsion of any excess aqueous solution from the gel; this solution was subsequently absorbed and removed from the sample using a Kimwipe. This process was carried out a total of four times and the mass of the sample, m_{gel}, was then recorded. The sample was then vitrified in liquid nitrogen and dried under high vacuum for 48 h before being dried to a constant weight under high vacuum at ~ 80 °C. The mass of the dry sample, m_{dry}, was recorded and the mass of water, m_{water}, was calculated using the expression

$m_{water} = m_{gel} - m_{dry}$ (this treatment assumes that mass loss under vacuum is only due to water). Elemental analysis (C, H, N) was subsequently performed on the dry sample to calculate the total acid content and the protonation state of the amphiphile (Table 1).

Small-Angle X-Ray Scattering (SAXS). Laboratory SAXS measurements were performed in the Materials Science Center at the University of Wisconsin-Madison on a Bruker D8 Discover diffractometer equipped with a VANTEC–500 detector (140 mm in diameter) calibrated with a silver behenate standard (d = 58.38 Å). Cu Kα X–rays generated from a micro X–ray source with a Montel mirror were collimated through a 0.5 mm diameter pinhole. Samples were loaded into either quartz capillaries or Kapton tubes (Cole-Parmer), and exposed to X-rays for 5-10 min. 2D-SAXS patterns collected at a sample-to-detector distance of 22.26 cm were azimuthally integrated to obtain one-dimensional intensity ($I(q)$) *versus* scattering wavevector (q) plots, which were analyzed using the DataSqueeze software package (http://www.datasqueezesoftware.com).

Synchrotron SAXS analyses were conducted at the Advanced Photon Source (beamline 12–ID–B) using a beam energy of 14.00 keV (λ = 0.8856 Å). Two-dimensional SWAXS patterns were collected on a Pilatus 2M detector with a sample to detector distance of either 2.000 or 3.616 m, calibrated with a silver behenate standard (d = 58.38 Å). Protonated amphiphile samples under aqueous solution were sealed in quartz capillary tubes and heated on a multi-capillary heating stage. Samples were allowed to equilibrate at each temperature for at least 10 min prior to X–ray exposure for ~0.1–1 s. The resulting 2D SAXS patterns were azimuthally-integrated using the DataSqueeze software package to obtain one-dimensional intensity versus q ($Å^{-1}$) scattering profiles. Le Bail refinement of synchrotron SAXS data (performed using the

JANA2006 software package) was used to determine structure factor intensities associated with each peak and to determine the refined unit cell parameters and space group symmetry. Application of charge-flipping algorithms in *SUPERFLIP* to the structure factor data enabled reconstruction of three-dimensional electron density maps for each phase, which could be visualized using the *VESTA* software package.

Results and Discussion

We synthesized a library of four six-tailed amphiphiles derived from the ring-opening reaction of (1,2)-epoxyalkanes with the tetraamine head group tris(2-aminoethyl)amine (TREN) (amphiphiles $\mathbf{1_9}$ **-** $\mathbf{1_{12}}$, Figure 1A). In the notation used here, the subscript refers to the number of carbon atoms in each amphiphile tail. This small library of amphiphiles was designed to yield compounds with aliphatic tails 9 to 12 methylene groups in length, as inspired by the most ubiquitous Lipid A derivatives.[10,11] We selected this molecular structure because past studies have demonstrated that these amphiphiles can undergo complex self-assembly in aqueous media and may be readily influenced by or respond to their environments.[30] In this study, we sought to expand on those initial observations and (i) comprehensively characterize the phase behaviors and identify LLC phases formed by these amphiphiles in a variety of acidic media that promote self-assembly, (ii) determine the effects of amphiphile protonation state, tail length, and counterion identity on LLC morphology and, (iii) develop molecular structure-property principles that can be used to select and tune the LLC morphologies of these six-tailed amphiphiles.

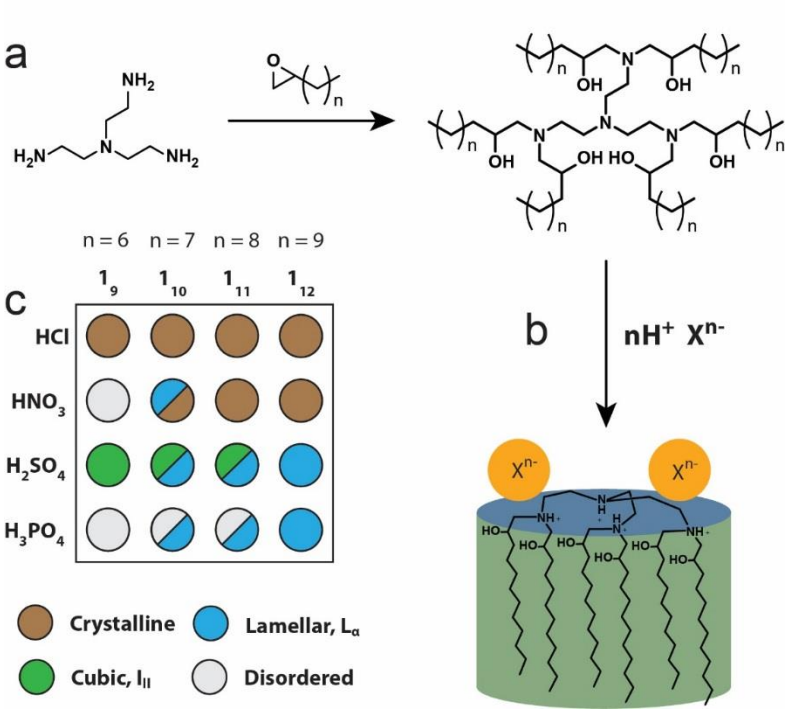

Figure 1. (a) Synthesis of six-tailed synthetic amphiphiles that undergo self-assembly into (b) lyotropic liquid crystalline phases upon protonation of the head group in strong acids. (c) Graphical summary of the results of screening acids used for protonation under different conditions, based on synchrotron SAXS characterization at room temperature.

The six-tailed amphiphiles shown in Figure 1A are all viscous oils that lack any inherent self-assembled morphology upon addition of water. We reasoned that protonation of the tetra-amine head group and a resulting increase in amphiphilicity could help drive self-assembly (Figure 1B). This hypothesis was guided, in part, by past reports of the pH-dependent self-assembly of Lipid A,[9,10,26,28] and our previously reported studies which showed that amphiphile **1$_{10}$** can self-assemble into complex inverse phases upon addition of H_2SO_4.[30] To test this hypothesis, dispersions of these amphiphiles were prepared at constant concentrations (0.133 wt% amphiphile) in hydrochloric acid ($HCl_{(aq)}$), nitric acid ($HNO_{3(aq)}$), phosphoric acid ($H_3PO_{4(aq)}$), and sulfuric acid ($H_2SO_{4(aq)}$), with equivalent ionic strengths, followed by sonication

and thermal annealing (90 °C; see Materials and Methods for complete details). We selected strong mono-, di-, and triprotic acids for these studies to elucidate the influence of the identity of the charge-compensating counterion at the head group on the observed self-assembled morphology. We used acid concentrations equivalent to an ionic strength of 6 M on the basis of our past initial studies on the self-assembly of amphiphile $\mathbf{1_{10}}$ using 1 M H_2SO_4.[30]

Several amphiphile samples transformed from viscous oils to stiff, gel-like materials upon acidification. From here on, we refer to these samples using the notation $\mathbf{1}_{\boldsymbol{n}}\textbf{-}\boldsymbol{x}\boldsymbol{A}$, where ***n*** denotes the number of carbon atoms in an amphiphile tail (e.g., see Figure 1B), and ***x*** denotes the molarity of acid ***A*** (where ***A*** = **C** (HCl), **N** (HNO_3), **P** (H_3PO_4), or **S** (H_2SO_4)). Figure 1C shows a graphical summary of self-assembly screening experiments on the four six-tailed amphiphiles treated with these four different acids, assessed by combined small- and wide-angle X-ray scattering (SAXS and WAXS, respectively). A number of samples exhibited molecular-level crystallinity in the surfactant tails, indicated by a large number of sharp diffraction peaks observed in the WAXS data. We disregarded these samples because amphiphile crystallinity overrides lyotropic self-assembly at a longer length scale. All amphiphiles prepared in 3 M HCl (i.e., $\mathbf{1_X}$**-3C**; Fig S1) were crystalline. Amphiphile crystallinity was also evident in samples prepared in 3 M HNO_3 ($\mathbf{1_{10}}$**-3N**, $\mathbf{1_{11}}$**-3N** and $\mathbf{1_{12}}$**-3N**; Fig S2), while SAXS analysis of $\mathbf{1_9}$**-3N** revealed only a single, broad scattering feature at low *q*, indicative of disorder and a lack of long-range order. In contrast, samples prepared using the triprotic acid 0.5 M H_3PO_4 with an ionic strength equivalent to all other acids did not exhibit crystallinity. We instead observed evenly spaced Bragg peaks in the low *q* region of the SAXS pattern for $\mathbf{1_{10}}$**-0.5P**, $\mathbf{1_{11}}$**-0.5P**, and $\mathbf{1_{12}}$**-0.5P**, indicating the formation of a lamellar (L_α) LLC phase. However, the SAXS patterns for $\mathbf{1_{10}}$**-0.5P** and $\mathbf{1_{11}}$**-0.5P** also displayed an underlying broad scattering peak indicative of coexistence with a

disordered micellar phase, with **1_9-0.5P** appearing entirely disordered (Fig S3). In stark contrast to the behaviors observed in these three acids, Figure 2 shows that the preparation of amphiphiles in 1M H_2SO_4 led to a remarkably rich tail length-dependent LLC polymorphism. The studies outlined below focus on our investigations of the detailed investigations of the tail length- and temperature-dependent LLC phases observed in these **1_X-*x*S** samples.

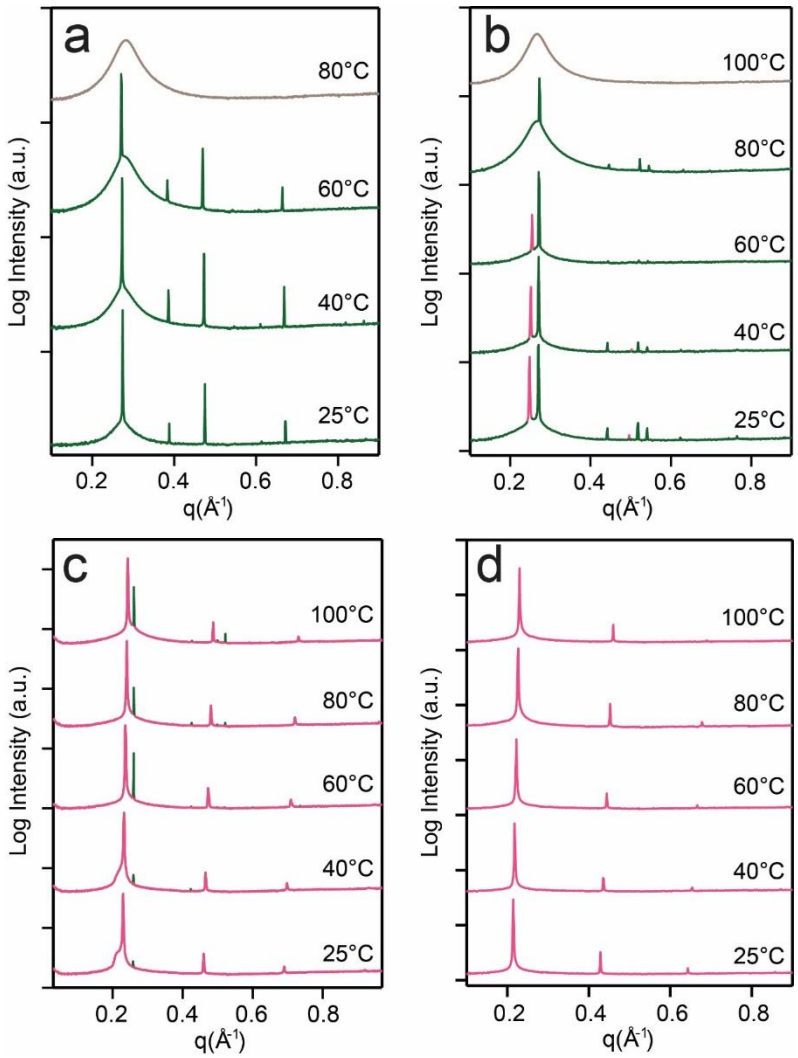

Figure 2. Temperature-dependent synchrotron SAXS analysis of amphiphiles (a) **1_9**, (b) **1_{10}**, (c) **1_{11}** and (d) **1_{12}** in 1M H_2SO_4. Peaks corresponding to lamellar (L_α) phases are pink, and peaks corresponding to cubic phases are green. The broad feature observed at high temperature in **1_9** and **1_{10}** (in grey) corresponds to a disordered phase.

Figure 2 shows temperature-dependent synchrotron SAXS patterns for **1_9-1S**, **1_{10}-1S**, **1_{11}-1S**, and **1_{12}-1S** samples, all of which form LLCs that displayed multiple sharp, low q SAXS peaks. In these samples, the absence of any high q WAXS peaks confirms the lyotropic liquid crystalline nature of these phases (Figure 2, Fig S4). Figure 2A shows that **1_9-1S**, with the shortest amphiphile tail-length, displays a scattering pattern with relative peaks positions q/q^* = √2, √4, √6, √8, √10, √12, √18, √20 and √24 [q^* = 0.194(7) Å^{-1}] consistent with the (110), (200), (211), (220), (310), (222), (411), (420), and (422) reflections of a body-centered cubic morphology. The intensity of a broad feature underneath the primary scattering peak increased upon heating, and an order-to-disorder transition was observed between 60 and 80 °C.

In our previously reported preliminary investigation into the phase behavior of this class of amphiphile, we observed a complex peak pattern for **1_{10}-1S** by low resolution lab-source SAXS measurements that we tentatively assigned as an inverse cubic phase.[30] Attempts to fit the high-resolution SAXS peaks for **1_{10}-1S** at 25 °C shown in Figure 2B to a single LLC phase were unsuccessful, therefore we reasoned that this sample might contain coexisting phases. By excluding the first scattering peak, q_L^* = 0.248 Å^{-1} and a higher order peak at q/q_L^* = √4 that we tentatively assigned to a L_α phase, the remaining peaks could be tentatively fit to a face-centered cubic lattice, with peaks located at q/q_C^* = √3, √8, √11, √12, √16, and √24 [q^* = 0.156(46) Å^{-1}], corresponding to the (111), (220), (311), (222), (400) and (422) reflections, respectively. The L_α peaks disappeared upon heating this sample to 80 °C, leaving the pure cubic morphology and a broad underlying feature which may be indicative of coexistence with a disordered micellar phase. Further heating to 100 °C resulted in a complete order-disorder phase transition. Figure 2C shows the SAXS pattern for **1_{11}-1S**. The series of equally spaced peaks indicates a L_α LLC phase, which persists up to 100 °C, together with a series of non-lamellar peaks that are similar

to those observed in **1_{10}-1S**. Finally, Figure 2D reveals exclusively lamellar peaks in **1_{12}-1S** from 25 to 100 °C, leading us to conclude that **1_{12}-1S** forms a lamellar LLC over the entire temperature range of interest. Overall, when amphiphiles were dispersed in 1 M H_2SO_4, we observed a progression from cubic → cubic and lamellar → pure lamellar with increasing amphiphile tail length, and we return to the detailed assignment of these cubic phases below.

The results above reveal a significant combined effect of acid type and amphiphile tail-length on the supramolecular assembly of these six-tailed amphiphiles. We hypothesized that the poly-basic (tetraamine-containing) structure of the amphiphile head group could impart a pH-dependent self-assembly response similar to that reported for Lipid A.[9,10,26,28] Figure 3 shows that changing the concentration of H_2SO_4 used to protonate the amphiphiles drives changes in self-assembled LLC phases. Figure 3A shows that **1_9** was largely unaffected by decreasing acid strength: **1_9-0.1S** yielded a body-centered cubic phase that appeared to be identical to that of **1_9-1S**, along with one additional low intensity peak that is tentatively assigned to a lamellar phase (definitive assignment is not possible in the absence of higher order peaks). At higher acid concentration, however, **1_9-3S** revealed a different peak pattern that exhibits cubic symmetry, consistent with a cubic-to-cubic phase change. We note here that, generally, in the **1_9-S** SAXS patterns there was a broad scattering feature, indicative of coexisting disordered reverse micelles within the sample. Figures 3B and 3C reveal that decreasing the acid strength by a factor of ten from 1 M to 0.1 M in **1_{10}-0.1S** and **1_{11}-0.1S** resulted in a shift to pure lamellar phases. However, upon increasing acid strength to 3 M in both samples, peaks corresponding to a face-centered cubic phase (discussed in detail below) appear with a concomitant decrease in the lamellar peak intensities. The lamellar LLC morphologies adopted by **1_{12}** (not shown) were invariant with changes in the acid concentration.

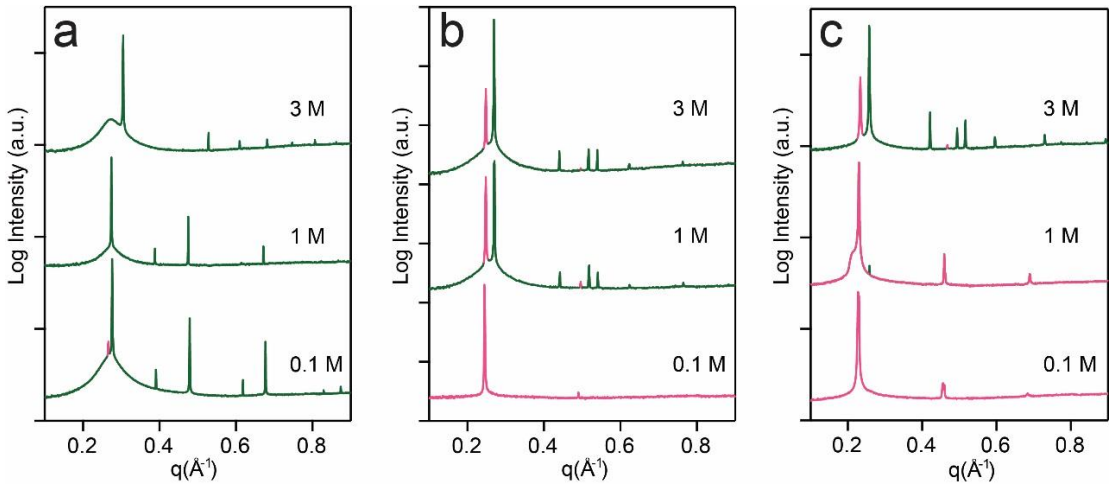

Figure 3. Acid strength-dependent synchrotron SAXS plots for amphiphiles (a) **1$_9$**, (b) **1$_{10}$** and (c) **1$_{11}$** at different H_2SO_4 concentrations. Peaks corresponding to lamellar (L_α) phases are pink, and peaks corresponding to cubic phase are green. The broad feature observed in **1$_9$** and at higher concentration in **1$_{10}$** corresponds to a disordered phase coexisting with the liquid crystalline structure.

We sought to elucidate the detailed nanostructured morphologies of the two distinct cubic phases observed in samples of (i) **1$_9$-0.1S/1S** and (ii) **1$_{10}$-1S/3S** and **1$_{11}$-1S/3S**, in order to determine whether the underlying morphologies were common to the different amphiphiles under different acid concentrations, and if the morphologies are bicontinuous or discontinuous micellar cubic LLCs. We began with **1$_9$-0.1S/1S** and found that based on the observed series of Bragg reflections, the underlying LLC morphology conforms to P23, I23, $I2_13$, $Pm\bar{3}$, $Im\bar{3}$, P432, I432, $P\bar{4}3m$, $I\bar{4}3m$, $P\bar{4}3n$, $Pn\bar{3}n$, $Pm\bar{3}n$, or $Im\bar{3}m$ space groups symmetries. Following crystallographic convention, we began by selecting $Im\bar{3}m$ (space group #229) as the highest symmetry group that fit the observed SAXS pattern of **1$_9$-1S**. Using this space group, we performed Le Bail refinement using the *JANA2006* software package to extract the structure factor intensities associated with each allowed reflection in this pattern with a unit cell dimension a = 3.24 nm. Application of a charge-flipping algorithm within the *SUPERFLIP* software

package to these structure factor intensities enabled reconstruction of the electron density contrast map for this phase. The electron density map in Figure 4A shows the expected body-centered cubic unit cell, in which reverse micelles (water-rich domains) of identical volumes are located at each of the corners and at the center of the cubic unit cell.

At least eight SAXS peaks in samples of **1_{10}-1S/3S** and **1_{11}-3S** could be tentatively fit to a face-centered cubic lattice, coexisting with a lamellar phase under most of the conditions studied here. Upon heating **1_{10}-1S** to 80°C, the coexisting lamellar phase disappeared leaving only peaks consistent with a face-centered cubic lattice. To facilitate cubic structure determination, we used the SAXS pattern with the largest number of cubic peaks (i.e., **1_{11}-3S**, 25 °C; see Fig S5), excluding the lamellar peaks from Le Bail refinement. In this SAXS pattern, the absence of the $q^*\sqrt{4}$ peak allowed us to narrow down to $F4_132$, $Fd\bar{3}$, or $Fd\bar{3}m$ space group symmetries. According to crystallographic convention, we conducted a Le Bail refinement of the SAXS data based on the $Fd\bar{3}m$ symmetry (space group #227) with a cubic unit cell parameter a = 4.22 nm, from which we reconstructed the electron density map for this phase. Figures 4B and C show that the unit cell arising from electron density reconstruction consisted of discontinuous micelles located at the positions of a diamond lattice: micelles are located at each corner and in the center of each face of the unit cell, with four additional micelles filling the tetrahedral interstitial sites located at (1/4, 1/4, 1/4), (3/4, 3/4, 1/4), (3/4, 1/4, 3/4), and (1/4, 3/4, 3/4). Notably, we also observed the same structure in an electron density reconstruction performed on the pure cubic phase in **1_{10}-1S** at 80 °C (data not shown). While tetrahedrally-closest packed inverse micellar cubic phases with $Fd\bar{3}m$ symmetry have been reported for biological lipid mixtures, those phases typically contain 24 reverse micelles per unit cell.[32-34] These structures are similar to those observed here, however they differ in that the remaining four tetrahedral interstitial sites are

filled with four particles arranged into a tetrahedron that maintains the overall space group symmetry. The SAXS peak intensities associated with the well-known inverse Fd$\bar{3}$m LLCs[32-34] significantly differ from those formed by **1_{11}-3S** at 25 °C, which results in the observed structural differences. Specifically, the unusual peak intensity ratios observed in the SAXS pattern for **1_{11}-3S** coupled with the absence of the (531) reflection and dramatically different peak positions in *q*-space, suggests that our new phase is different from previously reported Fd$\bar{3}$m LLCs. Ongoing molecular dynamics simulations will enable us to improve and confirm this tentative LLC phase assignment made by SAXS.

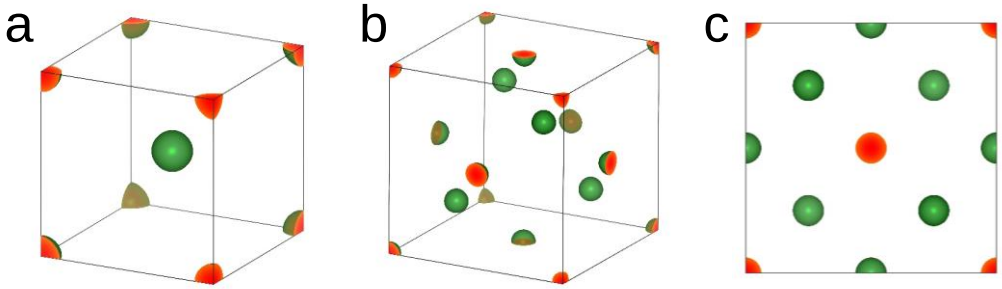

Figure 4. Electron density maps of the inverse cubic phases formed by six-tailed synthetic amphiphiles in 1M H_2SO_4. (a) BCC phase (space group Im$\bar{3}$m) formed by **1_9** and (b) and (c) different projections of the phase with Fd$\bar{3}$m symmetry formed by **1_{10}** and **1_{11}**. The unit cells were plotted using a 90% electron density isosurface, where the green regions represent the aqueous micelles dispersed in a matrix of hydrocarbon tails.

With the knowledge that LLC phases formed by our synthetic amphiphiles exist in excess aqueous solution, we deduce that these are inverse lyotropic phases comprising discrete hydrophilic micelles embedded within a matrix of the hydrophobic amphiphile tails. To the best of our knowledge, an inverse micellar phase with Im$\bar{3}$m symmetry has not been encountered in amphiphile-based LLCs. Ambiguities in the SAXS data reported in the literature for Lipid A

LLCs preclude direct comparisons of the phases formed by the biological lipid and synthetic mimics described here.[9,26] However, our results show that the unique multi-tailed structure of these synthetic amphiphiles, like Lipid A, enables self-assembly into both lamellar and rare inverse micellar cubic LLCs.

Table 1. Summary of compositional analysis of synthetic amphiphiles protonated under different conditions.

Sample	acid (conc /M)	LLC phase	Est. average Protonation[§]	mols water/ Amphiphile*
1_9-0.1SO	H_2SO_4 (0.1)	L+I+D	3.6+	9.5
1_9-1SO	H_2SO_4 (1)	I+D	4+	6.3
1_{10}-0.1SO	H_2SO_4 (0.1)	L	3.4+	11
1_{10}-1SO	H_2SO_4 (1)	L+I	4+	9.3
1_{10}-1NO	HNO_3 (1)	L+D	2.8+	25
1_{10}-0.5PO	H_3PO_4 (0.5)	L+D	3+	11.6
1_{12}-1SO	H_2SO_4 (1)	L	4+	13

[§]Estimated average protonation state was determined by elemental analysis; *mols of water per amphiphile was determined by gravimetry.

The variety of lyotropic phases observed within this small library of synthetic amphiphiles indicates that a balance among multiple factors governs their self-assembly behaviors and resulting morphologies, including: (i) the identity of the acid used for protonation, which determines the structure and position of the counterion, (ii) the acid strength, and (iii) the amphiphile tail length. The most striking observation is that only samples prepared in sulfuric acid yielded inverse cubic LLC morphologies, whereas all other acids investigated here resulted in lamellar LLC phases and/or crystalline materials. To shed light on the physicochemical origins of these differences in self-assembly behavior, we sought to quantify both (i) the protonation state of the head group and (ii) the extent of head group hydration, using a combination of

gravimetric and elemental analysis (see Materials and Methods for full details). Table 1 reveals that there exists a significant difference in protonation states for **1_{10}** in different acids. **1_{10}-1S** was found to contain ~2 divalent sulfate counterions, which suggested a fully protonated head group structure (i.e., $4H^+$), while **1_{10}-1N** had an average of ~2.8 nitrate counterions per amphiphile, suggesting a predominantly triply-protonated head group. In **1_{10}-0.5P**, a ratio of three phosphorous atoms per amphiphile was calculated, yielding three monovalent counterions to charge-balance a triply-protonated head group (at 0.5 M H_3PO_4, pH ~ 1.26 and the acid would primarily exist as $H_2PO_4^-$). The pH-dependence of the protonation state was also observed when comparing the compositions of **1_{10}-0.1S** and **1_{10}-1S**. Although our analysis suggests that **1_{10}-1S** was in the 4+ state, lowering the acid concentration as in **1_{10}-0.1S** gave an average protonation state of ~3.4+, suggesting that the amphiphile head group existed as a mixture of the 3+ and 4+ states. The water content of the LLC phases also varied widely: **1_{10}-1N**, **1_{10}-0.5P** and **1_{10}-0.1S** possessed more water molecules per amphiphile than **1_{10}-1S**. Data gathered for amphiphile **1_{10}** show that higher protonation states and lower degrees of hydration were present in samples forming cubic phases. Thus, our results point to a strong correlation between the amphiphile protonation state, the degree of hydration, and the resulting self-assembled morphology.

These experimental results allowed us to deduce the overall amphiphile shape as a function of both protonation state/counterion identity and tail length (Figure 5), leading us to draw the following general conclusions.

1) *Influence of protonation state/counterion identity*: Cubic phases were only observed in sulfuric acid, which coincided with the observation of fully protonated (4+) head groups. Nitric and phosphoric acids afforded mostly triply-protonated head groups, and only lamellar phases were observed. Based on our data, we surmise that a fully protonated head group is required for

these amphiphiles to adopt a conformation with the negative spontaneous curvature needed to drive the formation of inverse cubic phases (e.g. **1_9-1S**). Our results suggest that the coordination of more than three monovalent counterions at each head group may be electrostatically demanding as well as sterically hindered, and that amphiphiles are therefore limited to a triply-protonated state with these acids (e.g., **1_{10}-1N**, **1_{10}-0.5P**). The sulfuric acid strength also impacted self-assembly in **1_{10}** and **1_{11}**, with cubic phases becoming increasingly favored over L_α in stronger acids as a result of a more highly protonated head group. We propose that the increase in pH and the subsequent shift in the ratio of [divalent]:[monovalent] charge-balancing counterions at the head group (i.e., HSO_4^-:SO_4^{2}) increases the tendency of the head groups to exist in the 3+ state over the 4+ state, thereby promoting self-assembly into a lamellar phase. Elemental analysis also suggested that mixtures of triply- and fully-protonated head groups exist in **1_{10}** at the lower sulfuric acid strength (i.e., **1_{10}-0.1S**). The fact that cubic phase formation depends strongly on the presence of divalent anions at the amphiphile head group is a striking similarity to Lipid A, where inverse cubic phases are also promoted by the presence of the divalent cation Mg^{2+}.[8]

2) *Influence of amphiphile tail length*: Within the homologous series **1_9-1S**, **1_{10}-1S**, **1_{12}-1S**, a progression of phases from cubic → cubic coexisting with lamellar → lamellar is observed with increasing tail length, despite the observation of a fully-protonated head group in all cases (Table 1), suggesting that head group protonation state does not absolutely control the shape of six-tailed amphiphiles. We hypothesize that the prevalence of the lamellar phase in **1_{12}-1S** is a result of both the longer hydrophobic tails, and the increased extent of head group hydration (Table 1) leading to a significant increase in overall head group area. In addition, FTIR measurements were consistent with stronger hydrogen bonding interactions between the

amphiphile hydroxyl groups and the sulfate counterions in longer tail amphiphiles, as evidenced by OH stretching at lower wavenumbers (Fig S6). This evidence of stronger molecular interactions suggests a more closely associated counterion that could increase head group area and drive a more cylindrical amphiphile shape, and therefore promote the formation of a lamellar morphology. Only when tails are short enough is it possible to form inverse cubic phases. We conclude here that, similar to the behavior of Lipid A derivatives containing longer aliphatic tails,[10] analogous six-tailed amphiphiles also favor lamellar over inverse LLC phases.

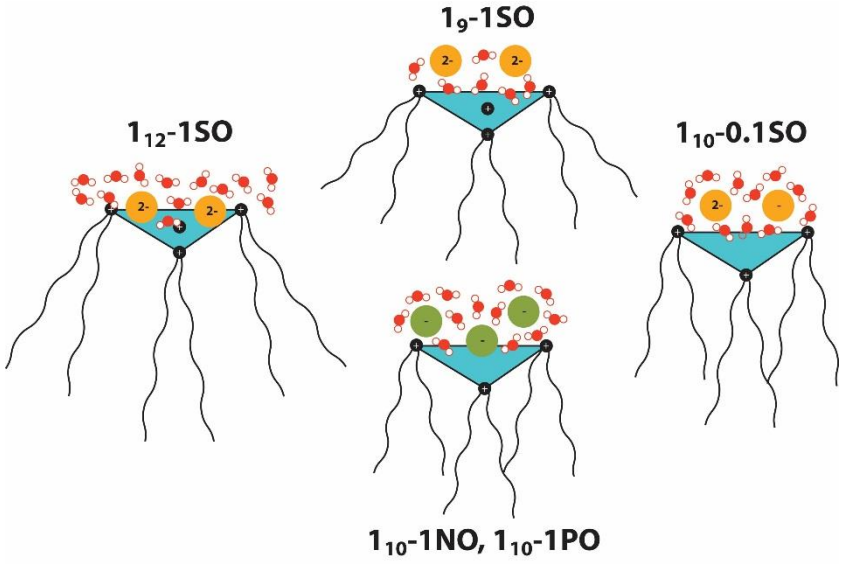

Figure 5. Cartoon illustrating the predicted conformations adopted by six-tailed synthetic amphiphiles with different tail lengths under different conditions.

Conclusions

We have reported on the LLC behavior of a series of homologous six-tailed synthetic amphiphiles that mimic key structural parameters of bacterial Lipid A. We showed that the acid used to protonate the tetra-amine head group in six-tailed amphiphiles plays a key role in determining the resulting LLC morphology. The dispersion of amphiphiles in sulfuric acid

promoted self-assembly into inverse discontinuous cubic LLC phases with rare micellar arrangements. An interplay between the protonation state of the amphiphile head group (controlled by the strength and identity of the acid used) and the amphiphile tail length are the key factors that determine overall amphiphile conformation and the resulting self-assembled morphology. These bioinspired six-tailed amphiphiles and their LLC materials mimic several aspects of Lipid A assemblies, including the propensity to self-assemble into lamellar and inverse cubic LLCs in an environmentally-responsive manner. Our results provide guiding principles for the future application of six-tailed synthetic amphiphiles in a number of contexts within the bulk, thin film, and dispersed-particle regimes.

Acknowledgments. This work was supported by the National Science Foundation through a grant to the Materials Research Science and Engineering Center (MRSEC) at the University of Wisconsin-Madison (DMR-1121288) and made use of NSF-supported facilities (DMR-1121288, CHE-9974839, CHE-1048642). We thank Arya Baghkhanian for organizing synchrotron SAXS studies conducted at Sector 12 of the Advanced Photon Source, a U.S. Department of Energy (DOE) Office of Science User Facility operated for the DOE Office of Science by Argonne National Laboratory under Contract No. DE-AC02-06CH11357. We thank C. Son and D. Demapan for performing ongoing molecular simulations experiments. M.C.D.C acknowledges the Natural Sciences and Engineering Research Council of Canada for a graduate fellowship.

References

(1) van Meer, G.; Voelker, D. R.; Feigenson, G. W. Membrane lipids: where they are and how they behave. *Nature Reviews Molecular Cell Biology* **2008,** *9* (2), 112.

(2) Dowhan, W.; Bogdanov, M.; Mileykovskaya, E.; McLeod, R. S. In *Biochemistry of Lipids, Lipoproteins and Membranes*; 6th ed.; Mcleod, R. S.;Ridgway, N., Eds.; Elsevier, 2016.

(3) Yoo, J.-W.; Irvine, D. J.; Discher, D. E.; Mitragotri, S. Bio-inspired, bioengineered and biomimetic drug delivery carriers. *Nature Reviews Drug Discovery* **2011,** *10* (7), 521.

(4) Martiel, I.; Sagalowicz, L.; Mezzenga, R. Phospholipid-based nonlamellar mesophases for delivery systems: Bridging the gap between empirical and rational design. *Advances in Colloid and Interface Science* **2014,** *209*, 127.

(5) Lagny, T. J.; Bassereau, P. Bioinspired membrane-based systems for a physical approach of cell organization and dynamics: usefulness and limitations. *Interface Focus* **2015,** *5* (4).

(6) Palivan, C. G.; Goers, R.; Najer, A.; Zhang, X.; Car, A.; Meier, W. Bioinspired polymer vesicles and membranes for biological and medical applications. *Chemical Society Reviews* **2016,** *45* (2), 377.

(7) van Rijn, P.; Tutus, M.; Kathrein, C.; Zhu, L.; Wessling, M.; Schwaneberg, U.; Boker, A. Challenges and advances in the field of self-assembled membranes. *Chemical Society Reviews* **2013,** *42* (16), 6578.

(8) Seydel, U.; Brandenburg, K.; Koch, M. H. J.; Rietschel, E. T. Supramolecular Structure of Lipopolysaccharide and Free Lipid-A under Physiological Conditions as Determined by Synchrotron Small-Angle X-ray Diffraction. *European Journal of Biochemistry* **1989,** *186* (1-2), 325.

(9) Brandenburg, K.; Koch, M. H. J.; Seydel, U. Phase-Diagram of Lipid-A from Samonella-Minnesota and Escherichia-coli Rough Mutant Lipopolysaccharide. *Journal of Structural Biology* **1990,** *105* (1-3), 11.

(10) Brandenburg, K.; Seydel, U.; Schromm, A. B.; Loppnow, H.; Koch, M. H. J.; Rietschel, E. T. Conformation of lipid A, the endotoxic center of bacterial lipopolysaccharide. *Journal of Endotoxin Research* **1996,** *3* (3), 173.

(11) Molinaro, A.; Holst, O.; Di Lorenzo, F.; Callaghan, M.; Nurisso, A.; D'Errico, G.; Zamyatina, A.; Peri, F.; Berisio, R.; Jerala, R.et al. Chemistry of Lipid A: At the Heart of Innate Immunity. *Chemistry-A European Journal* **2015,** *21* (2), 500.

(12) Fairhurst, C. E.; Fuller, S.; Gray, J.; Holmes, M. C.; Tiddy, G. J. T. *Handbook of liquid crystals*; Wiley-VCH: Weinheim ; Chichester, 1998.

(13) Mezzenga, R. In *Self-Assembled Supramolecular Architectures*; John Wiley & Sons, Inc.: Hoboken, NJ, 2012.

(14) Hyde, S. T. *Handbook of Applied Surface and Colloid Chemistry*; John Wiley & Sons, Inc., NewYork, 2001.

(15) Shearman, G. C.; Ces, O.; Templer, R. H.; Seddon, J. M. Inverse lyotropic phases of lipids and membrane curvature. *Journal of Physics-Condensed Matter* **2006,** *18* (28), S1105.

(16) Zabara, A.; Mezzenga, R. Controlling molecular transport and sustained drug release in lipid-based liquid crystalline mesophases. *Journal of Controlled Release* **2014,** *188*, 31.

(17) Koltover, I.; Salditt, T.; Radler, J. O.; Safinya, C. R. An inverted hexagonal phase of cationic liposome-DNA complexes related to DNA release and delivery. *Science* **1998,** *281* (5373), 78.

(18) Boyd, B. J.; Whittaker, D. V.; Khoo, S. M.; Davey, G. Lyotropic liquid crystalline phases formed from glycerate surfactants as sustained release drug delivery systems. *International Journal of Pharmaceutics* **2006,** *309* (1-2), 218.

(19) Negrini, R.; Mezzenga, R. pH-Responsive Lyotropic Liquid Crystals for Controlled Drug Delivery. *Langmuir* **2011,** *27* (9), 5296.

(20) Mulet, X.; Boyd, B. J.; Drummond, C. J. Advances in drug delivery and medical imaging using colloidal lyotropic liquid crystalline dispersions. *Journal of Colloid and Interface Science* **2013,** *393*, 1.

(21) Kerr, R. L.; Miller, S. A.; Shoemaker, R. K.; Elliott, B. J.; Gin, D. L. New Type of Li Ion Conductor with 3D Interconnected Nanopores via Polymerization of a Liquid Organic Electrolyte-Filled Lyotropic Liquid-Crystal Assembly. *Journal of the American Chemical Society* **2009,** *131* (44), 15972.

(22) Zhang, H.; Li, L.; Moller, M.; Zhu, X. M.; Rueda, J. J. H.; Rosenthal, M.; Ivanov, D. A. From Channel-Forming Ionic Liquid Crystals Exhibiting Humidity-Induced Phase Transitions to Nanostructured Ion-Conducting Polymer Membranes. *Advanced Materials* **2013,** *25* (26), 3543.

(23) Bara, J. E.; Kaminski, A. K.; Noble, R. D.; Gin, D. L. Influence of nanostructure on light gas separations in cross-linked lyotropic liquid crystal membranes. *Journal of Membrane Science* **2007,** *288* (1-2), 13.

(24) Gin, D. L.; Bara, J. E.; Noble, R. D.; Elliott, B. J. Polymerized lyotropic liquid crystal assemblies for membrane applications. *Macromolecular Rapid Communications* **2008,** *29* (5), 367.

(25) Brandenburg, K.; Richter, W.; Koch, M. H. J.; Meyer, H. W.; Seydel, U. Characterization of the nonlamellar cubic and H-II structures of lipid A from Salmonella enterica serovar Minnesota by X-ray diffraction and freeze-fracture electron microscopy. *Chemistry and Physics of Lipids* **1998,** *91* (1), 53.

(26) Brandenburg, K.; Mayer, H.; Koch, M. H. J.; Weckesser, J.; Rietschel, E. T.; Seydel, U. Influence of the Supramolecular Structure of Free Lipid A on its Biological Activity. *European Journal of Biochemistry* **1993,** *218* (2), 555.

(27) Brandenburg, K.; Koch, M. H. J.; Seydel, U. Phase-Diagram of Deep Rough Mutant Lipopolysaccharide from Salmonella-Minnesota R595. *Journal of Structural Biology* **1992,** *108* (2), 93.

(28) Faunce, C. A.; Paradies, H. H. Phase Transformations in Lipid A-Diphosphate Initiated by Sodium Hydroxide. *Journal of Physical Chemistry B* **2012,** *116* (43), 12997.

(29) Fukuoka, S.; Brandenburg, K.; Muller, M.; Lindner, B.; Koch, M. H. J.; Seydel, U. Physico-chemical analysis of lipid A fractions of lipopolysaccharide from Erwinia carotovora in relation to bioactivity. *Biochimica Et Biophysica Acta-Biomembranes* **2001,** *1510* (1-2), 185.

(30) Carter, M. C. D.; Miller, D. S.; Jennings, J.; Wang, X.; Mahanthappa, M. K.; Abbott, N. L.; Lynn, D. M. Synthetic Mimics of Bacterial Lipid A Trigger Optical Transitions in Liquid Crystal Microdroplets at Ultralow Picogram-per-Milliliter Concentrations. *Langmuir* **2015,** *31* (47), 12850.

(31) Tremblay, A. E.; Whittle, E.; Buist, P. H.; Shanklin, J. Stereochemistry of Delta(4) dehydrogenation catalyzed by an ivy (Hedera helix) Delta(9) desaturase homolog. *Organic & Biomolecular Chemistry* **2007,** *5* (8), 1270.

(32) Tyler, A. I. I.; Shearman, G. C.; Brooks, N. J.; Delacroix, H.; Law, R. V.; Templer, R. H.; Ces, O.; Seddon, J. M. Hydrostatic pressure effects on a hydrated lipid inverse micellar Fd3m cubic phase. *Physical Chemistry Chemical Physics* **2011,** *13* (8), 3033.

(33) Rappolt, M.; Cacho-Nerin, F.; Morello, C.; Yaghmur, A. How the chain configuration governs the packing of inverted micelles in the cubic Fd3m-phase. *Soft Matter* **2013,** *9* (27), 6291.

(34) Gillams, R. J.; Nylander, T.; Plivelic, T. S.; Dymond, M. K.; Attard, G. S. Formation of Inverse Topology Lyotropic Phases in Dioleoylphosphatidylcholine/Oleic Acid and Dioleoylphosphatidylethanolamine/Oleic Acid Binary Mixtures. *Langmuir* **2014,** *30* (12), 3337.

Supporting Information for Chapter 14

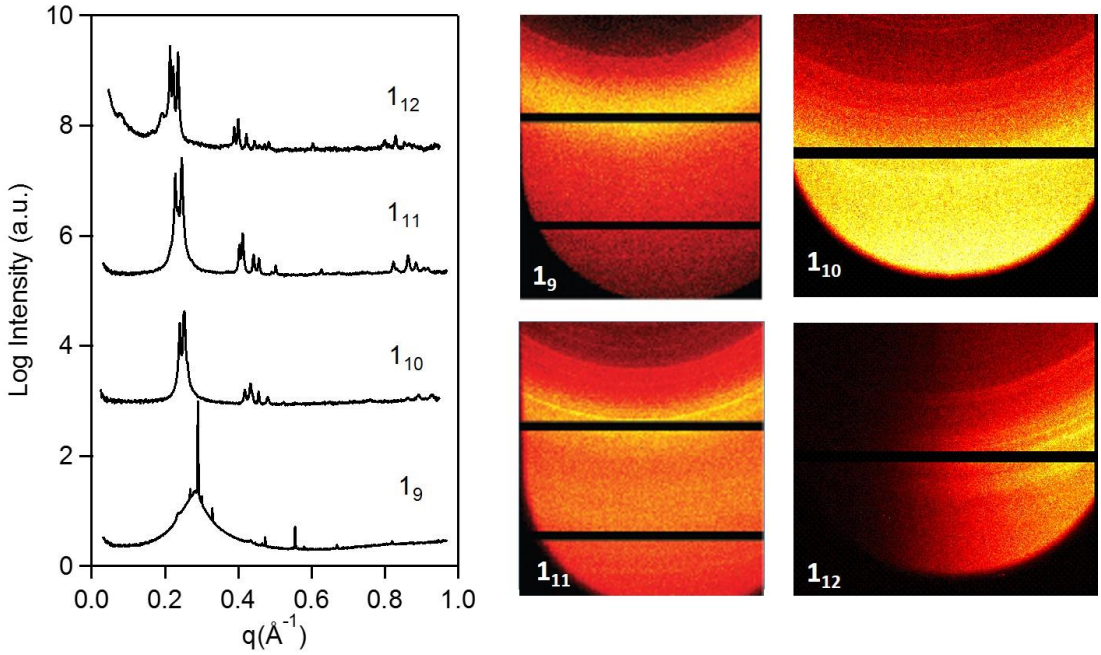

Figure S1. SAXS (left) and WAXS (right) for samples **1x-3C**. The two-dimensional WAXS data shows a large number of sharp diffraction peaks suggesting crystallinity.

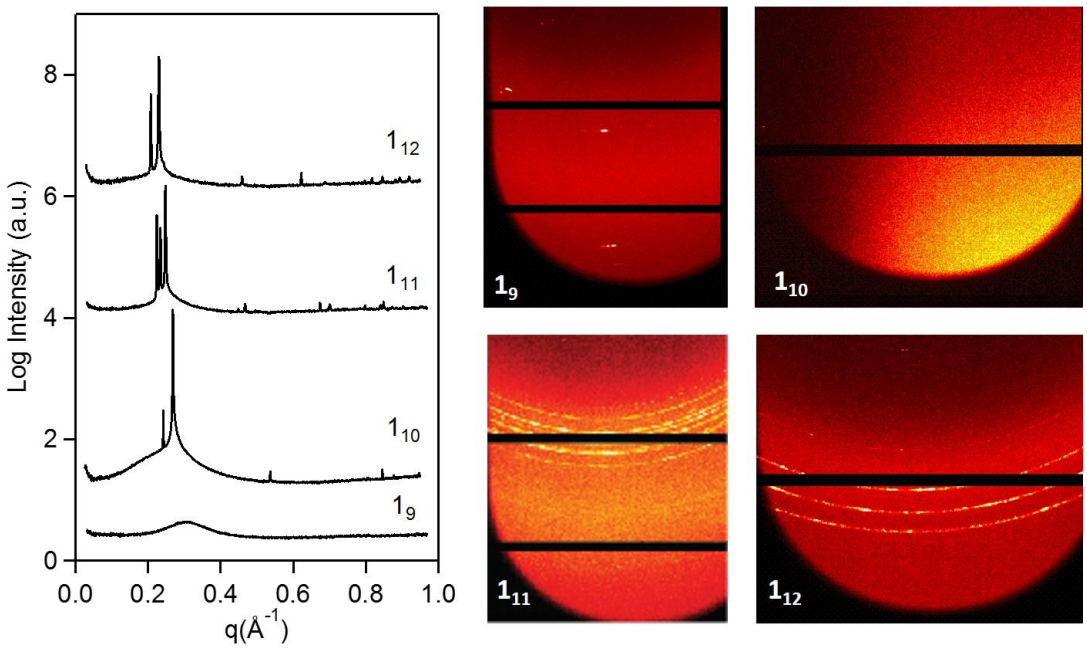

Figure S2. SAXS (left) and WAXS (right) for samples **1x-3N**. The two-dimensional WAXS data shows a large number of sharp diffraction peaks suggesting crystallinity.

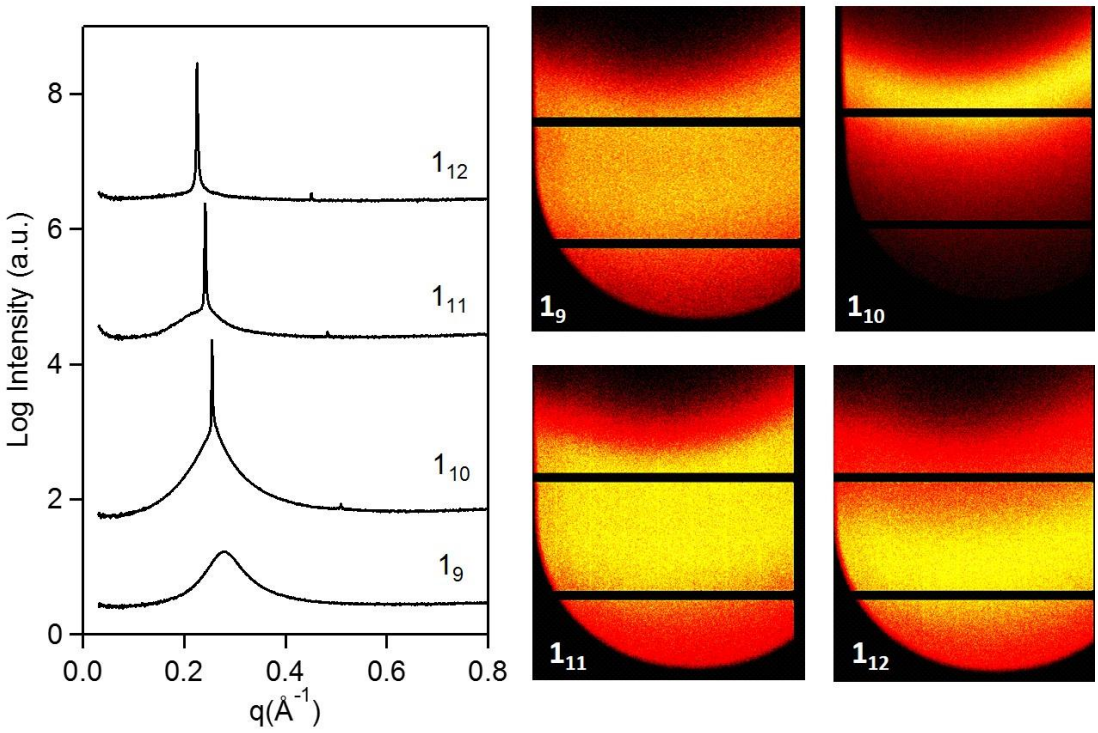

Figure S3. SAXS (left) and WAXS (right) for samples **1x-0.5P**. The two-dimensional WAXS data does not show a number of sharp peaks suggesting lamellar LLC self-assembly and coexistence with disorder when combined with the SAXS data.

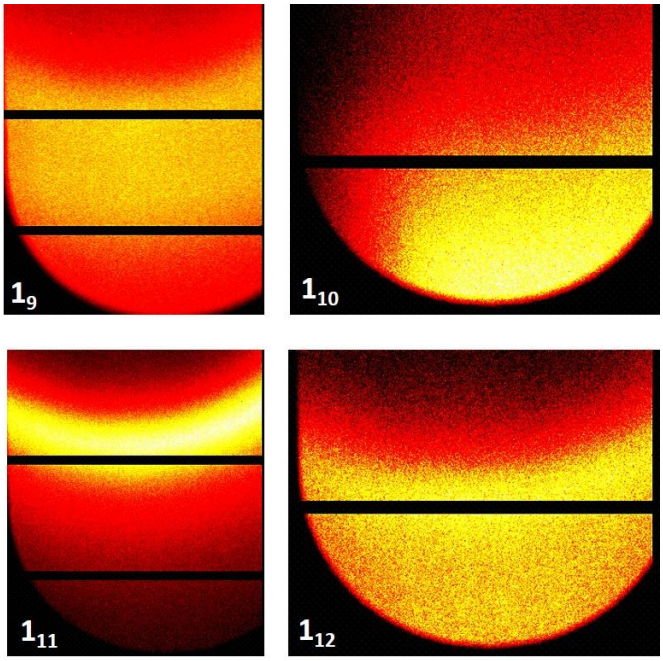

Figure S4. WAXS data for samples **1x-1S**. The two-dimensional WAXS data does not show a number of sharp peaks suggesting LLC self-assembly and the absence of crystallinity.

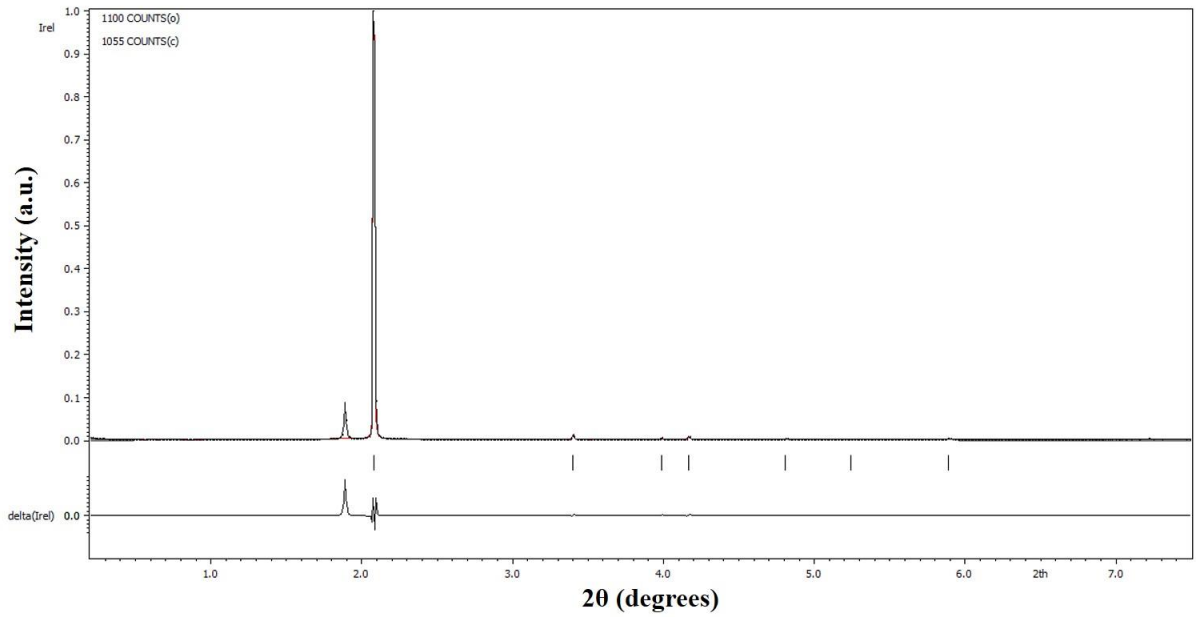

Figure S5. Azimuthally-integrated X-ray scattering pattern for **1_{11}-3S** at 25 °C, overlaid with the simulated pattern resulting from Le Bail refinement (using the *JANA2006* software package). The calculated peak positions and residuals are given below the diffractogram. This fit is based on the $Fd\bar{3}m$ symmetry, using the lattice parameter a = 4.22 nm. The peak at 2θ = 1.9 degrees arises from a coexistent lamellar phase; it was therefore deliberately excluded from the fitting.

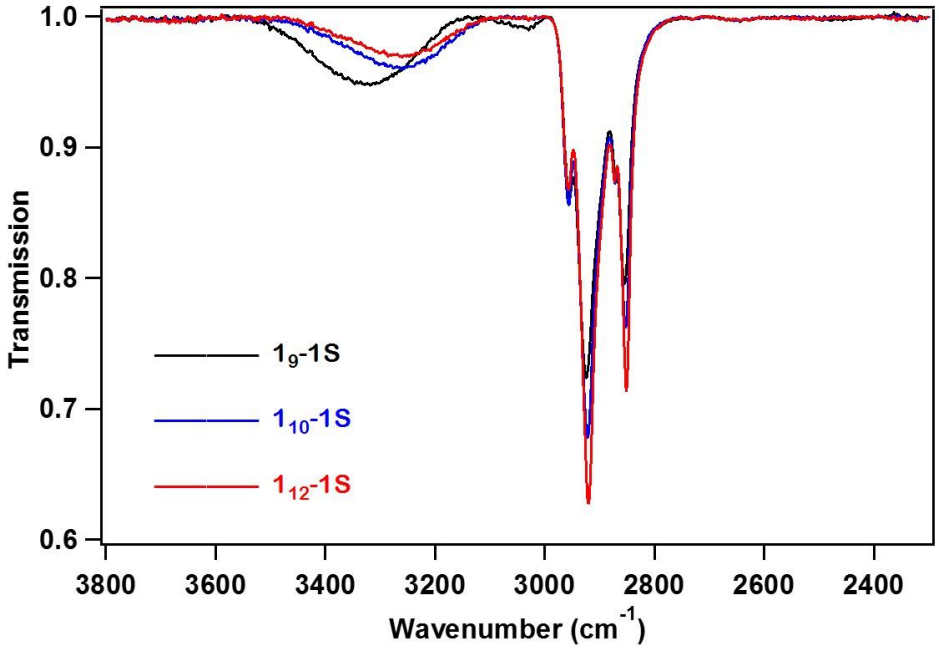

Figure S6. ATR IR analysis of **1x-1S** samples in the sp^2 and sp^3 CH and OH stretching region of the spectrum.

Chapter 15

Cubic and Lamellar Lyotropic Liquid Crystalline Particles from Synthetic Six-Tailed Amphiphiles‡

‡ Portions of this chapter are being prepared for publication as: Carter, M.C.D.; Jennings, J.; Guo, X.; Rodríguez-López, A. de L.; Lynn, D.M. "Cubic and Lamellar Lyotropic Liquid Crystalline Particles from Synthetic Six-Tailed Amphiphiles." J. Jennings and I synthesized the amphiphiles, fabricated the LLC particles, performed the physicochemical characterization experiments, and analyzed the data. X. Guo fabricated the hollow polymer capsules and A. Rodríguez-López performed the bacterial inhibition studies.

Introduction

The ability of lipids and amphiphiles to self-assemble into well-ordered morphologies provides unique opportunities to define the nanostructures and physicochemical properties of soft materials.[1-4] Self-assembled lipid phases in the bulk regime have been used in a range of applications, from molecular filtration and separation,[5,6] to the design of templates for the synthesis of new inorganic materials.[7-10] So-called 'isasome' particles are the dispersed-phase analogues of bulk self-assembled morphologies. These colloidally-stable particles contain internal LLC phases and are commonly fabricated using biological lipids (e.g., monoolein, DOPE, and DOPC), the structure of which determines particle morphology and properties.[11-13] Internal hexagonally-packed cylinder morphologies (hexasomes), bicontinuous or discrete micellar cubic phases (cubosomes), and internal lamellar morphologies (lamellarsomes) have all been obtained from the self-assembly of biological lipids, and these LLC particles have been used as hosts for drug delivery[13-19] and medical contrast imaging agents.[20-23] To date, the vast majority of isasomes have been fabricated using a small number of naturally-occuring biological lipids.[3,13] The relatively narrow range of particle physicochemical properties that can be accessed with this small set of lipids places limits on the functions and behaviors of dispersed LLC particles that can be achieved. The ability to modulate and tune internal structures, as well as design particles that contain or incorporate synthetic lipids with specific functionalities, could lead to the design of new LLC particles with unique properties.

We recently reported a synthetic route to six-tailed synthetic amphiphiles that self-assemble into a variety of inverse lyotropic liquid crystalline (LLC) phases under aqueous acidic conditions. That approach was based on amphiphiles obtained by the ring-opening reaction of (1,2)-epoxyalkanes with tris(2-aminoethyl)amine.[24] A survey of the LLC phase behavior in a

homologous series of those synthetic amphiphiles by small-angle X-ray scattering (SAXS) was presented in Chapter 14. Our analyses revealed a number of molecular design principles that guide supramolecular self-assembly in this system. One key observation arising from those studies is that these LLC phases persist under excess acidic conditions (e.g., when the amines in the amphiphile headgroup are protonated) and that the resulting LLC phases are inverse (or "type II"), where hydrophilic aqueous domains are well-ordered within a matrix of the hydrophobic amphiphile tails. Here, we demonstrate that these synthetic inverse phases can be used to fabricate colloidally stable, water-dispersed lamellarsomes and cubosomes. These particles represent fully synthetic analogues of conventional isasomes fabricated using common biological lipids. We demonstrate that LLC particles obtained from synthetic six-tailed amphiphiles with discontinuous cubic and lamellar morphologies are promising materials for the encapsulation of molecular cargo (e.g., model drugs) and that isasomes can be fabricated within hollow polymer capsules, providing new methods to template the sizes and size distributions, as well as define the surface chemistry and properties, of dispersed LLC particles. The fundamental insights and guiding principles reported here could open the door to the design of new colloidally-stable LLC particles with unique internal morphologies and tunable surface properties.

Materials and Methods

Amphiphiles **1$_9$**, **1$_{10}$**, and **1$_{12}$** were synthesized as previously described.[24] Pluronic F127 (BioReagent), cystamine dihydrochloride (≥98.0%), sulfuric acid (98%), acetonitrile (HPLC grade, (≥99.9%), acetone (reagent grade), diethyl ether (>99%), and chloroform ($CHCl_3$, HPLC grade, >99.8%) were purchased from Sigma (Milwaukee, WI). Methanol (MeOH, Semiconductor Grade) was purchased from VWR (West Chester, PA). 3-

Dimethylaminopropylamine (DMAPA, 99%) was purchased from Acros Organics (Morris Plains, NJ). Triclosan (5-chloro-2-(2,4-dichlorophenoxy)phenol) (99%) was purchased from Alfa Aesar (Ward Hill, MA). The diamine cystamine (Cys) was prepared by the deprotonation of the cystamine dihydrochloride salt, following a literature procedure.[25] 2-Vinyl-4,4-dimethylazlactone (VDMA) was a kind gift from Dr. Steven M. Heilmann (3M Corporation, Minneapolis, MN) and poly(2-vinyl-4,4-dimethylazlactone) (PVDMA) was synthesized as described previously.[26] Millipore Amicon Ultra 0.5 mL centrifuge tubes with a molecular weight cut-off of 3 kDa were purchased from Fisher Scientific (Pittsburgh, PA). SiO_2 microparticles (5 wt% in water; diameter = 7.96 ± 0.2 μm) were purchased from Microparticles GmbH (Berlin, Germany). *S. aureus* strain 33591 was obtained from ATCC (Manassas, VA). Mueller Hinton (MH) Broth, Tryptic Soy Agar (TSA), and Tryptic Soy Broth (TSB) were purchased from Sigma (Milwaukee, WI). Deionization of a distilled water source was performed using a Milli-Q system (Millipore, Bedford, MA) to give water with a resistivity of 18.2 MΩ•cm. All materials were used as received without further purification unless otherwise noted.

General Considerations. Dynamic light scattering (DLS) measurements were made using a Malvern Zetasizer Nano ZSP (Malvern Instruments, Malvern, UK) at 25 °C at a detector angle of 173°. Size measurements by intensity are an average of 3 runs of at least 10 scans each and are reported with the dispersity index. UV/Vis measurements were obtained using a Thermo Fisher NanoDrop 2000c and 2 μL of sample. Sonication was performed using a Branson 2510 laboratory-scale water bath sonicator operating at room temperature (Danbury, CT; 100 W, 42 kHz operating frequency). Optical micrographs and cross-polarized images were obtained using an Olympus IX71 inverted microscope (Center Valley, PA) with an objective magnification

power of 100x (oil-immersion lens) and a Hamamatsu 1394 ORCAER CCD camera (Bridgewater, NJ) controlled through SimplePCI imaging software (Compix, Inc., Cranberry Twp., NJ). Digital images were acquired using a Canon PowerShot SX130 IS digital camera.

Fabrication of LLC Particles. A sample of the desired amphiphile (~20 mg) was dissolved in diethyl ether or chloroform (250 μL) by brief vortex mixing and heating in a warm water bath. 800 μL of a 1 wt% Pluronic F127 solution in water was added, and the colloidal mixture was vortexed for 30 s and then sonicated for 30 mins to form a milky dispersion. 400 μL of a 3M H_2SO_4 solution in water was added to bring the overall acid strength to 1 mol/L of water, and the mixture was capped and vortexed for 30 s. The cap was removed and the mixture was sonicated for 1.5 hr to promote evaporation of the organic solvent and yield a dispersion of LLC particles. A sonication time of 1.5 hr was sufficient for complete removal of ether or chloroform, as determined by separate experiments where the mass of the vial was monitored over time (i.e., sonication was performed to a constant weight). For SAXS or DLS analysis, an aliquot of the dispersion was transferred by syringe to a quartz capillary or Kapton tube (SAXS), or diluted 100-fold (DLS).

Preparation of Loaded LLC Particles and Solvent-Exchange Protocol. The preparation of 1 wt% triclosan-loaded LLC particles is given as a representative example. A sample of the desired amphiphile (~20 mg) was dissolved in 20 μL of a 10 wt% solution of triclosan in chloroform by brief vortex mixing and heating in a warm water bath. 800 μL of a 1 wt% Pluronic F127 solution in water was added, and the resulting colloidal mixture was vortexed for 30 s and then sonicated for 30 mins to form a milky colloidal dispersion. 400 μL of a 3 M H_2SO_4 solution in water was

added to bring the overall acid strength to 1 M of water, and the mixture was capped and vortexed for 30 s. The cap was removed and the mixture was sonicated for 1.5 hr to promote evaporation of the organic solvent and yield a dispersion of loaded LLC particles. To exchange the acidic solution with PBS buffer (pH = 7.4), a 0.5 mL aliquot of the as-fabricated LLC particle dispersion was placed into a 0.5 mL centrifugal filter with a 3 kDa molecular weight cut-off and centrifuged at 14*g* for 30 mins. The resulting pellet was redispersed in 0.5 mL of a 1 wt% Pluronic F127 solution (in PBS buffer) by vigorous and prolonged vortex mixing. This centrifugation-redispersion process was repeated an additional two times to ensure complete replacement of the acidic solution with PBS buffer and to remove unloaded triclosan, as determined by UV/Vis analysis. After the final cycle, the centrifugal filter containing the LLC particles was placed upside down in a clean receiving tube and centrifuged at 8*g* for 30 mins to isolate the pellet of LLC particles. The particles were redispersed in 1.0 mL of a 1 wt% solution of Pluronic F127 in PBS buffer by vortex mixing and sonication. For control experiments using unloaded LLC particles, the same fabrication method was followed, but 20 μL of pure chloroform was used in the first step. To determine the presence of triclosan loaded into LLC particles, a small 50 μL aliquot of particle dispersion was centrifuge-filtered. The recovered pellet of particles was dissolved in methanol to yield a clear solution which was analyzed by UV/Vis photospectrometry.

Small-Angle X-Ray Scattering (SAXS) Analysis of LLC Particle Morphologies. *Lab-Source SAXS Measurements.* Laboratory SAXS measurements were performed in the Materials Science Center at the University of Wisconsin-Madison on a Bruker D8 Discover diffractometer equipped with a VANTEC–500 detector (140 mm in diameter) calibrated using a silver behenate

standard (d = 58.38 Å). Cu Kα X–rays generated from a micro X–ray source with a Montel mirror were collimated through a 0.5 mm diameter pinhole. Samples were loaded into either quartz capillaries or Kapton tubes (Cole-Parmer) and exposed to X-rays for 5-10 min at a sample-to-detector distance of 22.26 cm. The resulting 2D-SAXS patterns were azimuthally-integrated using the DataSqueeze software package to obtain one-dimensional intensity ($I(q)$) versus scattering wavevector (q) plots. *Synchrotron SAXS Measurements.* Synchrotron SAXS analyses were conducted at the Advanced Photon Source (beamline 12–ID–B) using a beam energy of 14.00 keV (λ = 0.8856 Å). Two-dimensional SAXS patterns were collected on a Pilatus 2M detector with a sample to detector distance of either 3.616 m, calibrated with a silver behenate standard (d = 58.38 Å). Samples were sealed in quartz capillary tubes and were allowed to equilibrate at room temperature for at least 5 min prior to X–ray exposure for 0.1–1 s. The resulting 2D SAXS patterns were azimuthally-integrated using the DataSqueeze software package to obtain one-dimensional ($I(q)$) versus scattering wavevector (q) plots.

Incubation of Triclosan-Loaded LLC Particles with *S. aureus*. *S. aureus* 33591 cells were stored in 50% glycerol at -80 °C and grown in TSB media. Prior to each experiment, *S. aureus* cells were grown at 37 °C to an OD_{600} of 0.4, harvested, washed with PBS buffer (pH = 7.4) and resuspended at a concentration of 2 x 10^6 CFU/mL in MH media. A 1.0 mL aliquot of triclosan-loaded $\mathbf{1}_{12}$ particles was incubated with an equal volume of *S. aureus* cell suspension at 37 °C for 24 hr. *S. aureus* cell viability was determined by plating eight 10-fold serial dilutions of LLC particle/cell suspension on TSB agar plates. The plates were incubated at 30 °C for 24 hr and the number of colonies formed was counted. Experiments were performed in duplicate and were repeated on two different days. Separate control experiments using the same volume of unloaded

1$_{12}$ particles and 1.0 mL of a 1 wt% solution of Pluronic F127 in PBS only were conducted in the same manner as described above.

Fabrication of Layer-by-Layer Capsules. Solutions of PVDMA (2.8 mg/mL) and the diamine cross-linker Cys (10 mM, also containing an equimolar amount of DMAPA) were prepared in acetonitrile. A 100 μL aliquot of a 5 wt% dispersion of SiO_2 microparticles (8 μm nominal diameter) was placed into a plastic microcentrifuge tube and suspended in 1.0 mL of acetonitrile prior to multilayer assembly. The first layer of Cys was deposited onto the SiO_2 particles by adding 1.0 mL of the Cys solution to the particle suspension and manually shaking the particles for 1 min to allow the small molecule to adsorb to the particle surface. The particles were then centrifuged for 1 min at 1500 rpm. The supernatant was removed by pipette and the particles were rinsed twice by resuspension and vortex mixing in 1.0 mL of acetonitrile. After each rinse in acetonitrile, the particles were centrifuged for 1 min at 1500 rpm and the supernatant was removed. 1.0 mL of the PVDMA solution was added and the particle suspension was manually shaken for 30 sec. The particles were then rinsed twice with 1.0 mL of acetonitrile as described above. Subsequent layers were fabricated by repeating this process (by alternatingly depositing Cys or PVDMA solutions and allowing the particles to incubate for 30 sec) until four polymer layer pairs (or 'bilayers') were deposited. After the first two bilayers, the particle suspensions were placed into a new micro-centrifuge tube to minimize particle aggregation. After film fabrication, the coated particles were placed into 1.0 mL of DMAPA solution in acetonitrile (40 mM) and mixed on a rotator plate for 1 hr to functionalize the remaining azlactone groups and install tertiary amine functionality. Coated particles were then rinsed with acetonitrile three times, dispersed in 1.0 mL of deionized water, and then treated with hydrofluoric acid (HF, 5 M)

for 10 minutes to etch away the silica cores [WARNING: HF solutions and vapors are extremely poisonous and corrosive, and may cause extreme burns that are not immediately painful! Handle with extreme caution, in a chemical fume hood, and using appropriate protective equipment (gloves, face/eye protection, lab coat, etc.), and neutralize waste appropriately. Do not store in glass containers]. The resulting hollow polymer capsules were washed, centrifuged, and resuspended five times using water prior to characterization and use.

Encapsulation of Amphiphile $\mathbf{1}_{12}$ in Hollow Polymer Microcapsules. Samples of amphiphile $\mathbf{1}_{12}$ were encapsulated in the hollow microcapsules synthesized above using a solvent-exchange procedure adopted from the literature for the fabrication of PVDMA-based capsules.[27,28] Hollow capsules were rinsed and washed with ethanol twice and then centrifuged down into a pellet. The ethanol supernatant was removed using a pipette, and the pellet was suspended in 5 μL of ethanol with gentle agitation. A solution of amphiphile $\mathbf{1}_{12}$ (20 mg dissolved in 25 μL of a 5:1 *v/v* acetone/ethanol mixture) was then added to the particle suspension, the tube was sealed with parafilm, and this mixture was mixed on a rotator plate at room temperature for 2 hr. The microcentrifuge tube was then opened and left uncapped at room temperature for 24 hr to allow the solvent mixture to evaporate. Excess and unloaded $\mathbf{1}_{12}$ was removed by centrifuging the particle suspension at 1500 rpm for 3 min. 400 μL of DI water was added to the tube, and the filled capsules were extracted into the aqueous phase with manual shaking. Filled capsules were then characterized using bright-field and polarized light microscopy.

Characterization of Amphiphile-Loaded Capsules. A 5 μL dispersion of $\mathbf{1}_{12}$-loaded capsules was placed onto a glass coverslip and the capsules were allowed to settle in order to facilitate

characterization by microscopy. For experiments designed to investigate the influence of protonation on the self-assembly behaviors of encapsulated **1$_{12}$** droplets, H_2SO_4 was added to the settled **1$_{12}$**-loaded capsules to achieve a final concentration of approximately 1.0 M [H^+]. In experiments designed to test the reversibility of self-assembly, the acidic solution was carefully removed by pipette and replaced by approximately 200 μL $NaHCO_3$ buffer (pH = 10.8). Changes in the optical appearance of the loaded capsules were then characterized using bright-field and polarized light microscopy.

Results and Discussion

We prepared a series of LLC isasome particles using synthetic amphiphiles that contain six aliphatic tails connected to a tris(2-aminoethyl)amine-based head group (amphiphile **1X**, where X is the number of carbon atoms of each of the six tails, Figure 1A).[24] Previously, in Chapter 14, we demonstrated that these amphiphiles could be induced to self-assemble into inverse cubic (for **1$_9$**, **1$_{10}$**, and **1$_{11}$**) and lamellar phases (for **1$_{12}$**) in the bulk by dispersion in strong acid (e.g., 1M H_2SO_4). We hypothesized that colloidally stable LLC particles with internal inverse cubic and lamellar phases could be fabricated using this homologous amphiphile series and that, in contrast to isasomes obtained from biological lipids, this synthetic system would provide control over particle morphology by changing amphiphile tail length only, and not amphiphile identity (i.e., the overall chemical make-up of the particles would be relatively invariant with changing morphology).

The fabrication of biological lipid-based isasomes generally involves bulk LLC phase preparation followed by addition of a stabilizer and subsequent dispersion into nano- or micrometer-sized particles by mechanical agitation (e.g., sonication and extrusion).[11,13] Because

we observed that bulk LLC phases of our homologous six-tailed amphiphiles resisted dispersion by mechanical methods over extended periods of time, our isasome design strategy instead exploits the *in situ* formation of LLC morphologies after particle formation. In this approach, the amphiphile was dissolved in a volatile hydrophobic organic solvent (diethyl ether or chloroform) and an aqueous solution of Pluronic block copolymer was added to create an oil-in-water emulsion by sonication. Self-assembly of the LLC morphology in the resulting droplets was then triggered by addition of an acidic aqueous solution to protonate the amphiphile head group and by subsequent removal of the solvent (see Materials and Methods for complete details). Figure 1B shows a representative image of a vial containing colloidally-stable particles obtained using amphiphile **1$_{10}$**; the solution has a homogeneous opaque appearance characteristic of well-dispersed particles and is consistent with past reports on the fabrication of nanometer-sized LLC particles.[11,13] Figure 1C shows the results of dynamic light scattering (DLS) analysis on particle dispersions for all samples, revealing average intensity-based particle diameters of 214, 254, and 271 nm for **1$_9$**, **1$_{10}$**, and **1$_{12}$**, respectively, with dispersity indices below 0.25 in all cases.

In past studies, we observed a relationship between the tail length and the bulk LLC phase obtained for amphiphiles **1$_9$**, **1$_{10}$**, and **1$_{12}$** after acidification using sulfuric acid and thermal annealing. The images in Figure 1D-E show tentative morphological assignments for bulk samples of **1$_9$** and **1$_{10}$**, as discussed earlier in Chapter 14, which we have proposed form inverse cubic phases of space groups Im$\bar{3}$m with a unit cell dimension of a = 3.24 nm, (1D, bottom; based on the position of the principal scattering vector q^* = 0.194 Å^{-1}) and Fd$\bar{3}$m with a unit cell dimension of a = 4.03 nm (1E, bottom; q^* = 0.156 Å^{-1}), respectively. Amphiphile **1$_{12}$** formed a lamellar phase with a domain spacing of 2.95 nm (1F, bottom, q^* = 0.214 Å^{-1}). We fabricated

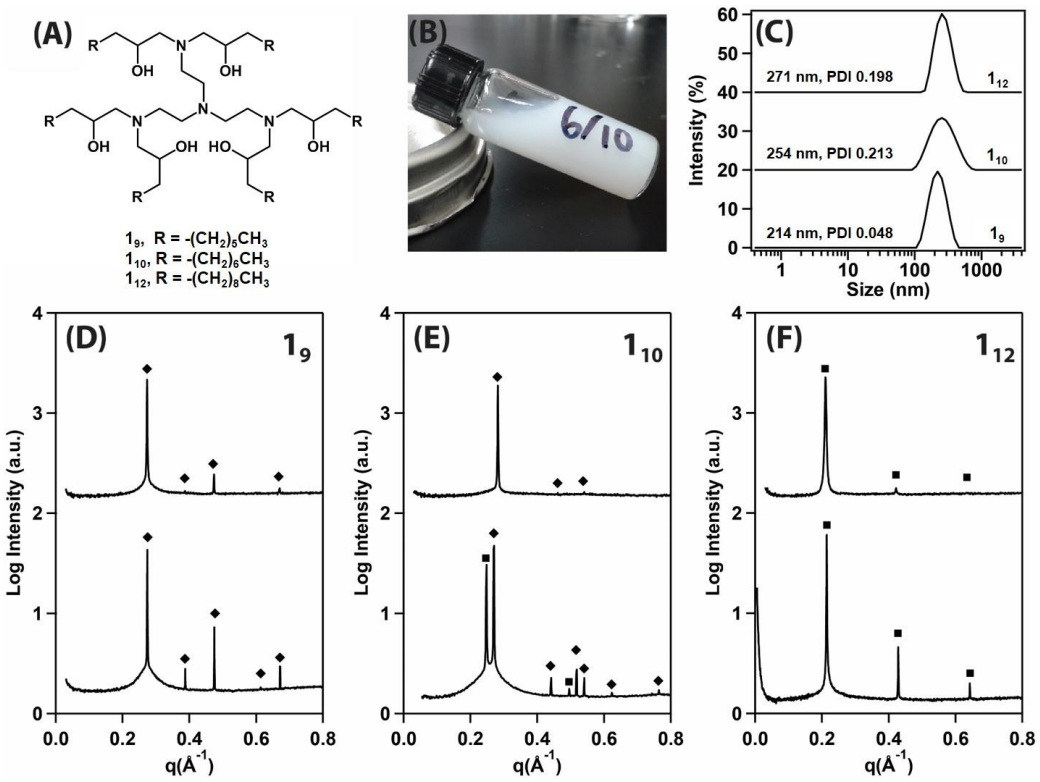

Figure 1. (A) Chemical structures of six-tailed amphiphiles $\mathbf{1_X}$ used to fabricate LLC particles. (B) Photo of a vial containing a colloidal dispersion of $\mathbf{1_{10}}$ LLC particles. (C) Dynamic light scattering (DLS) measurements of the sizes of LLC particles fabricated from amphiphiles $\mathbf{1_9}$ (bottom), $\mathbf{1_{10}}$ (middle), and $\mathbf{1_{12}}$ (top). (D-F) Azimuthally-integrated synchrotron SAXS patterns for bulk samples (bottom) and LLC particles (top) of amphiphiles $\mathbf{1_9}$ (D), $\mathbf{1_{10}}$ (E), and $\mathbf{1_{12}}$ (F).

LLC particles using each of these amphiphiles and investigated the self-assembled morphologies using high-resolution synchrotron small-angle X-ray scattering (SAXS). Figures 1D and F (top traces) show azimuthally-integrated SAXS patterns for the dispersed particle phases formed by amphiphiles $\mathbf{1_9}$ and $\mathbf{1_{12}}$; the positions of the observed reflections match well with the peaks observed for the bulk self-assembled phases (bottom traces), indicating that the morphology is the same in both particles and bulk samples prepared under similar conditions. Dispersed particles of $\mathbf{1_9}$ had an inverse body-centered cubic (BCC) morphology, while particles of $\mathbf{1_{12}}$ had an internal lamellar morphology. In bulk samples of $\mathbf{1_{10}}$, we observed a coexistence of a lamellar phase and a tentatively-assigned FCC phase (as discussed earlier in Chapter 14 and shown in Fig

1E, bottom). In contrast, the positions of the reflections in the SAXS pattern for the **1$_{10}$** particles (Figure 1E, bottom) suggest that the dispersed particle morphology is pure face-centered cubic (FCC). As noted in Chapter 14, further analysis will need to be carried out to definitively assign this tentative inverse cubic phase. Overall, we conclude that the polymorphic LLC behavior of this class of synthetic amphiphile is generally well-preserved when translated to the particle regime.

Numerous past studies have demonstrated that LLC particles fabricated using biological amphiphiles can be used to host and deliver molecular cargo. In this context, we hypothesized that particles assembled using our homologous series of synthetic amphiphiles could be advantageous in at least two ways: (i) whereas control over the phases LLC particles often requires the selection of chemically distinct lipids or mixtures of lipids with different functionalities, amphiphiles **1$_9$**, **1$_{10}$**, and **1$_{12}$** differ only by the number of carbon atoms in their tails. Thus, these synthetic amphiphiles provide access to particles with different internal morphologies but similar chemical properties, potentially obviating the need to study the *in vitro* effects of widely chemically different lipid formulations, and (ii) amphiphile **1$_X$** species should be highly stable to hydrolysis in physiologically-relevant environments, particularly when compared to commonly used ester bond-containing biological lipids (e.g, monoolein, DOPC, or DOPE),[11,13] a feature which could enable long-term particle stability in a variety of storage or delivery applications.

In an initial screening experiment designed to test the feasibility of loading isasomes with small molecules for storage and delivery, we fabricated loaded LLC particles using a modified preparation procedure. A solution of amphiphile and the small molecule to be encapsulated were co-dissolved in a hydrophobic organic solvent. After emulsification with Pluronic F127 solution

and acidification, the organic solvent was allowed to evaporate to give a dispersion of LLC particles. Using a solvent exchange protocol, we replaced the strongly acidic fabrication media with physiologically-relevant phosphate-buffered saline (PBS, pH = 7.4), simultaneously removing excess unloaded cargo as monitored by UV-Vis spectrophotometry (see Materials and Methods for full details on this solvent exchange protocol). We screened particle loading with a variety of different model compounds including pyrene, carboxyfluorescein, triclosan, aspirin, and ibuprofen, selected either because of their biological activities and/or the relative ease with which they could be detected by fluorimetry or UV/Vis spectrophotometry. In these initial screens, we found that hydrophilic molecules (e.g., aspirin and carboxyfluorescein) were released almost immediately after encapsulation and during the first several solvent exchange steps (as determined by UV/Vis analysis), whereas model hydrophobic molecules (e.g., pyrene, triclosan, and ibuprofen) could be encapsulated without significant disruption of the LLC morphology or domain sizes (as determined by UV/Vis and SAXS analysis). We address this second point in more detail in the discussion below.

The results of our screening study motivated the selection of triclosan—a moderately hydrophobic broad spectrum antibiotic with a readily measurable UV/Vis signal (λ = 280 nm)—for further study. To demonstrate that triclosan was loaded into the inverse cubic and lamellar phases of $\mathbf{1}_{10}$ and $\mathbf{1}_{12}$, respectively, we isolated $\mathbf{1}_{10}$ cubosomes and $\mathbf{1}_{12}$ lamellarsomes from particle dispersions in PBS solution (after washing away excess unloaded triclosan) by centrifugation-filtration. Figure 2A shows the results of UV/Vis analysis on a solution of the isolated particles after dissolution in methanol to disrupt the LLC morphology and release the loaded triclosan. The appearance of a peak at 280 nm confirmed that a significant quantity of triclosan was loaded in the particles (Figure 2A, solid line, $\mathbf{1}_{10}$; red line $\mathbf{1}_{12}$). Analysis of the PBS

supernatant showed that it did not contain triclosan (Figure 2A, dashed line), confirming that the solvent exchange and wash procedures used here were sufficient to remove unloaded triclosan after particle fabrication.

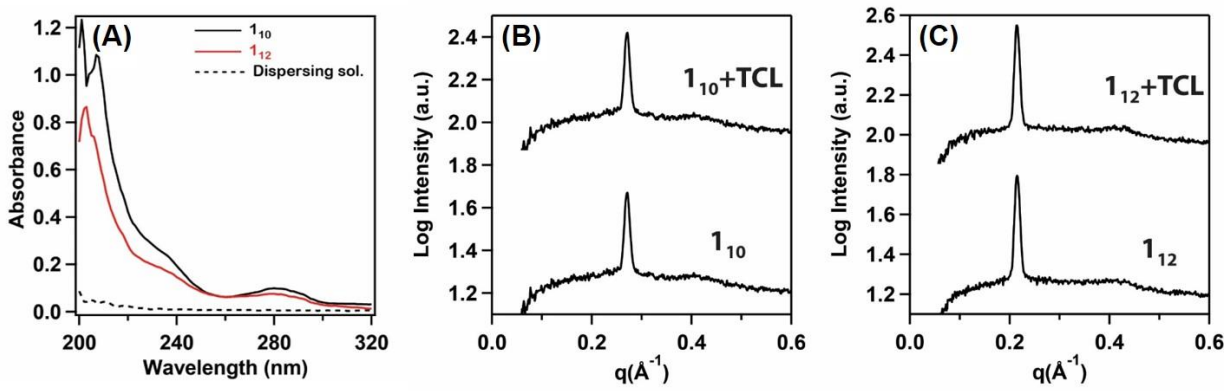

Figure 2. Analysis of triclosan loading into **1₁₀** and **1₁₂** LLC particles. (A) UV/Vis absorption spectra for solutions of triclosan-loaded **1₁₀** (black trace) and **1₁₂** (red trace) LLC particles after dissolution in methanol to liberate the loaded triclosan, together with the absorption of the aqueous media in which the particles were colloidally dispersed (dotted trace; triclosan, λ_{abs} = 280 nm). (B) and (C) Azimuthally-integrated SAXS traces for **1₁₀** and **1₁₂** LLC particles before (bottom) and after (top) loading with triclosan (TCL).

We performed experiments to determine whether the addition of triclosan significantly disrupted or altered the self-assembled morphologies of particles prepared with **1₁₀** and **1₁₂** at a loading of 1 wt% triclosan (relative to the amphiphile). Figures 2B and C show lab-source SAXS analysis of particles prepared from amphiphiles **1₁₀** and **1₁₂**, respectively; no difference in LLC morphology is apparent between triclosan-loaded and unloaded particles. We disregarded loaded **1₉** particles in these studies because initial SAXS analysis revealed a single broad peak suggesting a disordered state (Fig S2; we note that this could also be indicative of liposomes, but we did not pursue further characterization here). In addition, because the position of the principal scattering peak in the SAXS pattern of triclosan-loaded **1₁₀** and **1₁₂** particles is unchanged

relative to the unloaded particles, we conclude that the addition of 1 wt% triclosan does not substantially change the domain sizes in these structures. However, subsequent experiments revealed that the domain spacing in both $\mathbf{1_{10}}$ and $\mathbf{1_{12}}$ particles increased with increased loading fractions up to 5 wt% triclosan (based on a shift in the principal scattering peak to lower q^*; data not shown). The apparent loss of morphology in particles of $\mathbf{1_9}$ upon loading and the changes observed in the domain spacings for particles of $\mathbf{1_{10}}$ and $\mathbf{1_{12}}$ at higher loading fractions suggest that triclosan is interacting with the LLC phase, but it is not possible, from these experiments, to determine if it is localized within the hydrophobic tails or the hydrophilic aqueous domains.

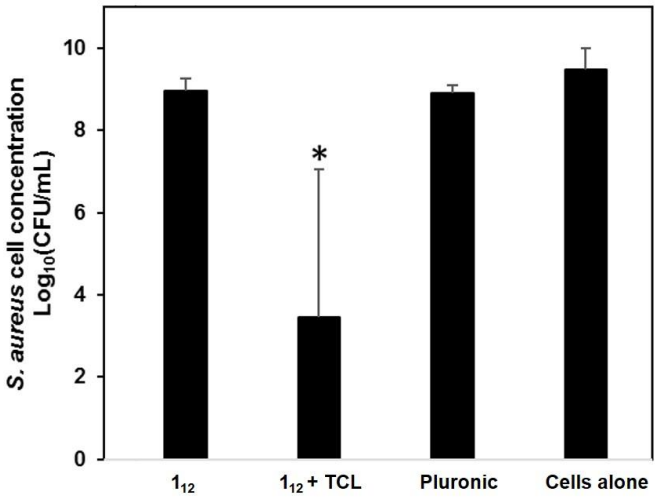

Figure 3. Plot showing the effect of triclosan-loaded $\mathbf{1_{12}}$ particles on *S. aureus*. The asterisk indicates that the reduction in cell viability for $\mathbf{1_{12}}$ triclosan-loaded particles ($\mathbf{1_{12}}$ + TCL) is statistically significant relative to treatment with $\mathbf{1_{12}}$ particles ($p < 0.05$). The effect of addition of Pluronic block copolymer (particle stabilizer) alone is also negligible.

We performed a final series of experiments to determine whether these triclosan-loaded LLC particles could promote cell death in a colony of *S. aureus*. For these experiments, samples of loaded and unloaded $\mathbf{1_{12}}$ lamellarsomes were incubated at 37 °C with cultures of *S. aureus* in a 6-well plate, and the number of colony forming units (CFUs) was subsequently analyzed after 24

hours of incubation. Figure 3 shows that cell viability was decreased significantly ($p < 0.05$) when *S. aureus* was treated with triclosan-loaded $\mathbf{1}_{12}$ particles relative to the untreated cell colony. A difference in viability was also apparent when the effect of triclosan-loaded particles was compared to control experiments performed by exposing cells to a solution of the LLC particle stabilizer (Pluronic F127) as well as to unloaded, but otherwise identically-fabricated, $\mathbf{1}_{12}$ particles. These results suggest that triclosan can be released from loaded $\mathbf{1}_{12}$ particles in a biologically active form and at concentrations sufficient enough to promote cell death in *S. aureus.*

Although many current applications for LLC particles including drug delivery could benefit from specific particle size distributions and surface chemistries (factors that control circulation time in the bloodstream and cellular uptake ability, for example),[13,16] conventional methods for isasome fabrication do not afford simultaneous control over these two properties. Previous reports have demonstrated that isasome particles can be coated, post-fabrication, with layer-by-layer (LbL) polymer thin films to define interfacial properties.[29,30] We hypothesized that a reverse approach, where LLC particles were encapsulated within pre-fabricated polymer capsules, could enable control over both particle size distributions and surface properties. We performed a series of experiments to determine if LLC particles could be formed and encapsulated reductively degradable hollow polymer capsules. To explore the feasibility of this approach, we used hollow capsules fabricated by a reactive LbL and sacrificial template approach based on the iterative deposition of the amine-reactive polymer poly(2-vinyl-4,4-dimethylazlactone) and the small molecule diamine cross-linker cystamine onto 8 μm silicon beads, followed by removal of the inorganic core to obtain hollow capsules (see Materials and Methods and past publications for details).[27,28] This approach affords both (i) reactive azlactone

groups at the outer and inner capsule walls that can be functionalized to install a range of physicochemical properties and functions, (ii) control over capsule size by selection of the silicon sphere template, and (iii) a degradable capsule of potential utility in controlled release.

To load the hollow microcapsules, we selected amphiphile **1$_{12}$** because lamellar LLC phases (in contrast to cubic phases, e.g., as formed by **1$_{10}$**) are anisotropic and therefore exhibit strong birefringence when self-assembled,[1,4] allowing us to study encapsulation and subsequent self-assembly using brightfield and cross-polarized microscopy. Figure 4A shows a representative brightfield microscopy image of hollow capsules prior to incubation in a solution of amphiphile **1$_{12}$**. Figure 4B shows the capsules after incubation and following extraction into deionized water. The appearance of spherical droplets fully contained within the capsules suggests that amphiphile **1$_{12}$** was successfully loaded into the capsules and that it does not diffuse out into the surrounding aqueous phase under these conditions. We also observed that the capsules were partially filled, behavior that has been observed in past reports with similar capsules loaded with droplets of thermotropic liquid crystal, and can be ascribed to the tendency of the capsules to swell after extraction into the aqueous phase.[27,31] Figure 4C shows a cross-polarized microscopy image of the loaded capsules; no birefringence is observed. However, as Figure 4D reveals, approximately 5 minutes after the addition of sulfuric acid to the surrounding media (such that the final concentration was ~ 1.0 M [H^+]), the capsules became strongly birefringent. This result suggests that protonation of the amphiphile by acid triggered self-assembly into a lamellar LLC phase within the capsule, which is consistent with past results from the self-assembly of bulk LLC phases, and observations made above during the fabrication of **1$_{12}$** LLC particles. Lab-source SAXS experiments further confirmed the presence of a lamellar phase for these **1$_{12}$**-loaded polymer capsules as evidenced by a sharp principal reflection at the same

position as for the dispersed **1$_{12}$** particles (SI Fig 2). The position of the principal scattering peak suggests a predominantly lamellar morphology, with a domain spacing that agrees well with the domain spacing for the non-encapsulated particles. We did, however, observe a secondary peak at higher *q* suggesting that a cubic or other unknown phase may coexist with the lamellae under these conditions. Further experiments will need to be performed in order to determine the conditions necessary for these encapsulated **1$_{12}$** particles to adopt a pure phase.

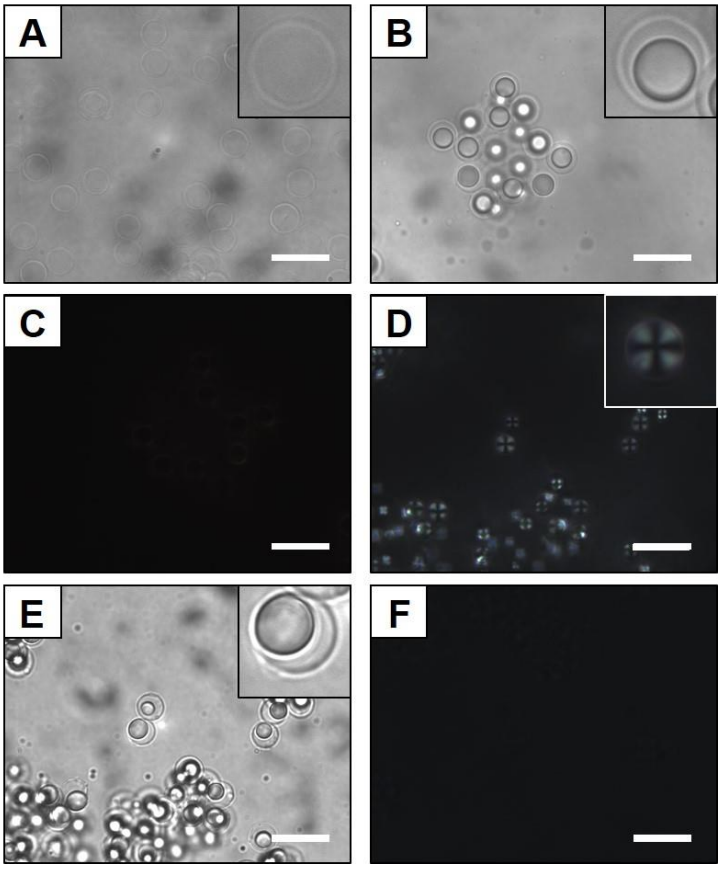

Figure 4. Microscopy images showing the results of loading hollow polymer capsules with **1$_{12}$** amphiphile and subsequent self-assembly. (A) Brightfield image of hollow polymer capsules before and (B) after loading with amphiphile **1$_{12}$**. (C) Cross-polarized image showing that the **1$_{12}$**-loaded capsules are non-birefringent after loading. (D) Cross-polarized image showing that after the addition of acid to the surrounding media, capsules are strongly birefringent. (E) Brightfield image of the loaded capsules after addition of $NaHCO_3$ buffer (pH = 10.8) and an increase in alkalinity of the surrounding media. (F) Corresponding cross-polarized image showing the transition back to a non-birefringent and disordered state. Scale bar = 20 μm.

Finally, Figures 4E and F show that the transition between the disordered and the self-assembled lamellar LLC morphology in **1$_{12}$**-loaded capsules is reversible upon exchange of the media with a basic buffer. Brightfield (E) and cross-polarized (F) images of the particle dispersion after exchanging the acidic media for $NaHCO_3$ buffer (pH = 10.8) reveal the encapsulated amphiphile droplets to have changed from birefringent to optically isotropic within ~5 minutes. This result is consistent with past unreported experiments from our lab demonstrating that bulk self-assembled samples of **1$_{12}$** can be disordered by the addition of base. The effect of pH on self-assembly in this system suggests opportunities to design responsive LLC particles and other stimuli-responsive LLC assemblies based on these six-tailed synthetic amphiphiles. Future experiments to determine the susceptibility of these self-assembled phases to treatment with minimal amounts of base will help guide the design of pH responsive systems, that could, for example be used to control and trigger drug or small molecule release.[17,32] Moreover, this new encapsulation approach could lead to experiments designed to investigate the interfacial wetting behaviors of encapsulated LLC particles and the effect of surface chemistry on the ordering transitions in encapsulated amphiphile droplets.[28,31]

Conclusions

LLC particles have been fabricated using a relatively limited number of naturally-occurring lipids and derivatives and access to different internal particle morphologies generally necessitates the use of chemically distinct lipids and mixtures of lipids, concomitantly changing other particle properties including size distribution and chemical functionality. We have reported here on the fabrication of inverse cubic and lamellar isasome particles that are fabricated using structurally homologous synthetic six-tailed amphiphiles. Our approach provides access to

different inverse LLC particle morphologies without significantly changing amphiphile chemistry, and thus the physicochemical properties of the particles. We demonstrated that LLC particles with lamellar structures can be used to host and deliver the antiobiotic triclosan, inducing cell death in *S. aureus*. We also reported methods for encapsulating particles within hollow polymer capsules and results suggesting that internal morphological changes can be triggered by changing the surrounding environment. Overall, this approach permits control over LLC particle size as well as surface chemistry, and could thus be useful in future applications such as targeting and drug delivery. Our approach to LLC particle fabrication and the methods reported here and should help guide the design of synthetic isasomes and enable their future development for potential applications including drug delivery, controlled release, and as hosts for imaging agents.

Acknowledgments. This work was supported by the National Science Foundation through a grant to the Materials Research Science and Engineering Center (MRSEC) at the University of Wisconsin-Madison (DMR-1121288) and made use of NSF-supported facilities (DMR-1121288, CHE-9974839, CHE-1048642). We thank Mahesh K. Mahanthappa for organizing synchrotron SAXS studies conducted at Sector 12 of the Advanced Photon Source, a U.S. Department of Energy (DOE) Office of Science User Facility operated for the DOE Office of Science by Argonne National Laboratory under Contract No. DE-AC02-06CH11357. We thank X. Guo for fabricating the hollow polymer capsules and A. Rodríguez-López for performing the bacterial inhibition studies. M.C.D.C acknowledges the Natural Sciences and Engineering Research Council of Canada for a graduate fellowship.

References

(1) Nguyen, S. T.; Gin, D. L.; Hupp, J. T.; Zhang, X. Supramolecular chemistry: functional structures on the mesoscale. *Proceedings of the National Academy of Sciences U.S.A.* **2001,** *98* (21), 11849.

(2) Zhao, X.; Pan, F.; Xu, H.; Yaseen, M.; Shan, H.; Hauser, C. A. E.; Zhang, S.; Lu, J. R. Molecular self-assembly and applications of designer peptide amphiphiles. *Chemical Society Reviews* **2010,** *39* (9), 3480.

(3) Fong, C.; Le, T.; Drummond, C. J. Lyotropic liquid crystal engineering-ordered nanostructured small molecule amphiphile self-assembly materials by design. *Chemical Society Reviews* **2012,** *41* (3), 1297.

(4) Miller, D. S.; Wang, X.; Abbott, N. L. Design of Functional Materials Based on Liquid Crystalline Droplets. *Chemistry of Materials* **2014,** *26* (1), 496.

(5) Gin, D. L.; Bara, J. E.; Noble, R. D.; Elliott, B. J. Polymerized lyotropic liquid crystal assemblies for membrane applications. *Macromolecular Rapid Communications* **2008,** *29* (5), 367.

(6) van Rijn, P.; Tutus, M.; Kathrein, C.; Zhu, L.; Wessling, M.; Schwaneberg, U.; Boker, A. Challenges and advances in the field of self-assembled membranes. *Chemical Society Reviews* **2013,** *42* (16), 6578.

(7) Archibald, D. D.; Mann, S. Template mineralization of self-assembled anisotropic lipid microstructures. *Nature* **1993,** *364* (6436), 430.

(8) Zhao, Y.; Liu, J.; Sohn, Y.; Fang, J. Synthesis of Stable Hybrid Silica-Lipid Cylinders with Nanoscale Helical Ripples. *Journal of Physical Chemistry C* **2007,** *111* (17), 6418.

(9) Delclos, T.; Aime, C.; Pouget, E.; Brizard, A.; Huc, I.; Delville, M.-H.; Oda, R. Individualized Silica Nanohelices and Nanotubes: Tuning Inorganic Nanostructures Using Lipidic Self-Assemblies. *Nano Letters* **2008,** *8* (7), 1929.

(10) Pal, N.; Bhaumik, A. Soft templating strategies for the synthesis of mesoporous materials: Inorganic, organic–inorganic hybrid and purely organic solids. *Advances in Colloid and Interface Science* **2013,** *189–190*, 21.

(11) Spicer, P. T. Progress in liquid crystalline dispersions: Cubosomes. *Current Opinion in Colloid & Interface Science* **2005,** *10* (5–6), 274.

(12) Yaghmur, A.; Glatter, O. Characterization and potential applications of nanostructured aqueous dispersions. *Advances in Colloid and Interface Science* **2009,** *147–148*, 333.

(13) Mulet, X.; Boyd, B. J.; Drummond, C. J. Advances in drug delivery and medical imaging using colloidal lyotropic liquid crystalline dispersions. *Journal of Colloid and Interface Science* **2013,** *393*, 1.

(14) Cervin, C.; Vandoolaeghe, P.; Nistor, C.; Tiberg, F.; Johnsson, M. A combined in vitro and in vivo study on the interactions between somatostatin and lipid-based liquid crystalline drug carriers and bilayers. *European Journal of Pharmaceutical Sciences* **2009,** *36* (4–5), 377.

(15) Nguyen, T.-H.; Hanley, T.; Porter, C. J. H.; Boyd, B. J. Nanostructured liquid crystalline particles provide long duration sustained-release effect for a poorly water soluble drug after oral administration. *Journal of Controlled Release* **2011,** *153* (2), 180.

(16) Zabara, A.; Mezzenga, R. Controlling molecular transport and sustained drug release in lipid-based liquid crystalline mesophases. *Journal of Controlled Release* **2014,** *188*, 31.

(17) Salentinig, S.; Tangso, K. J.; Hawley, A.; Boyd, B. J. pH-Driven Colloidal Transformations Based on the Vasoactive Drug Nicergoline. *Langmuir* **2014,** *30* (49), 14776.

(18) Martiel, I.; Baumann, N.; Vallooran, J. J.; Bergfreund, J.; Sagalowicz, L.; Mezzenga, R. Oil and drug control the release rate from lyotropic liquid crystals. *Journal of Controlled Release* **2015,** *204*, 78.

(19) Meli, V.; Caltagirone, C.; Falchi, A. M.; Hyde, S. T.; Lippolis, V.; Monduzzi, M.; Obiols-Rabasa, M.; Rosa, A.; Schmidt, J.; Talmon, Y.et al. Docetaxel-Loaded Fluorescent Liquid-Crystalline Nanoparticles for Cancer Theranostics. *Langmuir* **2015,** *31* (35), 9566.

(20) Liu, G.; Conn, C. E.; Waddington, L. J.; Mudie, S. T.; Drummond, C. J. Colloidal Amphiphile Self-Assembly Particles Composed of Gadolinium Oleate and Myverol: Evaluation as Contrast Agents for Magnetic Resonance Imaging. *Langmuir* **2010,** *26* (4), 2383.

(21) Moghaddam, M. J.; de Campo, L.; Waddington, L. J.; Drummond, C. J. Chelating phytanyl-EDTA amphiphiles: self-assembly and promise as contrast agents for medical imaging. *Soft Matter* **2010,** *6* (23), 5915.

(22) Moghaddam, M. J.; de Campo, L.; Waddington, L. J.; Weerawardena, A.; Kirby, N.; Drummond, C. J. Chelating oleyl-EDTA amphiphiles: self-assembly, colloidal particles, complexation with paramagnetic metal ions and promise as magnetic resonance imaging contrast agents. *Soft Matter* **2011,** *7* (22), 10994.

(23) Muir, B. W.; Acharya, D. P.; Kennedy, D. F.; Mulet, X.; Evans, R. A.; Pereira, S. M.; Wark, K. L.; Boyd, B. J.; Nguyen, T.-H.; Hinton, T. M.et al. Metal-free and MRI visible theranostic lyotropic liquid crystal nitroxide-based nanoparticles. *Biomaterials* **2012,** *33* (9), 2723.

(24) Carter, M. C. D.; Miller, D. S.; Jennings, J.; Wang, X.; Mahanthappa, M. K.; Abbott, N. L.; Lynn, D. M. Synthetic Mimics of Bacterial Lipid A Trigger Optical Transitions in Liquid Crystal Microdroplets at Ultralow Picogram-per-Milliliter Concentrations. *Langmuir* **2015,** *31* (47), 12850.

(25) Alferiev, I. S.; Connolly, J. M.; Levy, R. J. A novel mercapto-bisphosphonate as an efficient anticalcification agent for bioprosthetic tissues. *Journal of Organometallic Chemistry* **2005,** *690* (10), 2543.

(26) Buck, M. E.; Schwartz, S. C.; Lynn, D. M. Superhydrophobic Thin Films Fabricated by Reactive Layer-by-Layer Assembly of Azlactone-Functionalized Polymers. *Chemistry of Materials* **2010,** *22* (23), 6319.

(27) Manna, U.; Zayas-Gonzalez, Y. M.; Carlton, R. J.; Caruso, F.; Abbott, N. L.; Lynn, D. M. Liquid Crystal Chemical Sensors That Cells Can Wear. *Angewandte Chemie International Edition* **2013,** *52* (52), 14011.

(28) Guo, X.; Manna, U.; Abbott, N. L.; Lynn, D. M. Covalent Immobilization of Caged Liquid Crystal Microdroplets on Surfaces. *ACS Applied Materials & Interfaces* **2015,** *7* (48), 26892.

(29) Driever, C. D.; Mulet, X.; Johnston, A. P. R.; Waddington, L. J.; Thissen, H.; Caruso, F.; Drummond, C. J. Converging layer-by-layer polyelectrolyte microcapsule and cubic lyotropic liquid crystalline nanoparticle approaches for molecular encapsulation. *Soft Matter* **2011,** *7* (9), 4257.

(30) Driever, C. D.; Mulet, X.; Waddington, L. J.; Postma, A.; Thissen, H.; Caruso, F.; Drummond, C. J. Layer-by-Layer Polymer Coating on Discrete Particles of Cubic Lyotropic Liquid Crystalline Dispersions (Cubosomes). *Langmuir* **2013,** *29* (42), 12891.

(31) Carlton, R. J.; Zayas-Gonzalez, Y. M.; Manna, U.; Lynn, D. M.; Abbott, N. L. Surfactant-Induced Ordering and Wetting Transitions of Droplets of Thermotropic Liquid Crystals “Caged” Inside Partially Filled Polymeric Capsules. *Langmuir* **2014,** *30* (49), 14944.

(32) Liu, Q.; Dong, Y.-D.; Boyd, B. J. Selective Sequence for the Peptide-Triggered Phase Transition of Lyotropic Liquid-Crystalline Structures. *Langmuir* **2016,** *32* (20), 5155.

Supporting Information for Chapter 15

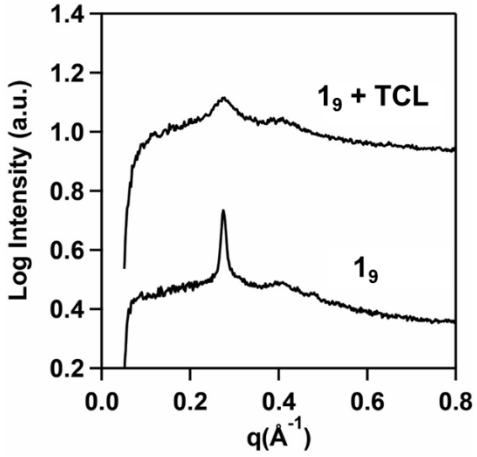

Figure S1. Azimuthally-integrated lab-source SAXS trace for **1₉** LLC particles (bottom) and **1₉** LLC particles loaded with triclosan (TCL, top). The SAXS pattern for the loaded particles is largely featureless, suggesting that the sample is predominantly disordered.

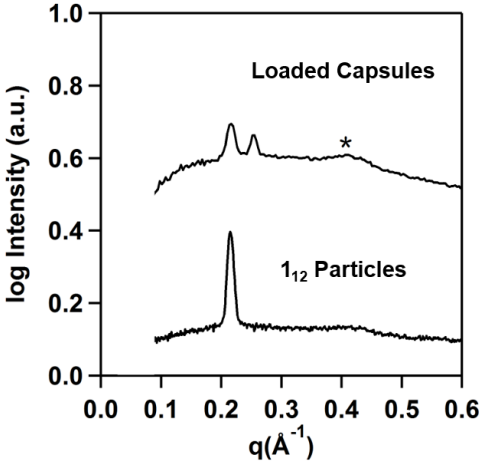

Figure S2. Azimuthally-integrated lab-source SAXS traces for dispersed-phase **1₁₂** LLC particles (bottom) and **1₁₂**-loaded hollow polymer capsules after extraction into deionized water and addition of H_2SO_4 such that the final [H+] ~ 1.0 M. The asterisk indicates a peak that arises from the Kapton tube used for SAXS measurements.

Chapter 16

Summary and Future Work

Summary

The work described in this thesis focused on (i) the design and fabrication of reactive polymers, surfaces, and interfaces that display the azlactone group, and (ii) the synthesis and physicochemical characterization of the self-assembly behavior of a class of homologous six-tailed amphiphiles. The work in the first section (Chapters 2-6) built upon past reports from our group demonstrating that multilayer films fabricated by the reactive layer-by-layer (LbL) assembly of poly(2-vinyl-4,4-dimethylazlactone) (PVDMA) and branched poly(ethylenimine) (PEI) contain residual azlactone groups that can be modified, post-fabrication, with primary amine-containing compounds to install new and useful surface and bulk properties.[1-12] The results of Chapter 2 significantly broaden the pool of nucleophiles available for post-fabrication functionalization reactions to include alcohol-, thiol-, and hydrazine-containing compounds; this advancement has enabled the introduction of degradable linkages and dynamic surface features in PEI/PVDMA multilayers. Chapters 3 and 4 presented further developments in the use of reactive azlactone-containing films as platforms for the design of biomolecule arrays, using both manual and automated synthesis methods. Chapter 5 described the development of a heat-shrinkable superhydrophobic material based on the LbL assembly of PEI and PVDMA that was readily amenable to reactive surface patterning and feature miniaturization by heat-induced shrinking. Chapter 6 continued to investigate the physicochemical properties of PEI/PVDMA multilayered films, and presented an emerging understanding and new insights into the fundamental physicochemical parameters that control the growth of nano- and microscale roughness and lead to the onset of superhydrophobicity in these materials.

Chapters 7 through 9 focused on the design, synthesis, and self-assembly of azlactone-containing block copolymers (BCPs). In Chapter 7, the results of initial self-assembly studies

with a lamellae-forming poly(styrene-*block*-2-vinyl-4,4-dimethylazlactone) (PS-*b*-PVDMA) BCP in both the bulk and thin film regime were reported, while Chapter 8 went on to describe self-assembly with a cylinder-forming BCP. The results of both chapters showed that PS-*b*-PVDMA BCP thin films can be used as reactive templates for surface patterning applications, by post-fabrication treatment with primary amine-containing nucleophiles to install new functionality on azlactone-containing nanometer-sized 'lines' or 'dots'. Chapter 9 exploited the reactivity of low molecular weight PS-*b*-PVDMA BCPs, using non-microphase-separated polymers to rapidly screen for microphase separation in side chain-functionalized polymer derivatives. This new method of identifying block-block combinations with high chemical incompatibility provided a framework for the discovery BCPs that microphase separate into morphologies with increasingly small feature sizes and could be useful in future lithography applications.

Chapters 10 through 12 reported on the development of new classes of azlactone-containing materials. Chapter 10 reported an approach to the introduction of degradable backbone ester units into the homopolymer PVDMA scaffold, yielding hydrolytically degradable and side chain-reactive polymers, as well as reactive assemblies including degradable capsules, gels, and cationic polymers that promote gene delivery. Chapter 11 illustrated the utility of side chain-functionalized PVDMA constructs for the conventional electrostatic LbL assembly of DNA-containing thin films. We showed that the combination of a side chain charge-shifting polymer and a poly(β-amino ester) into 'mixed multilayer' films resulted in coatings that promoted the long term and linear release of DNA. In a final new direction in azlactone-containing materials, Chapter 12 presented principles for the fabrication of electrospun

azlactone-containing polymer nanofibers, and illustrated the ability to immobilize diverse chemical functionality onto these non-woven mats.

The second major focus of this thesis, Chapters 13 through 15, reported on the synthesis and physicochemical characterization of synthetic six-tailed amphiphiles that mimic key structural properties and self-assembly behaviors of bacterial Lipid A. Chapter 3 focused on the ability of six-tailed amphiphiles to trigger optical ordering transitions in liquid crystal microdroplets, in a manner similar to that of Lipid A, at exceedingly low picogram-per-milliliter concentrations. Chapter 14 described synchrotron small-angle X-ray scattering (SAXS) studies on amphiphile self-assembly, varying tail length and headgroup counter-ion identity to systematically study lyotropic liquid crystalline (LLC) phase behavior. Chapter 15 exploited the self-assembly behavior of six-tailed described in detail in the previous chapter, showing that these synthetic amphiphiles could be used to fabricate colloidally-stable LLC particles, with applications in the encapsulation of molecular cargo. The remainder of this Chapter provides recommendations for future directions for the work described in this thesis.

Future Work (Chapters 2 to 6): Investigations into the Physicochemical Parameters that Control Growth and Morphology in PEI/PVDMA Multilayer Films

The studies in Chapters 2 through 6 exploited multilayered polymer films assembled using the mutually reactive polymers PEI and PVDMA. The continued and future deployment of these multilayered films in a variety of emerging applications (*e.g.*, drug delivery and controlled release,[13-15] as materials with special-wetting properties,[11,12,15,16] *etc.*) now depends on an understanding of the properties required to control and reproducibly predict film morphologies (*e.g.*, whether films are thin or thick, smooth or porous, *etc.*). The primary goal of Chapter 6 was

to present an emerging understanding of the physicochemical properties that control morphology in these multilayer films. Future studies should prove useful in further developing an understanding of growth mechanism in the PEI/PVDMA film system. First, additional studies to understand the degree to which electrostatic interactions between hydrolyzed azlactone groups (carboxylic acids) and amines in PEI play a role in promoting film growth, and to what extent these interactions determine film morphology, could shed light on the structures and functions of existing materials, as well as provide new tools for manipulating the properties of PEI/PVDMA thin films in unique ways (*e.g.*, to design films that grow and behave like conventional polyelectrolyte multilayers, covalently cross-linked assemblies, or as hybrids of the two). Second, in-depth kinetics studies of the reaction rates of azlactones in PVDMA with model primary amines-containing compounds in different solvents, by ^{1}H NMR and IR, followed by analogous studies to understand the reaction rates between azlactones and amines in PEI and other polyamines, could help to reveal the growth mechanism in multilayered films and provide potential new means to manipulate film growth and morphologies. Finally, a subsequent study to determine the effect of the solvent used for film fabrication solvent could prove useful in determining and potentially deconvoluting the contributions of ionic interactions and polymer-polymer cross-linking reactions to film morphology.

Future Work (Chapters 7 to 9): Synthesis, Self-Assembly, and Reactivity in Azlactone-Containing Block Copolymers

There is much that remains to be explored with azlactone-containing BCPs. PS-*b*-PVDMA represents the most well-characterized azlactone-containing BCP construct, and it is now among the most well-characterized reactive BCP systems with respect to thin film self-

assembly and reactive patterning.[17] It is one of several reactive BCPs successfully used for post-fabrication covalent surface patterning in the thin film regime.[18-20] An immediate future study that would be of fundamental interest would be to further map out the phase diagram for PS-*b*-PVDMA by varying PS and PVDMA volume fractions and thereby determine the full suite of accessible polymer morphologies. To date, hexagonal and lamellar BCPs have been reported by our group, but the addition of spherical and gyroidal BCPs to the toolkit would expand the range of templates available for reactive patterning in the both the bulk and thin film regimes. Additional synthetic studies targeting new BCP architectures would also increase the morphological diversity in this system. Triblock copolymers, for example, synthesized by homo- or heterobifunctional RAFT/ATRP agents would give rise to a range of new reactive morphologies and may enable future materials applications in the templated synthesis of inorganic materials or as nanoporous filtration scaffolds for liquid- or vapor-phase separations.[21-23] A final area of research would be to investigate the design of dually reactive BCPs, in which two or more blocks contains orthogonally reactive groups.[24,25] Such polymer constructs, once processed into bulk or thin film self-assemblies, could lead to new and unique templates for surface patterning and lithography.

In a final proposed area of research for azlactone-containing BCPs, the synthesis and characterization of polyanionic and polycationic polymers would be fundamentally interesting and potentially useful in a variety of settings. For example, permanently charged derivatives of azlactone-containing BCPs have not yet been studied, although these materials may display unique self-assembly behavior and provide access to exceedingly small domain sizes (*e.g.*, owing to high block-block repulsion).[26-28] Once in hand, copolymers with charged side chain groups could also be evaluated for their water solubility, potentially opening the door to self-

assembled aqueous particles (*e.g.*, liposomes, multilamellar vesicles, and worm-like micelles). Furthermore, water-soluble and reactive BCP polymers and particles could be designed, where only a minimum number of azlactone groups are functionalized to provide a sufficient number of charged side chains to increase water solubility, while the residual groups remain available for functionalization reactions in water. This general idea has been reported in the past,[29,30] but not in self-assembled aqueous nanostructures. Studies of this nature would require investigations into the stability of azlactones in these copolymers in aqueous media, as well as their reactivity with incoming compounds for further functionalization.

Future Work (Chapters 14 to 15): Cubosomes as Hosts for Molecular Cargo and Drug Delivery

In Chapters 14 and 15, we described the self-assembly behavior of a series of six-tailed synthetic amphiphiles and their subsequent fabrication into colloidally stable, water-dispersed LLC particles (so-called ‘isasome’ particles). In a proof of concept experiment, we showed that these synthetic nanometer-sized cubosomes and lamellarsomes (depending on internal structure) can be used to host molecular cargo (*e.g.*, the model antibacterial agent triclosan) and affect a response in living cells. These early investigations into this new system provide several avenues for future research and further experiments are suggested as follows: (i) a broad study on drug encapsulation to determine the physicochemical parameters (*e.g.*, hydrophobic, hydrophilic, and effects of functional groups) that govern loading and encapsulation within particles of each phase; (ii) a study to quantify the loading amount of selected model drugs into particles of each phase by varying the loading density and subsequently determining the effect on internal morphology by SAXS, and (iii) a full study of the release of a series of model drugs into

physiologically-relevant media (*e.g.*, PBS buffer or cell culture media) to determine both the release profiles and the total amount of drug that can be made available for a given concentration of particles.

A subsequent line of investigation into the general physiological effects of these particle dispersions *in vivo* could prove insightful. Experiments designed to characterize the residence time in the bloodstream of LLC particle formulations, as well as their mode of elimination, would guide potential future efforts to design injectable, particle-based drug formulations. In a related experiment, these particles could potentially be coated with polymer films to passivate the surface or otherwise install further functionality, using methods such as LbL assembly. Others have proposed methods for coating the surfaces of LLC particles, for example, to increase circulation time in the bloodstream, but LbL methods have yet to be extensively investigated.[31,32] In Chapter 15, we showed that amphiphiles could be loaded into pre-fabricated LbL capsules with well-defined size distributions and could be subsequently transformed into self-assembled encapsulated particles. However, experiments to coat pre-formed LLC particles with LbL films could prove exceedingly useful in the design of particles with tailored surface coatings. It could be possible, for example, to coat particles with polymer films that both increase residence time in the bloodstream and present targeting motifs on the surfaces of particles that promote localization at diseased sites.

Another line of inquiry for LLC particles falls under the broad category of hosting image-contrast agents or species that modulate relaxation times in medical imaging analyses. Past reports, for example, have shown that certain amphiphiles and assemblies can host or chelate contrast agents such as Gd^{3+} or Mn^{2+}, which are useful in magnetic resonance imaging.[33-36] The results of past experiments from our lab that have not been published suggest that synthetic six-

tailed amphiphiles can chelate certain transition metals with high affinity and form self-assembled phases. Transition metal ions useful as contrast agents could be screened for their ability to promote self-assembly in six-tailed amphiphiles. These results could lead to the design and synthesis of new LLC particles useful in magnetic resonance imaging, and could be combined with methods studied above for coating and passivating the surfaces of particles. Finally, the six-tailed amphiphiles described here for the preparation of LLC particles are entirely synthetic, in contrast to the common biological lipids used in past studies. The synthetic route to six-tailed amphiphiles reported here is straightforward but also modular, suggesting opportunities to incorporate functional elements within the amphiphile structures. For example, initial studies in our group have demonstrated that amphiphiles with double bond-containing tails could be easily synthesized. These structurally-related amphiphiles self-assemble into the same LLC phases as their aliphatic counterparts, and these results suggest new avenues for further amphiphile derivatization (*e.g.*, by thiol-ene coupling reactions) as well as the ability to polymerize a self-assembled nanostructure and lock it in place (*e.g.*, either in the bulk, as thin films, or the LLC particle regime). Future studies could focus on both (i) the use of alkene or other reactive groups within amphiphile tails for further derivatization and to install unique functionalities and properties, and (ii) post-fabrication polymerization of amphiphile self-assembled structures to increase mechanical rigidity and potentially open the door to applications for bulk amphiphile materials (*e.g.*, as materials for filtration membranes, to capture and sequester small molecules, or for the templated synthesis of hybrid materials within self-assembled hydrophobic or hydrophilic domains). Future work in this area should focus broadly on potential applications of both LLC particles, thin films, and bulk self-assembled materials.

References

(1) Buck, M. E.; Zhang, J.; Lynn, D. M. Layer-by-Layer Assembly of Reactive Ultrathin Films Mediated by Click-Type Reactions of Poly(2-Alkenyl Azlactone)s. *Advanced Materials* **2007,** *19* (22), 3951.

(2) Buck, M. E.; Breitbach, A. S.; Belgrade, S. K.; Blackwell, H. E.; Lynn, D. M. Chemical Modification of Reactive Multilayered Films Fabricated from Poly(2-alkenyl azlactone)s: Design of Surfaces that Prevent or Promote Mammalian Cell Adhesion and Bacterial Biofilm Growth. *Biomacromolecules* **2009,** *10* (6), 1564.

(3) Buck, M. E.; Lynn, D. M. Functionalization of Fibers Using Azlactone-Containing Polymers: Layer-by-Layer Fabrication of Reactive Thin Films on the Surfaces of Hair and Cellulose-Based Materials. *ACS Applied Materials & Interfaces* **2010,** *2* (5), 1421.

(4) Buck, M. E.; Schwartz, S. C.; Lynn, D. M. Superhydrophobic Thin Films Fabricated by Reactive Layer-by-Layer Assembly of Azlactone-Functionalized Polymers. *Chemistry of Materials* **2010,** *22* (23), 6319.

(5) Kinsinger, M. I.; Buck, M. E.; Abbott, N. L.; Lynn, D. M. Immobilization of Polymer-Decorated Liquid Crystal Droplets on Chemically Tailored Surfaces. *Langmuir* **2010,** *26* (12), 10234.

(6) Broderick, A. H.; Azarin, S. M.; Buck, M. E.; Palecek, S. P.; Lynn, D. M. Fabrication and Selective Functionalization of Amine-Reactive Polymer Multilayers on Topographically Patterned Microwell Cell Culture Arrays. *Biomacromolecules* **2011,** *12* (6), 1998.

(7) Buck, M. E.; Lynn, D. M. Azlactone-functionalized polymers as reactive platforms for the design of advanced materials: Progress in the last ten years. *Polymer Chemistry* **2012,** *3* (1), 66.

(8) Broderick, A. H.; Carter, M. C. D.; Lockett, M. R.; Smith, L. M.; Lynn, D. M. Fabrication of Oligonucleotide and Protein Arrays on Rigid and Flexible Substrates Coated with Reactive Polymer Multilayers. *ACS Applied Materials & Interfaces* **2013,** *5* (2), 351.

(9) Broderick, A. H.; Lynn, D. M. In *Functional Polymers by Post-Polymerization Modification*; Wiley-VCH Verlag GmbH & Co. KGaA, **2013**.

(10) Manna, U.; Lynn, D. M. Patterning and Impregnation of Superhydrophobic Surfaces Using Aqueous Solutions. *ACS Applied Materials & Interfaces* **2013,** *5* (16), 7731.

(11) Manna, U.; Lynn, D. M. Fabrication of Liquid-Infused Surfaces Using Reactive Polymer Multilayers: Principles for Manipulating the Behaviors and Mobilities of Aqueous Fluids on Slippery Liquid Interfaces. *Advanced Materials* **2015,** *27* (19), 3007.

(12) Manna, U.; Lynn, D. M. Synthetic Surfaces with Robust and Tunable Underwater Superoleophobicity. *Advanced Functional Materials* **2015,** *25* (11), 1672.

(13) Manna, U.; Kratochvil, M. J.; Lynn, D. M. Superhydrophobic Polymer Multilayers that Promote the Extended, Long-Term Release of Embedded Water-Soluble Agents. *Advanced Materials* **2013,** *25* (44), 6405.

(14) Kratochvil, M. J.; Tal-Gan, Y.; Yang, T.; Blackwell, H. E.; Lynn, D. M. Nanoporous Superhydrophobic Coatings that Promote the Extended Release of Water-Labile Quorum Sensing Inhibitors and Enable Long-Term Modulation of Quorum Sensing in Staphylococcus aureus. *ACS Biomaterials Science & Engineering* **2015,** *1* (10), 1039.

(15) Manna, U.; Raman, N.; Welsh, M. A.; Zayas-Gonzalez, Y. M.; Blackwell, H. E.; Palecek, S. P.; Lynn, D. M. Slippery Liquid-Infused Porous Surfaces that Prevent Microbial Surface Fouling and Kill Non-Adherent Pathogens in Surrounding Media: A Controlled Release Approach. *Advanced Functional Materials* **2016,** *26* (21), 3599.

(16) Kratochvil, M. J.; Welsh, M. A.; Manna, U.; Ortiz, B. J.; Blackwell, H. E.; Lynn, D. M. Slippery Liquid-Infused Porous Surfaces that Prevent Bacterial Surface Fouling and Inhibit Virulence Phenotypes in Surrounding Planktonic Cells. *ACS Infectious Diseases* **2016,** *2* (7), 509.

(17) Romulus, J.; Henssler, J. T.; Weck, M. Postpolymerization Modification of Block Copolymers. *Macromolecules* **2014,** *47* (16), 5437.

(18) Stadermann, J.; Riedel, M.; Komber, H.; Simon, F.; Voit, B. Functionalized block copolymers for preparation of reactive self-assembled surface patterns. *Journal of Polymer Science Part A: Polymer Chemistry* **2012,** *50* (7), 1351.

(19) Stadermann, J.; Riedel, M.; Voit, B. Nanostructured Films of Block Copolymers Functionalized With Photolabile Protected Amino Groups. *Macromolecular Chemistry and Physics* **2013,** *214* (2), 263.

(20) Killops, K. L.; Gupta, N.; Dimitriou, M. D.; Lynd, N. A.; Jung, H.; Tran, H.; Bang, J.; Campos, L. M. Nanopatterning Biomolecules by Block Copolymer Self-Assembly. *ACS Macro Letters* **2012,** *1* (6), 758.

(21) Bates, F. S.; Fredrickson, G. H. Block Copolymers—Designer Soft Materials. *Physics Today* **1999,** *52*, 32.

(22) Bates, C. M.; Maher, M. J.; Janes, D. W.; Ellison, C. J.; Willson, C. G. Block Copolymer Lithography. *Macromolecules* **2014,** *47* (1), 2.

(23) Epps, I. I. I. T. H.; O'Reilly, R. K. Block copolymers: controlling nanostructure to generate functional materials - synthesis, characterization, and engineering. *Chemical Science* **2016,** *7* (3), 1674.

(24) Lokitz, B. S.; Wei, J.; Hinestrosa, J. P.; Ivanov, I.; Browning, J. F.; Ankner, J. F.; Kilbey, S. M.; Messman, J. M. Manipulating Interfaces through Surface Confinement of Poly(glycidyl methacrylate)-block-poly(vinyldimethylazlactone), a Dually Reactive Block Copolymer. *Macromolecules* **2012,** *45* (16), 6438.

(25) Hoenders, D.; Tigges, T.; Walther, A. Combining the incompatible: Block copolymers consecutively displaying activated esters and amines and their use as protein-repellent surface modifiers with multivalent biorecognition. *Polymer Chemistry* **2015,** *6* (3), 476.

(26) Goswami, M.; Sumpter, B. G.; Huang, T.; Messman, J. M.; Gido, S. P.; Isaacs-Sodeye, A. I.; Mays, J. W. Tunable morphologies from charged block copolymers. *Soft Matter* **2010,** *6* (24), 6146.

(27) Wang, X.; Goswami, M.; Kumar, R.; G. Sumpter, B.; Mays, J. Morphologies of block copolymers composed of charged and neutral blocks. *Soft Matter* **2012,** *8* (11), 3036.

(28) Takahashi, R.; Sato, T.; Terao, K.; Yusa, S.-i. Intermolecular Interactions and Self-Assembly in Aqueous Solution of a Mixture of Anionic–Neutral and Cationic–Neutral Block Copolymers. *Macromolecules* **2015,** *48* (19), 7222.

(29) Gardner, C. M.; Stöver, H. D. H. Reactive Polyanions Based on Poly(4,4-dimethyl-2-vinyl-2-oxazoline-5-one-co-methacrylic acid). *Macromolecules* **2011,** *44* (18), 7115.

(30) Gardner, C. M.; Brown, C. E.; Stöver, H. D. H. Synthesis and properties of water-soluble azlactone copolymers. *Journal of Polymer Science Part A: Polymer Chemistry* **2012,** *50* (22), 4674.

(31) Mulet, X.; Boyd, B. J.; Drummond, C. J. Advances in drug delivery and medical imaging using colloidal lyotropic liquid crystalline dispersions. *Journal of Colloid and Interface Science* **2013,** *393*, 1.

(32) Zabara, A.; Mezzenga, R. Controlling molecular transport and sustained drug release in lipid-based liquid crystalline mesophases. *Journal of Controlled Release* **2014,** *188*, 31.

(33) Liu, G.; Conn, C. E.; Drummond, C. J. Lanthanide Oleates: Chelation, Self-assembly, and Exemplification of Ordered Nanostructured Colloidal Contrast Agents for Medical Imaging. *The Journal of Physical Chemistry B* **2009,** *113* (49), 15949.

(34) Liu, G.; Conn, C. E.; Waddington, L. J.; Mudie, S. T.; Drummond, C. J. Colloidal Amphiphile Self-Assembly Particles Composed of Gadolinium Oleate and Myverol: Evaluation as Contrast Agents for Magnetic Resonance Imaging. *Langmuir* **2010,** *26* (4), 2383.

(35) Moghaddam, M. J.; de Campo, L.; Waddington, L. J.; Weerawardena, A.; Kirby, N.; Drummond, C. J. Chelating oleyl-EDTA amphiphiles: self-assembly, colloidal particles, complexation with paramagnetic metal ions and promise as magnetic resonance imaging contrast agents. *Soft Matter* **2011,** *7* (22), 10994.

(36) Muir, B. W.; Acharya, D. P.; Kennedy, D. F.; Mulet, X.; Evans, R. A.; Pereira, S. M.; Wark, K. L.; Boyd, B. J.; Nguyen, T.-H.; Hinton, T. M.et al. Metal-free and MRI visible theranostic lyotropic liquid crystal nitroxide-based nanoparticles. *Biomaterials* **2012,** *33* (9), 2723.